Vaccine development and deep immune profiling in preclinical models of emerging outbreak viral pathogens



Jyothi Naidu Purushotham

Green Templeton College

University of Oxford

Thesis submitted for the degree of
Doctor of Philosophy

Hilary Term 2022

Word count: Approximately 50,000 (excluding figure legends, tables, references, and appendices)

Vaccine development and deep immune profiling in preclinical models of emerging outbreak viral pathogens

Jyothi Naidu Purushotham, Green Templeton College, University of Oxford

Thesis submitted for the degree of Doctor of Philosophy, Hilary Term 2022

Abstract

Emerging outbreak viral pathogens pose a significant threat to public health. Essential studies on the pathogenesis of and preventive tools for infectious threats often rely upon preclinical models to inform or supplant evaluations in humans. This thesis features studies characterising the immune responses after vaccination and infection in animal models, ranging from rodents to non-human primates, with a focus on two viral pathogens of epidemic/pandemic potential: Lassa virus (LASV) and severe acute respiratory syndrome coronavirus-2 (SARS-CoV-2).

LASV is endemic to regions in West Africa and circulates in rodent populations. Upon transmission to humans, LASV infection may cause an acute febrile illness called Lassa fever. Within the last several years, outbreaks of Lassa fever—associated with increased disease severity and mortality—have been reported in regions of endemicity. In the first half of this thesis, I present my work on the development and evaluation of a ChAdOx1-vectored vaccine for the prevention of Lassa fever, ChAdOx1-Lassa-GPC. The testing of this vaccine began with immunogenicity studies in mice and progressed to efficacy evaluations in guinea pig and non-human primate challenge models of LASV infection. Collectively, the results from these studies indicate that ChAdOx1-Lassa-GPC elicits strong, polyfunctional Th1 and cytotoxic T-cell responses targeting the viral surface glycoprotein. Although antibody titres are high, they are non-neutralising, and exhibit the capacity to elicit a variety of Fc-driven effector functions. Importantly, immunisation

with ChAdOx1-Lassa-GPC protected guinea pigs and non-human primates from direct challenge with a lethal dose of LASV and significantly reduced viral load in tissues.

SARS-CoV-2 emerged in Wuhan, China in late 2019 and has resulted in an on-going pandemic of a (primarily) respiratory disease, known as coronavirus disease-19 (COVID-19). Applying skills and techniques developed during prior studies on LASV, I subsequently shifted the focus of my thesis work to contribute to research efforts for SARS-CoV-2. Consequently, the second half of this thesis describes the immunological assessment of a COVID-19 vaccine, ChAdOx1 nCoV-19/AD1222 in rhesus macaques, first after intramuscular delivery and next after intranasal delivery. Results demonstrated the robust induction of humoral responses after vaccination, via both routes, and significant reductions in lower respiratory tract viral load and inflammation, which could be detected on a cellular level. Finally, a more detailed investigation of SARS-CoV-2 pathogenesis in rhesus macaques was carried out to profile age-related immune dynamics after infection in older versus younger animals. Overall, through the employment of various animal models, the data presented in this thesis have contributed to the advancement of two vaccine candidates to late stages of development and added to current understanding of host responses to infection.

Acknowledgements

First and foremost, I express deep gratitude towards my advisors, Professor Dame Sarah Gilbert, Professor Teresa Lambe, and Dr. Vincent Munster. I am so thankful for the opportunity to benefit from your mentorship and for your patience, support, and encouragement throughout the DPhil. Your commitment to the pursuit of science and the betterment of global health has inspired me and been formative in shaping my career goals. Next, I would like to thank Dr. Emmie de Wit and Dr. Emily Speranza, for exposing me to new scientific approaches, for instilling confidence in me, and for encouraging me in my academic/professional pursuits.

It would not have been possible for me to complete my thesis research without the support of Dr. Neeltje van Doremalen and Dr. Robert Fischer, who led the animal studies taking place in maximum containment. I am so appreciative for the opportunity to collaborate with and learn from you. I am also indebted to Aaron Carmody, Jonathan Schulz, and the members of the Rocky Mountain Veterinary Branch for their tremendous contributions to the animal studies featured in this thesis. Completion of my DPhil research would not have been possible without their essential help in executing experiments under maximum containment conditions.

I have had the privilege of conducting my research at the University of Oxford and at the NIH Rocky Mountain Laboratories. I am appreciative to have worked with and learned from the members of The Jenner Institute and the Laboratory of Virology at the NIH. Finally, thanks to the NIH Oxford-Cambridge Scholars Programme, International Biomedical Alliance, and the NIH Intramural Research Programme for enabling this research.

I am grateful that my DPhil experience has given me the opportunity to build a network of lifelong friendships across multiple countries. Thank you to Hannah Sharpe, Victoria Avanzato, Julia Port,

Robert Ragotte, Ciaran Gilbride, Rachel Wittenberg, Kwe Claude Yinda, and Myndi Holbrook for your love, kindness, scientific help, and emotional support over the years. Lastly, I am eternally grateful to my wonderful family—my parents and my sister—for their unconditional love, immense patience, unwavering support, incredible generosity, and continued confidence in me.

Table of Contents

Abstract……ii
Acknowledgements……iv
Table of Contents……vi
List of Figures……x
List of Tables……xiii
List of Abbreviations……xiv
Statement of Authorship……xviii
1. Introduction…… 1
1.1. Vaccine-mediated immunity and ChAdOx1…… 1
1.1.1. Cellular immunity …… 1
1.1.2. Humoral immunity……6
1.1.3. Immune correlates of protection…… 10
1.1.4. ChAdOx1……13
1.2. Lassa virus……15
1.2.1. Epidemiology……15
1.2.2. Clinical disease…… 17
1.2.3. Virology……19
1.2.4. Genetic diversity……20
1.2.5. Immunobiology of infection……22
1.2.6. Animal models of infection……24
1.2.7. Vaccines……27
1.3. Severe acute respiratory syndrome coronavirus-2……32
1.3.1. Epidemiology……32
1.3.2. Virology…… 33
1.3.3. Clinical disease…… 36
1.3.4. Immunobiology of infection…… 38
1.3.5. Vaccines……41
1.3.6. Variants of concern……46
1.3.7. Animal models of infection……51
1.4. Thesis aims and outline……54
1.4.1. Aims……54
1.4.2. Outline……55
2. Materials and methods…… 56
2.1. Materials……56
2.1.1. Reagents……56
2.1.2. Vaccines…… 59
2.1.2.1. ChAdOx1-Lassa-GPC……59
2.1.2.2. ChAdOx1 nCoV-19…… 60
2.1.3. Viruses…… 60
2.1.4. VSV-Lassa-GPc-cFLAG and VSV-SARS-CoV-2-S pseudotyped viruses……61
2.1.5. Cells…… 62
2.2. Methods – Animal experiments……62
2.2.1. Ethics……62

2.2.2. Biosafety…….. 63
2.2.3. Murine immunogenicity experiments…… 63
2.2.4. Efficacy of ChAdOx1-Lassa-GPC in Hartley guinea pigs…….63
2.2.5. Efficacy of ChAdOx1-Lassa-GPC in cynomolgus macaques……64
2.2.6. Efficacy of ChAdOx1 nCoV-19 (IM and IN) in rhesus macaques……65
2.2.6.1. IM delivery of ChAdOx1 nCoV-19……...65
2.2.6.2. IN delivery of ChAdOx1 nCoV-19……...66
2.2.7. SARS-CoV-2 infection of older and younger rhesus macaques……67
2.3. Methods – Immunology……....68
2.3.1. Cell sample processing……...68
2.3.1.1. Murine splenocytes……... 68
2.3.1.2. Non-human primate cell samples……...68
2.3.2. IgG ELISA……69
2.3.2.1. LASV IgG ELISA……..69
2.3.2.2. SARS-CoV-2 anti-S IgG ELISA……70
2.3.3. ELISpot assays……...70
2.3.3.1. Murine IFNγ ELISpot……70
2.3.3.2. NHP IFNγ and TNFα ELISpot……...71
2.3.3.3. NHP IgG B-cell ELISpot assay……..71
2.3.4. Intracellular cytokine staining (ICS) assays……...72
2.3.4.1. Murine ICS assay……...…72
2.3.4.2. NHP ICS assays…….……73
2.3.5. Activation-induced marker (AIM) assays……. 75
2.3.6. Immunophenotyping of T cells and innate cells in NHPs……..76
2.3.7. Antigen biotinylation…… ……78
2.3.8. B-cell phenotyping and SARS-CoV-2-specific B-cell staining……..78
2.3.9. Assessment of antibody-mediated effector functions……79
2.3.9.1. ADCD……....79
2.3.9.2. ADMP…….…… 80
2.3.9.3. ADNP…….……..……..80
2.3.9.4. ADNKA…….…… 81
2.3.10. Live virus neutralisation assays…….……82
2.3.10.1. LASV…….…….. 82
2.3.10.2. SARS-CoV-2……. ……83
2.3.11. VSV-based pseudotype neutralisation assays……... 83
2.3.11.1. Neutralisation of VSV-Lassa-GPc-cFLAG……... 83
2.3.11.2. Neutralisation of VSV-SARS-CoV-2 S……... 84
2.3.12. Multiplex analyte detection assays…….……..…. 84
2.3.12.1. MESO Scale Discovery Assays…… 84
2.3.12.2. MILLIPLEX Map 23-plex Kit……... 85
2.3.13. Transcriptomics……86
2.3.13.1. Bulk RNA sequencing in LASV-challenged cynomolgus macaques…….86
2.3.13.2. Single-cell RNA sequencing in SARS-CoV-2-infected rhesus macaques……88
2.3.14. Lipidomics…… 90
2.3.15. Multiplex IHC (mIHC)… ……91

2.4. Methods – Virology……..93
2.4.1. Real-time quantitative reverse-transcriptase PCR (qRT-PCR)……..93
2.4.1.1. LASV…..……93
2.4.1.2. SARS-CoV-2…..…… 94
2.4.2. Infectious virus titration assays…… 95
2.4.2.1. LASV……95
2.4.2.2. SARS-CoV-2…….…… 95
2.4.3. Histopathological evaluation of LASV-challenged animals…… 95
2.4.3.1. *In situ* hybridization of guinea pig tissues…… 95
2.4.3.2. IHC of cynomolgus macaque tissues……96
2.5. Methods – Data analysis and statistics……..96
2.5.1. Multivariate or high-dimensional data analyses……96
2.5.2. Testing for statistical significance……..97
3. Development of a ChAdOx1-vectored vaccine for LASV and testing in small animal models……..99
3.1. Introduction……...99
3.1.1. Authorship statement…….. .101
3.2. Results……102
3.2.1. Immunogenicity of ChAdOx1-Lassa-GPC in CD-1 mice……... 102
3.2.2. Antibody responses to ChAdOx1-Lassa-GPC in Hartley guinea pigs…… 107
3.2.3. Lethal LASV challenge in immunised Hartley guinea pigs……110
3.2.4. Cross-variant reactivity of vaccine-induced adaptive immune responses……120
3.3. Discussion……...121
4. Efficacy evaluation of ChAdOx1-Lassa-GPC in cynomolgus macaques……126
4.1. Introduction……126
4.1.1. Authorship statement……... 128
4.1.2. COVID-19 statement……..… 128
4.2. Results…….....129
4.2.1. Overview of animal experiment and outcome of hearing tests……129
4.2.2. Antigen-specific T-cell responses induced after vaccination……130
4.2.3. Antibody responses elicited by ChAdOx1-Lassa-GPC……136
4.2.4. Clinical and immunological outcomes of LASV challenge……140
4.2.5. Virological outcomes after LASV challenge……147
4.3. Discussion……...151
5. Immune profiling in rhesus macaques vaccinated with ChAdOx1 nCoV-19 and challenged with SARS-CoV-2……..157
5.1. Introduction……157
5.1.1. Authorship statement…..…… ……. 159
5.2. Results……160
5.2.1. IM ChAdOx1 nCoV-19 induces spike-specific T-cell responses……160
5.2.2. Circulating humoral responses induced by IM ChAdOx1 nCoV-19……...165
5.2.3. Local innate and cellular immunophenotypes on 3 and 5 DPC……170
5.2.4. Transcriptional shifts and cellular phenotypes within the lungs……..176
5.2.5. Systemic T-cell phenotypes at 7 DPC……..179
5.2.6. Systemic B-cell phenotypes at 7 DPC……..182
5.2.7. Humoral immunogenicity of IN-administered ChAdOx1 nCoV-19……185

5.2.8. SARS-CoV-2 challenge of IN-immunised ChAdOx1 nCoV-19 vaccinees…….189
5.3. Discussion……...193
6. Multi-omics evaluation of the age-related effects of SARS-CoV-2 infection in rhesus macaques……...198
6.1. Introduction…….……...198
6.1.1. Authorship statement…….…….. 201
6.2. Results…… 201
6.2.1. Baseline characterization of rhesus macaque cohorts…….. 201
6.2.2. Clinical and virological outcomes after SARS-CoV-2 infection……..…206
6.2.3. Local immune dynamics during acute SARS-CoV-2 infection……...208
6.2.4. Phenotypic analysis of lung T cells at 7 DPI…….213
6.2.5. Comparison of lung T-cell phenotypes and lymphoid tissue at 21 DPI……218
6.2.6. Systemic immune responses after infection……..224
6.2.7. Age-related differences in the resolution of systemic inflammation……227
6.3. Discussion…..…… 232
7. Discussion……..… 238
7.1. Overview…….…….. 238
7.2. Principal findings, limitations, and future work……. 239
7.2.1. Development of a ChAdOx1-vectored vaccine for LASV…….. 239
7.2.2. Assessment of a vaccine against and host responses to SARS-CoV-2……242
7.3. Concluding remarks……244
References……...246
Appendix……283

List of Figures

Figure 1-1. $CD4^+$ and $CD8^+$ T-cell effectors……5
Figure 1-2. Antibody structure, isotypes, and functions……..7
Figure 1-3. Geographic distribution of LASV……16
Figure 1-4. Structure of LASV and its surface GP……20
Figure 1-5. Phylogenetic lineages of LASV and their geographic localisation……22
Figure 1-6. Components of the SARS-CoV-2 virion, genome, and spike (S) protein……35
Figure 1-7. COVID-19 vaccines in use and under development……42
Figure 1-8. SARS-CoV-2 S mutations in VOCs…….....46
Figure 3-1. ChAdOx1-Lassa-GPC vaccination elicits cellular and humoral immune responses in CD-1 mice……....103
Figure 3-2. LASV-specific T-cell responses are polyfunctional……...105
Figure 3-3. LASV-specific T cells exhibit an effector phenotype 21 days post immunisation…107
Figure 3-4. Administration of ChAdOx1-Lassa-GPC in Hartley guinea pigs……..108
Figure 3-5. Antibodies elicited by ChAdOx1-Lassa-GPC vaccination are non-neutralising……109
Figure 3-6. ChAdOx1-Lassa-GPC-vaccinated guinea pigs are protected against lethal LASV challenge……..111
Figure 3-7. Viral load is significantly lower in the tissues and sera of ChAdOx1-Lassa-GPC vaccinees compared to controls……114
Figure 3-8. Replicating LASV is not detectable in tissues of ChAdOx1-Lassa-GPC-vaccinated animals by *in situ* hybridisation……116
Figure 3-9. Reductions in viral load measured in the tissues of vaccinated animals at the study endpoint……117
Figure 3-10. Vaccine-specific T cells and IgG antibodies exhibit cross-reactivity to antigen from heterologous LASV strains……..120
Figure 4-1. Efficacy of ChAdOx1-Lassa-GPC against LASV infection in cynomolgus macaques……..130
Figure 4-2. IFNγ ELISpot responses induced by ChAdOx1-Lassa-GPC vaccination……131
Figure 4-3. Functional assessment of LASV-specific T-cell responses……135
Figure 4-4. Characterisation of the vaccine-induced humoral response……139
Figure 4-5. Clinical disease signs after LASV challenge……141
Figure 4-6. Comparison of haematological profiles, serum chemistry, and cytokine milieu after LASV infection……143
Figure 4-7. Differential gene expression profiles in PBMC samples at 6 DPC……145

Figure 4-8. Comparison of cellular and immunological pathways affected by LASV challenge..146
Figure 4-9. Detection of LASV RNA in serum and tissues……...149
Figure 4-10. Immunohistochemistry of LASV-infected tissues……...150
Figure 5-1. Intramuscular vaccination-and-challenge study design and timeline……160
Figure 5-2. Spike protein-specific T-cell responses elicited by ChAdOx1 nCoV-19 vaccination……...164
Figure 5-3. Characterisation of serum antibody responses induced by ChAdOx1 nCoV-19 vaccination……...168
Figure 5-4. Characterisation of the ChAdOx1 nCoV-19-induced B cell response in circulation..170
Figure 5-5. Respiratory tract viral load and responses to SARS-CoV-2 challenge in BALF……173
Figure 5-6. Macrophage and T-cell phenotypes in BAL cell samples at 3 and 5 DPC……175
Figure 5-7. Lung T-cell phenotypes and cellular transcriptional profiles at 7 DPC……177
Figure 5-8. Lung macrophage/monocyte clusters and inflammatory signalling……..179
Figure 5-9. Comparison of systemic T-cell phenotypes at 7 DPC……181
Figure 5-10. Phenotypic and functional profiling of B cells after SARS-CoV-2 challenge…….184
Figure 5-11. Intranasal vaccination-and-challenge study design and timeline. ……..…185
Figure 5-12. Humoral responses induced by ChAdOx1 nCoV-19 vaccinees……..187
Figure 5-13. Characterisation of antibody functionality in 56 DPV serum……..189
Figure 5-14. Detection of SARS-CoV-2 in respiratory tract samples post challenge……..190
Figure 5-15. Characterising the relationship between the humoral response and outcomes post challenge……..192
Figure 6-1. SARS-CoV-2 inoculation and time-resolved sampling in older and younger rhesus macaques……..202
Figure 6-2. Baseline assessment of older and younger rhesus macaques……203
Figure 6-3. Comparison of baseline immunological parameters in older and younger rhesus macaques……..205
Figure 6-4. Comparison of clinical outcomes after SARS-CoV-2 inoculation……206
Figure 6-5. Comparison of shedding and viral load dynamics after SARS-CoV-2 inoculation...208
Figure 6-6. Single-cell RNA sequencing of BALF shows evidence of sustained inflammation associated with age……...…211
Figure 6-7. Elevated frequencies of dividing T cells in BALF of the younger animals compared to the older animals……..213
Figure 6-8. Age-related divergence in T-cell phenotypes in the lungs at 7 DPI……..215
Figure 6-9. Age-associated differences in the expression and frequency of T-cell markers of effector function……...218

Figure 6-10. Phenotypic analysis at 21 DPI reveals a potential age-related delay in local T-cell responses……..220

Figure 6-11. Comparison of the expression and frequency of T-cell markers associated with effector or memory function at 21 DPI……222

Figure 6-12. Advanced BALT structures in the lungs of the younger animals at 21 DPI detected by mIHC……...224

Figure 6-13. Comparison of circulating T-cell dynamics over the course of infection……...226

Figure 6-14. Higher frequencies of SARS-CoV-2-specific T cells in the younger animals at 21 DPI……..……..227

Figure 6-15. Circulating cytokines provide evidence of prolonged inflammation in the older animals…….228

Figure 6-16. LM profiles reveal an age-related delay in the return to homeostasis after infection……...231

Figure 6-17. Summary of the immune dynamics in younger and older rhesus macaques during SARS-CoV-2 infection……233

List of Tables

Table 1-1. LASV vaccine candidates under development……..30
Table 1-2. COVID-19 vaccines in currently in use……45
Table 1-3. SARS-CoV-2 variants of concern……50
Table 1-4. Animal models of experimental SARS-CoV-2 infection……..52
Table 2-1. Commercially available reagents……..56
Table 2-2. SARS-CoV-2 strain information……...60
Table 2-3. LASV strain information……...61
Table 2-4. Murine ICS panel for the characterisation of LASV GPC-specific T-cell responses…73
Table 2-5. NHP ICS panel for the characterisation of antigen-specific T-cell responses……..74
Table 2-6. AIM panel for the characterisation of SARS-CoV-2 S-specific T-cell responses……76
Table 2-7. T-cell phenotyping panel……...77
Table 2-8. Innate-cell phenotyping panel for BAL cells……77
Table 2-9. B-cell phenotyping panel……...79
Table 2-10. ADNP staining panel……...81
Table 2-11. ADNKA staining panel……...82
Table 2-12. Analytes and sample dilutions for MESO Scale Discovery assays……85
Table 2-13. mIHC primary antibody list……92
Table 2-14. LASV qRT-PCR primer and probe sequences……94
Table 2-15. SARS-CoV-2 qRT-PCR primer and probe sequences……94
Table 3-1. LASV RNA detected by qRT-PCR in lung, liver, spleen, and sera at 12 DPC…….....113
Table 3-2. LASV RNA detected by qRT-PCR in lung, liver, spleen, and sera at 28 DPC…….117
Table 5-1. AIM assay frequencies and pair-wise statistical comparisons……163
Table 5-2. BALF chemokine concentration statistical comparisons……172
Table 5-3. Vaccine-specific antibody responses in circulation, the upper and lower respiratory tract…….. 186

List of Abbreviations

ACE2	angiotensin-converting enzyme 2
ADCD	antibody-dependent complement deposition
ADCP	antibody-dependent cellular phagocytosis
ADE	antibody-dependent enhancement
ADMP	antibody-dependent monocyte phagocytosis
ADNP	antibody-dependent neutrophil phagocytosis
ADNKA	antibody-dependent NK-cell activation
AF	Alexa Fluor
AIM	activation-induced markers
ALP	alkaline phosphatase
APC	antigen-presenting cell
ARDS	acute respiratory distress syndrome
ASC	antibody-secreting cell
ASM	activated switched memory
ASP	animal study protocol
AUC	area under the curve
BAC	bacterial artificial chromosome
BAER	brainstem auditory evoked response
BAL	bronchoalveolar lavage
BALF	bronchoalveolar lavage fluid
BALT	bronchus associated lymphoid tissue
BCR	B cell receptor
BCS	body condition scores
BGH	bovine growth hormone
BSA	bovine serum albumin
BSL	biosafety level
BUV	brilliant ultraviolet
BV	brilliant violet
CCR	C-C motif chemokine receptor
CD	cluster of differentiation
CDC	Centers for Disease Control
CDR	complementarity-determining regions
CEPI	Coalition for Epidemic Preparedness Innovations
CoV	coronavirus
COVID-19	coronavirus disease 2019
COG-UK	COVID-19 Genomics UK Consortium
CTD	C-terminal domain
CTL	cytotoxic T lymphocyte
CTLA-4	cytotoxic T lymphocyte-associated protein 4
CXCR	CXC-chemokine receptor

Cy	cyanine
DAPI	4',6-diamidino-2-phenylindole
DC	dendritic cell
DMEM	Dulbecco's modified eagle medium
DPBS	Dulbecco's phosphate buffered saline
DPC	days post challenge
DPI	days post inoculation
DPV	days post vaccination
EEG	electroencephalography
ELISA	enzyme-linked immunosorbent assay
ELISpot assay	enzyme-linked immunospot assay
EUA	emergency use authorisation
Fab	fragment antigen binding
FBS	foetal bovine serum
Fc	fragment crystallisable
FcR	Fc receptor
FDA	Food and Drug Administration
FFU	focus forming units
FITC	fluorescein isothiocyanate
FOXP3	forkhead box protein 3
FPKM	fragment per kilobase of transcript per million mapped reads
GC	germinal centre
GM-CSF	granulocyte-macrophage colony-stimulating factor
GP	glycoprotein
GPA	guinea pig adapted
GPC	glycoprotein precursor
gRNA	genomic RNA
H	heavy (immunoglobulin chain)
HE	haematoxylin and eosin
HLA	human leukocyte antigen
IBC	institutional biosafety committee
IC_{50}	half-maximal inhibitory concentration
ICS	intracellular cytokine staining
IE CMV	human cytomegalovirus immediate early promoter
IFN	interferon
Ig	immunoglobulin
IHC	immunohistochemistry
IL	interleukin
IM	intramuscular
IN	intranasal
IP	intraperitoneal
ISH	*in situ* hybridisation

IT	intratracheal
IP-10	interferon γ-induced protein 10
IQR	interquartile range
IU	infectious units
JAK	janus kinase
L	light (immunoglobulin chain)
LASV	Lassa virus
LC-MS/MS	liquid chromatography with tandem mass spectrometry
LCMV	lymphocytic choriomeningitis virus
LD_{50}	median lethal dose
LLD	lower limit of detection
LLPC	long-lived plasma cell
LM	lipid mediator
mAb	monoclonal antibody
MCP	monocyte chemoattractant protein
MDC	macrophage-derived chemokine
MERS	Middle East Respiratory Syndrome
MHC	major histocompatibility complex
mIHC	multiplex immunohistochemistry
MIP	macrophage inflammatory protein
MV	measles virus
MVA	modified vaccinia virus Ankara
ORF	open reading frame
NHP	non-human primate
NIAID	National Institute of Allergy and Infectious Disease
NIH	National Institutes of Health
NK	natural killer
NP	nucleoprotein
NTD	N-terminal domain
PAMP	pathogen-associated molecular patterns
$PaO_2/FiO2$	ratio of arterial oxygen partial pressure to fraction of inspired oxygen
PBMC	peripheral blood mononuclear cell
PBS	phosphate buffered saline
PCA	principal component analysis
PE	phycoerythrin
PerCP	peridinin-chlorophyll-protein
PFA	paraformaldehyde
PFU	plaque forming units
PMA	phorbol myristate acetate
*p*NPP	*p*-nitrophenyl phosphate
PRR	pattern-recognition receptors
RABV	rabies virus
RBC	red blood cell

RBD	receptor binding domain
RBM	receptor binding motif
RMVB	Rocky Mountain Veterinary Branch
RML	Rocky Mountain Laboratories
RSM	resting switched memory
RSV	respiratory syncytial virus
RTB	Research Technologies Branch
S	spike protein
SA	streptavidin
SARS	Severe Acute Respiratory Syndrome
scRNAseq	single-cell RNA sequencing
SD	standard deviation
SEM	standard error of the mean
SFU	spot forming units
sgRNA	subgenomic RNA
SM	switched memory
αSMA	α-smooth muscle actin
SNP	single-nucleotide polymorphism
SPICE	simplified presentation of incredibly complex evaluations
SpO_2	oxygen saturation
$TCID_{50}$	median tissue culture infectious dose
TCR	T cell receptor
T_{CM}	central memory T cell
T_E	effector T cell
T_{EM}	effector memory T cell
T_{EEM}	effector or effector memory T cell
TetO	tetracycline operator
T_{fh}	T follicular helper cell
Th	helper T cell
TLR	Toll-like receptors
TLSM	tissue-like switched memory
TMPRSS2	transmembrane serine protease 2
TNF	tumour necrosis factor
USAMRIID	United States Army Medical Research Institute of Infectious Diseases
USM	unswitched memory
VEGF	vascular endothelial growth factor
VOC	variants of concern
VOI	variants of interest
VP	virus particles
VSV	vesicular stomatitis virus
VVCF	Viral Vector Core Facility
WHO	World Health Organization
YFV	yellow fever virus

Statement of Authorship

This thesis includes studies taking place under biosafety level 4 (BSL4) containment conditions at the Laboratory of Virology, Rocky Mountain Laboratories (RML), National Institute of Allergy and Infectious Diseases (NIAID), National Institutes of Health (NIH). Due to the nature of the work, many team members were involved in the production of data for these studies. Animal procedures, clinical monitoring, necropsies, and histopathological evaluations were conducted by the Rocky Mountain Veterinary Branch (RMVB), specifically Dr. Patrick Hanley, Dr. Dana Scott, Dr. Greg Saturday, Dr. Carl Shaia, and Friederike Feldmann. Dr. Neeltje van Doremalen and Dr. Robert Fischer were the Principal Investigators listed on the Animal Study Protocols (ASPs) associated with these studies. To complete experiments in BSL4, I developed protocols for BSL4-certified colleagues to execute and I would prepare all reagents or materials required for the procedures. In general, PBMC isolation and the generation of single-cell suspensions from tissues (taking place in BSL4) were performed by Jonathan Schulz. Cell thawing, plating, and extracellular staining (inside BSL4) was carried out by Aaron Carmody prior to inactivation and transfer to BSL2 where I would finish staining for intracellular markers and perform data acquisition on the cytometer. Inactivation of samples in TRIzol reagent, AVL buffer, formalin, or paraformaldehyde prior to remove from BSL4 was performed by Dr. Elaine Haddock. Single-cell and bulk RNA sequencing was carried out by the RML Research Technologies Branch (RTB) Genomics Core Facility, along with the preliminary analysis required to generate normalised gene count data. Lipidomics detection by liquid chromatography tandem mass spectrometry was conducted by Dr. Benjamin Schwarz. Finally, multiplex immunohistochemistry was performed on lung tissue sections by Dr. Carl Shaia and Dr. Emily Speranza. All other experimental work taking

place in BSL2 or BSL3 was performed by me, unless stated otherwise in the relevant methods or results sections.

I led the planning of analyses to be performed and integration of resulting data for the studies included in this thesis; collaborative efforts with others are indicated in the relevant results sections. Specifically, Dr. Emily Speranza directed the downstream assessment of all single-cell RNA sequencing and multiplex IHC data. She coached me through the appropriate techniques and pipelines for computational analysis given that these studies represented my first experience with transcriptomics data. Lipidomics data were independently analysed by Dr. Benjamin Schwarz, who kindly provided me with the individual and summed lipid signals, which I then visualised graphically and assessed via principal component analysis.

Finally, this thesis includes content that has been previously published. Appendix 1 contains a list of published papers that I have authored or co-authored over the course of my DPhil. These include research and review articles. Any content included in this thesis that was derived from these publications reflects data or writing that was originally my own. As mentioned above, data or methods produced by others have been attributed throughout the thesis. Results sections containing data from published papers include the corresponding reference within the chapter-specific authorship statement. I have received written approval from all co-authors and my supervisors to include content from these previously published works in my thesis.

1

Introduction

1.1 Vaccine-mediated immunity and ChAdOx1

Vaccines exploit the ability of the highly evolved mammalian immune system to respond to and recall encounters with specific pathogens. Also known as adaptive immunity, these specialized responses are facilitated by an expansive repertoire of somatically recombined receptors, which are collectively able to bind and recognise a vast number of unique epitopes (i.e., regions of pathogens' antigens)[1]. Vaccines are designed to mimic primary exposure to the target pathogen with the aim of generating immunological memory, which will mount rapid and robust responses upon secondary encounter. There are two mechanisms of acquired immunity—humoral and cellular. Early-stage vaccine development involves the detection and quantitative assessment of humoral and cellular immune responses generated against the target immunogen. Evaluation often encompasses the initial effector response as well as memory responses[1]. These investigations often begin in animal models and may eventually lead to testing in humans.

1.1.1 Cellular immunity

Cell-mediated immunity constitutes an important defence against intracellular pathogens and is governed by the activities of T lymphocytes. The T-cell receptor (TCR) is a member of the

immunoglobulin (Ig) superfamily and consists of a heterodimer of α and β chains or, less frequently, of γ and δ chains (0.5-5% of all T cells)[2]. Each of these chains contains a variable region and a constant region. The variable region of each chain contains three complementarity-determining regions (CDRs) which are responsible for antigen recognition. TCR diversity is generated by somatic recombination of variable (V), diversity (D), and joining (J) gene segments[3].

T cells complete their development in the thymus[2]. Naïve T cells are fully mature and migrate continuously between secondary lymphoid tissues, blood, and lymph. Upon encounter with cognate antigen, naïve T cells undergo proliferation and differentiation into effector T cells capable of contributing to the removal of infected cells displaying antigen[2]. Antigen recognition by naïve T cells primarily occurs in the T-cell zones of secondary lymphoid tissues. Specialized antigen-presenting cells (APC), primarily immature dendritic cell (DC) precursors, are highly efficient at ingesting and processing native proteins into peptides[4]. These cells are scattered throughout the body and phagocytise antigens. They then migrate into secondary lymphoid tissues, differentiate into partly mature DCs, and localise in T-cell zones while simultaneously degrading the antigen into immunogenic peptides that are displayed on major histocompatibility complex (MHC) molecules at the cell surface[5-8]. Macrophages and B cells may also serve as APCs[2].

Subsequently, T cells with a compatible TCR bind with the foreign peptide/MHC complexes on these cells, forming tight synapses, and trapping T cells within the T-cell zone. After T-cell trapping occurs, there is continuous recruitment of newly arriving naïve T cells to the immune response, potentially mediated by chemokines released by the influx of activated antigen-laden APCs[9-11]. The formation of the immunological synapse is associated with rapid clustering of TCR/CD3 complexes binding to peptide/MHC complexes. The CD4 and CD8 co-receptors play a role in TCR/CD3 triggering, along with a collection of costimulatory/adhesion molecules[9-11].

These molecules, which include CD28, LFA-1, CD40L, ICOS, OX40, CD2, CD27, and CD137 expressed on T cells, bind to complementary molecules on APCs. Together, they aid in T-cell activation, synapse stabilisation, and recruitment of intracellular signalling molecules[12]. The local accumulation of intracellular signalling molecules initiates downstream proliferation, cytokine synthesis, and effector-cell differentiation[13-15]. The resulting principal effectors of cellular immune responses are $CD4^+$ helper T (Th) cells and cytotoxic T lymphocytes (CTLs, or $CD8^+$ T cells).

$CD4^+$ Th cells recognise cognate antigen presented by MHC class II (MHC-II) molecules and subsequently undergo clonal expansion and differentiation into effector subtypes, while a few develop into memory T cells (Figure 1-1). Subtype or lineage differentiation of Th effectors is heavily influenced by a milieu of cytokines, transcription factors, and costimulatory/adhesion molecules[16,17]. Th1-cell polarisation is driven by IL-12 secretion by APCs and expression of the transcription factor T-bet. Th1 cells secrete pro-inflammatory cytokines, including IFNγ, TNFα, and IL-2, and contribute to the elimination of intracellular pathogens[16,17] (Figure 1-1). Th2 cells, defined by the expression of transcription factor GATA3 and production of IL-4, IL-5, and IL-13 assist B-cell responses, promoting the secretion of IgG, IgM, and IgA[16,17]. Th17 differentiation is mediated by the transcription factor RORγt; these cells produce IL-17 and IL-21 and exhibit multiple functional roles including in the maintenance of mucosal immunity and innate cell recruitment[18]. The regulatory subset, Treg, expresses FOXP3, regulates inflammatory responses, and inhibits self-reactive Th cells[19] (Figure 1-1). T follicular helper cells (T_{fh}) cells secrete IL-21 and support B-cell differentiation within germinal centre (GC) reactions[20]. Finally, Th9 and Th22 cells, which produce IL-9 and IL-22, respectively, are less well studied and likely have multiple roles that are still under investigation[21,22].

CTLs respond to endogenous antigenic peptides presented by APCs on MHC class I (MHC-I) molecules (Figure 1-1). Most $CD8^+$ T-cell activation requires assistance from $CD4^+$ T cells for optimal stimulation, although CD4-independent activation may also be triggered by certain pathogens[23]. Once activated, $CD8^+$ T cells undergo extensive clonal expansion to form a phenotypically and functionally heterogeneous pool of effector cells[24,25]. Activated CTLs may additionally upregulate the inflammatory chemokine receptor CXCR3, aiding their migration into inflamed peripheral tissues during infection[26]. Recognition of an infected target cell (displaying cognate peptide-MHC-I complexes) initiates CTL-mediated cell killing. Cytotoxic granules residing within the cytosol are released at point of contact, enabling specific cell targeting and limited bystander death; the granules contain perforin and granzyme (Figure 1-1). Perforin assembles on target membranes, allowing the delivery of granzymes into the target cell. Granzymes are a group of serine proteases that activate caspases, leading to cell death. CTLs may also induce apoptosis by ligation of the receptor Fas with Fas ligand expressed on infected cells[27]. CTLs specifically play a critical role in antiviral immunity. Within a week of viral infection, naïve $CD8^+$ T cells differentiate into effector cells[28]. Viral antigens are recognised by several pattern recognition receptors on innate immune cells, which leads to the production of type I interferon, which in turn initiates the development of $CD8^+$ T-cell effector responses. IL-12 produced by macrophages and DCs leads to the induction of T-bet, which drives the acquisition of antiviral cytotoxic functions[28]. Other cytokines, such as TNFα, IL-15, and IL-18 further augment the CTL response. Activated $CD8^+$ T cells also produce several cytokines that contribute to host defence, including IFNγ, TNFα, and lymphotoxin-α[29] (Figure 1-1). IFNγ inhibits viral replication while increasing expression of MHC-I, improving the chance that an infected cell will be recognised.

The bulk of the effector $CD4^+$ and $CD8^+$ T cells are short-lived (2-3 weeks) and die by apoptosis after clearance of the infection[2]. A small percentage (5-10%) survive as long-lived memory cells. Broadly, memory T cells are classified according to their degrees of effector function, proliferative capacity, and tissue-homing properties[30-32]. Central memory T cells (T_{CM}), circulate through secondary lymphoid tissues and express lymphoid homing markers (CCR7 and/or CD62L, in humans and mice), tissue-resident memory T cells (T_{RM}) are localised peripherally at the sites of pathogen entry, and effector memory T cells (T_{EM}) are present in circulation and in non-lymphoid tissues ($CCR7^{-/lo}$), serving as the first line of defence against re-infection[30-32].

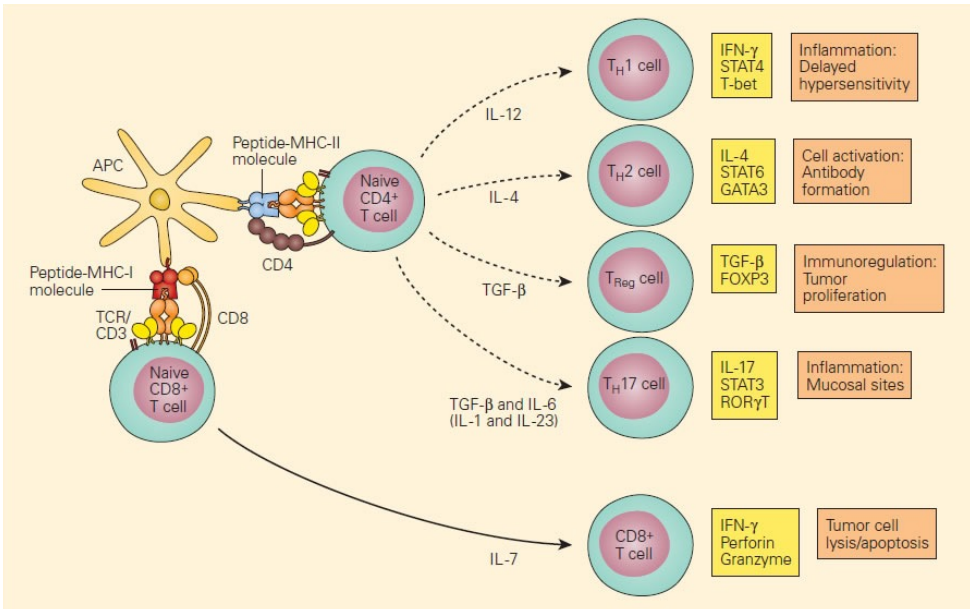


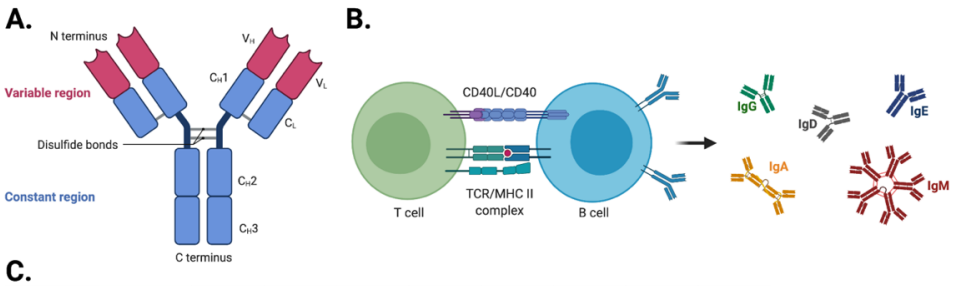
Figure 1-1. $CD4^+$ and $CD8^+$ T-cell effectors. Schematic representation of antigen presentation and activation of $CD4^+$ and $CD8^+$ T cells. Cytokines involved in driving effector T-cell differentiation are indicated. Some key classes of $CD4^+$ Th cells, including Th1, Th2, T_{reg}, and Th17 cells, as well as CTLs are shown. Defining cytokines and/or transcription factors for each effector subset are listed along with core functions. *Image sourced from*[33].

1.1.2 Humoral immunity

Extracellular spaces are protected by the humoral arm of the adaptive immune response, which is defined by the activities of antibodies, produced by B cells. B cells develop in the bone marrow; they undergo further maturation and activation within secondary lymphoid organs[34]. B cell activation begins when cognate antigen binds to the B cell receptor (BCR), and is primarily a T cell-dependent process, although T cell-independent activation is possible[35,36] (Figure 1-2). Antigen binding to the BCR initiates endocytosis, processing, and presentation of the antigen as peptides on MHC-II molecules to $CD4^+$ Th cells, also activated by antigen binding[37]. After TCR-peptide/MHC-II binding, Th cells, particularly T_{fh}, provide essential help to B cells via cytokine production (e.g., IL-4 and IL-21) and the expression of costimulatory molecules (e.g., CD40L and ICOS)[20,35]. B cells thereby undergo proliferation, Ig class-switching, and may differentiate into plasmablasts that secrete antibodies in extrafollicular responses.

Antibody diversity is governed by the BCR. Within BCR Ig loci, combinatorial rearrangement occurs in heavy (H) chain V, D, and J gene segments and light (L) chain V and J gene segments, creating an extensive number of BCR specificities[38-40]. Antibodies are a secreted form of the BCR; they are composed of four chains with two identical heavy chains and two identical light chains (Figure 1-2). These chains are further segmented into variable H or L domains and constant H or L domains. Each antibody comprises functional domains linked by a hinge region[38-41]. The antigen-binding fragment (Fab) confers antigen specificity and is composed of two Ig H chains and two Ig L chains. Fab domains evolve during an immune response, such as to vaccination or infection, to improve affinity to a foreign antigen[38-41]. Meanwhile, the crystallisable fragment (Fc) drives antibody function[42]. A single antibody consists of two Fab domains and one Fc domain; the resulting molecule can exist either as a monomer or form multimers. Fc domains will also undergo

rapid changes during an active immune response via the binding of Fc receptors (FcR) expressed on the surface of certain innate immune effectors aiding in pathogen clearance[42,43]. Variation in the Fc domain has resulted in the classification of antibodies into five isotypes—IgM, IgD, IgG, IgA, and IgE—each with unique structural features that impact antibody function[44-46] (Figure 1-2). Each isotype may be further divided into subclasses (e.g., IgG1, IgG2, IgG3, IgG4, IgA1, and IgA2), which also have distinct properties. Fc domain diversity is generated during an immune response via the selection of different antibody isotypes, subclasses, and post-translational glycosylation profiles[46]. Together, changes in isotype, subclass, and glycosylation influence the capacity of an antibody to interact with innate immune receptors and leads to key differences in function, persistence, stability, and distribution[46].



C.

Functional activity	IgD	IgE	IgM	IgA	IgG1	IgG2	IgG3	IgG4
Neutralisation	---	---	+	++	++	++	++	++
Opsonisation	---	---	+	+	+++	---	++	+
Sensitisation for killing by NK cells	---	---	---	---	++	---	++	---
Sensitisation of mast cells	---	+++	---	---	+	---	+	---
Activates complement system	---	---	+++	+	++	+	+++	---

--- Does not apply
\+ Applies
++ Strongly applies
+++ Heavily applies

Figure 1-2. Antibody structure, isotypes, and functions. (A) Basic antibody structure featuring variable (V) and constant (C) regions composed of Ig heavy$_{(H)}$ chains and light$_{(L)}$ chains. **(B)** T-cell dependent activation drives B-cell differentiation and antibody production; antibodies are classified into five different isotypes that may be monomeric (IgG, IgD, IgE), dimeric (IgA), or multimeric (IgM). **(C)** Different antibody isotypes and subclasses execute distinct functions (governed by the Fc domain) that initiate innate-immune effector responses. *Image sourced from BioRender; acknowledgements to Dr. Akiko Iwasaki and Dr. Ruslan Medzhitov for provision of content.*

Direct neutralisation of a pathogen or toxin is one mechanism by which antibodies can prevent disease. Interactions between a pathogen/toxin and host cell receptors are interrupted by Fab domain binding to a specific microbial target, which blocks cell entry and infection[47,48]. In addition to direct Fab-mediated neutralisation of infectious agents, antibodies may also induce innate immune effector activities in a Fc-dependent manner, as described above. Certain antibodies, such as pentameric IgM and clusters of highly glycosylated IgG forming hexameric complexes, can recruit and activate complement from blood and tissues[49-51]. The ensuing complement cascade leads to the production of peptide inflammatory mediators, phagocyte recruitment, opsonisation of immune complexes, and culminates in the assembly of the membrane attack complex that will destroy the pathogenic target. This process is known as antibody-dependent complement deposition (or activation) (ADCD)[50,51]. Meanwhile, antibody-dependent cellular cytotoxicity (ADCC) involves cross-linking of antibodies to FcγRIIIa on natural killer (NK) cells, resulting in perforin- and/or granzyme-driven death of the infected target cell[52,53]. Finally, certain antibodies may also trigger opsonophagocytosis, or the clearance of pathogens from circulation by mononuclear phagocytes (monocytes, macrophages, and dendritic cells) or granulocytes (neutrophils, eosinophils, basophils, and mast cells)[53,54]. Antibody-dependent cellular phagocytosis (ADCP) involves the formation of endocytic vesicles around antibody-coated pathogens, the fate of which is determined by the specificities of FcR signalling. Pathogens may be trafficked to lysosomes for degradation and direct antigen processing for presentation to T cells[53,54]. Or, whole antigens may be retained for subsequent transfer to B cells and the further induction of humoral immunity[55]. Phagocytic cells may integrate additional information via cooperative signals between FcRs and other pattern recognition receptors (PRRs), which are found on the surface of various immune cells[56,57]. This collaborative signalling may lead to additional

effector functions, including the release of proteases, defensins, cytokines, reactive oxygen species, and reactive nitrogen species, that together recruit and arm additional innate effector cells[57].

Interestingly, certain pathogens have evolved mechanisms to exploit antibody-mediated FcR pathways leading to the more rapid dissemination of infection and enhanced disease, rather than protection[58]. The classical example of this effect is in the case of viral infections, where primary infection and/or immunisation may result in incomplete protective humoral immunity that augments the subsequent infection of host cells with partially antibody-opsonised viruses. Antibody-dependent enhancement (ADE) of disease has been observed in dengue virus, Zika virus, and West Nile virus infections, as well as after respiratory syncytial virus (RSV) vaccination[59-63].

During an on-going humoral immune response, antibody-secreting plasmablasts are considered a transient population and are precursors of terminally differentiated effector cells[64-66]. Activated B cells may alternatively enter a lymphoid follicle and form a GC response. During GC reactions, B cells undergo class-switching, somatic hypermutation, and differentiation into memory B cells and long-lived plasma cells (LLPCs)[37,67]. LLPCs of high affinity will migrate to the bone marrow, where they can survive for decades and maintain pre-existing antibody levels, offering "constitutive humoral memory" [68,69]. Memory B cells are generated from lower-affinity GC B cells; they are long-lived quiescent cells that circulate between the blood and lymphoid tissues[37,70]. Upon antigen re-encounter, memory B cells mount an anamnestic response, also known as "reactive humoral memory". After an initial vaccination or infection, memory B cells may persist for decades in the absence of antigen[71]. Upon re-exposure to antigen these cells rapidly proliferate

and may either differentiate into antibody-secreting plasmablasts or re-enter a GC reaction to undergo further rounds of affinity maturation, supported by memory T_{fh}[64,72].

1.1.3 Immune correlates of protection

Immunological correlates of protection are biological markers exhibiting a correlation with immunity against disease or infection, which are measurable in experimental assays[73]. Identification of these immune markers may enable the optimal choice of antigens to include in vaccines; prediction of the extent of individual or population-wide immunity due to immunisation or previous exposure; facilitate immuno-bridging across studies, species, or populations; and may potentially supplant vaccine efficacy trials that are not feasible or ethical[1]. A correlate of protection may be defined in one of two ways. A mechanistic correlate reflects the specific functional immune mechanism that is believed to confer protection (e.g., pathogen-specific neutralising antibody titres)[74]. By contrast, a non-mechanistic correlate, or surrogate, of protection does not provide the protective function itself but has a statistical relationship with the mechanism of protection (e.g., total antigen-specific IgG antibody titres)[74]. Vaccine-induced protective mechanisms may differ from those resulting from natural infection, given the tendency of vaccines to deliver a single antigen and utilisation of technologies such as adjuvants or viral vector platforms, which may additionally modulate immune responses[75,76]. Notably, correlates may differ depending on the endpoint of interest, such as complete protection from infection (also known as sterilising immunity) versus protection from disease, severe disease, or mortality.

Vaccine-elicited correlates of protection are most often measured in clinical trials via the collection of sera and/or peripheral blood mononuclear cell (PBMC) samples from immunised individuals who do or do not develop disease upon subsequent pathogen encounter[74,75]. An alternative

approach to correlates estimation is through extrapolation from epidemiological seroprevalence studies performed in a vaccinated population and relation of these data to disease incidence rates[77,78]. Direct experimental challenges of immunised animals or humans have also been used to define correlates of protection[79]. In animal models, passive transfer of vaccine-induced antibodies or T cells, or B- or T-cell depletion (post immunisation) prior to challenge serve as a more direct approaches to determining the necessary and sufficient components of vaccine-mediated immunity[80-82]. However, the translatability of observations from challenge studies may be limited, given that inoculation doses and other experimental settings often do not closely reflect conditions of natural human exposure.

Traditionally applied correlates of protection for most vaccines have been based on antibody variables[74,75]. In many cases these may not be the only correlate of protection, but antibody levels are often easier to measure than cellular immune responses—typically by using enzyme-linked immunosorbent (ELISA) assays and/or neutralisation assays—and are therefore more straightforward to reliably compare across studies[76]. For example, a haemagglutination inhibition antibody titre of 1:40 may correlate with 50% protection from influenza A virus infection, according to the integration of data from standardised haemagglutination inhibition assays collected over many years from human vaccine cohorts and challenge studies[83,84]. These results have informed the annual reformulation of seasonal influenza vaccines. However, for diseases or vaccines eliciting humoral responses that are either subpar or insufficient to confer protection alone, tools for characterising the roles of other immune effectors are necessary.

Among the most common methods used to quantify the induction of antigen-specific cellular immune responses is by enzyme-linked immunospot (ELISpot) assay, which enables the detection of the number of cells (out of a defined sample) secreting cytokine(s) in response to stimulation

with antigenic peptides (or whole protein/pathogen). The quantification of antigen-specific IFNγ-secreting cells in PBMC samples collected post vaccination, specifically, is a widely adopted method for the estimation of the strength of vaccine-induced T-cell responses[85,86]. Intracellular cytokine staining (ICS) and flow cytometric assessment of antigen-stimulated cells, provides more detailed data on the phenotypic and functional profile of $CD4^+$ and $CD8^+$ T cells. This includes the characterisation of polyfunctional responses (i.e., multiple-cytokine secreting T cells), which are associated with superior effector and memory function[87]. Alternatively, activation-induced marker (AIM) assays may offer a more holistic method for identifying T cells responding to the antigen of interest—based on the upregulation of TCR-stimulated surface markers—particularly for subsets that are poor *ex vivo* cytokine secretors. This method was originally developed to detect antigen-specific GC T_{fh} cells but has since been validated as a tool for the reliable detection of other T-cell subsets[88,89]. Finally, direct flow cytometric quantification, visualisation, and phenotypic evaluation of epitope-specific T cells may also be achieved by staining with fluorescently labelled tetrameric MHC-peptide complexes[90,91]. Although, this method enables the identification of individual T-cell clones rather than the characterisation of an entire polyclonal response against an antigen/pathogen.

In the future, multi-omics methods—including single-cell and bulk transcriptomics, lipidomics, proteomics, metabolomics, and systems serology—may lead to new ways of defining correlates of protection[92]. For pathogens for which a single metric offers only a poor estimation of protection, multivariate profiles or signatures may instead demonstrate a stronger correlation with immunity. Furthermore, these tools may also bridge early and late immune responses, thus enabling the identification of features appearing shortly after vaccination, which are predictive of immunogenicity, efficacy, or even adverse events. For example, the integration of post-

immunisation transcriptional profiles with antibody and T-cell measurements led to the identification of early innate-immune signatures correlating with the immunogenicity of yellow fever virus (YFV) and influenza A virus vaccines in retrospective analyses of clinical trial samples[93,94]. However, the 'systems vaccinology' field is still in its infancy, and due to the significant financial, technical, and computational requirements associated with multi-omics investigations, they have yet to be applied broadly.

1.1.4 ChAdOx1

Recombinant adenoviruses have been used in gene therapy and as vaccine vectors for decades[95]. However, the widespread presence of pre-existing neutralising antibodies to common serotypes of human adenoviruses has raised concerns over their potential reduced immunogenicity[96,97]. Adoption of simian adenoviral vectors, to which human populations are less exposed, may circumvent potential problems related to anti-vector immunity[98]. The ChAdOx1 vector is derived from chimpanzee adenovirus (ChAd) Y25[99]. It is replication incompetent due to the deletion of a single transcriptional unit, E1, reducing the risk for adverse effects when administered to humans. Additional deletion of the E3 unit enables insertion of transgenes up to 8 kb in size[99]. Like other ChAd vectors, it achieves persistent, high-level expression of diverse antigens. Modification of the E4 region by substituting open reading frames from human adenovirus-5 has optimised replication rate and yield in E1-complemented human cell lines[99].

Like all adenoviruses, ChAdOx1 is a non-enveloped, icosahedral DNA virus. Upon intramuscular administration, the virus enters cells at the injection site by binding to coxsackie adenovirus receptors, uptake is aided by integrins[100]. The virus has a protruding trimeric fibre protein on its surface that is associated with the core hexon proteins forming the capsid; the former aids in host

cell attachment and the latter may serve as an intrinsic adjuvant[101]. Heterologous glycoproteins are not expressed on the virus surface. Once in the cell, viral DNA is trafficked to the nucleus and the antigen is expressed. Upon entry, host innate immune responses are initiated by the detection of viral nucleic acid sequences, known as pathogen-associated molecular patterns (PAMPs), by PRRs, such as Toll-like receptors (TLRs), C-type lectin receptors, and NOD- or RIG-I-like receptors[102]. PRR activation triggers a signalling cascade that culminates in a pro-inflammatory cytokine and chemokine milieu, resulting in local inflammation and the recruitment of leukocytes, including APCs. Expressed antigens can either be secreted into the extracellular environment for uptake by APCs or remain intracellular and be directed to host processing pathways[103,104]. The latter will undergo proteasomal degradation and presentation to $CD8^+$ T cells on MHC-I molecules. APCs at the injection site may also be directly infected and activated by the vector or may take-up vaccine antigens through phagocytosis of apoptotic cells. APCs migrate to draining lymph nodes where they prime and $CD4^+$ Th cells and $CD8^+$ CTLs, as well as B cells[103,104]. Thus, ChAdOx1, like other adenoviral vectors is associated with the robust induction of both cellular and humoral immune responses. Given that ChAdOx1 is completely replication deficient, antigen expression is largely confined to the injection site and draining lymph nodes.

The ChAdOx1 platform has been employed in the development of vaccine candidates for a diverse range of infectious threats. In preclinical studies, a single dose of ChAdOx1-vectored vaccine has uniformly afforded protection against disease associated with numerous pathogens, including (but not limited to) Rift Valley fever (RVF) virus[105], Middle East respiratory syndrome (MERS) coronavirus (CoV)[106], Zika virus[107], *Mycobacterium tuberculosis*[108], Nipah virus[109], Lassa virus (LASV)[110], and severe acute respiratory syndrome coronavirus-2 (SARS-CoV-2)[111,112]. Evaluations of ChAdOx1-vectored vaccines against LASV and SARS-CoV-2 are presented in this

thesis. ChAdOx1-vectored vaccines against MERS-CoV[113], Chikungunya virus[114], influenza A virus[115], and SARS-CoV-2[116] have further completed safety and immunogenicity evaluations in humans. ChAdOx1 nCoV-19, a SARS-CoV-2 vaccine, has been the first vaccine utilising this platform to progress through large-scale, multi-site phase III efficacy trials and to be deployed to millions of individuals worldwide under emergency use authorisation (EUA)[117,118].

1.2 Lassa virus

1.2.1 Epidemiology

First detected in Nigeria in 1969, LASV infections have been documented throughout countries of the Mano River Union (Sierra Leone, Guinea, Libera, Côte d'Ivoire), Mali, and Nigeria[119-122] (Figure 1-3). Regions like southern Nigeria and Sierra Leone are hyperendemic, and infections are thought to be seasonal. Isolated cases have also been reported in Benin and Togo[123] (Figure 1-3). Although an annual incidence of 100,000-300,000 cases is often cited, the burden of LASV infection remains poorly characterised, due to the limited availability of up-to-date epidemiological surveillance data[124,125]. An outbreak of LASV infection is defined as a significant increase in the number of cases over the baseline number occurring during a regular LASV season. For reasons that are not well understood, outbreaks take place in regions of endemicity at random intervals and have increased in frequency over the last several years[126,127].

LASV is a zoonotic pathogen, which circulates in rodent reservoirs. The natal multimammate rat, *Mastomys natalensis,* was long considered to be the only host of LASV[124]. However, LASV infections have recently been detected in other rodent species. The isolation of LASV from the African wood mouse, *Hylomyscus pamfi*, in Nigeria and the Guinea multimammate

mouse, *Mastomys erythroleucus*, in Nigeria and Guinea, led to the identification of novel strains belonging to a new phylogenetic lineage[128]. In all of these rodents, the virus causes persistent, asymptomatic infection. Although there are limited epidemiological data on viral transmission, human cases of LASV infection are believed to largely result from rodent-to-human transmission events, facilitated by contact with infectious rodent urine or faeces in the household environment. Consumption of contaminated food, inhalation of particles containing infectious virus, and skin contact with infected-rodent bodily fluids are likely modes of transmission[124,129,130]. This human-vector interface predominantly occurs in resource-limited communities, where access to health care and laboratory diagnostic testing is scarce[131]. Therefore, it is thought that many potential cases of infection go unreported. While less common, human-to-human transmission of the virus occurs via contact with infectious bodily fluids either in the household or during nosocomial outbreaks[124,131].

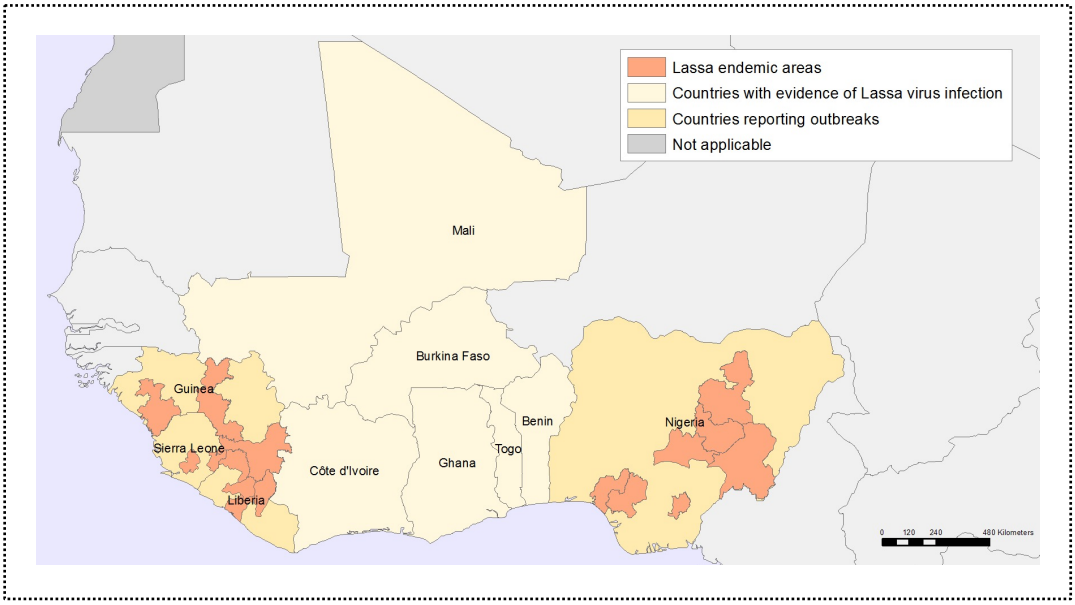


Figure 1-3. Geographic distribution of LASV. Regions where LASV is endemic, resulting in mostly seasonal outbreaks, are depicted in orange, and are concentrated within Nigeria, Sierra Leone, Guinea, and Liberia. Sporadic or infrequent outbreaks have been documented outside of regions of endemicity (as shown in yellow). Evidence of LASV infection has been detected in other West African countries based on seroprevalence surveys, isolation of infectious rodents, or reports of individual positive cases of infection. *Image sourced from*[132].

1.2.2 Clinical disease

The overall case fatality rate of LASV infection ranges between 1-15%[119,133,134]. The high degree of seroprevalence of LASV-specific antibodies in endemic regions, indicates that most infections are mild (or asymptomatic) and do not result in hospitalisation. However, in some individuals, it causes an acute febrile illness—Lassa fever—ranging in severity from mild to an often-fatal multisystem syndrome. An estimated 15-20% of infections result in moderate-to-severe disease[119,133,134]. The case fatality rate is approximately 20% amongst hospitalised patients and increases to greater than 50% in high-risk groups, including pregnant women and infants. Severe Lassa fever in pregnant women results in nearly 100% foetal mortality[135-138]. High mortality has also been observed during certain outbreaks; between 2016 and 2018 in Nigeria, 20-30% of confirmed cases of infection were fatal[139].

Symptoms of Lassa fever develop over an incubation period of 7-21 days[133,135,136]. Fever, vomiting, diarrhoea, chest pain, and headaches are common features of symptomatic infection. In most mild cases, symptoms abate, and recovery commences 8-10 days after disease onset[133,135,136]. Levels of viremia are highly predictive of disease outcome, and peak 4-9 days after symptoms appear. Most patients clear the virus from circulation about three weeks after the onset of illness[136].

By contrast, in severe cases, patients' conditions deteriorate after 6-10 days, resulting in respiratory distress, facial oedema, pleural effusion, and haemorrhage[133,135,136]. Many of these symptoms are a consequence of increased vascular permeability, which is an indicator of poor disease prognosis[140,141]. Moderate-to-severe hepatitis is also frequently observed in Lassa fever patients but is not implicated as a primary cause of death[142]. Instead, mortality is attributed to multiorgan failure, and generally occurs within two weeks of the onset of symptoms[133,135,136].

Post-mortem histopathological evaluation in fatal cases has revealed significant necrosis within hepatic, splenic, lymph node, and adrenocortical tissues, which is likely the result of direct viral infection[143]. Immunohistochemistry (IHC) has detected LASV antigens in (1) hepatocytes; (2) cells of the mononuclear phagocytic system such as Kupffer cells in hepatic sinusoids, alveolar macrophages, and endothelial cells; (3) mesothelial cells lining the pericardium, pleura, and peritoneum; and (4) specialized cells involved in hormone secretion, including those in the adrenal gland, ovary, uterus, placenta, and breast tissue[143]. Although, lymphoid tissues support the highest levels of virus replication.

Viral effects on platelets, inflammatory cells, macrophages, and endothelial cells likely play a critical role in pathogenesis. The infection of macrophages and endothelial cells may trigger secretion of cytokines and other inflammatory mediators, which ultimately leads to microvascular instability and capillary leak syndrome observed in many severe cases of disease[140,141]. The presence of viral antigens in hormone-secreting cells suggests that an interaction between LASV and hormone receptors may exist. This interaction may further enhance the pathogenicity of the virus and may account for the more severe pathophysiologic effects observed in LASV-infected pregnant women[138,143,144].

Survivors of Lassa fever may contend with chronic sequelae, including neurological complications like sensorineural hearing loss[145,146]. Loss of auditory function may occur after mild or severe illness and is estimated to effect 25-30% of cases. In approximately half of these individuals, hearing loss is permanent; in the remainder, partial restoration of hearing takes place between one and three months after recovery[145,146]. Although the precise mechanism underlying this effect is unknown, it is thought to be immune mediated[147].

Therapeutic management of Lassa fever is limited to off-label use of the antiviral ribavirin. According to one study, the drug may reduce the risk of mortality (to below 5%) if administered within the first six days of illness but demonstrates little benefit if started later in the course of disease[142]. However, contemporary reanalysis of this dataset has revealed conflicting findings, which suggest that ribavirin may increase the risk of death in some Lassa fever patients[148]. Two recent clinical trials (NCT02483260 and NCT00992693) have studied the effects of the intravenous (IV) administration of ribavirin to patients that are probable or suspected cases of Lassa fever or Crimean Congo Haemorrhagic Fever. Results from these trials have yet to be published. Favipiravir, an antiviral used against influenza virus infection in Japan, treated LASV infections in guinea pigs and cynomolgus macaques. It has also demonstrated some efficacy in mitigating symptoms in two human cases of Lassa fever, when used in combination with ribavirin[149-151]. However, larger clinical trials are still required to support widespread use of either or both drugs for treating Lassa fever. Additionally, further research to develop and test targeted treatments for LASV infection is urgently needed.

1.2.3 Virology

LASV belongs to the *Arenaviridae* family; it is an enveloped, single-stranded RNA virus with a bisegmented, ambisense genome[152]. The viral genome consists of a large (L) and small (S) RNA fragment, 3.4 and 7 kb in size, respectively[153]. The L fragment encodes the RNA-dependent RNA polymerase and a small, zinc-binding protein[154,155] (Figure 1-4). The S fragment encodes the viral glycoprotein precursor (GPC) and the nucleoprotein (NP)[155,156]. The glycoprotein (GP) spike complex drives host cell entry[157]. The mature form of GP is a trimer of heterodimers, each containing the receptor-binding subunit GP1 and the (class I) transmembrane, fusion-mediating subunit GP2[158] (Figure 1-4). GPC also encodes a stable signal peptide (SSP) that aids

in polyprotein processing into GP1 and GP2, regulation of the pH of infectivity, and provision of chaperone functions during GP maturation[159]. As the only antigen displayed on the viral surface, GP has been the major target for LASV antivirals and vaccine candidates under development.

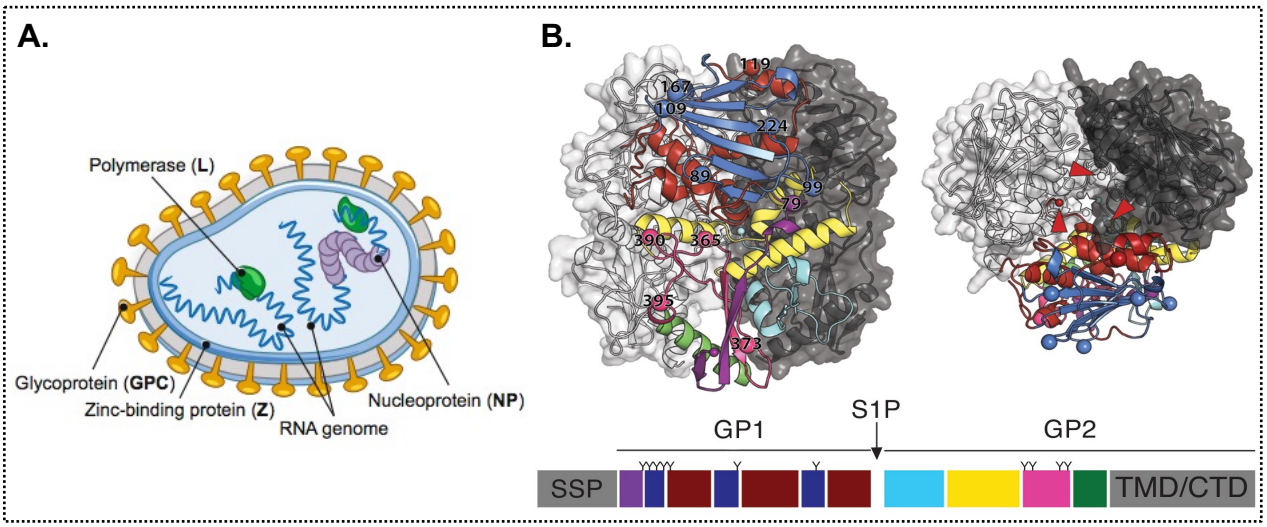


Figure 1-4. Structure of LASV and its surface GP. (A) An illustration of a LASV virion depicting the single-stranded ambisense RNA genome and major viral proteins: GP, NP, zinc-binding protein, and RNA-dependent RNA polymerase. **(B)** Depiction of a GP monomer. LASV GP1 can be divided into three subdomains: (1) the N-terminal β-strands (purple, interacting with GP2); (2) the upper, β-sheet core (blue); and (3) the lower helix-loop surface (dark red). LASV GP2 can be divided into four subdomains: (1) the fusion region (cyan), which is composed of the fusion peptide and fusion loop; (2) HR1a-d (yellow); (3) the T-loop (magenta); and (4) HR2 (green). N-linked glycosylation sites are shown as spheres and numbered on their respective asparagine residue. The C terminus of each GP1 subunit is indicated with an arrow and the N termini of the GP2 subunits, which are positioned at the threefold axis and 30 Å below the apex of the trimer, are indicated with a star. A linear representation of the GPC protomer is shown at the bottom with each subdomain of GPC colored according to the illustrated structure, with each N-linked glycosylation site indicated with a "Y". *Image A sourced from[155]; image B and legend sourced from[158].*

1.2.4 Genetic diversity

LASV exhibits significant nucleotide polymorphism. The L and S genomic segments of different strains may vary by up to 32% and 25%, respectively[120,155]. Although the total number of circulating strains is unknown, LASV variants cluster based on geographic location and at least seven distinct phylogenetic lineages exist[120,155]. Lineages I-III are found throughout Nigeria. Lineage IV circulates in Sierra Leone, Guinea, Liberia, and Côte d'Ivoire[120,155,160] (Figure 1-5).

The Josiah strain (lineage IV) from Sierra Leone is by far the most well-studied and is the dominant strain used in models of LASV infection and in vaccine development. Phylogenetic analysis of strains from Mali and Côte d'Ivoire revealed the emergence of lineage V[161] (Figure 1-5). Strain Kako, isolated from *Hylomyscus pamfi* in Nigeria, was putatively classified as lineage VI[128]. Finally, lineage VII was identified from a cluster of imported LASV infections, with the index case originating in Togo[123].

During the 2018 Nigerian Lassa fever season, a dramatic increase in case numbers raised concerns over the possible emergence of a new strain with a higher transmission rate[162]. However, two sequencing studies of patient derived LASV genomes, revealed multiple different strains representative of viruses in current geographic circulation rather than a single dominant strain[162,163]. Furthermore, LASV from samples collected at similar time points did not demonstrate close phylogenetic clustering, which would be expected in the event of increased human-to-human transmission. Therefore, LASV infections continue to principally occur via independent cross-species transmission events[162,163]. No clear reason for the increase in Lassa fever cases has been found; changes in the distribution of rodent reservoir populations or improved disease diagnosis and surveillance remain possible explanations[127,164].

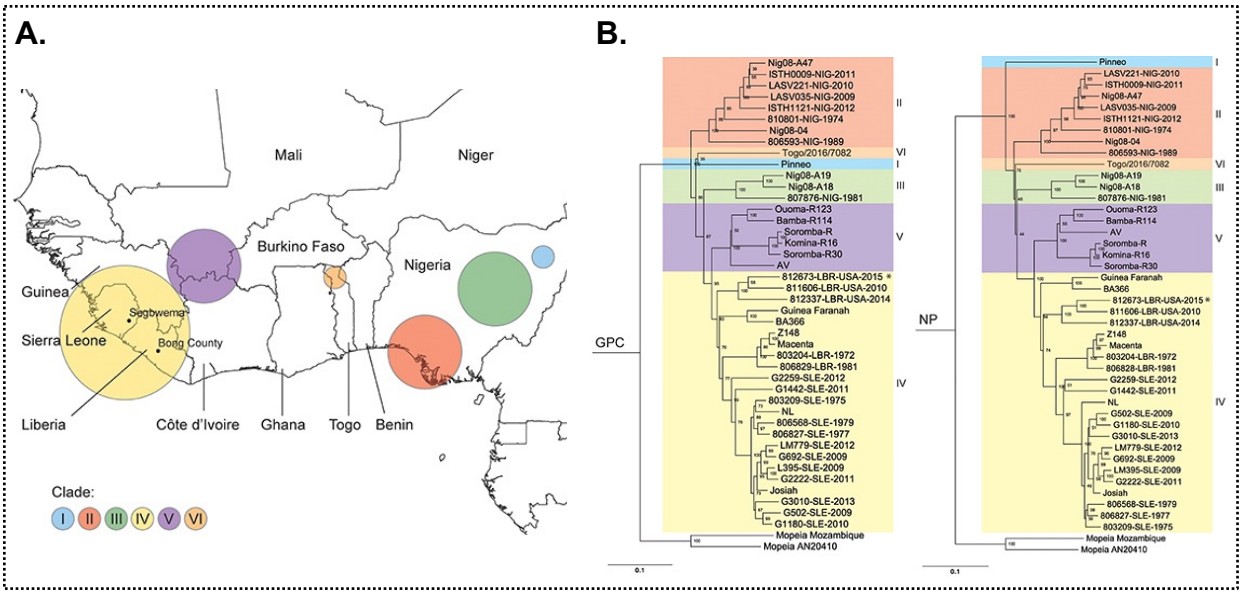


Figure 1-5. Phylogenetic lineages of LASV and their geographic localisation. (A) Sequence analysis of Lassa virus (LASV) strains demonstrates clustering based on geographical location, leading to the identification of major lineages. Clades I–III are found in different regions of Nigeria; Clade IV in Sierra Leone, Liberia, and Guinea; Clade V in southern Mali; and Clade VI (referred to as Clade VII in the main text) in Togo. **(B)** Phylogenetic analysis of full-length GPC (left) and NP (right) nucleotide sequences. Phylogenetic trees were rooted using Mopeia virus (MOPV) isolates, and isolates were grouped by clades. Node labels represent bootstrap values, 1000 replicates. Scale bar represents one change per 100 nucleotides. Note: This map does not include the Kako strain, isolated from *Hylomyscus pamfi* in Nigeria[128], as an independent lineage; thus, only six clades are shown. *Image and legend adapted from*[160].

1.2.5 Immunobiology of infection

LASV exhibits broad tissue tropism infecting the liver, spleen, adrenal glands, and other organs. The virus primarily targets myeloid cells, including APCs like DCs and macrophages, which support high levels of virus replication[165,166]. LASV infection antagonizes the activation and maturation of these cells resulting in impaired antigen processing and presentation. Although infected APCs migrate to the draining lymph nodes, their maturation remains impeded, causing dysregulation of the adaptive immune response and reduced viral clearance[165,166]. The presentation of LASV antigens by immature DCs may lead to immune tolerance and ultimately immunosuppression. The lack of adaptive immune responses observed in fatal cases of

Lassa fever may be associated with more severe disruption of APC function[165,166]. In contrast, Mopeia virus (MOPV), a similar, non-pathogenic arenavirus, also infects and replicates in DCs and macrophages at high levels. However, MOPV infection potently activates APCs, resulting in increased expression of CD40, CD80, CD86, type I interferon, TNFα, and IL-6[167]. Therefore, high levels of APC activation characterise a protective immune response whereas the impaired activation of these cells, in the case of LASV infection, is a determining feature of pathogenesis[167].

During the early stages of infection, the type-I-interferon response plays a critical role in suppressing viral replication and contributing to the initiation of virus-specific adaptive immune responses[168-170]. Mice deficient for the type-I-interferon receptor succumb to lethal infection[171,172]. Strong early (but transient) upregulation of IFNα is observed in non-human primates (NHPs) surviving infection, whereas in non-survivors IFNα production only increases at late stages of disease[173].

As antibody responses remain low during clinical disease, only increasing well after recovery, it is generally thought that resolution of LASV infection is principally mediated by cellular immunity[174]. This assertion is supported by experimental observations of Lassa fever in NHPs, where strong activation and proliferation of T cells (5-15 days post inoculation) occurs in animals that effectively control infection[173]. Meanwhile, severe disease is associated with T-cell depletion in secondary lymphoid tissues, lymphopenia, decreased T-cell activation and proliferation, and uncontrolled virus replication. In humans, LASV-specific $CD4^+$ and $CD8^+$ T cells are detected early during infection and are still present after recovery despite a low or absent antibody response[175]. Memory $CD4^+$ T-cell responses against LASV GPC and NP persist for several years after initial infection.

Generally, antibody production after LASV infection does not correlate with disease outcome. Although detectable, virus-specific IgM and IgG antibodies are produced at relatively low levels during early infection and are not neutralising[174]. Neutralising antibodies are often first detected in circulation months after the resolution of acute infection and at low titres. Neutralising antibody titres continue to rise months after convalescence, which may result from low levels of persisting virus that continues to stimulate B cells[174]. Seroconverted individuals primarily exhibit GP- and NP-specific antibodies[176,177]. The structure of the glycan shield of LASV GP has been implicated as a barrier to virus neutralisation, which may limit the role of antibodies in protection[158,178,179].

However, the significance of the humoral response in protection may be understated, as human monoclonal antibody therapy successfully protects guinea pigs and NHPs against severe Lassa fever[180,181]. The monoclonal antibodies used in these studies had a high neutralising index, suggesting that a strong neutralising response may be protective even if rarely observed after natural infection[180,181]. Finally, *in vitro* experiments have demonstrated viral clearance by non-neutralising antibodies via ADCC and ADCP[182]. Therefore, LASV vaccines capable of inducing high titre antibodies may confer significant protection regardless of the role of antibodies in naturally acquired immunity.

1.2.6 Animal models of infection

A variety of animal models have been employed in studies of Lassa fever, including mice, guinea pigs, and NHPs. Pathogenicity of LASV infection in mice is highly dependent upon the host strain, age, and route of infection. In fully immune competent mouse strains, LASV infection is rarely lethal, particularly when using peripheral routes of inoculation. Intracranial inoculation of CBA/J

mice results in fatal convulsive disease, which does not closely model Lassa fever in humans[183]. By contrast, several immunocompromised mouse strains demonstrate sensitivity to LASV infection. Mice deficient for the type-I-interferon receptor ($IFNAR^{-/-}$) or type-I- and type-II-interferon receptors ($IFN\text{-}a/bgR^{-/-}$) develop clinical signs including ruffled fur and weight loss after infection[169-171]. STAT1 knock out mice ($STAT1^{-/-}$)[184-186], chimeric $IFNAR^{-/-}$ mice transplanted with wildtype C57BL/6 bone marrow[187], and a humanised mouse model expressing human/mouse-chimeric HLA-A2.1[188,189] demonstrate severe (sometimes fatal) disease, viraemia, high tissue viral loads, histopathological lesions, and immune cell infiltration in multiple organs.

Inbred Strain 13 and outbred Hartley guinea pigs are the most widely utilised small animal models for studying Lassa fever. Pathogenicity differs based on host strain and virus strain. In inbred Strain 13 guinea pigs, intraperitoneal (IP) infection with Josiah strain LASV results in uniformly lethal disease characterised by fever, weight loss, and death within 14 days[190,191]. Viraemia is detectable within four days and peaks 10-12 days after infection. High viral titres are found in lymph nodes, salivary glands, spleen, pancreas, and lungs. The virus also replicates in the liver, heart, brain, kidney, and adrenal glands[190,191]. Haematological abnormalities resulting from LASV infection include lymphopenia, neutrophilia, and reduced levels of serum albumin. Damage is observed throughout cardiac, hepatic, and lymphoid tissues[192,193]. Animals may also suffer from interstitial pneumonia, but this does not usually account for lethal outcome[190,191].

In Hartley guinea pigs, the lethality of Josiah strain LASV infection varies from 30% to over 60%. Viral titres are lower in Hartley guinea pigs in comparison to Strain 13 animals[190,191]. An adapted Josiah strain LASV causing fatal disease in Hartley guinea pigs was developed after four passages of the wildtype virus in host animals[149]. Following IP inoculation with guinea pig-adapted (GPA)

LASV, animals uniformly succumb to disease after 15 days. Clinical manifestations of GPA LASV infection resemble those observed with the wildtype virus in the inbred Strain 13 guinea pig model[149].

NHP models are considered the gold standard for recapitulating key aspects of severe Lassa fever pathogenesis observed in humans. LASV (Josiah strain) infection has been well-characterised in rhesus[194,195] and cynomolgus[196,197] macaques, as well as in common marmosets[198]. In these species, viraemia typically appears 5-10 days post-infection and continues to increase until the animals succumb to disease. Like in humans, the extent of viraemia is highly predictive of disease prognosis. Common clinical symptoms may include lethargy, aphagia, depression, increased respiration or acute respiratory distress, gastrointestinal distress, weight loss, and low-grade fever shortly after infection[194-198]. NHPs may also develop confusion, tremors, seizures, or convulsions. Concurrent with viraemia, concentrations of liver enzymes (ALT and AST) rise, while serum albumin and total protein levels fall, as animals reach terminal illness. In survivors, levels return to normal after viral clearance[194-198]. The duration of disease varies between species. Macaques succumb to Lassa fever as early as 9 days after infection whereas marmosets typically do not reach terminal disease until 15 days post inoculation. Virus is detected in many organs; the largest quantities are typically found in the spleen, liver, adrenal glands, lungs, bone marrow, lymph nodes, and intestines[194-198]. In animals succumbing to disease, gross pathological changes include multi-focal hepatic necrosis and lesions in the spleen, heart, lymph nodes, and kidneys. Interstitial pneumonia of varying severity has been reported as well. Lesions in the central nervous system are less common, but do occur in the brain, spinal cord, and meninges[147,194-198]. These findings are consistent with clinical reports from severe Lassa fever patients. Interestingly, as in humans,

lesions do not account for death. Instead, mortality appears to be the result of multi-system organ failure[194-198].

1.2.7 Vaccines

There is currently no vaccine licensed for the prevention of Lassa fever. Although candidates have been in development for over a decade, there was previously limited impetus and funding to progress these candidates to late-stage preclinical and clinical evaluation. However, in 2018, the World Health Organization (WHO) R&D Blueprint listed LASV as a priority pathogen for research and development. Concurrently, a (then) new alliance called the Coalition for Epidemic Preparedness Innovations (CEPI) launched an initiative to finance and expedite promising LASV vaccines through preclinical development to evaluation in clinical trials in LASV-affected regions. This initiative revitalised LASV vaccine development efforts, leading to the generation of novel candidates and the progression of research on existing candidates. A summary of vaccine candidates under development is provided in Table 1-1. These include protein subunit, yellow fever (YF) virus-vectored[199], rabies virus (RABV)-vectored[182], vesicular stomatitis virus (VSV)-vectored[200,201], ChAd-vectored[110], modified vaccinia virus Ankara (MVA)-vectored[202], measles virus (MV)-vectored[203], alphavirus replicon[204], virus-like particle (VLP)[205], DNA[206], RNA, MOPV reassortant[207], and lymphocytic choriomeningitis virus (LCMV)-based[208] approaches.

To date, CEPI has awarded contracts to six vaccine developers/candidates. Through the support of CEPI, WHO, and the coordinated efforts of partner institutions globally, it appears likely that one or more of these vaccine candidates will advance to multi-site efficacy evaluation in West Africa. These platform-based vaccines are briefly discussed below and include VSV-vectored[200,201], MV-

vectored[203], ChAd-vectored[110], plasmid DNA[206], and mRNA candidates. They target the LASV GPC antigen alone or in combination with NP.

INO-4500 is a gene-optimised plasmid DNA vaccine encoding the GPC gene of LASV (Josiah strain)[206]. DNA vaccination involves introduction of a plasmid expressing the target immunogen into a tissue, relying upon *in situ* production of the antigen. INO-4500 is administered in a two-dose regimen via intradermal injection followed by electroporation. Efficacy has been demonstrated in guinea pig and NHP models of infection[206,209]. INO-4500 is the first LASV vaccine to be administered to humans and exhibited safety and immunogenicity in a phase IA trial (NCT03805984) conducted in healthy adults in the US. In early 2021, a phase IB trial (NCT04093076) began in Ghana, which will compare dosing schemes and inform dose selection for subsequent phase II studies in West Africa.

MV-LASV is a recombinant live attenuated viral vectored vaccine, based on the backbone of the MV (Schwarz strain)[203]. This replicating MV platform has been utilised in the development of vaccines for several pathogens, including for Chikungunya; MV-CHIK has completed phase II evaluation (NCT02851586) and is now in late stages of clinical development[210]. MV-LASV encodes the full-length GPC (Josiah strain) and NP sequences. After protecting NHPs from homologous and heterologous LASV challenge, MV-LASV has progressed to testing in a phase I trial (NCT04055454) to assess safety, tolerability, immunogenicity, and dosing of a prime-boost regimen[203,211].

The CEPI portfolio includes two replication-competent VSV-vectored vaccines for Lassa fever. VSV is a ubiquitous virus with broad species and tissue tropism; variations of the VSV vector have been used to develop vaccines for a wide range of pathogens[212]. Recombinant VSV is produced

by replacement of the VSV G gene with that of a heterologous glycoprotein, resulting in the presentation of foreign antigens on the viral surface. One of the two VSV-vectored vaccines contains the rVSVΔG vector, which was used to develop the first licensed vaccine for Zaire Ebola virus disease, rVSV-ZEBOV[213]. rVSVΔG-LASV-GPC encodes the Josiah strain GPC gene; this vaccine has demonstrated efficacy against homologous and heterologous LASV challenge in guinea pigs and NHPs[200,214]. A phase I safety, immunogenicity, and dose-escalation trial (NCT04794218) in healthy adults commenced in 2021. The second VSV-vectored candidate features an attenuated VSV vector, known as rVSV-N4CT1 (or VesiculoVax), which includes added truncation of the VSV glycoprotein and translocation of the nucleoprotein from position 1 to position 4 in the viral genome[215]. In clinical trials, administration of the attenuated vector has resulted in substantial reductions in vaccine-induced viraemia and side effects (HVTN 090 and HVTN 087)[216,217]. Two doses of rVSV-N4CT1-LASV, which encodes the LASV GPC (Josiah strain), successfully protected NHPs from challenge with a contemporary lineage II isolate[201].

Another vaccine targeting LASV GPC (Josiah strain), utilises a lipid nanoparticle-encapsulated mRNA platform; however, published data is not yet available for this candidate. The final CEPI-funded vaccine candidate employs the ChAOx1 vector described in section 1.1.4, ChAdOx1-Lassa-GPC. The preclinical development and evaluation of ChAdOx1-Lassa-GPC in mice, guinea pigs[110], and NHPs is discussed throughout Chapters 3 and 4 of this thesis.

The WHO Target Product Profile (WHO TPP)[218] for Lassa Virus Vaccines provides a set of minimum and preferred Lassa fever vaccine requirements to guide developers and regulatory agencies. In endemic regions, vaccines should at least be suitable for use in healthy adults and children, but preferably also safe in infants and pregnant women. Only mild, transient adverse

effects related to immunisation will be tolerated and additional data indicating that vaccination does not induce neurological complications associated with Lassa fever (including hearing loss and neuropsychiatric effects) are required[218]. Demonstration of at least 70% (but preferably over 90%) protective efficacy against infection or disease in clinical trials will be important. While a single-dose regimen will be ideal, up to three-doses conferring protection against LASV lineages I-IV for a minimum of three (but preferably over five) years may be deemed acceptable[218]. Finally, suitability for stockpiling evidenced by shelf life (at least 12 months at -20 °C and six months at 2-8 °C) and thermostability will also be essential. Evaluation of the above vaccine candidates in regions of LASV endemicity will provide the true test of alignment with the WHO TPP.

Table 1-1. LASV vaccine candidates under development.

Candidate	Platform or technology	LASV antigen(s)	Developers	Stage
VesiculoVax™ rVSVN4CT1-LASV **	Recombinant attenuated VSV vector	GPC	Profectus Biosciences & Emergent Biosolutions; Yale University; University of Texas Medical Branch	Preclinical
rVSVΔG-LASV-GPC **	Recombinant VSV vector	GPC	International AIDS Vaccine Initiative	Phase I clinical trials
MV-LASV **	Recombinant measles virus vector	GPC and NP	Themis Bioscience; Institut Pasteur	Phase I clinical trials
INO-4500 pLASV-GPC **	Plasmid DNA	GPC	Inovio Pharmaceuticals; US Army Medical Research Institute for Infectious Diseases (USARMIID)	Phase Ib clinical trials
Name not specified **	Lipid-nanoparticle-formulated mRNA	GPC	CureVac	Preclinical
ChAdOx1-Lassa-GPC **	Recombinant ChAd vector	GPC	University of Oxford; Janssen Pharmaceuticals	Preclinical
ChAdOx1 biLAMA	Recombinant ChAd vector	LASV GPC (and Marburg virus GP)	University of Oxford	Preclinical
MOPV ML29	Reassortant virus of LASV S segment and MOPV L segment	GPC and NP	Medigen; NIAID	Preclinical

ML29 L-AttV, rLCMV (IGR/S-S)	MOPV, LCMV, and LASV reassortant	GPC and NP	The Scripps Research Institute	Preclinical
rLCMV/CD	Live attenuated LCMV	Codon-deoptimised LCMV GP	The Scripps Research Institute, University of Rochester	Preclinical
Viral genome rearrangement for the development of live-attenuated arenavirus vaccines	Recombinant LCMV backbone	GPC and NP	University of Rochester; The Scripps Research Institute	Preclinical
MOPEVAC	Modified MOPV	GPC	Institut Pasteur	Preclinical
GPC441-449 subunit	HLA-A*0201-restricted epitope-based approach	Peptide (from GPC)	University of Vermont; The Scripps Research Institute; MWH Laboratories; University of North Carolina; PaxVax; University of California	Preclinical
PODS Lassa 1	Polyhedrin-encased protein	GP	IDT Biologika GmbH; Infectious disease research institute; Cell Guidance Systems; University of Cambridge; Imperial College London	Preclinical
LASV VLP	VLP	GPC, NP, Z	Tulane University Health Sciences Center; Autoimmune Technologies; Corgenix Medical Corporation; Vybion; USAMRIID	Preclinical
GEO-LM01	MVA-VLP	GPC and Z	GeoVax; The Scripps Research Institute; University of Maryland	Preclinical
LASSARAB	RABV virus vector	GPC	Thomas Jefferson University; NIAID; The Geneva Foundation; USAMRIID	Preclinical
MVA Lassa	MVA vector	GPC	University of Oxford	Preclinical
Alphavirus replicon	Alphavirus replicon	GPC	Medigen; University of Louisville; USAMRIID	Preclinical
Lassa GPC clamp	Recombinant protein (molecular clamp technology)	GPC	The University of Queensland; Australian Government National Health and Medical Research Council (NHMRC)	Preclinical

***Indicates candidates included in CEPI's portfolio of vaccines funded for accelerated development. Table adapted from[219,220].*

1.3 Severe acute respiratory syndrome coronavirus 2

1.3.1 Epidemiology

Severe acute respiratory syndrome coronavirus 2 (SARS-CoV-2) emerged in late 2019; the first cases of infection were detected in Wuhan, China in clusters of patients presenting with pneumonia of unknown cause. Since then, this highly transmissible pathogenic virus has caused a pandemic of acute respiratory disease, called coronavirus disease 2019 (COVID-19), resulting in over 400 million cases affecting all continents[221].

The introduction of SARS-CoV-2 into humans most likely resulted from zoonotic spill-over from a reservoir or intermediate host. Although the SARS-CoV-2 reservoir species has not been clearly determined, bats are natural hosts of many alpha- and beta-coronaviruses[222-225]. Among the closest phylogenetically related viruses to SARS-CoV-2 are bat coronaviruses, such as RaTG13 found in *Rhinolophus affinis* and RmYN02 in *Rhinolophus malyanus* bat species in Yunnan province, China. These viruses exhibit 96.2% and 93.3% genome sequence identity with SARS-CoV-2, respectively, suggesting that bats may also be the reservoir of SARS-CoV-2[222-225]. Pangolins are another wildlife host in which multiple highly related coronaviruses were identified, with greater than 90% sequence identity to SARS-CoV-2. However, there is no evidence demonstrating that pangolins were directly involved in the emergence of SARS-CoV-2[182,226,227].

Human-to-human transmission of SARS-CoV-2 largely occurs through close-range contact and transfer of respiratory droplets from an infected person. Although long-range airborne transmission via aerosolised particles has been demonstrated in animal models and other studies have detected viral RNA in air samples in hospital rooms of COVID-19 patients[228-231]. In addition,

the virus may stably persist on inanimate surfaces for days, but fomite transmission is not considered to be a principal contributor to the spread of SARS-CoV-2[228,232]. Upper respiratory tract shedding is the main source for viral transmission; viral loads in nasopharyngeal samples are highest during the first week of symptoms and appear to increase according to disease severity[233-235]. However, SARS-CoV-2 also transmits efficiently during mild or asymptomatic disease, which may account for the rampant geographic spread of the virus[236]. The virus has been detected in non-respiratory specimens, including stool, blood, ocular secretions, and semen, but the role of these sites in transmission is uncertain[237-244]. According to the WHO, transmission through the faecal-oral route does not appear to be a significant contributor to the spread of infection and the likelihood of bloodborne transmission also appears low and has not been reported for other respiratory coronaviruses[245,246]. Furthermore, there is no evidence that SARS-CoV-2 can be transmitted via contact with non-mucous membrane sites.

1.3.2 Virology

SARS-CoV-2 belongs to the sarbecovirus subgenus of the larger beta-coronavirus genus[247]. SARS-CoV-2 has an enveloped positive-sense single-stranded RNA genome encoding four structural proteins (membrane, envelope, nucleocapsid (N), and spike (S) proteins), multiple non-structural proteins (nsp), and eight accessory proteins[247] (Figure 1-6). The SARS-CoV-2 S trimeric glycoprotein is 1,273 amino acids in length and mediates virus entry into host cells. S monomers contain the S1 attachment domain (residues 1-686) and the S2 membrane fusion domain (residues 687-1273)[248,249] (Figure 1-6). A region within S1, called the receptor-binding domain (RBD, residues 306-534), when in the appropriate conformation, binds to the human angiotensin-converting enzyme 2 (ACE2) receptor to initiate cell entry. The residues forming the contact with human ACE2 are concentrated in a region of the RBD called the receptor-binding motif (RBM),

the surrounding region is known as the RBD core[250-253]. Both the RBD and much of the S1 amino-terminal domain (NTD) are exposed on the S trimer surface (Figure 1-6).

Like other coronaviruses, SARS-CoV-2 S requires proteolytic processing prior to endocytosis. Host cell proteases, including transmembrane serine protease 2 (TMPRSS2), cathepsin L, and furin, mediate S cleavage[254-256]. TMPRSS2 is highly expressed in multiple tissues and is co-expressed with ACE2 in nasal epithelial cells, lungs, and bronchial branches, which may explain some of the tissue tropism of SARS-CoV-2[257,258]. Besides human ACE2, SARS-CoV-2 also recognises ACE2 from a variety of species, including hamsters, pigs, ferrets, minks, civets, cats, pangolins, rabbits, dogs, and multiple NHP species[259-261]. The broad receptor usage of SARS-CoV-2—albeit with varied efficiency—implies a wide host range with different degrees of susceptibility to virus infection.

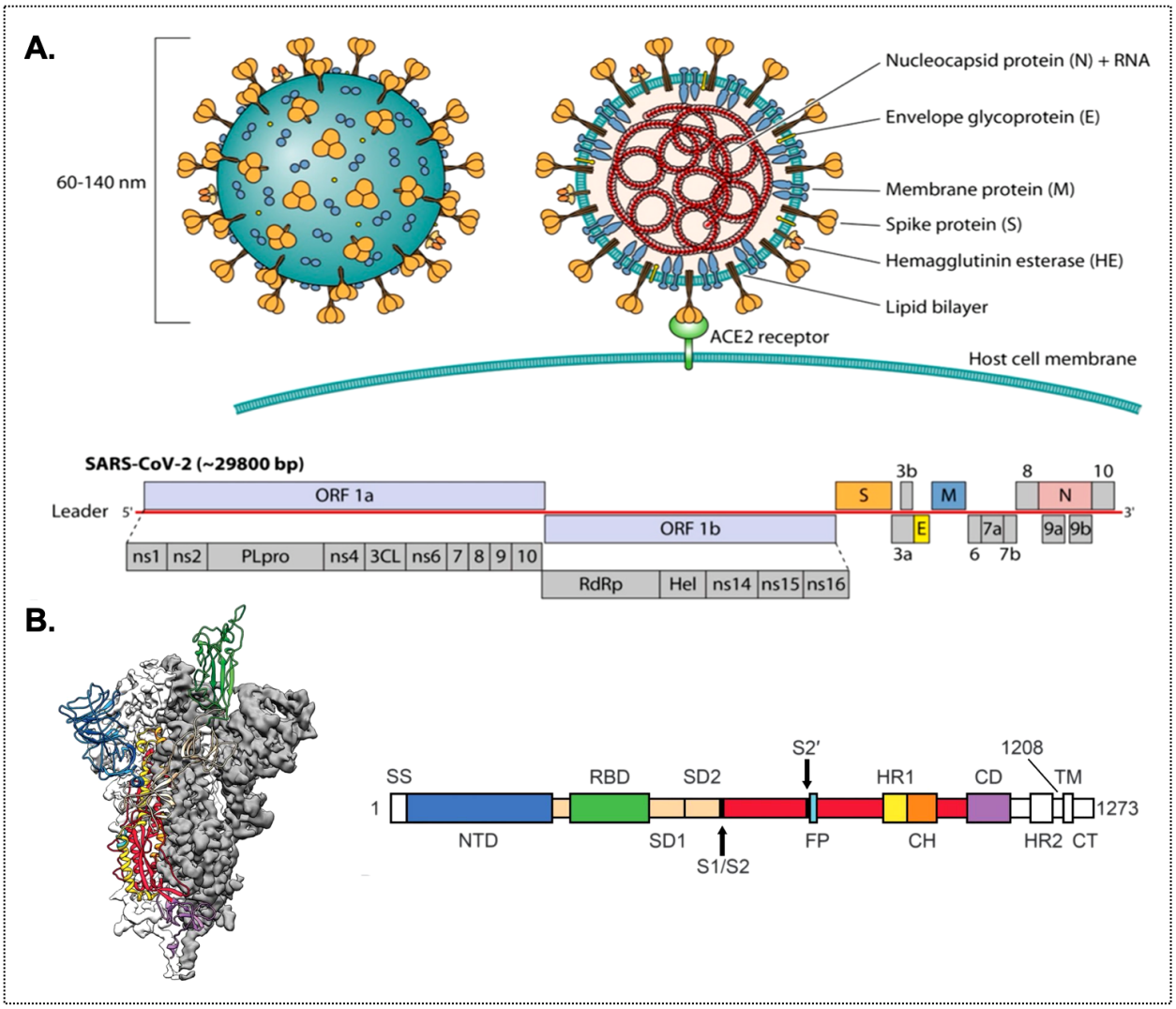


Figure 1-6. Components of the SARS-CoV-2 virion, genome, and spike (S) protein. **(A)** Diagram of the SARS-CoV-2 virion (top) with major structural proteins labelled. The SARS-CoV-2 genome (bottom) depicting the genes for major structural (S, E, M, and N) and nonstructural proteins (nsps, RNA-dependent RNA polymerase (RdRp), helicase (Hel), papin-like protease (PLpro), and cysteine protease (3CL)). **(B)** Side and top views of the prefusion structure of the S protein with a single RBD in the "up" conformation, colored by domain (left). Schematic of SARS-CoV-2 S primary structure colored by domain (right), including the signal sequence (SS), S2' protease cleavage site (S2'), fusion peptide (FP), heptad repeat 1 (HR1), central helix (CH), connector domain (CD), heptad repeat 2 (HR2), transmembrane domain (TM), cytoplasmic tail (CT). Arrows denote protease cleavage sites. Domains that could not be visualized in the final map are colored white. *Image A sourced from[262]; image B and legend adapted from[249].*

1.3.3 Clinical disease

SARS-CoV-2 pathogenesis in humans ranges from asymptomatic or mild symptoms to severe or fatal. The incubation period for COVID-19 is generally within 14 days following exposure, with most cases occurring approximately 4-5 days after exposure[263-265]. The National Institutes of Health (NIH) has issued guidelines classifying COVID-19 into five types based on the severity of clinical symptoms, laboratory or radiographic abnormalities, haematology, and organ function. These include asymptomatic or pre-symptomatic, mild, moderate, severe, and critical[266]. Data from reviews performed prior to the introduction of COVID-19 vaccines estimated that 17.9% to 33.3% of SARS-CoV-2 infections were asymptomatic[267-269]. Since the introduction of COVID-19 vaccination campaigns, the proportion of cases presenting as asymptomatic or as mild illness has increased significantly. Within specific demographics, particularly younger populations, even higher proportions of asymptomatic infections are reported. Mild illness is characterised by symptoms such as fever, cough, sore throat, malaise, headache, muscle pain, nausea, vomiting, diarrhoea, anosmia, or dysgeusia[269]. Individuals presenting with symptoms or radiologic evidence of lower respiratory tract disease with oxygen saturation (SpO_2) levels of ≥94% on room air are categorized as experiencing moderate illness. Meanwhile, SpO_2 levels ≤94% on room air, a ratio of arterial oxygen partial pressure to fraction of inspired oxygen (PaO_2/FiO_2) <300, tachypnoea, increased respiratory frequency (>30 breaths/min), or lung infiltrates >50% constitutes severe disease. Finally, individuals critically ill with COVID-19 experience septic shock, multiple organ dysfunction, or acute respiratory failure that may be designated acute respiratory distress syndrome (ARDS)[269-271]. Patients of older age (>60 years) and with comorbidities (obesity, diabetes, hypertension, chronic respiratory disease and cardiovascular disease) have a greater risk of developing ARDS and death[271-273]. Case fatality rates have varied broadly according to location,

population demographics, and severity of clinical disease[269]. Vaccination has led to dramatic reductions in the frequency of hospitalisation, severe disease, and mortality associated with SARS-CoV-2 infection. SARS-CoV-2 variants of concern with RBD mutations resulting in increased (or altered) affinity for the human ACE2 receptor and consequently enhanced viral entry may exhibit differences in pathogenesis with clinical manifestations.

Histopathological changes in patients with COVID-19 occur mainly in the lungs and reveal bilateral diffused alveolar damage, hyaline membrane formation, desquamation of pneumocytes and fibrin deposits in severe cases. Immunohistochemical analyses have shown SARS-CoV-2 antigen in the upper airway, bronchiolar and submucosal gland epithelia, as well as in type I and type II pneumocytes, alveolar macrophages and hyaline membranes[274-276]. Laboratory haematological abnormalities observed in COVID-19 patients include lymphopenia, leukopenia, elevated levels of C-reactive protein, elevated D-dimer, elevated erythrocyte sedimentation rate, leucocytosis, elevated cardiac enzymes, elevated procalcitonin, abnormal liver function tests, and abnormal renal function[277]. Elevated ratios of neutrophils-to-lymphocytes and platelets-to-lymphocytes are indicators of a 'cytokine-induced inflammatory storm', which is associated with severe disease[278]. Although the respiratory system is the principal target for SARS-CoV-2, as described above, it may affect other major organ systems such as the gastrointestinal tract, hepatobiliary, cardiovascular, renal, and central nervous systems. SARS-CoV-2-induced organ dysfunction may be the result of direct viral toxicity, ischemic injury caused by vasculitis, thrombosis or thrombo-inflammation, immune dysregulation, and/or renin-angiotensin-aldosterone system dysregulation[279,280].

A variety of therapeutic options are available for the treatment or mitigation of COVID-19. The broad-spectrum antiviral remdesivir has been approved by the US FDA for use in adults and

paediatric patients hospitalised with COVID-19; although, the effectiveness of this drug in improving recovery times and reducing mortality has been inconsistent across studies[281-283]. The FDA approved convalescent plasma therapy under EUA for patients with severe life-threatening COVID-19; however, results have been mixed[284,285]. By contrast, multiple anti-S monoclonal antibody cocktails have demonstrated promising results in phase II or phase III clinical trials and have been approved for clinical use by FDA EUA, these are: REGN-COV2 (casirivimab and imdevimab)[286,287], bamlanivimab/etesevimab[288], and sotrovimab[289]. In addition to the options listed above, a variety of immunomodulatory agents have also been used in the treatment of COVID-19, including (but not limited to): corticosteroids[290], anti-IL-6 receptor inhibitors[291,292], and janus kinase (JAK) inhibitors[98,293,294].

1.3.4 Immunobiology of infection

Within the respiratory tract, SARS-CoV-2 principally targets ciliated epithelial cells, type II pneumocytes, lung-resident (alveolar and interstitial) macrophages, and vascular endothelial cells[295,296]. Soon after infection, SARS-CoV-2 induces diminished or delayed type I and III interferon responses, creating a replication permissive microenvironment[297,298]. This initial dampening of innate immune signalling may explain the early high viral loads seen in COVID-19 patients, the uncharacteristically long incubation times, and high rates of asymptomatic or pauci-symptomatic infections[299,300]. In a productive immune response to infection, DCs, alveolar and interstitial tissue-resident macrophages, and NK cells at the site of infection release cytokines and chemokines—including TNFα, GM-CSF, IL-1, IL-6, IL-1β, IL-8, IL-12 and IFNγ—which first recruit neutrophils, then plasmacytoid DCs, and later monocytes within the span of a few days[301]. T- and B- cells appear 4-5 days after infection; antigen-specific adaptive responses develop 6-10 days later following adequate priming and clonal selection[302]. DCs and pDCs present viral antigens

to $CD4^+$ Th cells, which results in a Th1 response with enhanced IFNγ, IL-2 and TNFα secretion[303]. $CD8^+$ T-cell responses specific to SARS-CoV-2 also produce IFNγ, IL-2 and TNFα, resulting in direct cytotoxicity against infected cells. The early development of CTL responses correlates with less severe COVID-19 illness[302-304]. CTL responses also may contribute to protection from more severe clinical disease in NHPs in the presence of low titres of neutralising antibodies and in persons with impaired humoral immunity[82,305,306]. Many studies have identified specific human leukocyte antigen (HLA)-restricted Th cell and CTL epitopes within SARS-COV-2 S and N[307-309]. However, the number of recognised epitopes varies greatly between individuals according to HLA profile and is much lower than the total number of SARS-CoV-2 T-cell epitopes.

Like cellular immune responses, antibodies elicited by SARS-CoV-2 infection mainly target S and NP. IgA antibodies typically appear early during the first week of infection, followed by IgM (in 10-12 days), and later by IgG (after 21 days)[310-312]. S is the main target of neutralising antibodies[313-315]. Most neutralising antibodies target either the RBD RBM or the surrounding RBD core[316]. The epitopes in RBD account for ~90% of the neutralising activity of sera from individuals previously infected with SARS-CoV-2[317]. RBD-specific neutralising antibody titres correlate with protection in animal models, as well as in previously infected and vaccinated persons. Although, T-cells and non-neutralising antibodies may have also contributed to protection in these studies[82,318,319]. The development of neutralising antibodies early in the course of infection has been associated with lower viral load and enhanced protection against severe disease outcomes[320,321]. Some COVID-19 patients develop antibodies with minimal somatic mutation indicative of low-level affinity maturation; thus, a subset of patients may fail to mount robust long-lasting protective humoral responses against SARS-CoV-2[322]. Non-neutralising antibody Fc-effector functions such as complement activation, cellular cytotoxicity and phagocytosis have also been shown to afford

protection in animal models and in the initial weeks following vaccine administration[323,324]. However, the protection afforded by non-neutralising antibodies in the absence of neutralising antibodies is difficult to quantify[325,326]. Neutralising antibody levels have become the principal immune correlate of interest in predicting protection afforded by vaccination or previous infection, particularly in the context of heterosubtypic immunity against VOCs and waning immunity over time.

COVID-19 patients who experience the severe or critical form of the disease develop immunopathology due to an imbalance in pro- and anti-inflammatory mechanisms[299]. The transition from mild to moderate and ultimately to severe disease phenotype is coupled with metabolic, as well as innate and adaptive immune alterations. In severe COVID-19, the immune system's overactivation results in a 'cytokine storm' characterised by the release of high levels of circulating cytokines, especially IL-6 and TNFα, triggering uncontrolled local and systemic inflammation with damaging effects on tissues[327]. A disruption in lipid mediator levels and myeloid cell abnormalities, including dysfunctional neutrophils and monocytes, have also been observed in critical cases[328,329]. $CD4^+$ and $CD8^+$ T-cell lymphopenia is commonly found in COVID-19 patients, resulting either from direct cytotoxic effects of the virus, or from enhanced T-cell apoptosis due to dysregulation of the cytokine milieu or metabolism[330]. Decreased T-cell counts in severe COVID-19 have been associated with reduced expression of markers of T-cell activation and function[331]. Peripheral $CD8^+$ (and possibly also $CD4^+$) T cells also express high levels of exhaustion markers like PD1, TIM3, and CD57, suggesting a functional immune deficiency[332]. In severe COVID-19, exhausted T cells may also contribute to protracted inflammation through the secretion of cytokines (IL-1a, TNFα, IL-17, GM-CSF, IL-21, and IL-22) with broad chemotactic effects, which also promote vascular permeability and leakage[333,334].

Some severe COVID-19 patients have also exhibited increased serum concentrations of Th2 cytokines, including IL-4, IL-10, and IL-13, perhaps indicative of wide spectrum immune activation[335]. Analyses of circulating B cells in patients with severe COVID-19 have shown an expansion of oligoclonal plasmablasts and a reduced frequency of memory B cells[336].

1.3.5 Vaccines

Novel vaccines against SARS-CoV-2 were developed and tested at unprecedented speeds with multiple vaccines receiving EUA and even licensure. As of late 2021, over 8 billion vaccine doses have been administered, 23 vaccines have been deployed to the general population, and 10 vaccines are being monitored in wider phase IV surveillance studies[337] (Figure 1-7). In addition, 135 and 194 new vaccine candidates are undergoing clinical and preclinical evaluation, respectively. These vaccines (or vaccine candidates) comprise a diverse array of technologies including mRNA, DNA, viral vector, bacterial vector, recombinant protein, and whole virus approaches[337]. A brief description of some the 23 vaccines currently being administered to general populations globally follows; these vaccines are also listed in Table 1-2.

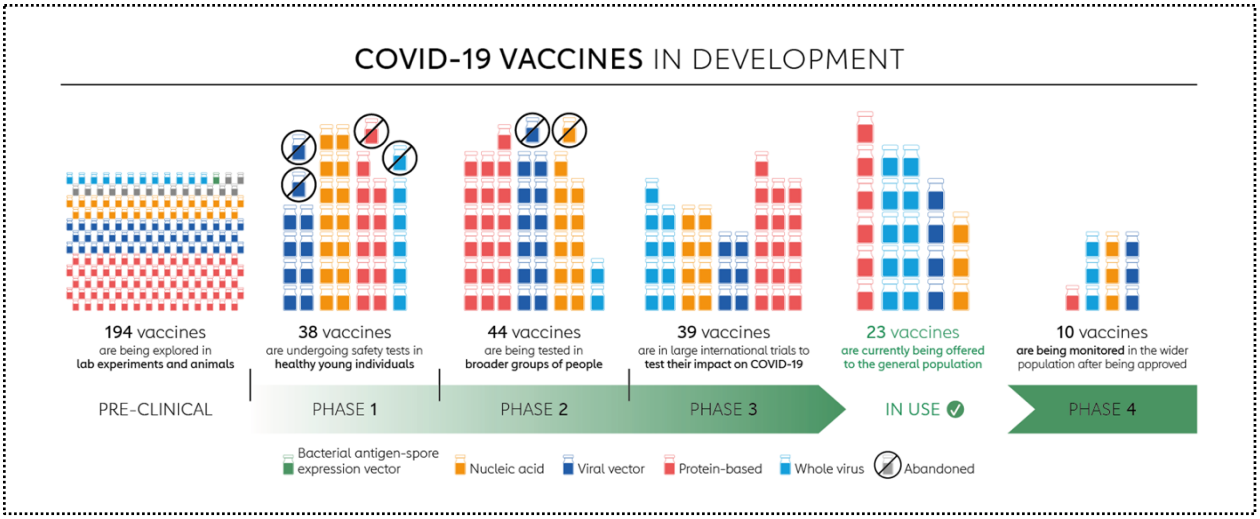


Figure 1-7. COVID-19 vaccines in use and under development. A schematic depicting the status of COVID-19 vaccine development (as of December 2021). The number of vaccines in pre-clinical versus clinical stages of development are shown. The number of vaccines authorised for use is indicated, as well as those under phase IV evaluation. Vaccines are depicted according to their platform or formulation. *Image sourced from*[337].

Multiple adenovirus-vectored COVID-19 vaccines are either approved or are in late-stage testing, including ChAdOx1 nCoV-19 (University of Oxford & AstraZeneca)[117,118,338,339], which is featured in Chapter 5 of this thesis, Gam-COVID-Vac (Gamaleya)[340], Ad26. COV2.S (Janssen & Janssen)[341], and Ad5-nCoV (CanSino Biologics)[342]. Although the recombinant adenoviruses differ between these vaccines, according to host species (human or simian) and strain/serotype, they are all replication-deficient and rely upon similar mechanisms for activating immune responses to those described for ChAdOx1 in section 1.1.4. BNT162b2 (Pfizer/BioNTech)[343,344] and mRNA-1273 (Moderna)[345,346] are lipid nanoparticle-encapsulated non-amplifying mRNA-based vaccines. ZyCoV-D (Zydus Cadila)[347] is a plasmid DNA vaccine. The target immunogen of primary interest in COVID-19 vaccine development has been the SARS-CoV-2 S protein. These viral-vectored, mRNA, and DNA vaccines all encode the full-length SARS-CoV-2 S protein and rely upon endogenous host cell machinery to transcribe, translate, process, and present the antigen *in vivo*. However, Ad26.COV2.S[348], BNT162b2[349], and mRNA-1273[350,351] contain specific modifications

within the S protein sequence resulting in two proline substitutions (i.e., K986P and V987P), combined with a furin cleavage-site mutation. These alterations maintain the S trimer in its pre-fusion conformation, thereby exposing key neutralising antibody conformational epitopes on the trimer surface that would otherwise be hidden in the more stable post-fusion protein, while also increasing S trimer yields[249,352]. Previous evidence revealed that the proline mutations were beneficial to the immunogenicity of the MERS-CoV S[353] and RSV fusion[354] glycoprotein trimers. These alterations to the antigen may play a role in the induction of potent neutralising antibody titres induced by these vaccines. The protein subunit vaccines NVX-CoV2373 (Novavax)[355,356] and MVC-COV1901 (Medigen, NCT05011526), also deliver S stabilised in its pre-fusion state with adjuvants (Matrix M and CpG, respectively). Several other protein subunit vaccines are in use and are listed in Table 1-2 below. Finally, multiple vaccines currently in use involve more traditional delivery of inactivated whole SARS-CoV-2 virus, and thus rely upon properties intrinsic to the virus and presentation of all viral proteins to activate robust adaptive immune responses; these include CoronaVac (Sinovac)[357,358], BBIBP-CorV (Sinopharm)[359], Covaxin/BBV152 (Bharat Biotech)[360,361], and several others listed in Table 1-2.

Although COVID-19 vaccines differ in immunogenicity, most induce dose-dependent titres of antibodies capable of neutralising live virus or S-protein-pseudotyped virus in *in vitro* assays[318]. Non-neutralising antibody effector functions, such as ADCC or ADCP, have been detected in vaccinee sera as well[319,362,363]. Furthermore, many currently deployed vaccines also demonstrate the induction of S-specific T-cell responses. Characterisation of vaccine-elicited cellular immune responses has detected polyfunctional Th1 and CTL effector responses, defined by the expression of IFNγ, TNFα, and IL-2[319,364-368]. For a few vaccines, S-specific T_{fh} cells have been detected in circulation, which could facilitate B-cell maturation and high-affinity antibody production in the

GCs of secondary lymphoid organs, as described in section 1.1.2[369]. Although T-cell responses have not received as much emphasis as a principal correlate of protection, they likely also play a role in protection and long-term memory as described in section 1.3.4[82,302-304].

Given differences in clinical trial designs, primary endpoints used in efficacy evaluations, populations and/or locations of vaccine deployment, and the time of efficacy assessment, it is difficult to directly compare the protective efficacies of the various COVID-19 vaccines. Importantly, most vaccines provide near complete protection against severe disease and substantially reduce the risk of hospitalisation[337]. The vaccines currently in use are delivered systemically via the intramuscular (IM) route, thereby inducing strong circulating adaptive immune responses, but not mucosal. Therefore, although immunisation is highly effective in preventing clinical disease, it does not fully block infection or transmission[370]. Virus-specific antibodies or T cells localised to the site of virus entry, namely the upper respiratory tract, may be necessary to completely avert infection[371,372]. At least two trials are underway to test the safety and immunogenicity of vaccine administration via intranasal (IN) spray (NCT04816019) or aerosol inhalation[373] (NCT04552366).

Table 1-2. COVID-19 vaccines in currently in use *(as of December 2021)*.

Vaccine	Type	Developer	Antigen	Doses	Current status
mRNA-1273	mRNA	Moderna/NIAID	S (pre-fusion stabilised)	Two doses	EUA by WHO, FDA, and multiple countries. Phase IV trials on-going.
BNT162b2	mRNA	Pfizer/BioNTech/Fosun Pharma	S (pre-fusion stabilised)	Two doses	FDA approved; EUA by WHO and multiple countries. Phase IV trials on-going.
ChAdOx1 nCoV-19 (AZD1222)	Adenoviral vector	AstraZeneca/University of Oxford	S	Two doses	EUA by WHO and multiple countries. Phase IV trials on-going.
Ad26.COV 2.S	Adenoviral vector	Janssen Pharmaceutical	S (pre-fusion stabilised)	One dose	EUA by WHO, FDA, and multiple countries. Phase IV trials on-going.
NVX-CoV2373	Protein subunit	Novavax, Inc	S (pre-fusion stabilised)	Two doses	EUA by WHO and multiple countries. Phase IV trials on-going.
CoronaVac	Inactivated virus	Sinovac Biotech	Whole virus	Two doses	EUA by WHO and multiple countries. Phase IV trials on-going.
BBiBP-CorV	Inactivated virus	Sinopharm 1/2	Whole virus	Two or three doses	EUA by WHO and multiple countries. Phase IV trials on-going.
BBV152	Inactivated virus	Bharat Biotech	Whole virus	Two doses	EUA in 16 countries
Ad5-nCoV	Adenoviral vector	CanSino Biological Inc/Beijing Institute of Biotechnology	S	Two doses	EUA in multiple countries.
Gam-COVID-Vac (rAd26-S + rAd5-S)	Adenoviral vector	Gamelya Research Institute/Health Ministry of the Russian Federation	S	Two doses	Approved (Russia, Belarus, and others)
MVC-COV1901	Protein subunit	Medigen	S (pre-fusion stabilised)	Two doses	EUA (Taiwan)
ZyCOV-D	DNA	Zydus Cadila	S	Three doses	EUA (India)
SpikoGen	Protein subunit	Vaxine/CinnaGen	S	Two doses	EUA (Iran)
EpiVacCorona	Peptide	Vektor State Research Center of Virology and Biotechnology	S peptides	Two doses	Approved (Russia, Belarus, Turkmenistan)
N/A	Inactivated virus	Wuhan Institute of Biological Products	Whole virus	Two doses	Approved in China and UAE
Vero Cells	Inactivated virus	Shenzen Kangtai Biological Products/ Beijing Minhai Biotechnology	Whole virus	Two doses	EUA in China
N/A	Inactivated virus	Chinese Academy of Medical Sciences, Institute of Medical Biology	Whole virus	Two doses	EUA in China
N/A	Protein subunit	Anhui Zhifei Longcom/ Chinese Academy of Medical Sciences, Institute of Medical Biology	S	Three doses	EUA in China and Uzbekistan

QazVac	Inactivated virus	Research Institute for Biological Safety Problems	Whole virus	Two doses	Phase III on-going.
COVIran	Inactivated virus	Shifa Pharmed Industrial Group	Whole virus	Two doses	Phase III on-going.
Abdala	Protein subunit	Center for Genetic Engineering and Biotechnology	S	Three doses	Phase III on-going. EUA in Cuba and Iran
Soberana 2	Protein subunit	Instituto Finlay De Vacunas	S	Two doses	Phase III on-going. EUA in Cuba and Iran
FAKHRA VAC	Inactivated virus	Organization of Defensive Innovation and Research	Whole virus	Two doses	EUA in Iran. Progress stopped after phase II trial, due to lack of demand

Table adapted from [374,375]. N/A = information not available.

1.3.6 Variants of concern

Merely a few months after the onset of the COVID-19 pandemic, the first reports of emergent SARS-CoV-2 variants materialised. Highly prevalent strains potentially associated with increased transmissibility, increased disease severity, or escape from humoral immunity generated after prior infection or vaccination have been classified as variants of concern (VOCs) by the WHO, US Centers for Disease Control and Prevention (CDC), and COVID-19 Genomics UK Consortium (COG-UK)[376-379]. Variants that have spread less widely but contain mutations like those present within VOCs have been classified as variants of interest (VOIs). SARS-CoV-2 variants are classified based on their lineage (named using the Greek alphabet) and defining mutations. Major SARS-CoV-2 VOCs have included Alpha (B.1.1.7), Beta (B.1.351), Gamma (P.1), Delta (B.1.617.2), and most recently Omicron (B.1.1.529) (Figure 1-8). VOIs include Epsilon (B.1.427 and B.1.429), Kappa (B.1.617.1), Iota (B.1.526), Eta (B.1.525), Zeta (P.2), Theta (P.3), and Lambda (C.37)[376-379].

SARS-CoV-2 variants harbour a distinctive repertoire of mutations. Most mutations of virological and epidemiological importance occur within the gene encoding S[316]. Generally, the S1 domain of SARS-CoV-2 S displays more amino acid variability than S2. Within S1, amino acid changes are

largely concentrated in the RBD and the NTD[317]. Within the RBD, the RBM is more variable than the RBD core. Some key mutations include D614G, P681R, and RBD mutations E848K, N501Y, K417N, L452R, N439K, and S477N[316] (Figure 1-8). Most of these mutations arose in multiple SARS-CoV-2 lineages.

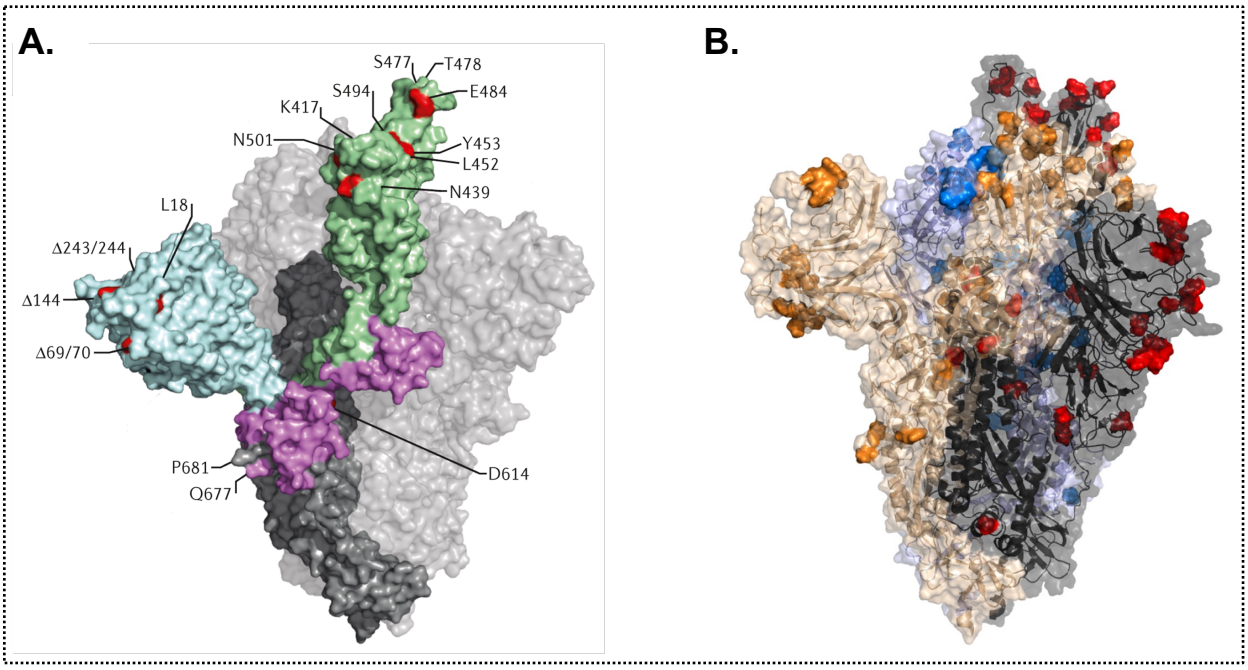


Figure 1-8. SARS-CoV-2 S mutations in VOCs. (A) Structural depiction of the sites of 16 key S1 mutations on the SARS-CoV-2 S trimer, including 9 in the RBD (green), four in the NTD (cyan), and three in the carboxy-terminal domain (CTD; purple). S2 is shown in dark grey. The S trimer figure was derived from a cryo-electron microscopy structure (Protein Databank Code: 7BNN). **(B)** S protein of SARS-CoV-2 Omicron VOC, with previously uncharacterized mutations shown in red, blue, gold, and black. *Image A and legend sourced from[379];image B sourced from The Centre for Virus Research, University of Glasgow, UK.*

S protein mutation D614G emerged early in the pandemic and is found in many circulating SARS-CoV-2 variants. The D614G mutation appears to increase the likelihood that RBD is in the open versus closed position, thereby increasing the probability of ACE2 binding[380]. D614G mutants replicate to higher levels in primary human airway cells and in the upper respiratory tract of hamsters and are also associated with increased transmission between hamsters[381]. In some studies,

viruses with D614G have been slightly more susceptible to neutralisation by monoclonal antibodies, convalescent plasma, and plasma from vaccinated individuals, but in other studies the opposite was observed[382,383].

As mentioned in section 1.3.3, SARS-CoV-2 S requires cleavage into S1 and S2 domains by cell proteases, like TMPRSS2, to complete virus-host membrane fusion. Mutations just upstream of the polybasic S1/S2 furin cleavage—including Q675H/R, Q677H/P, N679K and P681H/R—have occurred independently in many SARS-CoV-2 variants[384]. P681H is present in the Alpha VOC and the Theta VOI, whereas P681R is found in the Delta VOC and the Kappa VOI[385]. P681H/R substitutions appear to influence virus tropism by increasing S1/S2 cleavage in human airway epithelial cells, resulting in higher viral loads[386-388].

RBD mutations in particular influence the neutralisation activity of antibodies in diverse ways. Variants, such as Beta and Gamma, with the E484K mutation are associated with at least a three-fold reduction in susceptibility to 40% of convalescent plasma samples and 30% of plasma samples collected from mRNA-vaccinated persons[317,389-392]. N501Y is present in the Alpha, Beta, and Gamma VOCs. N501Y increases ACE2 affinity and increases virus replication in human upper-airway cells and in the upper respiratory tracts of hamsters[393-396]. N501Y does not influence binding or neutralisation by most monoclonal antibodies and is rarely associated with reduced sensitivity to plasma from previously infected or immunised individuals[397-399].

Other RBD mutations include, K417N/T, which are present in the Beta (as K417N) and Gamma (as K417T) VOCs. However, K417N/T rarely occur in the absence of other RBM mutations[317,400]. K417N confers over 100-fold and ten-fold reduced susceptibility to etesevimab and casirivimab, but retains susceptibility to other monoclonal antibody cocktails (bamlanivimab, imdevimab,

sotrovimab) and polyclonal sera/plasma from (mRNA) vaccinees or previously exposed individuals[389,401-403]. L452R is present in the Delta VOC, as well as the Kappa (B.1.617.1) and Epsilon (B.1.427/9) VOIs[404]. It reduces susceptibility to several monoclonal antibodies as well as to convalescent and vaccinee plasma samples[405-408]. Less common RBD mutations include, N439K, S477N, and T478K, which increase ACE2 binding affinity, but do not appear to impact susceptibility to convalescent or vaccinee plasma samples[409-411]. By contrast, F490S and S494P mutants may be significantly refractory to neutralisation by several monoclonal antibodies, including bamlanivimab and casirivimab[405,412,413].

NTD deletions are present in several VOCs and VOIs and have also been reported in patients with prolonged SARS-CoV-2 infections[414,415]. Deletions at positions 69-70 appear to be associated primarily with increased virus replication whereas those between positions 141-146 and 242-244 interfere with the neutralising activity of NTD-binding antibodies[416,417]. Other NTD mutations, including L18F and D253Y, also reduce susceptibility to NTD-neutralising antibodies. Finally, mutations outside the S protein have been reported to increase SARS-CoV-2 transmissibility by antagonising the host response to type I interferons[418]. But these are not associated with disruptions in neutralising antibody binding.

A brief summary of key VOCs, VOIs, and now de-escalated variants of concern (dVOC) is provided in Table 1-3. Key S protein mutations of interest are listed along with purported impacts on transmissibility, susceptibility to neutralisation, or disease severity. Published data on the Omicron variant is currently lacking, but this variant carries several previously uncharacterised mutations, the effects of which are currently under investigation (Figure 1-8).

Table 1-3. SARS-CoV-2 variants of concern.

Design-ation	WHO label	Lineage	Detection	S mutations of interest	Impact on transmission, immunity, or disease severity?
VOC	Beta	B.1.351	South Africa, September 2020	K417N, E484K, N501Y, D614G, A701V	T: Yes, I: Yes, S: Yes
VOC	Gamma	P.1	Brazil, December 2020	K417T, E484K, N501Y, D614G, H655Y	T: Yes, I: Yes, S: Yes
VOC	Delta	B.1.617.2	India, December 2020	L452R, T478K, D614G, P681R	T: Yes, I: Yes, S: Yes
VOC	Omicron	B.1.1.529	South Africa & Botswana, November 2021	A67V, Δ69-70, T95I, G142D, Δ143-145, Δ211-212, ins214EPE, G339D, S371L, S373P, S375F, K417N, N440K, G446S, S477N, T478K, E484A, Q493R, G496S, Q498R, N501Y, Y505H, T547K, D614G, H655Y, N679K, P681H, N764K, D796Y, N856K, Q954H, N969K, L981F	T: NA, I: NA, S: NA
VOI	Mu	B.1.621	Colombia, January 2021	R346K, E484K, N501Y, D614G, P681H	T: Yes, I: Yes, S: NA
VOI	Lambda	C.37	Peru, December 2020	L452Q, F490S, D614G	T: NA, I: Yes, S: NA
dVOC	Alpha	B.1.1.7	United Kingdom, September 2020	N501Y, D614G, P681H	T: Yes, I: No, S: Yes
dVOC	Epsilon	B.1.427/ B.1.429	USA, September 2020	L452R, D614G	T: NA, I: Yes, S: NA
dVOC	Eta	B.1.525	Nigeria, December 2020	E484K, D614G, Q677H	T: NA, I: Yes, S: NA
dVOC	Theta	P.3	The Philippines, January 2021	E484K, N501Y, D614G, P681H	T: Yes, I: Yes, S: NA
dVOC	Kappa	B.1.617.1	India, December 2020	L452R, E484Q, D614G, P681R	T: Yes, I: Yes, S: NA
dVOC	Iota	B.1.526	USA, December 2020	E484K, D614G, A701V	T: NA, I: Yes, S: NA
dVOC	Zeta	P.2	Brazil, January 2021	E484K, D614G	T: NA, I: Yes, S: NA

Table adapted from[419]. T = impact on transmission, I = impact on immunity, S = impact on disease severity, NA = data not available.

1.3.7 Animal models of infection

Diverse arrays of animal species were tested for susceptibility to SARS-CoV-2 infection at the onset of the COVID-19 pandemic. Suitable animal models have played an important role in studies of SARS-CoV-2 pathogenesis. Furthermore, the identification of models of infection providing measurable readouts to enable the testing of therapeutic agents, vaccines, and other medical countermeasures has been critical. Interspecies variability in ACE2 may be one factor determining host sensitivity to SARS-CoV-2[420]. For example, Old Word NHPs support high levels of SARS-CoV-2 replication and share 20 identical amino acid residues at the interface of the ACE2 binding site with RBD with humans[421,422]. Conversely, marmosets a New World NHP, harbour lower residue conservation and display (relatively) more resistance to SARS-CoV-2 infection[423]. Wildtype mice (expressing only murine ACE2) exhibit limited sensitivity to SARS-CoV-2; however, mice genetically engineered or transduced to express human ACE2 (hACE2) develop severe or fatal disease[424,425]. In addition to sequence similarity, the tissue distribution of ACE2 may also modulate susceptibility to and pathogenesis of SARS-CoV-2 infection. The ACE2 receptor of ferrets and minks both exhibit limited binding affinity with SARS-CoV-2 S[426,427]. Nevertheless, infection results in mild-to-moderate clinical signs in the former and fatal disease in the latter, which may be attributed to restricted ACE2 expression in the lower respiratory tract of ferrets[428,429]. However, it is likely that ACE2 only partially accounts for species differences in outcomes to SARS-CoV-2 infection. The actual host-pathogen interactions governing sensitivity to, and severity of, infection are likely more complex. To summarise briefly, hamsters, ferret, mink, African green monkeys, rhesus macaques, and cynomolgus macaques are highly susceptible to SARS-CoV-2 infection, while marmosets and wild-type mice are relatively less susceptible[426,427].

Interestingly, susceptibility to viral infection does not align with disease severity across species. For example, although rhesus and cynomolgus macaques support high levels of virus replication in the upper and lower respiratory tract within 48 hours after inoculation, the infection is cleared rapidly, and only mild-to-moderate clinical symptoms are observed[422,430,431]. Moreover, it has been challenging to identify an animal model which recapitulates the full spectrum of COVID-19 disease observed in humans[432]. Therefore, the selection of models for testing preventive or therapeutic interventions requires careful consideration of the outcome of interest, for example, prevention of severe disease versus a reduction in viral load. The rhesus macaque model, which has been employed for the SARS-CoV-2 studies featured in this thesis, is described in greater detail in Chapter 5. A summary of common COVID-19 animal models is provided in Table 1-4.

Table 1-4. Animal models of experimental SARS-CoV-2 infection.

Animal model	Route	Clinical and immunological features	Applications/limitations
hACE2 transgenic mice	IN	Bristled fur and weight loss. Moderate interstitial pneumonia. High viral titres in the nasal passage, lung, and brain. Lethal infection (dependent on dose).	App.: Vaccine and therapeutic testing. Lim.: Expression of hACE2 expression does not reflect natural ACE2 expression.
Syrian hamster	IN	Weight loss. Virus replication in the upper and lower respiratory tract. Nasal shedding detectable 1 day after inoculation. Significant lung pathology including inflammatory cell accumulation and consolidation.	App.: Vaccine and therapeutic testing. Studies on virus transmission. Testing of transmission-blocking interventions. Lim.: Short-lived infection kinetics. Severe lung damage without clinical signs of ARDS.
Ferrets	IN	Cough, elevated temperature, and lethargy. Transmission between animals observed. Viral RNA detected in upper and lower respiratory tract, and in intestines.	App.: Vaccine and therapeutic testing. Studies on virus transmission. Lim.: Mild clinical disease and mild lung pathology.
Mink	IN	Severe-to-fatal disease with signs of ARDS. Lung lesions similar to those found in severe COVID-19 patients.	App.: Studies on the pathogenesis of severe COVID-19. Lim.: Animals are not easily available or easy to work with.
Rhesus and cynomolgus macaques	IN, IT, Oral, Ocular	Changes in respiratory patten, loss of appetite, piloerection, dehydration, and weight loss. High viral loads in the upper respiratory tract. Low-to-moderate viral loads in the lower respiratory tract and intestines. Mild-to-moderate interstitial pneumonia with pulmonary infiltrates and radiographic abnormalities. Cynomolgus macaques exhibit slightly lower susceptibility to infection than rhesus macaques.	App.: Vaccine and therapeutic testing. Lim.: Self-limiting infection with transient clinical signs, severe or lethal disease outcomes are not observed.

Common marmoset	IN, IT	Slight elevation in temperature. Low levels of viral RNA detected in nasal swabs.	Lim.: Limited histopathological changes observed in lungs. Animals are relatively resistant to SARS-CoV-2 infection.
African green monkey	IN, IT, Oral, Ocular	Low grade fever. Changes in respiratory pattern. High viral loads in upper and lower respiratory tract. Viral RNA also detected in intestinal tract. Pulmonary pathology shows signs of acute bronchiolitis, interstitial pneumonia, and mild-to-severe lesions. ARDS may be observed in some older animals.	App.: Vaccine and therapeutic testing. Pathogenesis studies. Lim.: Not as accessible as other NHP models. Significant variation in infection outcomes between animals and between studies.

App. = model applications, Lim. = model limitations

1.4 Thesis aims and outline

Overall hypothesis: Through the employment of animal models, the research presented in this thesis will characterise immune responses to vaccination against and infection with LASV or SARS-CoV-2. These results will inform current knowledge of disease pathogenesis, subsequent vaccine clinical trials, and will critically highlight limitations of *in vivo* animal experimentation, thereby identifying areas for future improvement in research study design.

1.4.1 Aims

Aim 1: Evaluate the immunogenicity of ChAdOx1-vectored vaccines for Lassa fever.

Aim 2: Assess the efficacy of ChAdOx1-Lassa-GPC in lethal rodent and non-human primate models of LASV infection.

Aim 3: Characterise immune responses elicited by ChAdOx1 nCoV-19 in rhesus macaques and describe immunophenotypic changes occurring after SARS-CoV-2 challenge.

Aim 4: Elucidate age-related differences in the clinical, virological, and immunological outcomes of SARS-CoV-2 infection in rhesus macaques.

1.4.2 Outline

Chapter 2 outlines the materials and methods employed for this research.

Chapter 3 describes the early-stage development of a Lassa fever vaccine candidate, ChAdOx1-Lassa-GPC, immunogenicity testing in mice, and preliminary efficacy assessment in a rodent model of infection.

Chapter 4 demonstrates the efficacy of ChAdOx1-Lassa-GPC in protecting cynomolgus macaques against lethal LASV infection.

Chapter 5 characterises immune responses induced by ChAdOx1 nCoV-19 in rhesus macaques and investigates immunological and virological outcomes post SARS-CoV-2 challenge.

Chapter 6 compares immune dynamics after SARS-CoV-2 infection in older versus younger rhesus macaques.

Chapter 7 summarises the principal findings from this thesis and discusses limitations of the executed studies, overall significance, and future directions.

2

Materials and methods

2.1 Materials

2.1.1 Reagents

Commercially available reagents are listed in Table 2-1. These exclude flow cytometry antibodies, which are listed in panel-specific tables in the corresponding methods sections.

Table 2-1. Commercially available reagents

Reagent/material	Supplier	Catalogue number
15 mL falcons	Corning	430052
150 cm^2 tissue culture flask	Corning	431465
4% paraformaldehyde	Biotium	22023
5 mL polypropylene FACS tubes	Becton Dickinson	352063
50 mL falcons	Corning	430290
70 µM Falcon™ Cell Strainers	Fisher Scientific	352350
75cm^2 tissue culture flask	Corning	430641
96-well cell culture plate	Corning	3595
96-well U-bottom plates	Thermo Fisher	163320
96-well V-bottom plates	Thermo Fisher	277143
Alkaline phosphatase-conjugated goat anti-mouse IgG	Sigma	A3562
ALP conjugate substrate kit	BioRad	1706432
AMPure XP-bead purified using 0.95X beads	Beckman Coulter	E7420
AR6 buffer	Akoya Biosciences	AR600250ML
ArC™ Amine Reactive Compensation Bead Kit	Invitrogen	A10346
AVL Buffer	Qiagen	19073
BioAnalyzer DNA 1000 Chips	Agilent Technologies	5067-1504
Blocker Casein in PBS	Thermo Fisher	37528
Bovine serum albumin (BSA)	Sigma-Aldrich	A9418

Chromium Single Cell Reagent Kit (version 3.0 Chemistry)	10X Genomics	PN-1000075
ChromoMap DAB Kit	Roche Tissue Diagnostics	760-159
Cytofix/Cytoperm Fixation Permeabilization Solution	BD	554714
DAPI stain	Sigma-Aldrich	D9542-5MG
Dimethyl sulfoxide (DMSO)	Sigma-Aldrich	D2650
DNase I	Roche	3539121103
Dulbecco's modified eagle medium (DMEM)	Sigma-Aldrich	D6546
Dulbecco's phosphate buffered saline (DPBS)	Gibco	14190250
eBioscience™ Cell Stimulation Cocktail (PMA/ionomycin)	Invitrogen	00-4970-03
EZ-Link™ NHS-PEG4-Biotin, No-Weigh™ Format Kit	Thermo Fisher	A39259
FITC-conjugated-anti-C3 antibody	MP Biomedical	855385
Fluoromount-G	Southern Biotech	0100-01
Foetal bovine serum	Gibco	16000044
Gelatin veronal buffer	Boston Bioproducts	IBB-300X
gentleMACS™ dissociation	Miltenyi	130-093-237
Glo Lysis Buffer	Promega	E2661
GolgiPlug (Brefeldin A)	BD	555029
GolgiStop (Monensin)	BD	554724
GP1 LASV HuMAb 12.1F – Lassa virus glycoprotein subunit 1 Clone 12.1F	Zalgen Labs	---
GPC LASV HuMAb 25.10C – Lassa virus glycoprotein complex Clone 25.10C	Zalgen Labs	---
GPC LASV HuMAb 37.2D – Lassa virus glycoprotein complex Clone 37.2D	Zalgen Labs	---
GPC LASV HuMAb 8.9F – Lassa virus glycoprotein subunit 1 Clone 8.9F	Zalgen Labs	---
Guinea pig complement	Cedarlane Labs	CL4051
Histopaque®-1077 density-gradient medium	Sigma-Aldrich	10771-500ML
Human IFNγ Single-Color ELISPOT	Cellular Technologies Limited	---
Human IgG ELISpot BASIC Kit	Mabtech	3850-2A
Human TNFα Single-Color ELISPOT	Cellular Technologies Limited	---
Illumina NextSeq High Output Kit (150 cycle)	Illumina	20024907
Illumina Stranded mRNA Prep	Illumina	20040534
ImPress VR anti-rabbit IgG polymer	Vector Laboratories	MP-6401
Isotyping Panel 1 Human/NHP Kit	MESO Scale Diagnostics	K15203D
Kapa Quantification Kit for Illumina Sequencing	Kapa Biosystems	KR0405 - 7960166001
KPL affinity-purified polyclonal antibody peroxidase-labelled goat-anti-monkey IgG (H)	SeraCare	074-11-021
KPL peroxidase-labelled goat-anti-guinea pig IgG (H&L) antibody	SeraCare	5220-0366
L-glutamine	Gibco	5185-5990
LASV glycoprotein antigen, strain Josiah, pre-fusion GP monomer, lineage IV	Zalgen Labs	LASV-GP-017
LASV glycoprotein antigen, strain LASV237 Nigeria 2010H, pre-fusion GP monomer, lineage II	Zalgen Labs	LASV-GP-015
LASV glycoprotein antigen, strain NIG08-A18-2008H, pre-fusion GP monomer, lineage III	Zalgen Labs	LASV-GP-016
LASV glycoprotein antigen, strain Pinneo, pre-fusion GP monomer, lineage I	Zalgen Labs	LASV-GP-014

LASV NP antibody	Cusabio Technology	PA318401LA01LNP
LASV NP, full length lineage IV	Zalgen Labs	LASV-R-0041
LeucosepTM tubes	Greiner Bio-One	227290
Liberase TL	Roche	5401020001
MAD Nasal™ IN Mucosal Atomization Device	Teleflex	MAD110
Minimum essential medium - alpha modification (alpha-MEM)	Sigma-Aldrich	M4655
Mouse IFNγ ELISpot BASIC kit (ALP)	Mabtech	3321-2A
Nasosorption FX.i	Hunt Developments UK Ltd	---
Non-Human Primate Cytokine MILLIPLEX Map 23-plex Kit	Millipore	PCYTMG-40K-PX23
Nunc MaxiSorp plates	Thermo Fisher	44-2404-21
Opal 7-Color Automation IHC Kit	Akoya Biosciences	NEL821001KT
Opal polymer anti-mouse and anti-rabbit HRP-conjugated secondary antibodies	Akoya Biosciences	ARH1001EA
p-nitrophenyl phosphate (pNPP)	Sigma-Aldrich	32160405
Penicillin-streptomycin	Gibco	25030164
Perm/Wash Buffer	BD	554723
PureAffin R56	UTECH	EEPAR56
PVDF-membrane MSIP plates	Millipore	3654-WP-10
QIAamp Viral RNA Mini Kit	Qiagen	52904
Qiagen AllPrep DNA spin columns	Qiagen	80204
QuantiFast master mix	Qiagen	204654
Qubit™ RNA High Sensitivity Assay Kit	Thermo Fisher	Q32852
RBC Lysis Buffer	BioLegend	420302
Recombinant human IL-15	STEMCELL Technologies	78031
Red FluoSpheres™ NeutrAvidin™-Labeled Microspheres	Thermo Fisher	F8775
RLT buffer	Qiagen	79216
RNAscope 2.5 VS assay	Advanced Cell Diagnostics	312039
RNeasy Mini Kit	Qiagen	74104
RosetteSep™ Human NK Cell Enrichment Cocktail	STEMCELL Technologies	15065
Roswell Park Memorial Institute (RPMI) 1640 medium	Sigma-Aldrich	R8758
Rotor-Gene™ Probe Kit	Qiagen	204574
Savant™ DNA120 SpeedVac™	Thermo Fisher	13442549
Sep-Pak® 3 mL, 200 mg, C18	Waters Corporation	WAT054945
Spin filter	Agilent Technologies	5185-5990
Stop Solution	SeraCare	5150-0021
Streptavidin BV421	BioLegend	405225
Streptavidin PE-Dazzle 594	BioLegend	405248
Streptavidin PE-Cy7	BioLegend	405206
THP-1 cells (TIB-202)	ATCC	---
TMB 2-component peroxidase substrate	SeraCare	5120-0047
TRIS-buffered saline (TBS)	Thermo Fisher	J60764.K2
TRIzol™ Reagent	Thermo Fisher	15596026
Trypan Blue Solution, 0.4%	Gibco	15250061
Tween-20	Sigma-Aldrich	P9416
U-PLEX Chemokine Combo 1 (NHP) Kit	MESO Scale Diagnostics	K15055K
Ultra-LEAF™ purified anti-human CD49d antibody	BioLegend	304340
UltraComp eBeads™ Compensation Beads	Thermo Fisher	01-2222-42
V-PLEX COVID-19 Coronavirus Panel 1 (IgG) Kit	MESO Scale Diagnostics	K15362U
V-PLEX NHP Cytokine 24-Plex Kit	MESO Scale Diagnostics	K15058D
V-PLEX SARS-CoV-2 Panel 2 (IgA)	MESO Scale Diagnostics	K15385U
V-PLEX SARS-CoV-2 Panel 2 (IgG)	MESO Scale Diagnostics	K15383U

Ventana Discovery ULTRA slide auto staining system	Ventana Medical Systems	---
Water XBridge® Amide column (3.5 µm, 3 mm X 100 mm)	Waters Corporation	186004864
Xylene	Newcomer Supply	ABSB-04
Zeba™ Spin Desalting Columns	Thermo Fisher	89892

2.1.2 Vaccines

2.1.2.1 ChAdOx1-Lassa-GPC

ChAdOx1-Lassa-GPC was cloned by Dr. Sarah Sebastian and produced by the Viral Vector Core Facility (VVCF) of The Jenner Institute, University of Oxford. Briefly, the gene encoding GPC of Josiah strain LASV (GenBank accession number J04324.1, position 1872-3374) was codon optimised for expression in human cell lines and synthesised by GeneArt (Thermo Fisher). InFusion cloning (Clontech) was used to insert the antigen sequence into a shuttle plasmid containing a modified human cytomegalovirus immediate early promoter (IE CMV), with a tetracycline operator (TetO) and bovine growth hormone (BGH) polyadenylation signal, between Gateway® recombination sites. Gateway® recombination (Thermo Fisher) was carried out between the shuttle plasmid and a bacterial artificial chromosome (BAC) destination vector encoding the ChAdOx1 genome, as previously described[99]. Site-specific recombination resulted in insertion of the transgene into the ChAdOx1 E1 locus. Unique PmeI sites flanking the adenovirus genome sequence enabled excision of ChAdOx1 from the BAC backbone. The virus was rescued and propagated in T-Rex 293 HEK cells, which repress antigen expression during virus production. Purification was carried out by CsCl gradient ultracentrifugation. Virus titres were determined by hexon immunostaining assay; spectrophotometry was used to determine viral particle (VP) concentrations[433,434]. Vaccine doses in mice and guinea pigs were based on infectious units (IU), whereas doses in NHPs were based on VP numbers.

2.1.2.2 ChAdOx1 nCoV-19

ChAdOx1 nCoV-19 was synthesised by members of The Jenner Institute and VVCF. The S protein of SARS-CoV-2 (GenBank accession number YP_009724390.1) was codon optimised for expression in human cell lines and synthesised with a 5' tissue plasminogen activator (tPA) leader sequence by GeneArt (Thermo Fisher). Transgene cloning, Gateway recombination® with a ChAdOx1-encoding BAC, rescue of recombinant viruses, and virus titration was completed as described in section 2.1.2.1.

2.1.3 Viruses

SARS-CoV-2 and LASV isolates were obtained from the sources listed in Tables 2-2 (SARS-CoV-2) and 2-3 (LASV). All virus propagation was performed in Vero E6 cells in Dulbecco's Modified Eagle Medium (DMEM) supplemented with 2% foetal bovine serum (FBS), 1 mM L-glutamine, 50 U/ml penicillin and 50 µg/ml streptomycin (D2).

Table 2-2. SARS-CoV-2 strain information.

SARS-CoV-2 isolate	Virus (or sequence) identification number	Source
SARS-CoV-2/human/USA/WA-CDC-WA1/2020	MN985325.1	CDC, Atlanta, USA
SARS-CoV-2/human/USA/RML-7/2020	MW127503.1	Isolated at RML from a nasopharyngeal swab obtained on July 19, 2020.
hCoV-19/England/204820464/20200 (referred to as B.1.1.7 throughout the thesis)	GISAID: EPI_ISL_683466	Public Health England, UK and BEI, NIAID, NIH, USA
hCoV-19/USA/MD-HP01542/2021 (referred to as B.1.351 throughout the thesis)	GISAID: EPI_ISL_890360	Dr. Andrew Pekosz, Johns Hopkins University Bloomberg School of Public Health, Baltimore, USA
hCoV-19/USA/KY-CDC-2-4242084/2021 (referred to as B.1.617.2)	GISAID: EPI_ISL_1823618	BEI, NIAID, NIH, USA

Table 2-3. LASV strain information.

LASV isolate	Virus (or sequence) identification number	Source
Lassa mammarenavirus/Josiah-GPA/Cavia porcellus/11620/2011 (referred to as GPA LASV throughout this thesis)	L segment: MW004546.1; S segment: MW004547.1	Dr. Thomas Geisbert, University of Texas Medical Branch, Galveston, USA
Lassa mammarenavirus/Josiah/Homo sapiens/11620	L segment: JN650518.1; S segment: JN650517.1	USAMRIID, Fort Detrick, USA

2.1.4 VSV-Lassa-GPc-cFLAG and VSV-SARS-CoV-2-S pseudotyped viruses

Recombinant VSV was pseudotyped with LASV GPC (strain Josiah) or SARS-CoV-2 S (strain nCoV-WA1-2020) to create VSV-Lassa-GPc-cFLAG and VSV-SARS-CoV-2-S, respectively. Pseudotyped VSV particles were produced by Dr. Michael Letko. Briefly, antigenic (LASV GPC or SARS-CoV-2 S) sequences were codon optimised for human cells and appended to the nucleotide sequence for a FLAG-tag (DYKDDDDK). LASV GPC, specifically, was further modified by addition of a 3' tri-glycine linker (GGGS). Synthesised antigens were cloned into pcDNA3.1+ plasmids (GenScript); accuracy of the constructs was confirmed by Sanger sequencing (ACGT). Finally, replication-incompetent VSV particles, expressing GFP and luciferase reporters, were pseudotyped with the selected antigens by transfection of 293T cells as previously described[435-437].

2.1.5 Cells

Vero E6 and 293T cells were maintained in DMEM supplemented with 10% FBS, 1 mM L-glutamine, 50 U/ml penicillin and 50 µg/ml streptomycin (D10). Mycoplasma testing was performed at regular intervals and was not detected at any point during the studies.

2.2 Methods – Animal experiments

2.2.1 Ethics

CD-1 mice were used in accordance with the UK Animals (Scientific Procedures) Act under project license number P9804B4F1 granted by the UK Home Office. Animals were group housed in individually ventilated cages under specific pathogen free conditions, with constant temperature and humidity with lighting on a fixed light/dark cycle (12-hours/12-hours).

Approvals for guinea pig and NHP challenge experiments were provided by the Institutional Animal Care and Use Committee (IACUC) at RML, NIAID, NIH. Animal experiments were executed in an Association for Assessment and Accreditation of Laboratory Animal Care (AALAC)-approved facility by certified staff, following the basic principles and guidelines in the NIH Guide for the Care and Use of Laboratory Animals, the Animal Welfare Act, and the United States Department of Agriculture and United States Public Health Service Policy on Humane Care and Use of Laboratory Animals. Guinea pigs were companion housed, while rhesus and cynomolgus macaques were individually housed in cages allowing social interactions, in a climate-controlled room with a fixed light/dark cycle (12-hours/12-hours). Water was available ad libitum; food and environmental enrichment were provided by trained personnel. After virus challenge, animals were monitored a minimum of once daily.

2.2.2 Biosafety

The Institutional Biosafety Committee (IBC) approved work with infectious LASV and SARS-CoV-2 strains under BSL4 and BSL3 conditions, respectively. All NHP challenge experiments were carried out in the animal BSL4 (ABSL4) laboratory at RML, NIAID, NIH due to space and caging requirements. Inactivation of infectious samples was performed according to IBC approved standard operating procedures for removal of specimens from high containment.

2.2.3 Murine immunogenicity experiments

Female CD-1 mice, aged 6-8 weeks, were immunised via IM injection in the left hind leg. A dose of $1x10^8$ IU of the appropriate vaccine was delivered in a total volume of 50 µL and diluted in sterile Dulbecco's phosphate buffered saline (DPBS). Where applicable, prime and boost vaccinations were administered 28 days apart. Study endpoints were 21 days (single dose versus prime-boost vaccination experiment, section 3.2.1-3.2.2), 14 days (assessment of cross-reactive T-cell responses, section 3.2.4), and 28 days (evaluation of cross-reactive antibody responses, section 3.2.4) after immunisation. At the study endpoint, blood was collected via cardiac puncture, animals were euthanized via cervical dislocation, and spleens were harvested for further immunological analysis.

2.2.4 Efficacy of ChAdOx1-Lassa-GPC in Hartley guinea pigs

Mixed gender Hartley strain guinea pigs, age matched to 14 weeks at the time of challenge, were vaccinated with $3x10^8$ IU of ChAdOx1-Lassa-GPC or $1x10^8$ IU of ChAdOx1-GFP (control vaccine) via the IM route. Vaccines were diluted in sterile DPBS. Study procedures are reported chronologically in terms of days post challenge (DPC). The prime-boost group (n=10) was

immunised with ChAdOx1-Lassa-GPC on -56 and -28 DPC, the prime group (n=10) received a single dose of ChAdOx1-Lassa-GPC on -28 DPC, and control animals (n=10) received a single dose of ChAdOx1-GFP vaccine on -28 DPC. On 0 DPC, animals were challenged with $1x10^5$ $TCID_{50}$ of Josiah strain-derived GPA LASV, diluted in sterile DMEM, which is equivalent to 100 times 50% of the lethal dose (LD_{50}) via two IP injections[149]. Animals underwent daily post-challenge monitoring for body temperature, weight, and signs of disease (lethargy, guarded posture, and laboured respiration). At 12 DPC, four animals from each group were euthanized. The remaining animals in each group comprised the survival cohorts; these animals were euthanized upon meeting humane endpoint criteria (>20% weight loss) or, in the case of survivors, at the study endpoint (28 DPC). Sera were collected at -56, -28, 0, 12, and 28 DPC. During necropsies, blood, lung, liver, and spleen samples were collected from all animals for virological and histopathological analyses. Data from this study are presented in section 3.2.3.

2.2.5 Efficacy of ChAdOx1-Lassa-GPC in cynomolgus macaques

Adult female cynomolgus macaques received $2.5x10^{10}$ VP of ChAdOx1-Lassa-GPC or ChAdOx1-GFP (control vaccine), diluted in sterile DPBS, via the IM route. ChAdOx1-Lassa-GPC prime-boost recipients (n=4) and controls (n=4) were vaccinated on -56 and -28 DPC, whereas ChAdOx1-Lassa-GPC prime recipients (n=4) were immunised on -28 DPC only. EDTA whole blood and sera were collected on -56, -42, -28, -14, -7, and 0 DPC. All animals were challenged with $1x10^4$ $TCID_{50}$ of LASV strain Josiah (diluted in sterile DMEM), delivered IM, on 0 DPC. After LASV challenge, animals were monitored daily and scored for clinical indicators of disease by a trained member of RMVB. Standardised clinical scores were used to identify animals reaching humane endpoint criteria (cumulative score of ≥ 35), at which point they were euthanized. Scoring

was based on the following criteria: general appearance, temperature (fever), appearance of skin and coat, appetite, activity, respiration, discharge, and the appearance of faeces and urine. The scoring sheet can be found in Appendix 2[430]. Surviving animals were followed until the endpoint of the study, 42 DPC, prior to euthanasia. Post challenge, EDTA whole blood and sera were collected at 3, 6, 9, 12, 15, and 21 DPC, as well as at the time of euthanasia. Complete blood counts (CBC) and serum biochemistry assessment was carried out using the ProCyte Dx Haematology Analyzer (Idexx) and the Vetscan VS2 Chemistry Analyzer (Abaxis), respectively. Liver, lung, spleen, and cervical lymph node tissues were collected for virological and histopathological assessment at the time of necropsy. BAER auditory testing was performed to detect evidence of sensorineural hearing loss using a BAERCOM electroencephalography (EEG) portable instrument (UFI) at -56, -7, and 42 DPC. The results from this study are reported in Chapter 4.

2.2.6 Efficacy of ChAdOx1 nCoV-19 (IM and IN) in rhesus macaques

2.2.6.1 IM delivery of ChAdOx1 nCoV-19

Adult male rhesus macaques were vaccinated via the IM route with $2.5x10^{10}$ VP (diluted in sterile DPBS) of ChAdOx1 nCoV-19 at -56 and -28 DPC (n=6) or ChAdOx1 GFP at -28 DPC (n=6). EDTA whole blood and sera were obtained at -56, -42, -28, -14, and 0 DPC. Animals were challenged with SARS-CoV-2 strain nCoV-WA1-2020 (diluted in sterile DMEM) on 0 DPC; $4x10^5$ $TCID_{50}$/mL of virus suspension was administered through IT (4 mL), IN (1 mL), oral (1 mL), and ocular (0.5 mL) routes (total dose of $2.6x10^6$ $TCID_{50}$). Nasal swabs were collected on all exam dates. Bronchoalveolar lavage (BAL) fluid (BALF) and sera were collected on 3 and 5 DPC. BAL was performed by insertion of an endotracheal tube and bronchoscope into the trachea and subsequent installation of 10 mL of sterile DPBS. Manual suction was applied to retrieve the

BALF sample. Necropsy was performed on 7 DPC; EDTA whole blood and lung tissue (for flow cytometry and viral RNA detection) were collected from all animals (n=6 per group). Additionally, lung cells and splenocytes were obtained specifically for single-cell RNA sequencing (scRNAseq) and intracellular cytokine staining (ICS), respectively, from six vaccinees and three controls. The results from this study are reported in section 5.2.1-5.2.6.

2.2.6.2 IN delivery of ChAdOx1 nCoV-19

Adult rhesus macaques (5 female, 3 male) were vaccinated with 2.5 x 10^{10} VP (in 1 ml of sterile DPBS) of ChAdOx1 nCoV-19 (n=4) or ChAdOx1 GFP (n=4) using a MAD Nasal™ IN Mucosal Atomization Device (Teleflex) at -56 and -28 DPC. On 0 DPC, animals were challenged with 2x10^5 $TCID_{50}$/mL of SARS-CoV-2/human/USA/RML-7/2020 diluted in sterile DMEM, delivered IT (4 mL) and IN (1 mL). Clinical exams were performed on -56, -49, -42, -28, -21, -14, -7, 0, 1, 3, 5, and 7 DPC. Nasosorption samples and blood were collected at all exam dates. Nasosorption samples were collected as previously described[438]. Briefly, a nasosorption device (Hunt Developments UK Ltd) was inserted into the nasal cavity for 60 seconds prior to placement in 300 µl of AB-33K solution (DPBS containing 1% BSA and 0.4% Tween-20) and vortexing for 30 seconds. The swab and liquid were placed on a spin filter and centrifuged at 16,000 rpm for 20 minutes. Filtered liquid was aliquoted and stored at -80°C. Nasal swabs were collected on 0, 1, 3, 5, and 7 DPC. BAL was performed on 3, 5, and 7 DPI as described in section 2.2.6.1. Animals were euthanized on 7 DPC and multiple tissues were collected for virological assessment. Findings from this study are reported in section 5.2.7-5.2.8.

2.2.7 SARS-CoV-2 infection of older and younger rhesus macaques

Eight aged (16-23 years; 4 each female/male) and eight subadult (3-5 years; all male) rhesus macaques were inoculated with SARS-CoV-2 strain nCoV-WA1-2020 as described in section 2.2.6.1. Of note, the lifespan of rhesus macaques in captivity is around 35 years; the estimated equivalent age ranges corresponding with our study groups in humans are 48-69 years (older cohort) and 9-15 years (younger cohort) [439]. Animals were observed daily and scored for clinical signs using a standardised scoring sheet (Appendix 2), as described in section 2.2.5[430]. Clinical exams were performed on 0, 1, 3, 5, 7, 10, 14, 17, and 21 days post inoculation (DPI). On exam days, clinical parameters including weight, body temperature, and respiration rate were recorded, and ventro-dorsal and lateral chest radiographs were obtained. Body condition score (BCS) was assessed by a clinical veterinarian during each exam using a scale ranging from 1-9[440]. A BCS of 4-5 was considered ideal, scores of 1-3 were indicative of an underweight condition, and scores of 6-9 were indicative of an overweight condition. Blood and swabs (nasal, throat, and rectal) were collected during all clinical exams. Additionally, on -7, 3, and 7 DPI, BAL was performed as described in section 2.2.6.1. Four animals from each age group were euthanized at 7 and 21 DPI. Lung and spleen tissues were collected during necropsies. The results from this study are discussed in Chapter 6.

2.3 Methods – Immunology

2.3.1 Cell sample processing

2.3.1.1 Murine splenocytes

A single cell suspension of murine splenocytes was prepared by mechanical disruption of whole spleen tissue followed by filtration through a 70 µM cell strainer. Erythrocytes were lysed with ammonium-chloride-potassium (ACK) lysing buffer, and cells were resuspended in Minimum Essential Medium Eagle - alpha modification (alpha-MEM) supplemented with 10% FBS, 1 mM L-glutamine, 50 U/mL penicillin, and 50 µg/mL streptomycin.

2.3.1.2 Non-human primate cell samples

Peripheral blood mononuclear cells (PBMCs) were isolated from EDTA whole blood using Histopaque®-1077 density-gradient medium and Leucosep™ tubes according to the manufacturer's instructions. Cells were collected from BALF after filtration through a 70 µM cell strainer and centrifugation. Single cell suspension of lung cells and splenocytes were obtained by disrupting two pieces of tissue per organ (1 cm^3) using the gentleMACS™ dissociation system followed by enzymatic digestion with 0.1 mg/mL Liberase TL and 0.1 mg/mL DNase I in Roswell Park Memorial Institute (RPMI) 1640 medium at 37°C for 30 minutes. Undigested tissue was removed by pressing the sample through a 70 µM cell strainer and washing with RPMI-1640 medium supplemented with 10% FBS, 1 mM L-glutamine, 50 U/mL penicillin, and 50 µg/mL streptomycin (R10 medium). Erythrocyte removal was performed using RBC Lysis Buffer for 5 minutes at room temperature. All cell samples were treated to at least one final wash in R10

medium prior to resuspension in cryopreservation medium (FBS containing 10% DMSO) and transfer to -80ºC storage.

2.3.2 IgG ELISA

2.3.2.1 LASV IgG ELISA

IgG endpoint titre ELISAs were performed to detect LASV-specific antibodies in the sera of immunised CD-1 mice, Hartley guinea pigs, and cynomolgus macaques. Nunc MaxiSorp plates were coated with 2 μg/mL of LASV GP or NP antigen diluted in DPBS for overnight adsorption at 4°C. Plates were washed in DPBS with 0.1% Tween-20 (0.1% DPBS/T) and wells blocked using casein for one hour at room temperature. Serially diluted serum samples were added and incubated for two hours at room temperature. Plates were washed and a species-specific whole IgG conjugated antibody was added to the wells for one hour at room temperature: goat anti-mouse IgG conjugated to alkaline phosphatase (ALP, diluted 1:5000), peroxidase-labelled goat-anti-guinea pig IgG (dilute 1:1000), or peroxidase-labelled goat-anti-monkey IgG (diluted 1:1000). After washing, detection of LASV-specific mouse IgG was performed with *p*-nitrophenyl phosphate (*p*NPP) substrate and plates were read at 405 nm. Detection of LASV-specific guinea pig and macaque IgG was carried out with TMB 2-component peroxidase substrate and stop solution prior to reading plates at 450 nm. All sera samples were prepared in a two-fold dilution series starting at a 1:400 dilution in DPBS. A threshold for positivity was set using naïve CD-1 mouse, guinea pig, or macaque sera. A negative cutoff of the mean plus three times the standard deviation (SD) of the optical density (OD) of naïve sera was used to determine the endpoint titre.

2.3.2.2 SARS-CoV-2 anti-S IgG ELISA

SARS-CoV-2 anti-S IgG endpoint titre ELISA was performed on rhesus macaque sera as described in section 2.3.2.1 (for cynomolgus macaques), with the following modifications. Plates were coated overnight with 2 µg/mL of prefusion stabilised SARS-CoV-2 S protein with a T4 fibritin trimerization motif[441], which was obtained from the Vaccine Research Centre, Bethesda, USA. Endpoint titres were determined by establishing a negative cut-off of three times the OD value of the negative control (sera obtained from animals prior to start of the experiment) or 0.2— whichever value was higher.

2.3.3 ELISpot assays

2.3.3.1 Murine IFNγ ELISpot

Murine IFNγ ELISpot assays were performed using the Mouse IFNγ ELISpot^{BASIC} ALP Kit (Mabtech) according to the manufacturer's instructions. Briefly, ELISpot plates were coated overnight with an anti-mouse IFNγ capture antibody. Freshly isolated splenocytes were added to the wells of ELISpot plates in duplicates in a two-fold dilution series starting at $5x10^5$ cells/well. Cells were stimulated with pools of overlapping peptides spanning the LASV GPC sequence at a final concentration of 2 µg/mL per peptide (Mimotopes). A corresponding set of unstimulated, DMSO-treated samples and PMA/ionomycin-treated samples were established as negative and positive controls, respectively. ELISpot plates were incubated for 18-20 hours (at 37°C and 5% CO_2). IFNγ spot forming units (SFU) were detected by staining membranes with a species-specific anti-IFNγ biotinylated detection antibody (1µg/ml) for two hours, followed by streptavidin-ALP (1 µg/ml) for one hour, and development with an ALP conjugate substrate kit. Between each

staining step, plates were washed six times with DPBS. Following spot development, plates were rinsed in water. Antigen-specific T-cell responses were quantified by subtracting the responses in the unstimulated wells from those observed after peptide pool stimulation and reported in terms of SFU per $1.0x10^6$ cells. Once dry, murine ELISpot plates were read on an AID Classic ELISpot Reader (Autoimmun Diagnostika GmbH). Peptide library sequences are listed in Appendix 3.

2.3.3.2 NHP IFNγ and TNFα ELISpot

Cryopreserved PBMCs, splenocytes, and BAL cells were thawed, washed, and rested in R10 medium with 25 U/mL of Benzonase® Nuclease at 37ºC for six hours. Cells were plated at a concentration of $2.5x10^5$ cells per well in duplicates and were stimulated with three contiguous peptide pools spanning the LASV GPC amino acid sequence (GenScript) or two contiguous peptide pools spanning the sequences of the SARS-CoV-2 S protein subunits, S1 and S2, (GenScript). Again, peptide pools were diluted to a concentration of 2 µg/mL per peptide. ELISpot plates were incubated at 37ºC for 20-24 hours. Detection of cytokine-secreting cells was performed using the ImmunoSpot Human Single-Colour Enzymatic ELISpot Assay Kit for IFNγ and TNFα (Cellular Technologies Limited). Spot detection was carried out according to the manufacturer's protocol. Spots were counted using the CTL Analyzer and ImmunoSpot® 7 Software (Cellular Technologies Limited). Calculation of antigen-specific T-cell responses was carried out as described in section 2.3.3.1. Peptide library sequences are listed in Appendix 3.

2.3.3.3 NHP IgG B-cell ELISpot assay

PVDF-membrane MSIP plates were coated with capture anti-IgG antibody at a concentration of 15 µg/mL from the Human IgG B cell ELISpot Kit (Mabtech) and incubated overnight at 4ºC. On the following day, plates were washed and blocked with R10 medium at room temperature for at

least 30 minutes. Cryopreserved PBMCs were thawed, washed, and rested in R10 medium supplemented with Benzonase® Nuclease at a concentration of 25 U/mL at 37ºC for one hour. Cells were plated a concentration of $2.5x10^5$ cells per well. ELISpot plates were incubated at 37ºC for 20-24 hours. Detection of SARS-CoV-2 specific IgG antibody-secreting cells was performed using biotinylated S and RBD antigen at a concentration of 1 µg/mL. Spot development was performed according to the manufacturer's instructions. ELISpot plates were inactivated in 10% neutral buffered formalin overnight prior to removal from BSL4 and reading using the CTL Analyzer and ImmunoSpot® 7 Software.

2.3.4 Intracellular cytokine staining (ICS) assays

2.3.4.1 Murine ICS assay

Freshly isolated splenocytes ($1x10^6$ cells/well) were stimulated with a LASV GPC peptide pool (2 µg/mL per peptide), DMSO (unstimulated negative control), or PMA/ionomycin (positive control). Stimulation was carried out for six hours at 37ºC. GolgiPlug was added at a concentration of 1 µg/mL during the last 4 hours of stimulation. Subsequently, extracellular staining was carried out at 4ºC; the antibodies listed in Table 2-4 were diluted in DPBS with 0.05% bovine serum albumin (0.05% DPBS/BSA). Cells were subsequently permeabilized in 10% neutral buffered formalin. Intracellular staining was carried out at 4ºC, using the antibodies listed in Table 2-4 diluted in Perm/Wash Buffer. Finally, cells were washed twice (once in Perm/Wash Buffer and once in 0.05% DPBS/BSA) prior to resuspension in 0.05% DPBS/BSA and data acquisition on a LSRII flow cytometer (BD Biosciences). Antigen-specific T-cell responses were quantified by subtracting the percentage of cytokine-positive cells measured in matched unstimulated samples

from those observed after stimulation. A sample gating strategy for the identification of LASV GPC-specific T cells is provided in Appendix 4 (Figure A.4.1).

Table 2-4. Murine ICS panel for the characterisation of LASV GPC-specific T-cell responses.

Marker	Fluorochrome	Clone	Manufacturer	Catalogue number	Dilution
Extracellular staining cocktail					
CD16/32 (Fc block)	---	93	BioLegend	101302	1:50
CD8a	PerCP/Cy5.5	53-6.7	eBioscience	45-0081-82	1:200
CD4	BV650	RM4-5	BioLegend	100546	1:50
CD44	AF700	IM7	BioLegend	103026	1:100
CD62L	PeCy7	MEL-14	BioLegend	25-0621-81	1:50
CD127	eFluor 660	A7R34	Invitrogen	50-1271-82	1:50
LIVE/DEAD® Fixable Aqua Dead Cell Stain Kit	Aqua	---	Thermo Fisher Scientific	L34957	1:1000
Intracellular staining cocktail					
IFNγ	eFluor 450	XMG1.2	eBioscience	48-7311-82	1:100
TNFα	AF488	MP6-XT22	eBioscience	53-7321-82	1:100
IL-2	PE	J356-5H4	eBioscience	12-7021-82	1:100

2.3.4.2 NHP ICS assays

Cryopreserved PBMCs and splenocytes were thawed, washed, and rested as described in section 2.3.3.2. Cells were plated at a concentration of $1x10^6$ cells per well and were stimulated with LASV GPC or SARS-CoV-2 S1 and S2 peptide pools at a concentration of 2 µg/mL per peptide. Lists of peptide library sequences and pool configurations are included in Appendix 2. A corresponding negative control well was established for each sample, by treating cells with DMSO, to distinguish non-specific responses. Cells stimulated with PMA/ionomycin served as a positive control. Co-stimulatory antibodies, CD28 BUV661 and CD49d, were added to each well (both at 1 µg/mL). GolgiStop (0.67 µg/mL) and GolgiPlug (1 µg/mL) solutions were also added to each well. Plates were incubated at 37ºC for 16-18 hours prior to staining. First, viability staining was performed in DPBS, followed by extracellular staining in 0.05% DPS/BSA. To facilitate sample removal from

BSL4 (when required), cells were subsequently fixed with 2.5% paraformaldehyde (PFA) overnight. On the following day, cells were permeabilized in Cytofix/Cytoperm Solution and intracellular staining was carried out in Perm/Wash Buffer. Next, cells were washed twice (once in Perm/Wash Buffer and once in 0.05% DPBS/BSA) prior to resuspension in 0.05% DPBS/BSA and data acquisition on a FACSymphony A5 flow cytometer (BD Biosciences). To calculate antigen-specific T-cell responses, the frequencies of cytokine-positive cells in peptide pool-stimulated wells were adjusted for non-specific background by subtracting out cytokine-positive frequencies detected in DMSO-treated control wells. For the detection of SARS-CoV-2 S-specific responses, background-adjusted frequencies in S1- and S2-stimulated wells were summed for each sample. See Table 2-5 below for a list of the antibodies included in the ICS panels used to detect LASV-specific (Chapter 4) and SARS-CoV-2-specific (Chapters 5 and 6) T cells, respectively. A sample gating strategy is provided in Appendix 4 (Figure A.4.2).

Table 2-5. NHP ICS panel for the characterisation of antigen-specific T-cell responses.

Marker	Fluorochrome	Clone	Manufacturer	Catalogue number	Dilution
Viability staining					
Zombie Red™ Fixable Viability Kit	Zombie Red	---	BioLegend	423109	1:1000
Extracellular staining cocktail					
Human Fc block	---	---	BD	564220	1:50
CD3	BV650	SP34-2	BD	563916	1:200
CD4	BUV395	L200	BD	564107	1:200
CD8	PerCP-Cy5.5	SK1	BioLegend	344709	1:200
CD95	BUV737	DX2	BD	612790	1:200
CD45RA	BUV563	HI100	BD	564442	1:200
CCR7	BV510	G043H7	BioLegend	353231	1:100
CD14	PE-Dazzle594	M5E2	BioLegend	301851	1:200
CD16	PE-CF594	3G8	BD	562320	1:200
CD28*	BUV615	28.2	BD	751477	1 µg/mL
Intracellular staining cocktail					
IFNγ	AF488	4S.B3	BioLegend	502515	1:50
TNFα	BV785	mAb11	BioLegend	502948	1:50

IL-2/IL-5[#]	PE	MQ1-17H12/JES1-39D10[#]	eBioscience/BioLegend[#]	2017879/500904[#]	1:50
Granzyme B	APC	GB12	Invitrogen	MHGB05	1:50
IL-4	BV421	8D4-8	BD	562986	1:50
IL-10	BV711	JES3-9D7	BD	564050	1:50

**Marker stained for at the time of stimulation. [#]Antibody/marker substituted in LASV-specific ICS assay.*

2.3.5 Activation-induced marker (AIM) assays

AIM assays were performed as previously described[89,442]. Briefly, cryopreserved PBMCs were thawed, washed, and rested as described in section 2.3.3.2. Cells were plated at a concentration of $2x10^6$ cells per well and were stimulated with SARS-CoV-2 S1 and S2 peptide pools at a concentration of 2 μg/mL per peptide. Lists of peptide library sequences and pool configurations are included in Appendix 2. DMSO-treated negative control and PMA/ionomycin-treated positive control wells were created for each sample as explained in section 2.3.4.2. Anti-CD28 BUV661 and anti-CD49d antibodies were added to all wells as described in section 2.3.4.2. AIM assay plates were incubated at 37°C for 18 hours. After the end of the stimulation period, cells were stained with viability dye in DPBS and were subsequently stained with the extracellular antibody cocktail (in 0.05% DPBS/BSA) shown in Table 2-6. Cells were fixed in 2.5% PFA and, finally were washed and resuspended in 0.05% DPBS/BSA. Data acquisition was performed on a FACSymphony A5 flow cytometer. AIM^+ cells were identified as $OX40^+$ $CD25^+$, $OX40^+$ $PD\text{-}L1^+$, or $OX40^+$ $CD137^+$. The frequency of positive cells following S1 and S2 stimulation were adjusted for background, by subtraction of frequencies detected in corresponding DMSO-treated control samples and were subsequently summed. A sample gating strategy is depicted in Appendix 4 (Figure A.4.3).

Table 2-6. AIM panel for the characterisation of SARS-CoV-2 S-specific T-cell responses.

Marker	Fluorochrome	Clone	Manufacturer	Catalogue number	Dilution
Viability staining					
Zombie Red™ Fixable Viability Kit	Zombie Red	---	BioLegend	423109	1:1000
Extracellular staining cocktail					
Human Fc block	---	---	BD	564220	1:50
CD3	BV650	SP34-2	BD	563916	1:200
CD4	BUV395	L200	BD	564107	1:200
CD8	PerCP-Cy5.5	SK1	BioLegend	344709	1:200
CD95	BUV737	DX2	BD	612790	1:200
CD25	BUV496	M-A251	BD	741144	1:200
CD69	AF700	FN50	BioLegend	310921	1:50
CD38	FITC	MI15	STEM CELL	60131FI	1:200
CD138	PerCP-Cy5.5	SN3	BD	341087	1:200
CD137	PE	4B4-1	BioLegend	309804	1:100
OX40	BV711	L106	BD	745518	1:100
CD154	BV605	24-31	BioLegend	310825	1:100
PD-L1	BV421	29E.2A3	BioLegend	329714	1:100
CD14	PE-Dazzle594	M5E2	BioLegend	301851	1:200
CD16	PE-CF594	3G8	BD	562320	1:200
CD28*	BUV661	28.2	BD	751477	1:200

**Marker stained for at the time of stimulation.*

2.3.6 Immunophenotyping of T cells and innate cells in NHPs

Phenotypic characterizations of T-cell and/or innate-cell subsets were conducted in PBMC, lung, and BAL cell samples collected after viral infection. First, cryopreserved cells were thawed and washed in R10 medium. Subsequently, immunostaining was carried out as described in section 2.3.4.2. Briefly, cells were stained with viability dye followed by an extracellular staining cocktail. Cell fixation (and inactivation of infectious material) in 2.5% PFA took place overnight to enable sample removal from BSL4. On the next day, cell permeabilization and staining for intracellular markers was completed prior to data acquisition on a FACSymphony A5 flow cytometer. Individual panels and antibodies used for phenotyping are displayed in Tables 2-7 and 2-8. Sample gating strategies to identify major cell subsets are depicted in Appendix 4 (Figures A.4.4-A.4.5).

Table 2-7. T-cell phenotyping panel.

Marker	Fluorochrome	Clone	Manufacturer	Catalogue number	Dilution
Viability staining					
Zombie Red™ Fixable Viability Kit	Zombie Red	---	BioLegend	423109	1:1000
Extracellular staining cocktail					
Human Fc Block	---	---	BD	564220	1:50
CD3	BV650	SP34-2	BD	563916	1:200
CD4	BUV395	L200	BD	564107	1:200
CD8	PerCP-Cy5.5	SK1	BioLegend	344709	1:200
CD28	BUV615	28.2	BD	751477	1:200
CD95	BUV737	DX2	BD	612790	1:200
CD38 / CD103*	FITC	AT-1 / 2G5*	STEM CELL / Beckman Coulter*	60131FI / IM1856U*	1:200
CD49d	PE-Cy7	9F10	BioLegend	304313	1:200
CD69	AF700	FN50	BioLegend	310921	1:50
CD25	BUV496	M-A251	BD	741144	1:200
CD154	BV605	24-31	BioLegend	310825	1:100
HLA-DR	APC-Cy7	L243	BD	335796	1:200
CD45RA	BUV563	HI100	BD	564442	1:200
CCR7	BV510	G043H7	BioLegend	353231	1:100
CTLA4	BV785	BNI3	BioLegend	369623	1:100
CXCR3	BV421	1C6	BD	562558	1:100
CD14	PE-Dazzle594	M5E2	BioLegend	301851	1:200
CD16	PE-CF594	3G8	BD	562320	1:200
Intracellular staining cocktail					
Ki67	BV711	B56	BD	563755	1:50
FoxP3	PE	259D/C7	BD	560082	1:50

**Antibody/marker substituted for T-cell phenotyping of lung cell samples*

Table 2-8. Innate-cell phenotyping panel for BAL cells.

Marker	Fluorochrome	Clone	Manufacturer	Catalogue number	Dilution
Viability staining					
LIVE/DEAD® Fixable Blue Dead Cell Stain Kit	Blue UV	---	Thermo Fisher	L23105	1:1000
Extracellular staining cocktail					
Human Fc Block	---	---	BD	564220	1:50
CD11b	BV605	ICRF44	BioLegend	301332	1:200
CD14	BV421	M5E2	BioLegend	301830	1:200
CD16	BV510	3G8	BioLegend	302048	1:200
CD68	AF488	Y1/82A	BioLegend	333812	1:200
HLA-DR	APC-Cy7	L243	BD	335796	1:200
CD163	APC	GHI/61	BioLegend	333610	1:200
CD206	BUV737	19.2	BD	741860	1:200

CD80	BV785	2D10	BioLegend	305238	1:200
CD86	BV711	IT2.2	BioLegend	305440	1:200
CX3CR1	PerCP-Cy5.5	2A9-1	BioLegend	341614	1:200
CD49d	PE-Cy7	9F10	BioLegend	304313	1:200
CCR7	BV510	G043H7	BioLegend	353231	1:100
CD66abce	PE	TET2	Miltenyi	130-117-699	1:200
CD35	BUV615	E11	BD	751312	1:200
CD63	PE-CF594	H5C6	BD	565403	1:200
CCR5	BUV496	3A9	BD	750300	1:100

2.3.7 Antigen biotinylation

Purified LASV GP, SARS-CoV-2 S, and SARS-CoV-2 RBD proteins were biotinylated using the EZ-Link™ NHS-PEG4-Biotin, No-Weigh™ Format Kit according to the manufacturer's instructions. Excess biotin was removed using Zeba™ Spin Desalting Columns also in accordance with the manufacturer's protocol. LASV GP was biotinylated at a protein-to-biotin molar ratio of 1:50. SARS-CoV-2 S and RBD were biotinylated at a protein-to-biotin molar ratio of 1:20.

2.3.8 B-cell phenotyping and SARS-CoV-2-specific B-cell staining

Phenotypic of total B cells and staining to identify SARS-CoV-2-specific B cells was carried out using the panel of antibodies listed in Table 2-9. For the detection of SARS-CoV-2-specific B cells, probes were generated by tagging biotinylated S and RBD proteins with fluorochrome-conjugated streptavidin (SA) as previously described[322]. For added specificity of detection, cells were stained with two S protein probes, labelled with PE-Dazzle594 and BV421, which were made using a protein-to-SA molar ratio of 2:1. A RBD probe, labelled with PE-Cy7, was prepared by combining biotinylated protein with SA at a molar ratio of 4:1. Cryopreserved PBMCs were thawed and washed in R10 medium. Next, cells were stained with a cocktail of the three probes for 30 minutes at room temperature. Staining with general B-cell surface markers was subsequently carried out (as described in section 2.3.7) with a cocktail comprised of viability dye

and the antibodies listed in Table 2-9. To identify SARS-CoV-2 S-specific B cells, antigen-experienced B cells were first classified as $CD3^-$ $CD20^+$ IgD^- $CD27^+$. Within this population, cells staining as double positive for S-PE-Dazzle594$^+$ and S-BV421$^+$ were classified as S specific. RBD-specific B cells were identified as RBD-PE-Cy7$^+$ cells within the S-specific B-cell subset. A sample gating strategy for the identification of major B-cell subsets is shown in Appendix 4 (Figure A.4.6).

Table 2-9. B-cell phenotyping panel.

Marker	Fluorochrome	Clone	Manufacturer	Catalogue number	Dilution
LIVE/DEAD™ Fixable Blue Dead Cell Stain	Blue/UV	---	Thermo Fisher	L23105	1:1000
Human Fc Block	---	---	BD	564220	1:50
CD3	BV650	SP34-2	BD	563916	1:200
CD20	BV510	2H7	BioLegend	302339	1:200
CD27	BUV805	M-T271	BD	742012	1:200
CD21	BV786	B-Ly4	BD	740969	1:200
CD19	PE	J3.119	Beckman Coulter	IM1285U	1:200
CD19	PE	CB-19	Abcam	Ab1168	1:200
CD38	FITC	AT-1	STEM CELL	60131FI	1:200
CD138	PerCP-Cy5.5	MI15	BD	341087	1:200
IgD	AF647	---	Southern Biotech	2030-31	1:200
IgM	BUV395	G20-127	BD	563903	1:200
IgG	BUV563	G18-145	BD	741396	1:200
CD95	BUV737	DX2	BD	612790	1:200
CD69	APC-Cy7	FN50	BioLegend	310914	1:100
CD80	BUV661	2D10	BD	751731	1:200
CD39	BV605	A1	BioLegend	328236	1:200

2.3.9 Assessment of antibody-mediated effector functions

2.3.9.1 ADCD

ADCD assays were performed and analysed as previously described[348]. Briefly, 11 µl of Red FluoSpheres™ NeutrAvidin™-Labelled Microspheres were coated with biotinylated LASV GPC (5.5 µL at 1 mg/mL), SARS-CoV-2 S (25 µL at 1 mg/mL), or RBD protein (5 µL at 1 mg/mL) for

two hours at 37°C, washed, and diluted in 1 mL of DPBS. Serum samples were diluted 1:10 in RPMI-1640. 10 µL of antigen-coupled beads, 40 µL of RPMI-1640, and 50 µL of diluted sera were combined and incubated for two hours at 37°C. Next, 100 µL of guinea pig complement (diluted 1:25 in gelatin veronal buffer) was added to the serum:bead complexes and incubated at 37°C for 20 min. Serum:bead complexes were then washed with 15 mM EDTA and incubated with 50 µL FITC-conjugated-anti-C3 antibody (1:100 in PBS) for 15 min at room temperature in the dark. Serum:bead complexes were washed with DPBS and analysed on a FACSymphony A5 flow cytometer within one hour of completion of the protocol.

2.3.9.2 ADMP

ADMP assays were performed and analysed as previously described[348]. Antigen-coated neutravidin beads were prepared as described in section 2.3.9.1. Serum was diluted 1:100 in RPMI-1640. Diluted sera (100 µL) were mixed with 10 µL of beads and incubated at 37°C for 2 hours. Serum:bead complexes were washed with RPMI-1640. THP-1 cells (1.25 x 10^4 cells/well) or were added to the serum:bead complexes and incubated at 37°C for 18 hours. Cells were subsequently fixed in 4% PFA for 15 minutes at room temperature in the dark, washed with DPBS, and were run on a FACSymphony A5 flow cytometer. All samples were run in duplicate.

2.3.9.3 ADNP

ADNP was assessed according to previously described methods[348]. Antigen-coated neutravidin beads were prepared as described in section 2.3.9.1; serum was diluted and complexed with antigen-coated beads as explained in section 2.3.9.2. Leukocytes were freshly isolated through lysis of heparinised whole blood obtained from a healthy human donor (NIH IRB 01-I-N055) using RBC Lysis Buffer. Leukocytes (5x10^4 cells/well) were added to the serum:bead complexes and

incubated for one hour at 37°C. Next, cells were stained with the antibody cocktail shown in Table 2-10 diluted in DPBS, for 15 minutes in the dark. Finally, cells were fixed in 4% PFA and data acquisition was performed as described in section 2.3.9.2.

Table 2-10. ADNP staining panel.

Marker	Fluorochrome	Clone	Manufacturer	Catalogue number	Dilution
CD3	BUV395	SP34-2	BD	565983	1:200
CD14	BV605	M5E2	BioLegend	301834	1:200
CD66b	Pacific Blue	G10F5	BioLegend	305111	1:200

2.3.9.4 ADNKA

ADNKA was assessed using methods like those previously described[348]. Briefly, cells were isolated from 30 mL of heparin-treated whole blood collected from a healthy human donor (NIH IRB 01-I-N055) using the RosetteSep™ Human NK Cell Enrichment Cocktail according to the manufacturer's instructions. NK cells were rested overnight at 37°C in complete RPMI-1640 media supplemented with 10% FBS and 1 ng/mL of IL-15. Nunc MaxiSorp plates were coated with 3 µg/mL of antigen for two hours at 37°C. Plates were subsequently washed and blocked with a solution of 5% BSA in DPBS overnight at 4°C. Sera samples were diluted 1:25 in blocking buffer, plated in duplicates, and incubated on the coated plates for two hours at 37°C. NK cells were resuspended in a solution containing anti-CD107a antibody, GolgiStop (0.67 µg/mL), and GolgiPlug (1 µg/mL). After removal of sera from the plate, $5.0x10^4$ NK cells were added per well and incubated at 37°C for 6 hours. NK-cell surface staining involved the antibodies listed in Table 2.13. Next, cells were permeabilized using Cytofix/Cytoperm prior to intracellular staining with the antibodies listed in Table 2-11. Data acquisition was performed on a FACSymphony A5 flow cytometer. NK cells were defined as $CD3^-$ $CD16^+$ $CD56^+$.

Table 2-11. ADNKA staining panel.

Marker	Fluorochrome	Clone	Manufacturer	Catalogue number	Dilution
Extracellular staining cocktail					
Human Fc block	---	---	BD	564220	1:50
CD3	BV650	SP34-2	BD	563916	1:200
CD16	BV510	3G8	BioLegend	302048	1:200
CD56	BUV737	B159	BD	741842	1:200
CD107a*	PE-Cy7	H4A3	BioLegend	328618	1:100
Intracellular staining cocktail					
MIP-1β	PE	D21-1351	BD	550078	1:50
IFNγ	PerCP-Cy5.5	4S.B3	BioLegend	502526	1:50

**Marker stained for at the time of cell incubation.*

2.3.10 Live virus neutralisation assays

2.3.10.1 LASV

LASV neutralisation assays were carried out on Vero E6 cells in a 96-well plate format under BSL4 conditions by Dr. Robert Fischer (NIAID, NIH). Sera were heat inactivated at 56°C for 30 minutes and diluted two-fold in a series beginning from 1:10. A cocktail of human monoclonal antibodies—25.10C, 12.1F, 37.2D, and 8.9F—served as the positive control and was ten-fold serially diluted starting from a (total antibody) concentration of 15 μg/mL. Naïve guinea pig serum and wells containing only D2 media were used as negative controls. Each well of diluted sera or antibody cocktail was incubated with 20 $TCID_{50}$ of GPA LASV at 37°C for one hour. Next, following removal of existing cell culture supernatant, 100 μL of the above mixture was added to each well of Vero E6 cells. Infected cell cultures were incubated at 37˚C and scored for cytopathic effect (CPE) after ten days. Virus neutralising titres were reported as the maximum reciprocal sera dilution at which CPE was absent, or as <10 in the case of a negative result.

2.3.10.2 SARS-CoV-2

SARS-CoV-2 neutralisation assays were carried out on Vero E6 cells in a 96-well plate format under BSL3 conditions. Sera were heat-inactivated (at 56°C for 30 minutes) and two-fold serial dilutions were prepared in D2 media beginning with 1:10. Pooled sera from SARS-CoV-2-infected rhesus macaques (with previously confirmed neutralising activity) served as the positive control and naïve rhesus macaque sera served as the negative control. Diluted sera were mixed with 100 $TCID_{50}$ of SARS-CoV-2. After incubation for one hour at 37 °C, virus:serum mixtures were added to Vero E6 cells and incubated at 37°C for six days at which point cultures were scored for CPE. Virus neutralising titres were expressed as the reciprocal value of the highest dilution of the serum at which CPE was absent. Negative samples were represented graphically as having a titre of 3.

2.3.11 VSV-based pseudotype neutralisation assays

2.3.11.1 Neutralisation of VSV-Lassa-GPc-cFLAG

Sera were heat-inactivated and serially diluted (by a factor of 2.5) from 1:10 to 1:2441. Five-fold serial dilutions of human monoclonal antibodies 25.10C, 12.1F, 37.2D, and 8.9F from a starting concentration of 60 µg/mL served as positive controls. A cocktail of all four antibodies, at an initial (total antibody) concentration of 60 µg/mL, was serially diluted in the same way and was used as an additional positive control. Naïve guinea pig serum and virus only wells were used as negative controls. 1000 FFU of VSV-Lassa-GPc-cFLAG were added to the diluted sera or antibody and incubated for one hour at 37˚C. Serum:virus mixtures were overlayed on confluent Vero E6 cells and spin infection was carried out at 1200 x *g* and 4°C for one hour. Infected cells were incubated for 16 hours at 37˚C. Finally, GFP-positive cells were counted using the ImmunoSpot® 7 Software and CTL Analyzer (CTL Analyzers, LLC). The percent of infected cells was determined relative

to uninhibited virus only control wells. Half maximal inhibition (IC_{50}) values were calculated based on reciprocal sera dilution using a sigmoidal nonlinear fit model (4PL regression curve). Values above 100% infectivity were converted to 100%.

2.3.11.2 Neutralisation of VSV-SARS-CoV-2-S

Sera were heat-inactivated and serially diluted (by a factor of 2.5) from 1:10 to 1:6104. Pooled sera from SARS-CoV-2-infected and naïve rhesus macaques served as positive and negative controls, respectively. D2 media-only wells were also established as an additional negative control. Diluted sera were mixed with 1000 FFU of VSV-SARS-CoV-2-S for one hour at 37ºC. Infection of Vero E6 cells with serum:virus mixtures was carried out as described in section 2.3.11.1.After the 16-hour incubation period, cells were lysed with Cell Lysis Buffer and luciferase activity was measured in relative luminescence units (RLU) using a Biotek Synergy HT Microplate Reader with Gen5^{TM} Data Analysis Software (Agilent). Each sample was tested in duplicate. RLU were normalized to the 100% infectivity signal measured in a no sera control (maximum signal). The percent of infected cells was determined relative to uninhibited virus only control wells. IC_{50} values were calculated based on reciprocal sera dilution values using a sigmoidal nonlinear fit model (4PL regression curve).

2.3.12 Multiplex analyte detection assays

2.3.12.1 MESO Scale Discovery Assays

Multiplex detection of chemokines, cytokines, and antibodies was carried out in multiple studies featured in this thesis using kits developed and validated by MESO Scale Discovery. All assays were performed according to the manufacturer's protocol using kit reagents. Table 2-12 specifies the analytes tested and sample dilutions used with each kit. Post-infection samples were γ-

irradiated prior to removal from BSL4 for use in these assays. Assay plates were read using a MESO QuickPlex SQ 120 instrument (MESO Scale Diagnostics) according to the manufacturer's instructions.

Table 2-12. Analytes and sample dilutions for MESO Scale Discovery assays.

Kit and analytes	Sample type	Sample dilution
V-PLEX NHP Cytokine 24-Plex Kit Eotaxin-3, GM-CSF, IFNγ, IL-1β, IL-2, IL-5, IL-6, IL-7, IL-8, IL-8 (HA), IL-10, IL-12/IL-23p40, IL-15, IL-16, IL-17A, IP-10, MCP-1, MCP-4, MDC, MIP-1α, MIP-1β, TARC, TNFβ, VEGF-A	Sera	1:4
V-PLEX COVID-19 Coronavirus Panel 1 (IgG) Kit Flu A/Hong Kong H3, HCoV-HKU1 S, HCoV-OC43 S, MERS-CoV S, SARS-CoV-1 S, SARS-CoV-2 N, SARS-CoV-2 NTD, SARS-CoV-2 RBD, SARS-CoV-2 S	Sera	1:500
U-PLEX Chemokine Combo 1 (NHP) Kit Eotaxin, Eotaxin-3, IL-8, IP-10, MCP-1, MCP-4, MDC, MIP-1α, MIP-1β, TARC	BALF	1:2
Isotyping Panel 1 Human/NHP Kit IgA, IgG, IgM	Sera, nasosorption fluid, BALF	1:500, 1:10, 1:100
V-PLEX SARS-CoV-2 Panel 2 (IgG) SARS-CoV-2 S, RBD, N	Sera, nasosorption fluid, BALF	1:500, 1:10, 1:100
V-PLEX SARS-CoV-2 Panel 2 (IgA) SARS-CoV-2 S, RBD, N	Sera, nasosorption fluid, BALF	1:500, 1:10, 1:100

2.3.12.2 MILLIPLEX Map 23-plex Kit

Serum samples for analysis of cytokine/chemokine levels were inactivated by γ-radiation. Cytokine concentrations were measured on a Bio-Plex 200 instrument (Bio-Rad) using the Non-Human Primate Cytokine MILLIPLEX Map 23-plex Kit (Millipore) according to the manufacturer's instructions. Cytokines profiled included the following: G-CSF, GM-CSF, IFNγ, IL-1β, IL-1RA, IL-2, IL-4, IL-5, IL-6, IL-8, IL-10, IL-12/23 (p40), IL-13, IL-15, IL-17, MCP-1, MIP-1α, MIP-1β, sCD40L, TGFα, TNFα, VEGF, and IL-18. To account for batch effects resulting from the distribution of samples across different plates, the variance of the ratio of

observed:expected concentration multiplied by 100 was calculated for the each of the kit's 156.25 pg/mL, 625 pg/mL, and 2500 pg/mL reference ("spike-in" control) standards. Cytokines for which the summed variance was greater than 100 were removed from the analysis. Cytokine values were normalized across plates as follows. First, an average of the values of each standard across plates was calculated. Next, within each plate (for each of the standards analysed), a scaling factor was calculated as the ratio of the standard over the mean across plates. Then an average scaling value was calculated across the factors for each cytokine on each plate. These scaling factors were then applied to the experimental readouts for each cytokine on each plate. For values that could not be determined based on the standard curve (below the limit of detection), the readout value was set to zero.

2.3.13 Transcriptomics

2.3.13.1 Bulk RNA sequencing in LASV-challenged cynomolgus macaques

Cryopreserved PBMCs were thawed and inactivated by resuspension in TRIzol reagent (1 mL) for ten minutes. Samples were centrifuged at maximum speed for ten minutes prior to resuspension in fresh TRIzol (1 mL) and removal from BSL4. RNA was extracted from PBMC samples using the QIAmp Viral RNA Kit according to the manufacturer's instructions. Samples were fluorescently quantified using the Qubit™ 4 Fluorometer (Thermo Fisher) and Qubit™ RNA High Sensitivity Assay Kit following the manufacturer's protocol. In accordance with the Illumina Stranded mRNA Prep workflow, 100 ng of RNA was used as input for mRNA enrichment and next-generation sequencing (NGS) library preparation. NGS libraries were amplified for 14 cycles, AMPure XP-bead purified using 0.95X beads, assessed on BioAnalyzer DNA 1000 Chips, and quantified using the Kapa Quantification Kit for Illumina Sequencing. All libraries were diluted to 4 nM and pooled

equally. The library pool was denatured and further diluted to 1.8 pM for sequencing on the Illumina NextSeq 550 instrument (Illumina) using a High Output Kit (150 cycle). Sequencing runs were repeated to bring the reads per sample up to the target of 20 M. NGS library preparation and RNA sequencing was carried out by the RML RTB Genomics Core Facility.

Data analysis was performed, as described previously[443], with the RNA-seq workflow module of the Bioconductor "systemPipeR" package in R (version 4.1.0). Briefly, RNA-sequencing reads were demultiplexed, quality filtered, and trimmed. Quality reports were generated with the "seeFastq" function. Alignment of RNA-sequencing reads was performed against the annotated *Macaca fascicularis* (cynomolgus macaque) genome (GCA_000364345.1). Raw expression values in the form of gene read counts were generated with the "summarizeOverlaps*"* function, counting only the reads overlapping exonic regions of genes, and discarding reads mapping to ambiguous regions. The above steps were performed by Brittany Dulek of the RML RTB Genomics Core Facility. Subsequently, I carried out the normalization of raw counts (fragments per kilobase of transcript per million fragments mapped, FPKM) and statistical analysis of differentially expressed genes (DEGs) using the "fpkm" function and "edgeR*"* packages. Host DEGs were defined as those with a fold change ≥ 2 and a false discovery rate (FDR) corrected p-value < 0.05. Only protein coding genes were included for further analysis. Heatmaps of DEGs were generated using R packages "DESeq2" and "ggplot2". Gene set enrichment analysis to identify clusters of genes mapping to biological pathways, specifically to gene ontology terms, was performed using the "iDEP" (integrated Differential Expression and Pathway Analysis) package (version 0.93) available on Bioconductor. The results from these analyses are reported in Chapter 4.

2.3.13.2 Single-cell RNA sequencing in SARS-CoV-2-infected rhesus macaques

Chapters 5 and 6 include scRNAseq data from respiratory tract samples collected from SARS-CoV-2 infected rhesus macaques. BALF and lung cell samples were prepped according to the 10X Genomics protocol for gel bead in emulsion (GEM) creation. All samples were handled so that approximately 10,000 cells were captured as 10X Genomics GEMs. The 10X Genomics (version 3.1) chemistry was used to generate barcoded cDNA and to generate final libraries according to the manufacturer's protocol. After the final libraries were generated, samples were removed from containment following inactivation of the libraries. Inactivation involved combining 560 µL of AVL, 560µl of ethanol, and 140µL of the final library and incubation for a minimum of 10 minutes. Libraries were extracted from AVL using Qiagen AllPrep DNA spin columns. Samples were then quantified and sequenced using the Illumina NextSeq550 and the 10X Genomics' suggested cycling conditions. The above steps were carried out by members of the RML RTB Genomics Core Facility.

The analysis of scRNAseq data was led by Dr. Emily Speranza (NIAID, NIH) with assistance from me. After sequencing, samples were demultiplexed using the "cellRanger" pipeline. Reads were aligned against the annotated *Macaca mulatta* (rhesus macaque) genome (GCA_003339765.3) along with the SARS-CoV-2 genome (NC_045512.2) to parse out reads mapping to the host versus the virus. Samples were then read into R (version 3.6.2) using Seurat (version 3.1.5)[444]. To account for the differences in sample collection days across the two groups, sample integration was performed to help remove potential batch effects using the "IntegrateData" function in Seurat. Cells were filtered in a manner similar to that described previously[445]. In short, cells were filtered for high mitochondrial gene content (>20%) and abnormally high or low UMI counts. Samples were removed from the analysis if they either contained too high a level of ambient RNA (<70%

transcripts attributed to cells) or contained too few cells (< 1000) after filtering. The top 20 principal components of the data were calculated using the 2000 genes with the highest variance across the dataset. These principal components were used to calculate UMAP projections and to cluster cells. Gene set enrichment analysis was performed using the "fgsea" package[446] and the Molecular Signatures Database (MSigDB) annotated gene sets.

Cell type identification was performed using a previously described method[445]. Human lung single-cell sequencing samples[447] were used for reference sequencing data. Cell type identification was performed at the individual cell and cluster level. Dividing cell clusters were identified as having >98% of cells in the G2M or S phase of the cell cycle using the "CellCycleScoring" function in Seurat. To identify cell types exhibiting the greatest transcriptional shifts, we again used a method previously described[445]. In short, data were subset for each annotated cell type and the top 500 variable genes were used to calculate principal components. Next, principal components comprising 99% of the explained variance were selected and the mean differences in PC scores between experimental groups were calculated. A threshold of two standard deviations from the mean was applied to determine cell types exhibiting a high level of divergence.

In Chapter 5 specifically, an additional sub-clustering analysis was performed to differentiate macrophage/monocyte cells in vaccinees versus controls. Macrophage/monocyte cells were subset and re-analysed using the top 500 variable genes. The first two principal components were used to cluster the cells using a low result ion clustering value (0.1). Gene scores were assigned using the "AddModuleScore" function in Seurat to identify gene sets expressed at different levels across the clusters and between experimental groups. A Kolmogorov-Smirnov test was used to calculate a p-value for the difference in the gene scores across cell types over 1000 iterations; p-values were corrected using the Benjamini-Hochberg method.

2.3.14 Lipidomics

The detection of circulating lipids was carried out by Dr. Benjamin Schwarz (NIAID, NIH). Briefly, the extraction of bulk lipids was completed by adding 50 µL of serum to 400 µL of ice-cold methanol and 500 µL of ice-cold chloroform, followed by 400 µL of water. Samples were agitated and centrifuged to collect the organic fraction, which was dried in a Savant™ DNA120 SpeedVac™ concentrator and stored at -80°C. Dried samples were resuspended in butylated hydroxytoluene (5 µg/mL) in a 6:1 isopropanol:methanol solution prior to injection into the liquid chromatography tandem mass spectrometry (LC-MS/MS) pipeline. Lipid mediators were extracted from macaque serum as previously described[448]. Briefly 100 µL of serum was added to ice-cold methanol containing 1 ng each of d8-5-HETE, d5-RvD2, d5-LXA4, d4-LTB4, d4-PGE2. Macromolecules were precipitated, centrifuged, and the supernatant was collected. Oxy-lipid species were selectively extracted using solid phase columns as previously described[448]. Eluted samples were dried under nitrogen and resuspended in a 1:1 water:methanol solution. For LC-MS analysis, 30 µL of each sample was injected.

Bulk lipid and lipid mediator detection was completed using series of targeted multiple-reaction monitoring (MRM) hydrophilic interaction chromatography (HILIC) methods as previously described[448,449]. All samples were separated using a ExionLC™ AC System (Sciex) and analysed using a 5500 QTRAP® mass spectrometer (Sciex). Samples were separated on a Water XBridge® Amide column and eluted using a 12-minute binary gradient (from a solution of 100% 5 mM ammonium acetate and 5% water in acetonitrile to a solution of 95% 5 mM ammonium acetate and 50% water in acetonitrile). Target lipids were detected using scheduled MRM. Lipid signals were assessed by negative ion and positive ion modes; a separate injection was analysed for each method. A blank sample and a standard mix were serially injected every 10 injections. The

standard mix consisted of the following compounds (each at 10 ng/mL): RvE3, LXA4, LXA5, LXB4, PGE2, PGD2, PGF2a, TxB2, PD1, RvD5, Maresin 1, LTB4, 5,15-DiHETE, 14-HDHA, 18-HEPE, AA, EPA, DHA. Signal identities were confirmed using spectra and comparison to authentic standards. Raw data were analysed using the MultiQuant® Software (Sciex, version 3.0.3). Bulk lipid data was filtered by establishing thresholds of 50% and 30% for missing values and quality control coefficients of variance. Lipid mediator signals were normalized to internal standards based on the number of hydroxyl groups in each molecule. Bulk lipid class signals were calculated by summing the signals of lipid families within each class. Finally, I obtained the normalized signals of bulk lipid classes and individual lipid mediators for further downstream analyses; these results are presented in Chapter 6.

2.3.15 Multiplex IHC (mIHC)

Multiplex IHC panels were designed by me and Dr. Emily Speranza (NIAID, NIH). The preparation and staining of rhesus macaque lung tissues for mIHC analysis were carried out by Rebecca Rosenke and Dr. Carl Shaia (RMVB, NIAID, NIH). Briefly, rhesus macaque lung tissues were fixed for a minimum of seven days in 10% neutral buffered formalin and embedded in paraffin. The middle right lung lobe of each animal was selected for multiplex immunohistochemistry (mIHC) analysis, which was performed using the iterative bleaching extends multiplexity (IBEX) method for over-fixed tissue samples[450]. After sectioning, slides were de-waxed using xylene and 100% ethanol. Slides were subjected to a series of washes in 95% ethanol, 70% ethanol, water, 10% neutral buffered formalin, and water. Slides were stored in tris-buffered saline (TBS) with 0.05% Tween-20 (TBST). Antigen retrieval was performed using AR6 buffer and by heating tissues in a standard microwave first at 100% power for 45 seconds and next at 10% power for 15 minutes. Samples were cooled and rinsed in TBST. Staining was completed

with one primary antibody at a time. Following primary antibody staining, a mixture of anti-mouse and anti-rabbit peroxidase-conjugated secondary antibodies was added for 10 minutes, then washed in TBST. Finally, the assigned Opal dye was added for 3-10 minutes, then washed in TBST. After Opal dye deposition, antigen retrieval was performed again on the samples and the process was repeated for the next primary antibody in the panel. After completion of the staining sequence, slides were mounted with Fluoromount-G and imaged on the Leica Thunder system using a 20X oil objective with an additional autofluorescence channel collected to serve as a fiducial. After imaging of each panel, the coverslips were removed by soaking the slide overnight in TBST. A solution of $LiBH_4$ was used to remove fluorescent signal. Tissue was then stained and imaged sequentially using different panels until all desired markers were evaluated. DAPI was added to the final panel only. The antibodies used are listed in Table 2-13.

Analysis of mIHC images was led by Dr. Emily Speranza with assistance from me. The image files collected for the different panels were aligned according to autofluorescence using the Imaris XTension Software (Oxford Instrumentals) developed for IBEX. Linear modifications were made to images, as well as Gaussian blurring to reduce noise. All modifications were applied to the entire image, not a single area alone. Quantification of images, including counting of $Ki67^+$ nuclei, segmentation of the DAPI signal, identification of cell types, and quantification of bronchus-associated lymphoid tissue (BALT) structures were performed using Imaris Image Analysis Software (Oxford Instrumentals, version 9.5.0). These data are reported in Chapter 6.

Table 2-13. mIHC primary antibody list.

Marker	Fluoro-chrome	Clone	Manufacturer	Catalogue number	Dilution	Secondary	Opal dye
Lumican	---	EPR8898	Abcam	ab168348	1:100	Anti- mouse & rabbit HRP	520
CD206	---	---	Abcam	ab64693	1:100	Anti- mouse & rabbit HRP	650

αSMA	AF488	1A4	Invitrogen	53-9760-80	1:100	Anti- mouse & rabbit HRP	650
CD66abce	FITC	TET2	Miltenyi	130-166-522	1:100	Anti- mouse & rabbit HRP	780
EpCAM	---	---	Abcam	ab71916	1:50	Anti- mouse & rabbit HRP	570
CD4	---	---	R&D Systems	FAB8165G	1:50	Anti-goat HRP	480
Ki67	AF700	B56	BD Biosciences	561277	1:50	Anti- mouse & rabbit HRP	570
HLA-DR	---	EPR3692	Abcam	ab92511	1:100	Anti- mouse & rabbit HRP	570
Prosurfactant C	---	---	Abcam	ab90716	1:100	Anti- mouse & rabbit HRP	480
CD3	AF700	SP34-2	BD Biosciences	561805	1:100	Anti- mouse & rabbit HRP	570

2.4 Methods – Virology

2.4.1 Real-time quantitative reverse-transcriptase PCR (qRT-PCR)

2.4.1.1 LASV

Virus inactivation and RNA extraction were completed following approved institutional protocols. Briefly, 140 µL of blood was added to 560 mL of AVL and incubated at room temperature for ten minutes; this mixture was then added to 560 µL of absolute ethanol. RNA was extracted using a QIAamp Viral RNA Mini Kit according to the manufacturer's instructions. Tissues were weighed, homogenized in RLT buffer and adjusted to a concentration of 30 mg of tissue in 600 µL of RLT buffer. The homogenate was incubated at room temperature for ten minutes and subsequently added to 600 µL of 70% ethanol. RNA was then extracted using a RNeasy Mini Kit following the manufacturer's instructions. Presence of LASV RNA was detected using real-time quantitative reverse-transcriptase PCR (qRT-PCR). qRT-PCR assays were performed using 5 µL of template in 20 µL QuantiFast Master Mix on a Rotor-Gene instrument (Qiagen). The standard curve was

generated from a ten-fold dilution of RNA extracted from stock GPA LASV with a known virus concentration. Forward primer, reverse primer, and probe sequences are listed in Table 2-14[451].

Table 2-14. LASV qRT-PCR primer and probe sequences.

Primer/probe	Sequence
LaV F2 (forward)	CCACCATYTTRTGCATRTGCCA
LaV R (reverse)	GCACATGTNTCHTAYAGYATGGAYCA
LaV TM (probe)	FAM-AARTGGGGYCCDATGATGTGYCCWTT

2.4.1.2 SARS-CoV-2

Tissues (up to 30 mg) were homogenized in RLT buffer and RNA was extracted using the RNeasy Mini Kit according to the manufacturer's instructions. RNA was extracted from BAL fluid and nasal swabs using the QiaAmp Viral RNA kit according to the manufacturer's instructions. Viral genomic RNA (gRNA)[452] and subgenomic RNA (sgRNA)[453] specific qRT-PCR assays were used for the detection of viral RNA. Five µL RNA were tested with the Rotor-Gene™ Probe Kit according to instructions of the manufacturer. For each run, dilutions of RNA standards (with known genome counts) were run in parallel to calculate copy numbers in each sample. Forward primer, reverse primer, and probe sequences are listed in Table 2-15.

Table 2-15. SARS-CoV-2 qRT-PCR primer and probe sequences.

Primer/probe	Sequence (5' to 3')
E_Sarbeco_F1 (forward)	AACAGGTACGTTAATAGTTAATAGCGT
E_Sarbeco_R2 (reverse)	ATATTGCAGCAGTACGCACACA
E_Sarbeco_P1 (probe)	FAM-ACACTAGCCATCCTTACTGCGCTTCG-ZEN-IBHQ

2.4.2 Infectious virus titration assays

2.4.2.1 LASV

Endpoint titrations were carried out on Vero E6 cells inoculated with ten-fold dilutions of (LASV-infected) serum or tissue homogenates in a 96-well plate format by Dr. Robert Fischer. The titration plates were incubated for one hour at 37˚C and 5% CO_2. After incubation, the diluted sera or tissue solutions were removed, and the plates were rinsed twice with sterile DPBS. Finally, 200 µL of DMEM with 2% FBS were added to each well; plates were incubated at 37˚C and scored for CPE after ten days. $TCID_{50}$ values were calculated using four replicates according to the Spearman-Karber method.

2.4.2.2 SARS-CoV-2

Tissue sections were weighed and homogenized in 750 µL of DMEM. Vero E6 cells were inoculated with ten-fold serial dilutions of virus swab media, BALF, or tissue homogenates in 96-well plates. Plates were spun down for 1 hour at 1000 RPM. When titrating tissue homogenate, cells were washed with DPBS and 100 µl of DMEM with 2% FBS. Cells were incubated at 37°C for six days prior to reading CPE. Titrations of SARS-CoV-2-infected tissues were carried out by Dr. Neeltje van Doremalen (NIAID, NIH) in the BSL4 laboratory.

2.4.3 Histopathological evaluation of LASV-challenged animals

2.4.3.1 *In situ* hybridisation of guinea pig tissues

Hartley guinea pig liver, spleen, and lung samples were placed into paraffin-embedding cassettes and formalin fixed for seven days. Paraffin-embedded tissues were thinly sliced and probed for viral RNA by *in situ* hybridization (ISH). ISH was performed using the RNAscope 2.5 VS Assay

targeting Josiah strain LASV (GenBank accession number J04324.1, position 355-1782) positive sense mRNA on the Ventana Discovery ULTRA Slide Auto Staining System. A board-certified veterinary anatomic pathologist, Dr. Greg Saturday (RMVB, NIAID, NIH), performed ISH and evaluated all tissue slides.

2.4.3.2 IHC of cynomolgus macaque tissues

Tissues were fixed in 10% neutral buffered formalin for a minimum of seven days. Tissues were processed with a Sakura VIP-6 Tissue Tek (Sakura), on a 12-hour automated schedule, using a graded series of ethanol, xylene, and PureAffin R56. Embedded tissues were sectioned in 5 µm segments and dried overnight at 42°C prior to staining with haematoxylin and eosin (HE). LASV immunoreactivity was detected using LASV NP antibody followed by ImPress VR anti-rabbit IgG secondary antibody. The staining was performed using the Discovery Ultra Automated Stainer (Ventana Medical Systems) with a ChromoMap DAB Kit. Immunostaining and evaluation of slides was carried out by a board-certified veterinary anatomic pathologist, Dr. Carl Shaia, blinded to study group allocations.

2.5 Methods – Data analysis and statistics

2.5.1 Multivariate or high-dimensional data analyses

Statistical analyses and the generation of principal component analysis (PCA) graphs and dendrograms (euclidean distance, “complete” clustering algorithm) were performed in R (version 4.1.0), using the “ggplot2”, “factoextra” and “prcomp” packages. To generate the Simplified Presentation of Incredibly Complex Evaluations (SPICE) plots, SPICE 6 software (NIAID) was

used[454]. For t-stochastic neighbor embedding (t-SNE) and FlowSOM analyses, data from all animals were down-sampled and concatenated. Subsequently, t-SNE analysis[455] was performed in the FlowJo (Treestar, version 10.7) environment on compensated parameters (nearest neighbor = 15, minimum distance = 0.5, iterations = 1000), FlowSOM (version 2.9)[456] analysis was conducted using compensated parameters and fixed generation of 15 meta clusters (set speed = 3)[455]. Comparison of absolute fluorescence intensity values across individual cells within major T-cell subsets was performed by concatenating data from $CD4^+$ or $CD8^+$ T-cells across older or younger animals and exporting it to ViolinBox (version 5.1.8)[457].

2.5.2 Testing for statistical significance

Dr. Dean Follmann, Dr. Martha Nason, and Dr. Michael Proschan (NIAID, NIH) guided the selection of appropriate statistical analyses. Testing for statistical significance was complicated by small groups sizes ranging from four to eight animals in most of the studies featured in this thesis. To avoid employing the assumption that our data were normally distributed—particularly given that we could not adequately assess normality in our results—non-parametric tests were principally employed across experiments. Where feasible, medians with interquartile ranges (IQR) are presented for data compared via non-parametric tests. Differences between two groups were assessed using Mann-Whitney U tests. Differences between multiple groups were evaluated using Kruskal-Wallis tests with Dunn's correction for multiple comparisons. A Friedman test was used to compare matched data across multiple time points or conditions within a group. Spearman's (two-sided) rank was calculated for all correlations. Differences between multiple groups across multiple variables were conducted using two-way ANOVA or mixed-effects analysis with Tukey's or Šídák's correction for multiple comparisons, respectively. Data were corrected for multiplicity

within each statistical test, when more than two groups were compared, as described above for each respective test. Further adjustment for multiple comparisons across entire studies was not carried out given the relative consistency in results across corroborative datasets; moreover, such correction is not considered standard practice when sample sizes are low.

Area under the curve was calculated in GraphPad Prism (version 9.1.1); differences between means and standard errors (SEM) of net peak areas were compared by unpaired t tests. The polyfunctional cytokine profiles of antigen-specific T cells were compared within the SPICE 6 application by permutation test. During the analysis of single-cell and bulk transcriptomic data, the comparison of gene expression scores was carried out using a bootstrapping method to estimate p-values from 1000 iterations*;* p-values were adjusted for false discovery rate. For all statistical analyses $p<0.05$ was considered significant and all p-values are two-tailed. The p-values for significant comparisons are indicated on graphs or in an associated table. Analyses were performed in GraphPad Prism (version 9.1.1) or in R (version 4.1.0), unless indicated otherwise**.**

3

Development of a ChAdOx1-vectored vaccine for LASV and testing in small animal models

3.1 Introduction

Given the increasing number of outbreaks of unprecedented severity observed within the last several years, targeted countermeasures for Lassa fever are urgently needed[162]. The WHO and CEPI have identified LASV as a priority pathogen for research and development, and the WHO TPP lays out preferred criteria for a LASV vaccine candidate to be deployed in an endemic setting[218]. These include the following: safety across age groups and in pregnant women, efficacy after a single dose (or a maximum of three doses), durable protection, conferral of heterosubtypic immunity, thermostability, and ease of large-scale manufacturing for stockpiling. Fortunately, as detailed in section 1.2.7, numerous promising candidates are in the development pipeline. These include DNA[206], RNA, protein, live attenuated[458], VLP[205], viral reassortant[207], and multiple different viral-vectored[182,200,203] vaccine approaches. Nearly all candidates target the viral surface glycoprotein and encode the sequence for the full GPC gene, typically alone, but sometimes in combination with NP. LASV strain Josiah, first isolated in Sierra Leone in 1989, has served as the reference virus for the design of most vaccine immunogens and diagnostic tests. The protective

efficacy of these vaccine candidates has been demonstrated in rodent and NHP models of LASV infection. To date, three candidates—plasmid DNA delivered via dermal electroporation (NCT04093076), MV-vectored (NCT04055454), and VSV-vectored (NCT04794218) vaccines—have advanced to evaluation in phase I clinical trials.

Early-stage preclinical testing of new vaccine candidates for Lassa fever has been hampered by a lack of easily available small animal models. Immunocompetent mice exhibit limited susceptibility to LASV infection; thus, vaccine candidates are instead often evaluated in inbred Strain 13 or outbred Hartley guinea pigs[190]. Although IP inoculation with wildtype Josiah strain LASV produces uniformly lethal disease in the Strain 13 model, these inbred animals are not widely accessible. As described in section 1.2.6, a species-adapted variant of LASV (Josiah strain), referred to as GPA LASV, has been developed that causes fatal disease in outbred Hartley guinea pigs[149]. GPA LASV harbours a single nucleotide polymorphism in the S genomic segment compared to the wildtype Josiah strain virus. After IP inoculation with GPA LASV, animals develop fever, weight loss, and high tissue viral loads, before succumbing to disease within 15 days[149]. However, while Hartley guinea pigs represent a useful tool for the evaluation of vaccine-conferred protection from lethal illness, they do not easily facilitate the characterisation of vaccine-induced immune responses, due to a lack of species-specific reagents. Consequently, more detailed immunological investigations typically require use of a separate model.

The aim of this chapter is to report the results from the preclinical evaluation of the immunogenicity and efficacy of a novel ChAdOx1-vectored Lassa fever vaccine, ChAdOx1-Lassa-GPC. This vaccine candidate was previously generated by cloning the full-length Josiah strain LASV GPC sequence into the E1 deletion site of the ChAdOx1 vector, under the control of a modified human IE CMV promoter, as described in section 2.1.2.1. First, immunogenicity was

evaluated in outbred CD-1 mice and particular focus was given to the characterisation of vaccine-induced T-cell responses, including cross-reactivity to distinct strains. Subsequently, the Hartley guinea pig model was employed to evaluate the protective efficacy of ChAdOx1-Lassa-GPC delivered in a single-dose or prime-boost immunisation regimen. ChAdOx1-Lassa-GPC was found to be immunogenic, to confer protection against clinical disease, and significantly reduce tissue viral loads after challenge with a lethal dose of GPA LASV. The findings presented in this chapter support the continued development and testing of ChAdOx1-Lassa-GPC as a promising vaccine candidate for the prevention of Lassa fever.

3.1.1 Authorship statement

ChAdOx1-Lassa-GPC was synthesised by Dr. Sarah Sebastian and The Jenner Institute's VVCF. I performed all immunogenicity experiments carried out in CD-1 mice. Experimental LASV challenge of immunised Hartley guinea pigs took place under BSL4 conditions at the Laboratory of Virology, RML, NIH, and were conducted by Dr. Robert Fischer and RMVB. Please refer to the overall Statement of Authorship (page xviii) for an overarching description of procedures completed by colleagues; data generated by others are indicated throughout this chapter. I carried out the analysis and visualisation of all data included in this chapter, unless otherwise specified. The findings discussed here have been published in a research article, which I co-first authored[110].

3.2 Results

3.2.1 Immunogenicity of ChAdOx1-Lassa-GPC in CD-1 mice

The immunogenicity of ChAdOx1-Lassa-GPC was evaluated in CD-1 mice. ChAdOx1-Lassa-GPC was administered intramuscularly as either a single dose or prime-boost vaccination regimen (n=8 per group), with a 28-day interval between doses (Figure 3-1A). For the remainder of this chapter, animals receiving one dose of ChAdOx1-Lassa-GPC will be collectively referred to as LASV1, and those receiving two doses will be termed LASV2. Control animals (n=8) received a single dose of the empty vector control, ChAdOx1-GFP (referred to as GFP). After 21 days, LASV-specific T-cell and antibody responses were measured by IFNγ ELISpot assay (Figure 3-1B) and IgG ELISA (Figure 3-1C), respectively. The magnitude of the IFNγ T-cell response was determined by stimulating splenocytes with a pool of overlapping peptides spanning the full-length Josiah strain LASV GPC sequence. The median responses in animals immunised with one (p=0.0049) or two (p=0.0008) doses of ChAdOx1-Lassa-GPC were significantly elevated above those in animals receiving ChAdOx1-GFP (median [IQR] SFU/10^6 splenocytes: LASV1=707 [622.5-1841], LASV2=1018 [924-1310], GFP=2.5 [0.000-6.250]) by Kruskal-Wallis test with Dunn's multiple comparisons correction. GP-specific IgG serum antibodies were quantified by endpoint titre ELISA. Again, IgG titres after one (p=0.0030) or two (p=0.0007) vaccine doses were significantly higher than those measured in the control animals (median [IQR] $\log_{10}$ of reciprocal sera dilution: LASV1=4.107 [3.806-4.408], LASV2=4.258 [4.107-4.408], GFP=2.602 [2.602-2.602]) by Kruskal-Wallis test with Dunn's multiple comparisons correction. Statistically significant differences between single-dose and prime-boost vaccinees were not detected for either ELISpot assay (p>0.9999) or ELISA (p>0.9999). Spearman rank correlation analysis (two-sided)

comparing IFNγ ELISpot assay and IgG ELISA responses suggested that antigen-specific T-cell and antibody responses were fairly well correlated (Spearman r [95% CI]: r=0.6163 [0.1581-0.8561], *p*=0.0126) (Figure 3-1D). These assays illustrate induction of LASV-specific cellular and humoral immune responses after both single dose and prime-boost vaccination with ChAdOx1-Lassa-GPC.

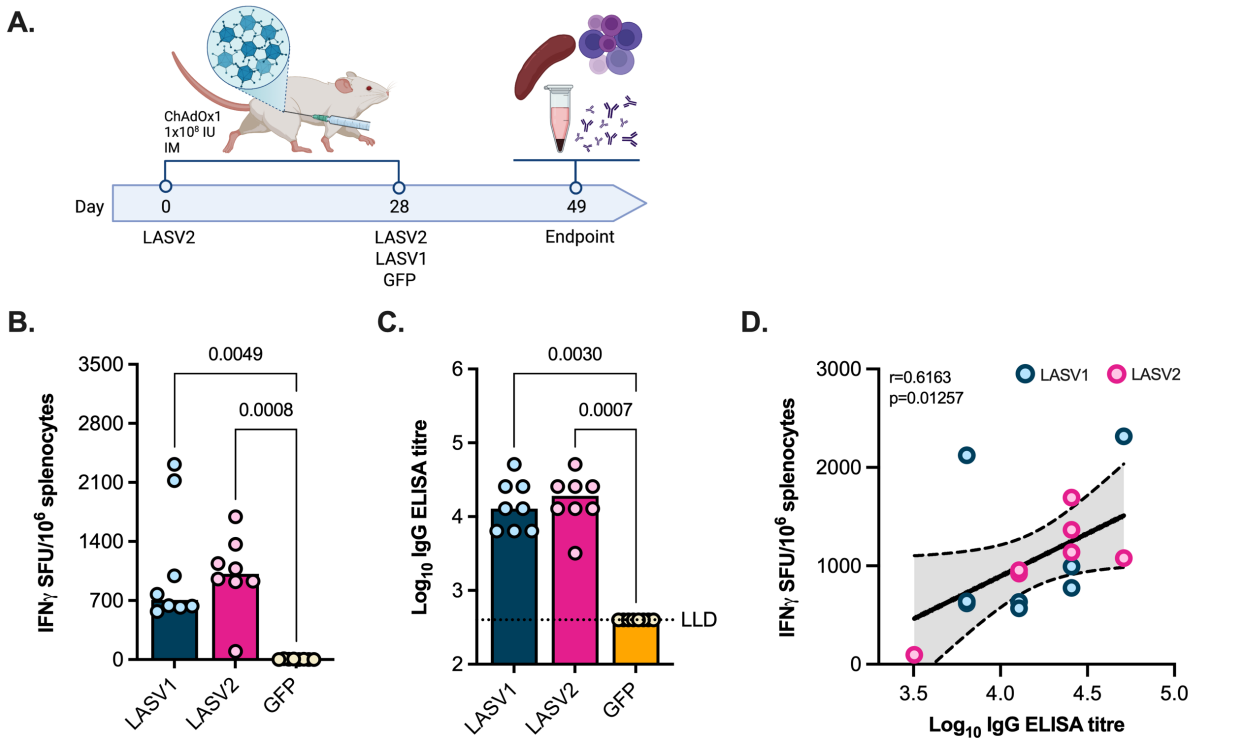


Figure 3-1. ChAdOx1-Lassa-GPC vaccination elicits cellular and humoral immune responses in CD-1 mice. **(A)** Outline of immunisation experiment and sampling performed in CD-1 mice. Experimental group abbreviations: ChAdOx1-Lassa-GPC prime (LASV1), ChAdOx1-Lassa-GPC prime-boost (LASV2), ChAdOx1-GFP control (GFP). **(B)** IFNγ ELISpot assay of murine splenocytes stimulated with a LASV GPC peptide pool measured in SFU per $1.0x10^6$ splenocytes (statistical test: Kruskal-Wallis, Dunn's multiple comparisons). **(C)** LASV GP-specific (log_{10}) IgG titres in two-fold serially diluted sera were measured by ELISA. Endpoint titres were determined using a threshold for positivity of the mean OD plus three-fold standard deviations detected in naïve sera. The lower limit of detection (LLD) line indicates the (reciprocal) lowest sera dilution tested (statistical test: Kruskal-Wallis, Dunn's multiple comparisons). **(D)** Correlation analysis and best-fit line comparing (log_{10}) IgG titres and IFNγ ELISpot responses of ChAdOx1-Lassa-GPC vaccinees (statistical test: two-sided Spearman rank correlation). All bars depict group medians. Significant p-values (<0.05) are denoted in the figures, all other comparisons are not significant.

There is some evidence suggesting that the resolution of LASV infection may be principally mediated by the cellular immune response; therefore, we further characterised LASV-specific and $CD4^+$ and $CD8^+$ T cells in the prime and prime-boost vaccine recipients by flow cytometric analysis[136,174,459]. ICS was carried out on splenocytes restimulated with a LASV GPC peptide pool. Antigen-specific T-cell responses were assessed by measuring the expression of proinflammatory cytokines—IFNγ, TNFα, and IL-2. $CD4^+$ T cells expressing IFNγ, TNFα, or IL-2 were observed post prime (median [IQR] %: IFNγ=0.174 [0.124-0.276], TNFα=0.161 [0.147-0.185], IL-2=0.046 [0.023-0.110]) and post boost (median [IQR] %: IFNγ=0.166 [0.104-0.230], TNFα=0.207 [0.150-0.331], IL-2=0.001 [0.001-0.030]) (Figure 3-2A). Comparatively higher frequencies of $CD8^+$ T cells responding to antigen re-exposure were detected. IFNγ (median [IQR] %: LASV1=2.381 [1.572-5.157], LASV2=1.376 [1.057-4.296]) and TNFα (median [IQR] %: LASV1=2.245 [1.480-4.053], LASV2=1.165 [0.915-2.948]) were expressed at the highest median frequencies in both prime and prime-boost animals. IL-2 was expressed by a lower percentage of $CD8^+$ T cells in both groups (median [IQR] %: LASV1=0.140 [0.018-0.198], LASV2=0.001 [0.001-0.001]) (Figure 3-2B). A significant reduction in the median frequency of IL-2-secreting $CD8^+$ T cells was observed in prime-boost animals compared to single-dose vaccinees (p=0.037) by two-way ANOVA with Tukey's multiple comparisons correction. However, all other comparisons of median cytokine expression after prime or prime-boost administration of ChAdOx1-Lassa-GPC were not statistically significant ($CD4^+$: $IFN\gamma^+$ p=0.599, $TNF\alpha^+$ p=0.599, IL-2^+ p=0.116; $CD8^+$: $IFN\gamma^+$ p=0.244, $TNF\alpha^+$ p=0.244).

The small subset of cytokine-producing $CD4^+$ T cells largely expressed a single cytokine, either IFNγ or TNFα (median [IQR] % of cytokine-secreting $CD4^+$ T cells expressing 1, 2, or 3 cytokines: LASV1=87.598 [80.124-90.675], 6.256 [4.088-8.361], 6.146 [4.512-8.046];

LASV2=88.167 [85.255-92.316], 5.349 [4.798-7.415], 6.484 [5.964-8.229]) (Figure 3-2C). By contrast, over 60% of vaccine-induced IFNγ$^+$, TNFα$^+$, or IL-2$^+$ CD8$^+$ T cells expressed more than one cytokine, indicating the development of a polyfunctional response (median [IQR] % of cytokine-secreting CD8$^+$ T cells expressing 1, 2, or 3 cytokines: LASV1=31.466 [29.411-33.677], 61.800 [52.484-63.290], 6.734 [4.115-9.648]; LASV2=31.944 [29.552-33.737], 61.454 [58.500-64.116], 6.602 [4.090-8.568]) (Figure 3-2C).

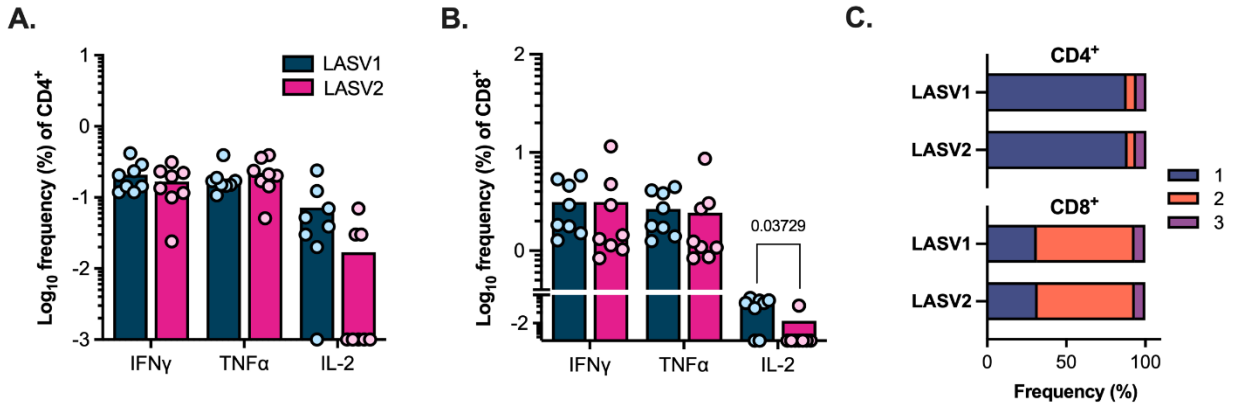


Figure 3-2. LASV-specific T-cell responses are polyfunctional. The percentage of splenic CD4$^+$ **(A)** and CD8$^+$ **(B)** T cells expressing IFNγ, TNFα, or IL-2 after GPC peptide pool stimulation and intracellular cytokine staining. Graphed values reflect adjustment to exclude non-specific cytokine expression measured from a corresponding set of unstimulated samples (statistical test: two-way ANOVA with Tukey's multiple comparisons). **(C)** Proportions of cytokine-secreting (IFNγ$^+$, TNFα$^+$, or IL-2$^+$) CD4$^+$ (top) and CD8$^+$ (bottom) T cells expressing one, two, or three cytokines. All bars depict group medians. Significant p-values (<0.05) are denoted in the figures, all other comparisons are not significant.

Surface phenotyping of CD4$^+$ and CD8$^+$ T cells revealed predominantly effector and effector memory subsets. IFNγ expression was used to distinguish LASV-specific T cells. Antigen-experienced effector and memory cells were further distinguished by surface expression of CD44, which is upregulated on activated T cells post antigen encounter. Effector (T_E), effector memory (T_{EM}), and central memory (T_{CM}) populations were classified based on surface expression of CD62L (L-selectin, lymphoid trafficking marker) and CD127 (IL-7 receptor, homeostatic survival

marker) as follows: $CD44^+$ $CD62L^-$ $CD127^-$ (T_E), $CD44^+$ $CD62L^-$ $CD127^+$ (T_{EM}), and $CD44^+$ $CD62L^+$ $CD127^+$ (T_{CM}). T_E, and to a lesser extent, T_{EM} phenotypes comprised the $IFN\gamma^+$ $CD4^+$ T-cell response (median [IQR] % T_E, T_{EM}, and T_{CM}: LASV1=42.000 [33.900-50.150], 29.850 [18.575-37.500], 1.775 [0.350-3.910]; LASV2=63.600 [50.325-66.050], 20.400 [15.750-27.500], 0.305 [0.000-1.150]) (Figure 3-3A). Similar results were observed for $IFN\gamma^+$ $CD8^+$ T cells (median [IQR] % T_E, T_{EM}, and T_{CM}: LASV1=51.850 [44.475-66.625], 44.700 [31.800-49.675], 0.770 [0.535-0.990]; LASV2=61.650 [56.850-76.075], 33.200 [22.250-37.100], 0.555 [0.348-1.535]) (Figure 3-3B). The T_{CM} phenotype was largely absent from the $CD4^+$ and $CD8^+$ T cells profiled. This finding is consistent with previous reports suggesting that the kinetics of the T_{CM} response (in mice) following adenovirus vaccination are slower than that of some other viral vectors and are only detectable a few months after immunisation[460,461]. Although the effect was only statistically significant in the $CD4^+$ T-cell subset, administration of a second dose of ChAdOx1-Lassa-GPC appeared to favour expansion of both $CD4^+$ (p=0.03729) and $CD8^+$ (p=0.2438) T_E cells. Comparisons of post prime and post boost frequencies for all other subsets were not statistically significant by two-way ANOVA with Tukey's multiple comparisons correction ($CD4^+$: T_{EM} p=0.2344, T_{CM} p=0.07977; $CD8^+$: T_{EM} p=0.2417, T_{CM} p=0.8200). Together, these data indicate that vaccination with ChAdOx1-Lassa-GPC induces a fully differentiated, polyfunctional T-cell response. Three weeks after immunisation, cellular immunity is dominated by effector and effector memory mechanisms. Furthermore, significant differences in the magnitude or quality of the T-cell response are largely not observed between single dose and prime-boost vaccination regimens.

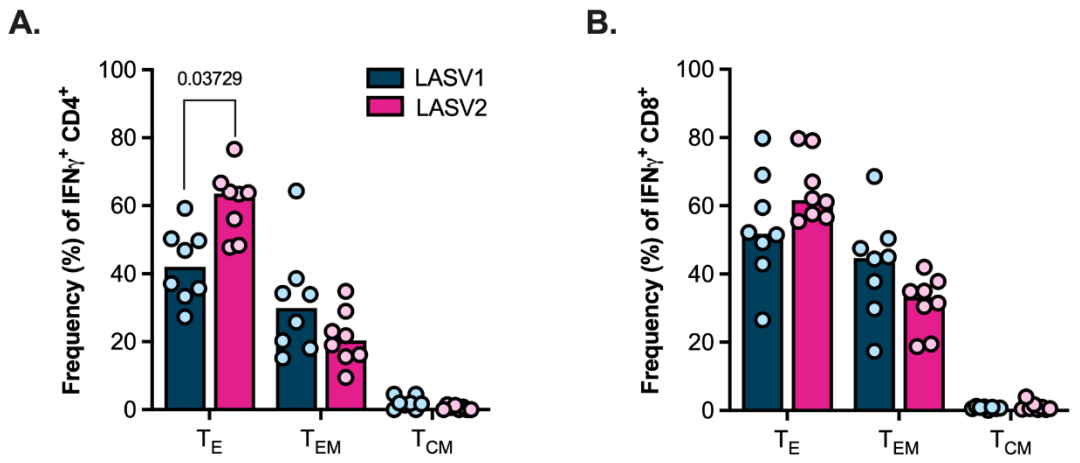


Figure 3-3. LASV-specific T cells exhibit an effector phenotype 21 days post immunisation. Percentages of LASV-specific IFNγ$^+$ CD4$^+$ **(A)** and CD8$^+$ **(B)** T cells exhibiting T_E, T_{EM}, and T_{CM} phenotypes as determined by immunostaining for CD44, CD62L, and CD127 surface markers (statistical test: two-way ANOVA with Tukey's multiple comparisons). All bars depict group medians. Significant p-values (<0.05) are denoted in the figures, all other comparisons are not significant.

3.2.2 Antibody responses to ChAdOx1-Lassa-GPC in Hartley guinea pigs

The protective efficacy of ChAdOx1-Lassa-GPC (after one or two doses) was evaluated in the Hartley guinea pig model of lethal Lassa fever. Animals were allocated into three experimental groups (n=10 per group) and administered the following immunisations: ChAdOx1-Lassa-GPC on -56 and -28 DPC (prime-boost, LASV2), ChAdOx1-Lassa-GPC on -28 DPC (prime, LASV1), or ChAdOx1-GFP on -28 DPC (control, GFP) (Figure 3-4A). The immunogenicity of ChAdOx1-Lassa-GPC in guinea pigs was confirmed by detection of GP-specific IgG antibodies 28 days post prime (-28 DPC) and boost (0 DPC) in the prime-boost group animals (median [IQR] $\log_{10}$ of reciprocal sera dilution: LASV2 -28 DPC=4.107 [4.032-4.408]; LASV2 0 DPC=4.709 [4.408-4.709]; GFP 0 DPC=2.602 [2.602-2.602]) (Figure 3-4B). LASV-specific IgG titres were significantly elevated post prime and post boost in ChAdOx1-Lassa-GPC vaccinees compared to the controls (p=0.0022 for both comparisons) by Kruskal-Wallis test with Dunn's multiple

comparisons correction. A significant increase in IgG antibody titre was observed after administration of a second dose of ChAdOx1-Lassa-GPC (p=0.0312) by Wilcoxon matched-pairs signed rank test.

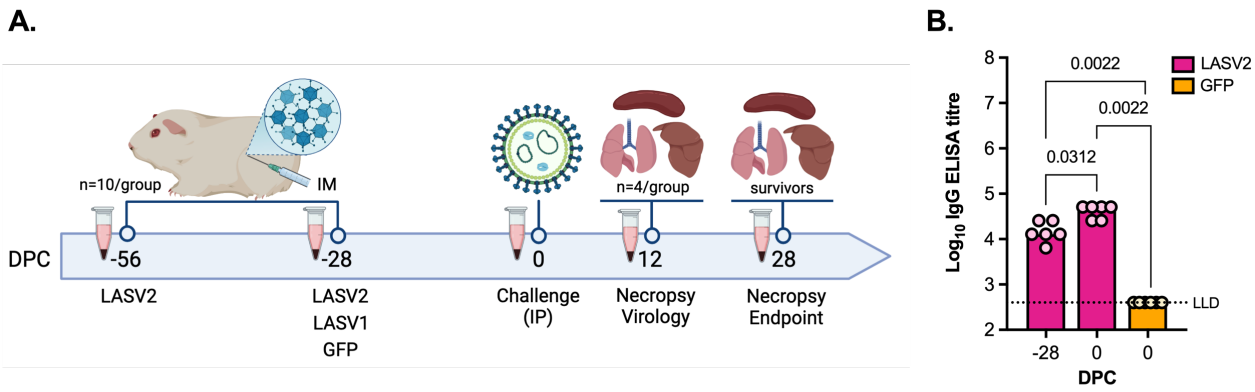


Figure 3-4. Administration of ChAdOx1-Lassa-GPC in Hartley guinea pigs. (A) Outline of immunisation and challenge experiment. Experimental group abbreviations: ChAdOx1-Lassa-GPC prime (LASV1), ChAdOx1-Lassa-GPC prime-boost (LASV2), ChAdOx1-GFP control (GFP). Timeline indicates days post challenge (DPC). **(B)** LASV GP-specific (log_{10}) IgG antibody titres in two-fold serially diluted sera were measured by endpoint titre ELISA. The threshold for positivity was set at the mean OD plus three-fold standard deviations detected in naïve sera. The LLD line refers to the (reciprocal) lowest sera dilution tested (statistical test: Kruskal-Wallis with Dunn's multiple comparisons, LASV2 -28 DPC vs. GFP 0 DPC and LASV2 0 DPC vs. GFP 0 DPC; Wilcoxon matched-pairs, LASV2 -28 DPC vs. LASV2 0 DPC). All bars depict group medians. Significant p-values (<0.05) are denoted in the figures, all other comparisons are not significant.

The neutralisation capacity of antibodies produced after immunisation with ChAdOx1-Lassa-GPC was assessed in a pseudotype neutralisation assay utilising a replication-deficient, GFP-expressing VSV pseudotyped with Josiah strain LASV GPC, VSV-Lassa-GPC-cFLAG. Sera collected on 0 DPC from guinea pigs receiving the prime-boost vaccination regimen were assayed as these animals developed the highest virus-specific IgG titres detected by ELISA. Sera samples were serially diluted 2.5-fold (starting at 1:10) and incubated with VSV-Lassa-GPC-cFLAG (1000 focus forming units, FFU) for one hour prior to infection of Vero E6 cells. After 16 hours, GFP-positive cells were counted and the proportion of infected cells relative to a virus-only control was determined. Human monoclonal antibodies (25.10C, 12.1F, 37.2D, and 8.9F) with previously

confirmed neutralising activity[176] were used as positive controls, both individually and in a cocktail, at a starting concentration of 30 µg/mL. Neutralising titres were reported as half maximal inhibition values (IC_{50}), which were extrapolated from a nonlinear regression variable slope curve derived by plotting log_{10} of sera dilution or antibody concentration versus the percent infectivity of VSV-Lassa-GPC-cFLAG. All four monoclonal antibodies neutralised VSV-Lassa-GPC-cFLAG individually and in combination. IC_{50} concentrations for these positive control antibodies ranged from 0.164 to 0.225 µg/mL, which was consistent with previous reports[176] (Figures 3-5A&B). Conversely, the sera from the immunised guinea pigs demonstrated little to no capacity to inhibit virus infection; IC_{50} values fell beyond the range of sera dilutions assayed and rivalled that of the naïve negative control sera (Figure 3-5C&D).

To verify the above results, the same sera samples were also tested for their capacity to neutralise live guinea pig-adapted (GPA) LASV; this assay was completed by Dr. Robert Fischer. Again, 0 DPC sera samples were serially diluted (two-fold) and incubated with 20 $TCID_{50}$ of virus. After ten days, CPE was observed in all samples at the lowest dilution (1:10). Therefore, all sera were considered negative and neutralising titres were documented as falling below the minimum dilution assayed (i.e., <10). A cocktail of the human monoclonal antibodies described above (25.10C, 12.1F, 37.2D, and 8.9F) served as a positive control and demonstrated inhibition at a total antibody concentration of 15 µg/mL, while CPE was observed at 1.5 µg/mL.

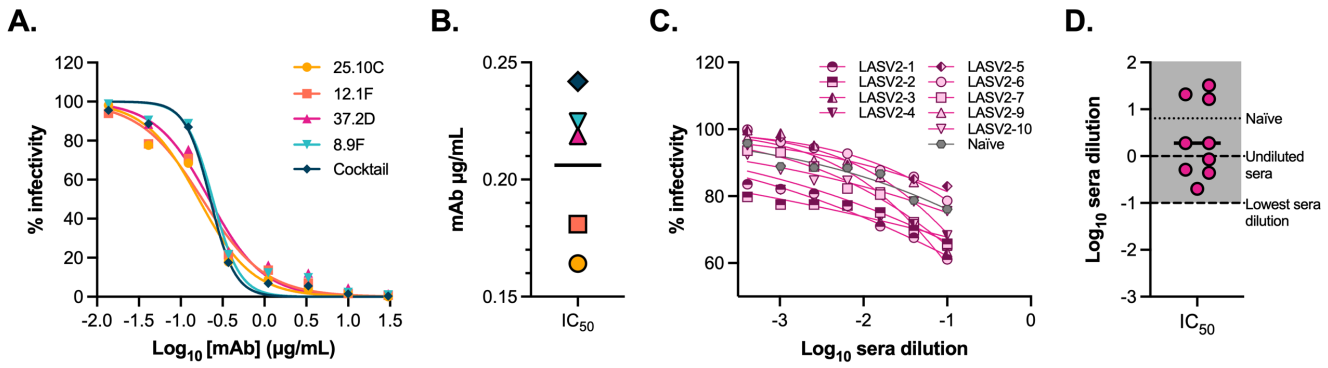


Figure 3-5. Antibodies elicited by ChAdOx1-Lassa-GPC vaccination are non-neutralising. (A) Variable slope nonlinear regression (least squares fit) curve of the percentage of VSV-Lassa-GPC-cFlag-infected Vero E6 cells versus log_{10} monoclonal antibody (mAb) concentration. Percent infectivity was determined by normalising the number of GFP-positive cells in antibody-treated wells against those in virus-only and cell-only control wells. **(B)** IC_{50} monoclonal antibody concentration (µg/mL) determined by nonlinear regression. **(C)** Variable slope nonlinear regression (least squares fit) curve of percent infectivity of VSV-Lassa-GPC-cFlag versus log_{10} sera dilution. Normalisation was performed as described above. **(D)** Best-fit half maximal inhibition (IC_{50}) values shown as log_{10} sera dilution determined by nonlinear regression. The IC_{50} of naïve (negative control) sera is indicated with a dotted line. The log_{10} y-axis values corresponding to the lowest sera dilution assayed (1:10) and undiluted sera are indicated with dashed lines. Values corresponding to negligible neutralising activity are captured in the grey shaded region.

3.2.3 Lethal LASV challenge in immunised Hartley guinea pigs

During the course of the study, prior to challenge, three animals died for reasons unrelated to vaccination or LASV challenge, altering the total number of animals in the ChAdOx1-Lassa-GPC prime-boost vaccination (n=9) and control (n=8) experimental groups. To account for this reduction, the numbers of animals in the survival cohorts of the prime-boost (n=5) and control (n=4) groups were adjusted accordingly.

On 0 DPC, all animals were challenged with $1x10^5$ $TCID_{50}$ of GPA Josiah strain LASV. On 12 DPC, four randomly selected animals from each group were euthanized to perform virological assessments in lung, liver, spleen, and sera. The remaining animals were used to assess survival; animals in this survival cohort were euthanized either after meeting humane endpoint criteria or on 28 DPC, which marked the study endpoint. All survival cohort guinea pigs vaccinated with

ChAdOx1-Lassa-GPC survived challenge and did not develop fevers, experience weight loss, or exhibit other signs of disease. No discernible differences in weight or temperature were observed between prime and prime-boost vaccinees. By contrast, all control animals in the survival cohort developed signs of terminal illness and met humane endpoint criteria (>20% weight loss) on or before 12 DPC, indicating that vaccination provided significant protection against lethality (p=0.0005) by Mantel-Cox log-rank test (Figure 3-6A). The temperatures of control animals began to increase on 3 DPC and animals became febrile by 8 DPC. Weight loss was apparent by 7 DPC and progressed until euthanasia by 12 DPC (Figures 3-6B&C). LASV inoculation and clinical monitoring were conducted by Dr. Robert Fischer and members of RMVB.

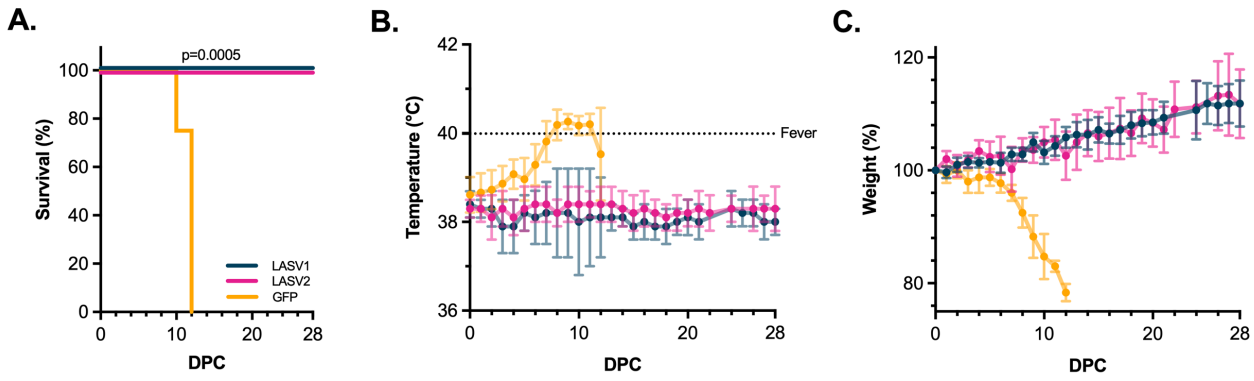


Figure 3-6. ChAdOx1-Lassa-GPC-vaccinated guinea pigs are protected against lethal LASV challenge. (A) Percent survival of guinea pigs following challenge with GPA LASV (statistical test: Mantel-Cox log rank test). **(B)** Temperature of challenged animals; animals with a temperature of ≥40ºC were diagnosed as febrile. **(C)** Weight loss post challenge expressed as a percentage of animals' weight on 0 DPC. In B and C, data points indicate group medians and error bars indicate 95% confidence intervals. Significant p-values (<0.05) are denoted in the figures (where relevant).

Despite conferring full protection against clinical disease after LASV challenge, vaccination with ChAdOx1-Lassa-GPC did not induce sterilising immunity in this model. As defined in section 1.1.3, sterile protection (or sterile immunity) refers to the complete preclusion of virus infection in a host. Low amounts of LASV RNA were detected in the tissues of immunised animals necropsied

on 12 DPC by qRT-PCR (Figure 3-7A). Median viral loads (with interquartile range) are listed for each group and tissue in Table 3-1. Median levels of viral RNA in the lungs of control animals exceeded those detected in prime-boost and single dose vaccinees by 6.664 and 6.832 $\log_{10}$ $TCID_{50}$/g equivalents, respectively. Similarly, median viral loads in the livers of control animals were elevated above those in the prime-boost and prime groups by 4.99 and 5.00 $\log_{10}$ $TCID_{50}$/g equivalents, respectively. Finally, vaccination with ChAdOx1-Lassa-GPC reduced splenic viral load by 6.09 and 5.47 $\log_{10}$ $TCID_{50}$/g equivalents after prime-boost or single dose delivery, respectively. Reductions in viral RNA in the vaccinated animals versus controls were statistically significant for all tissues ($p<0.0001$ for all comparisons, two-way ANOVA with Tukey's multiple comparisons correction). Meanwhile, no significant differences were observed between the prime-boost and prime immunisation groups (lung, liver, spleen: $p=0.9898$, 0.6238, 0.8813).

Overall, viral loads were much lower in sera than in the tissues (Figure 3-7B, Table 3-1). On 12 DPC, qRT-PCR analysis did not detect LASV RNA in the sera of ChAdOx1-Lassa-GPC vaccinees, apart from one animal in the prime-boost group (1.36 $\log_{10}$ $TCID_{50}$/mL equivalents). By contrast, sera from all but one control animal was positive for LASV RNA (median [IQR]: 2.152 [-0.386-3.208] $\log_{10}$ $TCID_{50}$/mL equivalents). Statistically significant differences in mean serum viral load were not observed between vaccinated and control animals by Kruskal-Wallis test with Dunn's multiple comparisons correction (LASV1 vs. LASV2: $p>0.9999$, LASV1 vs. GFP: $p=0.0687$, LASV2 vs. GFP: $p=0.2403$).

	LASV1	LASV2	GFP
Lung	1.360 [0.926 to 1.468]	1.528 [-0.179 to 2.125]	8.192 [7.763 to 8.494]
Liver	2.791 [2.344 to 3.930]	2.807 [0.197 to 4.142]	7.794 [7.756 to 7.988]
Spleen	2.756 [2.426 to 2.836]	2.145 [1.546 to 3.341]	8.230 [8.022 to 8.589]
Sera	-1.097 [-1.097 to 1.097]	-1.097 [-1.097 to 0.746]	2.152 [-0.386 to 3.208]

Table 3-1. LASV RNA detected by qRT-PCR in lung, liver, spleen, and sera at 12 DPC. For lung, liver, and spleen tissues, the table indicates median [IQR] $\log_{10}$ $TCID_{50}$/g equivalents determined for each group. For sera, median [IQR] $\log_{10}$ $TCID_{50}$/mL equivalents are shown for each group.

Antibody responses specific to LASV nucleoprotein (NP) were mounted in vaccinated and control animals by 12 DPC, which further suggested that low-level virus replication had occurred despite prior immunisation (median [IQR] $\log_{10}$ reciprocal sera dilution: LASV1=4.258 [3.881-4.634], LASV2=3.054 [2.677-3.430], GFP=4.408 [3.957-4.408]). The titre of anti-NP IgG antibodies was significantly lower in prime-boost vaccinees compared to single-dose vaccinees or controls (p=0.0492 for both comparisons), whereas titres in single-dose vaccinees and controls were similar (p>0.9999) by Kruskal-Wallis test with Dunn's multiple comparisons correction (Figure 3-7C). These results indicated that the two-dose vaccination regimen facilitated greater efficiency in viral clearance in comparison to one dose alone.

To determine if LASV RNA detected by qRT-PCR was indicative of infectious virus, lung, liver, and spleen tissues collected on 12 DPC were titrated on Vero E6 cells; this assay was performed by Dr. Robert Fischer. No viable LASV was isolated from the tissues of any of the animals immunised with ChAdOx1-Lassa-GPC, besides a single lung sample from an animal in the prime vaccination group (2.52 $\log_{10}$ $TCID_{50}$/g) at just above the limit of detection of the assay. Meanwhile, infectious virus was detected in all tissues isolated from control animals (median [IQR] $\log_{10}$ $TCID_{50}$/g in lung, liver, spleen: 7.636 [6.961-8.141], 6.648 [6.273-7.398], 7.148 [6.648-7.648]). Differences in virus titres between prime-boost vaccinees and controls (lung, liver,

spleen: p=0.0008, 0.0012, 0.0006), as well as between single-dose vaccinees and controls (lung, liver, spleen: p=0.0002, 0.0012, 0.0006) were statistically significant, but titres were not different between vaccination groups (lung: p=0.6259) by two-way ANOVA with Tukey's multiple comparisons correction (Figure 3-7D).

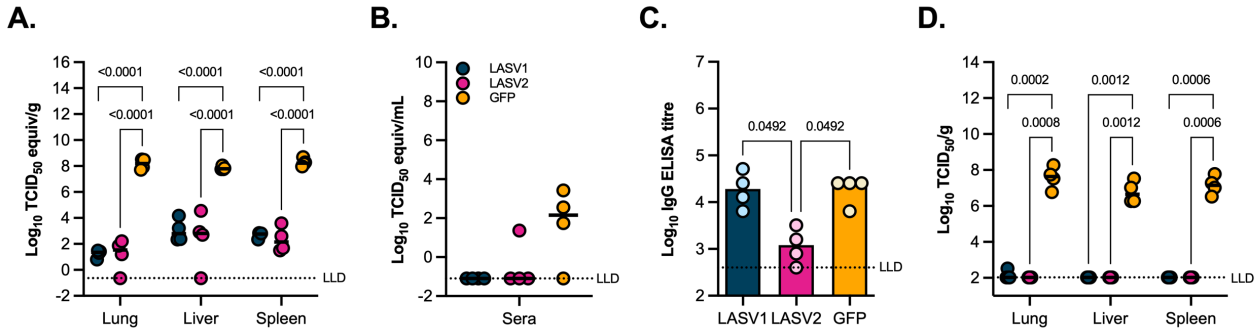


Figure 3-7. Viral load is significantly lower in the tissues and sera of ChAdOx1-Lassa-GPC vaccinees compared to controls. (A) qRT-PCR detection of LASV RNA (log_{10} $TCID_{50}$/g equivalents) in lung, liver, and spleen tissue collected at 12 DPC from animals (n=4 per group) randomly selected for necropsy to enable virological assessment. LLD for analysis (-0.638 log_{10} $TCID_{50}$/g equivalents) is indicated with a dotted line (statistical test: two-way ANOVA, Tukey's multiple comparisons). **(B)** LASV RNA (log_{10} $TCID_{50}$/mL equivalents) in 12 DPC sera. LLD for analysis (-1.097 log_{10} $TCID_{50}$/g equivalents) is indicated with a dotted line (statistical test: Kruskal-Wallis, Dunn's multiple comparisons). **(C)** Anti-NP (log_{10}) IgG antibody titres in two-fold serially diluted sera measured by ELISA. Endpoint titres were determined using the sum of the mean OD plus three-fold standard deviations of naïve sera as a negative cut-off. The LLD line indicates the lowest (reciprocal) sera dilution tested (statistical test: Kruskal-Wallis, Dunn's multiple comparisons). **(D)** Titration of infectious virus isolated from lung, liver, and spleen tissue on Vero E6 cells. Titres expressed as log_{10} $TCID_{50}$/g; the LLD for analysis (2.023 log_{10} $TCID_{50}$/g) is indicated with a dotted line (statistical test: two-way ANOVA, Tukey's multiple comparisons). All bars depict group medians. Significant p-values (<0.05) are denoted in the figures, all other comparisons are not significant.

Lung, liver, and spleen tissue sections were stained with HE or with LASV-specific *in situ* hybridisation (ISH) probes to detect replicating virus within cells (Figure 3-8). All slides were evaluated by a board-certified veterinary pathologist, Dr. Greg Saturday, who was blinded to study group allocations. Limited pathology was observed in the HE-stained tissues of vaccinated animals euthanized on 12 DPC post challenge. Marked and severe signs of vacuolar degeneration and centrilobular-midzonal bridging were detected in the livers of one and three control animals, respectively, but not in the vaccinated animals. Vacuolar degeneration is a response to stress or

damage to liver cells, which may be caused by disease processes, including but not limited to, infection, stress, and inflammation. Finally, the lung tissue in three of the four control animals exhibited mild-to-marked interstitial pneumonia with macrocytosis, while the lungs of vaccinees were free of this disease phenotype. ISH staining was largely absent in animals vaccinated with ChAdOx1-Lassa-GPC (Figure 3-8A-F). However, a single lung sample from the prime-boost vaccination group exhibited low-level ISH staining for positive-strand LASV RNA. By contrast, LASV RNA staining was abundantly present in all investigated tissues of control animals. Specifically, LASV replication was observed in type I and II pneumocytes and alveolar macrophages (Figure 3-8G). LASV replication was also observed in hepatic Kupffer cells (Figure 3-8H) and splenic reticuloendothelial cells (Figure 3-8I).

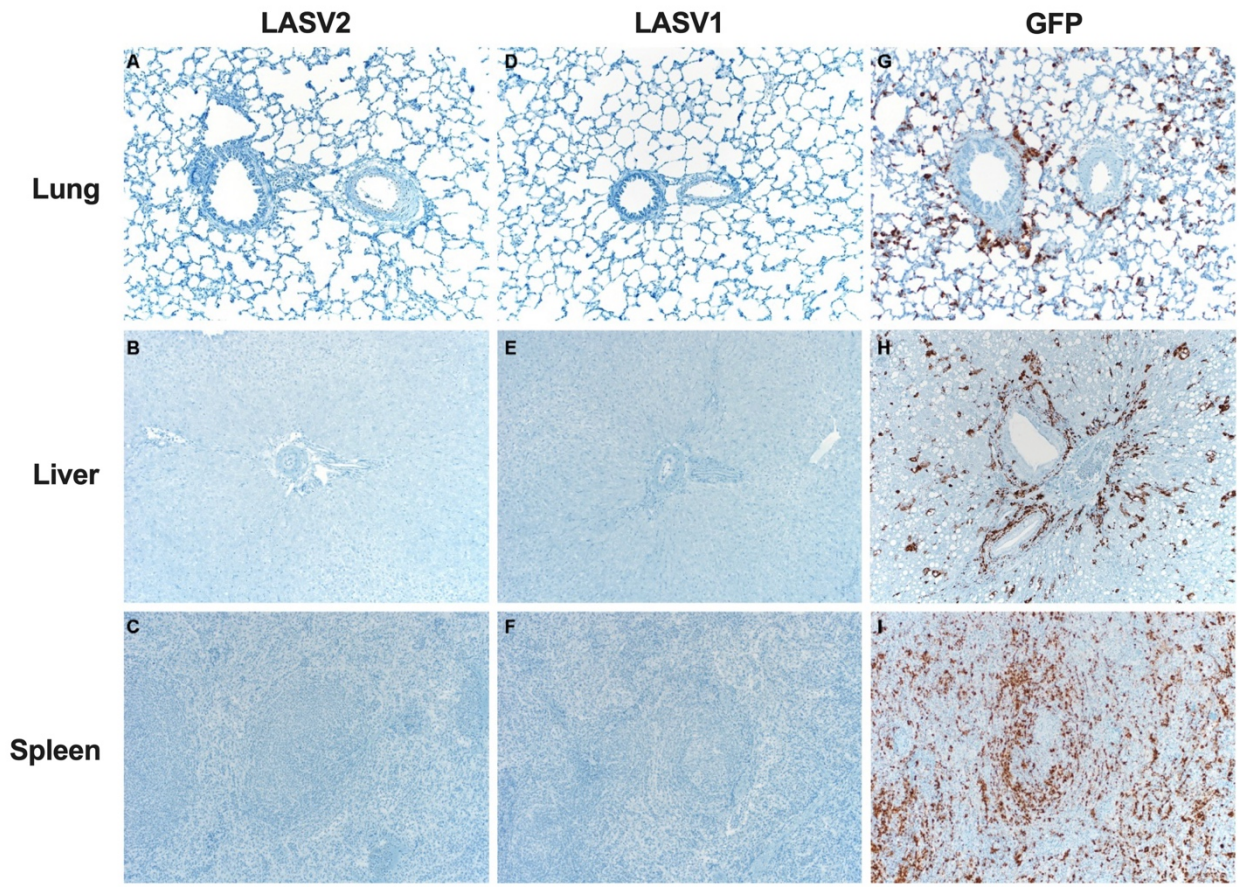


Figure 3-8. Replicating LASV is not detectable in tissues of ChAdOx1-Lassa-GPC-vaccinated animals by *in situ* hybridisation. Lung, liver, and spleen samples were collected from guinea pigs necropsied on 12 DPC (n=4 per group); tissue sections were stained with a LASV RNA-specific probe. Representative fields of view for each tissue collected from the prime-boost **(**LASV2) **(A-C)**, prime (LASV1) **(D-F**), and control (GFP) **(G-I)** groups are shown at 100X magnification. Positive-strand RNA, indicative of virus replication, is visible as brown staining.

Viral RNA was still detected in the terminal tissues of some survival cohort vaccinees at the study endpoint (28 DPC), but levels had decreased relative to those measured at 12 DPC, as indicated in Table 3-2 (Figure 3-9A). Sera were negative for viral RNA in all animals except for one animal in each group (LASV1=1.052, LASV2=0.223 $\log_{10}$ $TCID_{50}$/mL equivalents) (Figure 3-9B). Intergroup mean differences were not significant in tissues (lung, liver, spleen: p=0.9577, 0.92247, 0.9577) or sera (p>0.9999) by two-way ANOVA with Tukey's multiple comparisons correction. Consistent with findings at 12 DPC, significant titres of infectious virus could not be isolated from

lung, liver, or splenic tissues of the vaccinated animals at 28 DPC (Figure 3-9C). As above, tissue titration assays were carried out by Dr. Robert Fischer.

	LASV1	LASV2
Lung	0.934 [0.168 to 1.694]	0.779 [-0.638 to 1.602]
Liver	1.024 [-0.271 to 1.927]	1.788 [0.309 to 2.585]
Spleen	1.776 [1.043 to -2.321]	1.909 [0.933 to 2.435]
Sera	-1.097 [-1.097 to -0.560]	-1.097 [-1.097 to -0.437]

Table 3-2. LASV RNA detected by qRT-PCR in lung, liver, spleen, and sera at 28 DPC. For lung, liver, and spleen tissues, the table indicates median [IQR] log_{10} $TCID_{50}$/g equivalents determined for each group. For sera, median [IQR] log_{10} $TCID_{50}$/mL equivalents are shown for each group.

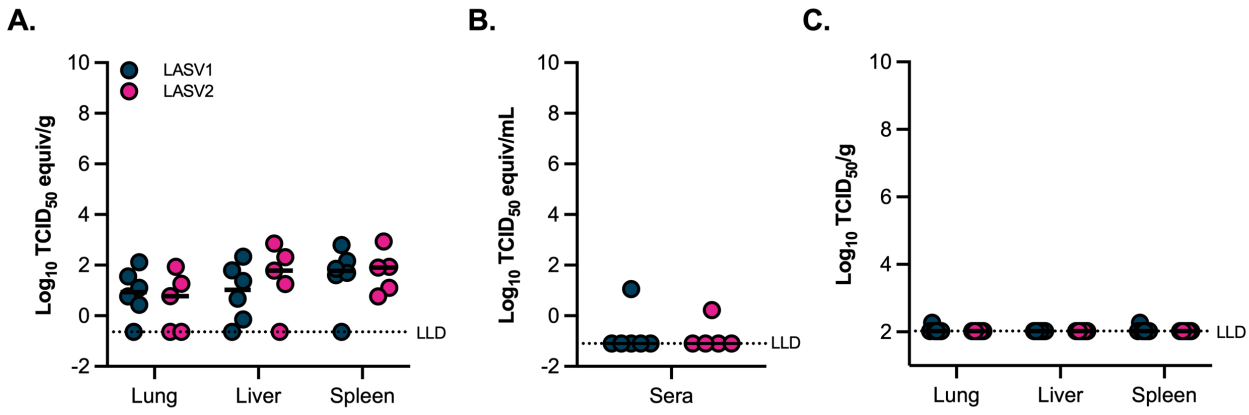


Figure 3-9. Reductions in viral load measured in the tissues of vaccinated animals at the study endpoint. (A) qRT-PCR detection of LASV RNA (log_{10} $TCID_{50}$/g equivalents) in lung, liver, and spleen tissue collected at 28 DPC from survival cohort animals immunised with ChAdOx1-Lassa-GPC. LLD for analysis (-0.638 log_{10} $TCID_{50}$/g equivalents) is indicated with a dotted line (statistical test: two-way ANOVA, Tukey's multiple comparisons). **(B)** LASV RNA (log_{10} $TCID_{50}$/mL equivalents) in 28 DPC sera. LLD for analysis (-1.097 log_{10} $TCID_{50}$/g equivalents) is indicated with a dotted line (statistical test: Mann-Whitney). **(C)** Titration of infectious virus isolated from lung, liver, and spleen tissue on Vero E6 cells. Titres expressed as log_{10} $TCID_{50}$/g; LLD for analysis (2.023 log_{10} $TCID_{50}$/g) is indicated with a dotted line (statistical test: two-way ANOVA, Tukey's multiple comparisons). All bars depict group medians. Significant p-values (<0.05) are denoted in the figures, all other comparisons are not significant.

3.2.4 Cross-variant reactivity of vaccine-induced adaptive immune responses

The ability to confer protection against infection by genetically diverse LASV strains is a critical feature for Lassa fever vaccine candidates. As mentioned in section 1.2.4, at least seven LASV lineages exist and nucleotide sequences of the short (S) genomic segment encoding the GPC gene may vary by up to 25%[155]. ChAdOx1-Lassa-GPC encodes antigen derived from the lineage IV Josiah strain virus. Prior to progressing to heterologous LASV challenge experiments in guinea pigs, we verified that vaccine-induced T-cell and antibody responses exhibited cross-reactivity to GP from multiple LASV lineages. CD-1 mice were immunised with a single dose of ChAdOx1-Lassa-GPC (n=8) or ChAdOx1-GFP control vaccine (n=2) and euthanized after 14 days (Figure 3-10A). Splenic T-cell responses were detected by IFNγ ELISpot assay. Cells were stimulated with pools of overlapping peptides spanning the GPC sequence of representative strains from LASV lineages I-IV. The median responses to heterologous strains Pinneo (lineage I), 803213 (lineage II), and GA391 (lineage III) were compared to those to the homologous strain Josiah (lineage IV). T-cell responses induced by ChAdOx1-Lassa-GPC demonstrated substantial cross-reactivity to the GPC of all variants (median [IQR] SFU/10^6 splenocytes: Pinneo-I=495.5 [240.0-1176], 803213-II=633 [442.5-1159], GA391-III=756.0 [562.0-995.0], Josiah-IV=879.0 [725.5-1535]) (Figure 3-10B). However, we detected slightly diminished reactivity of vaccine-induced T cells to heterologous versus homologous antigen. The greatest reduction in IFNγ ELISpot responses was observed for the most divergent strain Pinneo-I (93.1% amino acid sequence identity, p=0.0003), followed by 803213-II (93.9% amino acid sequence identity, p=0.0110) and GA391-III (93.6% amino acid sequence identity, p=0.0355) by Friedman test with Dunn's multiple comparisons correction.

Subsequently, the cross-reactivity of IgG antibody responses in mice vaccinated 28 days prior with a single dose of ChAdOx1-Lassa-GPC (n=8) were assessed by ELISA (Figure 3-10C). Sera from mice injected with ChAdOx1-GFP (n=2) served as a negative control. Sera was incubated with GP antigen from the Josiah strain or one of two heterologous strains: LASV237 Nigeria 2010H (lineage II, 93.5% amino acid sequence identity) or NIG08-A18 2008H (lineage III, 94.1% amino acid sequence identity). Again, the titres of IgG antibodies recognizing homologous and heterologous LASV GP were compared (median [IQR] $\log_{10}$ reciprocal sera dilution: LASV237 Nigeria 2010H=4.107 [3.881-4.333], NIG08-AI8 2008H=4.107 [3.806-4.333], Josiah=4.258 [4.107-4.634]). Although statistically significant, very minimal reductions in the capacity for vaccine-induced IgG to react with GP of LASV237 Nigeria 2010H-II (p=0.0489) and NIG-08-AI8 2008H-III (p=0.0173) were detected (Friedman test with Dunn's multiple comparisons correction) (Figure 3-10D). LASV GP-specific responses in the sera of ChAdOx1-GFP recipients fell below the limit of detection. These findings suggest that immune responses induced by ChAdOx1-Lassa-GPC demonstrate slightly diminished potency against heterologous antigen; however, given that quantitative correlates of protection for LASV infection have not yet been defined it is not clear if these minor reductions in immunogenicity will have any impact on vaccine efficacy. This information would best be obtained through vaccination-and-challenge experiments with diverse LASV isolates.

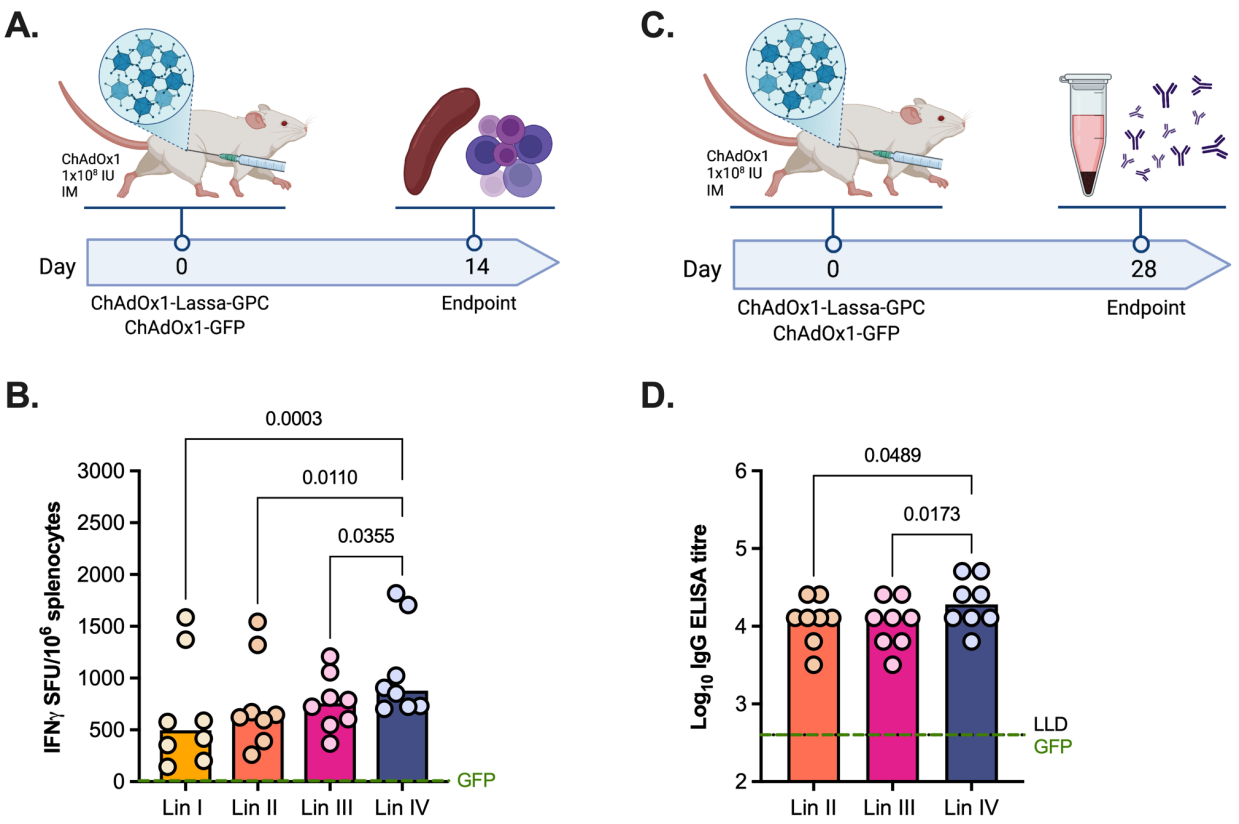


Figure 3-10. Vaccine-specific T cells and IgG antibodies exhibit cross-reactivity to antigen from heterologous LASV strains. (A) Outline of immunisation experiment in CD-1 mice. **(B)** IFNγ ELISpot assay of murine splenocytes stimulated with four different peptide pools corresponding to the GPC sequence of representative strains from LASV lineages I-IV. Responses measured in SFU per $1.0x10^6$ splenocytes. Dashed line (green) indicates mean response in (n=2) ChAdOx1-GFP control animals (statistical test: Friedman, Dunn's multiple comparisons). **(C)** Outline of immunisation experiment in CD-1 mice. **(D)** IgG antibody titres (log_{10}) binding to GP antigen of representative strains from LASV lineages II-IV in two-fold serially diluted sera were measured by ELISA. Endpoint titres were determined using the mean OD plus three-fold standard deviations for naïve sera. The (black) LLD line indicates the lowest (reciprocal) sera dilution tested. The (green) dashed line indicates mean titre in (n=2) ChAdOx1-GFP control animals (statistical test: Friedman, Dunn's multiple comparisons). All bars depict group medians. Significant p-values (<0.05) are denoted in the figures, all other comparisons are not significant.

3.3 Discussion

Lassa fever is a public health threat requiring continued research momentum due to its potential to cause significant morbidity and mortality. Availability of a safe and efficacious vaccine will be critical for disease prevention efforts in endemic and outbreak prone regions. This chapter principally reports the results from preclinical immunogenicity and efficacy evaluations of a novel chimpanzee adenovirus-vectored Lassa fever vaccine candidate, ChAdOx1-Lassa-GPC, in small animal models.

Our data shows that ChAdOx1-Lassa-GPC uniformly protects Hartley guinea pigs against Lassa fever. Animals receiving a single dose of ChAdOx1-Lassa-GPC survived lethal LASV challenge and did not develop notable signs of illness, in contrast to ChAdOx1-GFP control animals. At 12 DPC, no viable virus was recovered from animals receiving two doses of ChAdOx1-Lassa-GPC. Only one animal receiving a single dose of the vaccine had recoverable infectious virus in its lung tissue, at just over the limit of detection for the assay. However, the observation of low levels of LASV RNA in the tissues of vaccinees indicated that sterilising immunity was not achieved. Induction of a NP-specific antibody response in vaccinated (and control) animals provided further evidence of some degree of virus replication. Interestingly, although significant differences in viral load were not apparent between prime-boost and prime vaccinees, NP-specific IgG titres at 12 DPC were significantly higher in the latter (compared to the former). Together, these findings suggest that while administration of a booster dose is not necessary to protect against Lassa fever disease, it may facilitate more rapid control of virus replication in the early days after infection.

It is unclear if the observation of replicating virus in immunised animals reflects the stringency of this particular challenge model or if it will be predictive of outcomes following natural exposure

in humans. Few vaccine candidates have been tested in the lethal Hartley guinea pig model (with GPA LASV). Instead, most rodent efficacy studies have relied on the inbred Strain 13 guinea pig model. Multiple vaccine candidates, including leading candidates based on the VSV platform and the attenuated MOPV reassortant clone ML29, have reportedly conferred sterilising protection in these animals[200,462]. However, the same VSV-vectored vaccine candidate demonstrated only 83% efficacy in Hartley guinea pigs and infectious virus was isolated from the liver, lung, and spleen of vaccinated animals[463]. These findings may suggest that the Hartley guinea pig model represents a more stringent model of LASV infection, potentially increasing the likelihood of observing residual virus after challenge. Evaluation in NHPs may provide a clearer indication of a vaccine's ability to completely protect after lethal LASV challenge.

The correlates of protection for Lassa fever are poorly understood. It is widely hypothesised that a strong cellular immune response is necessary to protect against natural infection. This assertion is predicated on evidence that a strong humoral response is not observed in patients during the acute phase of the disease and neutralising antibodies are not detected until patients are well into convalescence[174]. Furthermore, in humans, LASV-specific $CD4^+$ and $CD8^+$ T-cell responses are activated early during infection and continue to be detected after recovery despite low (or absent) antibody responses[175]. Vaccine development for Lassa fever would be enhanced by more in-depth investigation into vaccine-mediated cellular immune mechanisms. However, tools for these investigations are not well-developed in the guinea pig model. For this reason, immunogenicity experiments were performed in mice, to assess the quality of the cellular immune response after vaccination with ChAdOx1-Lassa-GPC. Immunised mice developed a strong LASV-specific $CD8^+$ T-cell response. The majority of antigen-experienced $CD8^+$ T cells secreted IFNγ and TNFα. IL-2 expression was low overall. Evaluations of VSV-vectored and MV-vectored Lassa fever

vaccines have similarly observed an IFNγ- and TNFα-driven effector response post vaccination[203,214].

There is ample evidence suggesting that multiple-cytokine producing T cells are functionally superior to single-cytokine producing T cells, as the latter have a limited capacity to be sustained as memory cells[464]. Hence, vaccines, such as ChAdOx1-Lassa-GPC, which elicit a high proportion of polyfunctional T cells may be more likely to confer long-term protection. Studies characterizing vaccine-induced T-cell responses against HIV, hepatitis C virus, and influenza A virus, revealed a strong association between the level of protection and the induction of high frequencies of T cells co-producing IFNγ, TNFα, or IL-2[465-468].

At 21 days post immunisation, the vaccine-specific $CD8^+$ T-cell response was skewed towards effector or effector memory function. Data from other adenoviral-vectored vaccine candidates suggest that the central memory response is detectable only from a few months after vaccination. These kinetics may have contributed to low frequency IL-2 expression upon antigenic stimulation of splenocytes collected 21 days after immunisation, as T_{CM} are significant producers of this cytokine[464]. Administration of a second dose of ChAdOx1-Lassa-GPC favoured expansion of effector cells but did not significantly alter the overall proportion of activated cells or their functionality. This finding was not unexpected as some studies suggest that a larger interval between first and second doses or, alternatively, administration of a heterologous viral vector prime-boost regimen, may be required to efficiently boost and expand polyfunctional cellular immune responses[469-471].

A single dose of ChAdOx1-Lassa-GPC produced a humoral response, which was boosted by administration of a second dose. However, the observed increase in median IgG titres was only

statistically significant in guinea pigs and not in mice. Guinea pig sera did not demonstrate neutralising activity against pseudotyped or live virus. The functional role and relative importance of antibodies in controlling LASV infection has not been well-characterised. During natural infection, antibody production is thwarted due to viral targeting of antigen-presenting cells; antibodies, if present, may confer some degree of protection, as demonstrated by successful monoclonal antibody therapy in guinea pigs and non-human primates[180,181]. Neutralising antibodies to LASV GP have been detected in some survivors of LASV infection and primarily target epitopes exposed in the metastable prefusion trimer. However, it is postulated that the glycan arrangement around key neutralising sites of the prefusion trimer also precludes the selection and clonal expansion of B cells producing high-affinity neutralising antibodies[472]. In a recent study, adjuvanted virus-like particles expressing a stable native-like LASV Josiah GP trimer induced the production of hyperimmune sera in rabbits with the capacity to neutralise multiple strains of LASV *in vitro*. It has yet to be determined if this system can induce sufficiently high titres of neutralising antibodies to protect against LASV challenge in animal models[473].

The genetic diversity of LASV across West Africa poses a challenge for vaccine development. Lineages II and III are most epidemiologically relevant in Nigeria, while lineage IV circulates in Sierra Leone, Liberia, and Guinea[120,163]. An insufficient number of isolates or cases in lineages V, VI, and VII makes it difficult to assess their contribution to current caseloads or outbreaks[123,128,161]. In this chapter, the cross-reactivity of IFNγ T cells and serum IgG antibodies elicited by ChAdOx1-Lassa-GPC vaccination was evaluated, in CD-1 mice, against antigen from different LASV strains. Representative strains from LASV lineages I, II, and III were selected for ELISpot analysis and strains from lineages II and III were selected for ELISA analysis. We compared the strength of IFNγ T-cell responses and IgG titres for each of the heterologous antigens against those for the

homologous Josiah strain antigen. The results from these assays revealed a modest reduction in the magnitude of immune responses to the heterologous versus homologous antigens. However, from these data, we cannot predict the implication of these reductions in cross-strain immunogenicity for protection against disease. Indeed, in the case of SARS-CoV-2 VOCs, substantial reductions in neutralising antibody titres elicited by vaccination (in humans) have not correlated with a loss of protection against severe COVID-19 following infection with emerging variants[474]. It is likely that ChAdOx1-Lassa-GPC will demonstrate at least partially protective efficacy against a diverse array of LASV strains. But the true extent to which ChAdOx1-Lassa-GPC will confer cross-variant protection can only be assessed in heterologous experimental challenge models.

In summary, our findings collectively demonstrate that ChAdOx1-Lassa-GPC is effective in protecting Hartley guinea pigs against a uniformly lethal homologous LASV challenge. The results of this chapter lay the foundation for future work to assess the vaccine's capacity to protect against infection by virus strains of other LASV lineages in a heterologous challenge study. Additionally, they justify progression to expanded immunogenicity characterisation and efficacy determination in a NHP model.

4

Efficacy evaluation of ChAdOx1-Lassa-GPC in cynomolgus macaques

4.1 Introduction

The results from Chapter 3 suggested that ChAdOx1-Lassa-GPC protects Hartley guinea pigs from disease associated with LASV infection and elicits antigen-specific cellular and humoral immune responses in CD-1 mice. In mice, significant differences between the magnitude and functional profiles of Th and CTL responses were not detected between single-dose and prime-boost vaccinees. GP-specific IgG ELISA titres in mice also did not demonstrate a statistically significant boosting effect. However, in guinea pigs, IgG titres measured 28-days post boost were elevated above those measured 28-days post prime. Although levels of viral RNA and infectious virus titres were not different between prime and prime-boost vaccinees at 12 or 28 DPC, prime vaccinees developed significantly higher titres of NP-specific IgG (than prime-boost animals) post challenge. These findings suggest that booster vaccination may contribute to the more efficient control of virus replication in the early days after exposure, although it may not be required to prevent clinical disease.

The next step in our evaluation of ChAdOx1-Lassa-GPC, was the translation of findings in rodents to a model more closely correlated with humans. NHPs are considered ‘gold standard’ models for

preclinical vaccine evaluation and for the study of many viral infections, including LASV. Cynomolgus macaques, specifically, are the most widely used NHP species in LASV research and recapitulate many clinical and laboratory features of severe Lassa fever in humans. The characteristics of LASV infection in these animals are described in section 1.2.6. Briefly, upon IM inoculation with LASV Josiah, animals may exhibit lethargy, transient fever, weight loss, and abnormal respiration[196]. High levels of viraemia, elevated liver enzymes, elevated levels of certain circulating proinflammatory cytokines (e.g., IL-6), and depressed T-cell activation are predictors of terminal illness[173,197]. Histopathologic alterations are common in sites of virus replication, including in the liver, lungs, spleen, and lymph nodes. Animals typically succumb to disease between 9-14 days after infection[196].

In this chapter, we demonstrate that ChAdOx1-Lassa-GPC is immunogenic and efficacious in the cynomolgus macaque model of Lassa fever. Cellular and humoral immune responses are characterised after single-dose and prime-boost immunisation and indicate the induction of multifunctional antigen-specific T-cell and antibody responses. Upon challenge with a lethal dose of LASV Josiah, immunised animals exhibited limited clinical, pathological, and immunological signs associated with disease, whereas control animals progressed to terminal illness and euthanasia within 10 days. These findings were largely consistent with and expand upon those from mice and guinea pigs in Chapter 3. Collectively, the results from Chapters 3 and 4 support further evaluation of ChAdOx1-Lassa-GPC in phase I clinical trials and in heterologous challenge experiments.

4.1.1 Authorship statement

This chapter contains data from a vaccination-challenge study performed in cynomolgus macaques under BSL4 conditions. Dr. Robert Fischer was listed as the Principal Investigator on this Animal Study Protocol. Please see the overall Statement of Authorship (page xviii) for a summary of procedures conducted by colleagues. Data generated by others will be referenced in the corresponding figures throughout this chapter.

4.1.2 COVID-19 statement

Due to the COVID-19 pandemic, the use of BSL4 facilities for research unrelated to SARS-CoV-2 was deferred for over one year. As a consequence of the lengthy postponement of the study presented in this chapter, some experimental work could not be completed in time for inclusion in this thesis but is currently underway. Moreover, there are several studies included in my original thesis research plan, which I was not able to pursue due to their indefinite deferral or cancellation. These studies are briefly discussed at the end of this chapter.

4.2 Results

4.2.1 Overview of animal experiment and outcome of hearing tests

ChAdOx1-Lassa-GPC was administered via the IM route to cynomolgus macaques as either a single dose (LASV1) or prime-boost (LASV2) vaccination regimen (n=4 per group), with a 28-day interval between doses (Figure 4-1). Control macaques (n=4) received two doses of ChAdOx1-GFP (GFP) also administered 28 days apart. Clinical examinations were performed on each immunisation day (-56- and -42-days post challenge, DPC), 14 days after each immunisation (-42 and -14 DPC), seven days pre-challenge (-7 DPC), and on the day of challenge (0 DPC). All animals were challenged with $1x10^4$ $TCID_{50}$ of LASV strain Josiah, 28 days after receiving their final immunisation. After LASV challenge, animals were monitored daily and scored for clinical indicators of disease by a trained member of RMVB. Standardised clinical scores were used to identify animals reaching humane endpoint criteria, at which point they were euthanized. Surviving animals were followed until the endpoint of the study, 42 DPC, prior to euthanasia. Sera and PBMCs were collected on each exam day pre- and post-challenge. Multiple tissues were collected for virological and pathological assessment at the time of necropsy (Figure 4-1).

Natural LASV infection may result in long-term sensorineural hearing loss in up to 25% of survivors. Although the underlying mechanism is not fully understood, damaging immune responses to infection are implicated in this outcome. To address these concerns, BAER auditory testing was performed on the animals in our study to detect evidence of sensorineural hearing loss following ChAdOx1-Lassa-GPC vaccination and LASV challenge (Figure 4-1). Signs of hearing loss were not observed in any animal throughout the study.

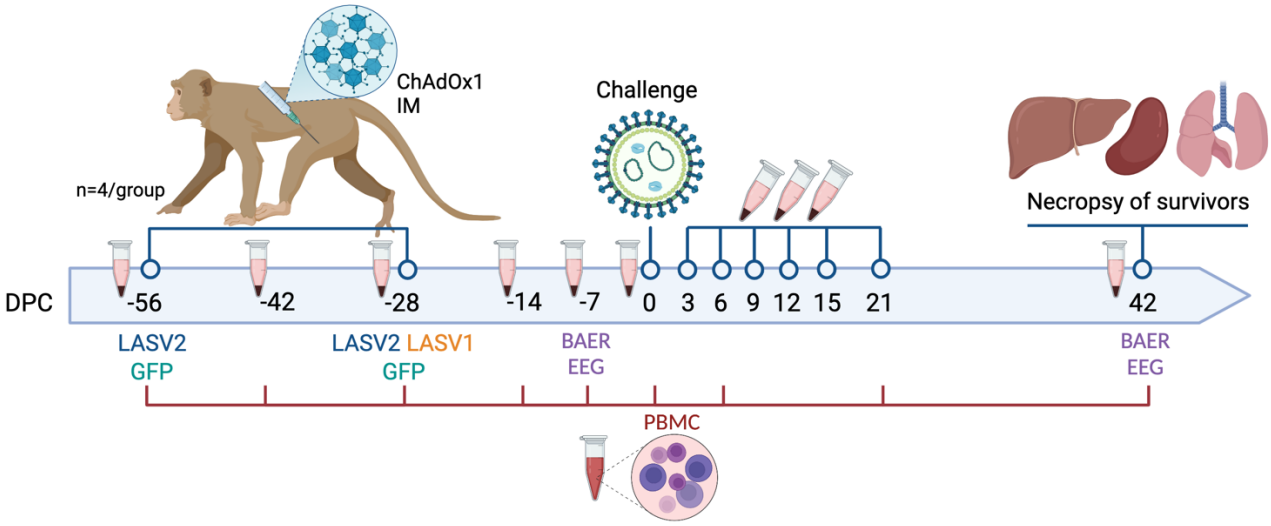


Figure 4-1. Efficacy of ChAdOx1-Lassa-GPC against LASV infection in cynomolgus macaques. Outline of immunisation experiment and sampling performed in 12 female cynomolgus macaques. Experimental group abbreviations: ChAdOx1-Lassa-GPC prime-boost (LASV2), ChAdOx1-Lassa-GPC prime only (LASV1), ChAdOx1-GFP control (GFP). Vaccinations took place on -56 and/or -28 DPC. Sera were collected during all clinical examinations, which occurred on -56, -42, -28, -14, -7, 0, 3, 6, 9, 12, 15, 21, and 42 DPC. PBMCs were isolated on -56, -42, -28, -14, -7, 0, 3, 6, 21, and 42 DPC. BAER auditory testing was performed on -7 and 42 DPC. Animals were euthanized upon reaching human endpoint criteria after LASV challenge or at the study endpoint (42 DPC). Liver, lung, spleen, and lymph node tissues were harvested during necropsies.

4.2.2 Antigen-specific T-cell responses induced after vaccination

Like in Chapter 3, the magnitude of the vaccine-induced T-cell response in macaques was first estimated by IFNγ ELISpot assay. PBMCs collected at -56, -42, -28, -14, and -7 DPC were stimulated with three pools of overlapping peptides spanning the full-length Josiah strain LASV GPC sequence. Median responses, summed across peptide pools, were monitored over time after vaccination (Figure 4-2A). In ChAdOx1-GFP controls, median responses remained at or below 5 SFU/10^6 PBMCs at all timepoints assayed. In prime-boost animals, circulating LASV-specific T cells were detectable 14 days after prime vaccination; their numbers dropped slightly by -28 DPC and were modestly augmented by the administration of a second vaccine dose (median [IQR] SFU/10^6 splenocytes at -56, -42, -28, -14, and -7 DPC, respectively: 4.5 [2.0-8.5], 187.0 [164.5-

229], 160.0 [154.5-189.5], 319.0 [222.5-465.0], 310.0 [210.0-414.5]) (Figure 4-2B). Peak responses were observed at -14 DPC, which were significantly elevated above baseline values (-56 vs. -14 DPC p=0.0032) and remained so through -7 DPC (-56 vs. -7 DPC p=0.0146) (Friedman test with Dunn's multiple comparisons correction). The magnitudes of the GPC-specific IFNγ T-cell responses in prime-boost and prime vaccinees were not significantly different at the time of peak responses (-14 DPC) in both groups (p=0.9753) (median [IQR] SFU/10^6 splenocytes: LASV2=319.0 [210-414.5], LASV1=196.0 [163.5-293], GFP=4.5 [4.0-5.0]) (Kruskal-Wallis with Dunn's multiple comparisons correction) (Figure 4-2C).

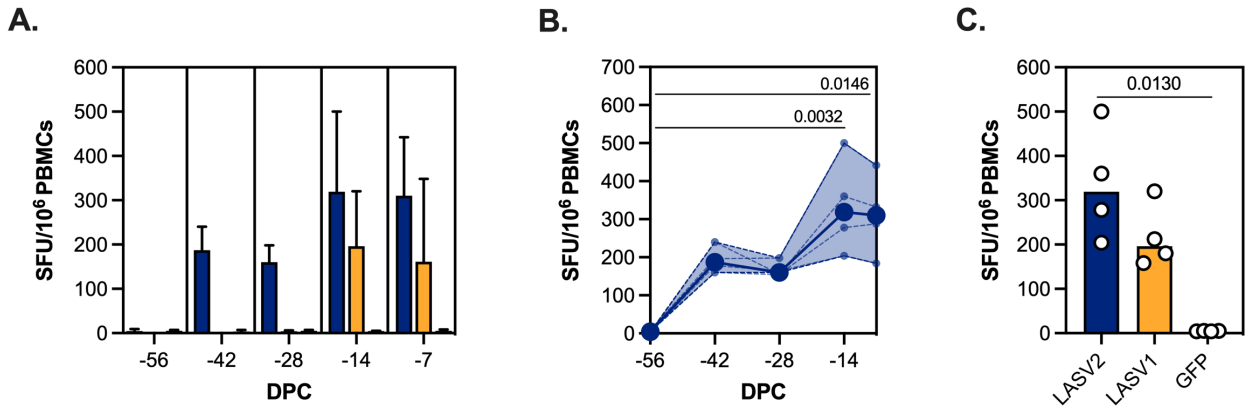


Figure 4-2. IFNγ ELISpot responses induced by ChAdOx1-Lassa-GPC vaccination. IFNγ ELISpot assay SFU per 10^6 PBMCs summed across cells stimulated with three peptide pools spanning the LASV GPC amino acid sequence after the subtraction of background responses detected in a corresponding set of DMSO-treated controls. **(A)** Responses in all groups over the time post vaccination. **(B)** Responses in prime-boost animals over time post vaccination (statistical test: Friedman test, Dunn's multiple comparisons). **(C)** Comparison of responses between prime-boost, prime, and control animals at -14 DPC (statistical test: Kruskal-Wallis, Dunn's multiple comparisons). All bars depict group medians. Error bars (where shown) indicate 95% confidence intervals. Significant p-values (<0.05) are denoted in figures B and C, all other comparisons are not significant.

LASV-specific $CD4^+$ and $CD8^+$ T-cell responses in vaccinees were subsequently characterised in greater detail by ICS and flow cytometric analysis of GPC-stimulated PBMCs at -14 DPC. Phenotypic assessment of GP-specific $CD4^+$ T cells suggested that vaccine-induced Th-cell responses were skewed towards a Th1-like phenotype. Total frequencies of $CD4^+$ T cells

expressing the Th1 cytokines IFNγ or TNFα (IFNγ$^+$/TNFα$^+$), in prime-boost (p=0.0477) and prime (p=0.0623) vaccinees, were elevated above those in controls, although only the former comparison was statistically significant (median [IQR] %: LASV2=0.440 [0.281-0.616], LASV1=0.418 [0.297-0.506], GFP=0.015 [0.010-0.0275]). Frequencies in prime-boost and prime vaccinees were also not significantly different (p>0.9999) (Kruskal-Wallis test with Dunn's multiple comparisons correction) (Figure 4-3A). Additional analysis of this subset of CD4$^+$ T cells (in vaccinees) revealed that a mean of 52% and 46% of CD4$^+$ IFNγ$^+$/TNFα$^+$ cells in prime-boost and prime vaccinees, respectively, were polyfunctional and expressed both IFNγ and TNFα (Figure 4-3A). By contrast, total frequencies of CD4$^+$ T cells expressing the Th2 cytokines IL-4 or IL-5 (IL-4$^+$/IL-5$^+$) did not surpass 0.03% in prime-boost or prime vaccinees, like those detected in controls (Figure 4-3B).

We subsequently further characterised the CD4$^+$ IFNγ$^+$/TNFα$^+$ population according to memory phenotypes. Unlike in humans or mice, effector and memory T-cell classes in macaques can be defined by expression of the co-stimulatory receptor, CD28, which is constitutively expressed on naïve T cells, and Fas receptor CD95, which is upregulated on antigen-experienced T cells. Accordingly, T cells were classified as effector/effector memory (T_{EEM}, CD28$^-$ CD95$^+$), central memory (T_{CM}, CD28$^+$ CD95$^+$), or naïve (CD28$^+$ CD95^{lo})[475].

Our phenotypic assessment of the GPC-specific CD4$^+$ IFNγ$^+$/TNFα$^+$ population revealed a substantial proportion of T_{EEM} cells, which appeared to be elevated in the prime-boost animals compared to prime vaccinees (median [IQR] %: LASV2=65.40 [60.33-69.50], LASV1=55.25 [53.10-60.33]) (Figure 4-3C). However, this difference was not statistically significant (p=0.0571, Mann-Whitney). Frequencies of T_{CM} cells within the CD4$^+$ IFNγ$^+$/TNFα$^+$ population were low

and similar between groups (median [IQR] %: LASV2=9.85 [9.03-11.73], LASV1=9.4 [7.43-12.58]) (p=0.6857, Mann-Whitney).

An analogous mode of analysis was applied to probe the $CD8^+$ T-cell subset for evidence of cytotoxic responses elicited by ChAdOx1-Lassa-GPC vaccination. First, total frequencies of $CD8^+$ T cells expressing at least one cytokine associated with cytotoxic function—IFNγ, TNFα, or Granzyme B (GrB)—were estimated. The magnitude of the $IFN\gamma^+/TNF\alpha^+/GrB^+$ response in prime-boost (median [IQR] %: 3.165 [2.533-3.940], p=0.0098) and prime (median [IQR] %: 2.330 [1.730-2.623], p=0.2327) vaccinees were significantly greater than those in control animals (median [IQR] %: 0.245 [0.0700-0.4125) (Figure 4-3D). Although the distinction did not reach statistical significance (p=0.7179), slightly elevated $IFN\gamma^+/TNF\alpha^+/GrB^+$ $CD8^+$ T-cell frequencies in the prime-boost versus prime vaccinees may suggest that a stronger cytotoxic response is associated with a two-dose vaccination regimen (Kruskal-Wallis test with Dunn's multiple comparisons correction). Comparison of cytokine expression profiles within the $IFN\gamma^+/TNF\alpha^+/GrB^+$ subset revealed that the largest fractions, summing to over 50% of all cells, were double positive for either $IFN\gamma^+$ $TNF\alpha^+$ (LASV2=32.2%, LASV1=28.1%) or $IFN\gamma^+$ GrB^+ (LASV2=27.4%, LASV1=30.6%) in both prime-boost and prime vaccinees. Notably, mean percentages of 15.2% and 12.4% of $IFN\gamma^+/TNF\alpha^+/GrB^+$ cells co-expressed IFNγ, TNFα, and GrB, in prime-boost and prime group animals, respectively (Figure 4-3D).

Antigen-specific $CD8^+$ $IFN\gamma^+/TNF\alpha^+/GrB^+$ T cells primarily exhibited a T_{EEM} phenotype (median [IQR] %: LASV2=82.2 [80.15-85.68], LASV1=80.65 [77.48-86.53]) rather than a T_{CM} phenotype (median [IQR] %: LASV2=4.10 [3.00-4.83], LASV1=4.15 [2.60-4.95]). The frequencies of these populations were similar between groups (T_{EEM} p>0.9999, T_{CM} p>0.9999) (Mann-Whitney test)

(Figure 4-3E). Together, these data indicate that ChAdOx1-Lassa-GPC elicits polyfunctional Th1 and cytotoxic T-cell responses, consistent with the findings presented in Chapter 3. At -14 DPC, these responses comprise predominantly T_{EEM} phenotypes. Although these data provide some indication that booster vaccination may enhance the magnitude of certain LASV-specific T-cell responses, larger group sizes to enable statistical comparisons of higher power would be required to facilitate proper differentiation of the results between vaccination regimens.

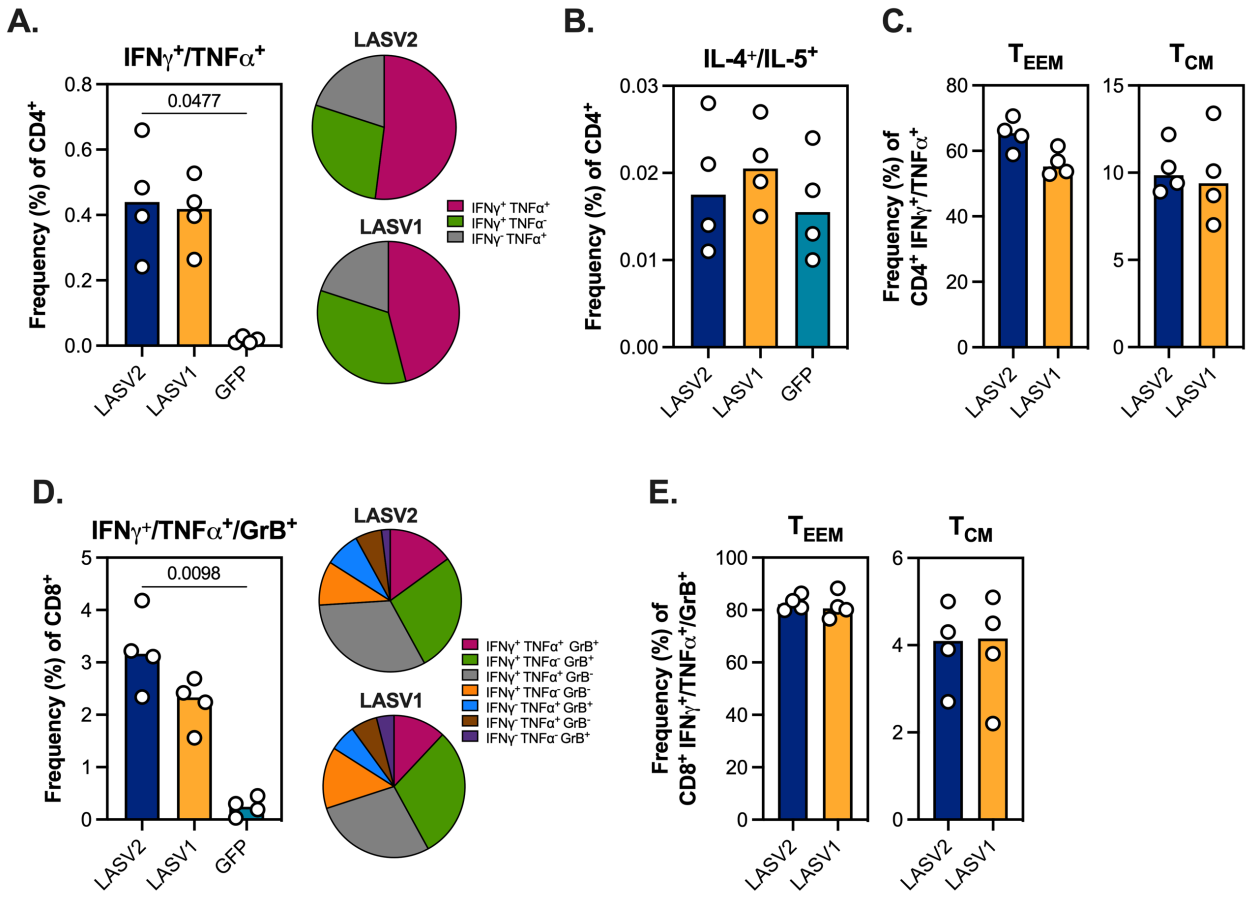


Figure 4-3. Functional assessment of LASV-specific T-cell responses. Frequencies of cytokine-expressing T cells after GPC peptide pool stimulation and ICS of PBMC samples collected at -14 DPC. Graphed values reflect adjustment to exclude non-specific cytokine expression measured from a corresponding set of unstimulated samples. **(A)** Bar chart (left) depicting the frequencies of $CD4^+$ T cells expressing IFNγ or TNFα for the animals within each group. Pie charts (right) indicating the mean fraction of total $IFN\gamma^+/TNF\alpha^+$ cells bearing a specific polyfunctional profile for prime-boost and prime group animals (statistical test: Kruskal-Wallis, Dunn's multiple comparisons). **(B)** Frequencies of $CD4^+$ T cells expressing IL-4 or IL-5 for the animals within each group (statistical test: Kruskal-Wallis, Dunn's multiple comparisons). **(C)** Frequencies of $CD4^+$ $IFN\gamma^+/TNF\alpha^+$ T cells exhibiting a T_{EEM} ($CD28^-$ $CD95^+$) or T_{CM} ($CD28^+$ $CD95^+$) phenotype (statistical tests: Mann-Whitney). **(D)** Bar chart (left) depicting the frequencies of $CD8^+$ T cells expressing IFNγ, TNFα, or Granzyme B (GrB) for the animals within each group. Pie charts (right) indicating the mean fraction of total $IFN\gamma^+/TNF\alpha^+/GrB^+$ cells bearing a specific polyfunctional profile for prime-boost and prime group animals (statistical test: Kruskal-Wallis, Dunn's multiple comparisons). **(E)** Frequencies of $CD8^+$ $IFN\gamma^+/TNF\alpha^+/GrB^+$ T cells exhibiting T_{EEM} ($CD28^-$ $CD95^+$) or T_{CM} ($CD28^+$ $CD95^+$) phenotype (statistical tests: Mann-Whitney). All bars depict group medians. Significant p-values (<0.05) are denoted in the figures, all other comparisons are not significant.

4.2.3 Antibody responses elicited by ChAdOx1-Lassa-GPC

GP-specific IgG antibodies were measured in sera at multiple time points after vaccination by endpoint titre ELISA (Figure 4-4A). At the time of LASV challenge (0 DPC), IgG titres after one (p=0.0672) or two (p=0.0290) vaccine doses were elevated above those measured in the control animals; however, only the latter difference met statistical significance (median [IQR] $\log_{10}$ of reciprocal sera dilution: LASV2=4.408 [3.881-4.709], LASV1=4.107 [3.881-4.559], GFP=2.602 [2.602-2.602]) (Kruskal-Wallis test with Dunn's multiple comparisons correction). Although it appeared that median IgG titres in prime-boost vaccinees were elevated relative to those in single-dose vaccinees, this difference was not statically significant (p>0.9999). Matched analyses of titres in prime-boost animals over time additionally suggested that titres were not substantially boosted after delivery of a second vaccine dose (-28 vs. 0 DPC, p>0.9013) (Friedman test with Dunn's multiple comparisons correction) (Figure 4-4A). However, as with the comparison of T-cell responses, larger group sizes will be required to confirm the presence or absence of a boosting effect. Nevertheless, these data indicate that ChAdOx1-Lassa-GPC elicits robust levels of GP-specific antibodies after just a single dose.

Next, we assessed the functional qualities of the vaccine-induced antibody response. First, the neutralising activity of sera collected from prime-boost and single-dose vaccinees at -7 DPC was assessed using the VSV-based pseudotype system (VSV-Lassa-GPc-cFLAG) and methods described in Chapter 3. The same human monoclonal antibodies (25.10C, 12.1F, 8.9F, 37.2D), alone and in a cocktail, served as positive controls. Again, neutralising titres (IC_{50} values) were extrapolated from a nonlinear regression variable slope curve derived by plotting the $\log_{10}$ of sera dilutions versus the percent infectivity of VSV-Lassa-GPC-cFLAG in Vero E6 cells (Figure 4-4B). Consistent with the findings in Chapter 3, the sera from the immunised macaques

demonstrated little to no capacity to inhibit virus infection; IC_{50} values fell beyond the range of sera dilutions assayed and were similar to those observed in ChAdOx1 GFP controls (Figure 4-4B).

There is increasing evidence supporting a role for non-neutralising antibodies in controlling viral infections[476-478]. Through Fc-receptor engagement, antibodies bound to cognate antigen can trigger numerous effector functions targeting infected cells, including phagocytosis, NK-cell cytotoxicity, and activation of the complement cascade, as described in section 1.1.2. To evaluate the non-neutralising functions of vaccine-elicited antibodies, we compared the relative induction of phagocytosis (by monocytes and neutrophils), complement activation, and NK-cell cytotoxicity by the sera of vaccinees and controls in *in vitro* assays (Figure 4-4C-F). GP-coated fluorescent microspheres were incubated with sera from ChAdOx1-Lassa-GPC vaccinees and ChAdOx1-GFP controls collected at -7 DPC. Antibody-bead complexes were then incubated with human monocyte THP-1 cells, freshly isolated human leukocytes, or guinea pig complement. Antibody-dependent monocyte and neutrophil phagocytosis (ADMP and ADNP), as well as complement deposition (ADCD), were measured by quantifying (1) cells engulfing GP antigen-coated fluorescent microspheres, and (2) the extent of the deposition of C3 complement protein on the surface of GP antigen-coated fluorescent microspheres, respectively. Phagocytosis scores represented the proportion and fluorescence intensity of bead-engulfing THP-1 cells (ADMP, Figure 4-4C) or neutrophils (ADNP, Figure 4-4D). Complement deposition was quantified using a labelled anti-(C3)-complement antibody and measurement of fluorescence intensity (ADCD, Figure 4-4E). Meanwhile, the frequency of activated NK cells with cytotoxic function (antibody-dependent NK cell activation, ADNKA) was estimated by the detection of CD107a expression (a marker of degranulation) after the co-culture of NK cells with serum-derived antibodies bound to

cognate (GP) antigen (Figure 4-4F). The results from all four assays suggested that both one and two doses of ChAdOx1-Lassa-GPC generated antibodies with Fc-mediated effector functions. However, only the differences between prime-boost animals and controls met statistical significance (ADMP p=0.0042, ADNP p=0.0059, ADCD p=0.0042, ADNKA p=0.0051) (Kruskal-Wallis with Dunn's multiple comparisons correction). Due to low sample sizes, the magnitudes of responses in prime-boost and prime vaccinees did not differ significantly, although prime-boost vaccination appeared to be associated with enhanced effector function (Figure 4-4C-F). A relatively high degree of concordance between the various non-neutralising functional variables was observed across (prime-boost and prime) vaccinees; correlation (r) coefficients were greater than 0.7 for all comparisons, and many met statistical significance (Spearman two-sided rank correlation analysis) (Figure 4-4G). Meanwhile, overall IgG ELISA responses on -7 DPC generally exhibited a lower degree of relatedness with these effector functions as suggested by weaker correlation (r) coefficients. Together, these data suggest that changes in the functional capacity of antibodies may not be entirely contingent on increases in overall IgG antibody titres.

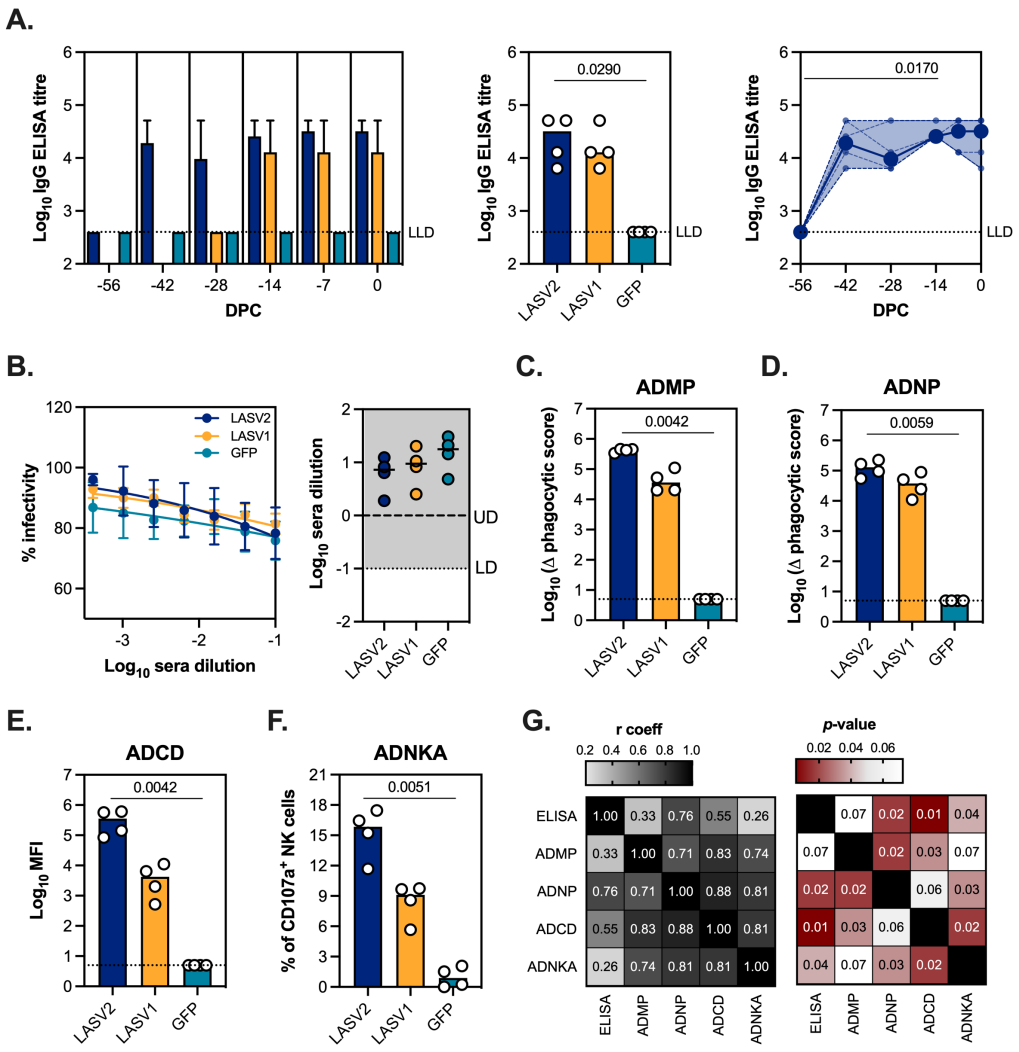


Figure 4-4. Characterisation of the vaccine-induced humoral response. (A) LASV GP-specific (log_{10}) IgG antibody titres in two-fold serially diluted sera were measured by ELISA. Responses in all groups over the time post vaccination (left). Comparison of responses between prime-boost, prime, and control animals at 0 DPC (middle, statistical test: Kruskal-Wallis, Dunn's multiple comparisons). Responses in prime-boost animals over time post vaccination (right, statistical test: Friedman test, Dunn's multiple comparisons). Endpoint titres were determined using a threshold for positivity of the mean OD plus three-fold standard deviations of pooled baseline (-56 DPC) sera. LLD lines indicate the lowest (reciprocal) sera dilution assayed. **(B)** Variable slope nonlinear regression (least squares fit) curve of percent infectivity of VSV-Lassa-GPC-cFlag versus log_{10} sera dilution. Percent infectivity was determined by normalising the number of GFP-positive cells in serum-treated wells against those in virus-only and cell-only control wells. Best-fit IC_{50} values shown as log_{10} sera dilution determined by nonlinear regression. The log_{10} y-axis values corresponding to the lowest sera dilution assayed (LD) and undiluted sera (UD) are indicated with dotted/dashed lines. Values indicative of negligible neutralising activity are captured in the grey shaded region. GP-specific **(C)** antibody-dependent monocyte phagocytosis (ADMP) and **(D)** antibody-dependent neutrophil phagocytosis (ADNP) scores, **(E)** antibody-dependent C3 complement deposition (ADCD) median fluorescent intensity (MFI), and **(F)** antibody-dependent activation of NK cells (ADNKA) assessed by frequencies of $CD107a^+$ NK cells ($CD3^-$ $CD56^+$ $CD16^+$) induced by sera collected on -7 DPC (statistical tests: Mann-Whitney). **(G)** Correlation matrix (left) depicting the Spearman two-sided rank correlation coefficients (r) values for the indicated pairwise comparisons; p-values are also shown (in the heatmap on the right). For graphs C-F, the dotted line indicates a negative response. All bars depict group medians. Error bars (where shown) indicate 95% confidence intervals. Significant p-values (<0.05) are denoted in the figures, all other comparisons are not significant.

4.2.4 Clinical and immunological outcomes of LASV challenge

Twenty-eight days after final immunisation, macaques were challenged with $1x10^4$ $TCID_{50}$ of Josiah strain LASV via IM injection. Standardised clinical scoring was carried out by a trained member of RMVB. Animals were then monitored for up to 42 days for disease signs according to body temperature, weight, food and water intake, behaviour, and other clinical indicators. Interestingly, clear differences in body temperature and weight were not observed between the groups; fever and weight loss did not appear to be characteristic features of disease in our model, with only two control animals developing transient fever (one at 6 DPC and one at 9 DPC) (Figure 4-5A-B). Between 0 and 7 DPC, nearly all animals exhibited a slightly reduced appetite, but only two (prime) vaccinees demonstrated additional signs of illness, namely hunched posture and ruffled fur, meriting clinical scores of 10 or above. During this period, control animals developed exacerbated symptoms including dehydration, abdominal respiration, sunken eyes, and facial oedema around 6 DPC. From 8 DPC onwards clinical signs in vaccinees resolved rapidly (score=0), whereas control animals progressed towards terminal disease characterized by severely depressed appetite, dehydration, reluctant movement requiring support, irregular/shallow respiration, facial oedema or swelling, and in some cases fever (n=1) or neurological signs (n=1). Peak disease occurred at 9 DPC and control animals met humane endpoint criteria (score=35 or above) resulting in euthanasia on 9 (n=2) or 10 (n=2) DPC (Figure 4-5C). By contrast, all vaccinees survived until the study endpoint (42 DPC), indicating that vaccination provided significant protection against uniformly lethal infection (p=0.0010, Mantel-Cox log-rank test) (Figure 4-5D). Notably, the clinical scores of the prime-boost animals did not exceed 3 at any point during infection, suggesting that a two-dose vaccination regimen may confer additional protection against illness after virus exposure. Area under the curve (AUC) comparison (AUC±SEM:

LASV2=4.500±2.121, LASV1=37.000±11.070, GFP=116.500±7.863) demonstrated a significant reduction in clinical signs in prime-boost recipients compared to single-dose vaccinees (LASV2 vs. LASV1: p=0.0124, LASV2 vs. GFP: p<0.0001, LASV1 vs. GFP: p<0.0001, AUC comparison by one-way ANOVA, Tukey's multiple comparisons).

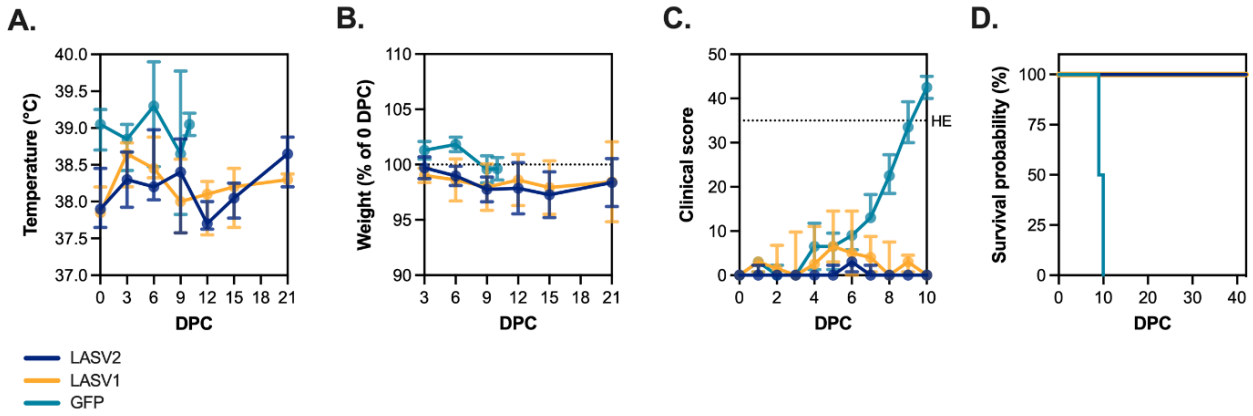


Figure 4-5. Clinical disease signs after LASV challenge. (A) Body temperature (°C) between 0 and 21 DPC; an animal with a temperature of ≥40°C was classified as febrile. **(B)** Changes in weight (as a percentage of weight in kg at 0 DPC) from 3 to 21 DPC. **(C)** Clinical scores between 0 and 10 DPC. Dotted line indicates human endpoint (HE) criteria for euthanasia (clinical score=35). **(D)** Percent survival of cynomolgus macaques following challenge with LASV (statistical test: Mantel-Cox log rank test). Scatter plots (A-C) depict median values and interconnecting line for each group; error bars indicate the 95% confidence interval.

Haematological evaluation revealed similar patterns in the changes in white blood cell, neutrophil, lymphocyte, and platelet counts between groups from 0 to 6 DPC. Post 6 DPC, control animals appeared to diverge slightly from prime-boost and prime vaccinees, as counts of total white blood cells, neutrophils, lymphocytes, and platelets decreased at 9 or 10 DPC in the former while increasing in the latter. Although, most of these differences did not meet statistical significance, the depression in leukocyte and platelet counts in controls, was consistent with clinical findings indicating that these animals developed severe disease between 7 and 10 DPC, while vaccinees exhibited signs of recovery (Figure 4-6A).

Serum chemistry analysis revelated more salient differences between vaccinees and controls. However, intra-group variation largely precluded observations reaching statistical significance. Specifically, elevated concentrations of alanine aminotransferase (ALT) and aspartate aminotransferase (AST), hallmarks of Lassa fever[479], were elevated in control animals at 9 and 10 DPC, while remaining largely unchanged in prime-boost and prime vaccinees after infection. AST levels in controls were significantly elevated at 9 DPC relative to vaccinees (LASV2 vs. GFP p=0.0163, LASV1 vs. GFP p=0.005, mixed-effects analysis with Tukey's multiple comparisons correction). Albumin, total protein, and calcium concentrations in the blood also decreased in controls at the time at which these animals succumbed to disease, as is consistent with LASV infection in this model (Figure 4-6B). Blood cell counts and chemistry data were procured by members of RMVB after each clinical exam.

Assessment of circulating cytokines revealed an increase in serum levels of IL-6, TNFβ, and IL-12/23, to a limited extent at 3 DPC and moderately at 6 DPC, relative to 0 DPC. These levels continued to rise in control animals as they reached terminal illness (at 9 DPC)—but not in prime-boost or prime vaccinees (Figure 4-6C). Chemoattractants, including MCP-1, MIP-1β, and IP-10, also increased in concentration in a similar manner and to a much greater extent in controls. Meanwhile, IL-8 appeared to be more transiently elevated at 3 DPC in all animals regardless of vaccination status. The levels of anti-inflammatory cytokines IL-5 and IL-10 increased dramatically from 6 DPC to death in control animals, whereas there was only a moderate increase in prime-boost and prime vaccinees during the same period. Finally, we assessed mediators of cytotoxic activities. We detected elevated levels of IFNγ, IL-2, and IL-15 at 6 DPC in all animals, which were augmented several-fold by 6 and 9 DPC in controls with a corresponding modest

increase in vaccinees. Overall, cytokine expression patterns were similar between animals receiving one or two doses of ChAdOx1-Lassa-GPC (Figure 4-6C).

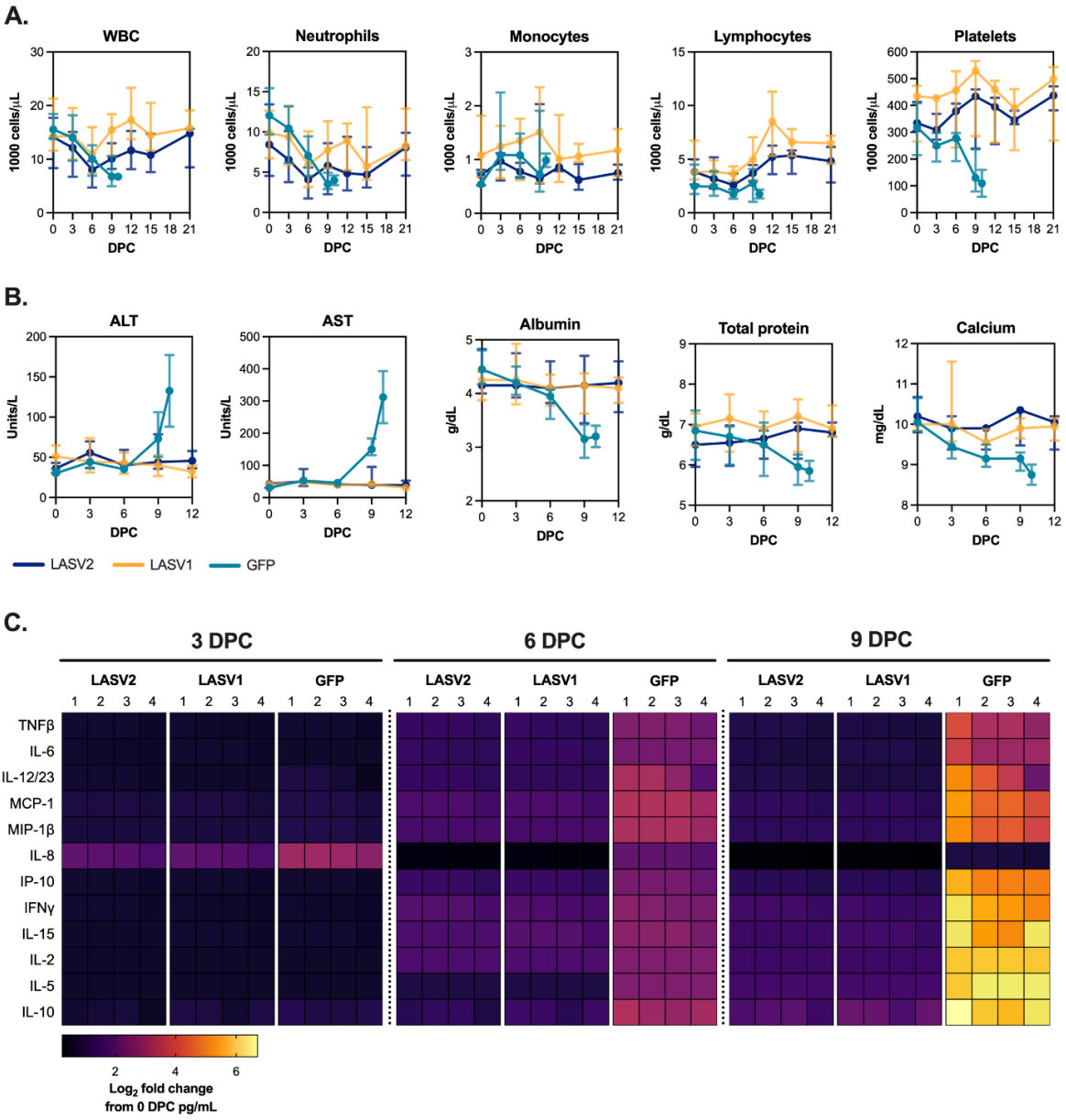


Figure 4-6. Comparison of haematological profiles, serum chemistry, and cytokine milieu after LASV infection. **(A)** Scatter plots of the counts (per μL of whole blood) of selected immunological cell populations determined by ProCyte haematological analysis over time. **(B)** Scatter plots of the concentration of selected enzymes (ALT, AST in units/L), proteins (albumin, total protein in grams/decilitre (dL)), and biomolecules (calcium, in mg/dL) in sera over time. Scatter plots (A-B) depict median values and interconnecting line for each group with error bars indicating the 95% confidence interval. **(C)** Panel of heatmaps depicting the changes (log_2 fold change) in the concentrations (pg/mL) of selected cytokines in sera at 3, 6, and 9 DPC relative to 0 DPC. Each cell represents an individual animal (numbered 1-4) within each group.

Next, we carried out bulk RNA sequencing of PBMC samples collected at 6 DPC—the last timepoint at which PBMCs were isolated from all 12 animals—to compare the effects of LASV challenge on the immunomodulatory environment between vaccinees and controls in greater detail. RNA extraction, sequencing, read mapping, and raw data normalisation was completed by the RML RTB Genomics Core Facility, specifically Brittany Dulek. Subsequently, we performed pairwise comparisons to identify differentially expressed (DE) genes between control samples and prime-boost or prime vaccinee samples (Figure 4-7). Although 6 DPC preceded the timing of peak disease in this model, some notable differences in transcriptional profiles were evident between vaccinees and controls. The majority of DE genes encoded proteins with known human homologues (>80%) and we focused our analysis on these protein-coding genes. We identified 172 genes with expression profiles that differed significantly between either prime-boost vaccinees and controls, or prime vaccinees and controls (significance was defined as a fold change in normalised gene counts ≥2 and a false-discovery rate adjusted p-value <0.05). Hierarchical clustering of gene expression data confirmed that control animals exhibited distinct upregulation of a majority of the DE genes and clustered away from vaccinees (Figure 4-7). Most notably, control animals demonstrated stronger expression of genes associated with innate immunity, early interferon responses, and inflammation, including *OAS1/2/3, TLR2/4/5/7, S100A8/9, IFI6/27/44, CCL2/8/23, CLEC5/7A, LY96, SIGLEC1, ISG15, IFIT1/3, GRZMA, CXCL10, APOBEC3A, CD1B, TRIM35, STAT2,* and *SOCS1*. Alongside augmented inflammatory signalling, control animals exhibited relatively reduced expression of genes governing leukocyte cell-to-cell adhesion (*CD5, CD28, CCR7, ADTRP, RGCC, CTLA4, CD3E, MYB, ZAP70, LEF1, LCK, CD6, IL21, SKAP1, LAX1, LAG3*), cell-cycle regulation (*MCM4/7, CDC6/20/45, PLK1/4, AURKA/B, CDKN3/2C, NUF2, and DSCC1*), as well as others involved in coagulation (*SERPIN, TFPI2*) and apoptosis

(*CLU, BCL2L14*) (Figure 4-7). By contrast, at 6 DPC, ChAdOx1-Lassa-GPC vaccinees were mounting adaptive immune responses to infection, evidenced by the upregulation of genes associated with T- and B-cell activation (*CD5, CD3D/E, LCK, CD79B, LAT, CD28, CCR7, CD22, BCL11B, CD19, CD40, ICOS, CXCR5, IL21, CMTM7, CD1C, IL27RA, IL23A, CR2, CTLA4, MYB, FCRL1, ZAP70, TCF7, LEF1, CD6, CD3D, LAX1, LAG3, MZB1, TIGIT, and GPR18)*.

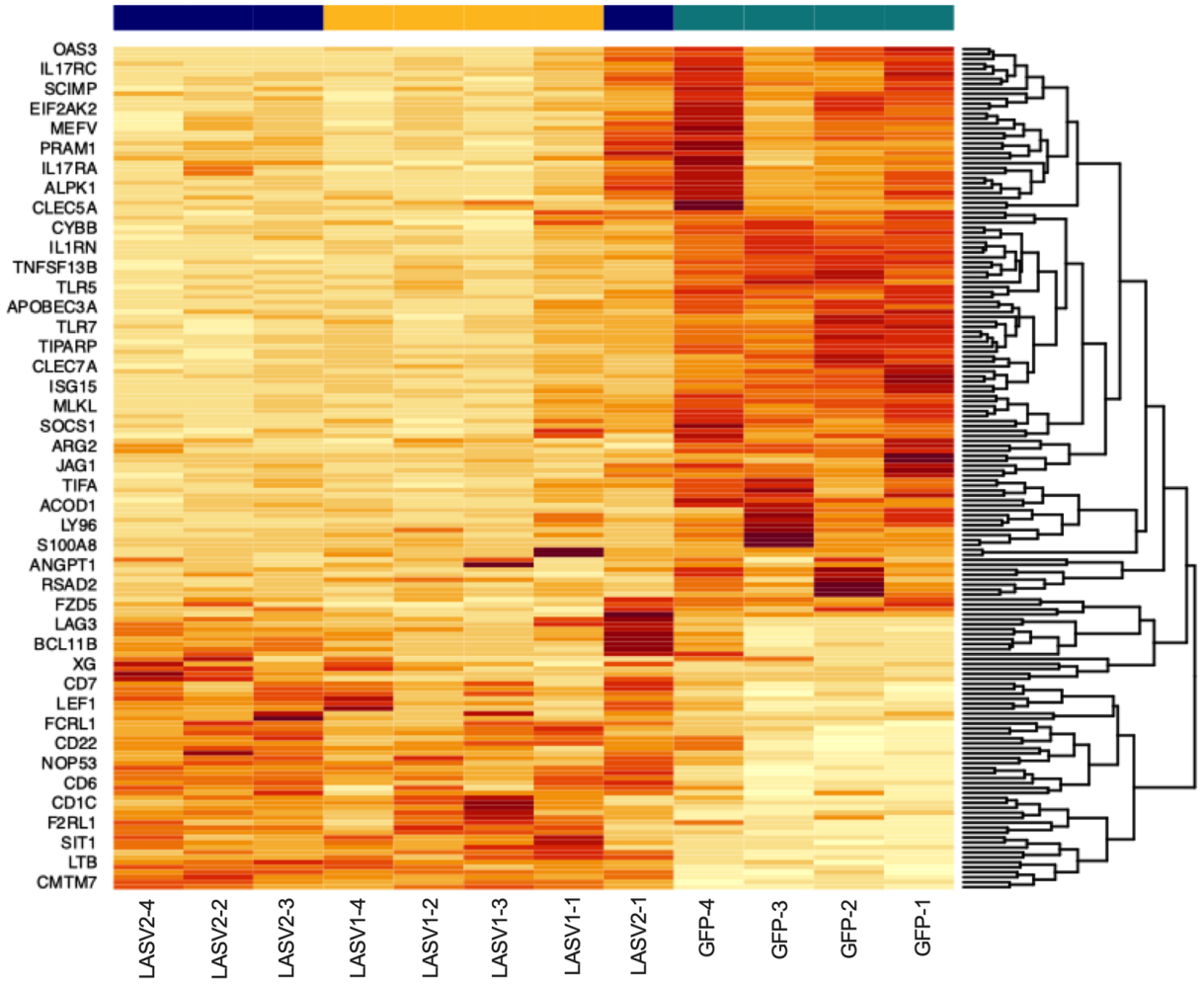


Figure 4-7. Differential gene expression profiles in PBMC samples at 6 DPC. Heatmaps depicting the top 172 differentially expressed genes, defined as those with a fold change ≥2 and false discovery rate adjusted p-value <0.05. Fragments per kilobase of transcript per million reads mapped (FPKM) normalised gene transcript counts in prime-boost (navy bar), prime (yellow bar), and control (green bar) group animals were scaled and hierarchically clustered. Scaled values are coloured such that dark red indicates relative increased expression and yellow indicates relative decreased expression. The dendrogram reflects Euclidean distances. Each column represents an individual animal (labelled 1-4 per group). Due to size constraints, not all 172 genes are labelled on the rows of the heatmap.

Finally, we confirmed the above findings by performing functional enrichment, using MetaCore™, to elucidate the overall biological impact of individual gene expression changes. To this end, DE genes were grouped according to function and enriched to Gene Ontology (GO) processes. Doing so revealed that genes demonstrating dramatic upregulation in controls (or downregulation in vaccinees) principally mapped to pathways associated with host defence mechanisms, virus response, and innate immunity (Figure 4-8, Figure A.5.1-A.5.4). Meanwhile, in vaccinees, upregulated DE genes were attributed to lymphocyte activation and regulation, immune effector, cell-to-cell adhesion, and cell cycle related processes.

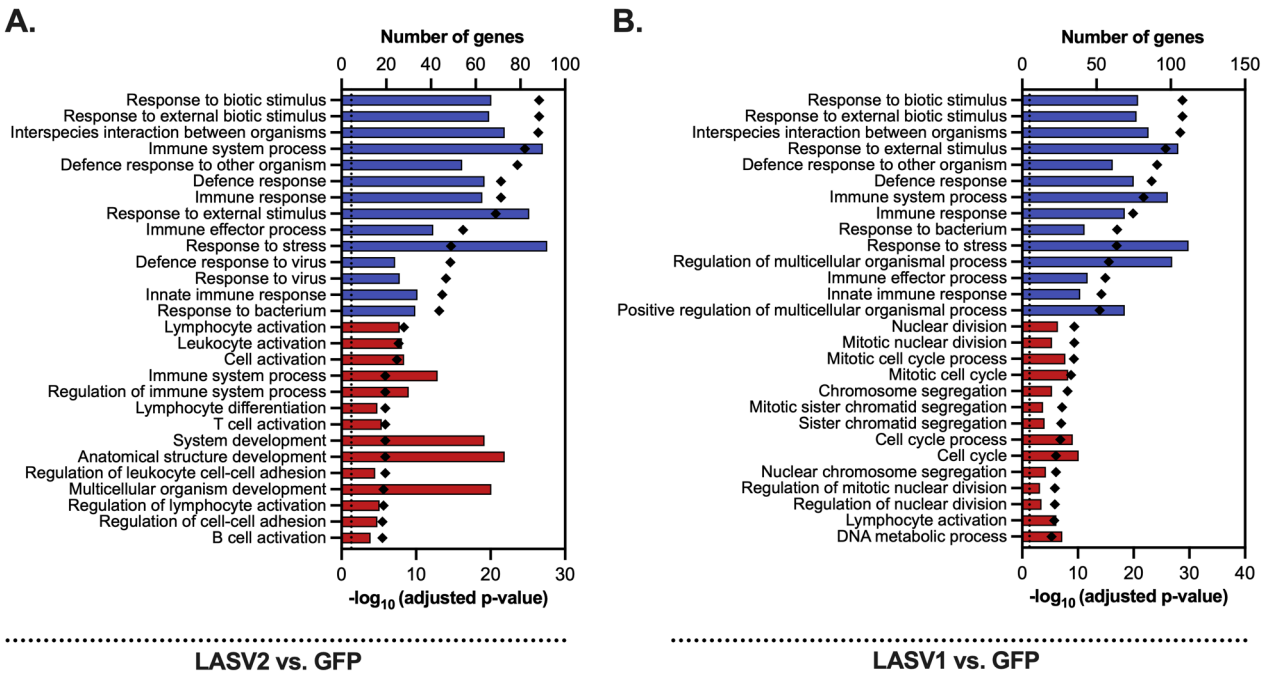


Figure 4-8. Comparison of cellular and immunological pathways affected by LASV challenge. Bar graphs comparing **(A)** prime-boost vaccinees versus controls and **(B)** prime vaccinees versus controls that depict statistically significant gene ontology (GO) terms to which differentially expressed genes enriched. Bars indicate the number of associated genes mapping to that process or pathway. Blue bars indicate relative downregulation of the process or pathway, and red bars indicate relative upregulation. The scatter plot represents the $-\log_{10}$(p-value) for the enriched term (adjusted for false-discovery rate); the dotted line represents the threshold for significance (p=0.05).

4.2.5 Virological outcomes after LASV challenge

The findings discussed above suggest that ChAdOx1-Lassa-GPC protects against lethal Lassa fever as well as major clinical and immunological indicators of disease after one or two doses. Next, we used qRT-PCR analysis of serum and tissue samples to assess the impact of vaccination on the dissemination of LASV and viral clearance after challenge (Figure 4-9). In the cynomolgus macaque model of Lassa fever, viraemia begins at 6-7 DPC and increases in severity during the terminal stages of disease[196]. LASV RNA was undetectable in all sera at 3 DPC. At 6 DPC, minimal quantities of viral RNA, just surpassing the limit of detection, were amplified from the sera of all four prime-boost and one prime vaccinee (median [IQR] $\log_{10}$ $TCID_{50}$ equivalents/mL: LASV2= 0.0 [0.0 to 0.0]; LASV1= -1.1 [-1.1 to -0.275]) (Figure 4-9A). The presence of viral RNA in vaccinee sera proved to be transient, as all previously positive samples were negative by 9 DPC. Meanwhile, all four control animals had detectable LASV RNA in circulation at 6 DPC, which further increased in quantity by 9 DPC (median [IQR] $\log_{10}$ $TCID_{50}$ equivalents/mL: 6 DPC=1.054 [0.226-1.915], 9 DPC=1.766 [1.667-2.114]). At 9 DPC, the elevation of serum viral load in the controls relative to prime-boost and prime vaccinees was statistically significant (p=0.0004 for both comparisons, two-way ANOVA with Tukey's multiple comparisons analysis) (Figure 4-9A). To quantify levels of infectious virus, sera were titrated on Vero E6 cells (by Dr. Robert Fischer). Infectious LASV was present at 6 and 9 DPC in all control animals (median [IQR] $\log_{10}$ $TCID_{50}$/mL: 6 DPC=3.250 [2.563-4.688], 9 DPC=4.875 [4.375-5.000]). By contrast, no viable virus was detected in any of the vaccinee samples at 3, 6, or 9 DPC (6 DPC p=0.0268, 9 DPC p=0.0003 for both comparisons, two-way ANOVA with Tukey's multiple comparisons analysis).

At the time of peak disease (i.e., euthanasia at 9-10 DPC) in the control animals, LASV RNA was detected in lung, liver, and splenic tissue at high copy numbers (median [IQR] log_{10} $TCID_{50}$ equivalents/g: lung=6.241 [5.466-7.110], liver=7.777 [6.877-8.206], spleen=7.277 [7.038-7.433]) (Figure 4-9C). Given that vaccinees survived until the study endpoint, a corresponding set of tissues harvested from immunised animals at the same time as controls were not available for comparison. Nevertheless, tissue samples were analysed at the time of necropsy (42 DPC) for prime-boost and prime vaccinees to quantify levels of residual virus that might be present after the resolution of clinical disease. LASV RNA was undetectable in the lungs of all vaccinees, as anticipated. However, viral RNA was detected in the liver of two prime-boost animals and one prime animal, as well as in the spleens of the same two prime-boost animals and three (different) prime animals. Median RNA levels in the liver (median [IQR] log_{10} $TCID_{50}$ equivalents/g: LASV2=0.531 [-0.640 to 2.365], LASV1= -0.640 [-0.640 to 1.048]) and spleen (median [IQR] log_{10} $TCID_{50}$ equivalents/g: LASV2=1.225 [-0.640 to 4.135], LASV1=1.597 [-0.136 to 2.582]) of vaccinees at 42 DPC were several log-fold lower than those in controls at 9 and 10 DPC (Figure 4-9C).

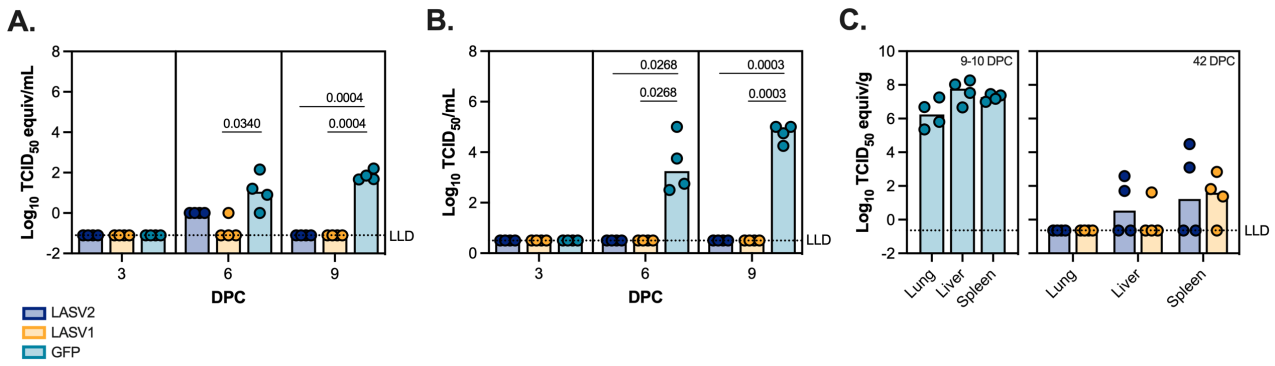


Figure 4-9. Detection of LASV RNA in serum and tissues. (A) Levels of LASV RNA (log_{10} $TCID_{50}$ equivalents/mL) in sera at 3, 6, and 9 DPC. The LLD for analysis (-1.10 log_{10} $TCID_{50}$ equivalents/mL) is indicated with a dotted line (statistical test: two-way ANOVA, Tukey's multiple comparisons). **(B)** Infectious virus titres (log_{10} $TCID_{50}$/mL) in sera at 3, 6, and 9 DPC. The LLD for analysis (0.5 log_{10} $TCID_{50}$/mL) is indicated with a dotted line (statistical test: two-way ANOVA, Tukey's multiple comparisons). **(C)** LASV RNA levels (log_{10} $TCID_{50}$ equivalents/g) in the lung, liver, and splenic tissue harvested at necropsy of control animals at 9-10 DPC (left) and prime-boost and prime vaccinees at 42 DPC (right). The LLD for analysis (-0.64 log_{10} $TCID_{50}$ equivalents/g) is indicated with a dotted line. Bars depict group medians. Where relevant, significant p-values (<0.05) are denoted in the figures, all other comparisons are not significant.

To further investigate the presence and effects of LASV within tissues, histopathological evaluation and immunohistochemistry (IHC) of lung, liver, splenic, and cervical lymph node (LN) tissue sections was carried out by Dr. Carl Shaia, a board-certified veterinary pathologist blinded to study group allocations. Lung, spleen, and LN tissues appeared largely normal across all animals, regardless of vaccination status. Meanwhile, the livers of control animals harvested during terminal disease exhibited histopathological lesions characterised by inflammatory cell accumulation within sinusoids and clusters of necrotic cells. IHC staining for LASV nucleoprotein (NP) revealed abundant immunoreactivity in pulmonary septal endothelial cells, foci of inflammation throughout the liver, splenic red pulp surrounding lymphoid follicles and peri-arteriolar sheaths, and the paracortex and lymphoid follicles of the cervical LN (Figure 4-10A). By contrast, at 42 DPC, histopathological lesions were not found in the tissues of prime-boost or prime vaccinees. Moreover, positive staining for LASV NP was absent from the tissues of all

prime-boost animals. Extremely rare immunoreactivity, limited to lymphoid tissues, was detected in some prime animals (Figure 4-10B).

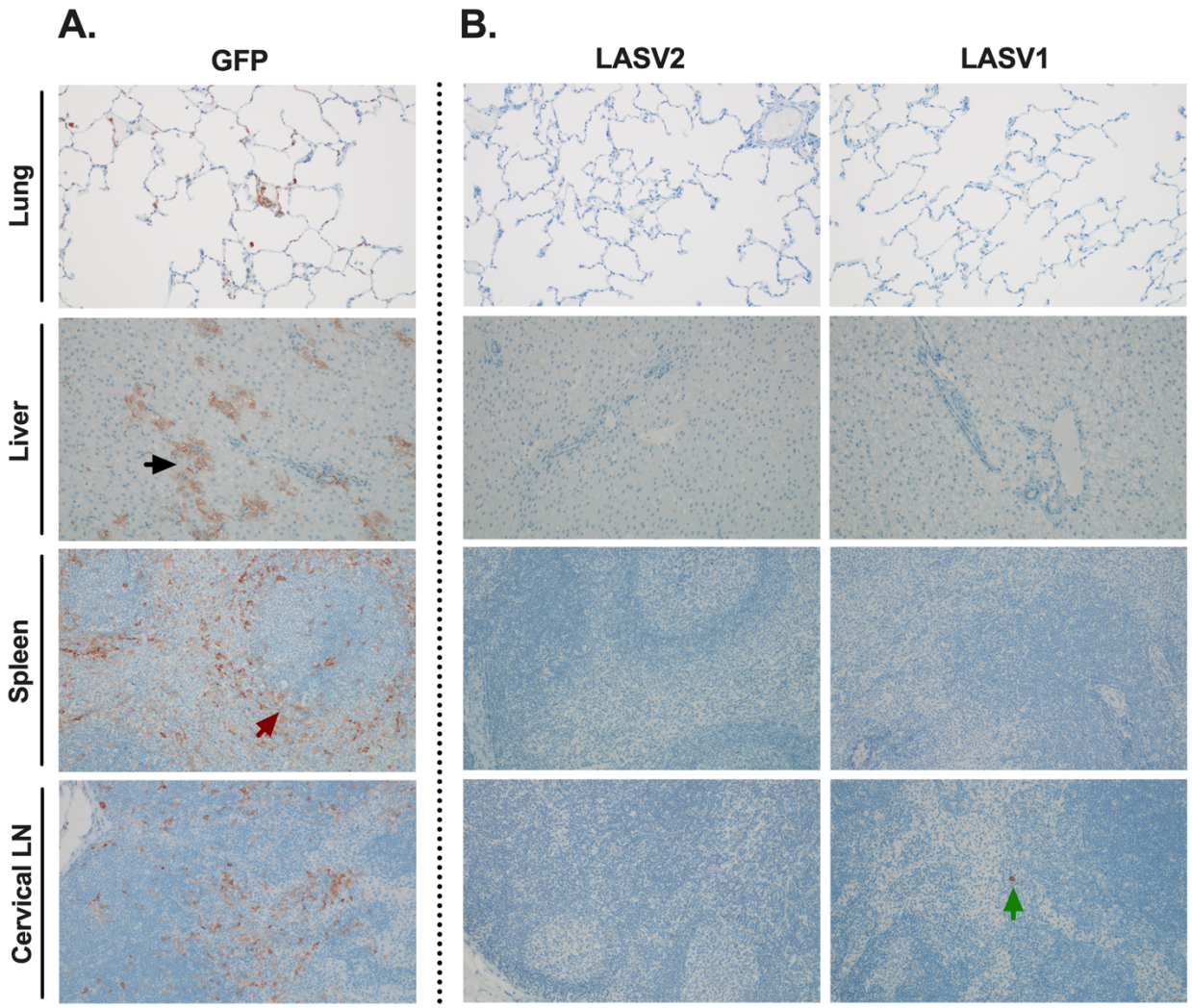


Figure 4-10. Immunohistochemistry of LASV-infected tissues. Representative images of lung, liver, spleen and cervical lymph node (LN) tissue samples collected at the time of necropsy in **(A)** control animals at 9-10 DPC and **(B)** prime-boost and prime vaccinees at 42 DPC. Fields of view are shown at 200X magnification. Immunoreactivity, to LASV NP, is visible as brown staining. Black arrow = example region of inflammatory cell accumulation; red arrow = lymphoid follicle; green arrow = rare immunoreactive mononuclear cell in medullary cord of cervical LN.

4.3 Discussion

In summary, the results presented in this chapter demonstrate that ChAdOx1-Lassa-GPC is immunogenic and confers protection against Lassa fever in a NHP model of infection, thereby supporting and building upon findings in mice and guinea pigs reported in Chapter 3. Our immunogenicity assessment in cynomolgus macaques revealed the induction of GP-specific T-cell responses in ELISpot and ICS assays, consistent with observations in mice. Moreover, antigen-specific cellular immune responses were polyfunctional, characterised by Th1 (versus Th2) polarisation, cytotoxic function (for $CD8^+$ T cells), and T_{EEM} phenotypes. Interestingly, comparison of ELISpot responses (1) between prime-boost and prime vaccinees at -14 DPC, and (2) at -42 DPC versus -14 DPC within the prime-boost group, suggested that administration of a second vaccine dose may be associated with a boosting effect. This observation was specifically reflected in differences between $IFN\gamma^+/TNF\alpha^+/GrB^+$ $CD8^+$ T-cell frequencies in prime-boost and prime vaccinees at -14 DPC detected via ICS assay. However, these differences were not statistically significant. As discussed in Chapter 3, we similarly observed comparable T-cell responses between single-dose and prime-boost vaccinees in mice. Furthermore, as previously mentioned, prior studies have suggested that cellular immune responses may be more refractory to boosting, requiring either a longer time interval between doses or heterologous prime-boost immunisation strategies for significant amplification of responses[86,460,469].

Although correlates of protection for Lassa fever are not well-defined, as explained in section 1.2.4, cellular immune responses are thought to play a dominant role in the resolution of infection. A recent report on the efficacy of several MV-vectored Lassa fever vaccines in cynomolgus macaques used transcriptomic profiling to demonstrate an association between the magnitude of

GP-specific $CD8^+$ (and to a lesser extent $CD4^+$) T-cell responses and low clinical scores and viremia[203]. In addition, efficient control of LASV was associated with cytotoxic T-cell activation. Therefore, future studies to investigate the conditions required to achieve maximal boosting of ChAdOx1-Lassa-GPC-induced cellular immune responses may be warranted.

Measurement of vaccine-elicited IgG titres revealed the robust induction of GP-specific responses after a single dose. Median IgG ELISA titres peaked 21-days post boost (at -7 DPC). Additionally, at the time of LASV challenge (0 DPC), higher levels of circulating GP-specific antibodies were detected in prime-boost compared to prime vaccinees. However, as in our assessment of T-cell responses, these differences failed to meet statistical significance. Functional evaluation of vaccine-induced antibodies revealed a principally non-neutralising response according to serum neutralisation assays involving VSV pseudotyped with LASV GP. These results are consistent with those from guinea pigs reported in Chapter 3; however, neutralisation assays with live, wildtype LASV (Josiah) are currently underway to obtain further confirmation. In the absence of neutralisation capacity, sera from immunised NHPs successfully induced a variety of Fc-dependent effector functions, including monocyte phagocytosis, neutrophil phagocytosis, complement activation, and NK-cell activation. Magnitudes of these responses were highly concordant across assays and indicated that booster administration augmented effector function (albeit not significantly). Given the lack of statistically significant relationships in our data, it is difficult to elucidate if this enhancement of function occurred concurrent with or in the absence of changes in overall IgG titres due to evolution of the Fc profiles of antibodies over time after vaccination[363,480]. Larger studies will be required, either in humans or in animals, to investigate the boosting potential of a second dose of ChAdOx1-Lassa-GPC and to optimise immunisation regimens to facilitate the augmentation of both cellular and humoral secondary responses.

Deeper investigation into the determinants of LASV-specific neutralising antibody responses would be a useful focus of future investigations. Although preclinical studies of other GPC-encoding LASV vaccine candidates have reported neutralising antibodies after vaccination, these have been extremely low in titre[206,211]. As explained in Chapter 3, the mapping of neutralising antibody epitopes in human cases of Lassa fever[176] and structural analysis of the LASV GP trimer[472,481] indicate that conformational epitopes present in the prefusion trimer are key neutralising targets. However, these susceptible regions are obscured when the antigen is in its more stable post-fusion conformation. Thus, initial exposure to LASV typically yields only low affinity, low titre neutralising antibodies. Development of high affinity neutralising antibodies may require prolonged or repeated antigen exposure, as has been observed in Lassa fever patients post convalescence[174,472]. Hence, it is possible that vaccination may only induce protective levels of neutralising antibodies through administration of multiple booster doses[473]. Alternatively, the design of modified vaccine immunogens involving stabilisation of the LASV GP prefusion trimer, via the introduction of amino acid substitutions, is another approach currently under exploration[481]. In fact, a study to compare the induction of neutralising antibodies, affinity maturation, and evolution of the BCR repertoire after a multi-dose immunisation series with ChAdOx1-Lassa-GPC or a new ChAdOx1-vectored vaccine encoding a prefusion GPC (over a period of several months) was planned. This investigation was deferred during the COVID-19 pandemic; however, if completed in the future, these results may inform the design of new LASV vaccine candidates and immunisation regimens.

After challenge with LASV (Josiah), macaques immunised with ChAdOx1-Lassa-GPC survived infection while control animals developed terminal disease and were euthanised by 9-10 DPC. Both prime and prime-boost vaccinees exhibited limited signs of clinical disease after infection

and these resolved before 7 DPC. Interestingly, despite the lack of salient differences in our immunogenicity comparisons after one or two doses of vaccine, clinical scores over the post-challenge time course were significantly reduced in prime-boost vaccinees relative to prime vaccinees. These findings imply added benefits may be associated with a two-dose immunisation strategy and further substantiate the need for additional immunogenicity studies with larger group sizes. Although, given that clinical scores were low in all vaccinees, regardless of group, it is unclear how this marginal benefit may translate to humans after natural exposure.

In addition to clinical monitoring, we also performed haematological, serum chemistry, cytokine, and transcriptomic evaluations after challenge. These analyses indicated that the control animals in our study exhibited classical signs of severe Lassa fever, including liver dysfunction, platelet disruption, systemic inflammation, and depressed lymphocyte activation. These observations correlate closely with findings in humans[124,174] and other studies of cynomolgus macaques[196,197]. Importantly, our results collectively suggest that both single-dose and prime-boost immunisation with ChAdOx1-Lassa-GPC protect against defining features of LASV pathogenesis, including immune dysregulation and the breakdown of productive antiviral adaptive immune responses.

Virological assessment after challenge revealed that while control animals developed progressive viraemia, prime and prime-boost vaccinees exhibited transient, negligible quantities of viral RNA and no infectious virus in sera. In addition to becoming severely viraemic, control macaques also developed high tissue viral loads during peak disease (9-10 DPC), evidenced by qRT-PCR analysis of lungs, liver, and spleen. At the endpoint of the study (42 DPC), we assessed viral loads in the tissues of vaccinees. LASV RNA was detected in the liver and spleen (but not lungs) of some prime-boost and prime vaccinees. IHC evaluation of these tissues demonstrated a lack of staining for intact viral antigen (NP), suggesting that RNA amplified from these tissues is likely not

representative of infectious virus. Instead, it is possible that these findings are indicative of genomic remnants from infected cells undergoing phagocytosis and clearance by effector cells within these tissues[482,483]. However, titration assays to quantify infectious virus in these tissues, as well as ISH to visualize LASV replicating within cells, are currently in progress to support this hypothesis.

Consistent with the results discussed in Chapter 3, ChAdOx1-Lassa-GPC does not elicit sterilising immunity in cynomolgus macaques. Our observation of minimal, transient viraemia at 6-7 DPC is consistent with results from NHP vaccine efficacy studies for ML29[207], VSV-vectored[200], MV-vectored[203], and DNA[206] vaccine candidates [200,207]. Tissues isolated from NHPs immunised with ML29 and MV-vectored vaccines were free from infectious LASV according to plaque titration assays[203,207]. Quantification of viral RNA by qRT-PCR, as presented in our study, is a highly sensitive method for quantifying viral loads and will amplify genomic material from both replicating virus and viral debris. Thus, as mentioned, it will be necessary to titre any infectious LASV isolated from the tissues of the vaccinees at 42 DPC. Although, direct comparison of our results with those from other studies may be complicated by differences in methods used for quantification of infectious virus (e.g., plaque versus $TCID_{50}$ assays) and their relative sensitivities. Given the high virus doses used in lethal challenge studies such as this one, low levels of virus detected at necropsy may not be an accurate representation of expected results in naturally infected humans. Nevertheless, it will be essential to confirm that LASV does not establish persistent, subclinical infection in the tissues of immunised animals or persons, due to the damaging effects of potential chronic inflammation over time, including T-cell exhaustion and immune-mediated sequelae like hearing loss[147,484].

In conclusion, the results presented in this chapter support the future development and assessment of ChAdOx1-Lassa-GPC in humans. Through the support of CEPI, a phase I clinical trial to test the safety, tolerability, and immunogenicity of this vaccine candidate will commence in the near future. Ultimately, vaccine evaluation in LASV-affected regions in West Africa will determine if ChAdOx1-Lassa-GPC sufficiently meets the criteria for a safe and effective Lassa fever vaccine as outlined in the WHO TPP[218]. Although the results presented in this chapter adequately demonstrate the preclinical immunogenicity and efficacy of ChAdOx1-Lassa-GPC, one major limitation of this work is the low number of animals (n=4) per group. Small group sizes coupled with the high degree of variation observed between outbred NHPs, led to underpowered analyses, thereby reducing our ability to detect statistically significant effects. Second, this study only reports outcomes of challenge with LASV Josiah, which is homologous to the vaccine antigen. Studies to assess the extent to which vaccine-induced immune responses protect against diverse LASV strains circulating in endemic areas will be a critical next step in the development of ChAdOx1-Lassa-GPC. To this end, we are currently in the process of obtaining contemporary virus isolates and evaluating their pathogenicity in inbred Strain 13 guinea pigs, Hartley guinea pigs, and cynomolgus macaques. Finally, there is some evidence to suggest that encoding multiple viral antigens into LASV vaccines may increase the likelihood of conferring cross-strain immunity[203,211]. To this end, we have also designed a bivalent ChAdOx1-vectored vaccine encoding both LASV GPC and NP; we plan to comparatively assess this vaccine alongside ChAdOx1-Lassa-GPC in future heterologous challenge studies.

5

Immune profiling in rhesus macaques vaccinated with ChAdOx1 nCoV-19 and challenged with SARS-CoV-2

5.1 Introduction

The COVID-19 pandemic launched the rapid development of vaccines based on a wide variety of platforms. Less than two years after the release of the first viral genome sequence, at least 33 are approved for emergency use, after demonstrating safety and efficacy in clinical trials. To date, over eight billion total vaccine doses have been administered globally[337]. ChAdOx1 nCoV-19/AZD1222 is among the major COVID-19 vaccines deployed worldwide. The extent of protection afforded by the various COVID-19 vaccines in use have varied between different populations and over time. However, a two-dose intramuscular (IM) regimen of ChAdOx1 nCoV-19 resulted in an estimated overall efficacy of 74% in adults, and 83.5% in individuals aged over 65 years, in phase III clinical trials conducted at 88 sites across the US, Chile, and Peru (a median of 61 days post boost). ChAdOx1 nCoV-19 immunisation was additionally associated with 64.3% efficacy in preventing SARS-CoV-2 infection (assessed by seroconversion) and nearly 100% protection against severe disease[117]. The vaccine features the ChAdOx1 vector encoding the

SARS-CoV-2 (Wuhan-1 strain) S sequence inserted into the E1 deletion site with the tPA leader sequence[111].

Prior to or concurrent with testing in phase I clinical trials, many COVID-19 vaccine candidates were evaluated in experimental challenge studies performed in NHPs[111,350,485,486]. Due to their susceptibility to infection and relative accessibility, rhesus macaques have been the most widely used NHP species in SARS-CoV-2 research, particularly for the assessment of vaccines and therapeutics. Stringent inoculation of naïve animals with SARS-CoV-2 via intranasal (IN) and intratracheal (IT) routes (and frequently also oral and ocular) results in self-limiting, mild-to-moderate respiratory disease[430,487,488]. Clinical signs are mild and short-lived, primarily consisting of irregular respiration, loss of appetite, and malaise. Animals exhibit abundant nasal shedding and high viral loads in the lower respiratory tract[430,487,488]. Viral kinetics are characterised by an early peak in virus replication, within 48 hours after inoculation, in the upper and lower respiratory tracts[430]. Viral loads are substantially reduced within seven days of infection, and the virus is essentially cleared from nasal passages, the airway, and lung tissue after 14 days. Histopathological findings indicate that animals' lungs present with some pulmonary lesions consistent with mild-to-moderate, multifocal interstitial pneumonia[430]. Thoracic radiographs also show some abnormalities indicative of an accumulation of pulmonary infiltrates, which resemble those observed in human COVID-19 patients[489]. Given the absence of major clinical or pathological signs associated with infection, salient outcome measures such as survival or the prevention of severe disease cannot be employed for vaccine or drug testing performed in this model—in contrast to the LASV challenge studies described in Chapters 3 and 4. Instead, a reduction in respiratory tract viral load has been applied as the principal criteria for establishing efficacy.

In Chapter 5, I present findings from two studies evaluating the performance of ChAdOx1 nCoV-19 in the rhesus macaque model of SARS-CoV-2. In the first study, animals received prime-boost IM vaccination with ChAdOx1 nCoV-19 or a ChAdOx1 GFP control vaccine. A chronological assessment of immunological and virological outcomes was conducted. Vaccine-elicited cellular and humoral responses were characterised in detail prior to challenge. After SARS-CoV-2 challenge, we assessed vaccine efficacy through a comparison of respiratory tract viral load in vaccinees versus controls. In addition, innate and adaptive immune responses were profiled in each group and compared between 3- and 7-days post challenge (DPC). In doing so, we aimed to model the effects of prior immunisation on local inflammation and adaptive immunity occurring within the first week after virus exposure. In the second study, we assessed the efficacy of prime-boost IN delivery of ChAdOx1 nCoV-19 (versus ChAdOx1 GFP) in rhesus macaques challenged with SARS-CoV-2. Informed by the results from our first study, we narrowed our focus to the characterisation of the vaccine-elicited humoral response, specifically. To this end, we measured antibody responses in circulation and in respiratory tract samples after immunisation. After virus challenge, we subsequently compared viral load dynamics in vaccinees versus controls to establish the efficacy of the IN-vaccination regimen.

5.1.1 Authorship statement

This chapter includes data from two vaccination-challenge studies performed in rhesus macaques under BSL4 conditions. Dr. Neeltje van Doremalen was the Principal Investigator on these Animal Study Protocols. Please see the overall Statement of Authorship (page xviii) for a summary of procedures conducted by colleagues. Data generated by others will be referenced in the corresponding figures throughout this chapter. Some of the findings discussed here have been published in two studies[111,112] on which I am a co-author.

5.2 Results

5.2.1 IM ChAdOx1 nCoV-19 induces spike-specific T-cell responses

To evaluate the immunogenicity and efficacy of a prime-boost IM vaccination regimen, we immunised rhesus macaques (n=6 per group) with ChAdOx1 nCoV-19 (nCoV-19) or ChAdOx1 GFP (GFP) (Figure 5-1). PBMCs and sera were collected from ChAdOx1 nCoV-19 vaccinees at baseline (i.e., 0 days post vaccination, DPV), 14 days post prime (14 DPV), on the day of boost (28 DPV), 14 days post boost (42 DPV), and on the day of challenge (56 DPV). Samples collected at 0, 14, and 28 DPV from ChAdOx1 GFP recipients were used for immunogenicity comparisons.

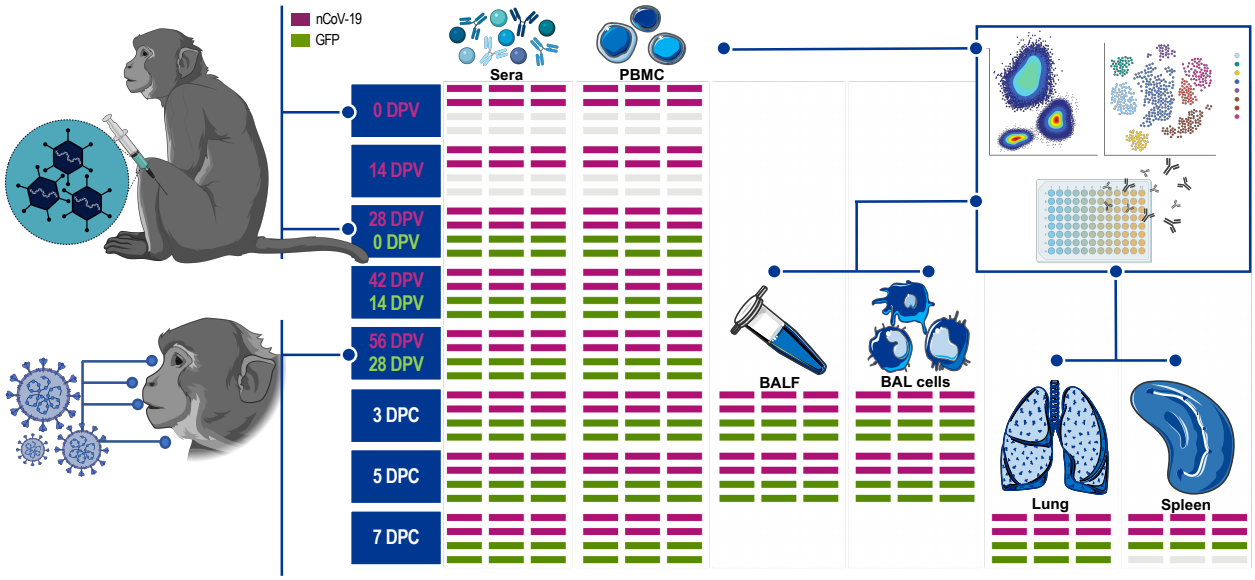


Figure 5-1. Intramuscular vaccination-and-challenge study design and timeline. Rhesus macaques received two intramuscular immunisations with $2.5x10^{10}$ VP of ChAdOx1 nCoV-19 (n=6), with a 28-day interval between doses. One dose of ChAdOx1 GFP was administered to control animals (n=6). Vaccinees (nCoV-19) are indicated in magenta and controls (GFP) are indicated in green. PBMCs and sera were collected from ChAdOx1 nCoV-19 vaccinees at baseline (i.e., 0 DPV), 14 days post prime (14 DPV), on the day of boost (28 DPV), 14 days post boost (42 DPV), and on the day of challenge (56 DPV). Samples collected at 0, 14, and 28 DPV from ChAdOx1 GFP recipients were used for immunogenicity comparisons. Twenty-eight days after final immunisation (i.e., 56 or 28 DPV), animals were challenged with $2.6x10^6$ $TCID_{50}$ SARS-CoV-2 strain nCoV-WA1-2020 via IN, IT, oral, and ocular routes. Sera was collected and bronchoalveolar lavage (BAL) was performed on 3 and 5 DPC. On 7 DPC, sera, PBMCs, and single-cell suspensions of lung and spleen tissue were harvested. Sera, BAL fluid (BALF), and lung tissue were collected from all 12 animals at the indicated timepoints for flow cytometric assays. Splenocytes and lung tissue for single-cell RNA sequencing were obtained from only nine animals: six nCoV-19 vaccinees and the three GFP controls.

First, we compared antigen-specific T-cell responses in vaccinees versus controls on 14 and 42 DPV using IFNγ and TNFα ELISpot assays (Figures 5-2A&B). Considerable variation was observed in the responses between ChAdOx1 nCoV-19 vaccinees. Median quantities of IFNγ-secreting T cells were significantly elevated in ChAdOx1 nCoV-19-vaccinated animals two weeks post prime (55.5 SFU/10^6 PBMCs, p=0.0076) and post boost (42.25 SFU/10^6 PBMCs, p=0.0428) compared to control animals at 14 DPV (2.50 SFU/10^6 PBMCs) (Kruskal-Wallis and Dunn's multiple comparisons tests) (Figure 5-2A). However, responses were not significantly altered after administration of a second vaccine dose (p=0.2188, Wilcoxon matched-pairs rank test). Median TNFα-secreting-cell ELISpot responses were also significantly higher in vaccinees at 14 (560.0 SFU/10^6 PBMCs, p=0.0200) and 42 (653.8 SFU/10^6 PBMCs, p=0.0424) DPV than those at 14 DPV in control animals (23.0 SFU/10^6 PBMCs) (Kruskal-Wallis and Dunn's multiple comparisons tests) (Figure 5-2B). Again, significant differences between post prime and post boost responses were not detected (p=0.6875, Wilcoxon matched-pairs rank test). Notably, the magnitudes of the vaccine-specific IFNγ- and TNFα-secreting T-cell responses did not exhibit a strong positive correlation (r=0.5569, p=0.0633) (Spearman two-sided rank correlation test) (Figure 5-2C).

Given the low magnitude of ELISpot responses in the vaccinated animals, we next employed TCR-dependent activation induced marker (AIM) assays to estimate S-specific T-cell responses. Studies performed to optimise these assays suggest that they enable the more comprehensive detection of (total) T cells responding to a given antigen than is achievable by assessment of single-cytokine responses via ELISpot or ICS[88,89,490]. To this end, we used three different marker combinations reported in published rhesus macaque studies: OX40 and CD25, OX40 and CD137, or OX40 and PD-L1[442,491]. Frequencies of $CD4^+$ and $CD8^+$ T cells co-expressing these marker pairs were

determined. The AIM assays revealed antigen-specific $CD4^+$ (Figure 5-2D) and $CD8^+$ (Figure 5-2E) T cells in all vaccinated animals at 14 and 42 DPV, although there was considerable variability between the three assays. Median frequencies (with interquartile range) and p-values associated with all statistical comparisons are listed in Table 5-1. Specifically, $OX40^+$ $CD25^+$ and $OX40^+$ $CD137^+$ populations appeared to differentiate ChAdOx1 nCoV-19 vaccinees most clearly from ChAdOx1 GFP controls. In vaccinees, median frequencies of $CD4^+$ and $CD8^+$ T cells that were $OX40^+$ $CD25^+$ or $OX40^+$ $CD137^+$ upon stimulation ranged between 0.45-1.1% and 0.21-0.78% (respectively) and were significantly elevated above values detected in the controls, which were below 0.1% (Kruskal-Wallis and Dunn's multiple comparisons tests, see Table 5-1 for p-values). In alignment with the ELISpot results, the AIM assays also indicated that significant changes in the magnitude of the vaccine-induced T-cell response were not achieved by boosting (Wilcoxon matched-pairs rank test, see Table 5-1 for p-values). By contrast, median frequencies of $OX40^+$ $PD\text{-}L1^+$ cells within both $CD4^+$ and $CD8^+$ T-cell subsets were detected at frequencies above 0.6% in all animals regardless of vaccination status, likely representative of some degree of non-specific upregulation of PD-L1. Although, frequencies of $OX40^+$ $PD\text{-}L1^+$ T cells in vaccinees were still significantly elevated over those in controls at both 14 ($CD4^+$ p=0.0041, $CD8^+$ p=0.0009) and 42 ($CD4^+$ p=0.0299, $CD8^+$ p=0.0401) DPV (Kruskal-Wallis and Dunn's multiple comparisons tests, see Table 5-1 for p-values). We thus predicted that OX40 and PD-L1 may demonstrate less specificity in distinguishing S protein-specific T cells from non-specifically activated T cells in this model (Figure 5-2D&E, Table 5-1). However, interestingly, frequencies of $OX40^+$ $CD25^+$ and $OX40^+$ $PD\text{-}L1^+$ $CD4^+$ (r=0.853, p=0.001) and $CD8^+$ (r=0.937, p<0.0001) T cells displayed a strong positive correlation (Figure 5-2F&G). Meanwhile, $CD4^+$ $OX40^+$ $CD25^+$ and $OX40^+$ $CD137^+$ were only fairly well correlated (r=0.608, p=0.04); all other comparisons were not significant (Spearman

two-sided rank correlation tests). Taken together, the ELISpot and AIM assays indicate that vaccination elicited a circulating antigen-specific T-cell response.

	Median [IQR] frequency			p-value (Kruskal-Wallis, Dunn's multiple comparisons)		p-value (Wilcoxon matched pairs)
	nCoV-19 14 DPV	nCoV-19 42 DPV	GFP 14 DPV	nCoV-19 14 DPV vs. GFP	nCoV-19 42 DPV vs. GFP	nCoV-19 14 DPV vs. 42 DPV
$CD4^+$ $OX40^+$ $CD25^+$	1.1 [0.54-1.30]	0.45 [0.26-0.99]	0.04 [0.02-0.08]	0.0016	0.0257	0.1250
$CD4^+$ $OX40^+$ $CD137^+$	0.47 [0.32-0.71]	0.64 [0.27-0.92]	0.06 [0.03-0.12]	0.0116	0.0041	0.4375
$CD4^+$ $OX40^+$ $PD\text{-}L1^+$	7.39 [4.07-8.91]	5.70 [2.99-8.41]	1.09 [1.01-1.65]	0.0041	0.0299	0.2188
$CD8^+$ $OX40^+$ $CD25^+$	0.34 [0.25-0.54]	0.21 [0.14-0.42]	0.01 [0.00-0.02]	0.0013	0.0295	0.2500
$CD8^+$ $OX40^+$ $CD137^+$	0.41 [0.31-0.56]	0.78 [0.34-1.04]	0.05 [0.02-0.11]	0.0299	0.0013	0.0625
$CD8^+$ $OX40^+$ $PD\text{-}L1^+$	3.75 [2.97-4.97]	2.33 [1.69-4.09]	0.68 [0.25-1.04]	0.0009	0.0401	0.0312

Table 5-1. AIM assay frequencies and pair-wise statistical comparisons. For each $CD4^+$ and $CD8^+$ AIM marker combination, median frequencies of positive cells are listed with interquartile range (in brackets) for 14 and 42 DPV samples for ChAdOx1 nCoV-19 vaccinees and for 14 DPV samples for ChAdOx1 GFP controls. Intergroup statistical comparisons between 14 DPV vaccinee and control samples, and 42 DPV vaccinee and control samples are indicated (Kruskal-Wallis, Dunn's multiple comparisons). Wilcoxon matched pairs rank test results assessing the impact of the delivery of a second vaccine dose are also indicated.

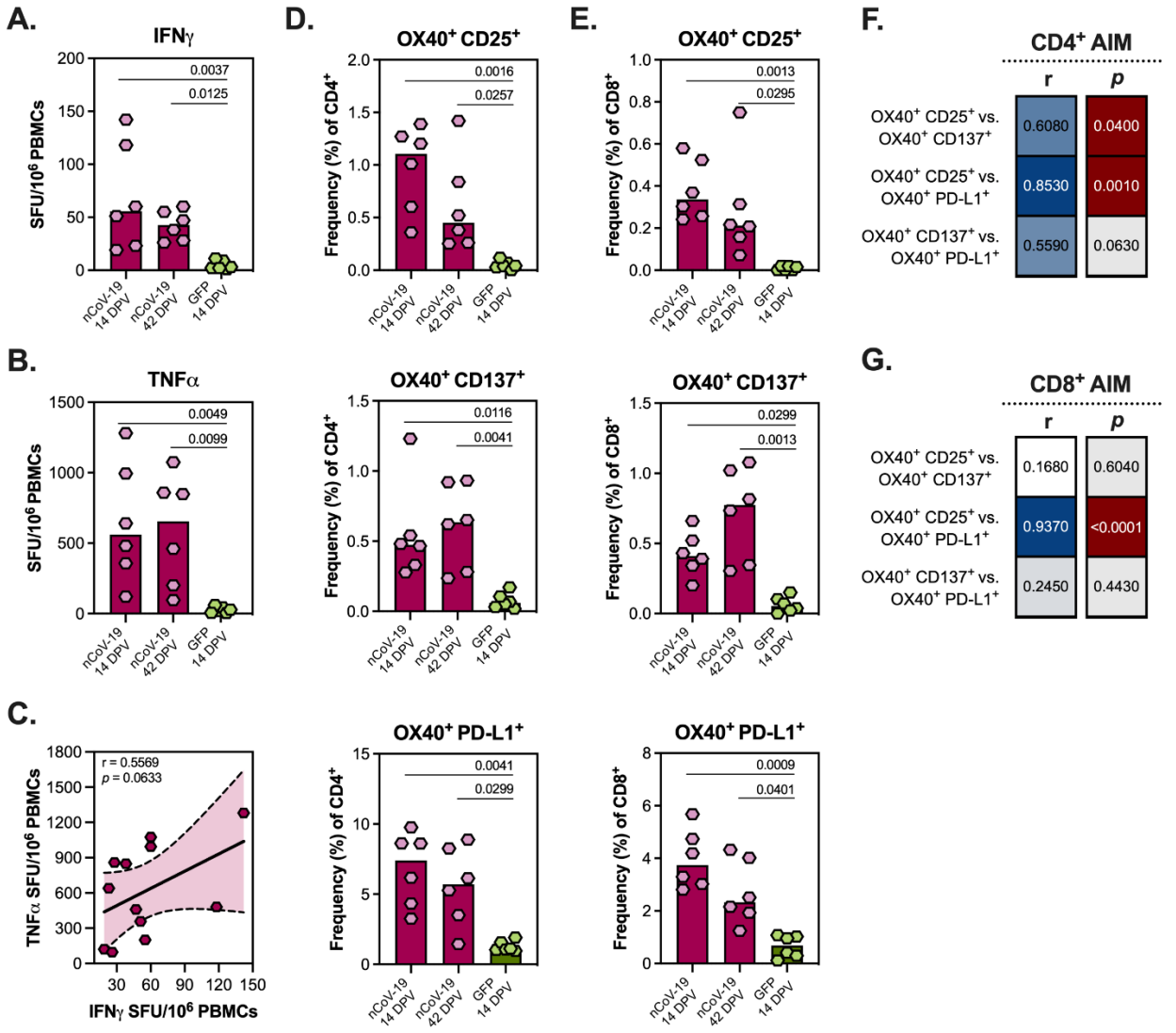


Figure 5-2. Spike protein-specific T-cell responses elicited by ChAdOx1 nCoV-19 vaccination. Antigen-specific T-cell responses were measured in PBMC samples collected 14-days post prime (14 DPV) and post boost (42 DPV) in ChAdOx1 nCoV-19 vaccinees and at 14 DPV in ChAdOx1 GFP controls. Summed **(A)** IFNγ and **(B)** TNFα ELISpot assay responses from PBMCs stimulated with four peptide pools spanning the spike protein sequence, represented as spot forming units (SFU) per $1.0x10^6$ cells (statistical test: Kruskal-Wallis, Dunn's multiple comparisons). **(C)** Spearman rank correlation analysis and best fit line comparing IFNγ versus TNFα ELISpot responses in ChAdOx1 nCoV-19 vaccinees. Activation induced surface marker (AIM) assays to detect frequencies of $OX40^+$ $CD25^+$ (top), $OX40^+$ $CD137^+$ (middle), and $OX40^+$ $PD\text{-}L1^+$ (bottom) populations within **(D)** $CD4^+$ and **(E)** $CD8^+$ T-cell subsets. Cells were stimulated with two peptide pools spanning the spike protein sequence; positive frequencies were summed after background adjustment (statistical test: Kruskal-Wallis, Dunn's multiple comparisons). Heatmaps depicting the results of spearman rank correlation analyses comparing frequencies of each AIM assay marker combination between vaccinees for **(F)** $CD4^+$ and **(G)** $CD8^+$ T-cell responses. Correlation (r) coefficients and p-values for each comparison are indicated by left and right heatmaps, respectively. All bars depict group medians. Significant p-values (<0.05) are denoted in the figures, all other comparisons are not significant.

5.2.2 Circulating humoral responses induced by IM ChAdOx1 nCoV-19

Next, we sought to characterise the vaccine-induced humoral response. Endpoint titre ELISA revealed an increase in median S-specific sera IgG titres following IM delivery of ChAdOx1 nCoV-19 that were boosted by administration of the second vaccine dose (Figure 5-3A). S-specific IgG titres were significantly amplified above baseline (0 DPV) levels by a nearly four log_{10}-fold increase at 42 DPV (p<0.0001, mixed-effects analysis and Dunnett's multiple comparisons). Like overall IgG titres measured by ELISA, virus neutralising (VN) titres were significantly elevated at 42 DPV, by at least two log_{10}-fold, relative to pre-vaccination or negative cut-off levels (p<0.0001, mixed-effects analysis and Dunnett's multiple comparisons) (Figure 5-3B). Subsequently, we employed a complementary assay to assess neutralisation of replication-deficient VSV, expressing luciferase and pseudotyped with SARS-CoV-2 S protein (VSV-SARS2-S). Inhibition of VSV-SARS2-S entry by serum antibodies was significantly enhanced at 42 (p=0.0008) and 56 (p=0.0261) DPV, as IC_{50} values increased by least two log_{10}-fold compared to baseline (mixed-effects analysis and Dunnett's multiple comparisons) (Figure 5-3C). IC_{50} values for VSV-SARS2-S exhibited a strong positive correlation (r=0.8050, p<0.0001) with live virus neutralising titres (Spearman two-sided rank correlation test) (Figure 5-3D).

As in Chapter 4, we also profiled the non-neutralising functions of vaccine-induced antibodies. To quantify support for antiviral phagocytic and complement-mediated activities, S and RBD protein-coated fluorescent beads were incubated with sera from ChAdOx1 nCoV-19 vaccinees and ChAdOx1 GFP controls collected at 42 DPV. ChAdOx1 nCoV-19-vaccinated animals achieved superior monocyte phagocytosis scores for both S- and RBD-specific sera antibodies compared to controls (p=0.004324 for both, Mann-Whitney tests with Holm-Šídák multiple comparisons correction) (Figure 5-3E). Similarly, the extent of complement deposition was significantly higher

on beads treated with sera from ChAdOx1 nCoV-19 versus ChAdOx1 GFP recipients (S: p=0.004324, RBD: p=0.008658, Mann-Whitney tests with Holm-Šídák multiple comparisons correction) (Figure 5-3F).

In lieu of direct measurement of NK cell-mediated killing of target cells, we measured cellular activation and degranulation as proxy indicators of cytotoxic function. S- and RBD-bound sera antibodies were incubated with freshly isolated human NK cells. The frequencies of NK cells expressing markers of degranulation (CD107a) or activation cytokines (MIP-1β and IFNγ) were measured by flow cytometry. NK cells exposed to S- and RBD-bound antibodies from the sera of ChAdOx1 nCoV-19 vaccinees exhibited degranulation and activation, indicating a transition from a resting to cytotoxic state, which was largely not induced by control sera (p=0.004324 for all comparisons, Mann-Whitney test) (Figure 5-3G). Collectively, these assays suggest that ChAdOx1 nCoV-19 elicits a multifunctional antibody response in rhesus macaques. A relatively high degree of concordance between neutralising and non-neutralising effector activities was detected by correlation analysis at 42 DPV, although most relationships were not statistically significant (two-sided Spearman rank correlation analyses) (Figure 5-3H).

Given the continued emergence of new SARS-CoV-2 variants, we investigated the extent to which ChAdOx1 nCoV-19-elicited antibodies that bind to or neutralise related coronaviruses or heterologous SARS-CoV-2 strains. We used a MESO Scale Discovery multiplex ELISA-like assay to measure relative levels of IgG, in the 56 DPV samples of the ChAdOx1 nCoV-19 vaccinees, that were able to bind to the surface antigens of other human respiratory coronaviruses—SARS-CoV-1 S, MERS-CoV S, OC43 S, and HKU1 S—in comparison to homologous SARS-CoV-2 S (Figure 5-3H). A decrease in IgG signal of approximately one $\log_{10}$-

fold was observed in the binding of vaccinee serum antibodies to SARS-CoV-1 S, but this was not statistically significant (p>0.9999). Significant decreases in IgG signals of two-or-more $\log_{10}$-fold were observed for MERS-CoV S (p=0.0010), HKU1 S (p=0.0010), and OC43 S (p=0.0423) (Friedman test with Dunn's multiple comparisons). Despite decreases of more than one $\log_{10}$-fold in IgG signal strength for SARS-CoV-1 S (p>0.9999), MERS-CoV-2 S (p=0.0010), HKU1 S (p=0.0010), and OC43 S (p=0.0423), vaccine-induced antibodies against SARS-CoV-2 S exhibited the capacity to bind to S of distantly-related coronaviruses in their linearised form. However, the ability to bind to linear epitopes was not representative of the functional ability to bind to conformational epitopes required for virus neutralisation. Heterologous neutralisation assays with live virus revealed substantial reductions in the susceptibility of strains B.1.351 (p=0.0016) and B.1.617.2 (p=0.0566) to neutralisation by vaccine-elicited antibodies compared to WA-1 (of more than a $\log_{10}$-fold reduction in titre), although the latter difference did not meet statistical significance (Friedman test with Dunn's multiple comparisons) (Figure 5-3I). Strain B.1.1.7 did not demonstrate decreased sensitivity to neutralisation (p>0.9999). Ultimately, these findings were consistent with data from clinical cohorts demonstrating that vaccine-induced antibodies display significantly reduced neutralising potential against VOCs with key RBD mutations[338,390,474].

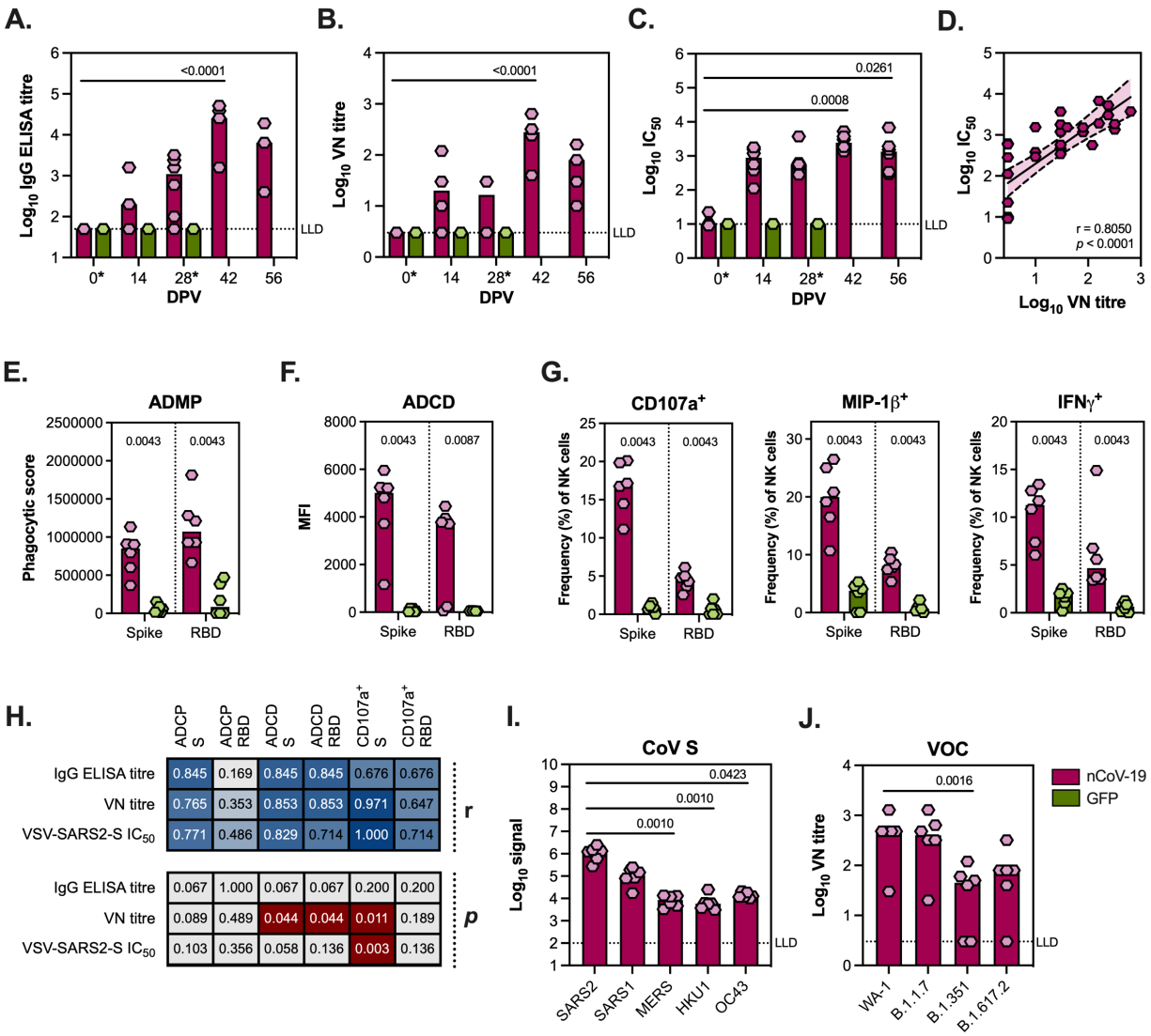


Figure 5-3. Characterisation of serum antibody responses induced by ChAdOx1 nCoV-19 vaccination. (A) SARS-CoV-2 spike protein-specific IgG ELISA titres represented as the $\log_{10}$ of the highest reciprocal sera dilution surpassing the negative cut-off. **(B)** Microneutralisation assay results of sera against 2000 $TCID_{50}$ of SARS-CoV-2 strain WA-1 reported as $\log_{10}$ of the highest reciprocal sera dilution absent for CPE. **(C)** $\log_{10}$ IC_{50} value determined for sera neutralisation of the SARS-CoV-2 spike-pseudotyped virus VSV-SARS2-S (statistical test A-C: mixed-effects analysis with Dunnett's multiple comparisons). **(D)** Correlation analysis and best-fit line relating $\log_{10}$ IC_{50} versus $\log_{10}$ virus neutralisation (VN) titre (statistical test: Spearman two-sided rank correlation coefficient). Spike- and RBD-specific **(E)** ADMP scores, **(F)** ADCD median fluorescent intensity (MFI), and **(G)** ADNKA assessed by frequencies of $CD107a^+$, MIP-$1\beta^+$, or $IFN\gamma^+$ $CD3^-$ $CD56^+$ $CD16^+$ cells (statistical test: Mann-Whitney with Holm-Šídák multiple comparisons). **(H)** Heatmaps depicting Spearman two-sided rank correlation coefficients (top) and p-values (bottom) for the indicated pairwise comparisons. **(I)** Relative concentrations of IgG antibodies in the sera of ChAdOx1 nCoV-19 and ChAdOx1 GFP animals binding to surface antigens of other respiratory coronaviruses compared to SARS-CoV-2 spike. **(J)** VN titres in 42 DPV sera of ChAdOx1 nCoV-19 vaccinees against SARS-CoV-2 variants of concern, in comparison to the challenge strain WA-1 (statistical test I-J: Friedman and Dunn's multiple comparisons test). All bars depict group medians. Dotted lines indicate the LLD or negative cut-off for each assay. Significant p-values (<0.05) are denoted in the figures, all other comparisons are not significant.

The longevity of protection afforded by vaccines is dependent on the induction of a robust memory response. We identified circulating B cells ($CD3^-$ $CD20^+$) exhibiting specificity to SARS-CoV-2 S and RBD using fluorescently labelled probes, as previously described[322]. Within the memory B-cell subset ($CD20^+$ IgD^- $CD27^+$), the median frequency of S-specific B cells steadily increased several-fold post immunisation with ChAdOx1 nCoV-19 (Figure 5-4A). Similarly, within the S-specific population, the median frequency of B cells recognizing RBD epitopes significantly increased (Figure 5-4A). As expected, the proportion of S-specific memory B cells that were also RBD-specific significantly increased between 14 DPV and 56 DPV (p=0.0009), to over 50%, reflecting the preferential targeting of the vaccine-induced humoral response to RBD epitopes (Figure 5-4B). Finally, the proportion of IgG^+ S-specific and RBD-specific memory B cells increased after vaccination, particularly post boost, to 60-70% by 56 DPV relative to IgM^+ or other Ig isotypes (Figure 5-4C). Collectively, these data highlight the induction of robust antigen-specific, multifunctional antibody and memory B-cell responses by ChAdOx1 nCoV-19, which may display attenuated specificity to emerging variants of concern.

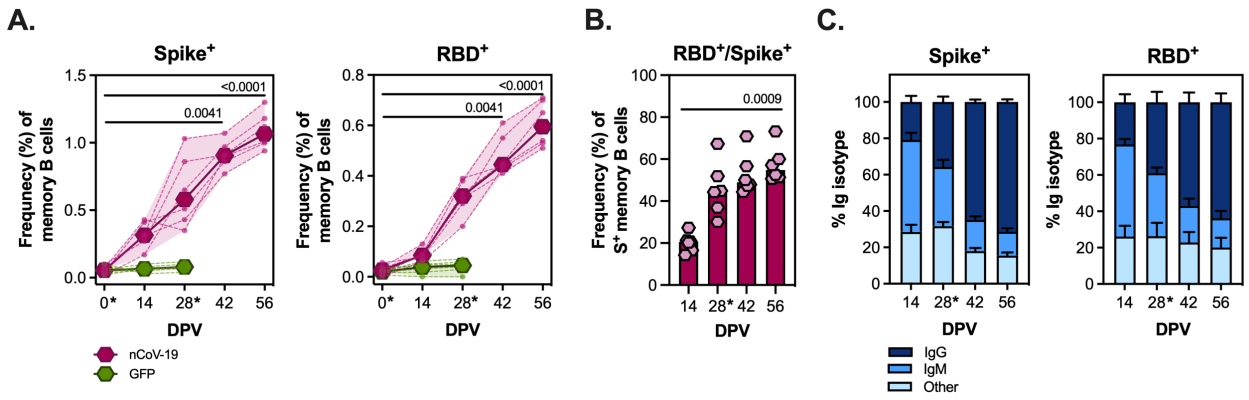


Figure 5-4. Characterisation of the ChAdOx1 nCoV-19-induced B cell response in circulation. (A) Dot plot with connecting line depicting the frequency of spike- (left) and RBD- (right) specific B cells as a percentage of total memory B cells over time. Small dots indicate individual animal frequencies. Large dots depict the group medians. The shaded region reflects the 95% confidence interval (statistical test: Friedman and Dunn's multiple comparisons test). **(B)** The proportion of spike-specific memory B cells also recognizing RBD in ChAdOx1 nCoV-19 vaccinees over time (statistical test: Friedman and Dunn's multiple comparisons test). Bars depict group medians. **(C)** Stacked bar chart depicting the median proportions of spike- (left) and RBD- (right) specific memory B cells expressing IgG, IgM, or neither Ig isotype. Error bars indicate the 95% confidence interval. Significant p-values (<0.05) are denoted in the figures, all other comparisons are not significant.

5.2.3 Local innate and cellular immunophenotypes on 3 and 5 DPC

Twenty-eight days after final immunisation, all animals were challenged with SARS-CoV-2 strain nCoV-WA1-2020. Animals were monitored for seven days prior to necropsy. For virological and immunological comparisons post challenge, sera and BAL fluid (BALF) were collected on 3 and 5 DPC. On 7 DPC, sera, PBMCs, lung cells, and splenocytes were obtained (Figure 5-1). As previously mentioned, SARS-CoV-2 infection causes mild respiratory disease in rhesus macaques with limited clinical signs or pulmonary damage. Therefore, the efficacy of ChAdOx1 nCoV-19 was primarily assessed based on the reduction of viral load and replication in the respiratory tract of vaccinees versus controls. Briefly, prime-boost vaccination substantially reduced genomic (gRNA) and subgenomic RNA (sgRNA) levels in the lower respiratory tract samples of vaccinees compared to controls; although, the difference only reached statistical significance for gRNA

comparisons in BALF at 3 (p=0.0043) and 5 (p=0.0151) DPC, as well as gRNA and sgRNA comparisons in lung tissue (p<0.0001 for both comparisons) (Mann-Whitney with Holm-Šídák's multiple comparisons test) (Figure 5-5A). Notably, only one vaccinee (nCoV-19 6) developed detectable levels of gRNA and sgRNA in BALF at 3 DPC. Differences in viral RNA levels in nasal swabs were not observed between vaccinees and controls.

Subsequently, we carried out immunological profiling of samples collected post challenge to evaluate the extent to which these variables were reflective of virological outcomes. Given the localised nature of infection in this model, we began our assessment by characterizing responses in the respiratory tract. First, we observed a reduction of multiple proinflammatory chemokine levels in BALF at 3 and 5 DPC associated with vaccination (Figure 5-5B). Comparisons of the z-scores of chemokine concentrations revealed significantly elevated concentrations of IL-8 (p<0.0001), IP-10 (p<0.0001), MCP-1 (p=0.0001), MIP-1α, (p<0.0001), MIP-1β (p<0.0001), eotaxin (p<0.0001), eotaxin-3 (p=0.0001), and macrophage-derived chemokine (MDC, p=0.0244) in controls compared to vaccinees (two-way ANOVA with Šídák's multiple comparisons test). MCP-4 (p=0.9988) concentrations were comparable between groups. These trends remained consistent, but were slightly less pronounced, at 5 DPC (Figure 5-5B, see Table 5-2 for list of p-values for pairwise comparisons). Slight elevations in the concentrations of certain chemokines were observed in nCoV-19 6, albeit to a lesser extent than in controls, in alignment with virological findings from the same BALF samples discussed above.

	3 DPC	5 DPC
IL-8	<0.0001	<0.0001
IP-10	<0.0001	<0.0001
MCP-1	0.0001	<0.0001
MIP-1α	<0.0001	<0.0001
MIP-1β	<0.0001	0.0022
Eotaxin	<0.0001	<0.0001
Eotaxin-3	0.0001	>0.9999
MCP-4	0.9988	0.6812
MDC	0.0244	0.9863

Table 5-2. BALF chemokine concentration statistical comparisons. P-values from two-way ANOVA and Šídák's multiple comparisons tests of the differences in the concentrations of individual chemokines detected in BALF at 3 and 5 DPC in ChAdOx1 nCoV-19 vaccinees versus ChAdOx1 GFP controls.

Alongside chemokine concentrations, we also compared relative levels of SARS-CoV-2 nucleoprotein (NP)-specific IgG and IgA in BALF post challenge by MESO Scale Discovery ELISA-like assay (Figure 5-7C). In corroboration with virus replication dynamics, significantly higher levels of NP-specific IgG and IgA antibodies were present in the BALF of control animals at 3 (IgG p=0.00003, IgA p=0.00006) and 5 (IgG p=0.02800, IgA p=0.03477) DPC, with a peak at 3 DPC. NP-specific antibodies were present in the BALF of vaccinated animals at levels just above the lower limit for the assay, which was consistent with little-to-no detection of viral RNA in these samples (Figure 5-5C).

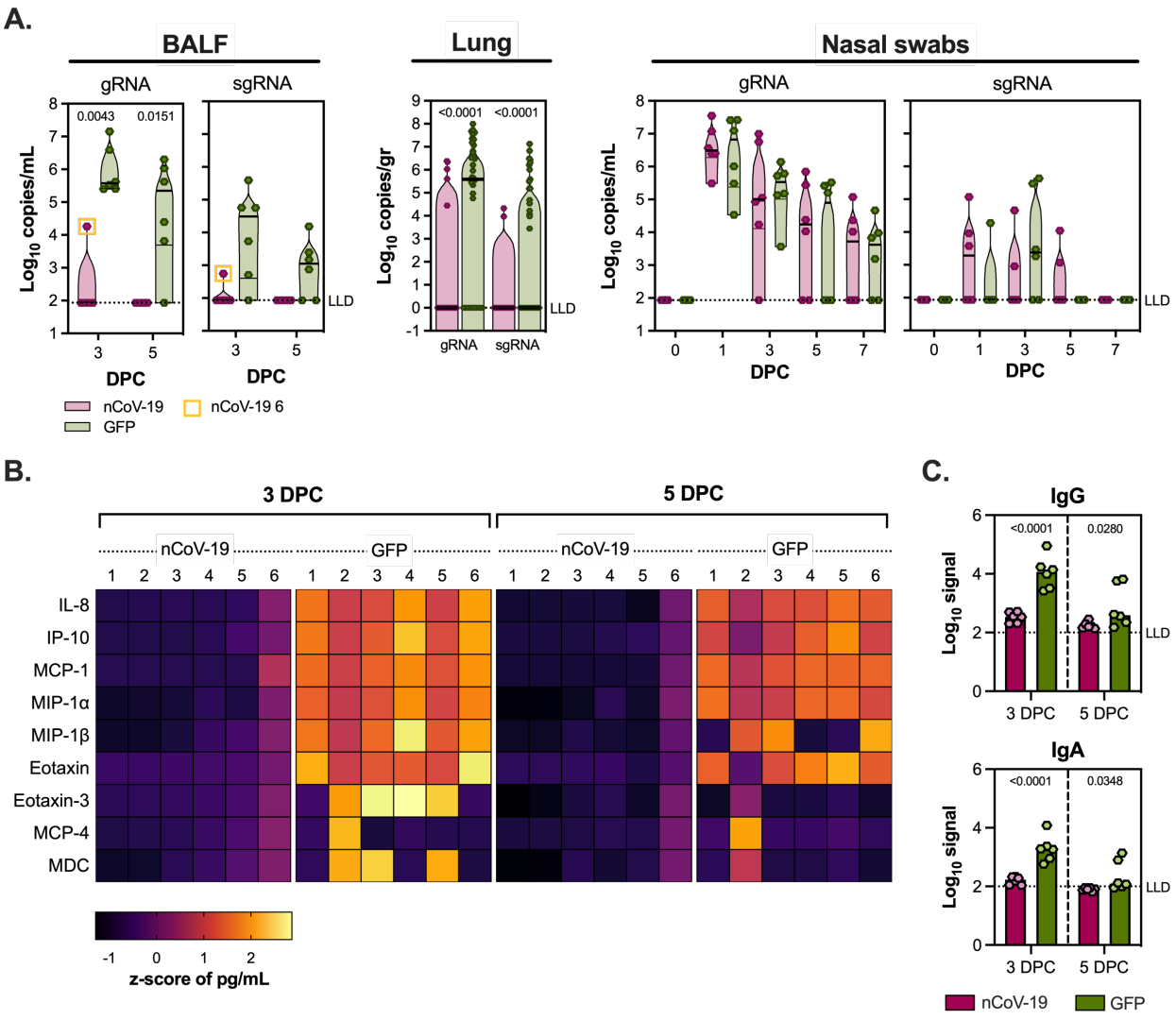


Figure 5-5. Respiratory tract viral load and responses to SARS-CoV-2 challenge in BALF. (A) Violin plots depicting genomic RNA (gRNA) and subgenomic RNA (sgRNA) detected by qRT-PCR in BALF at 3 and 5 DPC reported as $\log_{10}$ genome copies per mL (left), lung tissue at 7 DPC reported as $\log_{10}$ genome copies per gram (middle), and nasal swabs between 0 and 7 DPC reported as $\log_{10}$ genome copies per mL (right). A yellow square border has been used to highlight animal nCoV-19 6 in the BALF data (statistical test: Mann-Whitney with Holm-Šídák's multiple comparisons test). **(B)** Heatmaps depicting the z-scored concentrations (pg/mL) of chemokines in BALF at 3 (left) and 5 (right) DPC. Individual cells represent the z-scored data from individual animals (numbered 1-6) within each group. See Table 5-2 for p-values associated with comparison of the difference in concentrations between groups (statistical test: two-way ANOVA with Šídák's multiple comparisons tests). **(C)** Relative abundance of SARS-CoV-2 spike protein-specific IgG (top) and IgA (bottom) in BALF at 3 and 5 DPC reported as the $\log_{10}$ of the luminescence signal used to detect positive responses in the assay. Bars represent group medians (statistical test: Mann-Whitney with Holm-Šídák's multiple comparisons test). Dotted lines indicate the LLD or negative cut-off for each assay. Unless otherwise indicated, significant p-values (<0.05) are denoted in the figures, all other comparisons are not significant.

Next, we performed phenotyping of innate cells and T cells isolated from BALF collected at 3 and 5 DPC, respectively. During our assessment of innate cell populations at 3 DPC, we identified differences in macrophage phenotypes between vaccinees and controls. Specifically, within the subset of $CD163^+$ $CD206^+$ macrophages, which represented over 85% of total macrophages (classified as $CD66abce^-$ $CD68^+$ $CD11b^+$ HLA-DR^+), significantly larger $CD80^+$ $CD86^+$ and $CCR7^+$ populations were present in ChAdOx1 nCoV-19 vaccinees compared to controls (p=0.0159 for both comparisons, Mann-Whitney tests). Meanwhile, significantly higher frequencies of $CX3CR1^+$ macrophages were observed in control animals (p=0.0159, Mann-Whitney test) (Figure 5-6A). In previous studies, $CD80^+$ $CD86^+$ and $CCR7^+$ have been associated with resident macrophages with an activated or M1-polarised phenotype[492,493], whereas CX3CR1 may be upregulated on infiltrating (i.e., recently trafficked) or interstitial macrophages[494,495]. These observations suggest that the protection afforded by ChAdOx1 nCoV-19 may be reflected in significant phenotypic and functional differences in discrete local macrophage populations in comparison to controls.

At 5 DPC, the frequencies of $CD4^+$ (p=0.0087) and $CD8^+$ (p=0.0022) BAL T cells, as a proportion of total cells, were elevated in ChAdOx1 nCoV-19 vaccinees compared to controls (Mann-Whitney tests) (Figure 5-6B). Moreover, we noted phenotypic trends distinguishing vaccinees from controls, which were consistent across $CD4^+$ and $CD8^+$ T cells (Figures 5-6C&D). Specifically, frequencies of $CXCR3^+$ and $CD49d^+$ $CD4^+$ and $CD8^+$ T cells were significantly elevated in ChAdOx1 nCoV-19 recipients (p=0.0022 for all comparisons, Mann-Whitney tests). These markers are associated with T-cell homing to sites of inflammation/infection as well as effector memory function. Together, these data may reflect earlier recruitment of vaccine-primed T cells to the site of infection. By contrast, increased frequencies of $Ki67^+$ ($CD4^+$ p=0.0152, $CD8^+$

p=0.0043), CD38$^+$ (CD4$^+$ p=0.0022, CD8$^+$ p=0.0022), and HLA-DR$^+$ (CD4$^+$ p=0.0022, CD8$^+$ p=0.0043) T cells were detected in ChAdOx1 GFP recipients (Mann-Whitney tests) (Figure 5-6C&D). We predicted that the latter finding was representative of stronger local inflammatory signals (due to higher viral load) resulting in greater upregulation of markers of T-cell proliferation and activation in controls compared to vaccinees.

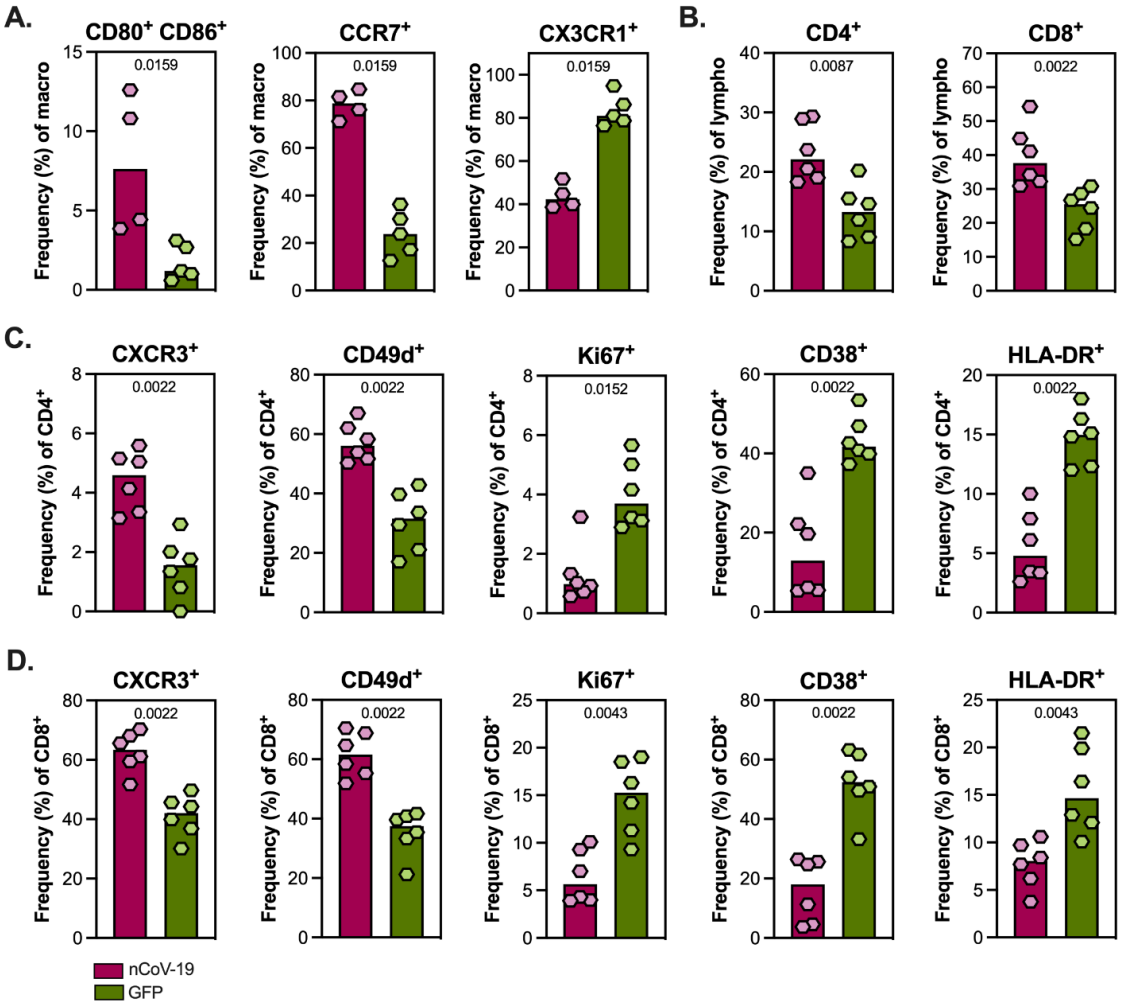


Figure 5-6. Macrophage and T-cell phenotypes in BAL cell samples at 3 and 5 DPC. (A) Frequencies of CD80$^+$ CD86$^+$ (left), CCR7$^+$ (middle), and CX3CR1$^+$ (right) macrophages at 3 DPC. The macrophage parent population was defined as CD66abce$^-$ CD68$^+$ CD11b$^+$ HLA-DR$^+$ CD163$^+$ CD206$^+$. Two nCoV-19 and one GFP samples were removed from the above analyses due to poor cell retrieval during the lavage procedure resulting in <250 total viable cells. **(B)** CD4$^+$(left) and CD8$^+$ (right) T-cell frequencies within the BALF lymphocyte fraction at 5 DPC. Frequencies of **(C)** CD4$^+$ and **(D)** CD8$^+$ T cells expressing (from left-to-right) CXCR3, CD49d, Ki67, CD38, and HLA-DR. Bars depict group medians (statistical tests for all comparisons: Mann-Whitney tests). Significant p-values (<0.05) are denoted in the figures, all other comparisons are not significant.

5.2.4 Transcriptional shifts and cellular phenotypes within the lungs

A similar flow cytometric phenotypic analysis was performed on T cells identified within single-cell suspensions of lung tissue harvested at 7 DPC. Findings from the lungs matched those from the BALF. Again, vaccinated animals exhibited increased frequencies of $CD4^+$ (p=0.0043) and $CD8^+$ (p=0.0022) T cells compared to controls (Mann-Whitney tests) (Figure 5-7A). Comparison of frequencies of $CD4^+$ and $CD8^+$ T cells positive for ten different phenotypic markers between vaccinees and controls revealed a trend consistent with that observed in the BALF. Frequencies of markers associated with antigen-experience (CD95) and homing or effector function (CXCR3 and CD49d) were higher in the vaccinated animals, and this effect was more pronounced on $CD8^+$ T cells compared to on $CD4^+$ T cells. Meanwhile, activation (CD69, CD38, HLA-DR) and proliferation (Ki67) markers were present at higher frequencies within T-cell subsets of the controls (significant p-values listed in the main figure, two-way ANOVA with Šídák's multiple comparisons test) (Figure 5-7B).

To expand our characterisation of the immune cell subsets in the lung post challenge, we performed single-cell RNA sequencing (scRNAseq) on samples from all six ChAdOx1 nCoV-19 recipients and three ChAdOx1 GFP controls. Lung sample processing, sequencing, and raw data normalisation was performed by the RML RTB Genomics Core Facility. Dr. Emily Speranza subsequently completed the analysis of the resulting scRNAseq data with assistance from me. Uniform manifold approximation and projection (UMAP) projections were calculated on the combined dataset generated from all animals and cell type identification was performed using an unbiased classification method as previously described[445] (Figure 5-7C). Comparison of major subset representation between groups revealed higher percentages of T (p=0.0357) and B (p=0.0357) cells in vaccinees versus controls (Figure 5-6D). Control animals exhibited a higher

proportion of actively or recently dividing cells (p=0.0357) (Mann-Whitney tests) (Figure 5-7D). These results closely recapitulated those from assessment via flow cytometry. To determine the cell types exhibiting the strongest identifiable transcriptional difference between groups, we applied a previously described clustering bias method (Figure A.6.1)[445]. Cell types demonstrating significant bias along one or more principal components were identified: macrophages/monocytes and dividing cells showed the strongest transcriptional shifts (Figure 5-7E). Cell type identification of dividing cells indicated that they were largely macrophages or monocytes.

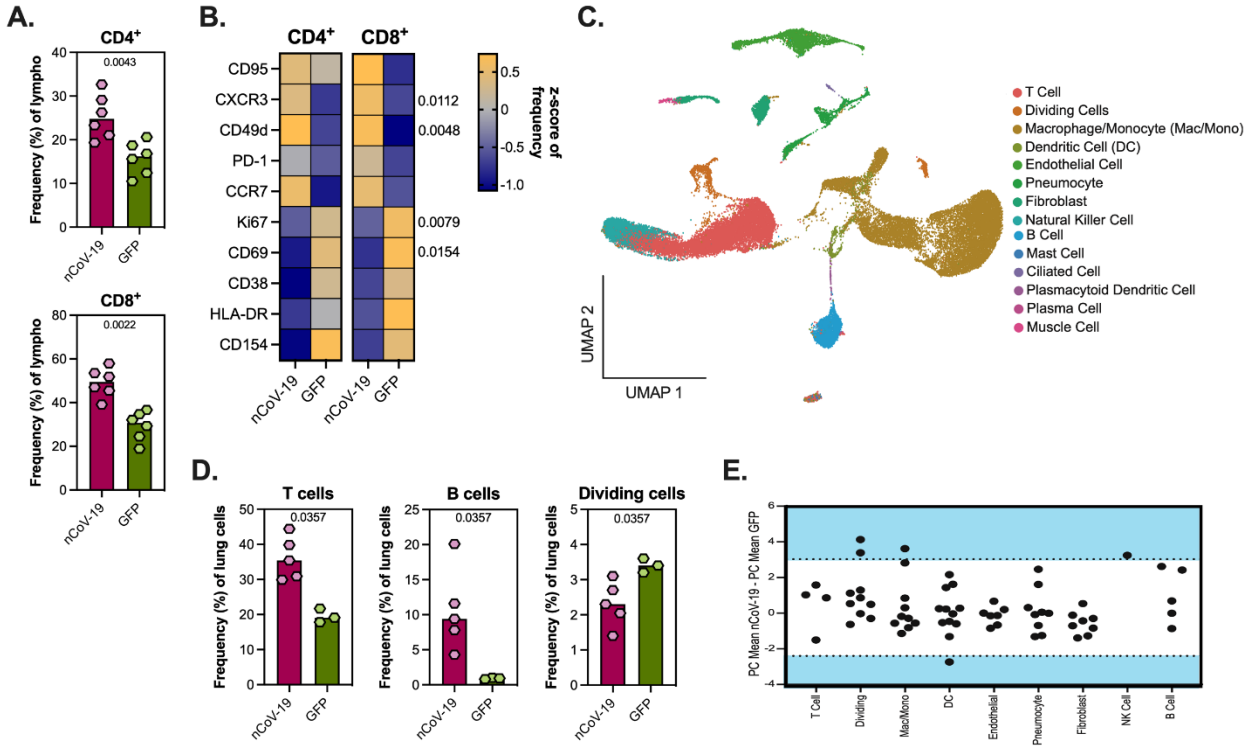


Figure 5-7. Lung T-cell phenotypes and cellular transcriptional profiles at 7 DPC. (A) CD4$^+$ and CD8$^+$ T-cell frequencies within the lung lymphocyte fraction (statistical test: Mann-Whitney)**. (B)** Heatmap comparing the z-scored frequencies of CD4$^+$ (left) and CD8$^+$ (right) T cells expressing specified phenotypic markers (statistical test: two-way ANOVA with Šídák's multiple comparisons test). **(C)** UMAP depiction of major cell types distinguished within the lung tissue across animals by single-cell RNA sequencing. Two nCoV-19 and one GFP samples were excluded from scRNAseq analyses due to cell suspensions that did not meet minimum sample quality thresholds. **(D)** Frequencies of T cells (left), B cells (middle), and actively or recently dividing cells (right) identified by scRNAseq, as a percentage of total lung cells (statistical test: Mann-Whitney). **(E)** Results from a clustering bias analysis calculating the difference in mean principal component scores between vaccinees and controls for each major cell type. Each data point represents a principal component for the given cell type; only components comprising 99% of the explained variance were included. Dotted lines represent ± two SD from the mean of all the points. Where relevant, bars depict group medians and significant p-values (<0.05) are denoted in the figures; all other statistical comparisons are not significant.

Therefore, we subsequently sought to better define drivers of the transcriptional differences observed between the macrophages of vaccinees and controls. To do so, we subset the data from these cells and performed a sub-clustering analysis (Figure A.6.1). When analysed independently, three distinct sub-clusters were identified within the total macrophage/monocyte population (Figure 5-8A). Cluster A represented alveolar macrophages with M2-like polarisation and expressed high levels of FABP4 and MARCO, as well as elevated levels of CD163 and CD63. Cluster B bore characteristics of M1-polarised macrophages, evidenced by elevated levels of HLA-associated genes, and included interstitial or newly recruited macrophages. Cluster C represented monocyte-like cells. We next looked at the relative distribution of cells from the vaccinated versus control animals between these phenotypic clusters. Cluster A macrophages were similarly represented in vaccinees and controls. But cluster B appeared to compose a significantly larger proportion of total macrophages in the control animals compared to the vaccinated animals (p=0.0096); differences in cluster C frequencies appeared to reflect a corresponding and proportional shift from cluster B (two-way ANOVA with Šídák's multiple comparisons test) (Figure 5-8B). Notably, the elevated frequencies of interstitial or recruited macrophages observed in the lungs of the controls by single-cell RNA sequencing corroborated with the increased frequency of $CX3CR1^{+}$ (infiltrating) macrophages in these animals in the BALF at 3 DPC. Finally, we elucidated gene sets that were strongly differentiated between the vaccinated and control animals in the three macrophage clusters. The highest divergence came from the type-I-interferon signalling pathway, which was elevated in the control animals in cluster A (p<0.0001) and cluster B (p<0.0001) macrophages (p-values estimated from 1000 iterations and adjusted for false discovery rate). Expression of this gene set was comparable between vaccinated and control animals in cluster C cells (Figure 5-8C). Together these data indicate that the vaccinated animals

exhibited limited detectable inflammation present in the deep lung tissue compared to control animals that demonstrated signs of inflammation and inflammatory cell accumulation persisting to 7 DPC.

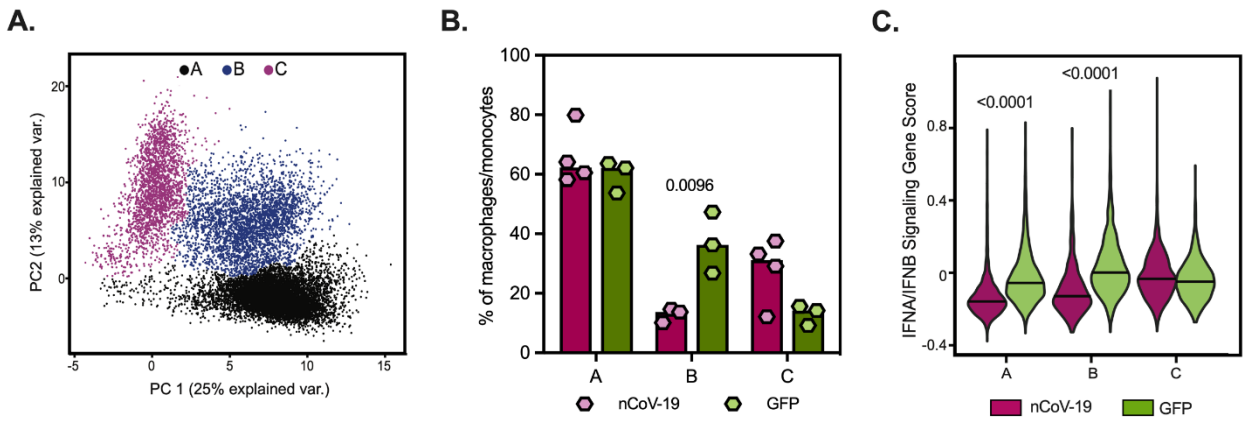


Figure 5-8. Lung macrophage/monocyte clusters and inflammatory signalling. (A) Principal component (PC) analysis for macrophage and monocyte like cells. Each data point on the dot plot represents an individual cell plotted according to PC1 and PC2 scores. Cells are coloured based on their cluster assignment: A (black), B (blue), or C (magenta). **(B)** Relative median frequency of cells belonging to clusters A, B, and C within the total macrophage/monocyte subset in vaccinees versus controls (statistical test: two-way ANOVA with Šídák's multiple comparisons test). **(C)** Violin plots depicting the type-I-interferon (IFNA/IFNB) gene signalling scores of each macrophage/monocyte cluster in vaccinees compared to controls. The horizontal lines represent the median value for each group (see methods for p-value estimation). Significant p-values (<0.05) are denoted in the figures; all other statistical comparisons are not significant.

5.2.5 Systemic T-cell phenotypes at 7 DPC

To conclude our assessment of cellular immune responses after infection, we next sought to determine if phenotypic trends observed on T cells from the respiratory tract also extended to systemic T cells. We primarily focused on T-cell responses in PBMC samples collected at 7 DPC. Unlike in BALF and lung samples, differences in the frequencies of total T cells (p=0.8182), $CD4^+$ (p>0.9999), or $CD8^+$ (p=0.3939) T cells were not discernible between groups in circulation (Mann-Whitney test) (Figure 5-9A). We hypothesised that migration of vaccine-primed cells to the lungs within the first few days after infection may have precluded the observation of increased

frequencies of circulating T cells in vaccinees relative to controls. To obtain evidence for this supposition, we calculated the (log_2) fold-change in frequencies between 0 and 7 DPC, for each animal. Doing so verified the occurrence of a uniform decrease in $CD4^+$ and $CD8^+$ T-cell frequencies in the vaccinated animals post challenge, which was not concurrently apparent in the controls (p=0.0022 nCoV-19 vs. GFP for both comparisons, Mann-Whitney tests) (Figure 5-9B&C). Differences in the ratios of $CD4^+$ to $CD8^+$ T cells were not detected between vaccinees and controls at 0 or 7 DPC (Appendix 7.1).

Finally, we carried out ICS on splenocytes harvested at 7 DPC to functionally characterise S-specific T cells in vaccinees versus controls (Figure 5-9D&E). The frequencies of $CD4^+$ and $CD8^+$ T cells expressing IFNγ, TNFα, IL-2, Granzyme B, IL-4, or IL-10 in response to stimulation were determined (Figure 5-9D&E). We could not detect significant differences in the frequencies of single cytokine-positive T cells between vaccinees and controls (two-way ANOVA with Šídák's multiple comparisons test). Moreover, Boolean gating to identify multiple cytokine-secreting populations and subsequent SPICE analysis revealed no significant differences in the polyfunctional cytokine profiles between the two groups (permutation test) (Figure 5-9F). Collectively, our assessment of the cellular immune response suggested that 7 DPC may have been too far post challenge to be able to detect clear phenotypic and functional differences in systemic T cell populations between vaccinees and controls, which was unsurprising given the rapid and localised nature of SARS-CoV-2 infection in this model.

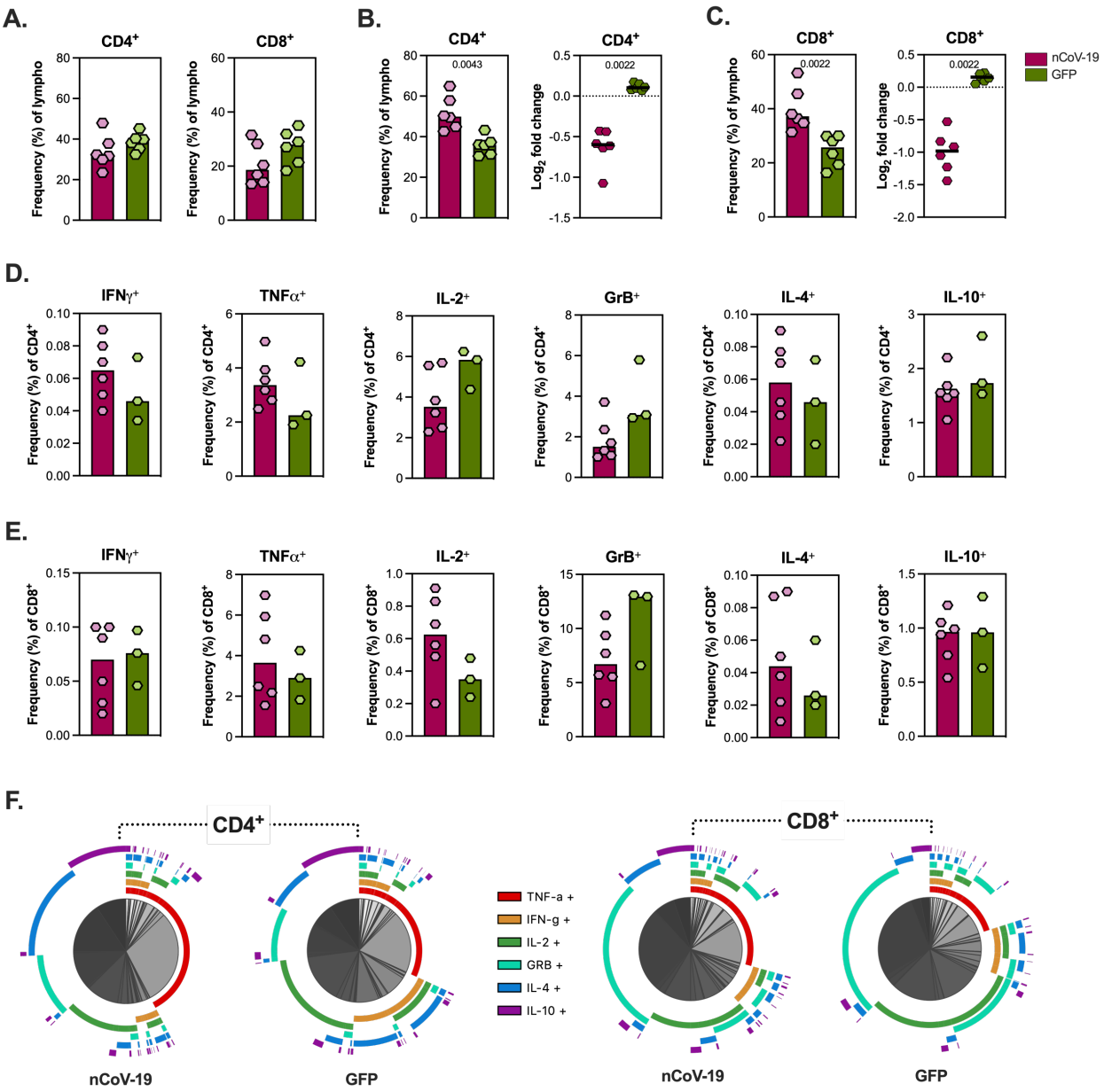


Figure 5-9. Comparison of systemic T-cell phenotypes at 7 DPC. (A) $CD4^+$ (top) and $CD8^+$ (bottom) T-cell frequencies within the PBMC lymphocyte fraction at 7 DPC (statistical test: Mann-Whitney)**. (B)** $CD4^+$ and **(C)** $CD8^+$ T-cell frequencies within the PBMC lymphocyte fraction at 0 DPC (left), alongside the $\log_2$ fold change in the frequency of each subset between 0 and 7 DPC (right) (statistical test: Mann-Whitney). ICS to quantify frequencies of **(D)** $CD4^+$ and **(E)** $CD8^+$ antigen-specific T-cell responses in splenocyte samples collected at 7 DPC from all six ChAdOx1 nCoV-19 vaccinees and three ChAdOx1 GFP control animals. Cells were stimulated with two peptide pools spanning the SARS-CoV-2 spike protein sequence; positive frequencies were summed after background adjustment. Frequencies of (form left-to-right) IFNγ, TNFα, IL-2, Granzyme B (GrB), IL-4, and IL-10 cells within (D) $CD4^+$ and (E) $CD8^+$ T-cell subsets are shown (statistical test: Mann-Whitney). **(F)** SPICE plots depicting cytokine expression profiles of SARS-CoV-2 spike-specific $CD4^+$ (left) and $CD8^+$ (right) T cells. Pie charts depict the weighted proportions of all cytokine permutations. Arcs mark populations positive for each cytokine (statistical test: permutation). Bars depict group medians. Significant p-values (<0.05) are denoted in the figures; all other statistical comparisons are not significant.

5.2.6 Systemic B-cell phenotypes at 7 DPC

Due to low quantities in the BALF and lung samples, assessment of B-cell responses was primarily restricted to comparison of phenotypes in PBMC samples at 7 DPC. We detected significantly higher frequencies of circulating B cells in vaccinees compared to the controls, likely due to the amplification of vaccine-primed B-cell responses (p=0.0022, Mann-Whitney test) (Figure 5-10A). To elucidate phenotypic differences between the groups, we subset B cells according to their memory and activation phenotypes. Doing so yielded 42 populations/phenotypes per animal which were inputted into a PC analysis. *K*-means clustering (k=3) was also applied. Each vaccinated (nCoV-19 1-6) and control (GFP 1-6) animal was plotted based on their PC1 and PC2 scores; these dimensions explained 43.75% and 18.27% of the total variance between animals, respectively (Figure 5-10B). Notably, five out of six ChAdOx1 nCoV-19 vaccinees clustered together (C1), distinctly from ChAdOx1 GFP controls that were grouped into a single cluster (C3). A single vaccinee (nCoV-19 6) was clustered independently (C2). Scores along PC1 clearly differentiated animals by vaccination status, except for nCoV-19 6, which appeared to resemble a control animal both by PC1 score and dendrogram placement (Figures 5-10B&C).

To identify drivers of the variation between vaccinees and controls, we ranked the contribution of all 42 variables to PC1 (Figure 5-10D). Eighteen above average contributors (>2.38% contribution to total PC1 variance) were selected for further analysis and groupwise comparisons (Figure 5-10E-G). As anticipated, ChAdOx1 nCoV-19 vaccinees exhibited higher frequencies of class-switched memory (SM, IgD^- IgM^-) B cells (p=0.0022), and lower frequencies of unswitched memory (USM, IgD^+ $CD27^+$) B cells (p=0.0022) and naïve (IgD^+ $CD27^-$ $CD21^+$) cells (p=0.0649) than the ChAdOx1 GFP controls, although the latter difference was not significant (Mann-Whitney

tests) (Figure 5-10E). The SM subset of vaccinees was composed of a significantly higher frequency of activated switched memory (ASM, $CD21^{-}$ $CD27^{+}$) B cells (p=0.0260). Meanwhile, the SM subset of controls consisted of greater percentages of resting switched memory (RSM, $CD21^{+}$ $CD27^{+}$, p=0.0368) and tissue-like switched memory (TLSM, $CD21^{lo}$ $CD27^{lo}$, p=0.0130) B cells (Mann-Whitney) (Figure 5-10E). Across most subpopulations, control animals demonstrated higher frequencies of cells positive for markers associated with the activation of early-stage B-cell responses (CD69, CD80, CD95, and IgM) (Figure 5-10F). By contrast, vaccinees exhibited higher frequencies of class-switched IgG^{+} cells composing the subsets examined (Figure 5-10G). Intriguingly, the frequencies of most B-cell sub-populations in animal nCoV-19 6 aligned more closely with the median values of the controls than those of the vaccinees, which corroborated with the clustering results from the PC analysis (Figures 5-10B&C). Moreover, nCoV-19 6 was the only vaccinee with detectable levels of BALF viral RNA and slight elevated BALF pro-inflammatory chemokines (Figure 5-7A&B). Finally, we further confirmed the above results by performing an antibody-secreting cell ELISpot to detect antigen-specific B cells actively secreting IgG in circulation on 7 DPC (Figure 5-10H). Significantly higher levels of S- (p=0.0022) and RBD-specific (p=0.0043) IgG-secreting cells were detected in PBMC samples from ChAdOx1 nCoV-19 vaccinees compared to controls (Mann-Whitney test). Collectively, these findings indicate that ChAdOx1 nCoV-19 vaccination elicited antigen-specific LLPC and/or mature memory B-cell development, which at 7 DPC, resulted in an active recall response to SARS-CoV-2. By contrast, at 7 DPC, systemic humoral immune responses to infection were mounting in control animals, characterised by significant populations of activated naïve B cells experiencing primary antigen exposure and recently differentiated memory cells that had yet to undergo class switching.

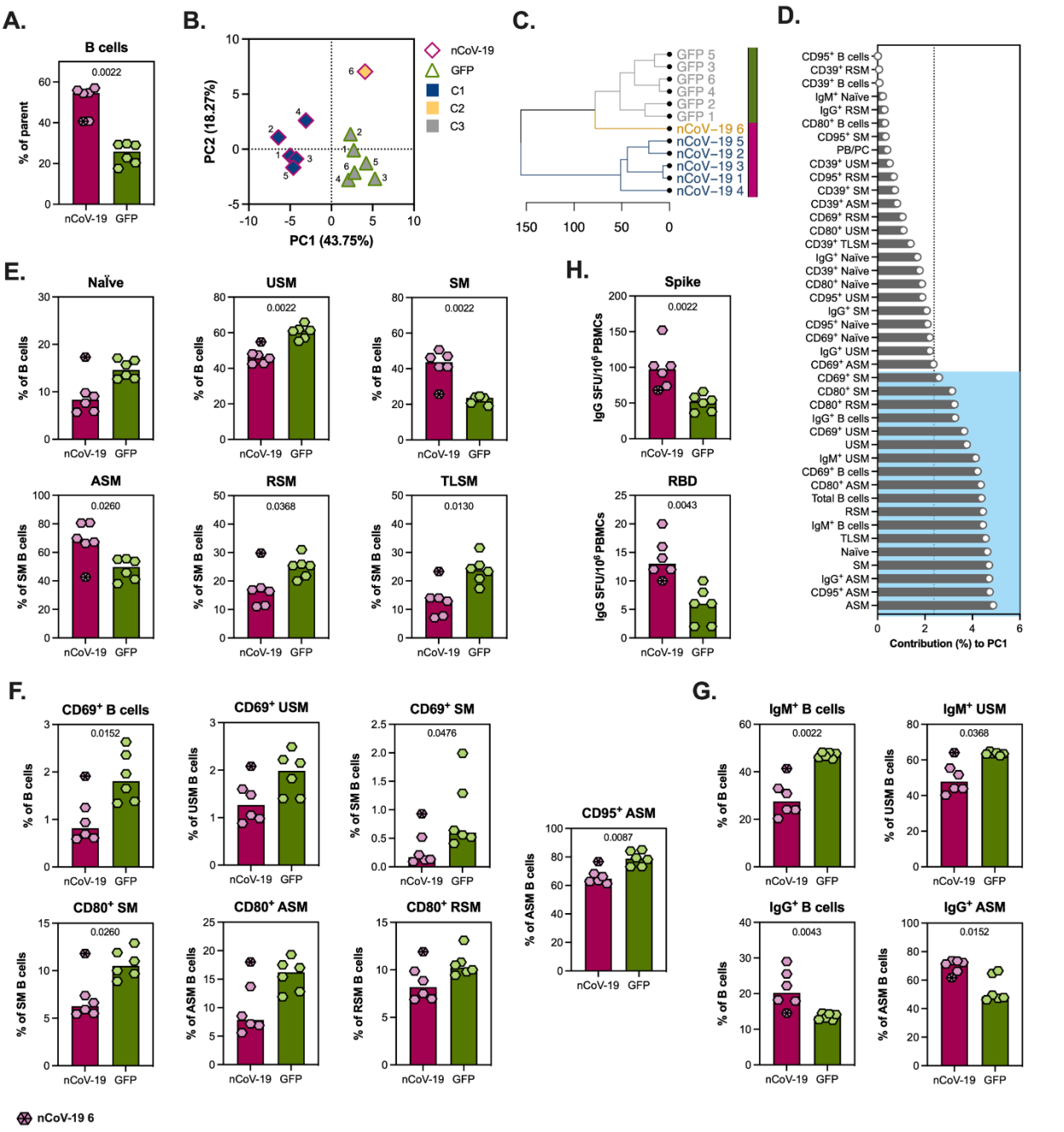


Figure 5-10. Phenotypic and functional profiling of B cells after SARS-CoV-2 challenge. (A) Frequency of total B cells within CD3$^-$ live lymphocytes**. (B)** PC analysis plot depicting PC1 and PC2 (left) with *k*-means clustering. Data were standardised (scaling such that mean=0, SD=1) and PCs were selected using the percentage of total explained variance. On the scatter plot: diamonds (magenta border) indicate nCoV-19 vaccinees and triangles (green border) indicate GFP controls; the numbers next to each datapoint indicate animals 1-6 within each group. The fill colour of each datapoint indicates the assigned cluster (C1-C3). **(C)** Dendrogram of *k*-means clustering with Euclidean distances; branch colours indicate the cluster (C1-C3) for each animal. **(D)** B-cell phenotypic variable contributions to PC1; above average contributions are captured in the blue shaded region. **(E-G)** Frequencies of B-cell populations identified in D. **(H)** S and RBD IgG antibody-secreting ELISpot; results reported as SFU per 10^6 cells. All bars depict group medians (statistical analyses for all comparisons: Mann-Whitney test). Significant p-values (<0.05) are denoted in the figures, all other comparisons are not significant.

5.2.7 Humoral immunogenicity of IN-administered ChAdOx1 nCoV-19

As a follow-up to our study examining the efficacy of IM administered ChAdOx1 nCoV-19, we next studied the effects of IN delivery of ChAdOx1 nCoV-19 in rhesus macaques challenged with SARS-CoV-2 (Figure 5-11). Animals received two doses of ChAdOx1 nCoV-19 or ChAdOx1 GFP on 0 and 28 DPV. Immunisation was performed using a mucosal atomisation device, which produced a spray of aerosols into the nasal cavity. PBMC samples, sera, and nasosorption (nasal fluid) samples were collected at baseline (0 DPV), post prime (14 and 28 DPV), and post boost (42 and 56 DPV). BALF was collected at 7 DPV and 35 DPV (Figure 5-11).

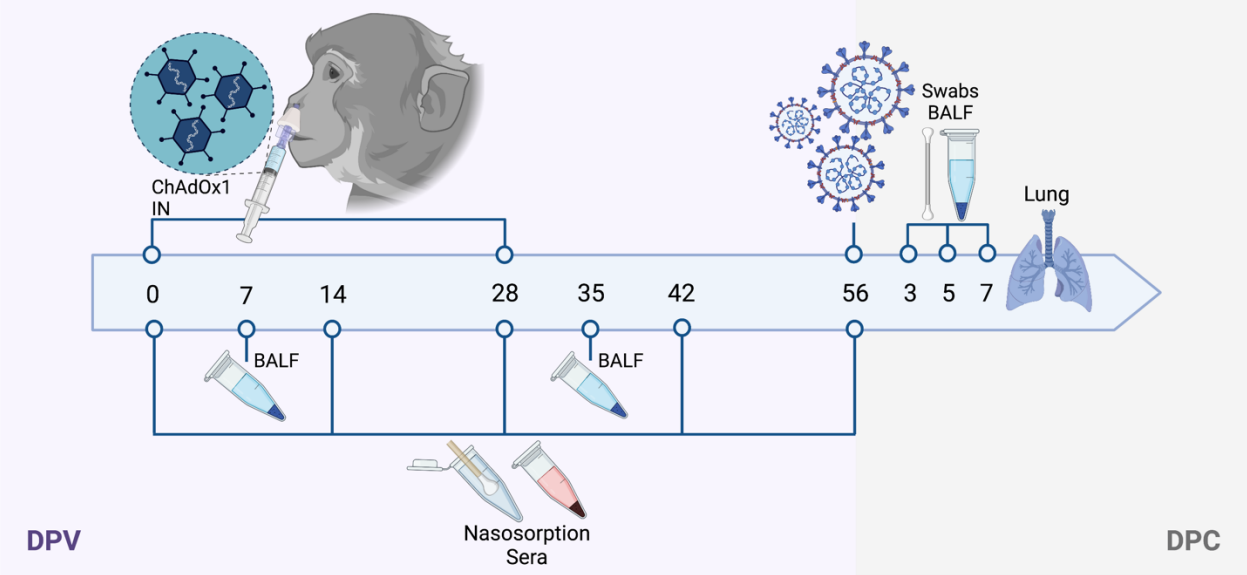


Figure 5-11. Intranasal vaccination-and-challenge study design and timeline. Overview of vaccination, challenge, and sampling schedule. Rhesus macaques (n=4 per group) received two doses of intranasally administered ChAdOx1 nCoV-19 or ChAdOx1 GFP ($2.5x10^{10}$ VP per dose) on 0 and 28 DPV. Vaccinees (nCoV-19) are indicated in magenta and controls (GFP) are indicated in green. PBMCs, sera, and nasosorption swabs were collected 0, 14, 28, 42, and 56 DPV. Nasosorption samples were obtained using a small piece of absorbent filter paper that was inserted into the nostril of the animal and closing of the nostril for 60 seconds. BAL was performed on 7 DPV and 35 DPV, to isolate performance of the lavage procedure from other sampling taking place on the previously listed exam days. Animals were challenged via the intratracheal and intranasal routes with 10^6 $TCID_{50}$ of SARS-CoV-2 (SARS-CoV-2/human/USA/RML-7/2020) on 56 DPV (or 0 DPC). Nasal swabs, BALF, and lung tissue samples were collected post challenge. Sampling timepoints are indicated in terms of days post vaccination (DPV) or days post challenge (DPC).

Based on our findings in recipients of IM ChAdOx1 nCoV-19, we decided to principally narrow our investigation to the assessment of the vaccine-mediated humoral response. Thus, we first evaluated the induction of antigen-specific antibody responses in circulation, and the upper and lower respiratory tract of IN-immunised macaques. A multiplex ELISA-like assay (MESO Scale Discovery) was carried out to measure relative concentrations of S- and RBD-specific IgG and IgA antibodies. S- and RBD-specific IgG were detected in serum and nasosorption samples 14 and 28 days after prime vaccination, but not in BAL, seven days post prime vaccination. Administration of a second vaccine dose boosted IgG titres in sera and nasosorption samples obtained at 42 and 56 DPV and elicited detectable IgG antibodies in BALF at 35 DPV (Figure 5-12A-C). S- and RBD-specific IgA antibodies were detected in serum upon prime vaccination but did not increase upon booster vaccination (Figure 5-12D). In contrast, SARS-CoV-2 specific IgA antibodies were only weakly detected in nasosorption samples upon prime vaccination but further increased upon boost vaccination (Figure 5-12E). As for IgG, no SARS-CoV-2 specific IgA antibodies were detected in BALF at 7 DPV but were elicited by seven days post boost vaccination (35 DPV, Figure 5-12F) (See Table 5-3 for statistical comparison of antibody levels between vaccinees and controls at 56 DPV). As expected, a higher fraction of IgA to total Ig was detected in nasosorption samples compared to BALF and serum samples (Figure 5-12G).

	Sera		Nasosorption		BALF	
	Spike	**RBD**	**Spike**	**RBD**	**Spike**	**RBD**
IgG	0.0286	0.0571	0.0286	0.0286	0.0286	0.0286
IgA	0.0286	0.0571	0.0286	0.0286	0.0286	0.1143

Table 5-3. Vaccine-specific antibody responses in circulation, the upper and lower respiratory tract. P-values for the statistical comparisons of the relative levels of SARS-CoV-2 S- and RBD-specific IgG and IgA antibodies in serum, nasosorption samples, and BALF detected by MESO Scale Discovery ELISA-like assay. Sera and nasosorption comparisons between vaccinee and control samples were performed at 56 DPV. BALF comparisons were performed on 35 DPV samples. P-values are the result of Mann-Whitney tests (all values shown).

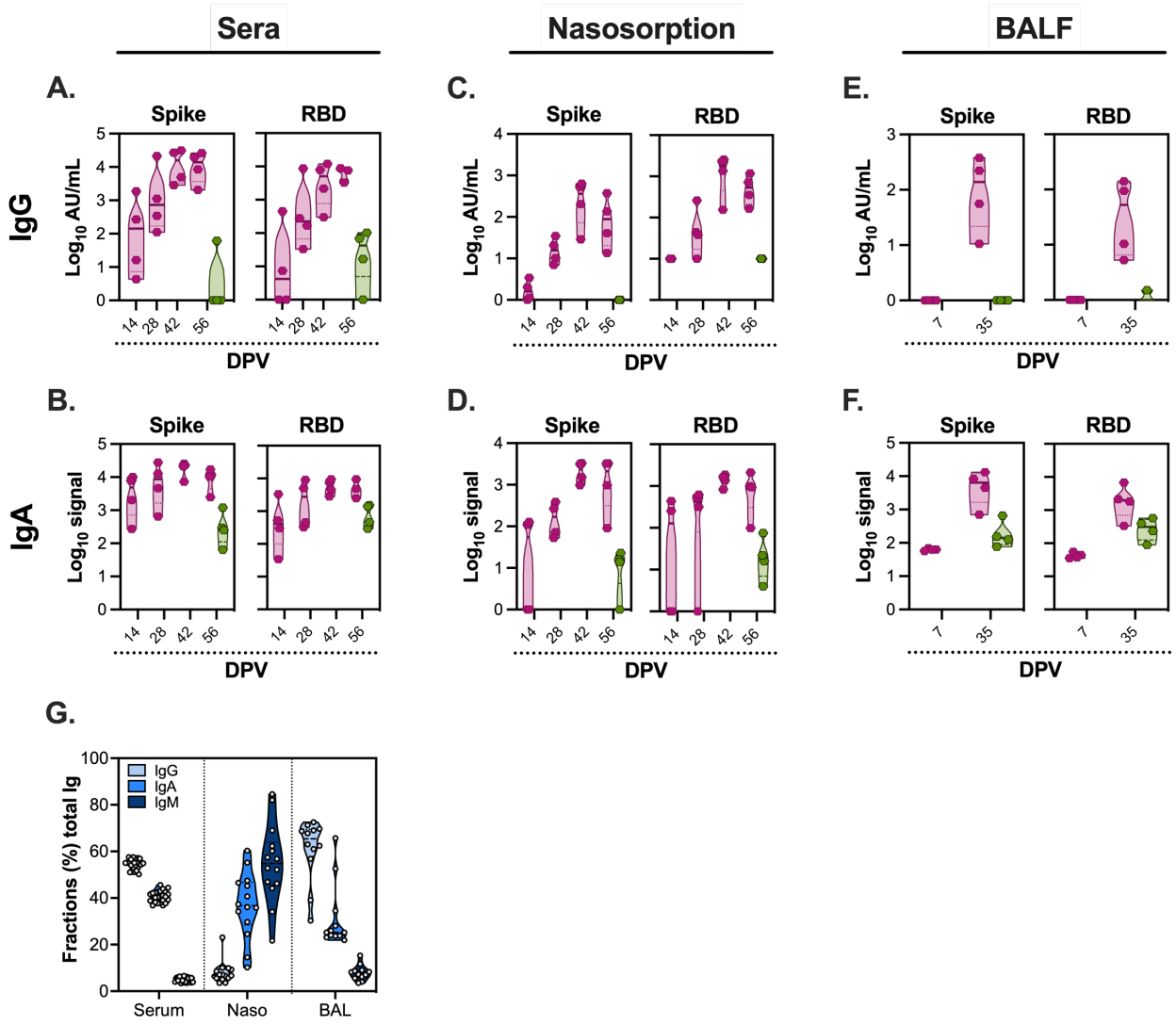


Figure 5-12. Humoral responses induced by ChAdOx1 nCoV-19 vaccinees. Truncated violin plots depicting the relative concentration or abundance of SARS-CoV-2 S- (left) and RBD-(right) specific IgG (log_{10} arbitrary units per mL) and IgA (log_{10} luminescence signal) antibodies measured in serum **(A, B)**, nasosorption samples **(C, D)**, and BALF **(E, F)**, respectively. Sera and nasosorption sample plots depict relative antibody concentrations in vaccinees at 14, 28, 42, and 56 DPV and in controls at 56 DPV. BALF plots depict relative antibody concentrations in vaccinees at 7 and 35 DPV and in controls at 35 DPV. (See Table 5-3 for a summary of statistical analyses performed and associated p-values). **(G)** Violin plots depicting the fractions of IgG, IgA, and IgM in serum, nasosorption, and BALF samples as a proportion of total immunoglobulin (Ig) obtained from animals from both groups between 14 and 56 DPV. Twenty-four serum, 14 nasosorption, and 12 BALF samples were investigated.

Circulating neutralising antibodies were detected in vaccinees at levels significantly above baseline by 42 DPV (p=0.0208, Friedman test with Dunn's multiple comparisons). These titres appeared slightly reduced compared to those in IM-immunised macaques, but not to an extent that

was statistically significant (p=0.6857, Mann-Whitney test) (Figure 5-13A). Serum antibodies at 42 DPV also demonstrated similar capacity to neutralise SARS-CoV-2 strains WA-1 and B.1.1.7. However, as previously observed, strains B.1.351 (p=0.1199) and B.1.617.2 (p=0.0.0278) were more refractory to neutralisation, although the reduction in titres relative to WA-1 was not quite statistically significant for the former (Friedman test with Dunn's multiple comparisons) (Figure 5-13B). Finally, the sera of IN-vaccinated macaques also demonstrated the ability to induce antibody Fc-mediated effector functions; these included ADCD, ADMP, and ADNKA (Figure 5-13C-E). The magnitude of S-specific antibody-mediated effector functions in vaccinees was substantially elevated in comparison to controls for all assays (ADCD: p<0.0001; ADMP: p<0.0001; ADNKA: CD107a p<0.0001, MIP-1β p=0.0016, IFNγ p=0.0010), differences for RBD-specific antibody effector functions did not meet statistical significance (two-way ANOVA with Šídák's multiple comparisons test). Thus, IN delivery of ChAdOx1 nCoV-19 elicited multifunctional, systemic and local antibody responses.

Although the detection of SARS-CoV-2 S-specific T cells was carried out by IFNγ ELISpot assay of PBMC and BAL cell samples collected post boost, on 56 and 49 DPV respectively, median responses in vaccinees fell below 80 SFU/10^6 cells in both assays and did not differ significantly from values measured in controls (Appendix 7.2). These low vaccine-elicited cellular immune responses were consistent with the previously reported observations in IM-immunised animals.

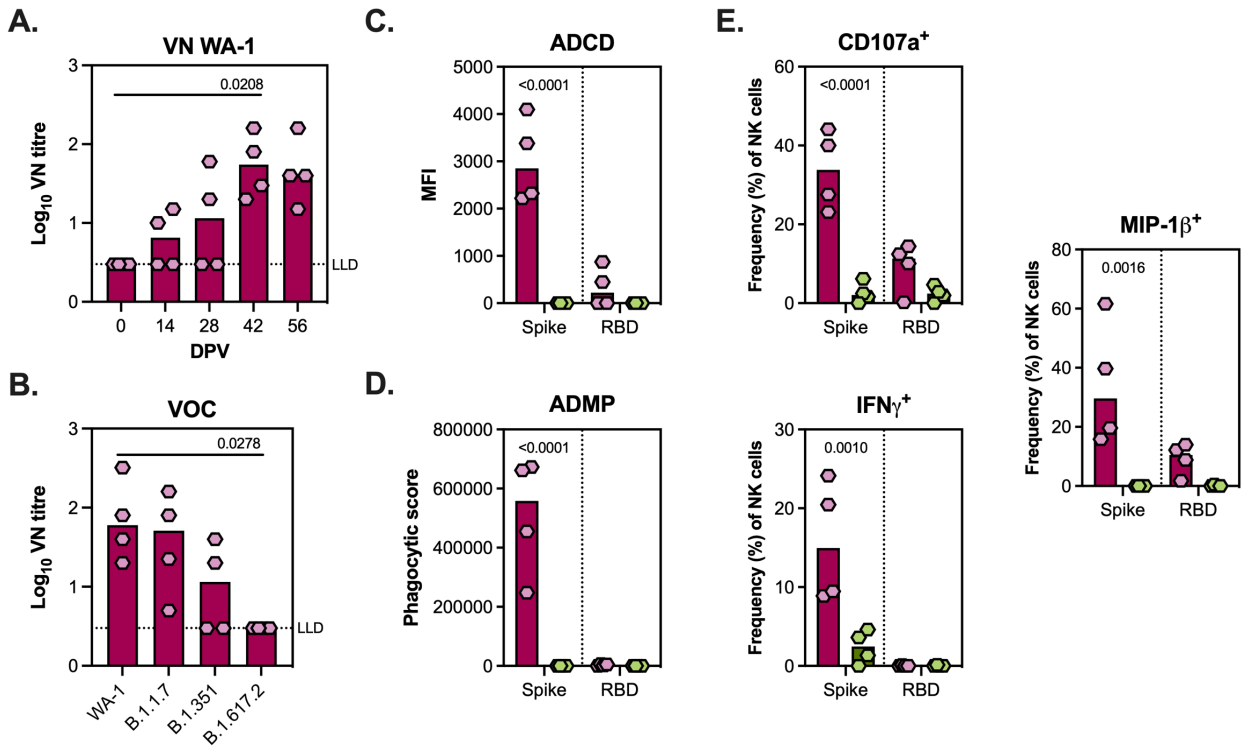


Figure 5-13. Characterisation of antibody functionality in 56 DPV serum. (A) Serum microneutralisation assay titres against 2000 $TCID_{50}$ of SARS-CoV-2 strain WA-1 reported as log_{10} of the highest reciprocal sera dilution absent for CPE. **(B)** VN titres in 42 DPV sera of ChAdOx1 nCoV-19 vaccinees against SARS-CoV-2 variants of concern, in comparison to the challenge strain WA-1 (statistical test I-J: Friedman and Dunn's multiple comparisons test). Spike- and RBD-specific **(C)** antibody-dependent monocyte phagocytosis (ADMP) scores of THP-1 cells, **(D)** antibody-dependent C3 complement deposition (ADCD) median fluorescent intensity (MFI), and **(E)** antibody-dependent activation of NK cells assessed by frequencies of $CD107a^+$, MIP-$1\beta^+$, or $IFN\gamma^+$ $CD3^-$ $CD56^+$ $CD16^+$ cells isolated from a healthy human donor (statistical test: Mann-Whitney with Holm-Šídák multiple comparisons). All bars depict group medians. Horizontal dotted lines indicate the lower limit of detection for the assay. Significant p-values (<0.05) are denoted in the figures, all other comparisons are not significant.

5.2.8 SARS-CoV-2 challenge of IN-immunised ChAdOx1 nCoV-19 vaccinees

On 56 DPV (or 0 DPC), animals were challenged with SARS-CoV-2. Nasal swabs, BALF, and lung tissue samples were investigated for the presence of gRNA, sgRNA and infectious virus at various timepoints post challenge (Figure 5-11). Titrations of infectious samples were carried out by Dr. Neeltje van Doremalen under BSL4 conditions. Notably, a downward trend in nasal shedding was associated with IN vaccination, according to sgRNA levels and infectious virus titres

between 0 and 7 DPC, particularly on 1 DPC (viral titre, p=0.0375, two-way ANOVA with Šídák's multiple comparisons test) (Figure 5-14A&B). Although the overall effect did not reach statistical significance by AUC comparisons of total shedding (sgRNA, p=0.2571; viral titre, p=0.1429, Mann-Whitney tests). Like the ChAdOx1 nCoV-19 IM vaccinees, IN-immunised animals showed salient reductions in lower respiratory tract viral load compared to controls, particularly evidenced by sgRNA levels in BALF between 3 and 7 DPC (AUC comparison, p=0.0286, Mann-Whitney test), as well as gRNA (p<0.0001) and sgRNA (p=0.001) levels in the lungs at 7 DPC (Mann-Whitney test) (Figure 5-14C-F).

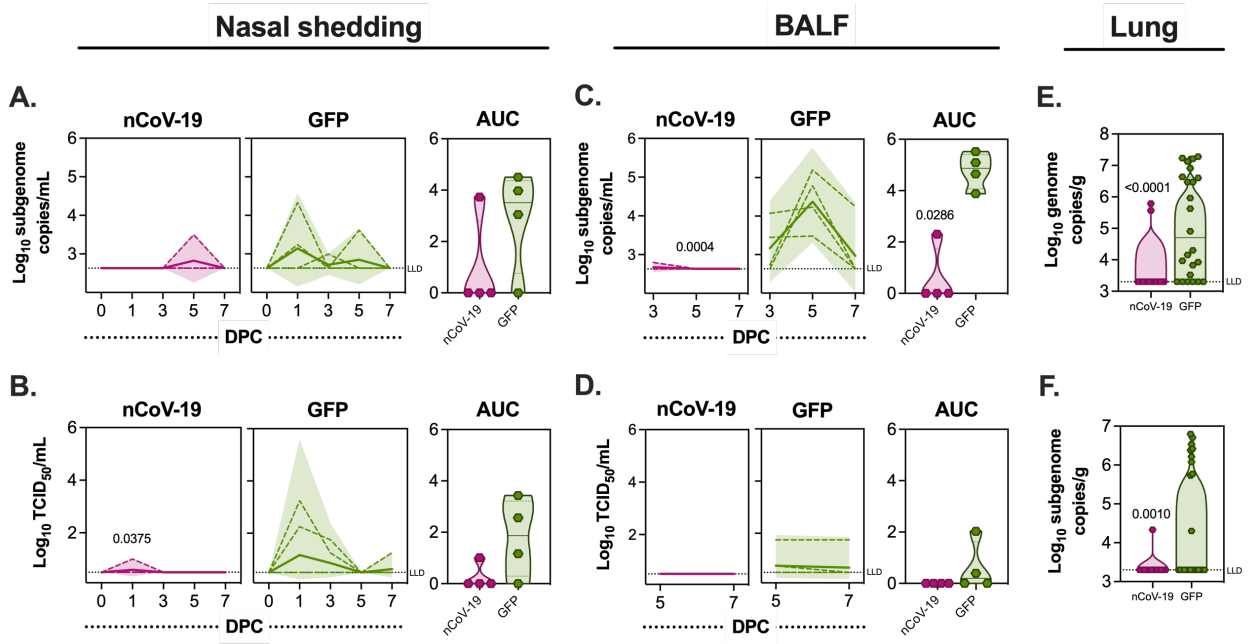


Figure 5-14. Detection of SARS-CoV-2 in respiratory tract samples post challenge. Viral load in nasal swabs and BALF by detection of **(A, C)** sgRNA (log_{10} copies per mL) by qRT-PCR and **(B, D)** infectious virus ($TCID_{50}$ per mL) by titration, respectively. In the line graphs for ChAdOx1 nCoV-19 (left) and ChAdOx1 GFP (middle), the dotted lines indicate individual animals, the solid line indicates the geometric mean, and the shaded region reflects the 95% confidence interval (statistical test: two-way ANOVA with Šídák's multiple comparisons test to compare mean viral loads at each timepoint in vaccinees versus controls). Area under the curve (AUC) was calculated as an indication of the total amount of virus shed in nasal swabs and BALF and displayed as a truncated violin plot (right) (statistical test: Mann-Whitney). Violin plots depicting the quantity of **(E)** gRNA and **(F)** sgRNA in lung tissue collected at 7 DPC reported as log_{10} copies per mL. Significant p-values (<0.05) are denoted in the figures, all other comparisons are not significant. Dotted lines indicate the LLD for each assay.

We subsequently sought to define the impact of the vaccine-specific humoral response on nasal shedding and viral load after challenge. The Spearman rank correlation coefficients computed for individual antibody-virology variable pairings were assessed (Figure 5-15A). Although the small group sizes precluded observations of statistical significance, some clear trends emerged. Whereas higher levels of serum (neutralising and Fc effector-function-inducing) antibodies and nasosorption antibodies correlated with reduced virus detection in nasal swabs, viral RNA in the BAL and lung tissue exclusively displayed strong negative correlations with BAL IgG and IgA titres. Of note, sgRNA levels generally appeared to correlate more strongly with antibody titres than gRNA levels. Although not conclusive due to the absence of sufficiently powered statistical comparisons, these findings may suggest a site-specific relationship between antibody titres and reductions in viral load in the upper versus lower respiratory tract.

Finally, drawing from our findings in the IM-immunised animals, which highlighted a level of concordance between B-cell phenotypes and virological outcomes, we performed similar staining of PBMC-derived B cells at 7 DPC in the IN vaccinees. Consistent with our previous observations, circulating B-cell responses were clearly differentiated between vaccinees and controls. The former exhibited evidence of the development of a mature, class-switched memory response whereas the latter demonstrated increased frequencies of early activation markers and IgM on most relevant B-cell subsets (Figure 5-15B&C)

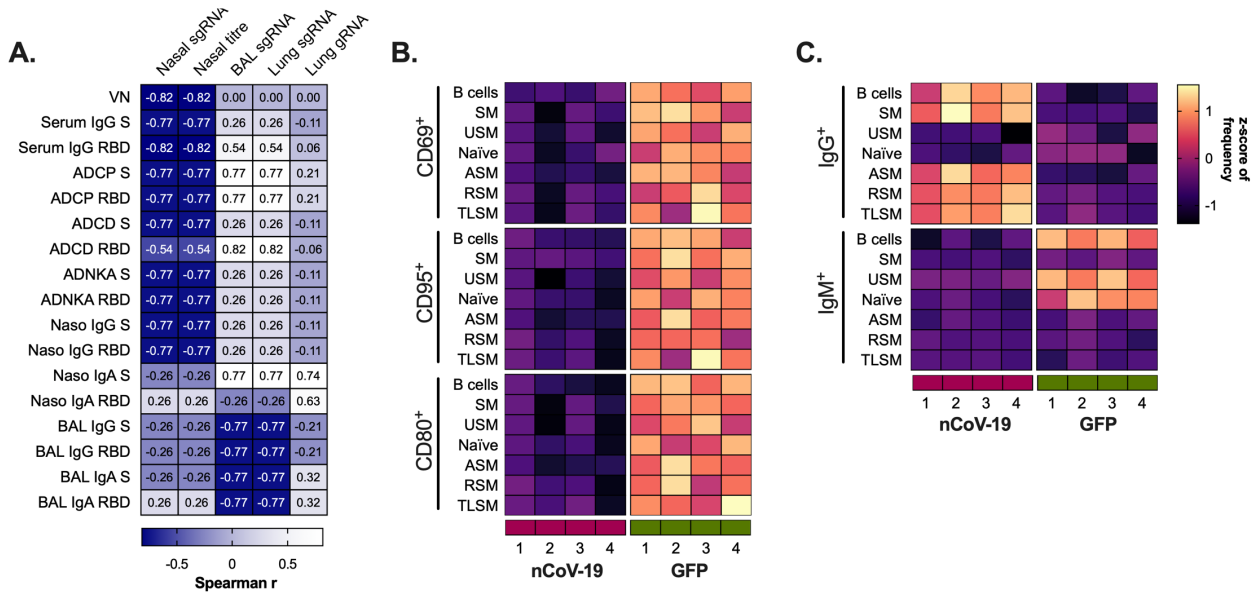


Figure 5-15. Characterising the relationship between the humoral response and outcomes post challenge. (A) Heatmap visualization of the correlations between antibody measures and viral RNA (AUC) titres for ChAdOx1 nCoV-19 vaccinees; r coefficients were generated by two-sided Spearman rank correlation tests. Heat maps depicting the z-scored frequencies comparing the relative size of circulating B-cell subsets expressing markers associated with **(B)** activation (CD69, CD95, CD80) and **(C)** the kinetics of the Ig response (IgG and IgM). Each heatmap square represents the data from a single animal.

5.3 Discussion

As is evident from substantial phase III efficacy data, ChAdOx1 nCoV-19 confers a significant degree of protection against COVID-19, particularly against hospitalisation and severe disease[117,118,338,339]. In 2020, some of the findings presented in this chapter provided the preclinical evidence required to progress the (then) candidate to assessment in phase I trials. Importantly, our results demonstrate that a two-dose regimen of IM or IN ChAdOx1 nCoV-19 provides near complete protection of the lower respiratory tract from SARS-CoV-2 infection, as evidenced by significant reductions in viral load in BALF and lung tissue. The vaccine also protects against clinical or histopathological signs of pneumonia[111,112]. As has been reported for other vaccines assessed in NHPs[348,350,496,497] and in epidemiological surveillance data[370,372], immunisation via the IM route does not eliminate upper respiratory tract shedding; in our study, viral RNA persistence in nasal swabs (between 1 and 7 DPC) was comparable between vaccinees and controls. However, our results indicate that vaccine delivery via the IN route may support a reduction in nasal shedding and therefore aid in the attenuation of transmission. Although, due to the underpowered nature of this study (n=4 per group), these differences in virus levels in nasal swabs largely did not meet statistical significance, apart from infectious virus titres on 1 DPC. But sgRNA and infectious virus were only detected in the nasal swabs of one vaccinee versus three controls, suggesting that in a larger study, a significant reduction in shedding might be observed. Indeed, additional studies performed in our lab, in hamsters, have demonstrated a significant reduction in viral RNA and infectious virus detected in oropharyngeal swabs from ChAdOx1 nCoV-19 IN-immunised hamsters compared to ChAdOx1 GFP controls following both (IN) inoculation with SARS-CoV-2 and in a direct-contact horizontal transmission setting[112].

Our immunogenicity assessments revealed that ChAdOx1 nCoV-19 induces robust levels of S- and RBD-specific serum IgG antibodies, particularly post boost. Memory B cells were detectable in circulation as well. IN vaccination additionally induced antigen-specific IgG and IgA responses in nasosorption samples and BALF. No nasosorption or BALF samples were collected pre-challenge in our IM study, but BALF collected at 3 and 5 DPC did not contain high titres of antigen-specific antibodies. SARS-CoV-2 specific neutralising and non-neutralising antibodies were detected in the sera of all IM and IN vaccinees post boost. Thus, IN delivery of the vaccine did not appear to result in diminished induction of systemic humoral responses. Similar observations have been noted in other studies involving IN vaccine administration in rodents[498].

Functional assessment of antibodies elicited by IM and IN vaccination revealed that S- and RBD-specific serum antibodies demonstrate the capacity to induce Fc-mediated effector functions, including cellular phagocytosis, complement deposition, and NK cell activation. These findings are consistent with those observed in the evaluation of ChAdOx1 nCoV-19 in clinical trials[362]. Although the importance of neutralising antibodies in protecting against SARS-CoV-2 infection has been convincingly demonstrated in rhesus macaques[81,82] and in humans[318], the importance of other effector functions remains more ambiguous. A selective delay or defect in IgG development has been linked to severe and fatal outcome in human patients[499]. A study in mice also demonstrated that *in vitro* neutralisation did not uniformly correlate with *in vivo* protection, and that binding to Fc receptors was of importance, suggesting that antibody effector functions play a pivotal role in protection against SARS-CoV-2[323]. Moreover, studies have demonstrated that the anti-SARS-CoV-2 efficacy of therapeutic monoclonal antibodies can be enhanced through modifications to the Fc region[500,501]. However, findings from another investigation suggest that antibodies capable of engaging Fcγ receptors decay more rapidly than those with neutralising

function, suggesting that they may have more limited protective benefits over time after immunisation[502].

In our study of IN-administered ChAdOx1 nCoV-19, we attempted to investigate the significance of antibody localisation for protection against SARS-CoV-2 infection. We found that the single vaccinee with detectable levels of virus in nasal swabs also exhibited low titres of IgG and IgA antibodies in nasosorption samples, coupled with low neutralising antibody and sera IgG titres, suggesting that a robust humoral response in the nasal mucosa and in circulation is necessary to efficiently control nasal shedding. Preliminary correlation analyses suggested that although both vaccine-induced circulating antibodies—with neutralising and non-neutralising functionality—and upper respiratory antibodies play a role in reducing nasal shedding, virus replication in the airway and lung tissue is primarily controlled by antibodies localised to the lower respiratory tract. However, given that low animal numbers prevented us from establishing correlations of statistical significance, further studies will be required to clearly define the relative impact of each component of the multifunctional humoral response on measures of protection.

In our study of IM-administered ChAdOx1 nCoV-19, post-challenge phenotypic characterisation of B cells and subsequent PC analysis revealed clear distinctions between vaccinees and controls at 7 DPC. While the B-cell subset of ChAdOx1 nCoV-19 vaccinees was characterised by significant frequencies of mature, class-switched memory IgG^+ B cells, control animals harboured higher frequencies of unswitched memory and naïve B cells expressing markers associated with early activation. Interestingly, the single IM vaccinee with detectable viral RNA in BALF at 3 DPC, also exhibited a B-cell phenotypic profile more closely resembling those of controls. This animal additionally displayed slightly elevated levels of inflammatory chemokines in BALF, unlike the five other vaccinees. Together, these results support the above claims regarding the

association between robust humoral responses and protection against the effects of SARS-CoV-2 infection.

Finally, our results demonstrate that although IM delivery of ChAdOx1 nCoV-19 does not completely prevent SARS-CoV-2 infection, vaccinees, unlike controls, are largely protected from inflammation and inflammatory cell infiltration within the lungs and airways, as evidenced by chemokine detection in BALF (at 3 and 5 DPC) and transcriptomic profiling of lung macrophages (at 7 DPC) by scRNAseq. These findings corroborated with our virological data suggesting that vaccination results in nearly full preclusion of virus replication in the lower respiratory tract.

There are several limitations of the work presented in this chapter. Again, animal numbers per group were low overall, but particularly in the IN study, which impaired our ability to clearly demonstrate the impacts of IN vaccination on upper respiratory tract shedding. Although we observed differences that were encouraging between IN-vaccinated and control animals, these were not significant. In addition, no IM-vaccinated group was included in this study, which would have facilitated direct comparison of the resultant shedding profiles between these two immunisation regimens. Finally, while not necessarily a limitation, a surprising result in both of our studies was the weak induction of S-specific cellular immune responses in vaccinees. Similar results have not been observed in ChAdOx1 nCoV-19-immunised humans[366,367,503,504]. Moreover, our findings are inconsistent with the findings from preclinical and clinical studies of other vaccines utilising the ChAdOx1 platform, which is typically a potent inducer of cellular immunity[114,115,505,506]. Additional experiments are underway, to elucidate factors contributing to this discrepancy.

In summary, the data presented here demonstrate the immunogenicity and efficacy of ChAdOx1 nCoV-19 following IM and IN delivery in the rhesus macaque model of SARS-CoV-2. In alignment with observations in humans, our results highlight the importance of the humoral response in immunity against SARS-CoV-2 and illustrate the protective effects of vaccination through reductions in viral load and inflammation in the lower respiratory tract. Lastly, the results in this chapter support the investigation of IN delivery of COVID-19 vaccines to attenuate virus transmission. The University of Oxford has conducted a phase I clinical trial to assess the safety and immunogenicity of different ChAdOx1 nCoV-19 IN vaccination regimens and dosing schemes in healthy adults (NCT04816019). Interestingly, this trial includes study groups of participants previously immunised against COVID-19 via the IM route, which will demonstrate the effect of introducing IN COVID-19 vaccines to populations with pre-existing systemic immunity against SARS-CoV-2.

6

Multi-omics evaluation of the age-related effects of SARS-CoV-2 infection in rhesus macaques

6.1 Introduction

In alignment with earlier studies, the findings presented in Chapter 5 demonstrate that SARS-CoV-2 infection of rhesus macaques results in largely mild, self-limiting disease[430,487]. Thus, although animals demonstrate a high degree of susceptibility to virus infection, they do not fully recapitulate the spectrum of COVID-19 disease observed in humans. As a follow-up investigation to the vaccine studies presented in Chapter 5, we attempted to identify conditions that would predispose rhesus macaques to develop a more severe disease phenotype. In doing so, we aimed to establish a NHP model of SARS-CoV-2 infection that could potentially be employed in future translational research, such as in the testing of prophylactics or therapeutics designed to mitigate the more adverse clinical features of COVID-19. In humans, increased rates of severe and fatal COVID-19 have been reported in individuals aged >65 years, males, and those with comorbidities, including hypertension, type II diabetes, cardiovascular disease, obesity, lung disease, and renal disease[507,508]. As such, age is a purported risk factor for worse COVID-19 prognosis. Predicting that a similar relationship would be observed in rhesus macaques, we set out to characterise the

differences in SARS-CoV-2 pathogenesis between older and younger animals, with a particular focus on immune responses to infection.

Aging results in numerous changes to cells and mediators of the immune system, which alter susceptibility to infection, disease progression, and clinical outcomes. Defining features of this process, termed immunosenescence, include cytokine dysregulation, an accumulation of senescent cells leading to chronic inflammation, a loss of naïve T and B cells, and defective responses by innate immune subsets[508,509]. The role of age-associated changes in the immune landscape to increased disease and tissue damage has been described for other viral respiratory pathogens, including influenza A virus and RSV[510-512]. These studies point to changes in the immune system and its interaction with the local cellular environment (e.g., the respiratory epithelium) in the breakdown of barriers against and protective responses to infectious agents. Ultimately, the confluence of these events may result in greater accrual of tissue damage, sustained local inflammation, severe clinical disease, and subpar induction of immune effector and memory responses.

The effects of age on disease outcome after SARS-CoV-2 infection has been explored in NHP species[431,513-517]. Several studies have been performed in aged rhesus macaques, but results have been inconsistent. An early study reported sustained virus replication in swabs (nasopharyngeal and anal) and higher viral load in lung tissue of older versus younger animals, accompanied by more severe interstitial pneumonia[518]. Conversely, a subsequent study detected higher viral loads in swabs (nasal, throat, and rectal) and tracheal brushes of younger animals, along with a higher degree of infiltration-induced lung damage within seven days post inoculation[515]. However, by 14 days post inoculation, these younger animals demonstrated more rapid resolution of clinical disease and tissue damage, whereas the older animals developed signs of elevated pro-

inflammatory signalling, suggestive of an age-related, inflammation-driven delay in disease progression. Contrasting results were obtained in a more recent study, which reported no significant differences in virus replication or cellular immune responses in aged versus juvenile rhesus macaques[513]. Finally, transcriptional profiling of macaque lungs 14 days after SARS-CoV-2 infection revealed stronger induction of genes associated with type-I-interferon and Notch signalling in younger animals, suggestive of the differential regulation of these pathways by age-associated factors[516].

The limited number of studies performed, and low animal numbers, have precluded the identification of clear age-related impacts on clinical, virological, and immunological outcomes of infection in this model. Furthermore, these studies have largely not addressed the relative roles of dysregulated immune responses versus virus-induced damage in driving differences in outcomes related to age. Finally, a potential link between underlying, age-associated immunological changes and subclinical effects of infection has not yet been described in detail.

In this study, to further characterise the relationship between age and host immune responses to SARS-CoV-2 infection, we conducted a time-resolved evaluation of disease in age-stratified cohorts of rhesus macaques. We performed extensive local and systemic sampling throughout the course of disease through swabbing and collection of blood, tissue, and BALF. Doing so facilitated the detection of immune-related differences, using single-cell and bulk approaches, at the site of infection during critical stages of disease progression: the acute phase, the post-acute phase, and the transition point between the two. Age-related divergences in inflammation, immune regulation, and adaptive immunity appeared several days after inoculation and were exacerbated over time. The research presented in this chapter represents an in-depth kinetic evaluation of the interaction between infection and the aging immune system in a NHP model.

6.1.1 Authorship statement

The study featured in this chapter was designed by Dr. Emmie de Wit, me, and Dr. Emily Speranza; however, significant contributions from many colleagues were required for the completion of this work. Dr. Emmie de Wit was listed as the Principal Investigator on the corresponding Animal Study Protocol. Please see the overall Statement of Authorship (page xviii) for a general summary of procedures conducted by colleagues. Data generated by others will be referenced in the corresponding figures throughout this chapter. The findings presented in the chapter have been compiled in a manuscript that has been submitted for publication on which I am co-first author[519].

6.2 Results

6.2.1 Baseline characterisation of rhesus macaque cohorts

We employed a multi-omics approach to profile local and systemic immune responses to SARS-CoV-2 infection in older and younger rhesus macaques (Figure 6-1). Animals were inoculated with $2.6x10^6$ $TCID_{50}$ of SARS-CoV-2 and clinical, virological, and immunological parameters were monitored over time using multiple modes of assessment on various sample types. Four animals from each age group were euthanized at 7 and 21 DPI to perform tissue-specific analyses during the acute and post-acute stages of infection (Figure 6-1).

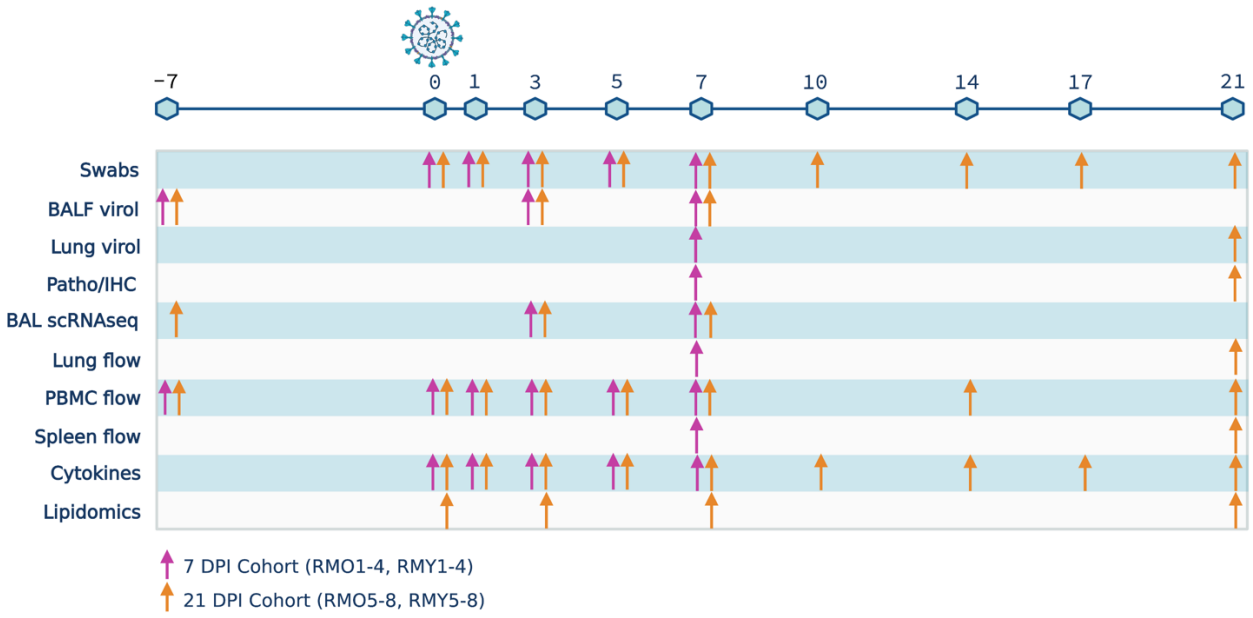


Figure 6-1. SARS-CoV-2 inoculation and time-resolved sampling in older and younger rhesus macaques. Older and younger rhesus macaques (n=8 per group) were inoculated with SARS-CoV-2 via (combined) IN, IT, and ocular routes. Four animals from each age cohort were euthanized at 7 (group 1) and 21 (group 2) DPI. Clinical exams were performed on 0, 1, 3, 5, 7, 10, 14, 17 and 21 DPI. Exams included measurement of weight, temperature, and respiration rate, as well as ventro-dorsal and lateral chest radiographs. Nasal and throat swabs were collected during all exams for viral RNA detection. BAL was performed at -7, 3, and 7 DPI for viral RNA detection and scRNAseq. PBMCs were isolated at -7, 1, 3, 5, 7, 14, and 21 DPI for immunophenotypic analysis by flow cytometry. Sera was collected at -7, 1, 3, 5, 7, 10, 14, 17, and 21 DPI for cytokine detection and lipidomics assessment. Lung tissue was harvested during both necropsies for viral RNA detection, multiplex immunohistochemistry (mIHC), and flow cytometry. Splenocytes were obtained at 7 and 21 DPI for ICS and flow cytometry. The coloured arrows indicate sampling for a subset of animals from each age cohort: animals necropsied at 7 DPI (pink) or 21 DPI (orange). Animals are identified as older (RMO) or younger (RMY) and belonging to the 7 DPI (1-4) or 21 DPI (5-8) necropsy group.

The mean ages of the older and younger animals were 18 and 3.37 years, respectively (Figure 6-2A). According to the estimated life span of rhesus macaques, the older animals were deemed moderately aged, while the younger animals were described as “subadult” (a stage preceding sexual maturity). The older animals were also classified as overweight, according to weight and body condition scores (Figure 6-2A). We additionally characterised the baseline circulating lipid content in these animals, because lipid mediators are important immune regulators that have been shown to influence COVID-19 severity in humans[448]. Liquid chromatography with tandem mass spectrometry (LC-MS/MS) and measurement of ~1200 lipid species across major classes was

carried out by Dr. Benjamin Schwarz. Upon comparison of the summation of signals from each lipid class, we noted that the older animals displayed elevated levels of neutral (p=0.0286), phospho- (p=0.0286), and lyso-phospho- (p=0.0286) lipids (Mann-Whitney tests) (Figure 6-2B). However, we did not detect substantial differences in sphingolipid, cholesterol-ester, or free fatty acid levels, which are primary markers of circulating lipid disruption in obese NHPs[26]. This lipidomic signature suggests that the older animals in this study exhibited some level of metabolic disruption but did not meet the criteria for obesity.

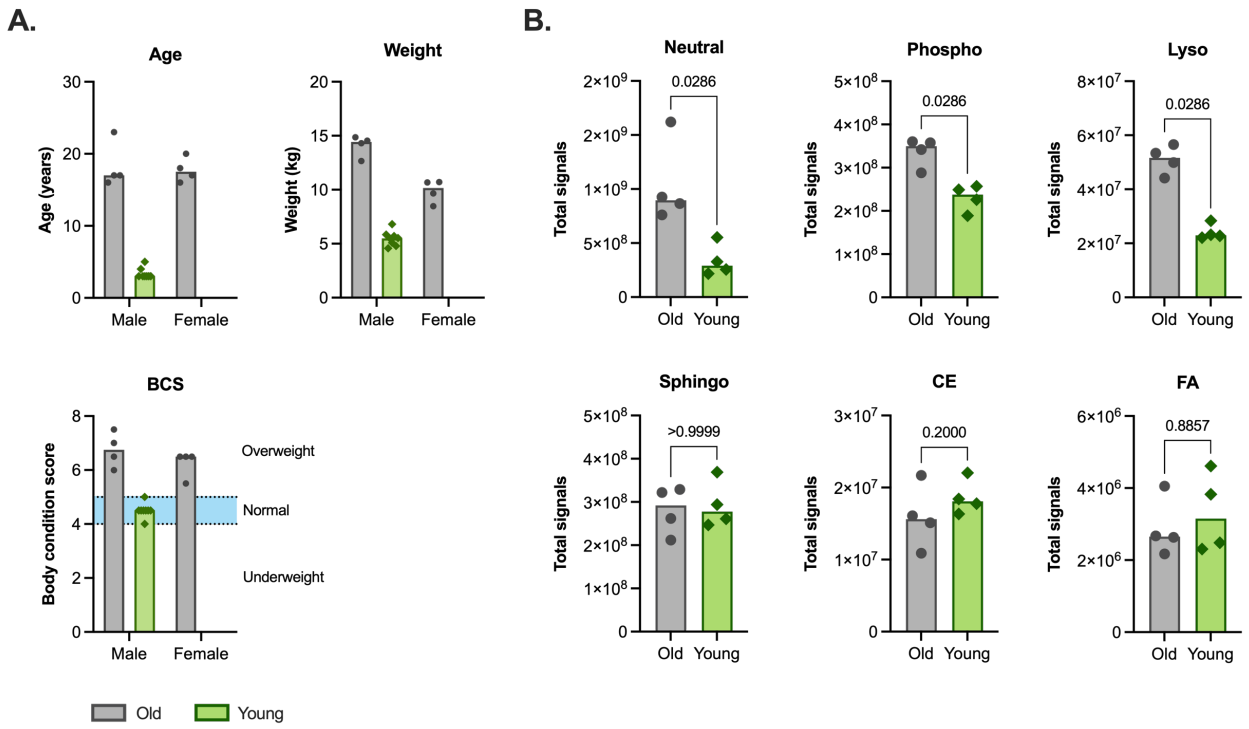


Figure 6-2. Baseline assessment of older and younger rhesus macaques. (A) Summary of age, weight, and body condition score (BCS) of the older and younger cohorts divided by sex. Underweight (1-3), normal (4-5), and overweight (6-9) BCS ranges are indicated on the relevant graph. **(B)** Relative signal strength of major lipid classes detected in serum samples: neutral lipids (neutral), phospholipids (phospho), lyso-phospholipids (lyso), sphingolipids (sphingo), cholesterol-esters (CE), and free fatty acids (FA) (statistical test: Mann-Whitney). All bars depict group medians. P-values are denoted in the lipid mediator figures, $p<0.05$ was considered significant.

Altered immune states in older individuals may include the development of a chronic inflammatory phenotype (also known as "inflammaging"), characterised by a persistent elevation of levels of pro-inflammatory cytokines[520]. Consistent with this phenotype, the older animals exhibited increased serum concentrations of IL-6 (p=0.0256) and to some extent MCP-1 (p=0.2786) at baseline in comparison to the younger animals (Mann-Whitney tests) (Figure 6-3A). However, salient elevations in the concentrations of other cytokines associated with chronic inflammation, like TNFα (p=0.6987) and IL-1RA (p=0.8785), were not detected[521-523]. Although the effect was not significant, IL-5 (p=0.1239) and IL-8 (p=0.0650) were detected at lower concentrations in the older animals compared to the younger, which may have reflected a diminished capacity for regulating the function or trafficking of eosinophils and neutrophils (Figure 6-3A)[524].

Declining adaptive immunity is another hallmark of immunosenescence. A reduction in thymic and bone marrow functions contributes to a loss of naïve T and B cells and the accumulation of terminally differentiated effector cells[525-528]. In alignment with this trend, the older animals exhibited lower frequencies of circulating naïve ($CD28^{+}CD95^{lo}$) $CD4^{+}$ (p=0.0006) and $CD8^{+}$ (p= 0.0002) T cells, as well as naïve (IgD^{+} $CD27^{-}$ $CD21^{+}$) (p=0.0047) and total (p=0.0148) $CD20^{+}$ B cells (Mann-Whitney tests) (Figure 6-3B&C). Corresponding elevated frequencies of effector/effector memory ($CD28^{-}$ $CD95^{+}$, T_{EEM}) $CD4^{+}$ (p=0.0148) and $CD8^{+}$ (p=0.0011) T cells, along with plasma cells ($CD20^{-}$ $CD38^{+}$ $CD138^{+}$, p=0.0047) were also observed in the older animals. In summary, the collective results from our baseline assessments revealed age-related differences in body condition, lipid metabolism, cytokine regulation, and adaptive immunity with the potential to impact responses to infection.

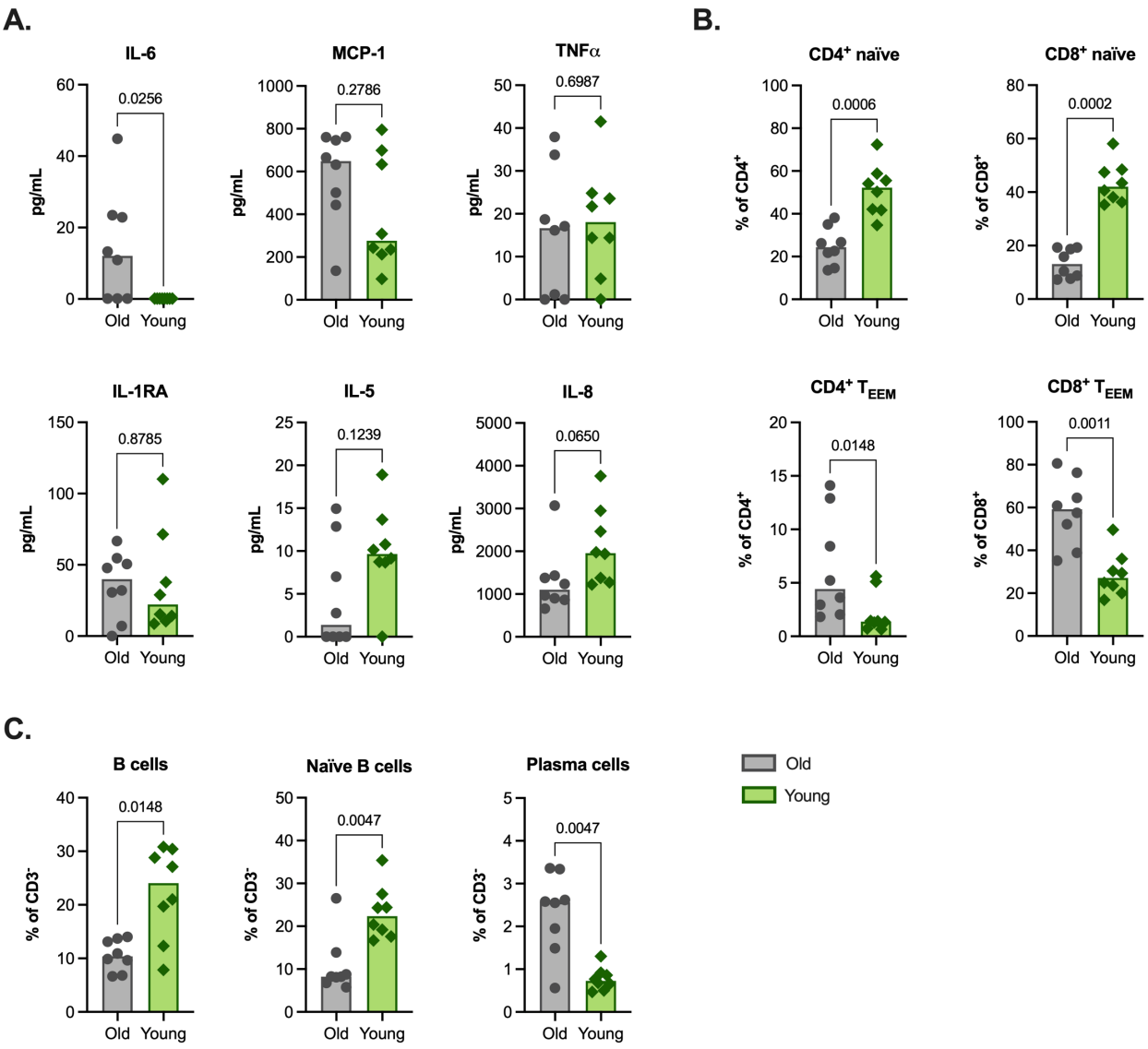


Figure 6-3. Comparison of baseline immunological parameters in older and younger rhesus macaques. Serum and PBMC samples were collected pre-inoculation (-7 DPI). **(A)** Serum concentrations (pg/mL) of selected cytokines (statistical test: Mann-Whitney). **(B)** Frequencies of $CD4^+$ and $CD8^+$ T cells with a naïve ($CD28^+$ $CD95^{lo}$) or effector/effector memory (T_{EEM}, $CD28^-$ $CD95^+$) phenotype (statistical test: Mann-Whitney). **(C)** Frequencies of total B cells ($CD20^+$), naïve B cells (IgD^+ $CD27^-$ $CD21^+$), and plasma cells ($CD20^-$ $CD38^+$ $CD138^+$) as a percentage of $CD3^-$ lymphocytes (statistical test: Mann-Whitney). All bars depict group medians. All p-values are denoted on the graphs, $p<0.05$ was considered significant.

6.2.2 Clinical and virological outcomes after SARS-CoV-2 infection

To assess differences in the progression of SARS-CoV-2 infection, we conducted standardised clinical scoring, scoring of pulmonary infiltrates on radiographs, and viral RNA measurements in respiratory tract samples. Clinical exams were performed by RMVB, and radiographs were scored by Dr. Atsushi Okumura. The older animals displayed slightly elevated clinical scores over the course of infection (AUC±SEM =150.2 ± 16.85) compared to the younger animals (AUC±SEM = 75.25 ± 9.45) (Figure 6-4A). By 21 DPI, 3 out of 4 younger animals had fully recovered, while mild clinical signs could still be observed in all older animals (p=0.0001, AUC comparison by unpaired t-test). Increased pulmonary infiltrates were observed in radiographs of the older cohort (AUC±SEM =19.88 ± 6.3) compared to the younger cohort (AUC±SEM = 7.00 ± 2.53) (p=0.0633, AUC comparison by unpaired t-test) (Figure 6-4B). However, infiltrates were no longer detected in either cohort by 10 DPI, indicating that respiratory disease was restricted to between 1-7 DPI.

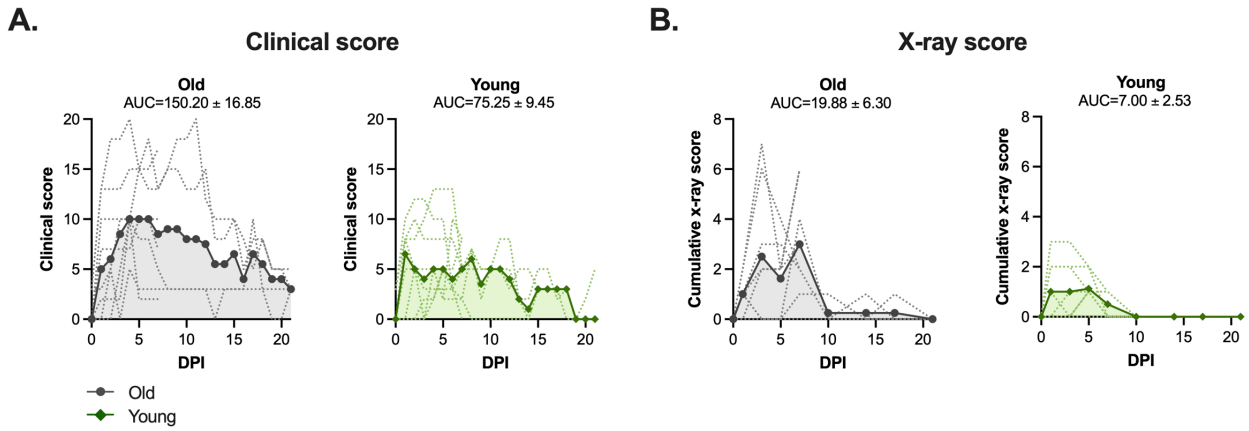


Figure 6-4. Comparison of clinical outcomes after SARS-CoV-2 inoculation. (A) Comparison of clinical scores over the course of infection for older (left) and younger (right) animals. Data from individual animals are indicated by dashed lines, group means are shown using solid lines, and the mean area under the curve (AUC) is represented by shading. **(B)** Cumulative x-ray scores from ventro-dorsal and lateral chest radiographs to detect pulmonary infiltrates graphed in the same format as in A. AUC ± standard error of the mean (SEM) is denoted on all graphs and were compared between the older and younger cohorts (statistical test: unpaired t-tests). All p-values are listed in the main text, $p<0.05$ was considered significant.

Virus replication in the upper and lower respiratory tract was assessed using nose swabs, throat swabs, BALF, and lung tissue. Viral loads were quantified using qRT-PCR for the detection of gRNA and sgRNA as a measure of recent virus replication. RNA extraction and qRT-PCR assays were performed by Dr. Manmeet Singh and Lizzette Pérez-Pérez. The older and younger animals demonstrated similar upper respiratory tract shedding profiles, as evidenced by gRNA and sgRNA levels in nose (gRNA p=0.1067, sgRNA p=0.5516) and throat (gRNA p=0.3238, sgRNA p=0.1987) swabs (AUC comparisons by unpaired t-tests) (Figure 6-5A&B). In the lower respiratory tract, levels of gRNA (old p=0.0054, young p<0.0001) and sgRNA (old p=0.0075, young p=0.0006) dropped substantially in BALF between 3 and 7 DPI, indicative of rapid clearance of the virus (paired t-tests) (Figure 6-5C). The rate of viral gRNA clearance was relatively consistent between the younger animals (mean±SD of change = -1.6±0.3), whereas substantial variability was observed within the older cohort, as evidenced by high variance in the mean change in viral load (mean±SD of change = -1.3±1.13). Meanwhile, levels of sgRNA in BALF between 3 and 7 DPI revealed similar control of virus replication, regardless of age (Figure 6-5C). Likewise, although comparison of gRNA in lung tissue at 7 DPI suggested that the younger animals cleared the virus material (p=0.1545) slightly more efficiently, levels of sgRNA did not differ between age cohorts (p=0.8472) (Mann-Whitney tests) (Figure 6-5D).

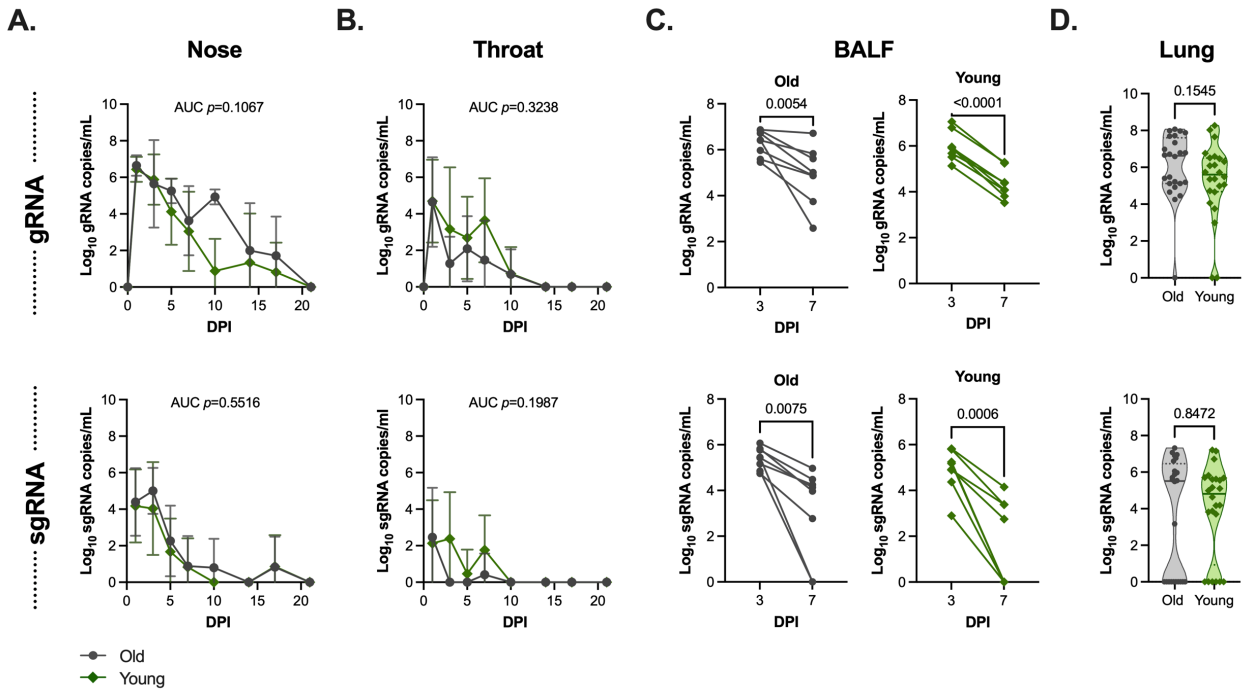


Figure 6-5. Comparison of shedding and viral load dynamics after SARS-CoV-2 inoculation. gRNA (top) and sgRNA (bottom) detected in **(A)** nasal swabs and **(B)** throat swabs expressed as log_{10} copies/mL. Data points and error bars indicate group means and standard deviation (SD). AUC analysis was performed to compare the shedding profiles between age cohorts (statistical test: unpaired t-test). **(C)** Viral RNA quantification in BALF collected at 3 and 7 DPI from the older (left) and younger (right) animals. Matched values between timepoints for each individual animal are indicated by a connecting line. Log_{10} copies/mL of gRNA (top) and sgRNA (bottom) are shown (statistical test: paired t-test). **(D)** Lung tissue viral load at 7 DPI based on the detection of gRNA (top) and sgRNA (bottom), expressed as log_{10} copies/mL. Six lung lobe sections were analysed per animal; each data point represents a single section. Violin plots depict the group median and interquartile range (statistical test: Mann-Whitney). All p-values are denoted on the graphs, $p<0.05$ was considered significant.

6.2.3 Local immune dynamics during acute SARS-CoV-2 infection

In the absence of major differences in the clinical course of disease, we pivoted our focus to explore the age-related variation in immune responses to SARS-CoV-2 infection. We performed scRNAseq in BALF (n=4 animals per age group at -7 DPI, n=8 animals per age group at 3, and 7 DPI). BALF sample processing, sequencing, and raw data normalisation were completed by the RML RTB Genomics Core Facility. Dr. Emily Speranza led the analysis of the scRNAseq data with assistance from me. All major cell types were identified in BALF using a computational

identification algorithm and we calculated the changes in cell frequencies over time[445] (Figure 6-6A, Figure A.6.2). Some general trends were noted across animals. We observed a reduction in the frequencies of macrophage/monocytes at 3 and 7 DPI, which appeared to reflect concurrent increases in the frequencies of other immune cell types, especially T cells (Figure 6-6B). Significant age-related differences in cell frequencies emerged at 7 DPI. Higher percentages of epithelial populations, specifically ciliated cells (p=0.0007) and pneumocytes (p=0.0272), were present in the BALF of the older animals (mixed-effects analysis with Šídák's multiple comparisons test). This effect may have resulted from the increased sloughing-off of lung cells during the lavage procedure in the older animals after infection. Meanwhile, elevated frequencies of BALF T cells were detected in the younger animals compared to the older animals at 7 DPI (p=0.0128), either due to enhanced expansion of local populations or systemic recruitment (mixed-effects analysis with Šídák's multiple comparisons test) (Figure 6-6B).

To evaluate changes in the transcriptional states of specific immune cell subsets, we applied a clustering bias method to identify cell types (or sub-clusters) demonstrating strong transcriptional shifts after SARS-CoV-2 inoculation (Figure A.6.2). We subsequently selected the two cell types demonstrating the strongest transcriptional shifts post inoculation, macrophages and dividing cells, for further assessment. An analysis of gene modules was performed to identify drivers of the observed transcriptional differences, starting in the macrophages. Macrophage gene expression was averaged for each timepoint (-7, 3, and 7 DPI) and clustered using 1000 iterations of k-means clustering into 10 distinct gene modules (Figure 6-6C). From these results, gene module 3 showed the strongest increase in expression after infection relative to baseline levels. This module comprised a subset of type I interferon-responsive genes, which are upregulated during the early inflammatory response to viral infection, such as *ISG15*, *IFIT2*, and *IRF7* (Figure 6-6C). Individual

gene module scores for the cells derived from the older versus younger animals were calculated to compare median expression (Figure 6-6D). Differences in expression were minimal pre-infection (p=0.2, estimated from 10000 iterations). However, by 3 DPI gene module 3 was expressed at significantly higher levels in the macrophages of the older animals than in that of the younger animals (p<0.0001, estimated from 10000 iterations), and this elevation persisted to 7 DPI (p<0.0001, estimated from 1000 iterations) (Figure 6-6D).

To determine if this finding in the older animals was a cell type-specific phenomenon or a consequence of generalised inflammation in the lower respiratory tract, we compared gene module 3 scores between the age cohorts in all BALF cell types (Figure 6-6E). Doing so revealed the presence of indiscriminate and sustained inflammation in the lungs of the older animals, as expression was upregulated across immune and non-immune cells at 3 DPI and persisted on immune cells at 7 DPI. The younger animals exhibited similar upregulation of this gene set across immune cells at 3 DPI, but not across non-immune cells. Moreover, nearly all cell types in the younger animals had returned to baseline levels of expression by 7 DPI, suggestive of more efficient regulation of inflammatory responses at the site of infection (Figure 6-6E).

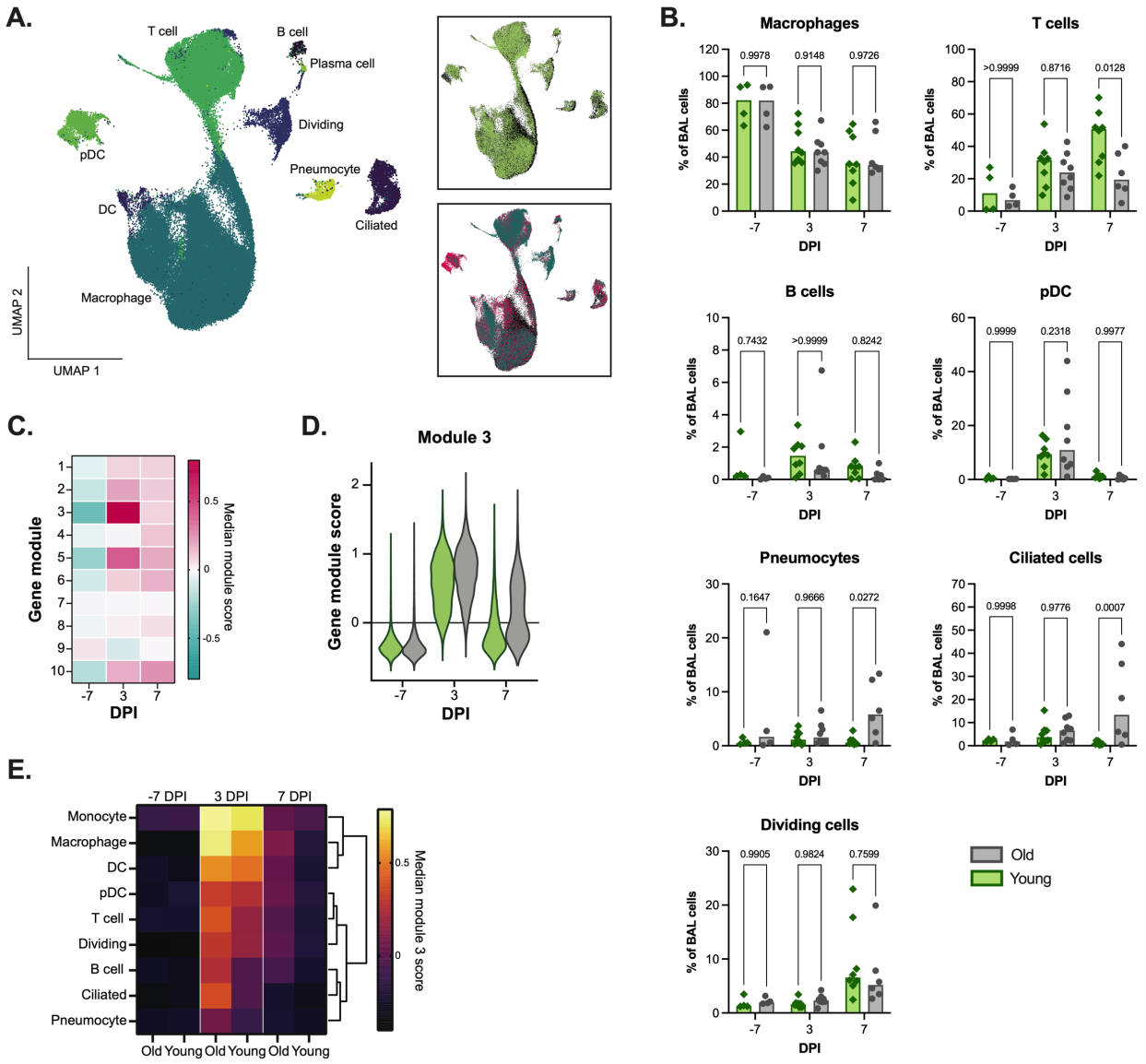


Figure 6-6. Single-cell RNA sequencing of BALF shows evidence of sustained inflammation associated with age. **(A)** Uniform manifold approximation projection (UMAP) depiction of the cell types detected in BALF by single-cell RNA sequencing (left). UMAP overlays of the total cells from each age cohort (top right, green= young, grey= old) and cells from each timepoint (bottom right, grey= -7 DPI, pink= 3 DPI, blue= 7 DPI) are also shown. **(B)** Comparison of the frequencies of major cell types (as a percentage of total BALF cells) between the older and younger animals at each timepoint. Bars represent median values (statistical test: mixed-effects analysis, Šídák's multiple comparisons). All p-values are denoted on graphs; $p<0.05$ was considered significant. **(C)** Heatmap illustration of the median macrophage gene module scores, across all animals, for 10 computationally determined gene modules at -7, 3, and 7 DPI. **(D)** Violin plots comparing the expression of gene module 3 in the macrophages of the older versus younger animals. **(E)** Heatmap comparison of the median expression score of gene module 3 in different cell types between the older and younger animals. The heatmap dendrogram indicates clustering based on Euclidian distance.

Next, we analysed the transcriptional changes occurring in BALF dividing cells, the second cell type identified in the clustering bias analysis described above. The dividing cell cluster was defined as containing more than 98% of cells in either the S or G2M phase of cell division. Subtyping of the dividing cells revealed predominantly T cells and macrophages/monocytes (Figure 6-7A). Six unique dividing cell sub-clusters were identified and included $CD8^+$ T cells (cluster 0), $CD4^+$ T cells (clusters 2 and 3), macrophages with a tissue-resident phenotype (cluster 1), macrophages with a monocyte-like or non-tissue-resident phenotype (cluster 4), and plasma cells (cluster 5). In general, cell dynamics revealed a decrease in macrophage frequencies and an increase in T-cell frequencies over time in the dividing cluster (Figure 6-7B).

Differentiating the changes occurring within the dividing cell subsets of the two age cohorts revealed slightly higher frequencies of dividing macrophages in the older animals at baseline (cluster 1, p=0.0435, two-way ANOVA with Šídák's multiple comparisons tests) (Figure 6-7C). At 7 DPI, a moderate increase in monocyte-like cells or non-tissue-resident macrophages was observed in the older animals (cluster 4, p=0.0655), which is consistent with previous data (Figure 6-6E) suggesting prolonged inflammation in the lungs of the older cohort. Meanwhile, an increase in the frequency of dividing $CD8^+$ T cells was selectively detected in the younger animals at this time (cluster 0, p=0.0138, two-way ANOVA with Šídák's multiple comparisons tests) (Figure 6-7C, Figure A.6.3). Together, these results suggest that in addition to achieving better control over inflammation, the younger animals may also exhibit more efficient local induction or systemic recruitment of T cells than the older animals.

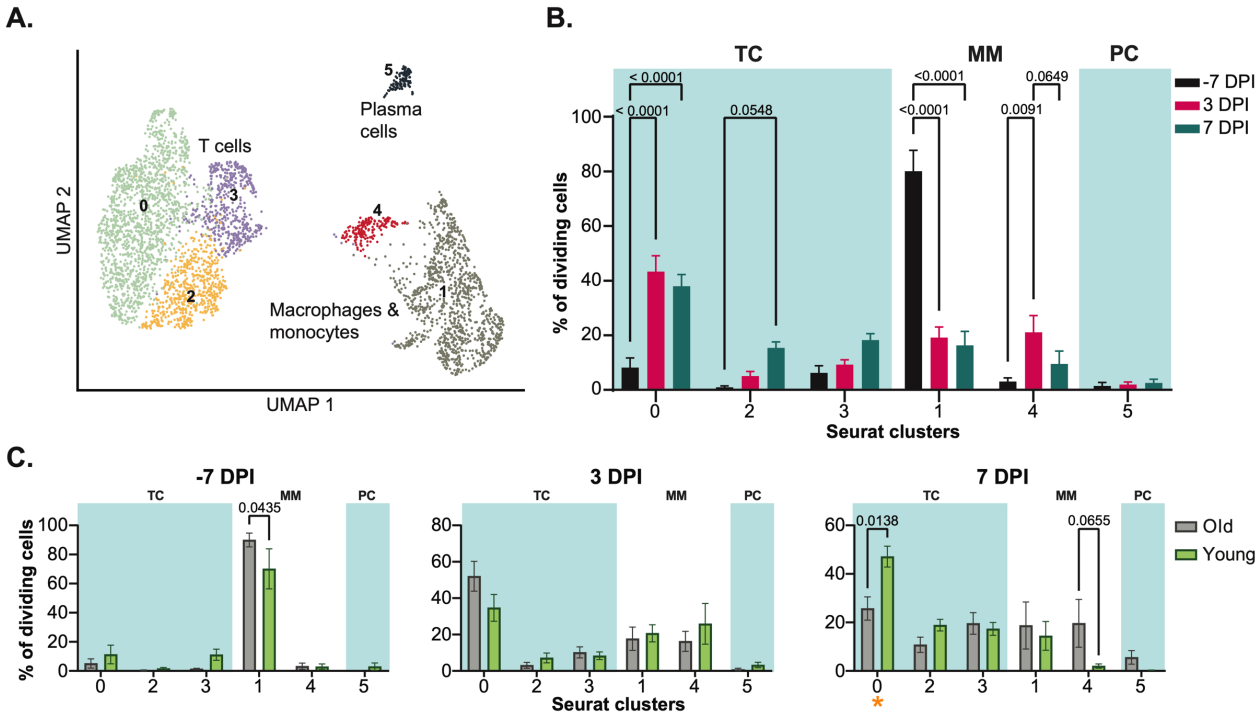


Figure 6-7. Elevated frequencies of dividing T cells in BALF of the younger animals compared to the older animals. (A) UMAP projection of dividing cells. Seurat clusters (0-5) are numbered, represented in different colours, and labelled to reflect cell type: T cells (TC, clusters 0, 2, and 3), macrophages/monocytes (MM, clusters 1 and 4), and plasma cells (PC, cluster 5). **(B)** Frequencies of Seurat clusters (as a percentage of dividing cells) at -7 (black), 3 (pink) and 7 DPI (teal). Bars represent mean frequencies and SEM; only p-values <0.1 are depicted on the graph (statistical test: mixed-effects analysis, Šídák's multiple comparisons). Significance was limited to $p<0.05$. **(C)** Frequencies of cells from each Seurat cluster derived from the older and younger animals at -7 (left), 3 (middle) and 7 (right) DPI (as a percentage of dividing cells). Asterisk indicates a dividing $CD8^+$ T-cell cluster present at elevated frequencies in the younger cohort. Bars represent mean frequencies and SEM; only p-values <0.1 are depicted on the graph (statistical test: two-way ANOVA with Šídák's multiple comparisons tests). Significance was limited to $p<0.05$.

6.2.4 Phenotypic analysis of lung T cells at 7 DPI

To determine if there were indeed more robust T-cell responses in the younger animals as suggested by the scRNAseq data, we used flow cytometry to profile the phenotypes of T cells isolated from lung tissue at 7 DPI. Consistent with the scRNAseq results, at 7 DPI, the younger animals exhibited higher frequencies of total ($CD3^+$) T cells in comparison to the older animals (p=0.0286), although this effect could not be completely attributed to differences in $CD4^+$ or $CD8^+$ T cells between the groups (p=0.2000 for both) (Mann-Whitney tests) (Figure 6-

8A). To capture subtle age-related trends in T-cell phenotypes, we adopted a previously described approach for unbiased clustering and classification of phenotypic patterns[529]. This method involved the concatenation of data from a random subset of $CD3^+$ T cells across animals and application of the FlowSOM algorithm to identify 15 phenotypically distinct meta-clusters based on the inclusion of 15 markers[530,531]. These clusters were visualized by t-distributed stochastic neighbour embedding (t-SNE) (Figure 6-8B). The composition of each cluster, according to the frequency of cells derived from each age cohort, was defined (Figure 6-8B).

To differentiate phenotypes, we selected clusters in which at least 60% of cells were derived from either older or younger animals and distinguished these as demonstrating cohort-specific enrichment. Application of this threshold yielded five clusters enriched in cells from the older animals (clusters 1, 5, 9, 13, and 15) and six clusters enriched in cells from the younger animals (clusters 2, 3, 7, 8, 10, and 11). Four clusters were categorised as not notably enriched for the cells of either cohort (clusters 4, 6, 12, and 14) (Figure 6-8C). Statistical comparisons of the relative median frequencies of cells composing each cluster from the older versus younger animals were performed, although none of the differences met statistical significance (Mann-Whitney tests) (Figure 6-8C). Nevertheless, we continued forwards with our evaluation of cluster phenotypes as an initial strategy for distinguishing potential age-related trends.

To this end, the major T-cell subset classifying each cluster was delineated according to the relative frequency of $CD4^+$ ($CD4^+$ $CD8^-$), $CD8^+$ ($CD4^-$ $CD8^+$), double negative (DN, $CD4^-$ $CD8^-$), and double positive (DP, $CD4^+$ $CD8^+$) T cells (Figure 6-8D). Older cohort clusters were composed primarily of $CD4^+$ T cells (clusters 1, 5, 9, and 13) and DP T cells (cluster 15). Meanwhile, clusters ascribed to the younger cohort consisted of $CD8^+$ (clusters 2, 7, and 10), DN (clusters 8 and 11) and DP (cluster 3) T cells (Figure 6-8D). To conduct an unbiased assessment of clusters ascribed

to the older versus younger cohorts, the median fluorescence intensities (MFI) of 15 phenotypic markers were determined within each cluster and z-scores were calculated to compare relative fluorescence intensity across clusters, as previously described[529] (Figure 6-8D). One clear trend differentiating the clusters attributed to each age cohort, was the relative increased fluorescence intensity of markers associated with proliferation (Ki67), antigen experience (CD95), and effector function or inflammatory homing (CD49d, and to some extent CXCR3) on the clusters enriched for younger animals' T cells. We also noted differences in activation profiles, with CD69 and HLA-DR exhibiting higher MFI z-scores on clusters ascribed to the older animals (Figure 6-8D).

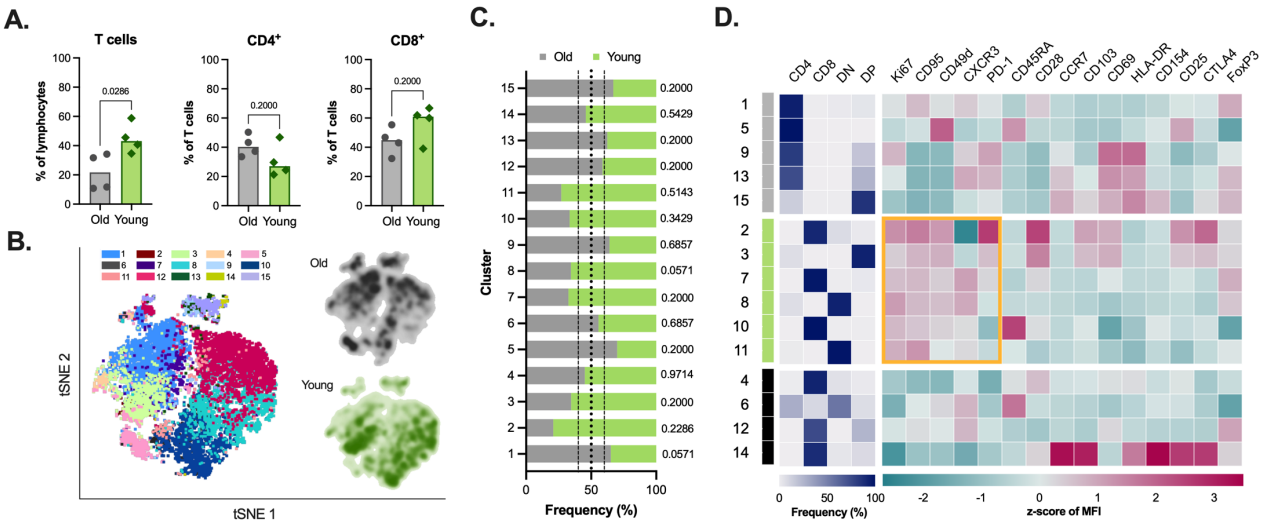


Figure 6-8. Age-related divergence in T-cell phenotypes in the lungs at 7 DPI. (A) Frequencies of $CD3^+$ T cells as a percentage of lymphocytes; frequencies of $CD4^+$ and $CD8^+$ T cells as percentages of $CD3^+$ T cells. Bars depict median frequencies (statistical test: Mann-Whitney). P-values are denoted on the graphs, $p<0.05$ was considered significant. **(B)** Visualization of concatenated $CD3^+$ T-cell subset across animals by t-SNE analysis. Stacked density plots (right) show the distribution of T cells derived from each age cohort. Dot plot depicts colour coded FlowSOM meta-clusters overlayed onto total combined T cells (left). **(C)** Stacked bar chart depicting the cumulative proportion of cells from animals of the older and younger cohort comprising each FlowSOM meta-cluster (1-15). Vertical dotted lines (from left to right) represent the (1) threshold of 10% for enrichment of cells from younger animals, (2) equal composition, and (3) the threshold for enrichment of cells from older animals. P-values comparing the median frequency of cells per animal within each cohort are listed to the right of the stacked-bars for each cluster (statistical test: Mann-Whitney). **(D)** Heat map representation of meta-cluster phenotypes. The clusters enriched for the cells of the older (grey), younger (green), and neither (black) are indicated (leftmost column). The major T-cell subset characterizing each cluster is shown by depicting the frequencies of $CD4^+$, $CD8^+$, DN, and DP T cells composing each cluster (central heat map). Cluster phenotypes were compared by calculation of the z-score of the MFI of the listed markers across all 15 clusters (rightmost heat map). Markers of interest on clusters enriched for cells from the younger animals are outlined in golden-yellow.

Next, we sought to confirm that the trends initially identified from the clustering analysis were representative of broader age-specific differences across major T-cell subsets (rather than a clustering artifact). We were specifically interested in the markers of antigen-experience, proliferation, and effector function that exhibited higher MFI z-scores on clusters enriched in younger animals' cells. So, we directly compared the fluorescence intensities of these markers on total $CD4^+$ and $CD8^+$ T cells aggregated across all animals within each age cohort, using a specialized software, ViolinBox, to generate fluorescence intensity values at the individual cell level[457]. The medians of the fluorescence intensities of CD95, CD49d, Ki67, and CXCR3 were significantly greater on the $CD4^+$ and $CD8^+$ T cells of younger compared to older animals (p<0.0001 for all, Mann Whitney tests); although, CXCR3 fluorescence intensity was low on $CD4^+$ T cells overall (Figure 6-9B). We also noted that the fluorescence intensity of PD-1 was significantly greater in the younger animals, although this difference was not clearly discernible from the clustering analysis. Like CXCR3, the fluorescence intensity of PD-1 was generally low on $CD4^+$ T cells.

Ideally, to support the above observations, we would have compared the frequencies of SARS-CoV-2-specific effector T cells within the lungs of the older and younger animals by ICS. However, the single-cell suspension yields (approximately two million cells per sample) from the lung tissue pieces collected at necropsy were insufficient to meet the total cell requirements for establishing multiple stimulation conditions in an ICS assay (over four million cells per sample). Therefore, we instead compared frequencies of $CD4^+$ and $CD8^+$ T cells expressing markers characteristically upregulated on antigen-experienced effectors and exhibiting signs of recent proliferation. Previous studies have suggested that Ki67 expression, in combination with other markers, may identify T cells expanding in response to antigen exposure[532,533]. As percentages of

non-naïve ($CD95^+$) $CD4^+$ or $CD8^+$ T cells, $CD49d^+$ $Ki67^+$, $CXCR3^+$ $Ki67^+$, and PD-1^+ $Ki67^+$ populations were present at significantly higher frequencies in the younger animals compared to the older animals (p=0.0286 for all comparisons, Mann-Whitney tests) (Figure 6-9C&D). As previously stated, CD49d and CXCR3 are both markers associated with antiviral effector and effector memory responses, as well as T cells with inflammatory homing capacity[26,534-536]. PD-1 is a multifunctional T-cell marker, but during acute infection it is preferentially expressed on early activated ($CD8^+$) effectors[537,538]. Collectively, these data suggest that at 7 DPI, the lungs of the younger animals contained more abundant populations of T cells bearing phenotypic characteristics of effector T cells. However, we acknowledge that the use of surrogate phenotypes does not truly enable the distinguishment of pathogen-specific responses from bystander effects.

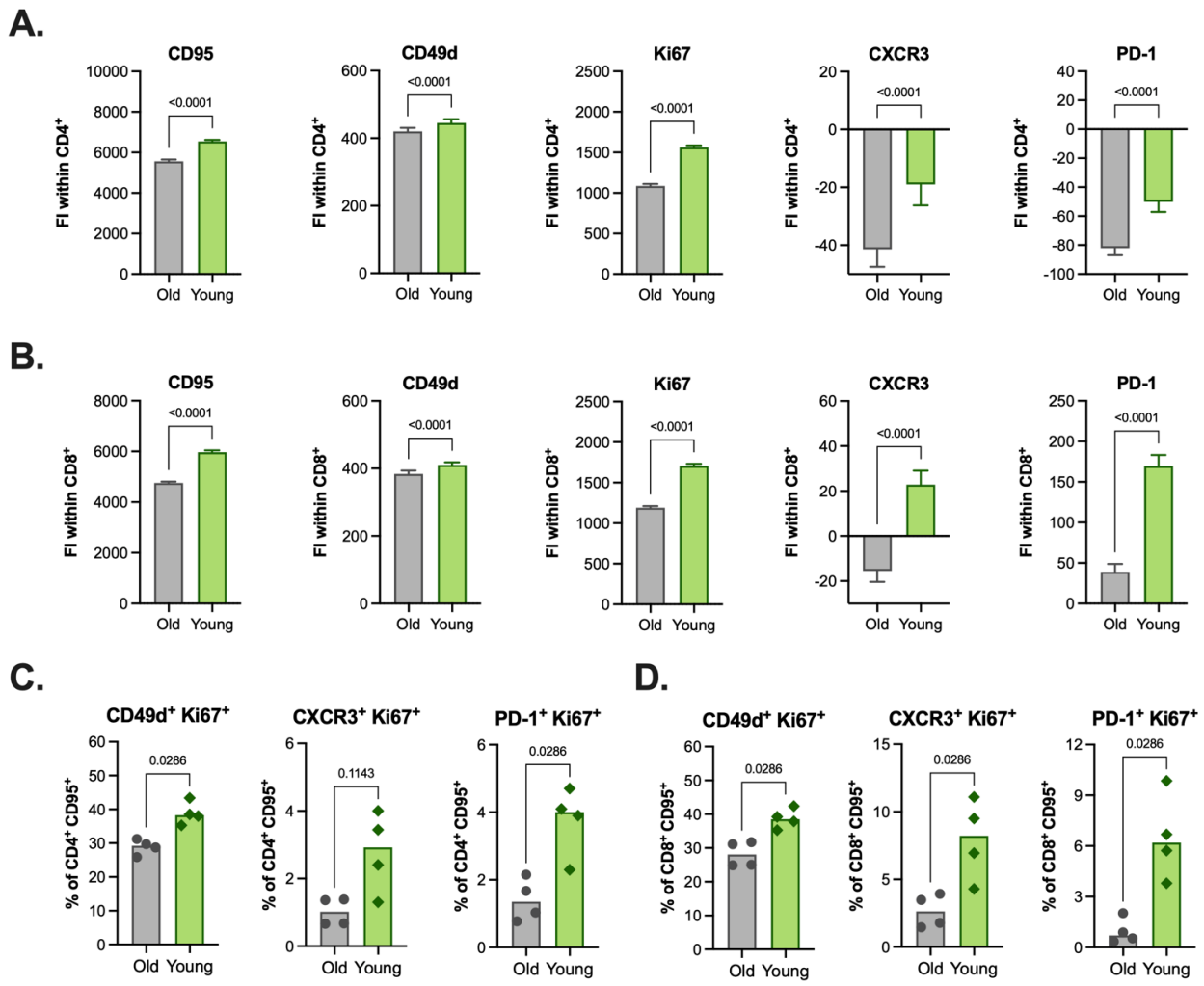


Figure 6-9. Age-associated differences in the expression and frequency of T-cell markers of effector function. The fluorescence intensities (FI) of selected markers assessed by flow cytometry on lung CD4$^+$ **(A)** and CD8$^+$ **(B)** T cells at 7 DPI were compared between older and younger animals. Bars depict the median and 95% CI calculated from all FI values of individual cells concatenated across animals within each age cohort (statistical test: Mann-Whitney). Frequencies of CD4$^+$ **(C)** and CD8$^+$ **(D)** CD49d$^+$ Ki67$^+$, CXCR3$^+$ Ki67$^+$, and PD-1$^+$ Ki67$^+$ T-cell populations as percentages of non-naïve (CD95$^+$) cells. Bars depict median frequencies (statistical test: Mann-Whitney). P-values are denoted on the graphs, $p<0.05$ was considered significant.

6.2.5 Comparison of lung T-cell phenotypes and lymphoid tissue at 21 DPI

To determine whether the phenotypic differences between the age cohorts at 7 DPI were maintained or altered during the post-acute phase of infection, we performed the same analyses on lung T cells at 21 DPI. Doing so revealed additional changes in the phenotypic trends appearing

in the period following virus clearance. In contrast to observations at 7 DPI, at 21 DPI, a substantial elevation in total T-cell frequencies was detected in the older animals, while a dramatic reduction was observed in the younger animals (p=0.0286, Mann-Whitney test). However, the frequencies of $CD4^+$ (p=0.4857) and $CD8^+$ (p=0.6857) T cells were similar between cohorts (Mann-Whitney tests) (Figure 6-10A). These data may have been indicative of a late-occurring expansion of local T cells or an influx of T cells from the peripheral blood of the older animals. Applying the same FlowSOM clustering analysis described above, we identified six clusters enriched for cells from the older animals (clusters 3, 4, 7, 13, 14, and 15) and six clusters enriched for cells from the younger animals (clusters 1, 2, 5, 8, 9, and 11) (Figure 6-10B). Notably, at 21 DPI, the segregation of cells from each age cohort into distinct clusters was more exaggerated than at 7 DPI, as evidenced by the statistical comparisons of the median cell frequencies within each cluster (Mann-Whitney tests) (Figure 6-10C). The clusters composed of cells from the older animals spanned all major subsets: $CD4^+$ (clusters 7, 13, 14), $CD8^+$ (cluster 3), DN (clusters 4 and 15), and DP (cluster 14) (Figure 6-10D). Meanwhile T cells in the younger animals were again largely found in $CD8^+$ (clusters 1, 2, 5, 8) or mixed $CD8^+$ and DN clusters (clusters 9 and 11). Comparisons of the z-scored MFIs of phenotypic markers revealed higher MFIs of Ki67, CD95, CD49d, and to some extent CXCR3 and PD-1 on clusters enriched for T cells from the older cohort compared to those for the younger cohort (Figure 6-10D). Remarkably, this combination of markers matched those demonstrating increased fluorescence intensity on the clusters ascribed to the younger animals at 7 DPI. Meanwhile, in the younger animals at 21 DPI, higher MFIs of CCR7, CD103, CD69, and HLA-DR were observed on multiple ($CD8^+$) clusters, relative to clusters ascribed to the older animals (Figure 6-10D). CCR7 is a marker for lymph node homing, whereas CD103 and CD69 are often upregulated together on T cells with a tissue-resident memory phenotype.

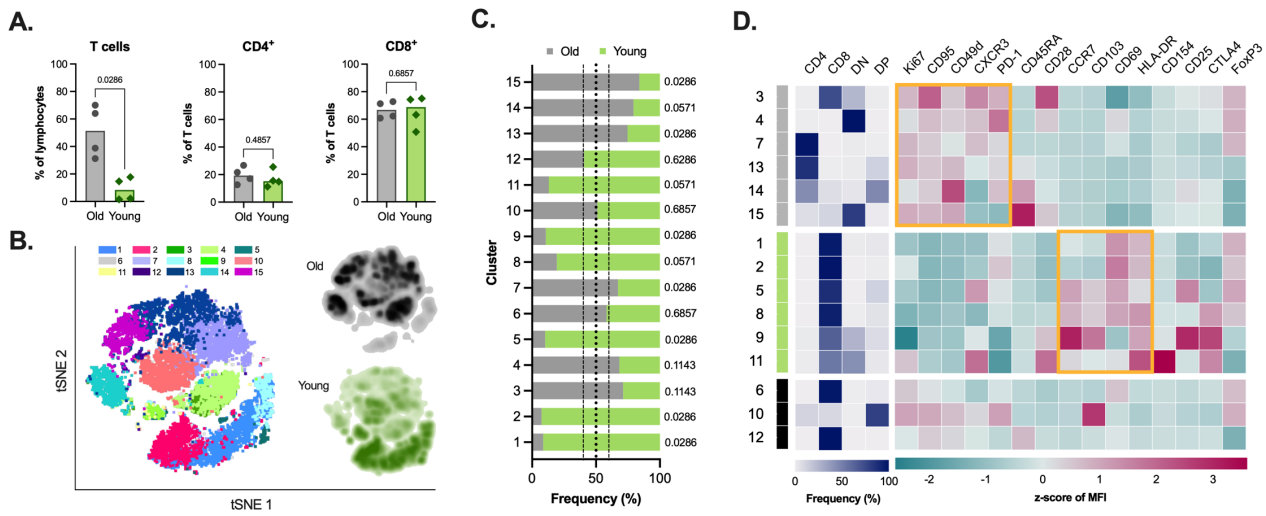


Figure 6-10. Phenotypic analysis at 21 DPI reveals a potential age-related delay in local T-cell responses. (A) Flow cytometric evaluation of lung cells collected at 21 DPI. Frequencies of $CD3^+$ T cells as a percentage of lymphocytes; frequencies of $CD4^+$ and $CD8^+$ T cells as percentages of $CD3^+$ T cells. Bars depict median frequencies (statistical test: Mann-Whitney). P-values are denoted on the graphs, $p<0.05$ was considered significant. **(B)** Visualization of concatenated $CD3^+$ T-cell subset across animals by t-SNE analysis. Stacked density plots (right) show the distribution of T cells derived from each age cohort. Dot plot depicts individually colour coded FlowSOM meta-clusters overlayed onto total combined T cells (left). **(C)** Stacked bar chart depicting the cumulative proportion of cells from animals of the older and younger cohort comprising each FlowSOM meta-cluster (1-15). Vertical dotted lines (from left to right) represent the (1) threshold of 10% for enrichment of cells from younger animals, (2) equal composition, and (3) the threshold for enrichment of cells from older animals. P-values comparing the median frequency of cells per animal within each cohort are listed to the right of the stacked-bars for each cluster (statistical test: Mann-Whitney). **(D)** Heat map representation of meta-cluster phenotypes. The clusters enriched for the cells of the older (grey), younger (green), and neither (black) are indicated (leftmost column). The major T-cell subset characterizing each cluster is shown by depicting the frequencies of CD4, CD8, DN, and DP T cells composing each cluster (central heat map). The phenotypic profiles of clusters were characterised and compared relative to one another by calculation of the z-score of the MFI of the listed markers across all 15 clusters (rightmost heat map). Markers of interest on clusters enriched for cells from either age cohort are outlined in golden-yellow.

Comparison of the fluorescence intensity of these markers across total $CD4^+$ and $CD8^+$ T cells from each age cohort confirmed that the intensities of CD95, CD49d, and Ki67 were now significantly elevated on the $CD4^+$ T cells of the older animals versus younger animals ($p<0.0001$); this effect was also observed for CD95 and CD49d on $CD8^+$ T cells ($p<0.0001$) (Mann-Whitney tests) (Figure 6-11A&B). Although, median fluorescent intensities of Ki67 on $CD8^+$ T cells, and CXCR3 and PD-1 on $CD4^+$ and $CD8^+$ T cells were significantly higher in the younger animals ($p<0.0001$), consistent with the results at 7 DPI (Figure 6-

11A&B). Meanwhile, in alignment with the clustering analysis, the fluorescence intensities of CCR7, CD103, CD69, and HLA-DR were significantly higher on $CD8^+$ T cells in the younger animals compared to the older animals ($p<0.0001$ for all, Mann-Whitney tests) (Figure 3-11B). These markers did not consistently display a similar effect on $CD4^+$ T cells (Figure 3-11A).

Next, we performed a comparison of population frequencies. At 21 DPI, frequencies of non-naïve ($CD95^+$) $CD4^+$ and $CD8^+$ T cells that were also $CD49d^+$ $Ki67^+$, $CXCR3^+$ $Ki67^+$, and $PD\text{-}1^+$ $Ki67^+$ increased relative to their 7 DPI levels in both cohorts, but particularly in the older animals, consistent with the fluorescence intensity data (Figure 6-11C&D). Finally, we corroborated the observed elevation in fluorescence intensity of markers associated with lymph node homing (CCR7) and tissue-residency (CD103, CD69) on $CD8^+$ T cells of the younger animals at 21 DPI via direct comparison of population frequencies. Significantly higher percentages ($p=0.0286$, Mann-Whitney test) of non-naïve ($CD95^+$) $CD8^+$ T cells expressing lymph node homing markers, specifically those consistent with a central memory phenotype ($CD28^+$ $CCR7^+$), were present in the younger animals in comparison to the older animals[539] (Figure 6-11E). We additionally detected elevated frequencies of $CD8^+$ $CD95^+$ T cells in the younger cohort that were also $CD103^+$ ($p=0.0286$) or $CXCR3^+$ $CD69^+$ $CD103^+$ ($p=0.0286$), which may have represented populations of effector-like memory cells exhibiting lung-specific, tissue-resident phenotypes[540-542] (Mann-Whitney tests) (Figure 6-11F).

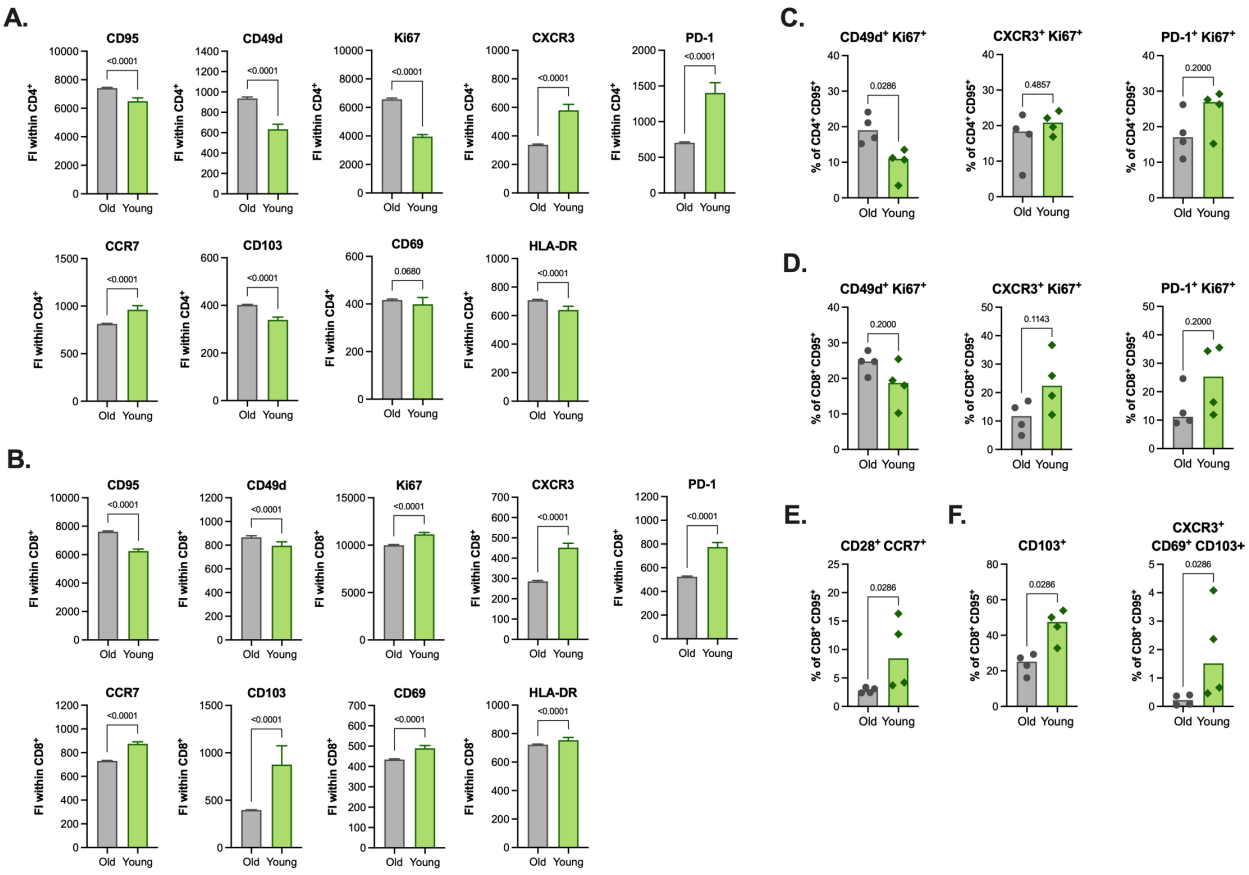


Figure 6-11. Comparison of the expression and frequency of T-cell markers associated with effector or memory function at 21 DPI. The fluorescence intensities (FI) of selected markers on lung $CD4^+$ **(A)** and $CD8^+$ **(B)** T cells at 21 DPI were compared between older and younger animals. Bars depict the median and 95% CI calculated across FI values of individual cells concatenated across animals within each cohort (statistical test: Mann-Whitney). Frequencies of $CD4^+$ **(C)** and $CD8^+$ **(D)** $CD49d^+$ $Ki67^+$, $CXCR3^+$ $Ki67^+$, and $PD\text{-}1^+$ $Ki67^+$ T cells as percentages of non-naïve ($CD95^+$) cells. Bars depict median frequencies (statistical test: Mann-Whitney). Frequencies of **(E)** $CD28^+$ $CCR7^+$, **(F)** $CD103^+$ and $CXCR3^+$ $CD69^+$ $CD103^+$ cells as percentages of $CD8^+$ $CD95^+$ T cells. Bars depict median frequencies (statistical test: Mann-Whitney). P-values are denoted on the graphs, $p<0.05$ was considered significant.

To supplement the results from our T-cell phenotyping by flow cytometry, we carried out multiplex IHC (mIHC) of lung tissue samples at 21 DPI. The staining and histopathological evaluation of lung tissue was performed by Dr. Carl Shaia, Rebecca Rosenke, and Dr. Emily Speranza. I assisted with the subsequent image analysis and quantification. We found evidence of the enhanced expansion of bronchus-associated lymphoid tissue (BALT) structures in the lungs of the younger animals compared to the older animals (Figure 7-12A). Previous studies suggest that

BALT expansion may be induced shortly after pulmonary infection[543,544]. These BALT formations were primarily found around large airways, denoted by EpCAM and α-smooth muscle actin (αSMA). Within the BALT, we identified cells co-expressing CD3, HLA-DR, and Ki-67, characteristic of activated and proliferating T cells[545] (Figure 7-12A). BALT structures were less abundant in the older animals, and those present were generally smaller in size and exhibited reduced proliferative capacity (i.e., lower Ki67 density) (Figure 7-12B). By contrast, the lungs of the younger animals contained a mixture of larger and smaller BALT, which contained GC-like structures with a high density of $CD3^-$ $Ki67^+$ $HLA\text{-}DR^+$ cells (Figure 7-12A&B). Notably, the lungs of the older animals did not exhibit signs of the advanced-stage development of full lymphoid-like tissue structures, such as endothelial vessel formation, $CD3^+$ $CD4^+$ cells surrounding clusters of $CD3^+$ $HLA\text{-}DR^+$ cells (representing activated T cells), or $CD3^-$ $HLA\text{-}DR^+$ populations (comprising APCs and B cells). However, it is possible that similarly mature BALT would appear in the older animals if given more time. In summary, combined with the kinetic differences observed by flow cytometry, these data provide additional evidence of an age-associated delay or deficiency in the local cellular immune response to infection.

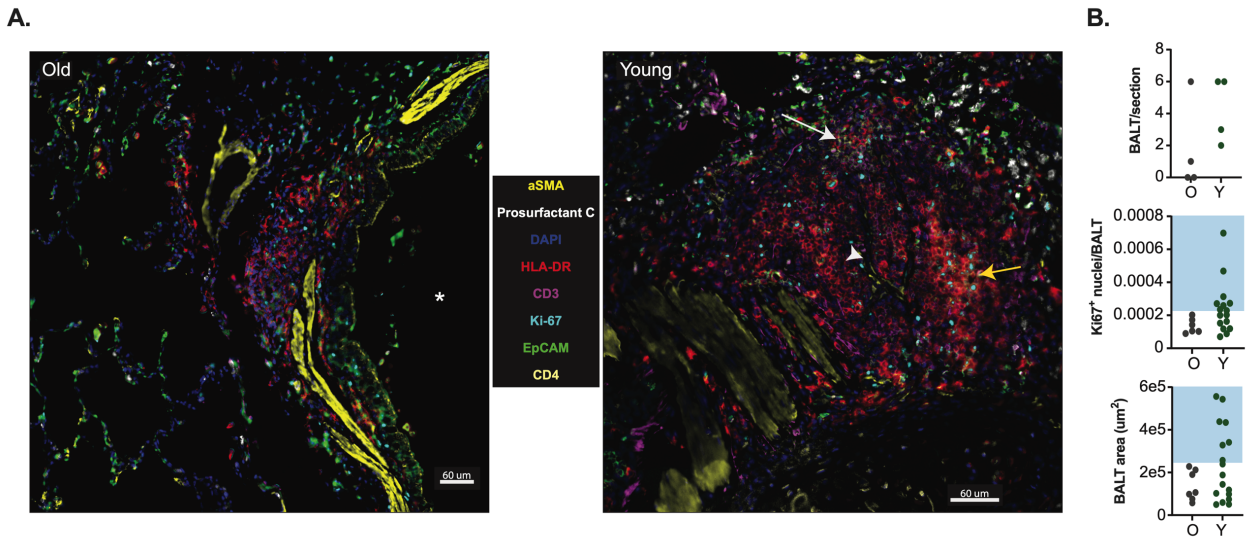


Figure 6-12. Advanced BALT structures in the lungs of the younger animals at 21 DPI detected by mIHC. (A) Representative mIHC of a lung section from an older (left) and a younger (right) rhesus macaque focusing on identified BALT; α-smooth muscle actin, prosurfactant C, DAPI, HLA-DR, CD3, Ki-67, EpCAM, and CD4 are shown. Some features are denoted such as a large airway (*), GC formation (yellow arrow), high endothelial venule (white arrowhead), and $CD4^+$ T-cell accumulation (white arrow). Scale bars represent 60 µm. **(B)** Quantification of mIHC images in older and younger animals. Graphs show the number of BALT found per the lung section for each animal (top), the density of $Ki67^+$ nuclei out of all BALT cells (middle), and the area (μm^2) of all identified BALT (bottom). Cut-offs for immature BALT (white area) versus more advanced BALT (blue shaded area) are indicated.

6.2.6 Systemic immune responses after infection

Next, to expand upon our findings in the lungs, we also mapped systemic T-cell responses over the course of infection. By 1 DPI, frequencies of circulating $CD4^+$ and $CD8^+$ T_{EEM} ($CD28^-$ $CD95^+$) cells increased relative to baseline levels in all animals (mean increase in frequency, older = 27.3%, younger = 35.3%) (Figure 6-13A&B). Corresponding decreases in the frequencies of central memory (T_{CM}, $CD28^+$ $CD95^+$) and naïve ($CD28^+$ $CD95^{lo}$) populations were observed during the same period. Between 3 and 21 DPI, the younger animals exhibited more salient reductions in frequencies of non-naïve (T_{EEM} and T_{CM}) cells, accompanied by a proportional increase in the frequency of naïve cells (Figure 6-13A&B). This effect was strongest for $CD8^+$ T_{EEM} cells (mean decrease in frequency, older = 23.6%, younger = 46.9%), and likely reflects the exodus of effector

T cells from the peripheral blood to the site of infection. AUC analysis between 1 and 21 DPI confirmed that the reduction of this cell type in circulation was significantly greater in the younger animals (AUC±SEM = 662.1±27.09) compared to the older animals (AUC±SEM = 304.7±95.06) (p=0.0006, unpaired t-test) (Figure 6-13A&B). The principal decrease occurred between 1 and 7 DPI, which aligned with data from the lungs at 7 DPI demonstrating elevated frequencies of T cells, particularly $CD8^+$ T cells, in the tissues of the younger animals. Comparison of the frequencies of $CXCR3^+$ cells as a percentage of non-naïve ($CD95^+$) $CD4^+$ and $CD8^+$ T cells between 1 and 21 DPI provided further evidence of more efficient homing of T cells to the site of infection in the younger animals (AUC±SEM = 509.8±50.21 and 618.6±57.18, $CD4^+$ and $CD8^+$, respectively) compared to the older animals (AUC±SEM = 345.4±57.61 and 384.7±83.25, $CD4^+$ and $CD8^+$, respectively) (Figure 6-13C&D). The augmented frequency of CXCR3 expression was evident on both $CD4^+$ $CD95^+$ and $CD8^+$ $CD95^+$ cells post inoculation, although the effect was stronger for the latter (p=0.0350 and p=0.0042, respectively, AUC comparisons by unpaired t-tests). In summary, these data suggest that the differences in T-cell dynamics observed in the lungs stemmed at least in part from the enhanced recruitment of circulating $CD8^+$ T cells to the site of infection in the younger animals. However, given the timing of this hypothesised migration effect, it is possible that a substantial proportion of bystander T cells are trafficked in the early days after inoculation. Alternatively, naïve T cells transitioning to an antigen-experienced phenotype may upregulate surface expression of CD95 well in advance of their differentiation into functionally mature antigen-specific T cells.

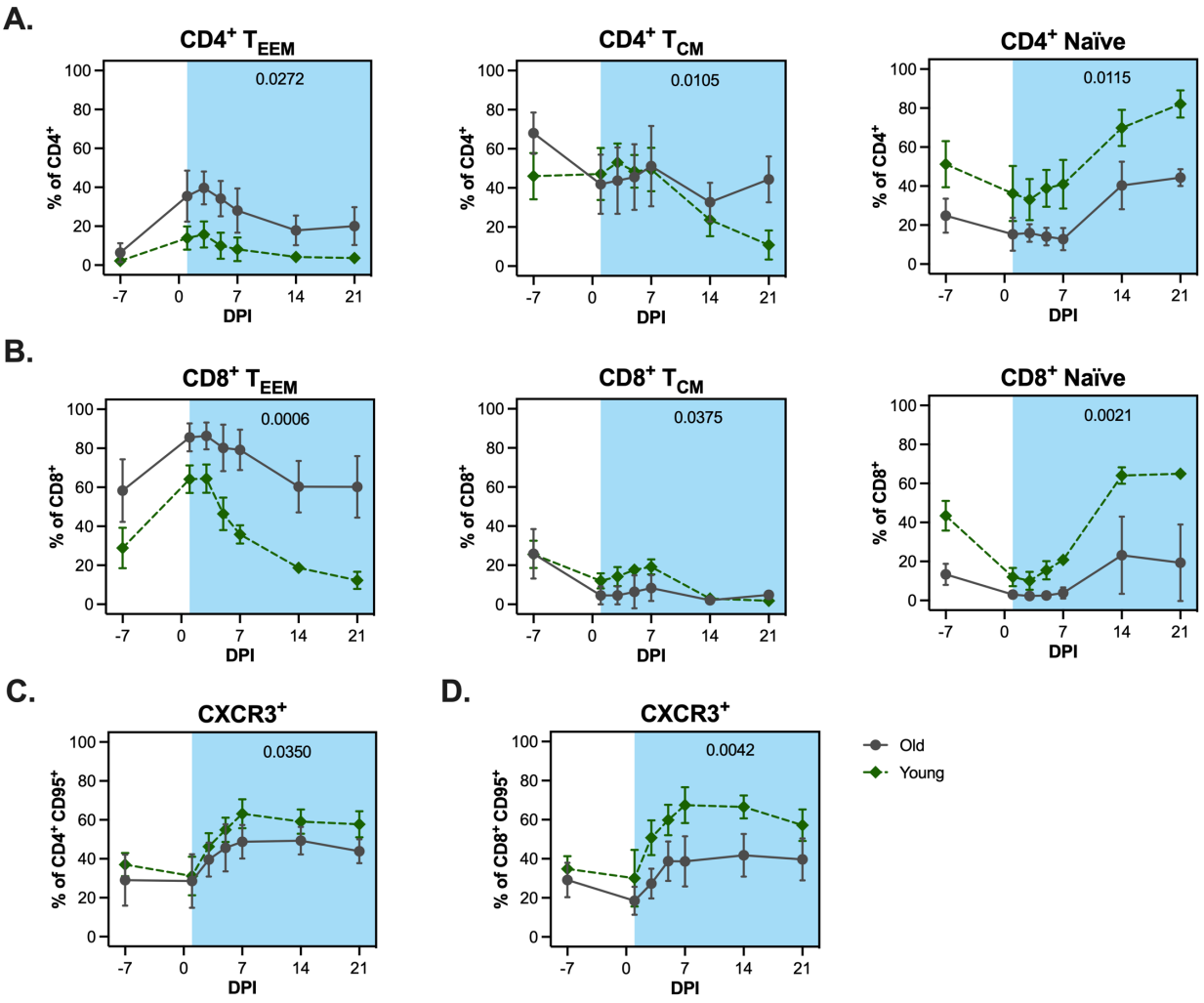


Figure 6-13. Comparison of circulating T-cell dynamics over the course of infection. Frequencies of T_{EEM} (left), T_{CM} (middle), and naïve (right) $CD4^+$ **(A)** and $CD8^+$ **(B)** T cells over time (DPI) as a percentage of total $CD4^+$ and $CD8^+$ T cells, respectively. Frequencies of $CXCR3^+$ populations over time (DPI) as a percentage of $CD4^+$ **(C)** and $CD8^+$ **(D)** non-naïve ($CD95^+$) T cells. Data points represent the mean frequency with standard deviation (error bars) connected across timepoints for the older and younger animals. AUC was calculated for the frequencies from 1-21 DPI; AUC was compared between the age cohorts (statistical test: unpaired t-test). P-values are denoted on the graphs, $p<0.05$ was considered significant.

Finally, we compared the functional profiles of SARS-CoV-2-specific T cells present in the spleen at 21 DPI by ICS. We determined the frequencies of $CD4^+$ and $CD8^+$ T cells expressing IFNγ, TNFα, IL-2, or Granzyme B in response to SARS-CoV-2 S-protein peptide pool stimulation. Notably, we observed higher frequencies of $CD4^+$ $IFN\gamma^+$, $CD8^+$ $IFN\gamma^+$, and $CD8^+$ $TNF\alpha^+$ T cells in the younger animals compared to the older animals (p=0.0286 for all comparisons, Mann-

Whitney tests) (Figure 6-14A&B). There additionally appeared to be a trend towards elevated frequencies of $CD4^+$ $TNF\alpha^+$ and $CD4^+$ $IL\text{-}2^+$ cells in the younger animals, but these differences were not statistically significant (p=0.0571 for both comparisons, Mann-Whitney tests). Collectively, these data suggest that the younger animals developed a more robust virus-specific pro-inflammatory (Th and CTL) cellular immune responses than the older animals by 21 DPI[464,466].

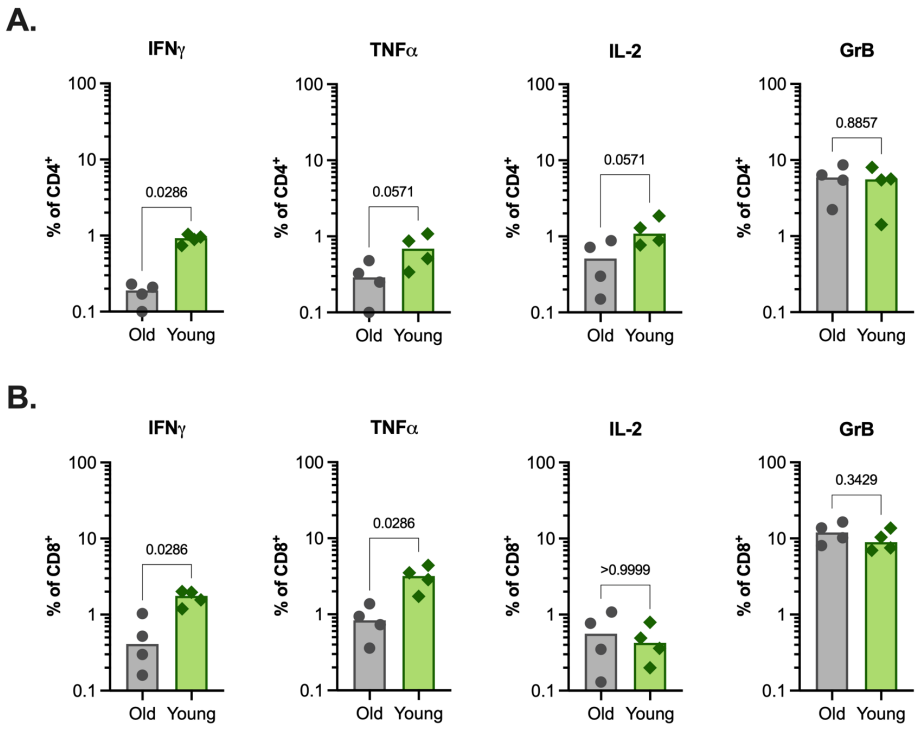


Figure 6-14. Higher frequencies of SARS-CoV-2-specific T cells in the younger animals at 21 DPI. The percentage of splenic $CD4^+$ **(A)** and $CD8^+$ **(B)** T cells expressing IFNγ, TNFα, IL-2, or Granzyme B (GrB) after SARS-CoV-2 S-protein peptide pool stimulation and ICS. Graphed values reflect adjustment to exclude non-specific cytokine expression measured from a corresponding set of unstimulated samples. All bars depict group medians (statistical test: Mann-Whitney). P-values are denoted on the graphs, $p<0.05$ was considered significant.

6.2.7 Age-related differences in the resolution of systemic inflammation

The previous findings highlighted age-specific differences in inflammation and cellular changes within the lungs, along with kinetic and functional incongruity in T-cell responses. These results prompted us to monitor patterns in the immunomodulatory signalling environment during

infection. To this end, levels of serum cytokines were assessed during the acute (1-7 DPI) and post-acute phases of infection (10-21 DPI). Principal component analysis (PCA) revealed little evidence of sample clustering according to age through 7 DPI (F=2.5, p=0.04, permanova test) (Figure 6-15A). However, from 10 DPI onwards, cohort separation became clearer (F=6.2, p=0.00009, permanova test), suggestive of the development of distinct cytokine profiles. From the PCA, we identified seven cytokines representing the most likely drivers of the age-associated variation observed between 10-21 DPI by applying a loadings cut-off of 0.2 and selecting for high loading scores along PC1: IL-2, IL-10, IL-17A, IL-13, IL-6, and MIP-1α (Figure 6-15B). To further examine these results, we directly compared the concentrations of these cytokines at each sampling timepoint. In alignment with the PCA data, no dramatic differences in the levels of individual serum cytokines were observed between age cohorts from 1-7 DPI (Figure 6-15C). However, at 10 DPI, concentrations of circulating pro-inflammatory cytokines IL-6, MIP-1α, TNFα, and IL-17A were elevated in the older animals in comparison to the younger animals (p=0.0002, 0.002, 0.0645, and 0.0474, respectively, two-way ANOVA with Šídák's multiple comparisons test). Concurrent spikes in the concentrations of regulatory cytokines IL-10 (p=0.03) and IL-13 (p=0.0011) were also apparent in the older animals while being absent in the younger. Notably, elevations in the levels of IL-6, IL-10, and IL-13 were sustained in the older animals from 10 DPI through at least 21 DPI (10-21 DPI AUC comparison of old versus young: p=0.0085, 0.0176, and 0.0256, respectively, by unpaired t-tests), suggesting prolonged systemic inflammation (Figure 6-15C).

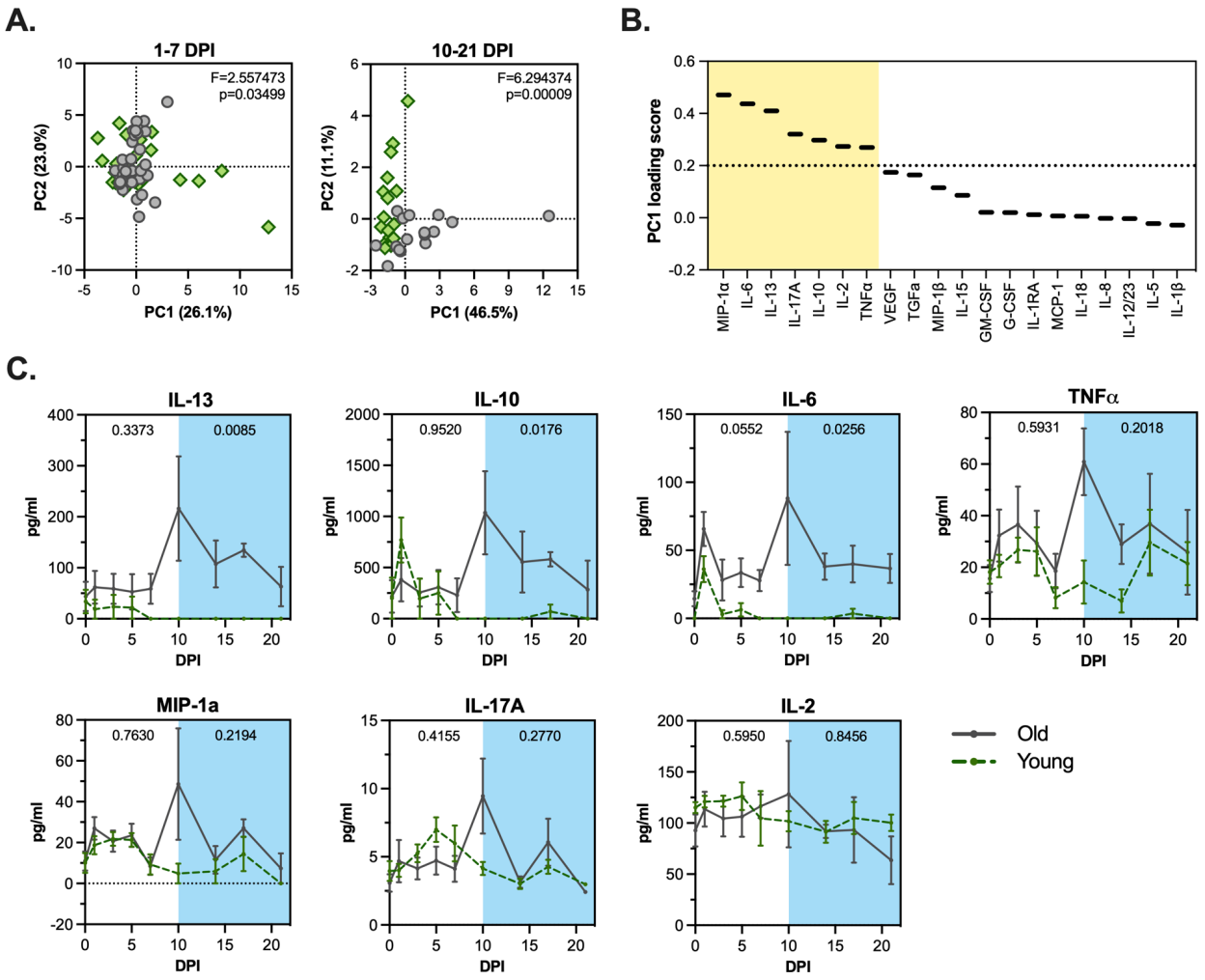


Figure 6-15. Circulating cytokines provide evidence of prolonged inflammation in the older animals. (A) PCA analysis of the serum cytokine data grouped to reflect the acute (1-7 DPI) and post-acute (10-21 DPI) phases of infection. Plots depict PC1 versus PC2 scores, which encompass 23.0% and 11.1% of the total variation, respectively. A data point for each older (grey) and younger (green) animal per sampling timepoint is depicted. The F-statistic and p-value for clustering across all significant principal components (up to 99% explained variance) is shown (statistical test: permanova). **(B)** PC1 variable loading scores for serum cytokine concentrations between 10-21 DPI. The vertical dashed line represents the cut-off for the significant loading values (0.2). **(C)** Selected serum cytokine concentrations (pg/mL) over the course of infection. Group means and standard error (SEM) are shown for each timepoint. P-values listed on the graphs represent AUC comparisons between the older and younger animals for 0-7 DPI (left) and 10-21 DPI (right) (statistical test: unpaired t-test).

Due to their role in regulating the activation and resolution phases of the inflammatory response, changes in immune lipid mediators (LMs) were also assessed at 3, 7, and 21 DPI (Figure 6-1). As before, LC-MS/MS analysis of LM levels in sera was carried out by Dr. Benjamin Schwarz. No

acute changes in circulating LM profiles were observed within the first few days after inoculation (3 DPI), although the nonspecific elevation of LMs present in the older animals prior to infection was preserved (log_2 fold change relative to 0 DPI) (Figure 6-16A). At 7 DPI, the LM profile of the older animals remained unchanged, but the younger animals began to display a trend of higher LM levels across multiple LM families in agreement with the observed inflection in cytokine behaviour on 7 DPI. By 21 DPI, these LM levels continued to increase in the younger cohort while remaining unchanged in the older cohort (Figure 6-16A). The responsive LMs in the younger animals were primarily localised to the cyclooxygenase (COX) family and the 12- and 15-lipoxygenase families, as evidenced by PCA and the corresponding PC1 loadings data (Figure 6-16B&C). Increases in similar LM and LM pathway signatures have been associated with an upregulation of tissue-repair processes. In combination with the findings in the lungs, the differences in LM profiles suggest that by 21 DPI the younger animals had efficiently transitioned away from an acute antiviral response to a pro-resolving or repair-promoting state, as would be expected during convalescence[546-548].

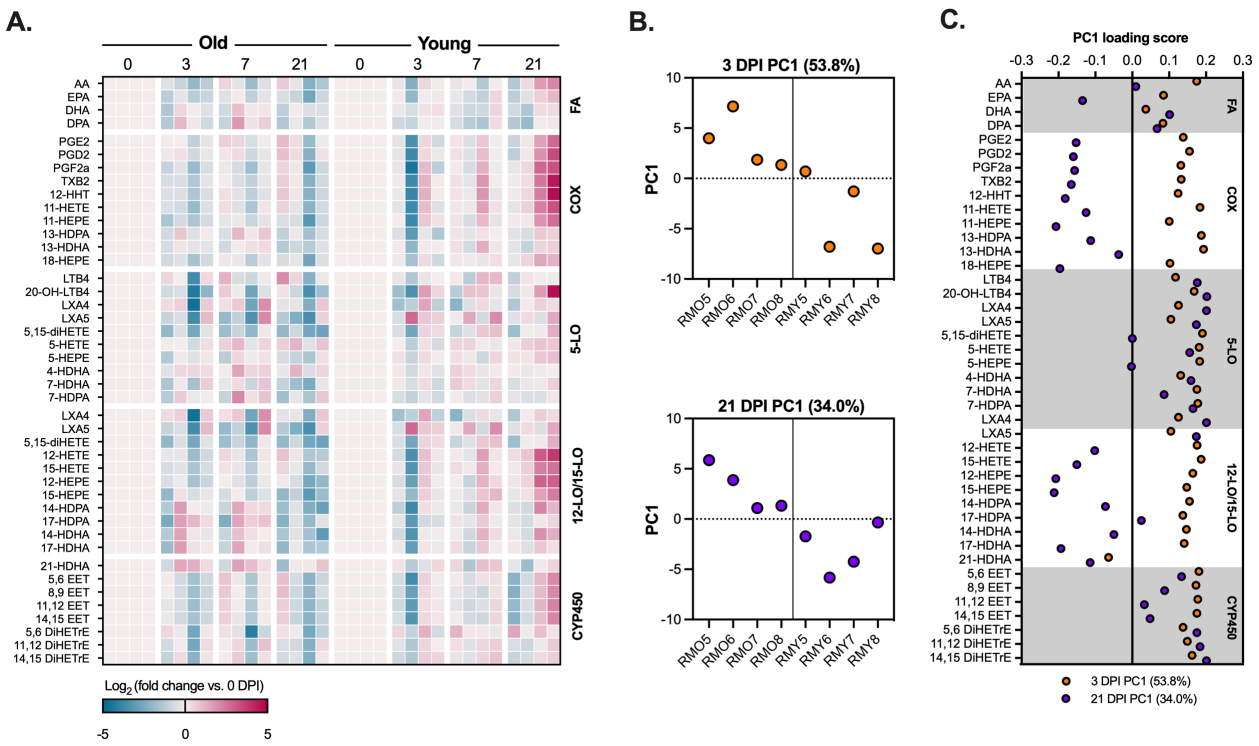


Figure 6-16. LM profiles reveal an age-related delay in the return to homeostasis after infection. (A) Circulating LM profiles for the old (left) and young (right) at 0, 3, 7 and 21 DPI. Each column represents a single animal, and the rows distinguish specific LM species. LMs are grouped into families by the synthesizing lipoxygenase (LO) enzyme noted to the right of the heatmap. Individual LM species produced by multiple LO enzymes are listed for each family. Values represent the $\log_2$ fold change of the lipid signal relative to 0 DPI, with teal indicating a decrease and red indicating an increase. **(B)** PCA of the LM data for 3 (top) and 21(bottom) DPI; PC1 scores for each animal are shown (older = RMO5-8, younger = RMY5-8). PC1 captured 53.8% and 34.0% of the total variation between animals at 3 and 21 DPI, respectively. **(C)** PC1 variable loading scores for LM species at 3 (orange) and 21 (purple) DPI.

6.3 Discussion

Increased age is a clear risk factor for severe COVID-19 in humans. Although the mechanism underlying this susceptibility is not fully understood, it is likely driven by impaired immune responses to infection in older individuals[507]. Following the COVID-19 vaccine studies discussed in Chapter 5, we aimed to select for host factors in rhesus macaques that might predispose animals to more severe SARS-CoV-2 pathogenesis. Our objective in doing so was to potentially identify a NHP model recapitulating features of severe COVID-19 in humans that could be applied in translational studies (e.g., for testing interventions aimed at ameliorating clinical disease). Based on observations in humans, we selected age as our host factor of interest. We subsequently set out to characterise, in detail, the differences in outcomes to SARS-CoV-2 infection in aged versus young animals. To this end, we employed multi-omics analyses to compare immune dynamics in older and younger rhesus macaques on a cellular level, with a particular focus on the lungs during two key phases of infection: the acute phase (1-7 DPI) and the post-acute phase (10-21 DPI). Ultimately, we found limited differences in the clinical course of disease in our animals regardless of age, counter to our initial hypothesis. Nevertheless, our time-resolved evaluation did reveal interesting age-related differences in the immune responses to SARS-CoV-2 infection. A summary of our findings has been depicted in Figure 6-17 below, and a discussion of these results follows.

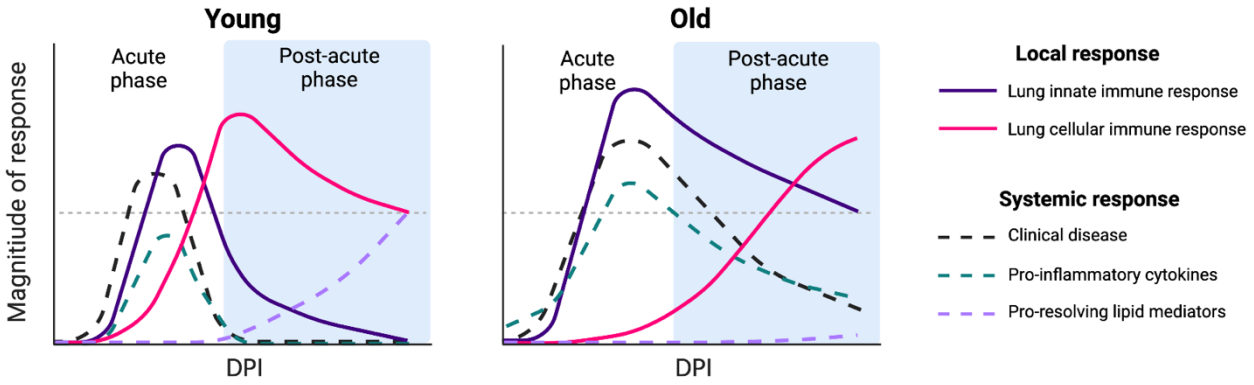


Figure 6-17. Summary of the immune dynamics in younger and older rhesus macaques during SARS-CoV-2 infection. Graphical representation of the relative magnitude of response over the course of SARS-CoV-2 infection in younger (left) and older (right) rhesus macaques. The white part of each graph indicates the acute phase of the disease and blue is the post-acute phase. The grey horizontal line is for reference between the two graphs at the same point. The different curves represent different local (lung innate immune and lung cellular immune) and systemic (clinical disease, pro-inflammatory cytokines, and pro-resolving lipid mediators) host responses to SARS-CoV-2 infection.

Baseline assessment of our older and younger cohorts, with a specific focus on host factors associated with COVID-19 severity in humans, revealed BCS and LM profiles for the older animals that were not indicative of an obese phenotype. Consistent with their moderately advanced age, the older animals also exhibited elevated concentrations of certain pro-inflammatory cytokines, including IL-6, and changes in adaptive immune cell subsets, such as a loss of naïve cells, which were reflective of some degree of immunosenescence.

In our model, like previous studies in NHPs[430,513,514], clinical disease was mild in both age groups with older animals demonstrating a slight elevation in disease signs and a longer time to recovery. Despite this limited effect of age on disease outcome, we found several striking differences in the response to SARS-CoV-2 infection through immunological and transcriptional profiling (summarised in Figure 6-17). During the acute phase of SARS-CoV-2 infection in the older animals, the local innate response was upregulated in both immune and non-immune cell populations through 7 DPI. By contrast, the younger animals appeared to achieve better control

over innate inflammatory response in the lungs, as evidenced by the more attenuated induction of innate pathways that occurred only in immune cells and had nearly resolved by 7 DPI. During the post-acute phase of the disease, the two groups diverged further, with older animals exhibiting a prolonged pro-inflammatory circulating response, as well as a delay in the activation and/or differentiation of T cells isolated from the lungs. Concomitant with these changes within the T-cell compartment, the younger animals displayed a pro-resolving circulating milieu of lipid mediators and cytokines at later timepoints, while the older animals did not (Figure 6-17). Collectively, our findings suggest that increasing age is associated with a protracted inflammatory state and delayed or less efficient mechanisms for inducing cellular immunity in response to SARS-CoV-2 exposure.

The initiation of the innate immune response is vital to controlling acute viral infections. Studies in humans suggest that younger individuals achieve superior control of SARS-CoV-2 replication and reduced severity of disease through an earlier induction of innate immune responses, especially in the upper respiratory tract[549]. In contrast, the rapid initiation of lung innate responses was observed in both age cohorts in our study, with elevated inflammatory signalling present in the older versus younger animals. This finding may explain the self-limiting nature of SARS-CoV-2 infection in the rhesus macaque model and the lack of severe disease, even in aged animals. However, innate responses resolved more slowly in the aged animals compared to the younger macaques. Prolonged inflammation has been linked to the dysregulation of adaptive immune responses, which play a critical role in the resolution of disease[550]. Together, these observations suggest that rather than being dependent on the initiation of innate responses, differences in infection dynamics in the rhesus macaque model are driven by the inability to properly dampen the initial innate inflammatory response and a failure to support rapid adaptive responses.

Defective or dysregulated innate and adaptive immune responses may contribute to the worsening COVID-19 outcomes observed with increased age[508]. Elevated concentrations of cytokines correlated with severe COVID-19, including IL-6 and IL-10[551], were present for a longer duration in the older animals than in the younger animals, along with protracted clinical signs. The timing and quality of virus-induced T-cell responses are also predictive of the outcomes of infection for multiple pathogens and are vulnerable to age-related disruption[552]. The efficient stimulation of virus-specific IFN-γ-secreting T cells is associated with decreased COVID-19 severity in humans[553]. Additionally, $CD8^+$ T cells have been found to be among the first cells to enter the lungs after influenza A virus infection and are important in the resolution of disease[554]. Indeed, rapid $CD8^+$ T-cell responses combined with efficient dampening of inflammatory responses are linked to recovery from COVID-19[555,556]. In alignment with this observation, ($CD8^+$) effector T-cell frequencies were increased in the lungs of the younger animals at 7 DPI, whereas frequencies of phenotypically similar cells were not elevated in the older animals until 21 DPI. Similarly delayed T-cell responses, measured in the circulating immune pool, have been associated with secondary waves of disease beyond the point of viral clearance in COVID-19 patients, especially when combined with pro-inflammatory signatures[555]. These immune dynamics observed in COVID-19 patients are present in our older rhesus macaque cohort. As such, differences between older and younger animals during the post-acute phase of infection may provide insight into contributing cell populations and immune processes that define the continuous scale of severity observed in mild-to-moderate COVID-19 and the prolonged symptoms seen in many COVID-19 patients[555].

A relationship is evident between the mild features of immunosenescence present in the older animals at baseline and the immune dynamics after infection indicative of a moderate, but not yet

catastrophic, decline in immune responsiveness and homeostatic control. The delay in local cellular immune responses observed in the older animals may additionally be explained by reduced priming capacity with advancing age, due to a reduction in the size of the naïve T-cell pool and intrinsic cellular defects, which may have a stronger toll on $CD8^+$ T-cell responses[557]. Meanwhile, the sustained local and systemic inflammation in these animals may be explained by the progressive tendency of aging immune systems to shift towards a pro-inflammatory phenotype due to an imbalance of pro- and anti-inflammatory cytokines and decreased efficiency of inflammation-resolving mechanisms[520]. Additionally, 12- and 15-lipoxygenase pathways have been linked to recovery of lung tissue following viral infection[558,559], and loss of these lipid mediator classes has been linked to higher instances of ICU admissions in COVID-19 patients[448]. The observed upregulation of the LM pathways in the younger, but not older animals in our study, may have contributed to lagging recovery times and potentially to slower repair of lung tissue in the older animals.

Our ability to significantly distinguish the age-related immune dynamics discussed above was limited by the group sizes (n=8) used in our study, only half of which were monitored up to 21 DPI, and a male-only cohort of younger animals due to a lack of available subadult females. Moreover, given that the study endpoint did not extend beyond 21 DPI, we could not ascertain if the differences in the immune responses identified between the age groups resolved or became more pronounced over time. Finally, our study did not include animals of exceedingly advanced age, and our older animals were additionally free from comorbidities associated with severe COVID-19 in humans and linked with increased age[507]. Therefore, we cannot rule out the possibility that significantly worse clinical outcomes would have been observed in severely aged animals with compromised innate immune defences.

Despite these limitations, the results presented in this chapter demonstrate a defined impact of viral respiratory tract infection on the aging immune system. Importantly, our findings highlight essential differences and similarities in the immune response to SARS-CoV-2 infection between rhesus macaques and humans that may be affected by age. As such, the research featured in this chapter may provide new insights into the age-related immune dynamics of SARS-CoV-2 infection and represents an advance in available models of age-associated changes in immunity.

7

Discussion

7.1 Overview

Within the last eight years, outbreaks of Ebola virus disease, Zika fever, MERS, Nipah virus disease, Lassa fever, and above all the COVID-19 pandemic have highlighted the need for enhanced preparedness against zoonotic viral pathogens of epidemic or pandemic potential. Effective vaccines are a critical component of the response to new infectious threats. To this end, preclinical vaccine evaluation to establish immunogenicity, efficacy, and mechanisms of vaccine-induced immunity, is an essential stage in the process to develop preventive technologies. Not only do these studies provide data necessary to advance promising vaccine candidates to assessment in humans, but they can also provide evidence to inform decisions on licensure or emergency use authorisation, particularly when epidemiological limitations preclude phase III efficacy trials. Finally, the ability to impose controlled experimental infection conditions and the breadth of feasible sampling in animals may enable a more diverse array of assessments than is achievable in human studies. Access to suitable small animal and NHP models of infection are necessary to facilitate the above investigations and may enhance fundamental knowledge of disease pathogenesis.

This dissertation encompasses preclinical investigations for two viral pathogens of public health importance, LASV and SARS-CoV-2. Appraisal of vaccines designed with the ChAdOx1 viral vector platform comprised a substantial portion of this work. Alongside these studies, I also conducted experiments to characterise the relationship between the aging immune system and SARS-CoV-2 infection. A summary of major research findings and discussion of some of the limitations and challenges associated with the models employed follows.

7.2 Principal findings, limitations, and future work

7.2.1 Development of a ChAdOx1-vectored vaccine for LASV

Like other major vaccine candidates for LASV, ChAdOx1-Lassa-GPC encodes the full-length GPC sequence of the canonical Josiah strain virus. We demonstrated that the vaccine was immunogenic in CD1 mice, Hartley guinea pigs, and cynomolgus macaques. The characterisation of vaccine-specific adaptive responses revealed the robust induction of cellular and humoral immunity. However, antibody responses elicited by vaccination were non-neutralising across studies.

Our ability to draw definitive conclusions from the immunogenicity assessments performed in macaques was hampered by low animal numbers (n=4 per group). Trends emerged in the data suggesting that antigen-specific T-cell responses and antibody Fc-mediated effector functions may be enhanced after prime-boost versus single-dose vaccination. However, these differences did not meet statistical significance, due to underpowered analyses and a relatively high degree of variation between animals, characteristic of outbred models.

Guinea pigs and cynomolgus macaques immunised with one or two doses of ChAdOx1-Lassa-GPC were protected against lethal Lassa fever. Minimal signs of disease were observed in vaccinees, based on weight and temperature monitoring in guinea pigs and clinical scores in macaques. Despite the lack of measurable differences between the immunogenicity of the single- and two-dose vaccination regimens, clinical and immunological outcomes in guinea pigs and macaques indicated that boosting may contribute to the more efficient resolution of infection. Vaccination may also protect animals from uncontrolled systemic inflammation and dysregulation of antiviral immune responses, characteristic of Lassa fever, as suggested by multiplex cytokine and transcriptomic evaluation performed on macaque blood samples post challenge. The detection of viral RNA in tissues, particularly the liver and spleen, of vaccinees indicated that immunised animals (both guinea pigs and macaques) were not completely protected from infection. This result is consistent with the absence of detectable neutralising antibodies in circulation at the time of challenge in both models. However, limited quantities of viable virus were isolated from the tissues of immunised guinea pigs, suggesting that there was no on-going latent infection in these animals. Live virus titration assays to quantify infectious virus and *in situ* hybridisation of probes targeting RNA from replicating virus within cells of tissues harvested from vaccinated macaques are currently underway and will indicate if LASV infection is persisting sub-clinically, as late as 42 days after challenge.

While it will be important to ensure that vaccination does not result in the establishment of latent infection following LASV exposure, a strong emphasis on the demonstration of sterilising immunity may not be practical or relevant during vaccine assessment in stringent experimental challenge models. Infection with artificially high doses of virus renders the detection of viral RNA, in at least one site at some point after infection, a near inevitability depending on the breadth of

sampling performed. Given that experimental challenge conditions do not reflect natural exposure in humans, the translation of these findings into real-world infection scenarios may be limited.

To summarise, although our data suggests that ChAdOx1-Lassa-GPC may be a promising vaccine candidate to protect against Lassa fever, more evidence will be required to determine if it will meet the WHO TPP criteria outlined in Chapter 1. One of the greatest challenges to the development of an effective LASV vaccine will be the extensive phylogenetic diversity of the virus. Although in Chapter 3, we showed that ChAdOx1-Lassa-GPC-induced T cells and antibodies displayed cross-reactivity against the GP antigen from lineage I, II, or III strains, we did see a reduction in these responses against heterologous isolates. Heterologous challenge studies will be necessary to determine if these diminished responses are still sufficient to confer protection against clinical disease. It will be important to conduct these studies with contemporary isolates—rather than historical—to ascertain the likelihood that vaccines developed against the Josiah strain will remain efficacious against strains circulating in hyperendemic or outbreak prone regions. We are currently endeavouring to acquire viruses isolated between 2018 and 2019 in Nigeria. Once obtained, it will be necessary to confirm susceptibility of common LASV animal models to these variants, given that distinct strains may demonstrate dramatically different levels of pathogenicity. Nonlethal infections may require either the development of a species-adapted viral variant, comparable to the GPA LASV variant established for Hartley guinea pigs, or the utilisation of alternate outcome measures for establishing efficacy, in the place of survival. If ChAdOx1-Lassa-GPC affords subpar protection in these studies, an alternative approach will be to modify the GPC antigenic sequence to more closely reflect epidemiologically relevant strains, or to consider a multivalent vaccine approach with additional immunogens, such as NP, which may be more conserved.

7.2.2 Assessment of a vaccine against and host responses to SARS-CoV-2

The COVID-19 pandemic prompted a shift in my research focus towards supporting the development of ChAdOx1 nCoV-19/AZD1222 and characterising the relationship between the aging immune system and SARS-CoV-2 pathogenesis. These studies were performed in NHPs. Unlike LASV (Josiah strain) infection in cynomolgus macaques, SARS-CoV-2 infection results in only mild-to-moderate acute respiratory disease in rhesus macaques. In the absence of survival as a principal outcome, we relied upon virological and immunological parameters to assess vaccine efficacy or changes in the progression of infection.

Rhesus macaques immunised intramuscularly with two doses of ChAdOx1 nCoV-19 exhibited a significant reduction in viral load in the lower, but not upper, respiratory tract compared to ChAdOx1 GFP control animals. Vaccine-induced adaptive immune responses featured robust titres of antibodies, which exhibited neutralising and non-neutralising functions. By contrast, cellular immune responses detected in circulation were weak. Interestingly, this finding did not align with results in humans, suggesting that reduced cellular immunogenicity of ChAdOx1 nCoV-19 may be a phenomenon unique to this model. Consistent with antigen-specific responses post immunisation, after SARS-CoV-2 challenge, we observed an association between B-cell phenotypes in circulation and lower respiratory tract viral load, which was not concurrently apparent for T-cell phenotypes. Specifically, higher frequencies of mature IgG^+ memory B cells were observed in vaccinees without detectable virus replication in the lower respiratory tract. Meanwhile, the expression of early activation markers was observed across B-cell subsets in animals (mainly controls) exhibiting higher viral loads. B-cell phenotypic clustering was also concordant with the degree of lower respiratory tract inflammation, which was reduced in almost all vaccinees in comparison to controls. Together, these results suggest that in the rhesus macaque

model, ChAdOx1 nCoV-19-induced immunity to SARS-CoV-2-associated disease was largely mediated by the humoral response. In a smaller follow-up study examining the effects of prime-boost intranasal delivery of ChAdOx1 nCoV-19, we obtained evidence suggesting that delivery of the vaccine to the upper respiratory tract may lead to reduced nasal shedding. Moreover, we again observed a potential association between multifunctional antibody responses—particularly those detected in respiratory tract samples—and virological outcomes post challenge. However, future studies conducted with larger group sizes (greater than n=4 per group) will be required to substantiate these hypotheses, as nearly all comparisons failed to meet statistical significance. Ideally, in order to elucidate the relative roles of vaccine-elicited cellular and humoral immune responses in conferring protection in the rhesus macaque model, we would perform follow up T- and B-cell depletion or antibody/T-cell transfer studies. However, the optimisation and implementation of such experiments are challenging, particularly in non-human primates. Furthermore, depletion studies carried out in unvaccinated rhesus macaques have shown only moderate impacts on disease pathogenesis following SARS-CoV-2 infection, suggesting that only subtle differences might be expected in a vaccination-depletion study, thus complicating the interpretability of results[82].

Overall, the ability to extrapolate findings from much of our SARS-CoV-2-related work in NHPs was hindered by reliance upon the rhesus macaque model. Rhesus macaques are more readily available than many other NHP species and also display susceptibility to SARS-CoV-2 infection. Thus, throughout the pandemic, they were a principal model utilised for our studies of the virus. However, the mild nature of clinical disease and the rapidity of viral clearance in these animals, highlight distinct features of pathogenesis. Indeed, our comparative characterisation of SARS-CoV-2 infection in aged versus subadult rhesus macaques illustrated this phenomenon. Although

the older animals exhibited evidence of delayed cellular immune responses and prolonged inflammation following infection, the absence of clear age-related differences in the clinical course of disease confirmed that this model is unable to recapitulate the full spectrum of COVID-19 disease severity observed in humans. Therefore, continued application of the rhesus macaque model for future studies on SARS-CoV-2 should be carefully considered. Baboons and African green monkeys have shown increased clinical signs associated with SARS-CoV-2 infection, and the former demonstrated an age-related increase in disease severity in one study[513,514]. These species, although less accessible, may serve as more representative models in which to conduct COVID-19 studies in the future.

7.3 Concluding remarks

The studies presented in this dissertation span the development of a ChAdOx1-vectored vaccine for Lassa fever, as well as the characterisation of vaccine-induced and host immune responses in the rhesus macaque model of SARS-CoV-2. Although not fully complete, evaluations of ChAdOx1-Lassa-GPC suggest that it is a promising vaccine candidate warranting further assessment in heterologous challenge models and in phase I clinical trials. It is unclear if a universal LASV vaccine will be achievable—these data may only be obtainable from future large-scale efficacy trials carried out in endemic regions of West Africa. In the meantime, additional epidemiological studies are required to elucidate dominant routes of transmission (for both rodent-to-human and human-to-human transmission events) to aid in the implementation of alternative, targeted countermeasures, such as vector control.

The research presented in this dissertation on SARS-CoV-2 contributed to the advancement of ChAdOx1 nCoV-19 to testing in phase I clinical trials during the early stages of the COVID-19

pandemic. Moreover, detailed immunological profiling revealed a potential association between the humoral response and protection, while also suggesting that intranasal delivery of the vaccine may improve performance by promoting a reduction in nasal shedding. Intranasal boosting of human populations previously immunised against COVID-19 may thus be advantageous to further attenuate transmission.

More broadly, this work demonstrates the value and limitations of using preclinical models, specifically NHPs, to address immunological questions. While data from NHPs is of considerable value given its perceived translatability to humans, our research shows that due to ethical, cost, and logistical restrictions, these studies are frequently underpowered. Consequently, clear conclusions regarding vaccine-induced mechanisms of immunity and correlates of protection are often not discernible from these experiments. A potential consideration for future research would be the application of high-throughput "-omics" tools and computational modelling, which may enable the verification of purported associations or correlations across an extensive number of variables and multiple systems. Doing so may provide an alternative method for the rigorous confirmation of trends documented in animal studies when larger group sizes are not feasible. Employment of such strategies will be considered in the planning of future NHP experiments to enable more informed predictive modelling of outcomes in humans. In summary, the studies presented here, although diverse in focus, collectively highlight both the utility and shortcomings of the application of animal models to studies of vaccine efficacy or disease pathogenesis. However, with more targeted study designs or novel approaches to data collection and analyses, these preclinical investigations will remain a critical part of the early scientific response to outbreaks.

References

1 Pollard, A. J. & Bijker, E. M. A guide to vaccinology: from basic principles to new developments. *Nature Reviews Immunology* **21**, 83-100, doi:10.1038/s41577-020-00479-7 (2021).

2 Sprent, J. & Surh, C. D. T cell memory. *Annual Review of Immunology* **20**, 551-579, doi:10.1146/annurev.immunol.20.100101.151926 (2002).

3 Alcover, A., Alarcón, B. & Di Bartolo, V. Cell biology of T cell receptor expression and regulation. *Annu Rev Immunol* **36**, 103-125, doi:10.1146/annurev-immunol-042617-053429 (2018).

4 Jenkins, M. K. *et al.* In vivo activation of antigen-specific CD4 T cells. *Annu Rev Immunol* **19**, 23-45, doi:10.1146/annurev.immunol.19.1.23 (2001).

5 Banchereau, J. & Steinman, R. M. Dendritic cells and the control of immunity. *Nature* **392**, 245-252, doi:10.1038/32588 (1998).

6 Banchereau, J. *et al.* Immunobiology of dendritic cells. *Annu Rev Immunol* **18**, 767-811, doi:10.1146/annurev.immunol.18.1.767 (2000).

7 Liu, Y. J., Kanzler, H., Soumelis, V. & Gilliet, M. Dendritic cell lineage, plasticity and cross-regulation. *Nat Immunol* **2**, 585-589, doi:10.1038/89726 (2001).

8 De Smedt, T. *et al.* Regulation of dendritic cell numbers and maturation by lipopolysaccharide in vivo. *J Exp Med* **184**, 1413-1424, doi:10.1084/jem.184.4.1413 (1996).

9 Chambers, C. A. & Allison, J. P. Costimulatory regulation of T cell function. *Curr Opin Cell Biol* **11**, 203-210, doi:10.1016/s0955-0674(99)80027-1 (1999).

10 Watts, T. H. & DeBenedette, M. A. T cell co-stimulatory molecules other than CD28. *Curr Opin Immunol* **11**, 286-293, doi:10.1016/s0952-7915(99)80046-6 (1999).

11 Coyle, A. J. & Gutierrez-Ramos, J. C. The expanding B7 superfamily: increasing complexity in costimulatory signals regulating T cell function. *Nat Immunol* **2**, 203-209, doi:10.1038/85251 (2001).

12 Bromley, S. K. *et al.* The immunological synapse. *Annu Rev Immunol* **19**, 375-396, doi:10.1146/annurev.immunol.19.1.375 (2001).

13 Monks, C. R. F., Freiberg, B. A., Kupfer, H., Sciaky, N. & Kupfer, A. Three-dimensional segregation of supramolecular activation clusters in T cells. *Nature* **395**, 82-86, doi:10.1038/25764 (1998).

14 Grakoui, A. *et al.* The immunological synapse: a molecular machine controlling T cell activation. *Science* **285**, 221-227, doi:10.1126/science.285.5425.221 (1999).

15 Lanzavecchia, A. & Sallusto, F. Dynamics of T lymphocyte responses: intermediates, effectors, and memory cells. *Science* **290**, 92-97, doi:10.1126/science.290.5489.92 (2000).

16 Luckheeram, R. V., Zhou, R., Verma, A. D. & Xia, B. $CD4^+$T cells: differentiation and functions. *Clin Dev Immunol* **2012**, 925135, doi:10.1155/2012/925135 (2012).

17 Raphael, I., Joern, R. R. & Forsthuber, T. G. Memory CD4(+) T cells in immunity and autoimmune diseases. *Cells* **9**, doi:10.3390/cells9030531 (2020).

18 Korn, T., Bettelli, E., Oukka, M. & Kuchroo, V. K. IL-17 and Th17 cells. *Annu Rev Immunol* **27**, 485-517, doi:10.1146/annurev.immunol.021908.132710 (2009).

19 Sakaguchi, S. Naturally arising Foxp3-expressing CD25+CD4+ regulatory T cells in immunological tolerance to self and non-self. *Nat Immunol* **6**, 345-352, doi:10.1038/ni1178 (2005).

20 Crotty, S. A brief history of T cell help to B cells. *Nature Reviews Immunology* **15**, 185-189, doi:10.1038/nri3803 (2015).

21 Schmitt, E., Klein, M. & Bopp, T. Th9 cells, new players in adaptive immunity. *Trends Immunol* **35**, 61-68, doi:10.1016/j.it.2013.10.004 (2014).

22 Jia, L. & Wu, C. The biology and functions of Th22 cells. *Adv Exp Med Biol* **841**, 209-230, doi:10.1007/978-94-017-9487-9_8 (2014).

23 Zhang, N. & Bevan, M. J. CD8(+) T cells: foot soldiers of the immune system. *Immunity* **35**, 161-168, doi:10.1016/j.immuni.2011.07.010 (2011).

24 Butz, E. A. & Bevan, M. J. Massive expansion of antigen-specific CD8+ T cells during an acute virus infection. *Immunity* **8**, 167-175, doi:10.1016/s1074-7613(00)80469-0 (1998).

25 Parish, I. A. & Kaech, S. M. Diversity in CD8(+) T cell differentiation. *Current opinion in immunology* **21**, 291-297, doi:10.1016/j.coi.2009.05.008 (2009).

26 Hickman, H. D. *et al.* CXCR3 chemokine receptor enables local CD8(+) T cell migration for the destruction of virus-infected cells. *Immunity* **42**, 524-537, doi:10.1016/j.immuni.2015.02.009 (2015).

27 Andersen, M. H., Schrama, D., Thor Straten, P. & Becker, J. C. Cytotoxic T cells. *J Invest Dermatol* **126**, 32-41, doi:10.1038/sj.jid.5700001 (2006).

28 Stipp, S. R., Iniguez, A., Wan, F. & Wodarz, D. Timing of CD8 T cell effector responses in viral infections. *R Soc Open Sci* **3**, 150661-150661, doi:10.1098/rsos.150661 (2016).

29 Mescher, M. F. *et al.* Signals required for programming effector and memory development by CD8+ T cells. *Immunol Rev* **211**, 81-92, doi:10.1111/j.0105-2896.2006.00382.x (2006).

30 Sallusto, F., Lenig, D., Förster, R., Lipp, M. & Lanzavecchia, A. Two subsets of memory T lymphocytes with distinct homing potentials and effector functions. *Nature* **401**, 708-712, doi:10.1038/44385 (1999).

31 Gebhardt, T. *et al.* Memory T cells in nonlymphoid tissue that provide enhanced local immunity during infection with herpes simplex virus. *Nat Immunol* **10**, 524-530, doi:10.1038/ni.1718 (2009).

32 Sathaliyawala, T. *et al.* Distribution and compartmentalization of human circulating and tissue-resident memory T cell subsets. *Immunity* **38**, 187-197, doi:10.1016/j.immuni.2012.09.020 (2013).

33 Stiehm, E. R. Joseph A. Bellanti (ed) immunology IV: clinical applications in health and disease. *J Clin Immunol* **32**, 647, doi:10.1007/s10875-012-9648-5 (2012).

34 Zou, Y.-R., Grimaldi, C. & Diamond, B. in *Kelley and Firestein's Textbook of Rheumatology (Tenth Edition)* (eds Gary S. Firestein *et al.*) 207-230.e203 (Elsevier, 2017).

35 Lee, S. K. *et al.* B cell priming for extrafollicular antibody responses requires Bcl-6 expression by T cells. *J Exp Med* **208**, 1377-1388, doi:10.1084/jem.20102065 (2011).

36 Vos, Q., Lees, A., Wu, Z. Q., Snapper, C. M. & Mond, J. J. B-cell activation by T-cell-independent type 2 antigens as an integral part of the humoral immune response to pathogenic microorganisms. *Immunol Rev* **176**, 154-170, doi:10.1034/j.1600-065x.2000.00607.x (2000).

37 Kurosaki, T., Kometani, K. & Ise, W. Memory B cells. *Nature Reviews Immunology* **15**, 149-159, doi:10.1038/nri3802 (2015).

38 Lu, L. L., Suscovich, T. J., Fortune, S. M. & Alter, G. Beyond binding: antibody effector functions in infectious diseases. *Nature Reviews Immunology* **18**, 46-61, doi:10.1038/nri.2017.106 (2018).

39 Brack, C., Hirama, M., Lenhard-Schuller, R. & Tonegawa, S. A complete immunoglobulin gene is created by somatic recombination. *Cell* **15**, 1-14, doi:10.1016/0092-8674(78)90078-8 (1978).

40 Li, Z., Woo, C. J., Iglesias-Ussel, M. D., Ronai, D. & Scharff, M. D. The generation of antibody diversity through somatic hypermutation and class switch recombination. *Genes Dev* **18**, 1-11, doi:10.1101/gad.1161904 (2004).

41 Janda, A., Bowen, A., Greenspan, N. S. & Casadevall, A. Ig constant region effects on variable region structure and function. *Front. Microbiol.* **7**, doi:10.3389/fmicb.2016.00022 (2016).

42 Park, H. I., Yoon, H. W. & Jung, S. T. The highly evolvable antibody Fc domain. *Trends Biotechnol* **34**, 895-908, doi:10.1016/j.tibtech.2016.04.005 (2016).

43 Alharbi, N. K. *et al.* ChAdOx1 and MVA based vaccine candidates against MERS-CoV elicit neutralising antibodies and cellular immune responses in mice. *Vaccine* **35**, 3780-3788, doi:10.1016/j.vaccine.2017.05.032 (2017).

44 Onoue, K., Grossberg, A. L., Yagi, Y. & Pressman, D. Immunoglobulin M antibodies with ten combining sites. *Science* **162**, 574-576, doi:10.1126/science.162.3853.574 (1968).

45 Ying, T., Gong, R., Ju, T. W., Prabakaran, P. & Dimitrov, D. S. Engineered Fc based antibody domains and fragments as novel scaffolds. *Biochim Biophys Acta* **1844**, 1977-1982, doi:10.1016/j.bbapap.2014.04.018 (2014).

46 Bengtén, E. *et al.* in *Origin and Evolution of the Vertebrate Immune System* (eds Louis Du Pasquier & Gary W. Litman) 189-219 (Springer Berlin Heidelberg, 2000).

47 Willey, S. & Aasa-Chapman, M. M. I. Humoral immunity to HIV-1: neutralisation and antibody effector functions. *Trends in Microbiology* **16**, 596-604, doi:https://doi.org/10.1016/j.tim.2008.08.008 (2008).

48 Pang, N. Y.-L., Pang, A. S.-R., Chow, V. T. & Wang, D.-Y. Understanding neutralising antibodies against SARS-CoV-2 and their implications in clinical practice. *Military Medical Research* **8**, 47, doi:10.1186/s40779-021-00342-3 (2021).

49 Diebolder, C. A. *et al.* Complement is activated by IgG hexamers assembled at the cell surface. *Science* **343**, 1260-1263, doi:10.1126/science.1248943 (2014).

50 Merle, N. S., Church, S. E., Fremeaux-Bacchi, V. & Roumenina, L. T. Complement system part I - molecular mechanisms of activation and regulation. *Front Immunol* **6**, 262, doi:10.3389/fimmu.2015.00262 (2015).

51 Merle, N. S., Noe, R., Halbwachs-Mecarelli, L., Fremeaux-Bacchi, V. & Roumenina, L. T. Complement system part II: role in immunity. *Front Immunol* **6**, 257, doi:10.3389/fimmu.2015.00257 (2015).

52 Hanton, G. & Pastoret, P. P. The reaction of antibody-dependent cell-mediated cytotoxicity (ADCC). *Ann Rech Vet* **15**, 443-454 (1984).

53 Reichert, J. M. Antibody Fc: linking adaptive and innate immunity. *mAbs* **6**, 619-621, doi:10.4161/mabs.28617 (2014).

54 Kamen, L. *et al.* A novel method for determining antibody-dependent cellular phagocytosis. *J Immunol Methods* **468**, 55-60, doi:10.1016/j.jim.2019.03.001 (2019).

55 Bergtold, A., Desai, D. D., Gavhane, A. & Clynes, R. Cell surface recycling of internalized antigen permits dendritic cell priming of B cells. *Immunity* **23**, 503-514, doi:10.1016/j.immuni.2005.09.013 (2005).

56 Rittirsch, D. *et al.* Cross-talk between TLR4 and FcgammaReceptorIII (CD16) pathways. *PLoS Pathog.* **5**, e1000464-e1000464, doi:10.1371/journal.ppat.1000464 (2009).

57 Anthony, R. M., Wermeling, F., Karlsson, M. C. & Ravetch, J. V. Identification of a receptor required for the anti-inflammatory activity of IVIG. *Proc Natl Acad Sci U S A* **105**, 19571-19578, doi:10.1073/pnas.0810163105 (2008).

58 Halstead, S. B., Mahalingam, S., Marovich, M. A., Ubol, S. & Mosser, D. M. Intrinsic antibody-dependent enhancement of microbial infection in macrophages: disease regulation by immune complexes. *Lancet Infect Dis* **10**, 712-722, doi:10.1016/S1473-3099(10)70166-3 (2010).

59 Ayala-Nunez, N. V. *et al.* How antibodies alter the cell entry pathway of dengue virus particles in macrophages. *Scientific Reports* **6**, 28768, doi:10.1038/srep28768 (2016).

60 Beltramello, M. *et al.* The human immune response to Dengue virus is dominated by highly cross-reactive antibodies endowed with neutralizing and enhancing activity. *Cell Host Microbe* **8**, 271-283, doi:10.1016/j.chom.2010.08.007 (2010).

61 Dejnirattisai, W. *et al.* Dengue virus sero-cross-reactivity drives antibody-dependent enhancement of infection with zika virus. *Nature Immunology* **17**, 1102-1108, doi:10.1038/ni.3515 (2016).

62 Hawkes, R. A. Enhancement of the infectivity of arboviruses by specific antisera produced in domestic fowls. *Aust J Exp Biol Med Sci* **42**, 465-482, doi:10.1038/icb.1964.44 (1964).

63 Polack, F. P. *et al.* A role for immune complexes in enhanced respiratory syncytial virus disease. *J Exp Med* **196**, 859-865, doi:10.1084/jem.20020781 (2002).

64 Palm, A.-K. E. & Henry, C. Remembrance of things past: long-term B cell memory after infection and vaccination. *Front. Immunol.* **10**, doi:10.3389/fimmu.2019.01787 (2019).

65 Qian, Y. *et al.* Elucidation of seventeen human peripheral blood B-cell subsets and quantification of the tetanus response using a density-based method for the automated identification of cell populations in multidimensional flow cytometry data. *Cytometry B Clin Cytom* **78 Suppl 1**, S69-82, doi:10.1002/cyto.b.20554 (2010).

66 Wrammert, J. *et al.* Rapid and massive virus-specific plasmablast responses during acute dengue virus infection in humans. *J Virol* **86**, 2911-2918, doi:10.1128/jvi.06075-11 (2012).

67 Blink, E. J. *et al.* Early appearance of germinal center-derived memory B cells and plasma cells in blood after primary immunization. *J Exp Med* **201**, 545-554, doi:10.1084/jem.20042060 (2005).

68 Zehentmeier, S. *et al.* Static and dynamic components synergize to form a stable survival niche for bone marrow plasma cells. *Eur J Immunol* **44**, 2306-2317, doi:10.1002/eji.201344313 (2014).

69 Brynjolfsson, S. F., Mohaddes, M., Kärrholm, J. & Wick, M. J. Long-lived plasma cells in human bone marrow can be either $CD19^{+}$ or $CD19^{-}$. *Blood Adv* **1**, 835-838, doi:10.1182/bloodadvances.2017004481 (2017).

70 McHeyzer-Williams, L. J. & McHeyzer-Williams, M. G. Antigen-specific memory B cell development. *Annu Rev Immunol* **23**, 487-513, doi:10.1146/annurev.immunol.23.021704.115732 (2005).

71 Amanna, I. J., Carlson, N. E. & Slifka, M. K. Duration of humoral immunity to common viral and vaccine antigens. *N Engl J Med* **357**, 1903-1915, doi:10.1056/NEJMoa066092 (2007).

72 Ise, W. *et al.* T follicular helper cell-germinal center B cell interaction strength regulates entry into plasma cell or recycling germinal center cell fate. *Immunity* **48**, 702-715.e704, doi:10.1016/j.immuni.2018.03.027 (2018).

73 Chen, X., Bailleux, F., Desai, K., Qin, L. & Dunning, A. J. A threshold method for immunological correlates of protection. *BMC Medical Research Methodology* **13**, 29, doi:10.1186/1471-2288-13-29 (2013).

74 Plotkin, S. A. & Gilbert, P. B. Nomenclature for immune correlates of protection after vaccination. *Clinical Infectious Diseases* **54**, 1615-1617, doi:10.1093/cid/cis238 (2012).

75 Plotkin Stanley, A. Correlates of protection induced by vaccination. *Clinical and Vaccine Immunology* **17**, 1055-1065, doi:10.1128/CVI.00131-10 (2010).

76 Krammer, F. A correlate of protection for SARS-CoV-2 vaccines is urgently needed. *Nature Medicine* **27**, 1147-1148, doi:10.1038/s41591-021-01432-4 (2021).

77 Folegatti, P. M. *et al.* A systematic review on malaria sero-epidemiology studies in the Brazilian Amazon: insights into immunological markers for exposure and protection. *Malar J* **16**, 107, doi:10.1186/s12936-017-1762-7 (2017).

78 Aziz, N. A. *et al.* Seroprevalence and correlates of SARS-CoV-2 neutralizing antibodies from a population-based study in Bonn, Germany. *Nat. Commun.* **12**, 2117, doi:10.1038/s41467-021-22351-5 (2021).

79 Haney, D. J., Lock, M. D., Simon, J. K., Harris, J. & Gurwith, M. Antibody-based correlates of protection against cholera analysis of a challenge study in a cholera-naïve population. *Clin Vaccine Immunol* **24**, e00098-00017, doi:10.1128/CVI.00098-17 (2017).

80 Zhao, J. *et al.* Airway memory $CD4^+$ T cells mediate protective immunity against emerging respiratory coronaviruses. *Immunity* **44**, 1379-1391, doi:10.1016/j.immuni.2016.05.006 (2016).

81 Corbett Kizzmekia, S. *et al.* Immune correlates of protection by mRNA-1273 vaccine against SARS-CoV-2 in nonhuman primates. *Science* **373**, eabj0299, doi:10.1126/science.abj0299.

82 McMahan, K. *et al.* Correlates of protection against SARS-CoV-2 in rhesus macaques. *Nature* **590**, 630-634, doi:10.1038/s41586-020-03041-6 (2021).

83 Coudeville, L. *et al.* Relationship between haemagglutination-inhibiting antibody titres and clinical protection against influenza: development and application of a bayesian random-effects model. *BMC Medical Research Methodology* **10**, 18, doi:10.1186/1471-2288-10-18 (2010).

84 Black, S. *et al.* Hemagglutination inhibition antibody titers as a correlate of protection for inactivated influenza vaccines in children. *Pediatr Infect Dis J* **30**, 1081-1085, doi:10.1097/INF.0b013e3182367662 (2011).

85 Forrest Bruce, D. *et al.* Correlation of cellular immune responses with protection against culture-confirmed influenza virus in young children. *Clinical and Vaccine Immunology* **15**, 1042-1053, doi:10.1128/CVI.00397-07 (2008).

86 Keating, S. M. *et al.* Durable human memory T cells quantifiable by cultured enzyme-linked immunospot assays are induced by heterologous prime boost immunization and correlate with protection against malaria. *J Immunol* **175**, 5675-5680, doi:10.4049/jimmunol.175.9.5675 (2005).

87 Sei, J. J. *et al.* Effector and central memory poly-functional $CD4^+$ and $CD8^+$ T cells are boosted upon ZOSTAVAX(®) vaccination. *Front Immunol* **6**, 553, doi:10.3389/fimmu.2015.00553 (2015).

88 Dan, J. M. *et al.* A cytokine-independent approach to identify antigen-specific human germinal center T follicular helper cells and rare antigen-specific CD4+ T cells in blood. *J Immunol* **197**, 983-993, doi:10.4049/jimmunol.1600318 (2016).

89 Bowyer, G. *et al.* Activation-induced markers detect vaccine-specific $CD4^+$ T cell responses not measured by assays conventionally used in clinical trials. *Vaccines (Basel)* **6**, doi:10.3390/vaccines6030050 (2018).

90 Dileepan, T. *et al.* MHC class II tetramers engineered for enhanced binding to CD4 improve detection of antigen-specific T cells. *Nature Biotechnology* **39**, 943-948, doi:10.1038/s41587-021-00893-9 (2021).

91 Novak, E. J., Liu, A. W., Nepom, G. T. & Kwok, W. W. MHC class II tetramers identify peptide-specific human CD4+ T cells proliferating in response to influenza A antigen. *The Journal of Clinical Investigation* **104**, R63-R67, doi:10.1172/JCI8476 (1999).

92 Raeven, R. H. M., van Riet, E., Meiring, H. D., Metz, B. & Kersten, G. F. A. Systems vaccinology and big data in the vaccine development chain. *Immunology* **156**, 33-46, doi:10.1111/imm.13012 (2019).

93 Querec, T. D. *et al.* Systems biology approach predicts immunogenicity of the yellow fever vaccine in humans. *Nature Immunology* **10**, 116-125, doi:10.1038/ni.1688 (2009).

94 Nakaya, H. I. *et al.* Systems analysis of immunity to influenza vaccination across multiple years and in diverse populations reveals shared molecular signatures. *Immunity* **43**, 1186-1198, doi:10.1016/j.immuni.2015.11.012 (2015).

95 Lasaro, M. O. & Ertl, H. C. J. New insights on adenovirus as vaccine vectors. *Mol. Ther.* **17**, 1333-1339, doi:10.1038/mt.2009.130 (2009).

96 Dudareva, M. *et al.* Prevalence of serum neutralizing antibodies against chimpanzee adenovirus 63 and human adenovirus 5 in Kenyan children, in the context of vaccine vector efficacy. *Vaccine* **27**, 3501-3504, doi:10.1016/j.vaccine.2009.03.080 (2009).

97 Buchbinder, S. P. *et al.* Efficacy assessment of a cell-mediated immunity HIV-1 vaccine (the Step Study): a double-blind, randomised, placebo-controlled, test-of-concept trial. *Lancet* **372**, 1881-1893, doi:10.1016/s0140-6736(08)61591-3 (2008).

98 Tatsis, N. *et al.* Chimpanzee-origin adenovirus vectors as vaccine carriers. *Gene Ther.* **13**, 421-429, doi:10.1038/sj.gt.3302675 (2006).

99 Dicks, M. D. J. *et al.* A novel chimpanzee adenovirus vector with low human seroprevalence: improved systems for vector derivation and comparative immunogenicity. *PLoS One* **7**, 12, doi:10.1371/journal.pone.0040385 (2012).

100 Horwitz, W. W. a. M. in *Fields Virology* (ed DM Knipe BN Fields, PM Howley) 1836-1844 (Lippincott-Raven, 2007).

101 Crawford-Miksza, L. & Schnurr, D. P. Analysis of 15 adenovirus hexon proteins reveals the location and structure of seven hypervariable regions containing serotype-specific residues. *J Virol* **70**, 1836-1844, doi:10.1128/JVI.70.3.1836-1844.1996 (1996).

102 Zhu, J., Huang, X. & Yang, Y. Innate immune response to adenoviral vectors is mediated by both Toll-like receptor-dependent and -independent pathways. *J Virol* **81**, 3170-3180, doi:10.1128/jvi.02192-06 (2007).

103 Shiver, J. W. *et al.* Replication-incompetent adenoviral vaccine vector elicits effective anti-immunodeficiency-virus immunity. *Nature* **415**, 331-335, doi:10.1038/415331a (2002).

104 Crosby, C. M., Nehete, P., Sastry, K. J. & Barry, M. A. Amplified and persistent immune responses generated by single-cycle replicating adenovirus vaccines. *J Virol* **89**, 669-675, doi:10.1128/jvi.02184-14 (2015).

105 Warimwe, G. M. *et al.* Chimpanzee adenovirus vaccine provides multispecies protection against rift valley fever. *Scientific Reports* **6**, 7, doi:10.1038/srep20617 (2016).

106 Doremalen, N. v. *et al.* A single dose of ChAdOx1 MERS provides protective immunity in rhesus macaques. *Science Advances* **6**, eaba8399, doi:doi:10.1126/sciadv.aba8399 (2020).

107 Lopez-Camacho, C. *et al.* Rational Zika vaccine design via the modulation of antigen membrane anchors in chimpanzee adenoviral vectors. *Nat. Commun.* **9**, 11, doi:10.1038/s41467-018-04859-5 (2018).

108 Stylianou, E. *et al.* Identification and evaluation of novel protective antigens for the development of a candidate tuberculosis subunit vaccine. *Infect. Immun.* **86**, 16, doi:10.1128/iai.00014-18 (2018).

109 van Doremalen, N. *et al.* A single-dose ChAdOx1-vectored vaccine provides complete protection against Nipah Bangladesh and Malaysia in Syrian golden hamsters. *Plos Neglect. Trop. Dis.* **13**, e0007462-e0007462, doi:10.1371/journal.pntd.0007462 (2019).

110 Fischer, R. J. *et al.* ChAdOx1-vectored Lassa fever vaccine elicits a robust cellular and humoral immune response and protects guinea pigs against lethal Lassa virus challenge. *npj Vaccines* **6**, 32, doi:10.1038/s41541-021-00291-x (2021).

111 van Doremalen, N. *et al.* ChAdOx1 nCoV-19 vaccine prevents SARS-CoV-2 pneumonia in rhesus macaques. *Nature* **586**, 578-582, doi:10.1038/s41586-020-2608-y (2020).

112 Doremalen, N. v. *et al.* Intranasal ChAdOx1 nCoV-19/AZD1222 vaccination reduces viral shedding after SARS-CoV-2 D614G challenge in preclinical models. *Science Translational Medicine* **13**, eabh0755, doi:doi:10.1126/scitranslmed.abh0755 (2021).

113 Bosaeed, M. *et al.* Safety and immunogenicity of ChAdOx1 MERS vaccine candidate in healthy Middle Eastern adults (MERS002): an open-label, non-randomised, dose-escalation, phase 1b trial. *Lancet Microbe*, doi:10.1016/s2666-5247(21)00193-2 (2021).

114 Folegatti, P. M. *et al.* A single dose of ChAdOx1 CHIK vaccine induces neutralizing antibodies against four chikungunya virus lineages in a phase 1 clinical trial. *Nat Commun* **12**, 4636, doi:10.1038/s41467-021-24906-y (2021).

115 Antrobus, R. D. *et al.* Clinical assessment of a novel recombinant simian adenovirus ChAdOx1 as a vectored vaccine expressing conserved influenza A antigens. *Mol. Ther.* **22**, 668-674, doi:10.1038/mt.2013.284 (2014).

116 Ramasamy, M. N. *et al.* Safety and immunogenicity of ChAdOx1 nCoV-19 vaccine administered in a prime-boost regimen in young and old adults (COV002): a single-blind, randomised, controlled, phase 2/3 trial. *Lancet* **396**, 1979-1993, doi:10.1016/s0140-6736(20)32466-1 (2021).

117 Falsey, A. R. *et al.* Phase 3 safety and efficacy of AZD1222 (ChAdOx1 nCoV-19) covid-19 vaccine. *N. Engl. J. Med.* **385**, 2348-2360, doi:10.1056/NEJMoa2105290 (2021).

118 Clemens, S. A. C. *et al.* Efficacy of ChAdOx1 nCoV-19 (AZD1222) vaccine against SARS-CoV-2 lineages circulating in Brazil. *Nat. Commun.* **12**, 5861, doi:10.1038/s41467-021-25982-w (2021).

119 Richmond, J. K. & Baglole, D. J. Lassa fever: epidemiology, clinical features, and social consequences. *Br. Med. J.* **327**, 1271-1275, doi:10.1136/bmj.327.7426.1271 (2003).

120 Bowen, M. D. *et al.* Genetic diversity among Lassa virus strains. *J Virol* **74**, 6992-7004, doi:10.1128/jvi.74.15.6992-7004.2000 (2000).

121 Safronetz, D. *et al.* Detection of Lassa virus, Mali. *Emerg Infect Dis* **16**, 1123-1126, doi:10.3201/eid1607.100146 (2010).

122 Kouadio, L. *et al.* Lassa virus in multimammate rats, Cote d'Ivoire, 2013. *Emerg Infect Dis* **21**, 1481-1483, doi:10.3201/eid2108.150312 (2015).

123 Whitmer, S. L. M. *et al.* New lineage of Lassa virus, Togo, 2016. *Emerg Infect Dis* **24**, 599-602, doi:10.3201/eid2403.171905 (2018).

124 McCormick, J. B., Webb, P. A., Krebs, J. W., Johnson, K. M. & Smith, E. S. A prospective-sudy of the epidemiology and Ecology of Lassa fever. *J. Infect. Dis.* **155**, 437-444, doi:10.1093/infdis/155.3.437 (1987).

125 Gibb, R., Moses, L. M., Redding, D. W. & Jones, K. E. Understanding the cryptic nature of Lassa fever in west Africa. *Pathog. Glob. Health* **111**, 276-288, doi:10.1080/20477724.2017.1369643 (2017).

126 Yaro, C. A. *et al.* Infection pattern, case fatality rate and spread of Lassa virus in Nigeria. *BMC Infectious Diseases* **21**, 149, doi:10.1186/s12879-021-05837-x (2021).

127 Redding, D. W. *et al.* Geographical drivers and climate-linked dynamics of Lassa fever in Nigeria. *Nat. Commun.* **12**, 5759, doi:10.1038/s41467-021-25910-y (2021).

128 Olayemi, A. *et al.* New hosts of the Lassa virus. *Scientific Reports* **6**, 6, doi:10.1038/srep25280 (2016).

129 Lecompte, E. *et al.* Mastomys natalensis and Lassa fever, west Africa. *Emerg Infect Dis* **12**, 1971-1974 (2006).

130 Ogbu, O., Ajuluchukwu, E. & Uneke, C. J. Lassa fever in west African sub-region: an overview. *J Vector Borne Dis* **44**, 1-11 (2007).

131 Ajayi, N. A. *et al.* Containing a Lassa fever epidemic in a resource-limited setting: outbreak description and lessons learned from Abakaliki, Nigeria (January-March 2012). *Int J Infect Dis* **17**, e1011-1016, doi:10.1016/j.ijid.2013.05.015 (2013).

132 in *Information Evidence and Research* (World Health Organization, 2018).

133 Asogun, D. A., Günther, S., Akpede, G. O., Ihekweazu, C. & Zumla, A. Lassa Fever: epidemiology, clinical features, diagnosis, management and prevention. *Infect Dis Clin North Am* **33**, 933-951, doi:10.1016/j.idc.2019.08.002 (2019).

134 Merson, L. *et al.* Clinical characterization of Lassa fever: A systematic review of clinical reports and research to inform clinical trial design. *Plos Neglect. Trop. Dis.* **15**, e0009788, doi:10.1371/journal.pntd.0009788 (2021).

135 Frame, J. D., Baldwin, J. M., Gocke, D. J. & Troup, J. M. Lassa Fever, a new virus disease of man from west Africa .1. clinical description and pathological findings. *Am. J. Trop. Med. Hyg.* **19**, 670-&, doi:10.4269/ajtmh.1970.19.670 (1970).

136 McCormick, J. B. *et al.* A case-control study of the clinical-diagnosis and course of Lassa fever. *J. Infect. Dis.* **155**, 445-455, doi:10.1093/infdis/155.3.445 (1987).

137 Price, M. E., Fisherhoch, S. P., Craven, R. B. & McCormick, J. B. A prospective-study of maternal and fetal-outcome in acute Lassa fever infection during pregnancy. *Br. Med. J.* **297**, 584-587, doi:10.1136/bmj.297.6648.584 (1988).

138 Kayem, N. D. *et al.* Lassa fever in pregnancy: a systematic review and meta-analysis. *Trans. Roy. Soc. Trop. Med. Hyg.* **114**, 385-396, doi:10.1093/trstmh/traa011 (2020).

139 Roberts, L. Nigeria hit by unprecedented Lassa fever outbreak. *Science* **359**, 1201-1202, doi:10.1126/science.359.6381.1201 (2018).

140 Horton, L. E., Sullivan, B., Garry, R. F., Grant, D. S. & Oldstone, M. B. Endothelial dysfunction in the pathogenesis of acute Lassa Fever. *The Journal of Immunology* **200**, 126.122 (2018).

141 Horton, L. E. *et al.* Endotheliopathy and platelet dysfunction as hallmarks of fatal Lassa fever. *Emerg Infect Dis* **26**, 2625-2637, doi:10.3201/eid2611.191694 (2020).

142 McCormick, J. B. *et al.* Lassa fever - effective therapy with ribavirin. *N. Engl. J. Med.* **314**, 20-26, doi:10.1056/nejm198601023140104 (1986).

143 Shieh, W.-J. *et al.* Pathology and pathogenesis of Lassa fever: novel immunohistochemical findings in fatal cases and clinico-pathologic correlation. *Clinical Infectious Diseases*, ciab719, doi:10.1093/cid/ciab719 (2021).

144 Price, M. E., Fisher-Hoch, S. P., Craven, R. B. & McCormick, J. B. A prospective study of maternal and fetal outcome in acute Lassa fever infection during pregnancy. *BMJ: British Medical Journal* **297**, 584-587 (1988).

145 Cummins, D. *et al.* Acute sensorineural deafness in Lassa fever. *JAMA-J. Am. Med. Assoc.* **264**, 2093-2096 (1990).

146 Mateer, E. J., Huang, C., Shehu, N. Y. & Paessler, S. Lassa fever-induced sensorineural hearing loss: A neglected public health and social burden. *Plos Neglect. Trop. Dis.* **12**, 11, doi:10.1371/journal.pntd.0006187 (2018).

147 Cashman, K. A. *et al.* Immune-mediated systemic vasculitis as the proposed cause of sudden-onset sensorineural hearing loss following Lassa virus exposure in cynomolgus macaques. *MBio* **9**, e01896-01818 (2018).

148 Salam, A. P. *et al.* Time to reconsider the role of ribavirin in Lassa fever. *Plos Neglect. Trop. Dis.* **15**, e0009522, doi:10.1371/journal.pntd.0009522 (2021).

149 Safronetz, D. *et al.* The broad-spectrum antiviral favipiravir protects guinea pigs from lethal Lassa virus infection post-disease onset. *Scientific Reports* **5**, 11, doi:10.1038/srep14775 (2015).

150 Rosenke, K. *et al.* Use of favipiravir to treat Lassa virus infection in macaques. *Emerg Infect Dis* **24**, 1696-1699, doi:10.3201/eid2409.180233 (2018).

151 Raabe, V. N. *et al.* Favipiravir and ribavirin treatment of epidemiologically linked cases of Lassa fever. *Clin Infect Dis* **65**, 855-859, doi:10.1093/cid/cix406 (2017).

152 Buckley, S. M. & Casals, J. Lassa fever, a new virus disease of man from west Africa .3. isolation and characterization of virus. *Am. J. Trop. Med. Hyg.* **19**, 680-&, doi:10.4269/ajtmh.1970.19.680 (1970).

153 Lukashevich, I. S., Stelmakh, T. A., Golubev, V. P., Stchesljenok, E. P. & Lemeshko, N. N. Ribonucleic-acids of Machupo and Lassa virsues. *Arch. Virol.* **79**, 189-203, doi:10.1007/bf01310811 (1984).

154 Vieth, S., Torda, A. E., Asper, M., Schmitz, H. & Gunther, S. Sequence analysis of L RNA of Lassa virus. *Virology* **318**, 153-168, doi:10.1016/j.virol.2003.09.009 (2004).

155 Andersen, K. G. *et al.* Clinical sequencing uncovers origins and evolution of Lassa virus. *Cell* **162**, 738-750, doi:10.1016/j.cell.2015.07.020 (2015).

156 Auperin, D. D., Romanowski, V., Galinski, M. & Bishop, D. H. L. Sequencing studies of pichinde arenavirus S-RNA indicate a novel coding strategy, an ambisense viral S-RNA. *J Virol* **52**, 897-904, doi:10.1128/jvi.52.3.897-904.1984 (1984).

157 Cohen-Dvashi, H., Cohen, N., Israeli, H. & Diskin, R. Molecular mechanism for LAMP1 recognition by Lassa virus. *J Virol* **89**, 7584-7592, doi:10.1128/jvi.00651-15 (2015).

158 Hastie, K. M. & Saphire, E. O. Lassa virus glycoprotein: stopping a moving target. *Current Opinion in Virology* **31**, 52-58, doi:https://doi.org/10.1016/j.coviro.2018.05.002 (2018).

159 Messina, E. L., York, J. & Nunberg, J. H. Dissection of the role of the stable signal peptide of the arenavirus envelope glycoprotein in membrane fusion. *J Virol* **86**, 6138-6145, doi:10.1128/JVI.07241-11 (2012).

160 Welch, S. R. *et al.* The S genome segment is sufficient to maintain pathogenicity in intra-clade Lassa virus reassortants in a guinea pig model. *Frontiers in Cellular and Infection Microbiology* **8**, doi:10.3389/fcimb.2018.00240 (2018).

161 Manning, J. T., Forrester, N. & Paessler, S. Lassa virus isolates from Mali and the Ivory Coast represent an emerging fifth lineage. *Front. Microbiol.* **6**, 10, doi:10.3389/fmicb.2015.01037 (2015).

162 Bhadelia, N. Understanding Lassa fever. *Science* **363**, 30-30, doi:10.1126/science.aav8958 (2019).

163 Kafetzopoulou, L. E. *et al.* Metagenomic sequencing at the epicenter of the Nigeria 2018 Lassa fever outbreak. *Science* **363**, 74-+, doi:10.1126/science.aau9343 (2019).

164 Uzoma, I. R. *et al.* Increasing trend of Lassa fever outbreak in Nigeria: The more you look, the more you see. *Int. J. Infect. Dis.* **101**, 357, doi:https://doi.org/10.1016/j.ijid.2020.09.936 (2020).

165 Baize, S. *et al.* Lassa virus infection of human dendritic cells and macrophages is productive but fails to activate cells. *J. Immunol.* **172**, 2861-2869, doi:10.4049/jimmunol.172.5.2861 (2004).

166 Schaeffer, J. *et al.* Lassa virus activates myeloid dendritic cells but suppresses their ability to stimulate T cells. *PLoS Pathog.* **14**, 25, doi:10.1371/journal.ppat.1007430 (2018).

167 Pannetier, D. *et al.* Human dendritic cells infected with the nonpathogenic mopeia virus induce stronger T-cell responses than those infected with Lassa virus. *J Virol* **85**, 8293-8306, doi:10.1128/jvi.02120-10 (2011).

168 Baize, S. *et al.* Role of interferons in the control of Lassa virus replication in human dendritic cells and macrophages. *Microbes Infect.* **8**, 1194-1202, doi:10.1016/j.micinf.2006.02.002 (2006).

169 Yun, N. E. *et al.* Functional interferon system is required for clearance of lassa virus. *J Virol* **86**, 3389-3392 (2012).

170 Muller, U. *et al.* Functional role of type I and type II interferons in antiviral defense. *Science* **264**, 1918-1921 (1994).

171 Rieger, T., Merkler, D. & Günther, S. Infection of type I interferon receptor-deficient mice with various old world arenaviruses: a model for studying virulence and host species barriers. *PLoS One* **8**, e72290 (2013).

172 Ehichioya, D. U. *et al.* Phylogeography of Lassa virus in Nigeria. *J Virol* **93**, 12, doi:10.1128/jvi.00929-19 (2019).

173 Baize, S. *et al.* Early and strong immune responses are associated with control of viral replication and recovery in Lassa virus-infected cynomolgus monkeys. *J Virol* **83**, 5890-5903, doi:10.1128/jvi.01948-08 (2009).

174 Johnson, K. M. *et al.* Clinical virology of Lassa fever in hospitalized-patients. *J. Infect. Dis.* **155**, 456-464, doi:10.1093/infdis/155.3.456 (1987).

175 Flatz, L. *et al.* T cell-dependence of Lassa fever pathogenesis. *PLoS Pathog.* **6**, 13, doi:10.1371/journal.ppat.1000836 (2010).

176 Robinson, J. E. *et al.* Most neutralizing human monoclonal antibodies target novel epitopes requiring both Lassa virus glycoprotein subunits. *Nat. Commun.* **7**, 14, doi:10.1038/ncomms11544 (2016).

177 Hufert, F. T., Ludke, W. & Schmitz, H. Epitope mapping of the Lassa virus nucleoprotein using monoclonal anti-nucleocapsid antibodies. *Arch. Virol.* **106**, 201-212, doi:10.1007/bf01313953 (1989).

178 Watanabe, Y. *et al.* Structure of the Lassa virus glycan shield provides a model for immunological resistance. *Proceedings of the National Academy of Sciences* **115**, 7320, doi:10.1073/pnas.1803990115 (2018).

179 Sommerstein, R. *et al.* Arenavirus glycan shield promotes neutralizing antibody evasion and protracted infection. *PLoS Pathog.* **11**, e1005276-e1005276, doi:10.1371/journal.ppat.1005276 (2015).

180 Cross, R. W. *et al.* Treatment of Lassa virus infection in outbred guinea pigs with first-in-class human monoclonal antibodies. *Antiviral Res.* **133**, 218-222, doi:10.1016/j.antiviral.2016.08.012 (2016).

181 Mire, C. E. *et al.* Human-monoclonal-antibody therapy protects nonhuman primates against advanced Lassa fever. *Nature Medicine* **23**, 1146-+, doi:10.1038/nm.4396 (2017).

182 Abreu-Mota, T. *et al.* Non-neutralizing antibodies elicited by recombinant Lassa-Rabies vaccine are critical for protection against Lassa fever. *Nat. Commun.* **9**, 16, doi:10.1038/s41467-018-06741-w (2018).

183 Lukashevich, I. Lassa virus lethality for inbred mice. *Ann Soc Belg Med Trop* **65**, 207-209 (1985).

184 Durbin, J. E., Hackenmiller, R., Simon, M. C. & Levy, D. E. Targeted disruption of the mouse Stat1 gene results in compromised innate immunity to viral disease. *Cell* **84**, 443-450 (1996).

185 Meraz, M. A. *et al.* Targeted disruption of the stat1 gene in mice reveals unexpected physiologic specificity in the JAK–STAT signaling pathway. *Cell* **84**, 431-442, doi:https://doi.org/10.1016/S0092-8674(00)81288-X (1996).

186 Yun, N. E. *et al.* Mice lacking functional stat1 are highly susceptible to lethal infection with Lassa virus. *J Virol* **87**, 10908-10911, doi:10.1128/jvi.01433-13 (2013).

187 Oestereich, L. *et al.* Chimeric mice with competent hematopoietic immunity reproduce key features of severe Lassa fever. *PLoS Pathog.* **12**, 22, doi:10.1371/journal.ppat.1005656 (2016).

188 Pascolo, S. *et al.* HLA-A2. 1–restricted education and cytolytic activity of CD8+ T lymphocytes from β2 microglobulin (β2m) HLA-A2. 1 monochain transgenic H-2Db β2m double knockout mice. *Journal of Experimental Medicine* **185**, 2043-2051 (1997).

189 Arnold, B. & Hämmerling, G. J. MHC class-I transgenic mice. *Annual review of immunology* **9**, 297-322 (1991).

190 Jahrling, P. B., Smith, S., Hesse, R. A. & Rhoderick, J. B. Pathogenesis of Lassa virus-infection in guinea-pigs. *Infect. Immun.* **37**, 771-778, doi:10.1128/iai.37.2.771-778.1982 (1982).

191 Peters, C. J. *et al.* Experimental studies of arenaviral hemorrhagic fevers. *Curr.Top.Microbiol.Immunol.* **134**, 5-68 (1987).

192 Bell, T. *et al.* Temporal progression of lesions in guinea pigs infected with Lassa virus. *Veterinary pathology* **54**, 549-562 (2017).

193 Walker, D., Wulff, H., Lange, J. & Murphy, F. A. Comparative pathology of Lassa virus infection in monkeys, guinea-pigs, and mastomys natalensis. *Bulletin of the World Health Organization* **52**, 523 (1975).

194 Callis, R. T., Jahrling, P. B. & DePaoli, A. Pathology of Lassa virus infection in the rhesus monkey. *Army Medical Research Inst of Infectious Diseases Fortr Detrick MD (1982).*

195 Jahrling, P. *et al.* Lassa virus infection of rhesus monkeys: pathogenesis and treatment with ribavirin. *J. Infect. Dis.* **141**, 580-589 (1980).

196 Hensley, L. E. *et al.* Pathogenesis of lassa fever in cynomolgus macaques. *Virol. J.* **8**, 15, doi:10.1186/1743-422x-8-205 (2011).

197 Baillet, N. *et al.* Systemic viral spreading and defective host responses are associated with fatal Lassa fever in macaques. *Communications Biology* **4**, 27, doi:10.1038/s42003-020-01543-7 (2021).

198 Carrion Jr, R. *et al.* Lassa virus infection in experimentally infected marmosets: liver pathology and immunophenotypic alterations in target tissues. *J Virol* **81**, 6482-6490 (2007).

199 Jiang, X. H. *et al.* Yellow fever 17D-vectored vaccines expressing Lassa virus GP1 and GP2 glycoproteins provide protection against fatal disease in guinea pigs. *Vaccine* **29**, 1248-1257, doi:10.1016/j.vaccine.2010.11.079 (2011).

200 Safronetz, D. *et al.* A recombinant vesicular stomatitis virus-based Lassa fever vaccine protects guinea pigs and macaques against challenge with geographically and genetically distinct Lassa viruses. *Plos Neglect. Trop. Dis.* **9**, 14, doi:10.1371/journal.pntd.0003736 (2015).

201 Cross, R. W. *et al.* Quadrivalent VesiculoVax vaccine protects nonhuman primates from viral-induced hemorrhagic fever and death. *The Journal of Clinical Investigation* **130**, 539-551, doi:10.1172/JCI131958 (2020).

202 Kennedy, E. M. *et al.* A vaccine based on recombinant modified vaccinia Ankara containing the nucleoprotein from Lassa virus protects against disease progression in a guinea pig model. *Vaccine* **37**, 5404-5413, doi:10.1016/j.vaccine.2019.07.023 (2019).

203 Mateo, M. *et al.* Vaccines inducing immunity to Lassa virus glycoprotein and nucleoprotein protect macaques after a single shot. *Science Translational Medicine* **11**, 17, doi:10.1126/scitranslmed.aaw3163 (2019).

204 Pushko, P., Geisbert, J., Parker, M., Jahrling, P. & Smith, J. Individual and bivalent vaccines based on alphavirus replicons protect guinea pigs against infection with Lassa and Ebola viruses. *J Virol* **75**, 11677-11685, doi:10.1128/jvi.75.23.11677-11685.2001 (2001).

205 Branco, L. M. *et al.* Lassa virus-like particles displaying all major immunological determinants as a vaccine candidate for Lassa hemorrhagic fever. *Virol J* **7**, 279, doi:10.1186/1743-422x-7-279 (2010).

206 Cashman, K. A. *et al.* A DNA vaccine delivered by dermal electroporation fully protects cynomolgus macaques against Lassa fever. *Human Vaccines Immunother.* **13**, 2902-2911, doi:10.1080/21645515.2017.1356500 (2017).

207 Lukashevich, I. S. *et al.* Safety, immunogenicity, and efficacy of the ML29 reassortant vaccine for Lassa fever in small non-human primates. *Vaccine* **26**, 5246-5254, doi:10.1016/j.vaccine.2008.07.057 (2008).

208 Cai, Y. *et al.* A Lassa fever live-attenuated vaccine based on codon deoptimization of the viral glycoprotein gene. *mBio* **11**, e00039-00020, doi:doi:10.1128/mBio.00039-20 (2020).

209 Cashman, K. A. *et al.* Enhanced efficacy of a codon-optimized DNA vaccine encoding the glycoprotein precursor gene of Lassa virus in a guinea pig disease model when delivered by dermal electroporation. *Vaccines* **1**, 262-277, doi:10.3390/vaccines1030262 (2013).

210 Reisinger, E. C. *et al.* Immunogenicity, safety, and tolerability of the measles-vectored chikungunya virus vaccine MV-CHIK: a double-blind, randomised, placebo-controlled and active-controlled phase 2 trial. *Lancet* **392**, 2718-2727, doi:10.1016/s0140-6736(18)32488-7 (2018).

211 Mateo, M. *et al.* A single-shot Lassa vaccine induces long-term immunity and protects cynomolgus monkeys against heterologous strains. *Sci Transl Med* **13**, doi:10.1126/scitranslmed.abf6348 (2021).

212 Ruedas, J. B. & Connor, J. H. Generating recombinant vesicular stomatitis viruses for use as vaccine platforms. *Methods Mol Biol* **1581**, 203-222, doi:10.1007/978-1-4939-6869-5_12 (2017).

213 Juan-Giner, A. *et al.* Safety of the rVSV ZEBOV vaccine against Ebola Zaire among frontline workers in Guinea. *Vaccine* **37**, 7171-7177, doi:https://doi.org/10.1016/j.vaccine.2018.09.009 (2019).

214 Geisbert, T. W. *et al.* Development of a new vaccine for the prevention of lassa fever. *PLos Med.* **2**, 537-545, doi:10.1371/journal.pmed.0020183 (2005).

215 Mire, C. E. *et al.* Single-dose attenuated VesiculoVax vaccines protect primates against Ebola Makona virus. *Nature* **520**, 688, doi:10.1038/nature14428 (2015).

216 Fuchs, J. D. *et al.* First-in-human evaluation of the safety and immunogenicity of a recombinant vesicular stomatitis virus human immunodeficiency virus-1 gag vaccine (HVTN 090). *Open Forum Infect Dis* **2**, v082, doi:10.1093/ofid/ofv082 (2015).

217 Elizaga, M. L. *et al.* Safety and tolerability of HIV-1 multiantigen pDNA vaccine given with IL-12 plasmid DNA via electroporation, boosted with a recombinant vesicular stomatitis virus HIV Gag vaccine in healthy volunteers in a randomized, controlled clinical trial. *PLoS One* **13**, e0202753, doi:10.1371/journal.pone.0202753 (2018).

218 WHO target product profile for Lassa virus vaccines. (2017).

219 Gouglas, D. *et al.* Estimating the cost of vaccine development against epidemic infectious diseases: a cost minimisation study. *Lancet Glob Health* **6**, e1386-e1396, doi:10.1016/s2214-109x(18)30346-2 (2018).

220 Salami, K., Gouglas, D., Schmaljohn, C., Saville, M. & Tornieporth, N. A review of Lassa fever vaccine candidates. *Current Opinion in Virology* **37**, 105-111, doi:https://doi.org/10.1016/j.coviro.2019.07.006 (2019).

221 *COVID-19 Dashboard*, <https://coronavirus.jhu.edu/map.html> (2021).

222 Zhou, P. *et al.* A pneumonia outbreak associated with a new coronavirus of probable bat origin. *Nature* **579**, 270-273, doi:10.1038/s41586-020-2012-7 (2020).

223 Paraskevis, D. *et al.* Full-genome evolutionary analysis of the novel corona virus (2019-nCoV) rejects the hypothesis of emergence as a result of a recent recombination event. *Infect Genet Evol* **79**, 104212, doi:10.1016/j.meegid.2020.104212 (2020).

224 Zhou, H. *et al.* A novel bat coronavirus closely related to SARS-CoV-2 contains natural insertions at the S1/S2 cleavage site of the spike protein. *Curr Biol* **30**, 2196-2203.e2193, doi:10.1016/j.cub.2020.05.023 (2020).

225 Zhang, Y. Z. & Holmes, E. C. A Genomic perspective on the origin and emergence of SARS-CoV-2. *Cell* **181**, 223-227, doi:10.1016/j.cell.2020.03.035 (2020).

226 Lam, T. T.-Y. *et al.* Identifying SARS-CoV-2-related coronaviruses in Malayan pangolins. *Nature* **583**, 282-285, doi:10.1038/s41586-020-2169-0 (2020).

227 Liu, P., Chen, W. & Chen, J.-P. Viral metagenomics revealed sendai virus and coronavirus infection of Malayan pangolins (manis javanica). *Viruses* **11**, 979, doi:10.3390/v11110979 (2019).

228 Port, J. R. *et al.* SARS-CoV-2 disease severity and transmission efficiency is increased for airborne compared to fomite exposure in Syrian hamsters. *Nat. Commun.* **12**, 4985, doi:10.1038/s41467-021-25156-8 (2021).

229 Stadnytskyi, V., Bax, C. E., Bax, A. & Anfinrud, P. The airborne lifetime of small speech droplets and their potential importance in SARS-CoV-2 transmission. *Proc Natl Acad Sci U S A* **117**, 11875-11877, doi:10.1073/pnas.2006874117 (2020).

230 Meselson, M. Droplets and aerosols in the transmission of SARS-CoV-2. *N. Engl. J. Med.* **382**, 2063-2063, doi:10.1056/NEJMc2009324 (2020).

231 van Doremalen, N. *et al.* Aerosol and surface stability of SARS-CoV-2 as compared with SARS-CoV-1. *N Engl J Med* **382**, 1564-1567, doi:10.1056/NEJMc2004973 (2020).

232 Kampf, G., Todt, D., Pfaender, S. & Steinmann, E. Persistence of coronaviruses on inanimate surfaces and their inactivation with biocidal agents. *J Hosp Infect* **104**, 246-251, doi:10.1016/j.jhin.2020.01.022 (2020).

233 Peiris, J. S. *et al.* Clinical progression and viral load in a community outbreak of coronavirus-associated SARS pneumonia: a prospective study. *Lancet* **361**, 1767-1772, doi:10.1016/s0140-6736(03)13412-5 (2003).

234 Zou, L. *et al.* SARS-CoV-2 viral load in upper respiratory specimens of infected patients. *N. Engl. J. Med.* **382**, 1177-1179 (2020).

235 Wolfel, R. *et al.* Virological assessment of hospitalized patients with COVID-2019 (vol 581, pg 465, 2020). *Nature* **588**, E35-E35 (2020).

236 Li, R. *et al.* Substantial undocumented infection facilitates the rapid dissemination of novel coronavirus (SARS-CoV-2). *Science* **368**, 489-493 (2020).

237 Chen, W. *et al.* Detectable 2019-nCoV viral RNA in blood is a strong indicator for the further clinical severity. *Emerg Microbes Infect* **9**, 469-473, doi:10.1080/22221751.2020.1732837 (2020).

238 Wang, W. *et al.* Detection of SARS-CoV-2 in different types of clinical specimens. *JAMA* **323**, 1843-1844, doi:10.1001/jama.2020.3786 (2020).

239 Colavita, F. *et al.* SARS-CoV-2 isolation from ocular secretions of a patient with COVID-19 in Italy with prolonged Viral RNA detection. *Ann Intern Med* **173**, 242-243, doi:10.7326/m20-1176 (2020).

240 Cheung, K. S. *et al.* Gastrointestinal manifestations of SARS-CoV-2 infection and virus load in fecal samples from a Hong Kong cohort: systematic review and meta-analysis. *Gastroenterology* **159**, 81-95, doi:10.1053/j.gastro.2020.03.065 (2020).

241 Zheng, S. *et al.* Viral load dynamics and disease severity in patients infected with SARS-CoV-2 in Zhejiang province, China, January-March 2020: retrospective cohort study. *Bmj* **369**, m1443, doi:10.1136/bmj.m1443 (2020).

242 Li, D., Jin, M., Bao, P., Zhao, W. & Zhang, S. Clinical characteristics and results of semen tests among men with coronavirus disease 2019. *JAMA Netw Open* **3**, e208292-e208292, doi:10.1001/jamanetworkopen.2020.8292 (2020).

243 Pham, T. D. *et al.* SARS-CoV-2 RNAemia in a healthy blood donor 40 days after respiratory illness resolution. *Ann Intern Med* **173**, 853-854, doi:10.7326/l20-0725 (2020).

244 Azzolini, C. *et al.* SARS-CoV-2 on Ocular surfaces in a cohort of patients with COVID-19 from the lombardy region, Italy. *JAMA Ophthalmol* **139**, 956-963, doi:10.1001/jamaophthalmol.2020.5464 (2021).

245 Report of the WHO-China joint mission on coronavirus disease 2019 (COVID-2019). (2020).

246 *AABB's Coronavirus Resources*, <http://www.aabb.org/advocacy/regulatorygovernment/Pages/AABB-Coronavirus-Resources.aspx> (2020).

247 Wu, A. *et al.* Genome composition and divergence of the novel coronavirus (2019-nCoV) originating in China. *Cell Host Microbe* **27**, 325-328, doi:10.1016/j.chom.2020.02.001 (2020).

248 Walls, A. C. *et al.* Structure, function, and antigenicity of the SARS-CoV-2 spike glycoprotein. *Cell* **181**, 281-292.e286, doi:10.1016/j.cell.2020.02.058 (2020).

249 Wrapp, D. *et al.* Cryo-EM structure of the 2019-nCoV spike in the prefusion conformation. *Science* **367**, 1260-1263, doi:doi:10.1126/science.abb2507 (2020).

250 Lan, J. *et al.* Structure of the SARS-CoV-2 spike receptor-binding domain bound to the ACE2 receptor. *Nature* **581**, 215-220, doi:10.1038/s41586-020-2180-5 (2020).

251 V'kovski, P., Kratzel, A., Steiner, S., Stalder, H. & Thiel, V. Coronavirus biology and replication: implications for SARS-CoV-2. *Nature Reviews Microbiology* **19**, 155-170, doi:10.1038/s41579-020-00468-6 (2021).

252 Shang, J. *et al.* Structural basis of receptor recognition by SARS-CoV-2. *Nature* **581**, 221-224, doi:10.1038/s41586-020-2179-y (2020).

253 Carvalho, T., Krammer, F. & Iwasaki, A. The first 12 months of COVID-19: a timeline of immunological insights. *Nature Reviews Immunology* **21**, 245-256, doi:10.1038/s41577-021-00522-1 (2021).

254 Hoffmann, M. *et al.* SARS-CoV-2 cell entry depends on ACE2 and TMPRSS2 and is blocked by a clinically proven protease inhibitor. *Cell* **181**, 271-280.e278, doi:10.1016/j.cell.2020.02.052 (2020).

255 Ou, X. *et al.* Characterization of spike glycoprotein of SARS-CoV-2 on virus entry and its immune cross-reactivity with SARS-CoV. *Nat Commun* **11**, 1620, doi:10.1038/s41467-020-15562-9 (2020).

256 Shang, J. *et al.* Cell entry mechanisms of SARS-CoV-2. *Proc Natl Acad Sci U S A* **117**, 11727-11734, doi:10.1073/pnas.2003138117 (2020).

257 Sungnak, W. *et al.* SARS-CoV-2 entry factors are highly expressed in nasal epithelial cells together with innate immune genes. *Nat Med* **26**, 681-687, doi:10.1038/s41591-020-0868-6 (2020).

258 Lukassen, S. *et al.* SARS-CoV-2 receptor ACE2 and TMPRSS2 are primarily expressed in bronchial transient secretory cells. *Embo j* **39**, e105114, doi:10.15252/embj.20105114 (2020).

259 Shi, J. *et al.* Susceptibility of ferrets, cats, dogs, and other domesticated animals to SARS-coronavirus 2. *Science* **368**, 1016-1020, doi:10.1126/science.abb7015 (2020).

260 Chandrashekar, A. *et al.* SARS-CoV-2 infection protects against rechallenge in rhesus macaques. *Science* **369**, 812-817, doi:10.1126/science.abc4776 (2020).

261 Zhao, X. *et al.* Broad and differential animal angiotensin-converting enzyme 2 receptor usage by SARS-CoV-2. *J Virol* **94**, doi:10.1128/jvi.00940-20 (2020).

262 Tali, S. H. S. *et al.* Tools and techniques for severe acute respiratory syndrome coronavirus 2 (SARS-CoV-2)/COVID-19 detection. *Clinical Microbiology Reviews* **34**, e00228-00220, doi:doi:10.1128/CMR.00228-20 (2021).

263 Chan, J. F. *et al.* A familial cluster of pneumonia associated with the 2019 novel coronavirus indicating person-to-person transmission: a study of a family cluster. *Lancet* **395**, 514-523, doi:10.1016/s0140-6736(20)30154-9 (2020).

264 Li, Q. *et al.* Early transmission dynamics in Wuhan, China, of novel coronavirus–infected pneumonia. *N. Engl. J. Med.* **382**, 1199-1207, doi:10.1056/NEJMoa2001316 (2020).

265 Guan, W. J. *et al.* Clinical characteristics of coronavirus disease 2019 in China. *N Engl J Med* **382**, 1708-1720, doi:10.1056/NEJMoa2002032 (2020).

266 McIntosh, K. *COVID-19 clinical features*, <https://www.uptodate.com/contents/covid-19-clinical-features> (2021).

267 Nishiura, H. *et al.* Estimation of the asymptomatic ratio of novel coronavirus infections (COVID-19). *Int J Infect Dis* **94**, 154-155, doi:10.1016/j.ijid.2020.03.020 (2020).

268 Zhu, J. *et al.* Clinicopathological characteristics of 8697 patients with COVID-19 in China: a meta-analysis. *Fam Med Community Health* **8**, doi:10.1136/fmch-2020-000406 (2020).

269 Li, J. *et al.* Epidemiology of COVID-19: A systematic review and meta-analysis of clinical characteristics, risk factors, and outcomes. *J Med Virol* **93**, 1449-1458, doi:10.1002/jmv.26424 (2021).

270 Ranieri, V. M. *et al.* Acute respiratory distress syndrome: the Berlin Definition. *Jama* **307**, 2526-2533, doi:10.1001/jama.2012.5669 (2012).

271 Wu, C. *et al.* Risk factors associated with acute respiratory distress syndrome and death in patients with coronavirus disease 2019 pneumonia in Wuhan, China. *JAMA Intern Med* **180**, 934-943, doi:10.1001/jamainternmed.2020.0994 (2020).

272 Liu, Y. *et al.* Association between age and clinical characteristics and outcomes of COVID-19. *Eur Respir J* **55**, doi:10.1183/13993003.01112-2020 (2020).

273 Tian, J. *et al.* Clinical characteristics and risk factors associated with COVID-19 disease severity in patients with cancer in Wuhan, China: a multicentre, retrospective, cohort study. *Lancet Oncol* **21**, 893-903, doi:10.1016/s1470-2045(20)30309-0 (2020).

274 Huang, C. *et al.* Clinical features of patients infected with 2019 novel coronavirus in Wuhan, China. *Lancet* **395**, 497-506, doi:10.1016/s0140-6736(20)30183-5 (2020).

275 Zeng, Z. *et al.* Pulmonary pathology of early-phase COVID-19 pneumonia in a patient with a benign lung lesion. *Histopathology* **77**, 823-831, doi:10.1111/his.14138 (2020).

276 Martines, R. B. *et al.* Pathology and pathogenesis of SARS-CoV-2 associated with fatal coronavirus disease, United States. *Emerg Infect Dis* **26**, 2005-2015, doi:10.3201/eid2609.202095 (2020).

277 Szklanna, P. B. *et al.* Routine hematological parameters may be predictors of COVID-19 severity. *Frontiers in Medicine* **8**, doi:10.3389/fmed.2021.682843 (2021).

278 Mehta, P. *et al.* COVID-19: consider cytokine storm syndromes and immunosuppression. *Lancet* **395**, 1033-1034, doi:10.1016/s0140-6736(20)30628-0 (2020).

279 Järhult, J. D., Hultström, M., Bergqvist, A., Frithiof, R. & Lipcsey, M. The impact of viremia on organ failure, biomarkers and mortality in a Swedish cohort of critically ill COVID-19 patients. *Scientific Reports* **11**, 7163, doi:10.1038/s41598-021-86500-y (2021).

280 Elezkurtaj, S. *et al.* Causes of death and comorbidities in hospitalized patients with COVID-19. *Scientific Reports* **11**, 4263, doi:10.1038/s41598-021-82862-5 (2021).

281 Beigel, J. H. *et al.* Remdesivir for the treatment of Covid-19 - final report. *N Engl J Med* **383**, 1813-1826, doi:10.1056/NEJMoa2007764 (2020).

282 Goldman, J. D. *et al.* Remdesivir for 5 or 10 days in patients with severe Covid-19. *N Engl J Med* **383**, 1827-1837, doi:10.1056/NEJMoa2015301 (2020).

283 Spinner, C. D. *et al.* Effect of remdesivir vs standard care on clinical status at 11 days in patients with moderate COVID-19: a randomized clinical trial. *Jama* **324**, 1048-1057, doi:10.1001/jama.2020.16349 (2020).

284 Joyner, M. J. *et al.* Safety Update: COVID-19 convalescent plasma in 20,000 hospitalized patients. *Mayo Clin Proc* **95**, 1888-1897, doi:10.1016/j.mayocp.2020.06.028 (2020).

285 Joyner, M. J. *et al.* Effect of convalescent plasma on mortality among hospitalized patients with COVID-19: initial three-month experience. *medRxiv*, doi:10.1101/2020.08.12.20169359 (2020).

286 Baum, A. *et al.* REGN-COV2 antibodies prevent and treat SARS-CoV-2 infection in rhesus macaques and hamsters. *Science* **370**, 1110-1115, doi:10.1126/science.abe2402 (2020).

287 Weinreich, D. M. *et al.* REGN-COV2, a neutralizing antibody cocktail, in outpatients with Covid-19. *N Engl J Med* **384**, 238-251, doi:10.1056/NEJMoa2035002 (2021).

288 Gottlieb, R. L. *et al.* Effect of bamlanivimab as monotherapy or in combination with etesevimab on viral load in patients with mild to moderate COVID-19: a randomized clinical trial. *Jama* **325**, 632-644, doi:10.1001/jama.2021.0202 (2021).

289 Gupta, A. *et al.* Early treatment for Covid-19 with SARS-CoV-2 neutralizing antibody sotrovimab. *N. Engl. J. Med.* **385**, 1941-1950, doi:10.1056/NEJMoa2107934 (2021).

290 Horby, P. *et al.* Dexamethasone in hospitalized patients with Covid-19. *N Engl J Med* **384**, 693-704, doi:10.1056/NEJMoa2021436 (2021).

291 Stone, J. H. *et al.* Efficacy of tocilizumab in patients hospitalized with Covid-19. *N Engl J Med* **383**, 2333-2344, doi:10.1056/NEJMoa2028836 (2020).

292 Gordon, A. C. *et al.* Interleukin-6 receptor antagonists in critically ill patients with Covid-19. *N Engl J Med* **384**, 1491-1502, doi:10.1056/NEJMoa2100433 (2021).

293 Richardson, P. *et al.* Baricitinib as potential treatment for 2019-nCoV acute respiratory disease. *Lancet* **395**, e30-e31, doi:10.1016/s0140-6736(20)30304-4 (2020).

294 Cao, Y. *et al.* Ruxolitinib in treatment of severe coronavirus disease 2019 (COVID-19): a multicenter, single-blind, randomized controlled trial. *J Allergy Clin Immunol* **146**, 137-146.e133, doi:10.1016/j.jaci.2020.05.019 (2020).

295 Ramos da Silva, S. *et al.* Broad severe acute respiratory syndrome coronavirus 2 cell tropism and immunopathology in lung tissues from fatal coronavirus disease 2019. *The Journal of Infectious Diseases* **223**, 1842-1854, doi:10.1093/infdis/jiab195 (2021).

296 Hou, Y. J. *et al.* SARS-CoV-2 reverse genetics reveals a variable infection gradient in the respiratory tract. *Cell* **182**, 429-446.e414, doi:10.1016/j.cell.2020.05.042 (2020).

297 Perry, A. K., Chen, G., Zheng, D., Tang, H. & Cheng, G. The host type I interferon response to viral and bacterial infections. *Cell Res* **15**, 407-422, doi:10.1038/sj.cr.7290309 (2005).

298 Sa Ribero, M., Jouvenet, N., Dreux, M. & Nisole, S. Interplay between SARS-CoV-2 and the type I interferon response. *PLoS Pathog* **16**, e1008737, doi:10.1371/journal.ppat.1008737 (2020).

299 Blanco-Melo, D. *et al.* Imbalanced host response to SARS-CoV-2 drives development of COVID-19. *Cell* **181**, 1036-1045.e1039, doi:10.1016/j.cell.2020.04.026 (2020).

300 Galani, I.-E. *et al.* Untuned antiviral immunity in COVID-19 revealed by temporal type I/III interferon patterns and flu comparison. *Nature Immunology* **22**, 32-40, doi:10.1038/s41590-020-00840-x (2021).

301 Wack, A. Monocyte and dendritic cell defects in COVID-19. *Nature Cell Biology* **23**, 445-447, doi:10.1038/s41556-021-00685-y (2021).

302 Sette, A. & Crotty, S. Adaptive immunity to SARS-CoV-2 and COVID-19. *Cell* **184**, 861-880, doi:10.1016/j.cell.2021.01.007 (2021).

303 Sekine, T. *et al.* Robust T cell immunity in convalescent individuals with asymptomatic or mild COVID-19. *Cell* **183**, 158-168.e114, doi:https://doi.org/10.1016/j.cell.2020.08.017 (2020).

304 DiPiazza, A. T., Graham, B. S. & Ruckwardt, T. J. T cell immunity to SARS-CoV-2 following natural infection and vaccination. *Biochem Biophys Res Commun* **538**, 211-217, doi:10.1016/j.bbrc.2020.10.060 (2021).

305 Yu, J. *et al.* DNA vaccine protection against SARS-CoV-2 in rhesus macaques. *Science* **369**, 806-811, doi:doi:10.1126/science.abc6284 (2020).

306 Bange, E. M. *et al.* CD8+ T cells contribute to survival in patients with COVID-19 and hematologic cancer. *Nature Medicine* **27**, 1280-1289, doi:10.1038/s41591-021-01386-7 (2021).

307 Saini, S. K. *et al.* SARS-CoV-2 genome-wide T cell epitope mapping reveals immunodominance and substantial CD8(+) T cell activation in COVID-19 patients. *Sci Immunol* **6**, doi:10.1126/sciimmunol.abf7550 (2021).

308 Gao, A. *et al.* Learning from HIV-1 to predict the immunogenicity of T cell epitopes in SARS-CoV-2. *iScience* **24**, 102311, doi:10.1016/j.isci.2021.102311 (2021).

309 Tarke, A. *et al.* Comprehensive analysis of T cell immunodominance and immunoprevalence of SARS-CoV-2 epitopes in COVID-19 cases. *Cell Rep Med* **2**, 100204, doi:10.1016/j.xcrm.2021.100204 (2021).

310 Ni, L. *et al.* Detection of SARS-CoV-2-specific humoral and cellular immunity in COVID-19 convalescent individuals. *Immunity* **52**, 971-977.e973, doi:10.1016/j.immuni.2020.04.023 (2020).

311 Boppana, S. *et al.* SARS-CoV-2-specific circulating T follicular helper cells correlate with neutralizing antibodies and increase during early convalescence. *PLoS Pathog* **17**, e1009761, doi:10.1371/journal.ppat.1009761 (2021).

312 Sterlin, D. *et al.* IgA dominates the early neutralizing antibody response to SARS-CoV-2. *Sci Transl Med* **13**, doi:10.1126/scitranslmed.abd2223 (2021).

313 Weisblum, Y. *et al.* Escape from neutralizing antibodies by SARS-CoV-2 spike protein variants. *Elife* **9**, doi:10.7554/eLife.61312 (2020).

314 Wec, A. Z. *et al.* Broad neutralization of SARS-related viruses by human monoclonal antibodies. *Science* **369**, 731-736, doi:doi:10.1126/science.abc7424 (2020).

315 McCallum, M. *et al.* N-terminal domain antigenic mapping reveals a site of vulnerability for SARS-CoV-2. *Cell* **184**, 2332-2347.e2316, doi:10.1016/j.cell.2021.03.028 (2021).

316 Piccoli, L. *et al.* Mapping neutralizing and immunodominant sites on the SARS-CoV-2 spike receptor-binding domain by structure-guided high-resolution serology. *Cell* **183**, 1024-1042.e1021, doi:https://doi.org/10.1016/j.cell.2020.09.037 (2020).

317 Greaney, A. J. *et al.* Comprehensive mapping of mutations in the SARS-CoV-2 receptor-binding domain that affect recognition by polyclonal human plasma antibodies. *Cell Host Microbe* **29**, 463-476.e466, doi:10.1016/j.chom.2021.02.003 (2021).

318 Khoury, D. S. *et al.* Neutralizing antibody levels are highly predictive of immune protection from symptomatic SARS-CoV-2 infection. *Nature Medicine* **27**, 1205-1211, doi:10.1038/s41591-021-01377-8 (2021).

319 Sahin, U. *et al.* COVID-19 vaccine BNT162b1 elicits human antibody and TH1 T cell responses. *Nature* **586**, 594-599, doi:10.1038/s41586-020-2814-7 (2020).

320 Atyeo, C. *et al.* Distinct early serological signatures track with SARS-CoV-2 survival. *Immunity* **53**, 524-532.e524, doi:https://doi.org/10.1016/j.immuni.2020.07.020 (2020).

321 Garcia-Beltran, W. F. *et al.* COVID-19-neutralizing antibodies predict disease severity and survival. *Cell* **184**, 476-488.e411, doi:https://doi.org/10.1016/j.cell.2020.12.015 (2021).

322 Seydoux, E. *et al.* Analysis of a SARS-CoV-2-infected individual reveals development of potent neutralizing antibodies with limited somatic mutation. *Immunity* **53**, 98-105.e105, doi:https://doi.org/10.1016/j.immuni.2020.06.001 (2020).

323 Schäfer, A. *et al.* Antibody potency, effector function, and combinations in protection and therapy for SARS-CoV-2 infection in vivo. *J Exp Med* **218**, doi:10.1084/jem.20201993 (2021).

324 Winkler, E. S. *et al.* Human neutralizing antibodies against SARS-CoV-2 require intact Fc effector functions for optimal therapeutic protection. *Cell* **184**, 1804-1820.e1816, doi:10.1016/j.cell.2021.02.026 (2021).

325 Bartsch, Y. C. *et al.* Discrete SARS-CoV-2 antibody titers track with functional humoral stability. *Nat. Commun.* **12**, 1018, doi:10.1038/s41467-021-21336-8 (2021).

326 Earle, K. A. *et al.* Evidence for antibody as a protective correlate for COVID-19 vaccines. *Vaccine* **39**, 4423-4428, doi:10.1016/j.vaccine.2021.05.063 (2021).

327 Melo, A. K. G. *et al.* Biomarkers of cytokine storm as red flags for severe and fatal COVID-19 cases: A living systematic review and meta-analysis. *PLoS One* **16**, e0253894, doi:10.1371/journal.pone.0253894 (2021).

328 Wilk, A. J. *et al.* A single-cell atlas of the peripheral immune response in patients with severe COVID-19. *Nature Medicine* **26**, 1070-1076, doi:10.1038/s41591-020-0944-y (2020).

329 Giamarellos-Bourboulis, E. J. *et al.* Complex immune dysregulation in COVID-19 patients with severe respiratory failure. *Cell Host & Microbe* **27**, 992-1000.e1003, doi:https://doi.org/10.1016/j.chom.2020.04.009 (2020).

330 Tan, L. *et al.* Lymphopenia predicts disease severity of COVID-19: a descriptive and predictive study. *Signal Transduction and Targeted Therapy* **5**, 33, doi:10.1038/s41392-020-0148-4 (2020).

331 Li, J. *et al.* Virus-host interactome and proteomic survey reveal potential virulence factors influencing SARS-CoV-2 pathogenesis. *Med (N Y)* **2**, 99-112.e117, doi:10.1016/j.medj.2020.07.002 (2021).

332 Diao, B. *et al.* Reduction and functional exhaustion of T cells in patients with coronavirus disease 2019 (COVID-19). *Front. Immunol.* **11**, doi:10.3389/fimmu.2020.00827 (2020).

333 De Biasi, S. *et al.* Marked T cell activation, senescence, exhaustion and skewing towards TH17 in patients with COVID-19 pneumonia. *Nat. Commun.* **11**, 3434, doi:10.1038/s41467-020-17292-4 (2020).

334 Asrani, P. & Hassan, M. I. SARS-CoV-2 mediated lung inflammatory responses in host: targeting the cytokine storm for therapeutic interventions. *Mol Cell Biochem* **476**, 675-687, doi:10.1007/s11010-020-03935-z (2021).

335 Pavel, A. B. *et al.* Th2/Th1 Cytokine imbalance is associated with higher COVID-19 risk mortality. *Frontiers in Genetics* **12**, doi:10.3389/fgene.2021.706902 (2021).

336 Kuri-Cervantes, L. *et al.* Comprehensive mapping of immune perturbations associated with severe COVID-19. *Science Immunology* **5**, eabd7114, doi:doi:10.1126/sciimmunol.abd7114 (2020).

337 Gavi. *The COVID-19 vaccine race - weekly update*, <https://www.gavi.org/vaccineswork/covid-19-vaccine-race> (2021).

338 Madhi, S. A. *et al.* Efficacy of the ChAdOx1 nCoV-19 Covid-19 vaccine against the B.1.351 variant. *N. Engl. J. Med.* **384**, 1885-1898, doi:10.1056/NEJMoa2102214 (2021).

339 Voysey, M. *et al.* Safety and efficacy of the ChAdOx1 nCoV-19 vaccine (AZD1222) against SARS-CoV-2: an interim analysis of four randomised controlled trials in Brazil, South Africa, and the UK. *Lancet* **397**, 99-111, doi:10.1016/s0140-6736(20)32661-1 (2021).

340 Logunov, D. Y. *et al.* Safety and efficacy of an rAd26 and rAd5 vector-based heterologous prime-boost COVID-19 vaccine: an interim analysis of a randomised controlled phase 3 trial in Russia. *Lancet* **397**, 671-681, doi:10.1016/s0140-6736(21)00234-8 (2021).

341 Sadoff, J. *et al.* Safety and efficacy of single-dose Ad26.COV2.S vaccine against Covid-19. *N Engl J Med* **384**, 2187-2201, doi:10.1056/NEJMoa2101544 (2021).

342 Zhu, F. C. *et al.* Immunogenicity and safety of a recombinant adenovirus type-5-vectored COVID-19 vaccine in healthy adults aged 18 years or older: a randomised, double-blind, placebo-controlled, phase 2 trial. *Lancet* **396**, 479-488, doi:10.1016/s0140-6736(20)31605-6 (2020).

343 Polack, F. P. *et al.* Safety and efficacy of the BNT162b2 mRNA Covid-19 vaccine. *N. Engl. J. Med.* **383**, 2603-2615, doi:10.1056/NEJMoa2034577 (2020).

344 Thomas, S. J. *et al.* Safety and efficacy of the BNT162b2 mRNA Covid-19 vaccine through 6 Months. *N. Engl. J. Med.* **385**, 1761-1773, doi:10.1056/NEJMoa2110345 (2021).

345 Baden, L. R. *et al.* Efficacy and safety of the mRNA-1273 SARS-CoV-2 vaccine. *N. Engl. J. Med.* **384**, 403-416, doi:10.1056/NEJMoa2035389 (2020).

346 El Sahly, H. M. *et al.* Efficacy of the mRNA-1273 SARS-CoV-2 vaccine at completion of blinded phase. *N. Engl. J. Med.* **385**, 1774-1785, doi:10.1056/NEJMoa2113017 (2021).

347 Momin, T. *et al.* Safety and immunogenicity of a DNA SARS-CoV-2 vaccine (ZyCoV-D): results of an open-label, non-randomized phase I part of phase I/II clinical study by intradermal route in healthy subjects in India. *EClinicalMedicine* **38**, 101020, doi:10.1016/j.eclinm.2021.101020 (2021).

348 Mercado, N. B. *et al.* Single-shot Ad26 vaccine protects against SARS-CoV-2 in rhesus macaques. *Nature* **586**, 583-588, doi:10.1038/s41586-020-2607-z (2020).

349 Vogel, A. B. *et al.* BNT162b vaccines protect rhesus macaques from SARS-CoV-2. *Nature* **592**, 283-289, doi:10.1038/s41586-021-03275-y (2021).

350 Corbett, K. S. *et al.* Evaluation of the mRNA-1273 vaccine against SARS-CoV-2 in nonhuman primates. *N. Engl. J. Med.* **383**, 1544-1555, doi:10.1056/NEJMoa2024671 (2020).

351 Corbett, K. S. *et al.* SARS-CoV-2 mRNA vaccine design enabled by prototype pathogen preparedness. *Nature* **586**, 567-571, doi:10.1038/s41586-020-2622-0 (2020).

352 Riley, T. P. *et al.* Enhancing the prefusion conformational stability of SARS-CoV-2 spike protein through structure-guided design. *Front. Immunol.* **12**, doi:10.3389/fimmu.2021.660198 (2021).

353 Pallesen, J. *et al.* Immunogenicity and structures of a rationally designed prefusion MERS-CoV spike antigen. *Proc Natl Acad Sci U S A* **114**, E7348-e7357, doi:10.1073/pnas.1707304114 (2017).

354 Mukhamedova, M. *et al.* Vaccination with prefusion-stabilized respiratory syncytial virus fusion protein induces genetically and antigenically diverse antibody responses. *Immunity* **54**, 769-780.e766, doi:10.1016/j.immuni.2021.03.004 (2021).

355 Dunkle, L. M. *et al.* Efficacy and safety of NVX-CoV2373 in adults in the United States and Mexico. *N. Engl. J. Med.*, doi:10.1056/NEJMoa2116185 (2021).

356 Heath, P. T. *et al.* Safety and efficacy of NVX-CoV2373 Covid-19 vaccine. *N. Engl. J. Med.* **385**, 1172-1183, doi:10.1056/NEJMoa2107659 (2021).

357 Wu, Z. *et al.* Safety, tolerability, and immunogenicity of an inactivated SARS-CoV-2 vaccine (CoronaVac) in healthy adults aged 60 years and older: a randomised, double-blind, placebo-controlled, phase 1/2 clinical trial. *Lancet Infect Dis* **21**, 803-812, doi:10.1016/s1473-3099(20)30987-7 (2021).

358 Jara, A. *et al.* Effectiveness of an Inactivated SARS-CoV-2 Vaccine in Chile. *N. Engl. J. Med.* **385**, 875-884, doi:10.1056/NEJMoa2107715 (2021).

359 Xia, S. *et al.* Safety and immunogenicity of an inactivated SARS-CoV-2 vaccine, BBIBP-CorV: a randomised, double-blind, placebo-controlled, phase 1/2 trial. *Lancet Infect Dis* **21**, 39-51, doi:10.1016/s1473-3099(20)30831-8 (2021).

360 Ella, R. *et al.* Efficacy, safety, and lot-to-lot immunogenicity of an inactivated SARS-CoV-2 vaccine (BBV152): interim results of a randomised, double-blind, controlled, phase 3 trial. *Lancet* **398**, 2173-2184, doi:10.1016/s0140-6736(21)02000-6 (2021).

361 Ella, R. *et al.* Safety and immunogenicity of an inactivated SARS-CoV-2 vaccine, BBV152: interim results from a double-blind, randomised, multicentre, phase 2 trial, and 3-month follow-up of a double-blind, randomised phase 1 trial. *Lancet Infect Dis* **21**, 950-961, doi:10.1016/s1473-3099(21)00070-0 (2021).

362 Barrett, J. R. *et al.* Phase 1/2 trial of SARS-CoV-2 vaccine ChAdOx1 nCoV-19 with a booster dose induces multifunctional antibody responses. *Nature Medicine* **27**, 279-288, doi:10.1038/s41591-020-01179-4 (2021).

363 Gorman, M. J. *et al.* Fab and Fc contribute to maximal protection against SARS-CoV-2 following NVX-CoV2373 subunit vaccine with Matrix-M vaccination. *Cell reports. Medicine* **2**, 100405-100405, doi:10.1016/j.xcrm.2021.100405 (2021).

364 Mateus, J. *et al.* Low-dose mRNA-1273 COVID-19 vaccine generates durable memory enhanced by cross-reactive T cells. *Science (New York, N.Y.)* **374**, eabj9853-eabj9853, doi:10.1126/science.abj9853 (2021).

365 Woldemeskel, B. A., Garliss, C. C. & Blankson, J. N. SARS-CoV-2 mRNA vaccines induce broad CD4+ T cell responses that recognize SARS-CoV-2 variants and HCoV-NL63. *J Clin Invest* **131**, doi:10.1172/jci149335 (2021).

366 Ewer, K. J. *et al.* T cell and antibody responses induced by a single dose of ChAdOx1 nCoV-19 (AZD1222) vaccine in a phase 1/2 clinical trial. *Nature Medicine* **27**, 270-278, doi:10.1038/s41591-020-01194-5 (2021).

367 Kim, J. Y. *et al.* Comparison of antibody and T cell responses induced by single doses of ChAdOx1 nCoV-19 and BNT162b2 vaccines. *Immune Netw* **21**, e29, doi:10.4110/in.2021.21.e29 (2021).

368 Keech, C. *et al.* Phase 1–2 trial of a SARS-CoV-2 recombinant spike protein nanoparticle vaccine. *N. Engl. J. Med.* **383**, 2320-2332, doi:10.1056/NEJMoa2026920 (2020).

369 Lederer, K. *et al.* SARS-CoV-2 mRNA vaccines foster potent antigen-specific germinal center responses associated with neutralizing antibody generation. *Immunity* **53**, 1281-1295.e1285, doi:https://doi.org/10.1016/j.immuni.2020.11.009 (2020).

370 Singanayagam, A. *et al.* Community transmission and viral load kinetics of the SARS-CoV-2 delta (B.1.617.2) variant in vaccinated and unvaccinated individuals in the UK: a prospective, longitudinal, cohort study. *Lancet Infect Dis*, doi:10.1016/s1473-3099(21)00648-4 (2021).

371 Rubin, R. Trying to block SARS-CoV-2 transmission with intranasal vaccines. *JAMA* **326**, 1661-1663, doi:10.1001/jama.2021.18143 (2021).

372 Shah, A. S. V. *et al.* Effect of vaccination on transmission of SARS-CoV-2. *N. Engl. J. Med.* **385**, 1718-1720, doi:10.1056/NEJMc2106757 (2021).

373 Wu, S. *et al.* Safety, tolerability, and immunogenicity of an aerosolised adenovirus type-5 vector-based COVID-19 vaccine (Ad5-nCoV) in adults: preliminary report of an open-label and randomised phase 1 clinical trial. *The Lancet Infectious Diseases* **21**, 1654-1664, doi:https://doi.org/10.1016/S1473-3099(21)00396-0 (2021).

374 Creech, C. B., Walker, S. C. & Samuels, R. J. SARS-CoV-2 vaccines. *JAMA* **325**, 1318-1320, doi:10.1001/jama.2021.3199 (2021).

375 Dong, Y. *et al.* The way of SARS-CoV-2 vaccine development: success and challenges. *Signal Transduction and Targeted Therapy* **6**, 387, doi:10.1038/s41392-021-00796-w (2021).

376 *SARS-CoV-2 variants of concern and variants of interest*, <https://www.who.int/en/activities/tracking-SARS-CoV-2-variants> (2021).

377 *SARS-CoV-2 variant classifications and definitions*, <https://www.cdc.gov/coronavirus/2019-ncov/variants/variant-info.html > (2021).

378 An integrated national scale SARS-CoV-2 genomic surveillance network. *Lancet Microbe* **1**, e99-e100, doi:10.1016/s2666-5247(20)30054-9 (2020).

379 Tao, K. *et al.* The biological and clinical significance of emerging SARS-CoV-2 variants. *Nature Reviews Genetics* **22**, 757-773, doi:10.1038/s41576-021-00408-x (2021).

380 Zhang, L. *et al.* SARS-CoV-2 spike-protein D614G mutation increases virion spike density and infectivity. *Nat. Commun.* **11**, 6013-6013, doi:10.1038/s41467-020-19808-4 (2020).

381 Plante, J. A. *et al.* Spike mutation D614G alters SARS-CoV-2 fitness. *Nature* **592**, 116-121, doi:10.1038/s41586-020-2895-3 (2021).

382 Weissman, D. *et al.* D614G spike mutation increases SARS CoV-2 susceptibility to neutralization. *Cell Host Microbe* **29**, 23-31.e24, doi:10.1016/j.chom.2020.11.012 (2021).

383 Zou, J. *et al.* The effect of SARS-CoV-2 D614G mutation on BNT162b2 vaccine-elicited neutralization. *npj Vaccines* **6**, 44, doi:10.1038/s41541-021-00313-8 (2021).

384 Hodcroft, E. B. *et al.* Emergence in late 2020 of multiple lineages of SARS-CoV-2 Spike protein variants affecting amino acid position 677. *medRxiv*, 2021.2002.2012.21251658, doi:10.1101/2021.02.12.21251658 (2021).

385 Tablizo, F. A. *et al.* Genome sequencing and analysis of an emergent SARS-CoV-2 variant characterized by multiple spike protein mutations detected from the central Visayas region of the Philippines. *medRxiv*, 2021.2003.2003.21252812, doi:10.1101/2021.03.03.21252812 (2021).

386 Brown, J. C. *et al.* Increased transmission of SARS-CoV-2 lineage B.1.1.7 (VOC 2020212/01) is not accounted for by a replicative advantage in primary airway cells or antibody escape. *bioRxiv*, 2021.2002.2024.432576, doi:10.1101/2021.02.24.432576 (2021).

387 Johnson, B. A. *et al.* Loss of furin cleavage site attenuates SARS-CoV-2 pathogenesis. *Nature* **591**, 293-299, doi:10.1038/s41586-021-03237-4 (2021).

388 Saito, A. *et al.* SARS-CoV-2 spike P681R mutation, a hallmark of the Delta variant, enhances viral fusogenicity and pathogenicity. *bioRxiv*, 2021.2006.2017.448820, doi:10.1101/2021.06.17.448820 (2021).

389 Wang, P. *et al.* Antibody resistance of SARS-CoV-2 variants B.1.351 and B.1.1.7. *Nature* **593**, 130-135, doi:10.1038/s41586-021-03398-2 (2021).

390 Liu, Z. *et al.* Identification of SARS-CoV-2 spike mutations that attenuate monoclonal and serum antibody neutralization. *Cell Host Microbe* **29**, 477-488.e474, doi:10.1016/j.chom.2021.01.014 (2021).

391 Jangra, S. *et al.* SARS-CoV-2 spike E484K mutation reduces antibody neutralisation. *Lancet Microbe* **2**, e283-e284, doi:10.1016/s2666-5247(21)00068-9 (2021).

392 Tada, T. *et al.* Convalescent-phase sera and vaccine-elicited antibodies largely maintain neutralizing titer against global SARS-CoV-2 variant spikes. *mBio* **12**, e0069621, doi:10.1128/mBio.00696-21 (2021).

393 Liu, Y. *et al.* The N501Y spike substitution enhances SARS-CoV-2 infection and transmission. *Nature*, doi:10.1038/s41586-021-04245-0 (2021).

394 Starr, T. N. *et al.* Deep mutational scanning of SARS-CoV-2 receptor binding domain reveals constraints on folding and ACE2 binding. *Cell* **182**, 1295-1310.e1220, doi:10.1016/j.cell.2020.08.012 (2020).

395 Zhu, X. *et al.* Cryo-electron microscopy structures of the N501Y SARS-CoV-2 spike protein in complex with ACE2 and 2 potent neutralizing antibodies. *PLoS Biol* **19**, e3001237, doi:10.1371/journal.pbio.3001237 (2021).

396 Laffeber, C., de Koning, K., Kanaar, R. & Lebbink, J. H. G. Experimental evidence for enhanced receptor binding by rapidly spreading SARS-CoV-2 variants. *J Mol Biol* **433**, 167058, doi:10.1016/j.jmb.2021.167058 (2021).

397 Shen, X. *et al.* SARS-CoV-2 variant B.1.1.7 is susceptible to neutralizing antibodies elicited by ancestral spike vaccines. *Cell Host Microbe* **29**, 529-539.e523, doi:10.1016/j.chom.2021.03.002 (2021).

398 Rees-Spear, C. *et al.* The effect of spike mutations on SARS-CoV-2 neutralization. *Cell Rep* **34**, 108890, doi:10.1016/j.celrep.2021.108890 (2021).

399 Edara, V. V., Hudson, W. H., Xie, X., Ahmed, R. & Suthar, M. S. Neutralizing antibodies against SARS-CoV-2 variants after infection and vaccination. *Jama* **325**, 1896-1898, doi:10.1001/jama.2021.4388 (2021).

400 Collier, D. A. *et al.* Sensitivity of SARS-CoV-2 B.1.1.7 to mRNA vaccine-elicited antibodies. *Nature* **593**, 136-141, doi:10.1038/s41586-021-03412-7 (2021).

401 Chen, R. E. *et al.* Resistance of SARS-CoV-2 variants to neutralization by monoclonal and serum-derived polyclonal antibodies. *Nature Medicine* **27**, 717-726, doi:10.1038/s41591-021-01294-w (2021).

402 Wang, R. *et al.* Analysis of SARS-CoV-2 variant mutations reveals neutralization escape mechanisms and the ability to use ACE2 receptors from additional species. *Immunity* **54**, 1611-1621.e1615, doi:10.1016/j.immuni.2021.06.003 (2021).

403 Starr, T. N. *et al.* Prospective mapping of viral mutations that escape antibodies used to treat COVID-19. *Science* **371**, 850-854, doi:10.1126/science.abf9302 (2021).

404 Deng, X. *et al.* Transmission, infectivity, and neutralization of a spike L452R SARS-CoV-2 variant. *Cell* **184**, 3426-3437.e3428, doi:10.1016/j.cell.2021.04.025 (2021).

405 Copin, R. *et al.* The monoclonal antibody combination REGEN-COV protects against SARS-CoV-2 mutational escape in preclinical and human studies. *Cell* **184**, 3949-3961.e3911, doi:10.1016/j.cell.2021.06.002 (2021).

406 Ferreira, I. *et al.* SARS-CoV-2 B.1.617 mutations L452R and E484Q are not synergistic for antibody evasion. *J Infect Dis* **224**, 989-994, doi:10.1093/infdis/jiab368 (2021).

407 Li, Q. *et al.* The impact of mutations in SARS-CoV-2 spike on viral infectivity and antigenicity. *Cell* **182**, 1284-1294.e1289, doi:10.1016/j.cell.2020.07.012 (2020).

408 Zhang, L. *et al.* Ten emerging SARS-CoV-2 spike variants exhibit variable infectivity, animal tropism, and antibody neutralization. *Communications Biology* **4**, 1196, doi:10.1038/s42003-021-02728-4 (2021).

409 Thomson, E. C. *et al.* Circulating SARS-CoV-2 spike N439K variants maintain fitness while evading antibody-mediated immunity. *Cell* **184**, 1171-1187.e1120, doi:10.1016/j.cell.2021.01.037 (2021).

410 Chen, J., Wang, R., Wang, M. & Wei, G. W. Mutations strengthened SARS-CoV-2 infectivity. *J Mol Biol* **432**, 5212-5226, doi:10.1016/j.jmb.2020.07.009 (2020).

411 Muecksch, F. *et al.* Affinity maturation of SARS-CoV-2 neutralizing antibodies confers potency, breadth, and resilience to viral escape mutations. *Immunity* **54**, 1853-1868.e1857, doi:10.1016/j.immuni.2021.07.008 (2021).

412 Baum, A. *et al.* Antibody cocktail to SARS-CoV-2 spike protein prevents rapid mutational escape seen with individual antibodies. *Science* **369**, 1014-1018, doi:10.1126/science.abd0831 (2020).

413 Cathcart, A. L. *et al.* The dual function monoclonal antibodies VIR-7831 and VIR-7832 demonstrate potent in vitro and in vivo activity against SARS-CoV-2. *bioRxiv*, 2021.2003.2009.434607, doi:10.1101/2021.03.09.434607 (2021).

414 McCarthy, K. R. *et al.* Recurrent deletions in the SARS-CoV-2 spike glycoprotein drive antibody escape. *Science* **371**, 1139-1142, doi:doi:10.1126/science.abf6950 (2021).

415 Kemp, S. A. *et al.* SARS-CoV-2 evolution during treatment of chronic infection. *Nature* **592**, 277-282, doi:10.1038/s41586-021-03291-y (2021).

416 Liu, L. *et al.* Potent neutralizing antibodies against multiple epitopes on SARS-CoV-2 spike. *Nature* **584**, 450-456, doi:10.1038/s41586-020-2571-7 (2020).

417 Chi, X. *et al.* A neutralizing human antibody binds to the N-terminal domain of the Spike protein of SARS-CoV-2. *Science* **369**, 650-655, doi:10.1126/science.abc6952 (2020).

418 Guo, K., Barrett, B. S., Mickens, K. L., Hasenkrug, K. J. & Santiago, M. L. Interferon resistance of emerging SARS-CoV-2 variants. *bioRxiv : the preprint server for biology*, 2021.2003.2020.436257, doi:10.1101/2021.03.20.436257 (2021).

419 *SARS-CoV-2 variants of conern as of 26 November 2021*, <https://www.ecdc.europa.eu/en/covid-19/variants-concern> (2021).

420 Damas, J. *et al.* Broad host range of SARS-CoV-2 predicted by comparative and structural analysis of ACE2 in vertebrates. *Proceedings of the National Academy of Sciences* **117**, 22311, doi:10.1073/pnas.2010146117 (2020).

421 Melin, A. D., Janiak, M. C., Marrone, F., Arora, P. S. & Higham, J. P. Comparative ACE2 variation and primate COVID-19 risk. *Communications Biology* **3**, 641, doi:10.1038/s42003-020-01370-w (2020).

422 Salguero, F. J. *et al.* Comparison of rhesus and cynomolgus macaques as an infection model for COVID-19. *Nat. Commun.* **12**, 1260, doi:10.1038/s41467-021-21389-9 (2021).

423 Singh, D. K. *et al.* Responses to acute infection with SARS-CoV-2 in the lungs of rhesus macaques, baboons and marmosets. *Nat. Microbiol* **6**, 73-86, doi:10.1038/s41564-020-00841-4 (2021).

424 Yinda, C. K. *et al.* K18-hACE2 mice develop respiratory disease resembling severe COVID-19. *PLoS Pathog.* **17**, e1009195, doi:10.1371/journal.ppat.1009195 (2021).

425 Tseng, S.-H. *et al.* A novel pseudovirus-based mouse model of SARS-CoV-2 infection to test COVID-19 interventions. *Journal of Biomedical Science* **28**, 34, doi:10.1186/s12929-021-00729-3 (2021).

426 Muñoz-Fontela, C. *et al.* Animal models for COVID-19. *Nature* **586**, 509-515, doi:10.1038/s41586-020-2787-6 (2020).

427 Shou, S. *et al.* Animal models for COVID-19: hamsters, mouse, ferret, mink, tree shrew, and non-human primates. *Front. Microbiol.* **12**, doi:10.3389/fmicb.2021.626553 (2021).

428 Lean, F. Z. X. *et al.* Differential susceptibility of SARS-CoV-2 in animals: evidence of ACE2 host receptor distribution in companion animals, livestock and wildlife by immunohistochemical characterisation. *Transbound Emerg Dis*, doi:10.1111/tbed.14232 (2021).

429 Fenollar, F. *et al.* Mink, SARS-CoV-2, and the human-animal interface. *Front. Microbiol.* **12**, doi:10.3389/fmicb.2021.663815 (2021).

430 Munster, V. J. *et al.* Respiratory disease in rhesus macaques inoculated with SARS-CoV-2. *Nature*, doi:10.1038/s41586-020-2324-7 (2020).

431 Rockx, B. *et al.* Comparative pathogenesis of COVID-19, MERS, and SARS in a nonhuman primate model. *Science* **368**, 1012-1015, doi:10.1126/science.abb7314 (2020).

432 Ehaideb, S. N., Abdullah, M. L., Abuyassin, B. & Bouchama, A. Evidence of a wide gap between COVID-19 in humans and animal models: a systematic review. *Critical Care* **24**, 594, doi:10.1186/s13054-020-03304-8 (2020).

433 Bewig, B. & Schmidt, W. E. Accelerated titering of adenoviruses. *Biotechniques* **28**, 870-873, doi:10.2144/00285bm08 (2000).

434 Maizel, J. V., Jr., White, D. O. & Scharff, M. D. The polypeptides of adenovirus. I. Evidence for multiple protein components in the virion and a comparison of types 2, 7A, and 12. *Virology* **36**, 115-125, doi:10.1016/0042-6822(68)90121-9 (1968).

435 Letko, M. *et al.* Adaptive evolution of MERS-CoV to species variation in DPP4. *Cell Reports* **24**, 1730-1737, doi:10.1016/j.celrep.2018.07.045 (2018).

436 Letko, M., Marzi, A. & Munster, V. Functional assessment of cell entry and receptor usage for SARS-CoV-2 and other lineage B betacoronaviruses. *Nat. Microbiol* **5**, 562-+, doi:10.1038/s41564-020-0688-y (2020).

437 Marzi, A. *et al.* Vesicular stomatitis virus-based Ebola vaccines with improved cross-protective efficacy. *J. Infect. Dis.* **204**, S1066-S1074, doi:10.1093/infdis/jir348 (2011).

438 Thwaites, R. S. *et al.* Nasosorption as a minimally invasive sampling procedure: mucosal viral load and inflammation in primary RSV bronchiolitis. *The Journal of infectious diseases* **215**, 1240-1244, doi:10.1093/infdis/jix150 (2017).

439 Tigges, J., Gordon, T. P., McClure, H. M., Hall, E. C. & Peters, A. Survival rate and life span of rhesus monkeys at the Yerkes regional primate research center. *Am J Primatol* **15**, 263-273, doi:10.1002/ajp.1350150308 (1988).

440 Clingerman, K. J. & Summers, L. Validation of a body condition scoring system in rhesus macaques (Macaca mulatta): inter- and intrarater variability. *J Am Assoc Lab Anim Sci* **51**, 31-36 (2012).

441 Wrapp, D. *et al.* Cryo-EM structure of the 2019-nCoV spike in the prefusion conformation. *Science* **367**, 1260-1263, doi:10.1126/science.abb2507 (2020).

442 Havenar-Daughton, C. *et al.* Cytokine-independent detection of antigen-specific germinal center T follicular helper cells in immunized nonhuman primates ssing a live cell activation-induced marker technique. *J Immunol* **197**, 994-1002, doi:10.4049/jimmunol.1600320 (2016).

443 Menicucci, A. R., Sureshchandra, S., Marzi, A., Feldmann, H. & Messaoudi, I. Transcriptomic analysis reveals a previously unknown role for $CD8^+$ T-cells in rVSV-EBOV mediated protection. *Sci Rep* **7**, 919, doi:10.1038/s41598-017-01032-8 (2017).

444 Stuart, T. *et al.* Comprehensive integration of single-cell data. *Cell* **177**, 1888-1902 e1821, doi:10.1016/j.cell.2019.05.031 (2019).

445 Speranza, E. *et al.* Single-cell RNA sequencing reveals SARS-CoV-2 infection dynamics in lungs of African green monkeys. *Sci Transl Med* **13**, doi:10.1126/scitranslmed.abe8146 (2021).

446 Sergushichev, A. An algorithm for fast preranked gene set enrichment analysis using cumulative statistic calculation. *bioRxiv*, doi:10.1101/060012 (2016).

447 Madissoon, E. *et al.* scRNA-seq assessment of the human lung, spleen, and esophagus tissue stability after cold preservation. *Genome Biol* **21**, 1, doi:10.1186/s13059-019-1906-x (2019).

448 Schwarz, B. *et al.* Cutting Edge: Severe SARS-CoV-2 infection in humans is defined by a shift in the serum lipidome, resulting in dysregulation of eicosanoid immune mediators. *J Immunol* **206**, 329-334, doi:10.4049/jimmunol.2001025 (2021).

449 Pearson, M., Kapil, S. K., Norris, P. & Hunter, C. Achieve broad lipid quantitation using a high-throughput targeted lipidomics method. *SCIEX* (2020).

450 Radtke, A. J. *et al.* IBEX: A versatile multiplex optical imaging approach for deep phenotyping and spatial analysis of cells in complex tissues. *Proc Natl Acad Sci U S A* **117**, 33455-33465, doi:10.1073/pnas.2018488117 (2020).

451 Nikisins, S. *et al.* International external quality assessment study for molecular detection of Lassa virus. *Plos Neglect. Trop. Dis.* **9**, 9, doi:10.1371/journal.pntd.0003793 (2015).

452 Corman, V. M. *et al.* Detection of 2019 novel coronavirus (2019-nCoV) by real-time RT-PCR. *Euro Surveill* **25**, doi:10.2807/1560-7917.ES.2020.25.3.2000045 (2020).

453 Wölfel, R. *et al.* Virological assessment of hospitalized patients with COVID-2019. *Nature* **581**, 465-469, doi:10.1038/s41586-020-2196-x (2020).

454 Roederer, M., Nozzi, J. L. & Nason, M. C. SPICE: exploration and analysis of post-cytometric complex multivariate datasets. *Cytometry A* **79**, 167-174, doi:10.1002/cyto.a.21015 (2011).

455 UMAP: uniform manifold approximation and projection for dimension reduction. *arXIV*, v3,1802.03426 (2020).

456 Van Gassen, S. *et al.* FlowSOM: Using self-organizing maps for visualization and interpretation of cytometry data. *Cytometry Part A* **87**, 636-645, doi:https://doi.org/10.1002/cyto.a.22625 (2015).

457 Allen, M. *et al.* Raincloud plots: a multi-platform tool for robust data visualization. *Wellcome Open Res* **4:63** (2021).

458 Cai, Y. Y. *et al.* A Lassa fever live-attenuated vaccine based on codon deoptimization of the viral glycoprotein gene. *Mbio* **11**, 17, doi:10.1128/mBio.00039-20 (2020).

459 Laposta, V. J., Auperin, D. D., Kaminlewis, R. & Cole, G. A. Cross-protection against lymphocytic choriomeningitis virus mediated by a CD4+ T-cell clone specific for an envelope glycoprotein epitope of Lassa virus. *J Virol* **67**, 3497-3506, doi:10.1128/jvi.67.6.3497-3506.1993 (1993).

460 Reyes-Sandoval, A. *et al.* Mixed vector immunization with recombinant adenovirus and MVA can improve vaccine efficacy while decreasing antivector immunity. *Mol. Ther.* **20**, 1633-1647, doi:10.1038/mt.2012.25 (2012).

461 Penaloza-MacMaster, P. *et al.* Inhibitory receptor expression on memory CD8 T cells following Ad vector immunization. *Vaccine* **34**, 4955-4963, doi:10.1016/j.vaccine.2016.08.048 (2016).

462 Carrion, R. *et al.* A ML29 reassortant virus protects guinea pigs against a distantly related Nigerian strain of Lassa virus and can provide sterilizing immunity. *Vaccine* **25**, 4093-4102, doi:10.1016/j.vaccine.2007.02.038 (2007).

463 Stein, D. R. *et al.* A recombinant vesicular stomatitis-based Lassa fever vaccine elicits rapid and long-term protection from lethal Lassa virus infection in guinea pigs. *npj Vaccines* **4**, 7, doi:10.1038/s41541-019-0104-x (2019).

464 Panagioti, E., Klenerman, P., Lee, L. N., van der Burg, S. H. & Arens, R. Features of effective T cell-inducing vaccines against chronic viral infections. *Front. Immunol.* **9**, 276-276, doi:10.3389/fimmu.2018.00276 (2018).

465 Van Braeckel, E. *et al.* Polyfunctional $CD4^+$ T cell responses in HIV-1-infected viral controllers compared with those in healthy recipients of an adjuvanted polyprotein HIV-1 vaccine. *Vaccine* **31**, 3739-3746, doi:10.1016/j.vaccine.2013.05.021 (2013).

466 Kannanganat, S., Ibegbu, C., Chennareddi, L., Robinson, H. L. & Amara, R. R. Multiple-cytokine-producing antiviral CD4 T cells are functionally superior to single-cytokine-producing cells. *J Virol* **81**, 8468-8476, doi:10.1128/jvi.00228-07 (2007).

467 Park, S. H. *et al.* Successful vaccination induces multifunctional memory T-cell precursors associated with early control of hepatitis C virus. *Gastroenterology* **143**, 1048-+, doi:10.1053/j.gastro.2012.06.005 (2012).

468 Sridhar, S. *et al.* Cellular immune correlates of protection against symptomatic pandemic influenza. *Nature Medicine* **19**, 1305-+, doi:10.1038/nm.3350 (2013).

469 Coughlan, L. *et al.* Heterologous two-dose vaccination with simian adenovirus and poxvirus vectors elicits long-lasting cellular immunity to influenza virus A in healthy adults. *EBioMedicine* **29**, 146-154, doi:10.1016/j.ebiom.2018.02.011 (2018).

470 Afolabi, M. O. *et al.* Safety and immunogenicity of ChAd63 and MVA ME-TRAP in west African children and infants. *Mol. Ther.* **24**, 1470-1477, doi:10.1038/mt.2016.83 (2016).

471 Bliss, C. M. *et al.* Viral vector malaria vaccines induce high-level T cell and antibody responses in west African children and infants. *Mol. Ther.* **25**, 547-559, doi:10.1016/j.ymthe.2016.11.003 (2017).

472 Hastie, K. M. *et al.* Convergent structures illuminate features for germline antibody binding and pan-Lassa virus neutralization. *Cell* **178**, 1004-+, doi:10.1016/j.cell.2019.07.020 (2019).

473 Muller, H. *et al.* Adjuvant formulated virus-like particles expressing native-like forms of the Lassa virus envelope surface glycoprotein are immunogenic and induce antibodies with broadly neutralizing activity. *npj Vaccines* **5**, 17, doi:10.1038/s41541-020-00219-x (2020).

474 Emary, K. R. W. *et al.* Efficacy of ChAdOx1 nCoV-19 (AZD1222) vaccine against SARS-CoV-2 variant of concern 202012/01 (B.1.1.7): an exploratory analysis of a randomised controlled trial. *Lancet* **397**, 1351-1362, doi:10.1016/s0140-6736(21)00628-0 (2021).

475 Vaccari, M. & Franchini, G. Memory T cells in rhesus macaques. *Advances in experimental medicine and biology* **684**, 126-144, doi:10.1007/978-1-4419-6451-9_10 (2010).

476 Pedreño-Lopez, N. *et al.* Non-neutralizingantibodies may contribute to suppression of SIVmac239 viremia in Indian rhesus macaques. *Front. Immunol.* **12**, doi:10.3389/fimmu.2021.657424 (2021).

477 Ko, Y.-A. *et al.* A non-neutralizing antibody broadly protects against influenza virus infection by engaging effector cells. *PLoS Pathog.* **17**, e1009724, doi:10.1371/journal.ppat.1009724 (2021).

478 Carragher, D. M., Kaminski, D. A., Moquin, A., Hartson, L. & Randall, T. D. A novel role for non-neutralizing antibodies against nucleoprotein in facilitating resistance to influenza virus. *The Journal of Immunology* **181**, 4168, doi:10.4049/jimmunol.181.6.4168 (2008).

479 McCormick, J. B. *et al.* Lassa virus hepatitis - a study of fatal Lassa fever in humans. *Am. J. Trop. Med. Hyg.* **35**, 401-407, doi:10.4269/ajtmh.1986.35.401 (1986).

480 Wang, T. T. & Ravetch, J. V. Functional diversification of IgGs through Fc glycosylation. *The Journal of Clinical Investigation* **129**, 3492-3498, doi:10.1172/JCI130029 (2019).

481 Hastie, K. M. *et al.* Structural basis for antibody-mediated neutralization of Lassa virus. *Science* **356**, 923-+, doi:10.1126/science.aam7260 (2017).

482 Lang, P. A. *et al.* Tissue macrophages suppress viral replication and prevent severe immunopathology in an interferon-I-dependent manner in mice. *Hepatology* **52**, 25-32, doi:10.1002/hep.23640 (2010).

483 Lang, K. S. & Lang, P. A. Balancing viral replication in spleen and liver determines the outcome of systemic virus infection. *Z Gastroenterol* **53**, 1432-1435, doi:10.1055/s-0041-109631 (2015).

484 Mueller, S. N. & Ahmed, R. High antigen levels are the cause of T cell exhaustion during chronic viral infection. *Proceedings of the National Academy of Sciences* **106**, 8623, doi:10.1073/pnas.0809818106 (2009).

485 Yadav, P. D. *et al.* Immunogenicity and protective efficacy of inactivated SARS-CoV-2 vaccine candidate, BBV152 in rhesus macaques. *Nat Commun* **12**, 1386, doi:10.1038/s41467-021-21639-w (2021).

486 Chen, H. *et al.* Immunological evaluation of an inactivated SARS-CoV-2 vaccine in rhesus macaques. *Mol Ther Methods Clin Dev* **23**, 108-118, doi:10.1016/j.omtm.2021.08.005 (2021).

487 Deng, W. *et al.* Primary exposure to SARS-CoV-2 protects against reinfection in rhesus macaques. *Science* **369**, 818-823, doi:doi:10.1126/science.abc5343 (2020).

488 Aid, M. *et al.* Vascular disease and thrombosis in SARS-CoV-2-infected rhesus macaques. *Cell* **183**, 1354-1366.e1313, doi:https://doi.org/10.1016/j.cell.2020.10.005 (2020).

489 Yang, W. *et al.* Clinical characteristics and imaging manifestations of the 2019 novel coronavirus disease (COVID-19):A multi-center study in Wenzhou city, Zhejiang, China. *J Infect* **80**, 388-393, doi:10.1016/j.jinf.2020.02.016 (2020).

490 Grifoni, A. *et al.* Targets of T cell responses to SARS-CoV-2 coronavirus in humans with COVID-19 disease and unexposed individuals. *Cell* **181**, 1489-1501.e1415, doi:10.1016/j.cell.2020.05.015 (2020).

491 Reiss, S. *et al.* Comparative analysis of activation induced marker (AIM) assays for sensitive identification of antigen-specific CD4 T cells. *PLoS One* **12**, e0186998-e0186998, doi:10.1371/journal.pone.0186998 (2017).

492 Xuan, W., Qu, Q., Zheng, B., Xiong, S. & Fan, G. H. The chemotaxis of M1 and M2 macrophages is regulated by different chemokines. *J Leukoc Biol* **97**, 61-69, doi:10.1189/jlb.1A0314-170R (2015).

493 Kwiecień, I. *et al.* CD163 and CCR7 as markers for macrophage polarization in lung cancer microenvironment. *Cent Eur J Immunol* **44**, 395-402, doi:10.5114/ceji.2019.92795 (2019).

494 Held-Feindt, J. *et al.* CX3CR1 promotes recruitment of human glioma-infiltrating microglia/macrophages (GIMs). *Exp Cell Res* **316**, 1553-1566, doi:10.1016/j.yexcr.2010.02.018 (2010).

495 Ben-Mordechai, T. *et al.* CX3CR1 Expressing macrophages infiltrate the tumor microenvironment and promote radiation resistance in a mouse model of lung cancer. *International Journal of Radiation Oncology* **105**, S125-S126, doi:10.1016/j.ijrobp.2019.06.103 (2019).

496 Gao, Q. *et al.* Development of an inactivated vaccine candidate for SARS-CoV-2. *Science* **369**, 77-81, doi:doi:10.1126/science.abc1932 (2020).

497 Wang, H. *et al.* Development of an inactivated vaccine candidate, BBIBP-CorV, with potent protection against SARS-CoV-2. *Cell* **182**, 713-721.e719, doi:10.1016/j.cell.2020.06.008 (2020).

498 Bricker, T. L. *et al.* A single intranasal or intramuscular immunization with chimpanzee adenovirus-vectored SARS-CoV-2 vaccine protects against pneumonia in hamsters. *Cell Rep* **36**, 109400, doi:10.1016/j.celrep.2021.109400 (2021).

499 Zohar, T. *et al.* Compromised humoral functional evolution tracks with SARS-CoV-2 Mortality. *Cell* **183**, 1508-1519.e1512, doi:10.1016/j.cell.2020.10.052 (2020).

500 Chan, C. E. Z. *et al.* The Fc-mediated effector functions of a potent SARS-CoV-2 neutralizing antibody, SC31, isolated from an early convalescent COVID-19 patient, are essential for the optimal therapeutic efficacy of the antibody. *PLoS One* **16**, e0253487, doi:10.1371/journal.pone.0253487 (2021).

501 Yamin, R. *et al.* Fc-engineered antibody therapeutics with improved anti-SARS-CoV-2 efficacy. *Nature* **599**, 465-470, doi:10.1038/s41586-021-04017-w (2021).

502 Lee, W. S. *et al.* Decay of Fc-dependent antibody functions after mild to moderate COVID-19. *Cell Rep Med* **2**, 100296, doi:10.1016/j.xcrm.2021.100296 (2021).

503 Folegatti, P. M. *et al.* Safety and immunogenicity of the ChAdOx1 nCoV-19 vaccine against SARS-CoV-2: a preliminary report of a phase 1/2, single-blind, randomised controlled trial. *Lancet* **396**, 467-478, doi:10.1016/s0140-6736(20)31604-4 (2020).

504 Voysey, M. *et al.* Single-dose administration and the influence of the timing of the booster dose on immunogenicity and efficacy of ChAdOx1 nCoV-19 (AZD1222) vaccine: a pooled analysis of four randomised trials. *Lancet* **397**, 881-891, doi:10.1016/s0140-6736(21)00432-3 (2021).

505 Warimwe, G. M. *et al.* Immunogenicity and efficacy of a chimpanzee adenovirus-vectored Rift Valley Fever vaccine in mice. *Virol. J.* **10**, 9, doi:10.1186/1743-422x-10-349 (2013).

506 Folegatti, P. M. *et al.* Safety and immunogenicity of a candidate Middle East respiratory syndrome coronavirus viral-vectored vaccine: a dose-escalation, open-label, non-randomised, uncontrolled, phase 1 trial. *Lancet Infect Dis* **20**, 816-826, doi:10.1016/s1473-3099(20)30160-2 (2020).

507 Thakur, B. *et al.* A systematic review and meta-analysis of geographic differences in comorbidities and associated severity and mortality among individuals with COVID-19. *Sci Rep* **11**, 8562, doi:10.1038/s41598-021-88130-w (2021).

508 Bajaj, V. *et al.* Aging, immunity, and COVID-19: how age influences the host immune response to coronavirus infections? *Front Physiol* **11**, 571416, doi:10.3389/fphys.2020.571416 (2020).

509 Aiello, A. *et al.* Immunosenescence and Its hallmarks: how to oppose aging strategically? A review of potential options for therapeutic intervention. *Front Immunol* **10**, 2247, doi:10.3389/fimmu.2019.02247 (2019).

510 Chason, K. D. *et al.* Age-associated changes in the respiratory epithelial response to influenza infection. *J Gerontol A Biol Sci Med Sci* **73**, 1643-1650, doi:10.1093/gerona/gly126 (2018).

511 Cusi, M. G. *et al.* Age related changes in T cell mediated immune response and effector memory to Respiratory Syncytial Virus (RSV) in healthy subjects. *Immun Ageing* **7**, 14, doi:10.1186/1742-4933-7-14 (2010).

512 Bissel, S. J. *et al.* Age-related pathology associated with H1N1 A/California/07/2009 influenza virus infection. *Am J Pathol* **189**, 2389-2399, doi:10.1016/j.ajpath.2019.08.017 (2019).

513 Singh, D. K. *et al.* Responses to acute infection with SARS-CoV-2 in the lungs of rhesus macaques, baboons and marmosets. *Nat Microbiol* **6**, 73-86, doi:10.1038/s41564-020-00841-4 (2021).

514 Blair, R. V. *et al.* Acute respiratory distress in aged, SARS-CoV-2-infected African green monkeys but not rhesus macaques. *Am J Pathol* **191**, 274-282, doi:10.1016/j.ajpath.2020.10.016 (2021).

515 Song, T. Z. *et al.* Delayed severe cytokine storm and immune cell infiltration in SARS-CoV-2-infected aged Chinese rhesus macaques. *Zool Res* **41**, 503-516, doi:10.24272/j.issn.2095-8137.2020.202 (2020).

516 Rosa, B. A. *et al.* IFN signaling and neutrophil degranulation transcriptional signatures are induced during SARS-CoV-2 infection. *Commun Biol* **4**, 290, doi:10.1038/s42003-021-01829-4 (2021).

517 Linderman G. C. Dimensionality Reduction of Single-Cell RNA-Seq Data. *Methods in molecular biology*, **2284**, 331-342. doi:10.1007/978-1-0716-1307-8_18 (2021).

518 Yu, P. *et al.* Age-related rhesus macaque models of COVID-19. *Animal Model Exp Med* **3**, 93-97, doi:10.1002/ame2.12108 (2020).

519 Speranza, E. *et al.* Age-related differences in immune dynamics during SARS-CoV-2 infection in rhesus macaques. *bioRxiv*, 2021.2009.2008.459430, doi:10.1101/2021.09.08.459430 (2021).

520 Rea, I. M. *et al.* Age and age-related diseases: role of inflammation triggers and cytokines. *Front Immunol* **9**, 586, doi:10.3389/fimmu.2018.00586 (2018).

521 Tran, G. T. *et al.* IL-5 promotes induction of antigen-specific CD4+CD25+ T regulatory cells that suppress autoimmunity. *Blood* **119**, 4441-4450, doi:10.1182/blood-2011-12-396101 (2012).

522 Apostolopoulos, V., McKenzie, I. F., Lees, C., Matthaei, K. I. & Young, I. G. A role for IL-5 in the induction of cytotoxic T lymphocytes in vivo. *Eur J Immunol* **30**, 1733-1739, doi:10.1002/1521-4141(200006)30:6<1733::AID-IMMU1733>3.0.CO;2-E (2000).

523 Bernhard, S. *et al.* Interleukin 8 Elicits Rapid Physiological Changes in Neutrophils That Are Altered by Inflammatory Conditions. *J Innate Immun*, 1-17, doi:10.1159/000514885 (2021).

524 Brubaker, A. L., Rendon, J. L., Ramirez, L., Choudhry, M. A. & Kovacs, E. J. Reduced neutrophil chemotaxis and infiltration contributes to delayed resolution of cutaneous wound infection with advanced age. *J Immunol* **190**, 1746-1757, doi:10.4049/jimmunol.1201213 (2013).

525 Ferrando-Martinez, S. *et al.* Age-related deregulation of naive T cell homeostasis in elderly humans. *Age (Dordr)* **33**, 197-207, doi:10.1007/s11357-010-9170-8 (2011).

526 Cicin-Sain, L. *et al.* Dramatic increase in naive T cell turnover is linked to loss of naive T cells from old primates. *Proc Natl Acad Sci U S A* **104**, 19960-19965, doi:10.1073/pnas.0705905104 (2007).

527 Zharhary, D. Age-related changes in the capability of the bone marrow to generate B cells. *J Immunol* **141**, 1863-1869 (1988).

528 Ma, S., Wang, C., Mao, X. & Hao, Y. B Cell dysfunction associated with aging and autoimmune diseases. *Front Immunol* **10**, 318, doi:10.3389/fimmu.2019.00318 (2019).

529 Mathew, D. *et al.* Deep immune profiling of COVID-19 patients reveals distinct immunotypes with therapeutic implications. *Science* **369**, doi:10.1126/science.abc8511 (2020).

530 Quintelier, K. *et al.* Analyzing high-dimensional cytometry data using FlowSOM. *Nature Protocols* **16**, 3775-3801, doi:10.1038/s41596-021-00550-0 (2021).

531 Van Gassen, S. *et al.* FlowSOM: Using self-organizing maps for visualization and interpretation of cytometry data. *Cytometry A* **87**, 636-645, doi:10.1002/cyto.a.22625 (2015).

532 Soares, A. *et al.* Novel application of Ki67 to quantify antigen-specific in vitro lymphoproliferation. *J Immunol Methods* **362**, 43-50, doi:10.1016/j.jim.2010.08.007 (2010).

533 Rydyznski Moderbacher, C. *et al.* Antigen-Specific Adaptive Immunity to SARS-CoV-2 in Acute COVID-19 and Associations with Age and Disease Severity. *Cell* **183**, 996-1012.e1019, doi:https://doi.org/10.1016/j.cell.2020.09.038 (2020).

534 Christiaansen, A. F. *et al.* CD11a and CD49d enhance the detection of antigen-specific T cells following human vaccination. *Vaccine* **35**, 4255-4261, doi:10.1016/j.vaccine.2017.06.013 (2017).

535 Jian, J.-Y. *et al.* CD49d marks Th1 and Tfh-like antigen-specific CD4+ T cells during Plasmodium chabaudi infection. *International Immunology* **33**, 409-422, doi:10.1093/intimm/dxab020 (2021).

536 De Simone, G. *et al.* CXCR3 Identifies human naive CD8(+) T cells with enhanced effector differentiation potential. *J Immunol* **203**, 3179-3189, doi:10.4049/jimmunol.1901072 (2019).

537 Ahn, E. *et al.* Role of PD-1 during effector CD8 T cell differentiation. *Proceedings of the National Academy of Sciences* **115**, 4749-4754, doi:10.1073/pnas.1718217115 (2018).

538 Petrelli, A. *et al.* PD-1+CD8+ T cells are clonally expanding effectors in human chronic inflammation. *The Journal of clinical investigation* **128**, 4669-4681, doi:10.1172/JCI96107 (2018).

539 Pitcher, C. J. *et al.* Development and homeostasis of T cell memory in rhesus macaque. *J Immunol* **168**, 29-43, doi:10.4049/jimmunol.168.1.29 (2002).

540 Liu, Y., Ma, C. & Zhang, N. Tissue-specific control of tissue-resident memory T cells. *Crit Rev Immunol* **38**, 79-103, doi:10.1615/CritRevImmunol.2018025653 (2018).

541 Ogongo, P., Porterfield, J. Z. & Leslie, A. Lung tissue resident memory T-cells in the immune response to mycobacterium tuberculosis. *Front Immunol* **10**, 992, doi:10.3389/fimmu.2019.00992 (2019).

542 Wu, T. *et al.* Lung-resident memory CD8 T cells (TRM) are indispensable for optimal cross-protection against pulmonary virus infection. *J Leukoc Biol* **95**, 215-224, doi:10.1189/jlb.0313180 (2014).

543 Wiley, J. A. *et al.* Inducible bronchus-associated lymphoid tissue elicited by a protein cage nanoparticle enhances protection in mice against diverse respiratory viruses. *PLoS One* **4**, e7142, doi:10.1371/journal.pone.0007142 (2009).

544 Cesta, M. F. Normal structure, function, and histology of mucosa-associated lymphoid tissue. *Toxicol Pathol* **34**, 599-608, doi:10.1080/01926230600865531 (2006).

545 Viallard, J. F. *et al.* CD8+HLA-DR+ T lymphocytes are increased in common variable immunodeficiency patients with impaired memory B-cell differentiation. *Clin Immunol* **119**, 51-58, doi:10.1016/j.clim.2005.11.011 (2006).

546 Haworth, O. & Levy, B. D. Endogenous lipid mediators in the resolution of airway inflammation. *Eur Respir J* **30**, 980-992, doi:10.1183/09031936.00005807 (2007).

547 Bonnans, C. & Levy, B. D. Lipid mediators as agonists for the resolution of acute lung inflammation and injury. *Am J Respir Cell Mol Biol* **36**, 201-205, doi:10.1165/rcmb.2006-0269TR (2007).

548 Murata, T. *et al.* Anti-inflammatory role of PGD2 in acute lung inflammation and therapeutic application of its signal enhancement. *Proc Natl Acad Sci U S A* **110**, 5205-5210, doi:10.1073/pnas.1218091110 (2013).

549 Loske, J. *et al.* Pre-activated antiviral innate immunity in the upper airways controls early SARS-CoV-2 infection in children. *Nat Biotechnol*, doi:10.1038/s41587-021-01037-9 (2021).

550 Tahaghoghi-Hajghorbani, S. *et al.* The role of dysregulated immune responses in COVID-19 pathogenesis. *Virus Res* **290**, 198197, doi:10.1016/j.virusres.2020.198197 (2020).

551 Dhar, S. K., K, V., Damodar, S., Gujar, S. & Das, M. IL-6 and IL-10 as predictors of disease severity in COVID-19 patients: results from meta-analysis and regression. *Heliyon* **7**, e06155, doi:10.1016/j.heliyon.2021.e06155 (2021).

552 Schmidt, M. E. & Varga, S. M. The CD8 T cell response to respiratory virus infections. *Front Immunol* **9**, 678, doi:10.3389/fimmu.2018.00678 (2018).

553 Sattler, A. *et al.* SARS-CoV-2-specific T cell responses and correlations with COVID-19 patient predisposition. *J Clin Invest* **130**, 6477-6489, doi:10.1172/JCI140965 (2020).

554 McGill, J. & Legge, K. L. Cutting edge: contribution of lung-resident T cell proliferation to the overall magnitude of the antigen-specific CD8 T cell response in the lungs following murine influenza virus infection. *J Immunol* **183**, 4177-4181, doi:10.4049/jimmunol.0901109 (2009).

555 Bergamaschi, L. *et al.* Longitudinal analysis reveals that delayed bystander CD8+ T cell activation and early immune pathology distinguish severe COVID-19 from mild disease. *Immunity* **54**, 1257-1275 e1258, doi:10.1016/j.immuni.2021.05.010 (2021).

556 Wang, Z. *et al.* COVID-19 severity correlates with weaker T-cell immunity, hypercytokinemia, and lung epithelium injury. *Am J Respir Crit Care Med* **202**, 606-610, doi:10.1164/rccm.202005-1701LE (2020).

557 Quinn, K. M. *et al.* Age-related decline in primary CD8(+) T cell responses is associated with the development of senescence in virtual memory CD8(+) T cells. *Cell Rep* **23**, 3512-3524, doi:10.1016/j.celrep.2018.05.057 (2018).

558 Morita, M. *et al.* The lipid mediator protectin D1 inhibits influenza virus replication and improves severe influenza. *Cell* **153**, 112-125, doi:10.1016/j.cell.2013.02.027 (2013).

559 Ramon, S. *et al.* The specialized proresolving mediator 17-HDHA enhances the antibody-mediated immune response against influenza virus: a new class of adjuvant? *J Immunol* **193**, 6031-6040, doi:10.4049/jimmunol.1302795 (2014).

Appendix

Appendix 1. Publications and presentations completed as a DPhil student

A1.1. Publications

**Indicates shared first authorship on the author list*

- Speranza, E.*, **Purushotham, J. N.***, Port, J.R., Schwarz, B., Flagg, M., Williamson, B.N., Feldmann, F., Singh, M., Perez-Perez, L., Sturdevant, G.L., Roberts, L.M., Carmody, A., Schulz, J.E., van Doremalen, N., Okumura, A., Lovaglio, J., Hanley, P.W., Shaia, C., Germain, R.N., Best, S.M., Munster, V.J., Bosio, C.M., de Wit, E. (2022). Age-related differences in immune dynamics during SARS-CoV-2 infection in rhesus macaques. *Life Science Alliance*, 5(4), e202101314.
- **Purushotham, J. N.**, van Doremalen, N., & Munster, V. J. (2021). SARS-CoV-2 vaccines: anamnestic response in previously infected recipients. *Cell Res*, *31*(8), 827-828.
- Fischer, R. J.*, **Purushotham, J. N.***, van Doremalen, N., Sebastian, S., Meade-White, K., Cordova, K., Letko, M., Jeremiah Matson, M., Feldmann, F., Haddock, E., LaCasse, R., Saturday, G., Lambe, T., Gilbert, S. C., & Munster, V. J. (2021). ChAdOx1-vectored Lassa fever vaccine elicits a robust cellular and humoral immune response and protects guinea pigs against lethal Lassa virus challenge. *npj Vaccines*, *6*(1), 32.
- van Doremalen, N., **Purushotham, J. N.**, Schulz, J. E., Holbrook, M. G., Bushmaker, T., Carmody, A., Port, J. R., Yinda, C. K., Okumura, A., Saturday, G., Amanat, F., Krammer, F., Hanley, P. W., Smith, B. J., Lovaglio, J., Anzick, S. L., Barbian, K., Martens, C., Gilbert, S. C., Lambe, T., & Munster, V. J. (2021). Intranasal ChAdOx1 nCoV-19/AZD1222 vaccination reduces viral shedding after SARS-CoV-2 D614G challenge in preclinical models. *Science Translational Medicine*, eabh0755.
- **Purushotham, J.**, Lambe, T., & Gilbert, S. C. (2019). Vaccine platforms for the prevention of Lassa fever. *Immunol Lett*, *215*, 1-11.
- Warimwe, G. M., **Purushotham, J.**, Perry, B. D., Hill, A. V. S., Gilbert, S. C., Dungu, B., & Charleston, B. (2018). Tackling human and animal health threats through innovative vaccinology in Africa. *AAS Open Res*, *1*, 18.

A1.2. Oral presentations

- Purushotham, J.N. Age-related differences in immune dynamics during SARS-CoV-2 infection in rhesus macaques. WHO Working Group on COVID-19 Animal Models. Virtual, 30 September 2021.
- Purushotham, J.N. Multi-omics analysis of the age-related effects of SARS-CoV-2 infection in rhesus macaques. 6th European Congress of Immunology. Virtual, 1-4 September 2021.
- Purushotham, J.N. ChAdOx1 nCoV-19/AZD1222 vaccination induces a multifunctional humoral response as well as distinct cellular and innate immunophenotypes in a rhesus macaque model of SARS-CoV-2 infection. American Society for Virology Annual Meeting. Virtual, 19-23 July 2021.
- Purushotham, J.N. ChAdOx1 nCoV-19/AZD1222 induced immunity to SARS-CoV-2 is characterized by robust humoral immunophenotypes and a reduction in markers of inflammation. XVth International Nidovirus Symposium. Virtual, 7-8 June 2021.
- Purushotham, J.N. Chimpanzee adenoviral vector vaccines for Lassa fever. NIH Oxford-Cambridge 2019 Annual Workshop. University of Oxford, 26 June 2019.

A.1.3. Manuscripts in preparation

- **Purushotham, J.N.***, Speranza, E.*, Port, J.R., et al. ChAdOx1 nCoV-19/AZD1222 induced immunity to SARS-CoV-2 is characterized by robust humoral immunophenotypes and a reduction in markers of inflammation. (Manuscript in final stages of preparation).

- **Purushotham, J.N.***, Fischer, R.J.*, van Doremalen, N., et al. ChAdOx1-Lassa-GPC protects cynomolgus macaques against lethal Lassa fever after single dose and prime-boost immunization. (Manuscript draft under composition).

Appendix 2. NHP clinical scoring sheet.

The humane endpoint threshold was established as a total score of 35 or above, at which point immediate euthanasia was required.

Animal Tattoo:			Study ID:			
Species:	Room:		Date:			
			Time			
	Clinical Signs		Tech:			
				Score	Score	Score
General Appearance	Normal, Alert		0			
	a)Abnormal or Hunched Posture, b)Dull Appearance to Eyes		5			
	a)Dehydration b)Notable Weight Loss c)Obvious Swelling d) Tissue mass		10			
	Bleeding from any orifice (not related to routine procedures or menstruation)		15			
Skin and Haircoat	Normal		0			
	a)Ruffled Fur, b)Unkept Appearance		5			
	a)Rash, b)Pallor, c)Redness, d)Icterus, e)Petechiae, f)Ecchymoses, g) Wound, h)Abscess, i)Ulcer		10			
Nose, Mouth, Eyes, Head	Normal		0			
	a)Nasal discharge, b)Excessive Salivation, c)Ocular Discharge, d)Lacrimation, e)Reddened Eyes, f)Ptosis		5			
Resp	Normal		0			
	a)Increased or b)Decreased Respiration, c)cough, d)sneezing		5			
	a)Dyspnea, b)Open Mouth Breathing, c)Cyanosis		15			
Stool	NS – Normal SNS- Soft normal PS- Pasty Stool	WPS- Wet Pasty TLS – Thick liquid LS – Liquid DS – Dry Hard				
Feces & Urine	Normal		0			
	a)Decreased Feces, b)Dry, Wet and Pasty, c)Watery Feces, d)Discoloration e)Decreased urine, f)Discoloration		2			
	Feces absent		5			
	a)Liquid Feces (if debilitating), b)Urine Absent, c)Blood in Feces or Urine		10			
Appetite	Normal (eating more than half the biscuits)		0			
	Decreased (eating less than half the biscuits)		3			
	Eating Fruit but no biscuits		5			
	Severely decreased (not eating biscuits or fruit)		10			
Activity	Normal		0			
	a) Hyperactivity (circling, increased aggression), b) Hypoactivity (hunched, inactive on camera, active with people in room)		5			
	a)Ataxia, b)Neurological Signs (tremors, head tilt,), c)Loss of Interest in Treats		10			
	a)Reluctant to Move, b)Uses Cage for Support, c)Difficulty Getting to Food or Water (decreased response to human presence), d)Seizures		15			
	a)Down with no or Minimal Response to Human Approach, b)Coma		35			
Food eaten						
Water Given						
TOTAL SCORE						

Appendix 3. Peptide sequences and pool configurations.

A3.1 LASV GPC (strains Josiah, GA391, 803213, and Pinneo) peptide sequences

The peptide libraries were used in the murine immunogenicity experiments detailed in Chapter 3.

Josiah - Lineage IV	No.
MGQIVTFFQEVPHVIEEVMN	1
VPHVIEEVMNIVLIALSVLA	2
IVLIALSVLAVLKGLYNFAT	3
VLKGLYNFATCGLVGLVTFL	4
CGLVGLVTFLLLCGRSCTTS	5
LLCGRSCTTSLYKGVYELQT	6
LYKGVYELQTLELNMETLNM	7
LELNMETLNMTMPLSCTKNN	8
TMPLSCTKNNSHHYIMVGNE	9
SHHYIMVGNETGLELTLTNT	10
TGLELTLTNTSIINHKFCNL	11
SIINHKFCNLSDAHKKNLYD	12
SDAHKKNLYDHALMSIISTF	13
HALMSIISTFHLSIPNFNQY	14
HLSIPNFNQYEAMSCDFNGG	15
EAMSCDFNGGKISVQYNLSH	16
KISVQYNLSHSYAGDAANHC	17
SYAGDAANHCGTVANGVLQT	18
GTVANGVLQTFMRMAWGGSY	19
FMRMAWGGSYIALDSGRGNW	20
IALDSGRGNWDCIMTSYQYL	21
DCIMTSYQYLIIQNTTWEDH	22
IIQNTTWEDHCQFSRPSPIG	23
CQFSRPSPIGYLGLLSQRTR	24
YLGLLSQRTRDIYISRRLLG	25
DIYISRRLLGTFTWTLSDSE	26
TFTWTLSDSEGKDTPGGYCL	27
GKDTPGGYCLTRWMLIEAEL	28
TRWMLIEAELKCFGNTAVAK	29
KCFGNTAVAKCNEKHDEEFC	30
CNEKHDEEFCDMLRLFDFNK	31
DMLRLFDFNKQAIQRLKAEA	32
QAIQRLKAEAQMSIQLINKA	33
QMSIQLINKAVNALINDQLI	34
VNALINDQLIMKNHLRDIMG	35
MKNHLRDIMGIPYCNYSKYW	36
IPYCNYSKYWYLNHTTTGRT	37
YLNHTTTGRTSLPKCWLVSN	38
SLPKCWLVSNGSYLNETHFS	39
GSYLNETHFSDDIEQQADNM	40
DDIEQQADNMITEMLQKEYM	41
ITEMLQKEYMERQGKTPLGL	42
ERQGKTPLGLVDLFVFSTSF	43
VDLFVFSTSFYLISIFLHLV	44
YLISIFLHLVKIPTHRHIVG	45
KIPTHRHIVGKSCPKPHRLN	46
KSCPKPHRLNHMGICSCGLY	47
HMGICSCGLYKQPGVPVKWK	48
KQPGVPVKWKR	49

GA391 - Lineage III	No.
MGQIVTFFQEVPHVIEEVMN	1
VPHVIEEVMNIVLIALSILA	2
IVLIALSILAILKGLYNVAT	3
ILKGLYNVATCGLIGLVTFL	4
CGLIGLVTFLLLSGRSCSLI	5
LLSGRSCSLIYKGTYELQTL	6
YKGTYELQTLELNMETLNMT	7
ELNMETLNMTMPLSCTKNNS	8
MPLSCTKNNSHHYIRVGNET	9
HHYIRVGNETGLELTLTNTS	10
GLELTLTNTSILNHKFCNLS	11
ILNHKFCNLSDAHKRNLYDH	12
DAHKRNLYDHSLMSIISTFH	13
SLMSIISTFHLSIPNFNQYE	14
LSIPNFNQYEAMSCDFNGGK	15
AMSCDFNGGKITVQYNLSHS	16
ITVQYNLSHSFAVDAAGHCG	17
FAVDAAGHCGTLANGVLQTF	18
TLANGVLQTFMRMAWGGSYI	19
MRMAWGGSYIALDSGRGNWD	20
ALDSGRGNWDCIMTSYQYLI	21
CIMTSYQYLIIQNTTWDDHC	22
IQNTTWDDHCQFSRPSPIGY	23
QFSRPSPIGYLGLLSQRTRD	24
LGLLSQRTRDIYISRRLLGT	25
IYISRRLLGTFTWTLSDSEG	26
FTWTLSDSEGNETPGGYCLT	27
NETPGGYCLTRWMLIEAELK	28
RWMLIEAELKCFGNTAVAKC	29
CFGNTAVAKCNEKHDEEFCD	30
NEKHDEEFCDMLRLFDFNKQ	31
MLRLFDFNKQAIRRLKTEAQ	32
AIRRLKTEAQMSIQLINKAV	33
MSIQLINKAVNALINDQLIM	34
NALINDQLIMKNHLRDIMGI	35
KNHLRDIMGIPYCNYSRYWY	36
PYCNYSRYWYLNHTSTGKTS	37
LNHTSTGKTSLPRCWLISNG	38
LPRCWLISNGSYLNETKFSD	39
SYLNETKFSDDIEQQADNMI	40
DIEQQADNMITEMLQKEYID	41
TEMLQKEYIDRQGKTPLGLV	42
RQGKTPLGLVDLFVFSTSFY	43
DLFVFSTSFYLISIFLHLVK	44
LISIFLHLVKIPTHRHIVGK	45
IPTHRHIVGKPCPKPHRLNH	46
PCPKPHRLNHMGICSCGLYK	47
MGICSCGLYKQPGVPVRWKR	48

803213 - Lineage II	No.
MGQIITFFQEVPHVIEEVMN	1
VPHVIEEVMNIVLIALSLLA	2
IVLIALSLLAILKGIYNVAT	3
ILKGIYNVATCGLFGLISFL	4
CGLFGLISFLLLCGRSCSVT	5
LLCGRSCSVTYKGVYELQTL	6
YKGVYELQTLELNMANLNMT	7
ELNMANLNMTMPLSCTKNNS	8
MPLSCTKNNSHHYIMVGNET	9
HHYIMVGNETGLELTLTNTS	10
GLELTLTNTSIINHKFCNLS	11
IINHKFCNLSDAHKKNLYDH	12
DAHKKNLYDHALMSIISTFH	13
ALMSIISTFHLSIPNFNQYE	14
LSIPNFNQYEAMSCDFNGGK	15
AMSCDFNGGKISVQYNLSHS	16
ISVQYNLSHSFAVDAANHCG	17
FAVDAANHCGTIANGVLQTF	18
TIANGVLQTFMRMAWGGSYI	19
MRMAWGGSYIALDSGKGNWD	20
ALDSGKGNWDCIMTSYQYLI	21
CIMTSYQYLIIQNTTWEDHC	22
IQNTTWEDHCQFSRPSPIGY	23
QFSRPSPIGYLGLLSQRTRD	24
LGLLSQRTRDIYISRRLLGT	25
IYISRRLLGTFTWTLSDSEG	26
FTWTLSDSEGNEAPGGYCLT	27
NEAPGGYCLTRWMLIEAELK	28
RWMLIEAELKCFGNTAVAKC	29
CFGNTAVAKCNEKHDEEFCD	30
NEKHDEEFCDMLRLFDFNKQ	31
MLRLFDFNKQAIKRLKTEAQ	32
AIKRLKTEAQMSIQLINKAV	33
MSIQLINKAVNALINDQLIM	34
NALINDQLIMKNHLRDIMGI	35
KNHLRDIMGIPYCNYSRYWY	36
PYCNYSRYWYLNHTVTGKTS	37
LNHTVTGKTSLPRCWLVSNG	38
LPRCWLVSNGSYLNETHFSD	39
SYLNETHFSDDIEQQADNMI	40
DIEQQADNMITEMLQKEYMD	41
TEMLQKEYMDRQGKTPLGLV	42
RQGKTPLGLVDLFVFSTSFY	43
DLFVFSTSFYLISIFLHLVK	44
LISIFLHLVKIPTHRHIVGK	45
IPTHRHIVGKPCPKPHRLNH	46
PCPKPHRLNHMGICSCGLYK	47
MGICSCGLYKHPGVPVKWKR	48

Pinneo - Lineage I	No.
MGQIITFFQEVPHVIEEVMN	1
VPHVIEEVMNIVLIALSLLA	2
IVLIALSLLAILKGLYNIAT	3
ILKGLYNIATCGIIGLVAFL	4
CGIIGLVAFLFLCGKSCSLT	5
FLCGKSCSLTLKGGYELQTL	6
LKGGYELQTLELNMETLNMT	7
ELNMETLNMTMPLSCTKNSS	8
MPLSCTKNSSHHYIRVGNET	9
HHYIRVGNETGLELTLTNTS	10
GLELTLTNTSIINHKFCNLS	11
IINHKFCNLSDAHKKNLYDH	12
DAHKKNLYDHALMSIISTFH	13
ALMSIISTFHLSIPNFNQYE	14
LSIPNFNQYEAMSCDFNGGK	15
AMSCDFNGGKISVQYNLSHS	16
ISVQYNLSHSYAGDAAEHCG	17
YAGDAAEHCGTVANGVLQTF	18
TVANGVLQTFMRMAWGGRYI	19
MRMAWGGRYIALDSGKGNWD	20
ALDSGKGNWDCIMTSYQYLI	21
CIMTSYQYLIIQNTTWEDHC	22
IQNTTWEDHCQFSRPSPIGY	23
QFSRPSPIGYLGLLSQRTRD	24
LGLLSQRTRDIYISRRLLGT	25
IYISRRLLGTFTWTLSDSEG	26
FTWTLSDSEGNETPGGYCLT	27
NETPGGYCLTRWMLIEAELK	28
RWMLIEAELKCFGNTAVAKC	29
CFGNTAVAKCNEKHDEEFCD	30
NEKHDEEFCDMLRLFDFNKQ	31
MLRLFDFNKQAIRRLKAEAQ	32
AIRRLKAEAQMSIQLINKAV	33
MSIQLINKAVNALINDQLIM	34
NALINDQLIMKNHLRDIMGI	35
KNHLRDIMGIPYCNYSKYWY	36
PYCNYSKYWYLNHTSSGRTS	37
LNHTSSGRTSLPKCWLISNG	38
LPKCWLISNGSYLNETQFSD	39
SYLNETQFSDDIEQQADNMI	40
DIEQQADNMITEMLQKEYIE	41
TEMLQKEYIERQGKTPLGLV	42
RQGKTPLGLVDIFIFSTSFY	43
DIFIFSTSFYLISIFLHLIK	44
LISIFLHLIKIPTHRHIVGK	45
IPTHRHIVGKPCPKPHRLNH	46
PCPKPHRLNHMGVCSCGLYK	47
MGVCSCGLYKHPGVPTKWKR	48

A3.2 LASV Josiah GPC NHP peptide sequences and pool configurations

The peptide libraries were used in the NHP immunogenicity experiments detailed in Chapter 4.

Peptide no.	Sequence	ELISpot pools
peptide_1	MGQIVTFFQEVPHVI	A
peptide_2	VTFFQEVPHVIEEVM	A
peptide_3	QEVPHVIEEVMNIVL	A
peptide_4	HVIEEVMNIVLIALS	A
peptide_5	EVMNIVLIALSVLAV	A
peptide_6	IVLIALSVLAVLKGL	A
peptide_7	ALSVLAVLKGLYNFA	A
peptide_8	LAVLKGLYNFATCGL	A
peptide_9	KGLYNFATCGLVGLV	A
peptide_10	NFATCGLVGLVTFLL	A
peptide_11	CGLVGLVTFLLLCGR	A
peptide_12	GLVTFLLLCGRSCTT	A
peptide_13	FLLLCGRSCTTSLYK	A
peptide_14	CGRSCTTSLYKGVYE	A
peptide_15	CTTSLYKGVYELQTL	A
peptide_16	LYKGVYELQTLELNM	A
peptide_17	VYELQTLELNMETLN	A
peptide_18	QTLELNMETLNMTMP	A
peptide_19	LNMETLNMTMPLSCT	A
peptide_20	TLNMTMPLSCTKNNS	A
peptide_21	TMPLSCTKNNSHHYI	A
peptide_22	SCTKNNSHHYIMVGN	A
peptide_23	NNSHHYIMVGNETGL	A
peptide_24	HYIMVGNETGLELTL	A
peptide_25	VGNETGLELTLTNTS	A
peptide_26	TGLELTLTNTSIINH	A
peptide_27	LTLTNTSIINHKFCN	A
peptide_28	NTSIINHKFCNLSDA	A
peptide_29	INHKFCNLSDAHKKN	A
peptide_30	FCNLSDAHKKNLYDH	A
peptide_31	SDAHKKNLYDHALMS	A
peptide_32	KKNLYDHALMSIIST	A
peptide_33	YDHALMSIISTFHLS	A
peptide_34	LMSIISTFHLSIPNF	A
peptide_35	ISTFHLSIPNFNQYE	A
peptide_36	HLSIPNFNQYEAMSC	A
peptide_37	PNFNQYEAMSCDFNG	A
peptide_38	QYEAMSCDFNGGKIS	A
peptide_39	MSCDFNGGKISVQYN	A
peptide_40	FNGGKISVQYNLSHS	A

Peptide no.	Sequence	ELISpot pools
peptide_41	KISVQYNLSHSYAGD	B
peptide_42	QYNLSHSYAGDAANH	B
peptide_43	SHSYAGDAANHCGTV	B
peptide_44	AGDAANHCGTVANGV	B
peptide_45	ANHCGTVANGVLQTF	B
peptide_46	GTVANGVLQTFMRMA	B
peptide_47	NGVLQTFMRMAWGGS	B
peptide_48	QTFMRMAWGGSYIAL	B
peptide_49	RMAWGGSYIALDSGR	B
peptide_50	GGSYIALDSGRGNWD	B
peptide_51	IALDSGRGNWDCIMT	B
peptide_52	SGRGNWDCIMTSYQY	B
peptide_53	NWDCIMTSYQYLIIQ	B
peptide_54	IMTSYQYLIIQNTTW	B
peptide_55	YQYLIIQNTTWEDHC	B
peptide_56	IIQNTTWEDHCQFSR	B
peptide_57	TTWEDHCQFSRPSPI	B
peptide_58	DHCQFSRPSPIGYLG	B
peptide_59	FSRPSPIGYLGLLSQ	B
peptide_60	SPIGYLGLLSQRTRD	B
peptide_61	YLGLLSQRTRDIYIS	B
peptide_62	LSQRTRDIYISRRLL	B
peptide_63	TRDIYISRRLLGTFT	B
peptide_64	YISRRLLGTFTWTLS	B
peptide_65	RLLGTFTWTLSDSEG	B
peptide_66	TFTWTLSDSEGKDTP	B
peptide_67	TLSDSEGKDTPGGYC	B
peptide_68	SEGKDTPGGYCLTRW	B
peptide_69	DTPGGYCLTRWMLIE	B
peptide_70	GYCLTRWMLIEAELK	B
peptide_71	TRWMLIEAELKCFGN	B
peptide_72	LIEAELKCFGNTAVA	B
peptide_73	ELKCFGNTAVAKCNE	B
peptide_74	FGNTAVAKCNEKHDE	B
peptide_75	AVAKCNEKHDEEFCD	B
peptide_76	CNEKHDEEFCDMLRL	B
peptide_77	HDEEFCDMLRLFDFN	B
peptide_78	FCDMLRLFDFNKQAI	B
peptide_79	LRLFDFNKQAIQRLK	B

Peptide no.	Sequence	ELISpot pools
peptide_80	DFNKQAIQRLKAEAQ	C
peptide_81	QAIQRLKAEAQMSIQ	C
peptide_82	RLKAEAQMSIQLINK	C
peptide_83	EAQMSIQLINKAVNA	C
peptide_84	SIQLINKAVNALIND	C
peptide_85	INKAVNALINDQLIM	C
peptide_86	VNALINDQLIMKNHL	C
peptide_87	INDQLIMKNHLRDIM	C
peptide_88	LIMKNHLRDIMGIPY	C
peptide_89	NHLRDIMGIPYCNYS	C
peptide_90	DIMGIPYCNYSKYWY	C
peptide_91	IPYCNYSKYWYLNHT	C
peptide_92	NYSKYWYLNHTTTGR	C
peptide_93	YWYLNHTTTGRTSLP	C
peptide_94	NHTTTGRTSLPKCWL	C
peptide_95	TGRTSLPKCWLVSNG	C
peptide_96	SLPKCWLVSNGSYLN	C
peptide_97	CWLVSNGSYLNETHF	C
peptide_98	SNGSYLNETHFSDDI	C
peptide_99	YLNETHFSDDIEQQA	C
peptide_100	THFSDDIEQQADNMI	C
peptide_101	DDIEQQADNMITEML	C
peptide_102	QQADNMITEMLQKEY	C
peptide_103	NMITEMLQKEYMERQ	C
peptide_104	EMLQKEYMERQGKTP	C
peptide_105	KEYMERQGKTPLGLV	C
peptide_106	ERQGKTPLGLVDLFV	C
peptide_107	KTPLGLVDLFVFSTS	C
peptide_108	GLVDLFVFSTSFYLI	C
peptide_109	LFVFSTSFYLISIFL	C
peptide_110	STSFYLISIFLHLVK	C
peptide_111	YLISIFLHLVKIPTH	C
peptide_112	IFLHLVKIPTHRHIV	C
peptide_113	LVKIPTHRHIVGKSC	C
peptide_114	PTHRHIVGKSCPKPH	C
peptide_115	HIVGKSCPKPHRLNH	C
peptide_116	KSCPKPHRLNHMGIC	C
peptide_117	KPHRLNHMGICSCGL	C
peptide_118	LNHMGICSCGLYKQP	C
peptide_119	GICSCGLYKQPGVPV	C
peptide_120	CGLYKQPGVPVKWKR	C

A3.3 SARS-CoV-2 S peptide sequences and pool configurations

Peptide No.	Sequence	ELIspot pools	ICS pools
peptide_1	MFVFLVLLPLVSSQC	1	S1
peptide_2	LVLLPLVSSQCVNLT		
peptide_3	PLVSSQCVNLTTRTQ		
peptide_4	SQCVNLTTRTQLPPA		
peptide_5	NLTTRTQLPPAYTNS		
peptide_6	RTQLPPAYTNSFTRG		
peptide_7	PPAYTNSFTRGVYYP		
peptide_8	TNSFTRGVYYPDKVF		
peptide_9	TRGVYYPDKVFRSSV		
peptide_10	YYPDKVFRSSVLHST		
peptide_11	KVFRSSVLHSTQDLF		
peptide_12	SSVLHSTQDLFLPFF		
peptide_13	HSTQDLFLPFFSNVT		
peptide_14	DLFLPFFSNVTWFHA		
peptide_15	PFFSNVTWFHAIHVS		
peptide_16	NVTWFHAIHVSGTNG		
peptide_17	FHAIHVSGTNGTKRF		
peptide_18	HVSGTNGTKRFDNPV		
peptide_19	TNGTKRFDNPVLPFN		
peptide_20	KRFDNPVLPFNDGVY		
peptide_21	NPVLPFNDGVYFAST		
peptide_22	PFNDGVYFASTEKSN		
peptide_23	GVYFASTEKSNIIRG		
peptide_24	ASTEKSNIIRGWIFG		
peptide_25	KSNIIRGWIFGTTLD		
peptide_26	IRGWIFGTTLDSKTQ		
peptide_27	IFGTTLDSKTQSLLI		
peptide_28	TLDSKTQSLLIVNNA		
peptide_29	KTQSLLIVNNATNVV		
peptide_30	LLIVNNATNVVIKVC		
peptide_31	NNATNVVIKVCEFQF		
peptide_32	NVVIKVCEFQFCNDP		
peptide_33	KVCEFQFCNDPFLGV		
peptide_34	FQFCNDPFLGVYYHK		
peptide_35	NDPFLGVYYHKNNKS		
peptide_36	LGVYYHKNNKSWMES		
peptide_37	YHKNNKSWMESEFRV		
peptide_38	NKSWMESEFRVYSSA		
peptide_39	MESEFRVYSSANNCT		
peptide_40	FRVYSSANNCTFEYV		
peptide_41	SSANNCTFEYVSQPF		
peptide_42	NCTFEYVSQPFLMDL		
peptide_43	EYVSQPFLMDLEGKQ		
peptide_44	QPFLMDLEGKQGNFK		
peptide_45	MDLEGKQGNFKNLRE		
peptide_46	GKQGNFKNLREFVFK		
peptide_47	NFKNLREFVFKNIDG		
peptide_48	LREFVFKNIDGYFKI		
peptide_49	VFKNIDGYFKIYSKH		
peptide_50	IDGYFKIYSKHTPIN		
peptide_51	FKIYSKHTPINLVRD		
peptide_52	SKHTPINLVRDLPQG		
peptide_53	PINLVRDLPQGFSAL		
peptide_54	VRDLPQGFSALEPLV		
peptide_55	PQGFSALEPLVDLPI		
peptide_56	SALEPLVDLPIGINI		
peptide_57	PLVDLPIGINITRFQ		
peptide_58	LPIGINITRFQTLLA		
peptide_59	INITRFQTLLALHRS		
peptide_60	RFQTLLALHRSYLTP		
peptide_61	LLALHRSYLTPGDSS		
peptide_62	HRSYLTPGDSSSGWT		
peptide_63	LTPGDSSSGWTAGAA		
peptide_64	DSSSGWTAGAAAYYV		
peptide_65	GWTAGAAAYYVGYLQ		
peptide_66	GAAAYYVGYLQPRTF		
peptide_67	YYVGYLQPRTFLLKY		
peptide_68	YLQPRTFLLKYNENG		
peptide_69	RTFLLKYNENGTITD		
peptide_70	LKYNENGTITDAVDC		
peptide_71	ENGTITDAVDCALDP		
peptide_72	ITDAVDCALDPLSET		
peptide_73	VDCALDPLSETKCTL		
peptide_74	LDPLSETKCTLKSFT		
peptide_75	SETKCTLKSFTVEKG		
peptide_76	CTLKSFTVEKGIYQT		
peptide_77	SFTVEKGIYQTSNFR		

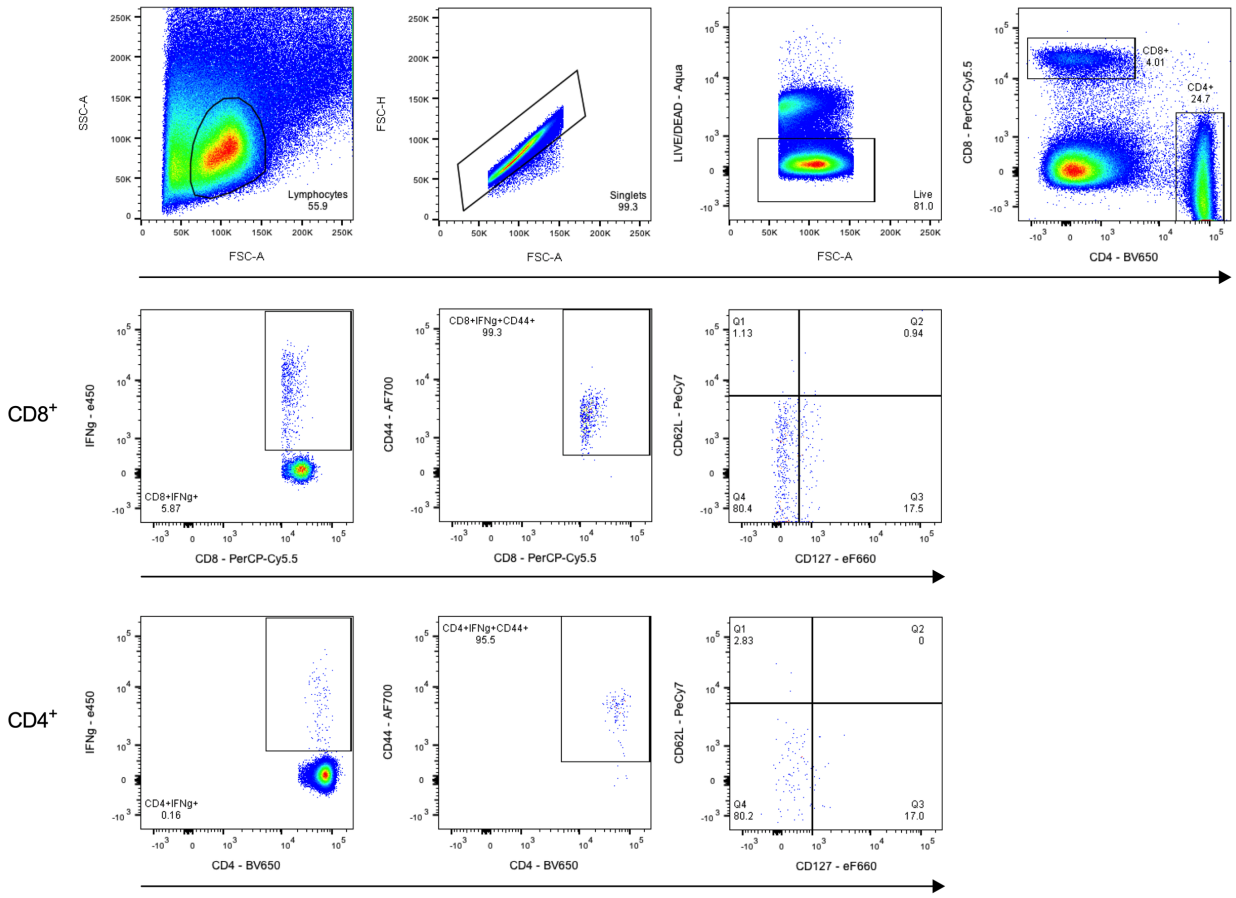
Peptide No.	Sequence	ELIspot pools	ICS pools
peptide_78	EKGIYQTSNFRVQPT	2	S1
peptide_79	YQTSNFRVQPTESIV		
peptide_80	NFRVQPTESIVRFPN		
peptide_81	QPTESIVRFPNITNL		
peptide_82	SIVRFPNITNLCPFG		
peptide_83	FPNITNLCPFGEVFN		
peptide_84	TNLCPFGEVFNATRF		
peptide_85	PFGEVFNATRFASVY		
peptide_86	VFNATRFASVYAWNR		
peptide_87	TRFASVYAWNRKRIS		
peptide_88	SVYAWNRKRISNCVA		
peptide_89	WNRKRISNCVADYSV		
peptide_90	RISNCVADYSVLYNS		
peptide_91	CVADYSVLYNSASFS		
peptide_92	YSVLYNSASFSTFKC		
peptide_93	YNSASFSTFKCYGVS		
peptide_94	SFSTFKCYGVSPTKL		
peptide_95	FKCYGVSPTKLNDLC		
peptide_96	GVSPTKLNDLCFTNV		
peptide_97	TKLNDLCFTNVYADS		
peptide_98	DLCFTNVYADSFVIR		
peptide_99	TNVYADSFVIRGDEV		
peptide_100	ADSFVIRGDEVRQIA		
peptide_101	VIRGDEVRQIAPGQT		
peptide_102	DEVRQIAPGQTGKIA		
peptide_103	QIAPGQTGKIADYNY		
peptide_104	GQTGKIADYNYKLPD		
peptide_105	KIADYNYKLPDDFTG		
peptide_106	YNYKLPDDFTGCVIA		
peptide_107	LPDDFTGCVIAWNSN		
peptide_108	FTGCVIAWNSNNLDS		
peptide_109	VIAWNSNNLDSKVGG		
peptide_110	NSNNLDSKVGGNYNY		
peptide_111	LDSKVGGNYNYLYRL		
peptide_112	VGGNYNYLYRLFRKS		
peptide_113	YNYLYRLFRKSNLKP		
peptide_114	YRLFRKSNLKPFERD		
peptide_115	RKSNLKPFERDISTE		
peptide_116	LKPFERDISTEIYQA		
peptide_117	ERDISTEIYQAGSTP		
peptide_118	STEIYQAGSTPCNGV		
peptide_119	YQAGSTPCNGVEGFN		
peptide_120	STPCNGVEGFNCYFP		
peptide_121	NGVEGFNCYFPLQSY		
peptide_122	GFNCYFPLQSYGFQP		
peptide_123	YFPLQSYGFQPTNGV		
peptide_124	QSYGFQPTNGVGYQP		
peptide_125	FQPTNGVGYQPYRVV		
peptide_126	NGVGYQPYRVVVLSF		
peptide_127	YQPYRVVVLSFELLH		
peptide_128	RVVVLSFELLHAPAT		
peptide_129	LSFELLHAPATVCGP		
peptide_130	LLHAPATVCGPKKST		
peptide_131	PATVCGPKKSTNLVK		
peptide_132	CGPKKSTNLVKNKCV		
peptide_133	KSTNLVKNKCVNFNF		
peptide_134	LVKNKCVNFNFNGLT		
peptide_135	KCVNFNFNGLTGTGV		
peptide_136	FNFNGLTGTGVLTES		
peptide_137	GLTGTGVLTESNKKF		
peptide_138	TGVLTESNKKFLPFQ		
peptide_139	TESNKKFLPFQQFGR		
peptide_140	KKFLPFQQFGRDIAD		
peptide_141	PFQQFGRDIADTTDA		
peptide_142	FGRDIADTTDAVRDP		
peptide_143	IADTTDAVRDPQTLE		
peptide_144	TDAVRDPQTLEILDI		
peptide_145	RDPQTLEILDITPCS		
peptide_146	TLEILDITPCSFGGV		
peptide_147	LDITPCSFGGVSVIT		
peptide_148	PCSFGGVSVITPGTN		
peptide_149	GGVSVITPGTNTSNQ		
peptide_150	VITPGTNTSNQVAVL		
peptide_151	GTNTSNQVAVLYQDV		
peptide_152	SNQVAVLYQDVNCTE		
peptide_153	AVLYQDVNCTEVPVA		
peptide_154	QDVNCTEVPVAIHAD		
peptide_155	CTEVPVAIHADQLTP		
peptide_156	PVAIHADQLTPTWRV		
peptide_157	HADQLTPTWRVYSTG		
peptide_158	LTPTWRVYSTGSNVF		
peptide_159	WRVYSTGSNVFQTRA		
peptide_160	STGSNVFQTRAGCLI		
peptide_161	NVFQTRAGCLIGAEH		
peptide_162	TRAGCLIGAEHVNNS		
peptide_163	CLIGAEHVNNSYECD		
peptide_164	AEHVNNSYECDIPIG		
peptide_165	NNSYECDIPIGAGIC		
peptide_166	ECDIPIGAGICASYQ		
peptide_167	PIGAGICASYQTQTN		

Peptide No.	Sequence	ELIspot pools	ICS pools
peptide_168	GICASYQTQTNSPRR	3	S2
peptide_169	SYQTQTNSPRRARSV		
peptide_170	QTNSPRRARSVASQS		
peptide_171	PRRARSVASQSIIAY		
peptide_172	RSVASQSIIAYTMSL		
peptide_173	SQSIIAYTMSLGAEN		
peptide_174	IAYTMSLGAENSVAY		
peptide_175	MSLGAENSVAYSNNS		
peptide_176	AENSVAYSNNSIAIP		
peptide_177	VAYSNNSIAIPTNFT		
peptide_178	NNSIAIPTNFTISVT		
peptide_179	AIPTNFTISVTTEIL		
peptide_180	NFTISVTTEILPVSM		
peptide_181	SVTTEILPVSMTKTS		
peptide_182	EILPVSMTKTSVDCT		
peptide_183	VSMTKTSVDCTMYIC		
peptide_184	KTSVDCTMYICGDST		
peptide_185	DCTMYICGDSTECSN		
peptide_186	YICGDSTECSNLLLQ		
peptide_187	DSTECSNLLLQYGSF		
peptide_188	CSNLLLQYGSFCTQL		
peptide_189	LLQYGSFCTQLNRAL		
peptide_190	GSFCTQLNRALTGIA		
peptide_191	TQLNRALTGIAVEQD		
peptide_192	RALTGIAVEQDKNTQ		
peptide_193	GIAVEQDKNTQEVFA		
peptide_194	EQDKNTQEVFAQVKQ		
peptide_195	NTQEVFAQVKQIYKT		
peptide_196	VFAQVKQIYKTPPIK		
peptide_197	VKQIYKTPPIKDFGG		
peptide_198	YKTPPIKDFGGFNFS		
peptide_199	PIKDFGGFNFSQILP		
peptide_200	FGGFNFSQILPDPSK		
peptide_201	NFSQILPDPSKPSKR		
peptide_202	ILPDPSKPSKRSFIE		
peptide_203	PSKPSKRSFIEDLLF		
peptide_204	SKRSFIEDLLFNKVT		
peptide_205	FIEDLLFNKVTLADA		
peptide_206	LLFNKVTLADAGFIK		
peptide_207	KVTLADAGFIKQYGD		
peptide_208	ADAGFIKQYGDCLGD		
peptide_209	FIKQYGDCLGDIAAR		
peptide_210	YGDCLGDIAARDLIC		
peptide_211	LGDIAARDLICAQKF		
peptide_212	AARDLICAQKFNGLT		
peptide_213	LICAQKFNGLTVLPP		
peptide_214	QKFNGLTVLPPLLTD		
peptide_215	GLTVLPPLLTDEMIA		
peptide_216	LPPLLTDEMIAQYTS		
peptide_217	LTDEMIAQYTSALLA		
peptide_218	MIAQYTSALLAGTIT		
peptide_219	YTSALLAGTITSGWT		
peptide_220	LLAGTITSGWTFGAG		
peptide_221	TITSGWTFGAGAALQ		
peptide_222	GWTFGAGAALQIPFA		
peptide_223	GAGAALQIPFAMQMA		
peptide_224	ALQIPFAMQMAYRFN		
peptide_225	PFAMQMAYRFNGIGV		
peptide_226	QMAYRFNGIGVTQNV		
peptide_227	RFNGIGVTQNVLYEN		
peptide_228	IGVTQNVLYENQKLI		
peptide_229	QNVLYENQKLIANQF		
peptide_230	YENQKLIANQFNSAI		
peptide_231	KLIANQFNSAIGKIQ		
peptide_232	NQFNSAIGKIQDSLS		
peptide_233	SAIGKIQDSLSSTAS		
peptide_234	KIQDSLSSTASALGK		
peptide_235	SLSSTASALGKLQDV		
peptide_236	TASALGKLQDVVNQN		
peptide_237	LGKLQDVVNQNAQAL		
peptide_238	QDVVNQNAQALNTLV		
peptide_239	NQNAQALNTLVKQLS		
peptide_240	QALNTLVKQLSSNFG		
peptide_241	TLVKQLSSNFGAISS		

Peptide No.	Sequence	ELIspot pools	ICS pools
peptide_242	QLSSNFGAISSVLND	4	S2
peptide_243	NFGAISSVLNDILSR		
peptide_244	ISSVLNDILSRLDKV		
peptide_245	LNDILSRLDKVEAEV		
peptide_246	LSRLDKVEAEVQIDR		
peptide_247	DKVEAEVQIDRLITG		
peptide_248	AEVQIDRLITGRLQS		
peptide_249	IDRLITGRLQSLQTY		
peptide_250	ITGRLQSLQTYVTQQ		
peptide_251	LQSLQTYVTQQLIRA		
peptide_252	QTYVTQQLIRAAEIR		
peptide_253	TQQLIRAAEIRASAN		
peptide_254	IRAAEIRASANLAAT		
peptide_255	EIRASANLAATKMSE		
peptide_256	SANLAATKMSECVLG		
peptide_257	AATKMSECVLGQSKR		
peptide_258	MSECVLGQSKRVDFC		
peptide_259	VLGQSKRVDFCGKGY		
peptide_260	SKRVDFCGKGYHLMS		
peptide_261	DFCGKGYHLMSFPQS		
peptide_262	KGYHLMSFPQSAPHG		
peptide_263	LMSFPQSAPHGVVFL		
peptide_264	PQSAPHGVVFLHVTY		
peptide_265	PHGVVFLHVTYVPAQ		
peptide_266	VFLHVTYVPAQEKNF		
peptide_267	VTYVPAQEKNFTTAP		
peptide_268	PAQEKNFTTAPAICH		
peptide_269	KNFTTAPAICHDGKA		
peptide_270	TAPAICHDGKAHFPR		
peptide_271	ICHDGKAHFPREGVF		
peptide_272	GKAHFPREGVFVSNG		
peptide_273	FPREGVFVSNGTHWF		
peptide_274	GVFVSNGTHWFVTQR		
peptide_275	SNGTHWFVTQRNFYE		
peptide_276	HWFVTQRNFYEPQII		
peptide_277	TQRNFYEPQIITTDN		
peptide_278	FYEPQIITTDNTFVS		
peptide_279	QIITTDNTFVSGNCD		
peptide_280	TDNTFVSGNCDVVIG		
peptide_281	FVSGNCDVVIGIVNN		
peptide_282	NCDVVIGIVNNTVYD		
peptide_283	VIGIVNNTVYDPLQP		
peptide_284	VNNTVYDPLQPELDS		
peptide_285	VYDPLQPELDSFKEE		
peptide_286	LQPELDSFKEELDKY		
peptide_287	LDSFKEELDKYFKNH		
peptide_288	KEELDKYFKNHTSPD		
peptide_289	DKYFKNHTSPDVDLG		
peptide_290	KNHTSPDVDLGDISG		
peptide_291	SPDVDLGDISGINAS		
peptide_292	DLGDISGINASVVNI		
peptide_293	ISGINASVVNIQKEI		
peptide_294	NASVVNIQKEIDRLN		
peptide_295	VNIQKEIDRLNEVAK		
peptide_296	KEIDRLNEVAKNLNE		
peptide_297	RLNEVAKNLNESLID		
peptide_298	VAKNLNESLIDLQEL		
peptide_299	LNESLIDLQELGKYE		
peptide_300	LIDLQELGKYEQYIK		
peptide_301	QELGKYEQYIKWPWY		
peptide_302	KYEQYIKWPWYIWLG		
peptide_303	YIKWPWYIWLGFIAG		
peptide_304	PWYIWLGFIAGLIAI		
peptide_305	WLGFIAGLIAIVMVT		
peptide_306	IAGLIAIVMVTIMLC		
peptide_307	IAIVMVTIMLCCMTS		
peptide_308	MVTIMLCCMTSCCSC		
peptide_309	MLCCMTSCCSCLKGC		
peptide_310	MTSCCSCLKGCCSCG		
peptide_311	CSCLKGCCSCGSCCK		
peptide_312	KGCCSCGSCCKFDED		
peptide_313	SCGSCCKFDEDDSEP		
peptide_314	CCKFDEDDSEPVLKG		
peptide_315	DEDDSEPVLKGVKLH		
peptide_316	SEPVLKGVKLHYT		

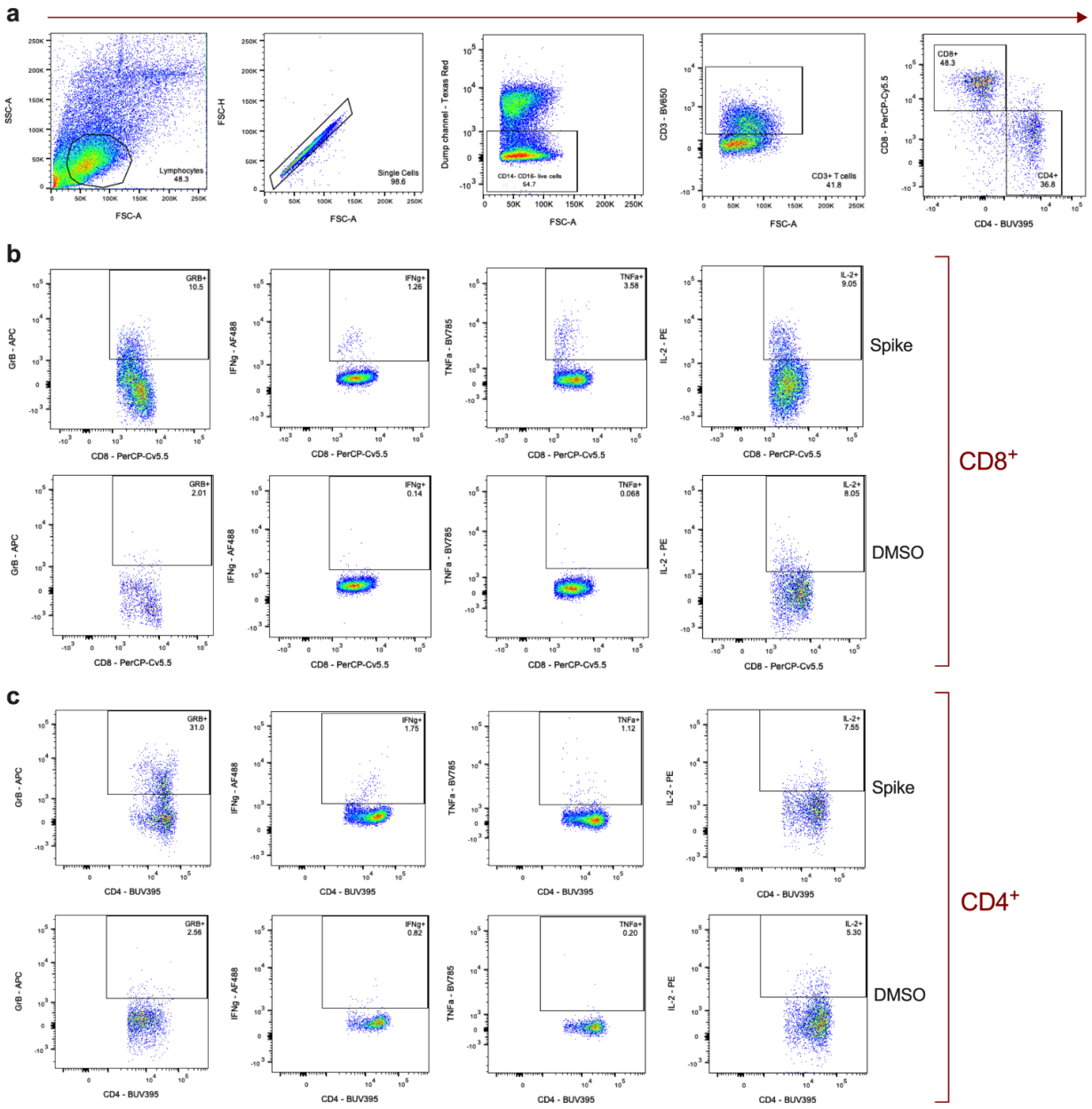
Appendix 4. Flow cytometry gating strategy examples.

A4.1 Identification of LASV GPC-specific T cells in murine ICS assays.



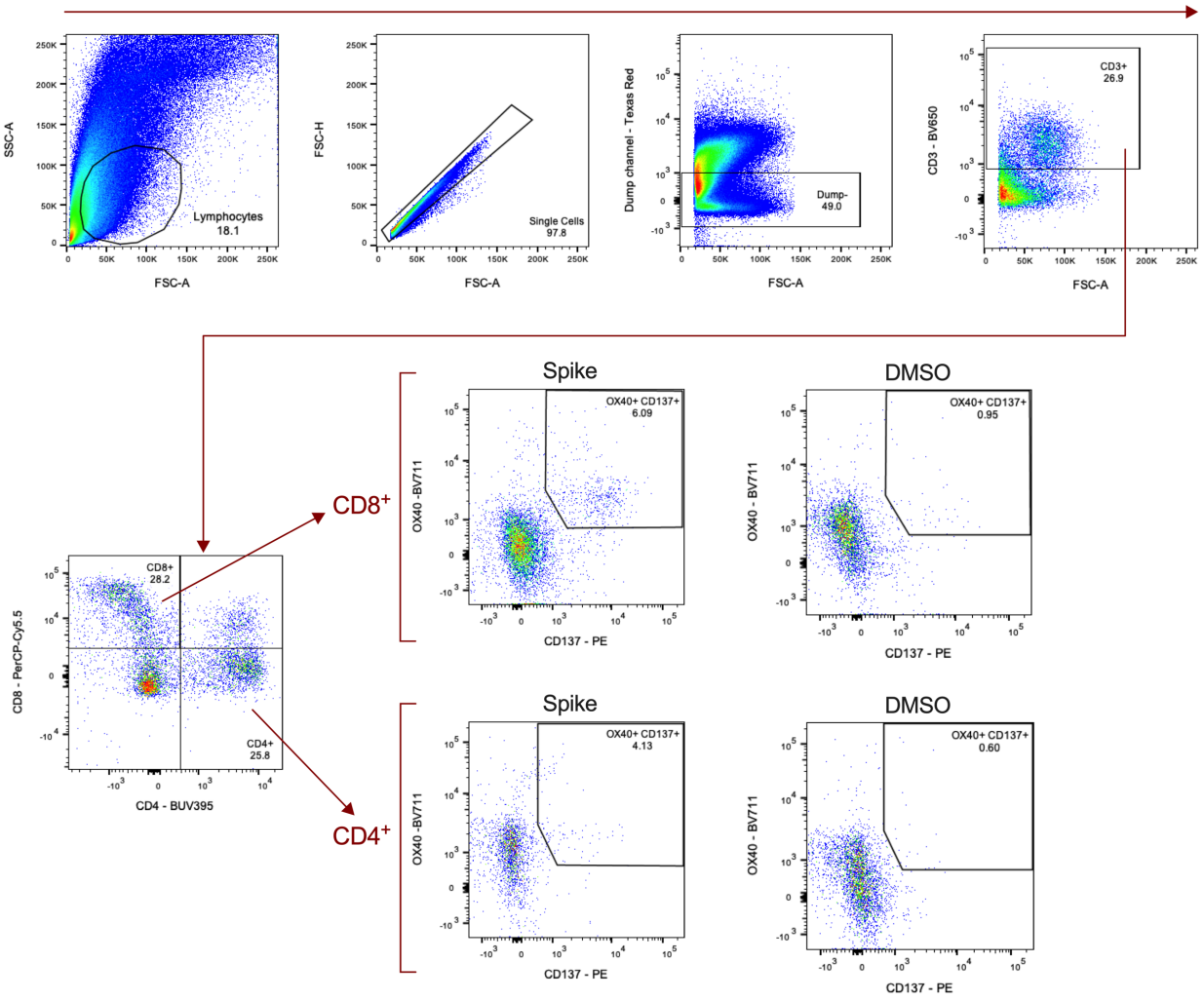
All events were first depicted using a combination of forward scatter area (FSC-A) and side scatter area (SSC-A). Lymphocytes were gated and displayed using a combination of FSC-A and forward scatter height (FSC-H), singlets were isolated, and live cells were gated using LIVE/DEAD and FSC-A. $CD8^+$ and $CD4^+$ T cell gates are shown. LASV-specific cells were identified as IFN-γ^+. All memory subsets were distinguished by first gating $CD44^+$ cells; effector cells (T_E) were identified as $CD62L^-$ $CD127^-$, effector memory cells (T_{EM}) were identified as $CD62L^-$ $CD127^+$, and central memory cells (T_{CM}) were identified as $CD62L^+$ $CD127^+$.

A4.2 Identification of antigen-specific T cells in NHP ICS assays.



All events were depicted using forward scatter area (FSC-A) and side scatter area (SSC-A) and lymphocytes were gated. Singlets were isolated using FSC-A and forward scatter height (FSC-H). Dead cells, $CD14^+$, and $CD16^+$ cells were excluded by gating on negative cells in the dump channel. **(A)** T cells were identified as $CD3^+$, and further classified as $CD4^+$ ($CD4^+$ $CD8^-$), $CD8^+$ ($CD4^-$ $CD8^+$). Gating to isolate single-cytokine positive populations (GrB, IFNγ, TNFα, and IL-2) within $CD8^+$ **(B)** and $CD4^+$ **(C)** T-cell subsets is indicated. An example of a sample stimulated with the SARS-CoV-2 spike (S1) protein-peptide pool (top) is shown along with the corresponding DMSO-treated control (bottom) for each cytokine.

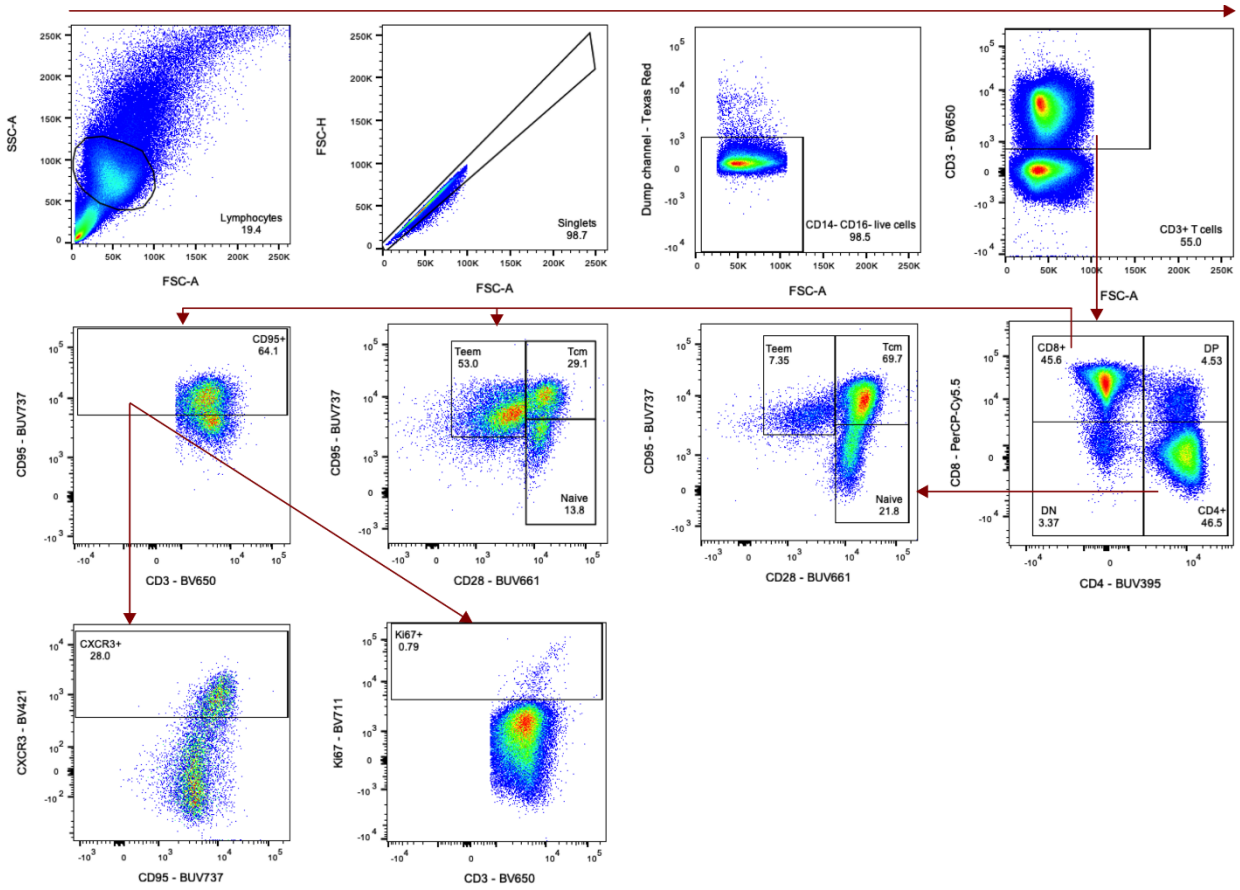
A4.3 Gating strategy to identify antigen-specific T cells in NHP AIM (OX40$^+$ CD137$^+$) assay.



All events were depicted using forward scatter area (FSC-A) and side scatter area (SSC-A) and lymphocytes were gated. Singlets were isolated using FSC-A and forward scatter height (FSC-H). Dead cells, CD14$^+$, and CD16$^+$ cells were excluded by gating on negative cells in the dump channel. T cells were identified as CD3$^+$, and further classified as CD4$^+$ (CD4$^+$ CD8$^-$), CD8$^+$ (CD4$^-$ CD8$^+$). Gating to isolate OX40$^+$ CD137$^+$ cells within CD8$^+$ (top) and CD4$^+$ (bottom) T-cell subsets is indicated. For each, a spike (S1) protein-peptide pool stimulated sample (left) with the corresponding DMSO-treated well (right) is shown.

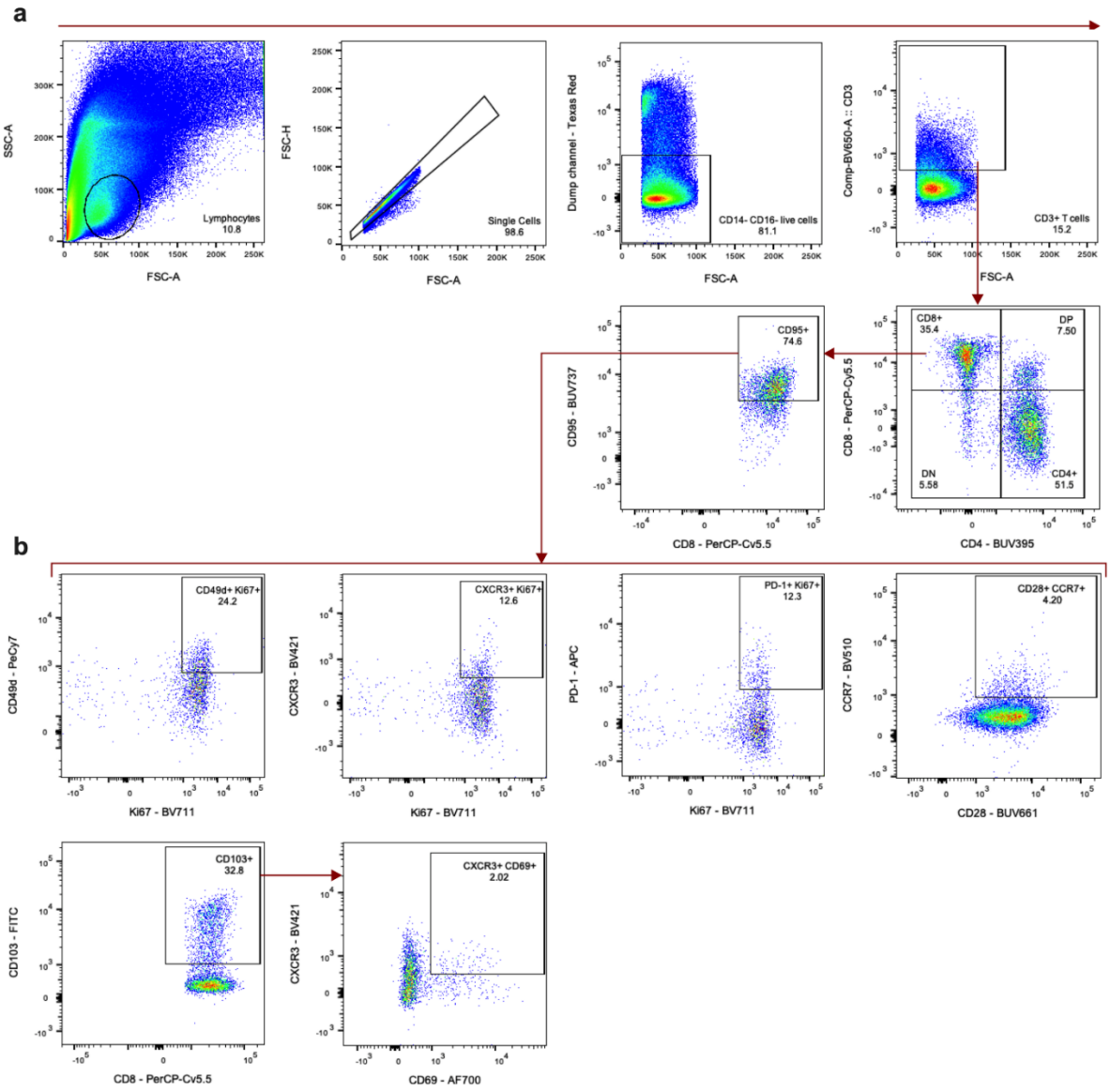
A4.4 Phenotyping of T cells in SARS-CoV-2 infected macaques.

A.4.4.1 PBMC-derived T cells



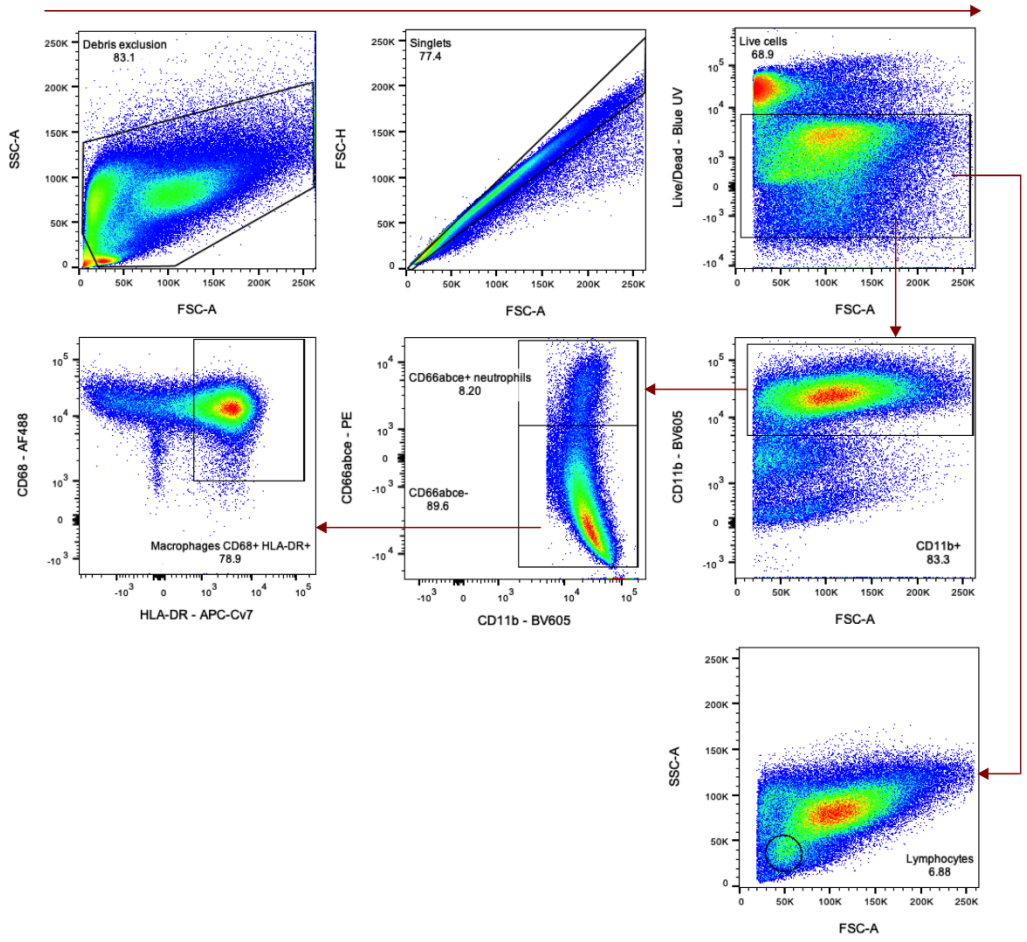
All events were depicted using forward scatter area (FSC-A) and side scatter area (SSC-A) and lymphocytes were gated. Singlets were isolated using FSC-A and forward scatter height (FSC-H). Dead cells, $CD14^{+}$, and $CD16^{+}$ cells were excluded by gating on negative cells in the dump channel. T cells were identified as $CD3^{+}$, and further classified as $CD4^{+}$ ($CD4^{+}$ $CD8^{-}$), $CD8^{+}$ ($CD4^{-}$ $CD8^{+}$), DP ($CD4^{+}$ $CD8^{lo}$), and DN ($CD4^{-}$ $CD8^{-}$). Memory subsets of $CD4^{+}$ and $CD8^{+}$ T cells were characterized as follows: naïve ($CD28^{+}$ $CD95^{lo}$), central memory (T_{CM}, $CD28^{+}$ $CD95^{hi}$), or effector/effector memory (T_{EEM}, $CD28^{-}$ $CD95^{+}$). $CD8^{+}$ T cells were additionally gated to isolate the total non-naïve ($CD95^{+}$) population; within this gate, $CXCR3^{+}$ and $Ki67^{+}$ cells were identified.

A.4.4.2 Lung-derived T cells



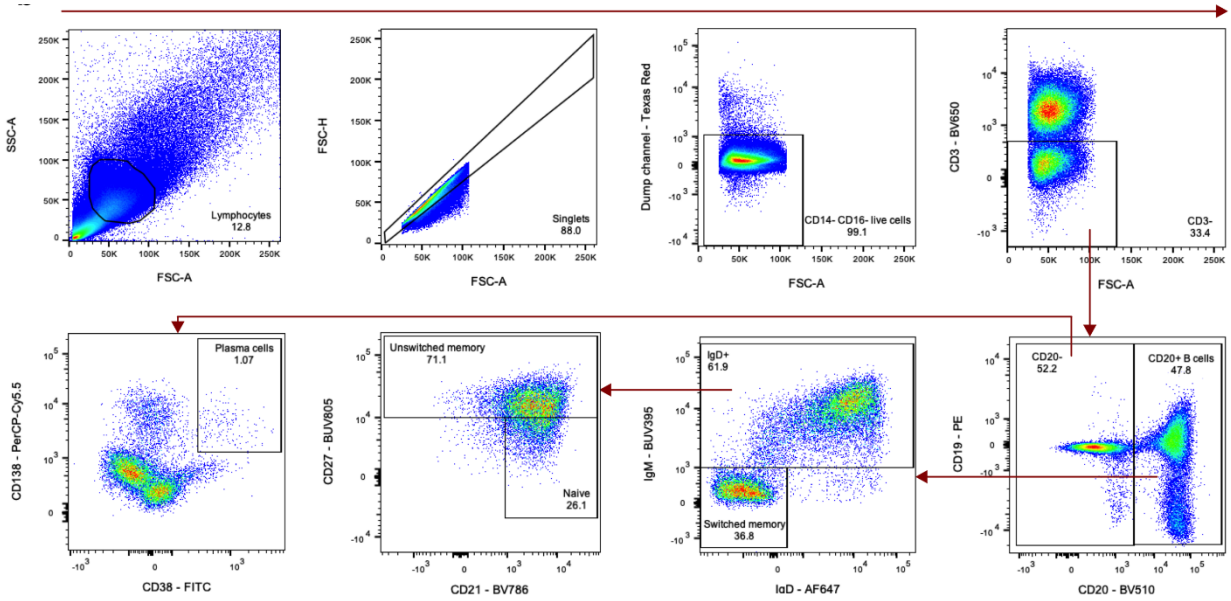
All events were depicted using forward scatter area (FSC-A) and side scatter area (SSC-A) and lymphocytes were gated. Singlets were isolated using FSC-A and forward scatter height (FSC-H). Dead cells, $CD14^{+}$, and $CD16^{+}$ cells were excluded by gating on negative cells in the dump channel. **(A)** T cells were identified as $CD3^{+}$, and further classified as $CD4^{+}$ ($CD4^{+}$ $CD8^{-}$), $CD8^{+}$ ($CD4^{-}$ $CD8^{+}$), DP ($CD4^{+}$ $CD8^{lo}$), and DN ($CD4^{-}$ $CD8^{-}$). **(B)** Within the $CD8^{+}$ non-naïve ($CD95^{+}$) T-cell gate, the following populations were identified: $CD49d^{+}$ $Ki67^{+}$, $CXCR3^{+}$ $Ki67^{+}$, $PD\text{-}1^{+}$ $Ki67^{+}$, $CD28^{+}$ $CCR7^{+}$, and $CD103^{+}$. A sub-population of $CXCR3^{+}$ $CD69^{+}$ cells was further isolated within the $CD103^{+}$ gate.

A4.5 Identification of macrophages within BALF of SARS-CoV-2-infected macaques.



Gating to exclude debris was performed using FSC-A and SSC-A prior to doublet discrimination using FSC-A and FSC-H. Dead cells were excluding by gating on the population of cells negative for LIVE/DEAD staining. A $CD11b^{+}$ population was isolated; within this gate, neutrophils were classified as $CD66abce^{+}$. Macrophages were identified by gating on $CD66abce^{-}$ cells followed by $CD68^{+}$ $HLA\text{-}DR^{+}$ cells. Lymphocytes were classified as $FSC\text{-}A^{lo}$ and $SSC\text{-}A^{lo}$ within the live cell gate.

A4.6 Phenotyping of B cells in SARS-CoV-2-infected macaques.



All events were depicted using forward scatter area (FSC-A) and side scatter area (SSC-A) and lymphocytes were gated. Singlets were isolated using FSC-A and forward scatter height (FSC-H). Dead cells, $CD14^{+}$, and $CD16^{+}$ cells were excluded by gating on negative cells in the dump channel. B-cells were classified as $CD3^{-}$ and $CD20^{+}$. Class-switched memory B-cells were further characterized as IgD^{-} IgM^{-}. Within the IgD^{+} gate, unswitched memory and naïve B-cells were identified as $CD27^{+}$ and $CD27^{-}$ $CD21^{+}$, respectively. Plasma cells were isolated within the $CD20^{-}$ gate and classified as $CD38^{+}$ $CD138^{+}$.

Appendix 5. DE genes mapped to GO processes in LASV-infected macaques.

A5.1 Pathways and associated differentially expressed genes that were downregulated in PBMC samples of ChAdOx1-Lassa-GPC prime-boost vaccinees versus ChAdOx1 GFP controls at 6 DPC

Pathways	nGenes	adj.Pval	Genes
Response to biotic stimulus	78	1.68E-29	GBP3 STAT2 MPO OASL S100A9 OAS2 TLR4 CCL8 TRIM35 HERC5 NOD2 OAS1 FER TICAM1 TLR7 DHX58 TIFA CGAS NAIP CXCL10 SLFN13 APOBEC3A S100A8 MPEG1 OAS3 TLR5 IFI44L DDX60 FAM20A IFI44 PML CSF1 GCH1 SASH1 FPR2 BATF2 MLKL EXT1 C3 SBNO2 SOCS1 IFI6 FKBP5 MRC1 DDX58 NOD1 CYBB CDHR2 SLC11A1 ALPK1 PYGL TLR2 CMPK2 RSAD2 CLEC5A IFIT1 MEFV IL17RC IDO1 IL6 MR1 ABCA1 TRIB1 ANXA3 PLAC8 PARP14 TENT5A GRN CEBPB IL27 TNF ISG15 DTX3L FZD5 SCIMP ACOD1 IFIT2 PLSCR2
Response to external biotic stimulus	77	1.68E-29	GBP3 STAT2 MPO OASL S100A9 OAS2 TLR4 CCL8 TRIM35 HERC5 NOD2 OAS1 FER TICAM1 TLR7 DHX58 TIFA CGAS NAIP CXCL10 SLFN13 APOBEC3A S100A8 MPEG1 OAS3 TLR5 IFI44L DDX60 FAM20A IFI44 PML CSF1 GCH1 SASH1 FPR2 BATF2 MLKL EXT1 C3 SBNO2 SOCS1 IFI6 FKBP5 MRC1 DDX58 NOD1 CYBB SLC11A1 ALPK1 PYGL TLR2 CMPK2 RSAD2 CLEC5A IFIT1 MEFV IL17RC IDO1 IL6 MR1 ABCA1 TRIB1 ANXA3 PLAC8 PARP14 TENT5A GRN CEBPB IL27 TNF ISG15 DTX3L FZD5 SCIMP ACOD1 IFIT2 PLSCR2
Interspecies interaction between organisms	85	4.24E-29	GBP3 STAT2 MVB12B MPO OASL S100A9 OAS2 TLR4 CCL8 TRIM35 HERC5 NOD2 OAS1 FER TICAM1 TLR7 DHX58 TIFA CGAS NAIP CXCL10 SIGLEC1 SLFN13 APOBEC3A S100A8 MPEG1 OAS3 TLR5 IFI44L DDX60 FAM20A IFI44 PML CSF1 GCH1 SASH1 FPR2 BATF2 MLKL EXT1 C3 FAM111A SBNO2 SOCS1 IFI6 FKBP5 MRC1 DDX58 NOD1 CYBB SLC11A1 ALPK1 PYGL IGF2R TLR2 CMPK2 RSAD2 CLEC5A ROCK2 IFIT1 MEFV IL17RC CTSB IDO1 IL6 MR1 ABCA1 TRIB1 ANXA3 PLAC8 PARP14 TENT5A GRN INSR EIF2AK2 CEBPB IL27 TNF ISG15 DTX3L FZD5 SCIMP ACOD1 IFIT2 PLSCR2
Response to external stimulus	105	1.73E-26	GBP3 STAT2 MPO OASL S100A9 OAS2 TLR4 CCL8 CASP5 PLAU TRIM35 HERC5 TNFAIP6 NOD2 OAS1 FER TICAM1 TLR7 DHX58 TIFA ZSWIM4 TEC CGAS NAIP CXCL10 GRN SLFN13 CMKLR1 APOBEC3A S100A8 MPEG1 OAS3 TLR5 CAPN3 IFI44L DDX60 FAM20A IFI44 SCARF1 PML CSF1 GCH1 TRPM2 SASH1 FPR2 BATF2 MLKL EXT1 FOSL1 C3 EGR2 SBNO2 SOCS1 IFI6 FKBP5 MRC1 DDX58 NOD1 SERPING1 JUP CYBB SLC11A1 ALPK1 CCRL2 NGFR PYGL TRIO SLC8A1 TLR2 CMPK2 RSAD2 CLEC5A LILRA5 SLC9A1 IFIT1 MEFV IL17RC IDO1 IL6 MR1 LTBR CSF3R ABCA1 TRIB1 ANXA3 PLAC8 PARP14 GLUL TENT5A PTPRO HSD3B7 CEBPB IL27 PLA2G2D TNF DAGLA ISG15 DTX3L FZD5 SCIMP SOCS3 PTGES ACOD1 IFIT2 PLSCR2
Defense response to other organism	61	5.85E-25	GBP3 STAT2 MPO OASL OAS2 TLR4 CCL8 TRIM35 HERC5 NOD2 OAS1 FER TLR7 DHX58 TIFA CGAS NAIP SLFN13 APOBEC3A MPEG1 OAS3 TLR5 IFI44L DDX60 PML CSF1 GCH1 FPR2 BATF2 S100A9 MLKL C3 SOCS1 IFI6 MRC1 DDX58 NOD1 CYBB SLC11A1 ALPK1 TICAM1 TLR2 RSAD2 CLEC5A IFIT1 MEFV IL17RC IL6 MR1 CXCL10 ANXA3 PLAC8 PARP14 GRN S100A8 CEBPB IL27 TNF ISG15 DTX3L PLSCR2
Defense response	75	5.78E-24	GBP3 STAT2 TLR5 MPO OASL S100A9 OAS2 TLR4 CCL8 CASP5 TRIM35 HERC5 TNFAIP6 NOD2 OAS1 IL1RN CYBB FER TICAM1 TLR7 DHX58 TIFA CGAS NAIP CXCL10 GRN SLFN13 CMKLR1 APOBEC3A S100A8 MPEG1 OAS3 IFI44L DDX60 PML CSF1 GCH1 FPR2 BATF2 MLKL EXT1 C3 SBNO2 SOCS1 IFI6 MRC1 DDX58 NOD1 SLC11A1 ALPK1 TLR2 RSAD2 CLEC5A LILRA5 IFIT1 MEFV IL17RC IDO1 IL6 MR1 TRIM55 ANXA3 PLAC8 PARP14 CEBPB IL27 PLA2G2D TNF DAGLA ISG15 DTX3L SOCS3 PTGES ACOD1 PLSCR2
Immune system process	98	1.72E-22	GBP3 STAT2 IFI44L FCGR1A OASL S100A9 DYSF OAS2 CCL8 TRIM35 HERC5 OAS1 IL1RN FER TICAM1 TLR7 DHX58 TIFA TEC PRAM1 CGAS CXCL10 SLFN13 MARCHF1 CMKLR1 APOBEC3A S100A8 IL27 OAS3 PDE1B TLR5 SCIN DDX60 MITF MPO PML CSF1 GCH1 MAFB TRPM2 FPR2 BATF2 MLKL EXT1 C3 TLR4 MERTK SBNO2 SOCS1 IFI6 MRC1 NOD2 DDX58 NOD1 SERPING1 CYBB SLC11A1 RBFOX2 ALPK1 IL15RA TLR2 RSAD2 CLEC5A GAB2 IFIT1 MEFV JAG1 IL17RC TNFSF10 IDO1 IL6 MR1 LTBR EPS8 CSF3R TRIM55 TRIB1 ANXA3 PARP14 HFE GRN STK3 EIF2AK2 HSD3B7 ITGAM CEBPB PLA2G2D TNF ACVR1B ISG15 NFAM1 EGR1 DTX3L FZD5 SCIMP CD300A ACOD1 PLSCR2
Immune response	69	1.26E-20	GBP3 STAT2 IFI44L FCGR1A S100A9 DYSF CCL8 TRIM35 IL1RN FER TICAM1 TLR7 DHX58 TIFA TEC PRAM1 CGAS CXCL10 MARCHF1 CMKLR1 IL27 TLR5 PML CSF1 GCH1 FPR2 OASL OAS2 EXT1 C3 TLR4 SBNO2 SOCS1 IFI6 MRC1 NOD2 DDX58 SERPING1 OAS1 CYBB SLC11A1 ALPK1 TLR2 RSAD2 CLEC5A IFIT1 MEFV JAG1 TNFSF10 IDO1 IL6 MR1 LTBR ANXA3 PARP14 HFE GRN ITGAM S100A8 PLA2G2D TNF OAS3 ISG15 NFAM1 FZD5 SCIMP CD300A ACOD1 PLSCR2
Response to bacterium	42	8.81E-18	GBP3 MPO S100A9 TLR4 NOD2 TICAM1 NAIP CXCL10 S100A8 MPEG1 TLR5 FAM20A IFI44 GCH1 SASH1 FPR2 OAS2 C3 SBNO2 FKBP5 MRC1 NOD1 SLC11A1 FER PYGL DHX58 TLR2 CMPK2 IDO1 IL6 MR1 ABCA1 TRIB1 ANXA3 PLAC8 TENT5A CEBPB TNF ISG15 FZD5 SCIMP ACOD1
Response to stress	112	1.07E-17	GBP3 STAT2 TLR5 MPO SASH1 OASL S100A9 DYSF OAS2 TLR4 CCL8 CASP5 PLAU TRIM35 HERC5 ARHGEF10L TNFAIP6 NOD2 OAS1 IL1RN CYBB FER TICAM1 TLR7 DHX58 LIMK2 TIFA ERCC4 HELB TEC CGAS NAIP CXCL10 GRN SLFN13 GSR CMKLR1 APOBEC3A S100A8 MPEG1 OAS3 CAPN3 IFI44L DDX60 SCARF1 PML CSF1 ATF6 GCH1 TRPM2 FPR2 BATF2 NCF1 RREB1 KDM6B MLKL EXT1 C3 NKX3-1 MERTK FAM111A MSRB2 SBNO2 SOCS1 IFI6 MRC1 DDX58 NOD1 SERPING1 SLC11A1 ALPK1 TLR2 RSAD2 CLEC5A TRIM72 LILRA5 IFIT1 MEFV IL17RC IDO1 NIBAN1 IL6 MR1 LTBR TRIM55 TRIB1 BOD1L1 ANXA3 PLAC8 PARP14 GLUL MTF1 STK3 UBXN8 EIF2AK2 TFEC CEBPB IL27 PLA2G2D TNF DAGLA ISG15 EGR1 DTX3L HSPB1 FZD5 SCIMP SOCS3 PTGES ACOD1 SNAI1 PLSCR2
Regulation of multicellular organismal process	101	2.89E-16	SCARF1 PLAU DISC1 TICAM1 TLR7 DHX58 ZSWIM4 TEC CGAS IL27 MAFF AGRN TLR5 SCIN CAPN3 DDX60 MITF B4GALT5 ENG PML CSF1 GCH1 MAFB SASH1 ACVRL1 CPNE5 ARSB SHTN1 PHLDA2 RREB1 KDM6B OAS2 C3 TLR4 NKX3-1 MERTK RIN2 EGR2 SOCS1 ACSL1 NOD2 NOD1 SERPING1 IL1RN JUP SLC11A1 RBFOX2 NGFR IL15RA SLC8A1 TLR2 RSAD2 CLEC5A ADM LILRA5 ROCK2 SLC9A1 MEFV JAG1 IL17RC DAAM2 P2RY2 IDO1 IL6 GRB10 CSF3R ABCA1 CXCL10 TRIB1 TWIST2 GOLGA4 ANXA3 IL17RA PLAC8 ELOVL3 TCF7L2 GLUL HFE GRN INSR STK3 PTPRO EIF2AK2 SMTNL1 SERPINB1 CEBPB G0S2 TNF ACVR1B RGS2 ISG15 KCNE3 NFAM1 EGR1 HSPB1 KCNJ2 FZD5 SCIMP YWHAG PTGES SNAI1
Immune effector process	44	1.22E-15	OASL DYSF OAS2 HERC5 OAS1 FER TICAM1 TLR7 CGAS SLFN13 APOBEC3A IL27 OAS3 STAT2 IFI44L DDX60 MPO MLKL C3 TLR4 SBNO2 IFI6 NOD2 DDX58 SERPING1 SLC11A1 DHX58 RSAD2 IFIT1 JAG1 IL6 MR1 CXCL10 ANXA3 HFE GRN ITGAM TNF ISG15 DTX3L FZD5 SCIMP CD300A PLSCR2
Innate immune response	39	5.99E-15	GBP3 STAT2 CCL8 TRIM35 FER DHX58 TIFA CGAS TLR5 PML CSF1 GCH1 FPR2 OASL S100A9 OAS2 C3 TLR4 SOCS1 IFI6 MRC1 NOD2 DDX58 OAS1 CYBB SLC11A1 ALPK1 TICAM1 TLR7 TLR2 CLEC5A IFIT1 MEFV PARP14 GRN S100A8 OAS3 ISG15 PLSCR2
Positive regulation of multicellular organismal process	69	1.25E-14	SCARF1 TICAM1 TLR7 DHX58 CGAS TLR5 SCIN DDX60 B4GALT5 ENG CSF1 GCH1 SASH1 ACVRL1 CPNE5 SHTN1 RREB1 KDM6B C3 TLR4 NKX3-1 RIN2 EGR2 SOCS1 ACSL1 NOD2 NOD1 JUP DISC1 SLC11A1 NGFR IL15RA SLC8A1 TLR2 RSAD2 CLEC5A ADM LILRA5 ROCK2 SLC9A1 JAG1 IL17RC P2RY2 IDO1 IL6 GRB10 ABCA1 TRIB1 GOLGA4 ANXA3 IL17RA PLAC8 ELOVL3 TCF7L2 EIF2AK2 SMTNL1 CEBPB IL27 G0S2 TNF ACVR1B RGS2 ISG15 NFAM1 EGR1 HSPB1 FZD5 SCIMP SNAI1

A5.2 Pathways and associated differentially expressed genes that were upregulated in PBMC samples of ChAdOx1-Lassa-GPC prime-boost vaccinees versus ChAdOx1 GFP controls at 6 DPC

Pathways	nGenes	adj.Pval	Genes
Nuclear division	24	4.43E-10	NUF2 DSCC1 RAD51 NCAPG2 CENPK CCNB1 CDCA5 ZWINT PTTG1 KIF11 AURKA AURKB CDC20 CDC6 TOP2A RGCC CDT1 PLK1 MYBL2 CCNE1 KIF2C CCNB2 MKI67 CD28
Mitotic nuclear division	20	4.43E-10	NUF2 DSCC1 NCAPG2 CENPK CCNB1 CDCA5 ZWINT PTTG1 KIF11 AURKA AURKB CDC20 CDC6 RGCC CDT1 PLK1 MYBL2 KIF2C MKI67 CD28
Mitotic cell cycle process	29	5.24E-10	AURKA NUF2 DSCC1 AURKB CDC6 CCNA2 NCAPG2 MCM4 CENPK CCNB1 CDCA5 CDK1 CCNE1 CDC45 ZWINT PTTG1 KIF11 CDC20 RAD51 RGCC CDT1 PLK1 MYBL2 CDKN2C MRNIP KIF2C MKI67 SPC25 CD28
Mitotic cell cycle	31	1.77E-09	AURKA NUF2 DSCC1 AURKB CDC6 CCNA2 NCAPG2 CDT1 MCM4 CENPK PLK1 CCNB1 CDCA5 TUBA4A CDK1 CCNE1 CDC45 ZWINT PTTG1 KIF11 CDC20 RAD51 RGCC MYBL2 CDKN2C MRNIP KIF2C CENPW MKI67 SPC25 CD28
Chromosome segregation	20	7.36E-09	NUF2 DSCC1 NCAPG2 ESCO2 CENPK CCNB1 CDCA5 ZWINT PTTG1 AURKB CDC20 CDC6 TOP2A CDT1 PLK1 CCNE1 KIF2C CENPW MKI67 SPC25
Mitotic sister chromatid segregation	14	7.13E-08	NUF2 DSCC1 NCAPG2 CENPK CCNB1 CDCA5 ZWINT PTTG1 AURKB CDC20 CDC6 CDT1 PLK1 KIF2C
Sister chromatid segregation	15	1.03E-07	NUF2 DSCC1 NCAPG2 ESCO2 CENPK CCNB1 CDCA5 ZWINT PTTG1 AURKB CDC20 CDC6 CDT1 PLK1 KIF2C
Cell cycle process	34	1.49E-07	AURKA NUF2 DSCC1 AURKB RAD51 CDC6 CCNA2 CDKN3 NCAPG2 CDT1 MCM4 ESCO2 CENPK PLK1 CCNB1 CDCA5 CDK1 CCNE1 CDC45 ZWINT PTTG1 KIF11 CDC20 PLK4 TOP2A RGCC MYBL2 CDKN2C MRNIP KIF2C CCNB2 MKI67 SPC25 CD28
Cell cycle	38	8.85E-07	AURKA NUF2 DSCC1 AURKB RAD51 CDC6 CCNA2 CDKN3 NCAPG2 CDT1 MCM4 ESCO2 CENPK PLK1 CCNB1 CDCA5 TUBA4A CDK1 CCNE1 CDC45 ZWINT PTTG1 KIF11 CDC20 PLK4 TOP2A RGCC MCM7 MYBL2 CDKN2C MRNIP KIF2C CENPW PCLAF CCNB2 MKI67 SPC25 CD28
Nuclear chromosome segregation	16	8.85E-07	NUF2 DSCC1 NCAPG2 ESCO2 CENPK CCNB1 CDCA5 ZWINT PTTG1 AURKB CDC20 CDC6 CDT1 PLK1 CCNE1 KIF2C
Regulation of mitotic nuclear division	12	1.40E-06	CDCA5 PTTG1 AURKB CDC6 RGCC CDT1 PLK1 CCNB1 ZWINT KIF11 MKI67 CD28
Regulation of nuclear division	13	1.40E-06	CDCA5 PTTG1 AURKB CDC20 CDC6 RGCC CDT1 PLK1 CCNB1 ZWINT KIF11 MKI67 CD28
Lymphocyte activation	23	1.88E-06	ICOS CD40 IL23A LCK CD79B CD28 SIT1 MS4A1 CD19 UNG CMTM7 CD1C CTLA4 CD22 MYB FCRL1 CD3D IL21 TIGIT MZB1 KIT F2RL1 GPR18
DNA metabolic process	27	5.55E-06	DNASE2B CD40 POLE2 RAD51 PARPBP UNG CDT1 MCM4 NDUFAB1 CDCA5 GINS2 CDC45 PCLAF MMS22L RNASEH2A GZMA DSCC1 MAGEF1 AURKB CDC6 TOP2A MCM7 ESCO2 CCNE1 MRNIP TK1 CD28

A5.3 Pathways and associated differentially expressed genes that were downregulated in PBMC samples of ChAdOx1-Lassa-GPC single-dose vaccinees versus ChAdOx1 GFP controls at 6 DPC

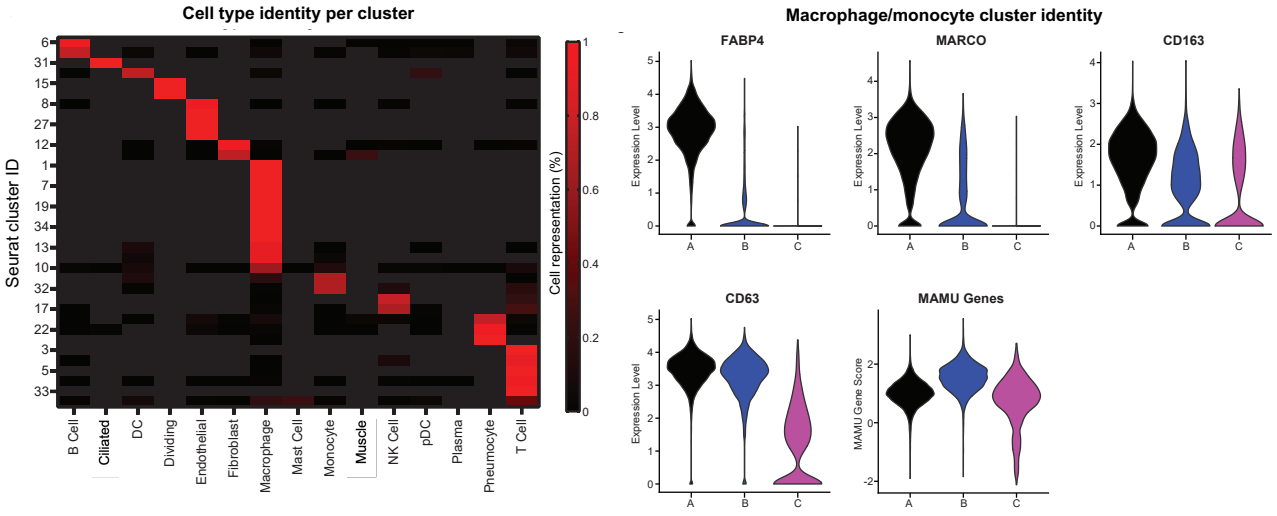
Pathways	nGenes	adj.Pval	Genes
Response to biotic stimulus	67	3.53E-27	RNASE6 MPO OASL S100A9 OAS2 TLR4 CCL8 TRIM35 HERC5 OAS1 TLR7 TIFA CGAS NAIP CXCL10 SLFN13 APOBEC3A S100A8 MPEG1 OAS3 TLR5 IFI44L DDX60 CLEC7A IFI44 LY96 GCH1 FPR2 BATF2 RNF135 MLKL EXT1 LYZF1 STAP1 SOCS1 IFI6 DDX58 CYBB CDHR2 SLC11A1 PYGL TLR2 ARG2 CMPK2 RSAD2 CLEC5A IFIT1 IL17RC IDO1 IL6 MR1 ABCA1 TRIB1 ANXA3 PLAC8 TENT5A GRN IFI27 IL27 ISG15 DEFB1 SCIMP EREG ACOD1 IFIT2 RAB20 PLSCR2
Response to external biotic stimulus	66	3.53E-27	RNASE6 MPO OASL S100A9 OAS2 TLR4 CCL8 TRIM35 HERC5 OAS1 TLR7 TIFA CGAS NAIP CXCL10 SLFN13 APOBEC3A S100A8 MPEG1 OAS3 TLR5 IFI44L DDX60 CLEC7A IFI44 LY96 GCH1 FPR2 BATF2 RNF135 MLKL EXT1 LYZF1 STAP1 SOCS1 IFI6 DDX58 CYBB SLC11A1 PYGL TLR2 ARG2 CMPK2 RSAD2 CLEC5A IFIT1 IL17RC IDO1 IL6 MR1 ABCA1 TRIB1 ANXA3 PLAC8 TENT5A GRN IFI27 IL27 ISG15 DEFB1 SCIMP EREG ACOD1 IFIT2 RAB20 PLSCR2
Interspecies interaction between organisms	73	4.46E-27	MVB12B RNASE6 MPO OASL S100A9 OAS2 TLR4 CCL8 TRIM35 HERC5 OAS1 TLR7 TIFA CGAS NAIP CXCL10 SIGLEC1 SLFN13 APOBEC3A S100A8 MPEG1 OAS3 TLR5 IFI44L DDX60 CLEC7A IFI44 LY96 GCH1 FPR2 BATF2 RNF135 MLKL EXT1 LYZF1 STAP1 FAM111A SOCS1 IFI6 DDX58 CYBB SLC11A1 PYGL IGF2R TLR2 ARG2 CMPK2 RSAD2 CLEC5A IFIT1 IL17RC IDO1 DYNLT1 IL6 MR1 ABCA1 TRIB1 ANXA3 PLAC8 TENT5A GRN IFI27 EIF2AK2 IL27 ISG15 DEFB1 SCIMP EREG ACOD1 CAV2 IFIT2 RAB20 PLSCR2
Immune system process	90	2.46E-25	IFI44L RNASE6 FCGR1A VEGFA OASL S100A9 DYSF OAS2 LIG4 CCL8 TRIM35 HERC5 OAS1 IL1RN TLR7 TIFA TEC CGAS CXCL10 SLFN13 MARCHF1 CMKLR1 APOBEC3A S100A8 IL27 OAS3 TIPARP TLR5 SCIN DDX60 MITF CLEC7A RHEX MPO LY96 GCH1 TRPM2 MPP1 FPR2 BATF2 RNF135 TNFSF13B MLKL EXT1 TLR4 STAP1 MERTK SOCS1 IFI6 DDX58 SERPING1 CYBB SLC11A1 RBFOX2 IL15RA TLR2 ARG2 RSAD2 CLEC5A IFIT1 ANGPT1 IL17RC TNFSF10 IDO1 IL6 MR1 EPS8 CSF3R C1QC PLA2G4A TRIM55 TRIB1 ANXA3 HFE GRN IFI27 STK3 EIF2AK2 HSD3B7 ITGAM ACVR1B ISG15 DEFB1 SCIMP EREG CD300A ACOD1 RAB20 C1QA PLSCR2
Defense response to other organism	54	2.47E-24	RNASE6 MPO OASL OAS2 TLR4 CCL8 TRIM35 HERC5 OAS1 TLR7 TIFA CGAS NAIP SLFN13 APOBEC3A MPEG1 OAS3 TLR5 IFI44L DDX60 CLEC7A LY96 GCH1 FPR2 BATF2 S100A9 RNF135 MLKL LYZF1 SOCS1 IFI6 DDX58 CYBB SLC11A1 TLR2 ARG2 RSAD2 CLEC5A IFIT1 IL17RC IL6 MR1 CXCL10 ANXA3 PLAC8 GRN IFI27 S100A8 IL27 ISG15 DEFB1 EREG RAB20 PLSCR2
Defense response	64	4.19E-22	TLR5 RNASE6 MPO OASL S100A9 OAS2 TLR4 CCL8 CASP5 TRIM35 HERC5 TNFAIP6 OAS1 IL1RN CYBB TLR7 TIFA CGAS NAIP CXCL10 GRN SLFN13 CMKLR1 APOBEC3A S100A8 MPEG1 OAS3 IFI44L DDX60 CLEC7A LY96 GCH1 FPR2 BATF2 RNF135 MLKL EXT1 LYZF1 STAP1 SOCS1 IFI6 DDX58 SLC11A1 TLR2 ARG2 RSAD2 CLEC5A IFIT1 IL17RC SMAD1 IDO1 IL6 MR1 TRIM55 ANXA3 PLAC8 IFI27 IL27 ISG15 DEFB1 EREG ACOD1 RAB20 PLSCR2
Immune response	63	4.19E-22	IFI44L RNASE6 FCGR1A S100A9 DYSF CCL8 TRIM35 IL1RN TLR7 TIFA TEC CGAS CXCL10 MARCHF1 CMKLR1 IL27 TLR5 CLEC7A LY96 GCH1 FPR2 OASL RNF135 TNFSF13B OAS2 EXT1 LIG4 TLR4 STAP1 SOCS1 IFI6 DDX58 SERPING1 OAS1 CYBB SLC11A1 TLR2 ARG2 RSAD2 CLEC5A IFIT1 ANGPT1 TNFSF10 IDO1 IL6 MR1 PLA2G4A ANXA3 HFE GRN IFI27 ITGAM S100A8 OAS3 ISG15 DEFB1 SCIMP EREG CD300A ACOD1 RAB20 C1QA PLSCR2
Response to external stimulus	84	2.02E-21	RNASE6 MPO VEGFA OASL S100A9 OAS2 TLR4 CCL8 CASP5 PLAU TRIM35 HERC5 TNFAIP6 OAS1 TLR7 TIFA TEC CGAS NAIP CXCL10 GRN SLFN13 CMKLR1 APOBEC3A S100A8 MPEG1 OAS3 TLR5 IFI44L DDX60 CLEC7A IFI44 LY96 GCH1 TRPM2 MPP1 FPR2 SLC1A3 BATF2 RNF135 MLKL EXT1 LYZF1 STAP1 SOCS1 IFI6 DDX58 SERPING1 CYBB SLC11A1 CCRL2 PYGL SLC8A1 TLR2 ARG2 CMPK2 RSAD2 CLEC5A IFIT1 ANGPT1 IL17RC IDO1 IL6 MR1 CSF3R ABCA1 PLA2G4A TRIB1 ANXA3 PLAC8 GLUL KANK2 TENT5A IFI27 HSD3B7 IL27 ISG15 DEFB1 SCIMP EREG ACOD1 IFIT2 RAB20 PLSCR2
Immune effector process	41	5.49E-17	OASL DYSF OAS2 HERC5 OAS1 TLR7 CGAS SLFN13 APOBEC3A IL27 OAS3 IFI44L RNASE6 DDX60 CLEC7A MPO RNF135 MLKL LIG4 TLR4 STAP1 IFI6 DDX58 SERPING1 SLC11A1 RSAD2 IFIT1 ANGPT1 IL6 MR1 CXCL10 ANXA3 HFE GRN IFI27 ITGAM ISG15 SCIMP CD300A C1QA PLSCR2
Response to stress	92	1.88E-15	TLR5 RNASE6 MPO VEGFA OASL S100A9 DYSF OAS2 LIG4 TLR4 CCL8 CASP5 PLAU TRIM35 HERC5 TNFAIP6 OAS1 IL1RN CYBB TLR7 LIMK2 TIFA TEC CGAS NAIP CXCL10 GRN SLFN13 CMKLR1 APOBEC3A S100A8 MPEG1 OAS3 IFI44L DDX60 CLEC7A LY96 GCH1 TRPM2 FPR2 SLC1A3 COMP BATF2 RNF135 MLKL EXT1 LYZF1 STAP1 NKX3-1 MERTK FAM111A SOCS1 RAB3D IFI6 DDX58 SERPING1 GFAP SLC11A1 TLR2 ARG2 RSAD2 CLEC5A NET1 IFIT1 IL17RC SMAD1 DPYSL3 IDO1 NIBAN1 IL6 MR1 PLA2G4A TRIM55 TRIB1 ANXA3 PLAC8 GLUL IFI27 STK3 EIF2AK2 TFEC IL27 ISG15 DEFB1 MGST1 SCIMP EREG ACOD1 SNAI1 RAB20 PPM1J PLSCR2
Defense response to virus	24	2.67E-15	OASL OAS2 HERC5 OAS1 TLR7 CGAS SLFN13 APOBEC3A OAS3 IFI44L RNASE6 DDX60 RNF135 MLKL IFI6 DDX58 RSAD2 IFIT1 IL6 CXCL10 IFI27 IL27 ISG15 PLSCR2
Response to virus	26	8.96E-15	OASL OAS2 HERC5 OAS1 TLR7 CGAS SLFN13 APOBEC3A OAS3 IFI44L RNASE6 DDX60 RNF135 MLKL EXT1 IFI6 DDX58 RSAD2 IFIT1 IL6 CXCL10 IFI27 IL27 ISG15 IFIT2 PLSCR2
Innate immune response	34	3.43E-14	RNASE6 CCL8 TRIM35 TIFA CGAS TLR5 CLEC7A LY96 GCH1 FPR2 OASL S100A9 RNF135 OAS2 TLR4 SOCS1 IFI6 DDX58 OAS1 CYBB SLC11A1 TLR7 TLR2 CLEC5A IFIT1 GRN IFI27 S100A8 OAS3 ISG15 DEFB1 EREG RAB20 PLSCR2
Response to bacterium	33	8.43E-14	RNASE6 MPO S100A9 TLR4 NAIP CXCL10 S100A8 MPEG1 TLR5 IFI44 LY96 GCH1 FPR2 OAS2 LYZF1 STAP1 SLC11A1 PYGL TLR2 ARG2 CMPK2 IDO1 IL6 MR1 ABCA1 TRIB1 ANXA3 PLAC8 TENT5A ISG15 DEFB1 SCIMP ACOD1

A5.4 Pathways and associated differentially expressed genes that were upregulated in PBMC samples of ChAdOx1-Lassa-GPC single-dose vaccinees versus ChAdOx1 GFP controls at 6 DPC

Pathways	nGenes	adj.Pval	Genes
Lymphocyte activation	26	4.36E-09	CD5 CD3E LCK CD79B LAT CD28 CCR7 BCL11B CD19 CXCR5 CMTM7 CD1C IL27RA CR2 CTLA4 MYB FCRL1 ZAP70 TCF7 LEF1 CD6 CD3D IL21 LAX1 LAG3 MZB1
Leukocyte activation	27	2.21E-08	CD5 CD3E LCK CD79B LAT CD28 CCR7 BCL11B CD19 CXCR5 CMTM7 CD1C CAMK4 IL27RA CR2 CTLA4 MYB FCRL1 ZAP70 TCF7 LEF1 CD6 CD3D IL21 LAX1 LAG3 MZB1
Cell activation	28	3.60E-08	CD5 CD3E LCK CD79B LAT CD28 CCR7 BCL11B CD19 CXCR5 CMTM7 CD1C RGCC CAMK4 IL27RA CR2 CTLA4 MYB FCRL1 ZAP70 TCF7 LEF1 CD6 CD3D IL21 LAX1 LAG3 MZB1
Immune system process	43	1.39E-06	CCR7 CD19 CXCR5 CD5 CD3E XG ZAP70 AZGP1 CXCR3 LCK CD79B LAT CD28 BCL11B CNR2 ADTRP GFI1 LTB CMTM7 CD1C RGCC CAMK4 SUSD4 NOP53 IL27RA CR2 NCAPG2 CTLA4 GCSAM MYB FCRL1 MMP28 TCF7 LEF1 CD6 CD3D IL21 SKAP1 LAX1 GPR68 LAG3 MZB1 CD7
Regulation of immune system process	30	1.39E-06	CD19 CD5 XG LCK CD79B LAT CD28 CCR7 ADTRP RGCC SUSD4 NOP53 IL27RA CR2 NCAPG2 CTLA4 GCSAM CD3E MYB ZAP70 MMP28 LEF1 CXCR3 CD6 IL21 SKAP1 LAX1 GPR68 LAG3 MZB1
Lymphocyte differentiation	16	1.39E-06	CD3E LCK CD79B CCR7 BCL11B CD19 CMTM7 CR2 CTLA4 MYB ZAP70 TCF7 LEF1 CD3D LAG3 CD28
T cell activation	18	1.39E-06	CD5 CD3E LCK LAT CD28 CCR7 BCL11B CD1C CTLA4 MYB ZAP70 TCF7 LEF1 CD6 CD3D IL21 LAX1 LAG3
System development	64	1.39E-06	STMN1 GBX2 MARCKSL1 CD3E ADGRB2 LCK CD79B AMIGO1 BIN1 PKP2 CCR7 ITGA6 QARS1 CDC20 BCL11B ADTRP GFI1 ZNF219 CD19 DOK5 LTB CXCR5 BCL9L KIF26A CMTM7 NYAP1 BICDL1 LSR RGCC CAMK4 PTPRF IL27RA CR2 NCAPG2 SORL1 SALL2 HIP1R CTLA4 LMNA TP63 MRTFB MYB PAX5 ZAP70 DHCR24 ANKH TCF7 PHGDH LEF1 CSMD1 LTBP3 CXCR3 GCNT4 CD3D GDF7 GPR68 LAG3 CD28 STMN3 RFLNB TPPP TMEM204 SFRP5 ACTG2
Anatomical structure development	73	1.39E-06	STMN1 GBX2 MARCKSL1 MRTFB CD3E ADGRB2 LCK CD79B AMIGO1 BIN1 PKP2 CCR7 ITGA6 RYR1 QARS1 CDC20 BCL11B ADTRP GFI1 ZNF219 CD19 DOK5 VSIG1 LTB CXCR5 BCL9L KIF26A CARMIL2 CMTM7 NYAP1 BICDL1 LSR RGCC CAMK4 PTPRF IL27RA CR2 NCAPG2 SORL1 SALL2 HIP1R CTLA4 LMNA TP63 SCMH1 MYB CDC25B PAX5 ZAP70 DHCR24 ANKH RAB25 TCF7 STRBP PHGDH LEF1 CSMD1 LTBP3 CXCR3 GCNT4 CD3D IL21 GDF7 GPR68 LAG3 CD28 STMN3 PID1 RFLNB TPPP TMEM204 SFRP5 ACTG2
Regulation of leukocyte cell-cell adhesion	15	1.39E-06	CD5 CD28 CCR7 ADTRP CTLA4 CD3E MYB ZAP70 LEF1 LCK CD6 IL21 SKAP1 LAX1 LAG3
Multicellular organism development	67	2.31E-06	STMN1 GBX2 MARCKSL1 CD3E ADGRB2 LCK CD79B AMIGO1 BIN1 PKP2 CCR7 ITGA6 RYR1 QARS1 CDC20 BCL11B ADTRP GFI1 ZNF219 CD19 DOK5 LTB CXCR5 BCL9L KIF26A CMTM7 NYAP1 BICDL1 LSR RGCC CAMK4 PTPRF IL27RA CR2 NCAPG2 SORL1 SALL2 HIP1R CTLA4 LMNA TP63 SCMH1 MRTFB MYB PAX5 ZAP70 DHCR24 ANKH TCF7 STRBP PHGDH LEF1 CSMD1 LTBP3 CXCR3 GCNT4 CD3D GDF7 GPR68 LAG3 CD28 STMN3 RFLNB TPPP TMEM204 SFRP5 ACTG2
Regulation of lymphocyte activation	17	2.31E-06	CD5 LAT CD28 CCR7 CD19 IL27RA CTLA4 CD3E MYB ZAP70 LEF1 LCK CD6 IL21 LAX1 LAG3 MZB1
Regulation of cell-cell adhesion	16	3.32E-06	CD5 CD28 CCR7 ADTRP RGCC CTLA4 CD3E MYB ZAP70 LEF1 LCK CD6 IL21 SKAP1 LAX1 LAG3
B cell activation	13	3.32E-06	CD79B CD19 CXCR5 CMTM7 IL27RA CR2 CTLA4 FCRL1 LEF1 IL21 LAX1 CD28 MZB1

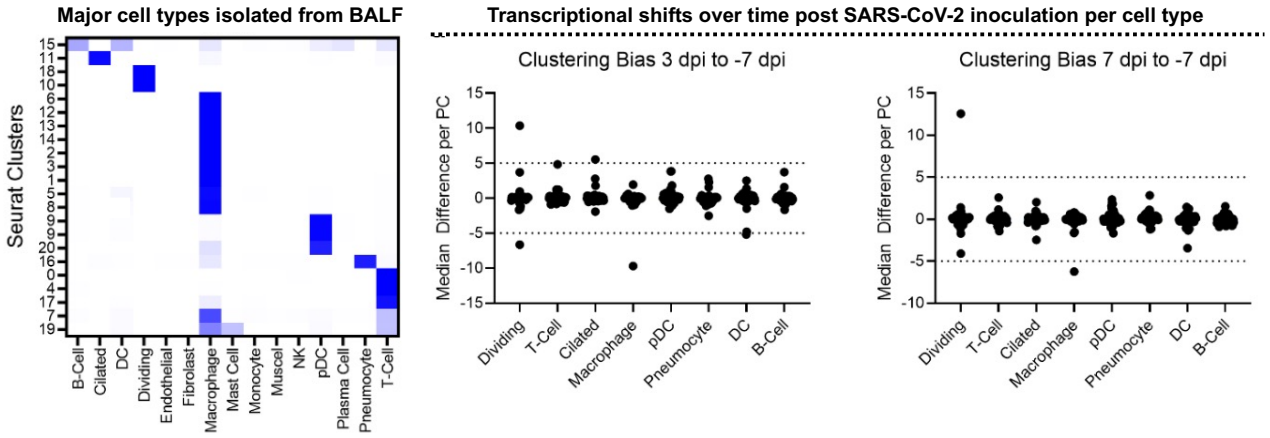
Appendix 6. Supplemental data for scRNAseq results.

A6.1 Cell type identification within Seurat clusters and characterisation of macrophage/ monocyte subclusters in the lungs of ChAdOx1 nCoV-19 and ChAdOx1 GFP recipients at 7 DPC



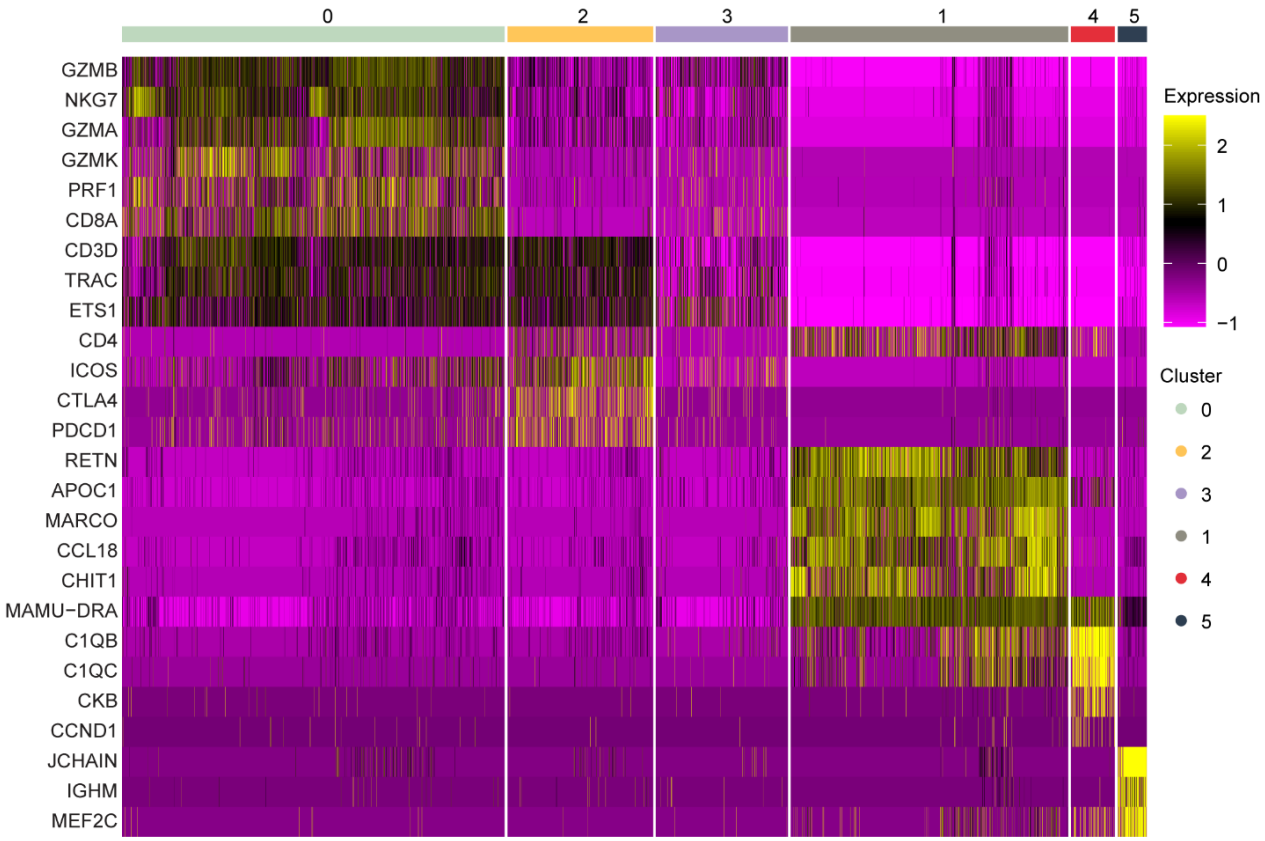
The heatmap (left) depicts the results of the unbiased cell identification algorithm. The columns represent the various cell types identified and the rows represent the different Seurat clusters. Cell percentages within a given cluster are indicated by colour (black=0% and red=100%). Violin plots (right) showing the gene expression information for selected markers within the macrophage/monocyte subclusters: A (black), B (blue), and C (magenta) exhibiting transcriptional differences between ChAdOx1 nCoV-19 vaccinees and ChAdOx1 GFP controls. Expression is shown for FABP4, MARCO, CD163, CD63, and the macaque HLA genes, MAMU. A single cumulative score across all MAMU genes is shown. Cluster A is shown in black, B is in blue, and C is in magenta.

A6.2 Cell type identification within Seurat clusters and clustering bias analysis in BALF at 3 and 7 dpi in SARS-CoV-2-infected older and younger rhesus macaques.



Comparison of computationally determined individual cell type identification with Seurat-determined clusters at a resolution of 0.8 in BALF (top left). Columns represent individual cell types and rows represent the Seurat clusters. Cell percentages within a given cluster are indicated by colour (white=0% and dark blue=100%). Dot plots (right) depicting transcriptional clustering bias across different cell types. Principal component (PC) analysis was performed, and scores calculated for each PC within each cell type. Each data point depicts the difference in the median score along each PC, for 3 vs. -7 dpi (left dot plot) or 7 vs. -7 dpi (right dot plot). Dashed lines at 5 and -5 represent the cut-offs for differences sufficiently large to warrant further analysis.

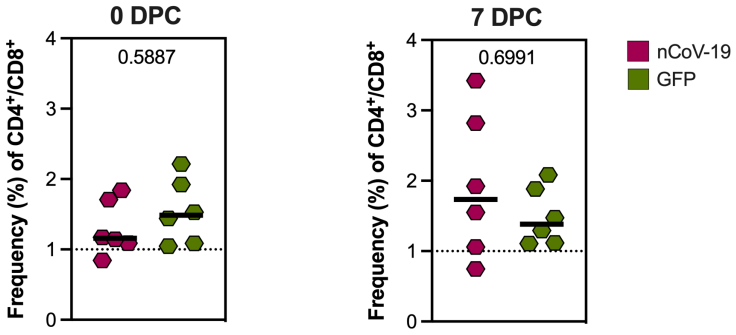
A6.3 Expression of marker genes within the dividing cell cluster in BALF in SARS-CoV-2-infected older and younger rhesus macaques.



Marker gene expression in individual cells (columns) is shown from the BALF dividing cell cluster. The groups across the top are the Seurat clusters determined by a resolution of 0.2. Colouring indicates the normalised expression of the gene per cell with purple representing low to no expression and yellow representing high expression values.

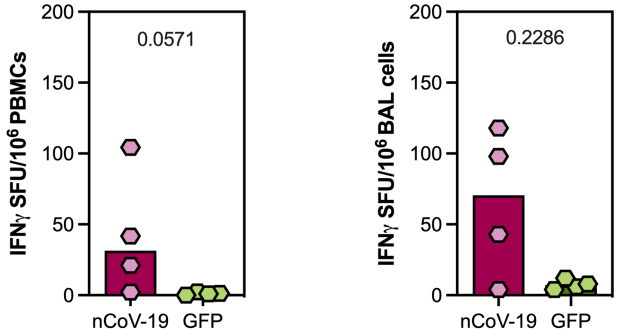
Appendix 7. Supplemental cellular immunity data for ChAdOx1 nCoV-19.

A7.1 Ratio of $CD4^+$-to-$CD8^+$ T cells in ChAdOx1 nCoV-19 vaccinees versus ChAdOx1 GFP controls.



Ratios were determined by dividing the frequency of $CD4^+$ T cells by the frequency of $CD8^+$ T cells (as percentages of total lymphocytes) in PBMC samples collected at 0 DPC (left) and 7 DPC (right). The horizontal lines indicate the group medians (statistical test: Mann-Whitney).

A7.2 SARS-CoV-2 S-specific T-cell responses detected by IFNγ ELISpot in PBMC and BAL cell samples collected at 42 DPV and 35 DPV, respectively, in recipients of IN ChAdOx1 nCoV-19 or ChAdOx1 GFP.



IFNγ ELISpot assay to detect SARS-CoV-2 S-specific T-cell responses elicited by ChAdOx1 nCoV-19 delivered via the IN route. Responses are indicated in terms of SFU per 10^6 cells. Antigen-specific T cells detected in PBMC samples at 42 DPV (left) and BAL cell samples at 35 DPV (right) are shown. Bars depict group medians (statistical tests: Mann-Whitney).